A Sensitive Search in the Dark Matter Halo of the Milky Way for Unknown Spectral Emission Lines in the X-Ray Regime

Dissertation
zur Erlangung des Doktorgrades Dr. rer. nat.
an der Fakultät für
Mathematik, Informatik und Naturwissenschaften
des Fachbereichs Physik der Universität Hamburg

vorgelegt von

Alexander Gewering-Peine (geb. Gewering)
aus Stadtlohn

Nürnberg
Dezember 2018

Gutachter der Dissertation:

1. Prof. Dr. Dieter Horns

2. Prof. Dr. Jürgen H. M. M. Schmitt

Gutachter der Disputation:

1. Prof. Dr. Dieter Horns

2. Dr. Michael J. Freyberg

Datum der Disputation:

10. Mai 2019

Vorsitzender des Prüfungsausschusses:

Prof. Dr. Caren Ines Hagner

Vorsitzender des Promotionsausschusses:

Prof. Dr. Michael Potthoff

Dekan der MIN-Fakultät:

Prof. Dr. Heinrich Graener

"I have loved the stars too truly to be fearful of the night."
Sarah Williams (1868), "The Old Astronomer".

Abstract

The Standard Model of particle physics can be extended to include sterile (right-handed) neutrinos or axions to solve the dark matter problem. Depending upon the mixing angle between active and sterile neutrinos, the latter have theoretically the opportunity to decay into monoenergetic active neutrinos and photons in the keV-range while axions can couple to two photons, respectively. In this study, data taken with the X-ray telescope XMM-Newton for the search of line emissions were used. Especially pointings with high exposures and large expected dark matter column densities with respect to the dark matter halo of the Milky Way were chosen and analysed. The posterior predictive p-value analysis was applied as a hypothesis test to locate parameter space regions which favour additional emission lines. In addition, upper limits of the parameter space of several dark matter and dark matter distribution models were generated such that the preexisting limits were significantly improved.

Zusammenfassung

Das Standardmodell der Teilchenphysik kann um sterile (rechtshändige) Neutrinos oder Axionen erweitert werden, um das Problem der dunklen Materie zu lösen. Je nach Mischungswinkel zwischen aktiven und sterilen Neutrinos haben sterile Neutrinos und Axionen theoretisch die Möglichkeit, respektive in monoenergetisch aktive Neutrinos und Photonen im keV-Bereich zu zerfallen oder an zwei Photonen zu koppeln. In dieser Arbeit wurden für die Suche nach Linienemissionen Daten des Röntgenteleskops XMM-Newton verwendet. Inbesondere wurden Beobachtungen mit hohen Belichtungszeiten und großen zu erwartenden Säulendichten der dunklen Materie in Bezug auf den Halo der Milchstraße ausgewählt und analysiert. Die “Posterior Predictive p-value Analysis” wurde als Hypothesentest zur Lokalisierung von Parameterraumbereichen eingesetzt, in welchen zusätzliche Emissionslinien favorisiert werden. Weiter wurden Obergrenzen des Parameterraumes verschiedener Teilchenmodelle dunkler Materie und Verteilungsmodelle dunkler Materie generiert, welche die bestehenden Grenzen deutlich verbesserten.

Contents

Chapter 1

Introduction

The search for the origin of dark matter is an ongoing endeavour which already lasts several decades. As early as 1933, Fritz Zwicky published results regarding observations of the dynamics of the Coma Cluster (30, 31). He realised that the visible mass was not sufficient to explain the dynamics of the galaxies in the Coma Cluster. Hence, he introduced the term 'dark matter' ("Dunkle Materie") to title the unobservable mass in the Coma Cluster. By the application of the virial theorem[1], he was able to derive an overall mean density of the Coma Cluster about 400 times higher than the mean density of the observable mass in the Coma Cluster.

Decades earlier, in 1895, Wilhelm Conrad Röntgen detected a new kind of radiation which he called X-rays ("X-Strahlen") in a laboratory of the University of Würzburg, Germany (1). He further discovered that these X-rays are not visible to the human eye and are able to transmit through human tissue such as the tissue of a human hand. It turned out that X-rays are electromagnetic waves with energies in the keV-regime. In 1901, Röntgen earned the first Nobel Price in physics for the discovery of the X-rays or "Röntgenstrahlen".

Decades later, X-rays have been established as a means to observe the sky. After a series of first experiments based on X-ray detectors mounted on sub-orbital rockets (3), the first satellite merely intended to perform observations of the sky in the X-ray regime was launched in 1970 (4). This mission was called "UHURU" and was the beginning of a series of further missions with the same goal, such as the X-ray Multi Mirror Mission or XMM-Newton[2] (39) whose captured data play an

[1]The virial theorem states that the average kinetic energy of a system consisting of $N_{\text{particles}}$ is equal to minus half of the sum of all mean scalar products of the force on the ith particle $\vec{F}_i$ and its individual location denoted by the vector $\vec{r}_i$: $\langle T \rangle = -\frac{1}{2} \sum_i^{N_{\text{particles}}} \langle \vec{F}_i \cdot \vec{r}_i \rangle$

[2]XMM was renamed XMM-Newton soon after launch into orbit.

important role in the present study. Over the last years, sights have been set on X-rays as a potential observation channel to tackle down the origin of dark matter (88).
A contemporary approach to describe the universe on cosmological scales is provided by the so-called ΛCDM[3] model. The ΛCDM model comprises a non-baryonic dark matter component (35) to account for the undiscovered mass component.
Furthermore, observations of the kinematics of galaxies and the Milky Way galaxy revealed that the velocity of rotation around the individual centers of gravity of these objects do not decrease with increasing distance from these centers of gravity or, in other words, the rotation curves do not behave as predicted by the Keplerian laws (36, 37). Many attempts have been made to find an explanation for the behavior of the rotation curves like the modification of the theories of gravity, e.g., Modified Newtonian Dynamics (MOND) (32) or modified theories of general relativity (33).
The flatness of the rotation curves can be described by the gravitational influence of a dark matter component predicted by the ΛCDM model. Dark matter is believed to be distributed as spherical halos, or radial density profiles which on average are spherical, surrounding galaxies such as the Milky Way (29, 98). Observations allow to interpret the constituents of dark matter halos as non-relativistic and non-baryonic particles (38). One relatively simple approach to describe the density distribution of dark matter halos is by means of isothermal spheres (27) or Navarro-Frenk-White profiles (18).
In the scope of the observational situation, dark matter particles seem to fulfill three specific properties: Firstly, the interactions between standard model particles and dark matter particles have to be weak, otherwise such particles would have been detected so far. Secondly, their distribution of momenta had to be non-relativistic to allow the structure formation in the early universe that has the universe as we see it today as an outcome. Thirdly, dark matter particles have to be stable on cosmological time-scales (38).
The majority of contemporary dark matter models describe dark matter as (elementary) particles which interact gravitationally and weakly with the baryonic matter in the universe. The most common theoretically predicted dark matter particle candidates can be assigned as follows:

a) Weakly interacting massive particles (WIMPs) (34)

[3] The abbreviation ΛCDM is a sequence of the Greek letter Λ which stands for the cosmological constant and the term "CDM" which stands for "Cold Dark Matter".

b) Ultra-light and cold weakly interacting slim particles (WISPs) like axions (141)

c) Warm Dark Matter particles (WDMPs) like right-handed or sterile neutrinos with masses in the keV-regime (88, 93)

The afore-mentioned models predict the decay of WISPs or WDMPs into X-rays by coupling weakly to known particles of the Standard Model of Particle Physics (SM). X-rays generated by such decay processes are believed to shape a signal formed as an emission line broadened by doppler shifts and/or natural line broadening (95).
The present study is a search for unknown emission lines in X-ray spectra taken by the European Photon Imaging Camera PN (EPIC-PN) detector of XMM-Newton (47). Such unknown emission lines could correspond to decays of WISPs or WDMPs as predicted by the above theoretical or phenomenological models.
Previous studies investigated data sets of three classes of astrophysical objects with respect to WISPs or WDMPs:

a) Galaxies (150, 167, 172, 198)
in particular the Milky Way (148, 149, 151, 152, 171),
as well as the Andromeda Galaxy, M31 (147, 148, 151, 153, 165, 168, 169, 172)

b) Dwarf spheroidals (146, 149, 171)

c) Galaxy clusters (153, 154, 170)

In addition, the diffuse galactic and/or extragalactic background has been analysed by A. Boyarsky et al. (153), Essig et al. (166) and Boyarsky et al. (173).
In the previous studies, mostly data of the satellite missions XMM-Newton (39), Chandra (58, 59) and HEAO-1 (61) have been used for the respective analyses.
The characteristic predicted dark matter column densities as observed from earth as well as the exposures of the observations of the corresponding data sets are of the order of $\mathcal{O}(10^{28})$ keV cm^{-2} and $\mathcal{O}(10-1000)$ ks, respectively.
In 2010, Prokhorov & Silk (143) claimed an excess emission originating from decays of sterile neutrinos on top of the Fe XXVI Ly$_\gamma$ emission line in spectra of the diffuse X-ray background of the Galactic Center measured by Koyama et al. (142). Further, in 2014, Koyama et al. (144) claimed two emission lines at 9.4 keV and 10.1 keV, respectively, in spectra of the Galctic bulge region also explained by

decays of sterile neutrinos. In 2014, a detection of an unknown emission line at an energy of $3.55\,\mathrm{keV}$ was claimed by Bulbul et al. (154) and A. Boyarsky et al. (153). Intensive debates followed the preceding claim (135, 145, 147, 148, 149, 150, 151, 152, 155, 156, 157, 158, 159, 160, 161, 162, 163, 164, 174, 175, 197) as well as numerous publications comprising theoretical or phenomenological models with the intention to describe the claimed emission line (99, 100, 101, 102, 103, 104, 105, 106, 107, 108, 109, 110, 111, 112, 113, 114, 115, 116, 117, 118, 119, 120, 121, 122, 123, 124, 125, 126, 127, 128, 129, 130, 131, 132, 133, 134). Laboratory measurements (80, 81, 82) are able to explain the claimed emission line at an energy of $3.55\,\mathrm{keV}$ via charge exchange processes like sulfur S XVI transitions from principal quantum numbers $n \geq 9$ to the ground state due to interactions of plasmas with cold dense clouds in galaxy clusters. A consensus with respect to the physical (or statistical) origin of the claimed line has not been reached so far.

The present work can be divided into the following steps, namely, a selection of dark matter distribution models, a selection of dark matter particle models, an estimation of the expected signal form (Chapter 2), a selection of an instrument to best observe the expected signal (Chapter 3), a selection of data sets according to a ranking and a selection of statistical methods to search for the expected signals in a given parameter space dependent on the selected data sets and the selected dark matter distributions and particle models. Specifically, the data sets taken by the PN-detector of XMM-Newton up to the year 2013 were ranked by their raw exposure and the predicted dark matter column densities dependent on the direction of observation. Consequently, a first group of $\mathbf{N_1} = 33$ data sets, denoted as $\mathbf{D_1}$, and a second group of $\mathbf{N_2} = 23$ data sets, denoted as $\mathbf{D_2}$, were selected from the group of data sets with the best ranking (Chapter 4).

The afore-mentioned publications, in particular Boyarsky et al. (147), Jeltema et al. (148), Malyshev et al. (149), Anderson et al. (150), Boyarsky et al. (151), Riemer-Sorensen (152) and Franse et al. (135), mostly applied similar statistical methods, especially $\Delta\chi^2$-statistics, to obtain upper limits on the flux normalisations of possible unknown emission lines. Conversely, the present study focuses on an optimised selection of data sets suitable to search for unknown emission lines, and among another, applies a powerful statistical method, the Posterior Predictive p-value Analysis (PPPA) (75), which fundamentally differs from the statistical methods applied in the above publications. The Posterior Predictive p-value Analysis was applied to perform an hypothesis test posing the following question: Could there be one or more unknown emission lines which can be explained by decays of WISPs or WDMPs and, in the affirmative, how are the corresponding

regions in the parameter space, in particular the energy-flux-normalisation parameter space, of these emission lines formed (Chapter 5)?
The results include limits on the normalisation of possible unknown spectral emission lines, limits on the sterile neutrino-photon coupling or mixing as well as the axion-photon coupling, and parameter space regions in which the models comprising additional spectral emission lines (alternative hypothesis models) are favoured over models sans such an additional component (nullhypothesis models) (Chapter 6).
A discussion, a conclusion and an outlook are given in Chapter 7 succeeded by a bibliography and an appendix 8.

In the scope of the present work, the refereed journal article Gewering-Peine et al. (199) was published.

Chapter 2

Models and Assumptions

2.1 The Dark Matter Problem

Since several decades, physicists are trying to grasp the nature and/or the origin of dark matter. So far, no direct measurements of dark matter have been carried out. Nonetheless, a great number of theoretical or phenomenological models have been introduced. Most of these models have the goal to describe unknown elementary particles which act as dark matter particles. With other words, the main strategy of these models is to presume a particle nature of dark matter and therefore to embed dark matter into the existing quantum field theories, e.g. the Standard Model of Particle Physics. Naturally, such an microscopic approach is contestable since until now the gravitational interactions of dark matter seem to be indirectly measurable on galactic, extragalactic or cosmological scales but not on microscopic scales. However, the present study focuses on two dark matter models which describe dark matter as one or more elementary particles, wherein the masses of these elementary particles are located within the keV-range.

2.2 Dark Matter Particle Models

2.2.1 First Dark Matter Particle Model: Sterile Neutrino

The right-handed or sterile neutrino belongs to the class of warm dark matter particle (WDMP) candidates (87, 88). An extensive overview of the actual state

of theory, models and experiments with respect to sterile neutrinos can be found in the publications Abazajian et al. (91), Adhikari et al. (96) and Boyarsky et al. (93).
The following sections intend to become the reader acquainted with the basic idea behind sterile neutrinos. For this purpose a system of notations and definitions is introduced at first, which applies for the present chapter.

Notations

The notations used in this chapter are the notations introduced in the text book Weinberg (5). The complex conjugate, the transpose and the Hermitian adjoint of a vector or matrix A is denoted as A^*, A^T, and $A^\dagger = (A^*)^T$, respectively. The Hermitian conjugate of an operator O is represented as $O^\dagger$. The abbreviations H.c. and c.c. stand for the Hermitian conjugates and the complex conjugates, respectively. The imaginary number $\sqrt{-1}$ is abbreviated as $\imath$.

Definitions

The definitions of the Pauli σ-Matrices were overtaken from Peskin et al. (6),

$$\sigma^1 = \begin{pmatrix} 0 & 1 \\ 1 & 0 \end{pmatrix}; \quad \sigma^2 = \begin{pmatrix} 0 & -\imath \\ \imath & 0 \end{pmatrix}; \quad \sigma^3 = \begin{pmatrix} 1 & 0 \\ 0 & -1 \end{pmatrix}, \tag{2.1}$$

as well as the Dirac matrices γ^μ,

$$\gamma^0 = \begin{pmatrix} 1 & 0 & 0 & 0 \\ 0 & 1 & 0 & 0 \\ 0 & 0 & -1 & 0 \\ 0 & 0 & 0 & -1 \end{pmatrix} \quad \text{and} \quad \gamma^i = \begin{pmatrix} 0 & \sigma^i \\ -\sigma^i & 0 \end{pmatrix}, \quad i \in \{1, 2, 3\}. \tag{2.2}$$

$$\gamma^5 = \imath\gamma^0\gamma^1\gamma^2\gamma^3 = \begin{pmatrix} 0 & 0 & 1 & 0 \\ 0 & 0 & 0 & 1 \\ 1 & 0 & 0 & 0 \\ 0 & 1 & 0 & 0 \end{pmatrix}. \tag{2.3}$$

The Dirac spinor consists of a 4-component wave function defined as a column vector

$$\psi = \begin{pmatrix} \psi_1 \\ \psi_2 \\ \psi_3 \\ \psi_4 \end{pmatrix}, \tag{2.4}$$

and its Hermitian conjugate $\psi^\dagger$ is a row vector (7),

$$\psi^\dagger = \left(\psi_1^*, \psi_2^*, \psi_3^*, \psi_4^*\right). \tag{2.5}$$

The adjunct spinor is the product of the Hermitian conjugate of the spinor with the Dirac matrix γ^0,

$$\overline{\psi} \coloneqq \psi^\dagger \gamma^0 = \left(\psi_1^*, \psi_2^*, -\psi_3^*, -\psi_4^*\right). \tag{2.6}$$

Weyl Equations

The Dirac representation the of Lorentz group is reducible to two instead of four components (6),

$$\psi \coloneqq \begin{pmatrix} \psi_L \\ \psi_R \end{pmatrix}, \tag{2.7}$$

in which the two components ψ_L and ψ_R are the left-handed and right-handed 2-component Weyl spinors, respectively. If the mass m contained in the Dirac equation,

$$(\imath\gamma^\mu \partial_\mu - m)\,\psi = \begin{pmatrix} -m & \imath\left(\partial_0 + \vec{\sigma}\cdot\vec{\nabla}\right) \\ \imath\left(\partial_0 - \vec{\sigma}\cdot\vec{\nabla}\right) & -m \end{pmatrix} \begin{pmatrix} \psi_L \\ \psi_R \end{pmatrix} = 0, \tag{2.8}$$

is zero, it breaks down to the so-called Weyl equations.

$$\imath\left(\partial_0 - \vec{\sigma}\cdot\vec{\nabla}\right)\psi_L = 0, \tag{2.9}$$

$$\imath\left(\partial_0 + \vec{\sigma}\cdot\vec{\nabla}\right)\psi_R = 0. \tag{2.10}$$

The formal scalar product $\vec{\sigma}\cdot\vec{\nabla}$ can be rewritten as the operator

$$\vec{\sigma}\cdot\vec{\nabla} = \sum_{i=1}^{3} \sigma^i \frac{\partial}{\partial x_i}, \tag{2.11}$$

in the two last equations 2.9 and 2.10, wherein these so-called Weyl equations describe massless neutrinos.

Helicity and Chirality

The projection of the spin onto the direction of the impulse of a particle,

$$\lambda = \frac{\vec{s} \cdot \vec{p}}{|\vec{p}|}, \tag{2.12}$$

is defined as the helicity of the particle (7). A fifth Dirac matrix $\gamma^5 := \imath\gamma^0\gamma^1\gamma^2\gamma^3$ allows the definition of the projection operators of chirality or "handedness".

$$P_L = \frac{1}{2}\left(1 + \gamma^5\right) \quad \text{and} \quad P_R = \frac{1}{2}\left(1 - \gamma^5\right). \tag{2.13}$$

These projection operators ensure the negative helicity of the neutrinos embedded in the standard model of particles. It is important to notice that the chirality coincides with the helicity for massless particles as the standard model neutrinos (91). This condition is formalised as

$$P_L\psi_\nu^{\lambda=+\frac{1}{2}} = \psi_\nu^{\lambda=+\frac{1}{2}} \quad \text{and} \quad P_L\psi_\nu^{\lambda=-\frac{1}{2}} = 0. \tag{2.14}$$

The General Lagrangian of the Neutrino

Neutrinos can be their own antiparticles. A charge and parity or CP-transformation instead of a pure charge or C-transformation is necessary to generate an antineutrino in the correct state of helicity (8, 91),

$$\psi_R^C = CP\psi_L = C\gamma^0\psi_L^* = \imath\gamma^2\gamma^0\gamma^0\psi_L^* = 2\imath\gamma^2\psi_L^*. \tag{2.15}$$

The most general Lagrangian term (8, 91) which includes active (left-handed) and sterile (right-handed) Dirac neutrinos, which are not their own antiparticles, as well as active and sterile Majorana neutrinos, which are their own antiparticles, can be written as

$$\begin{aligned}
\mathcal{L}_\nu &= \mathcal{L}_{\text{Dirac}} && + \mathcal{L}_{\text{active Majorana}} && + \mathcal{L}_{\text{sterile Majorana}} \\
&= -\, m^D\left(\overline{\psi}_L\psi_R + \overline{\psi}_R^C\psi_L^C\right) && -\frac{m_L^M}{2}\left(\overline{\psi}_L\psi_R^C + \overline{\psi}_R^C\psi_L\right) && -\frac{m_R^M}{2}\left(\overline{\psi}_L^C\psi_R + \overline{\psi}_R\psi_L^C\right) \\
&= \overline{\Psi}_L\mathcal{M}\Psi_R^C + \overline{\Psi}_R^C\mathcal{M}\Psi_L,
\end{aligned} \tag{2.16}$$

with

$$\Psi_R = \begin{pmatrix} \psi_R \\ \psi_R^C \end{pmatrix} \quad \text{and} \quad \Psi_L = \begin{pmatrix} \psi_L \\ \psi_L^C \end{pmatrix}, \tag{2.17}$$

and the symmetric matrix

$$\mathcal{M} = \begin{pmatrix} m_L^M & m^D \\ m^D & m_R^M \end{pmatrix}. \tag{2.18}$$

The dimension of the matrix $\mathcal{M}$ can be expressed by the number of active neutrinos n_a and the number of sterile neutrinos n_s as $\dim\left((n_a + n_s) \times (n_a + n_s)\right)$, wherein $\mathcal{M}$ is diagonisable by a unitary matrix $\mathcal{U}$ (8, 91),

$$\mathcal{U}^\dagger \mathcal{M} \mathcal{U}^* = \mathcal{U}^\dagger \begin{pmatrix} m_L^M & m^D \\ m^D & m_R^M \end{pmatrix} \mathcal{U}^* = \begin{pmatrix} m_1 & 0 \\ 0 & m_2 \end{pmatrix}, \tag{2.19}$$

with mass eigenvalues

$$m_{1,2} = \frac{1}{2}\left(\left(m_L^M + m_R^M\right) \pm \sqrt{\left(m_L^M - m_R^M\right)^2 + 4\left(m^D\right)^2}\right). \tag{2.20}$$

The authors of the publications (8, 91) derive four or rather five physical scenarios from equation 2.20.

1. The pure Majorana case takes place for vanishing Dirac-masses, $m^D = 0$. The mixing among active and sterile states is suppressed so that the sterile neutrino is decoupled.

2. The pure Dirac case, $m_L^M = m_R^M = 0$, with two degenerate Majorana neutrinos. These can be combined to build a Dirac neutrino with a conserved lepton number.

3. The pseudo-Dirac limit for $m^D \gg m_L^M$ and $m^D \gg m_R^M$ or $m_R^M \approx m_L^M$ which leads to a minor shift of the mass eigenvalues, $|m_{1,2}| = m^D \pm 0.5\left(m_L^M + m_R^M\right)$, $m \in \mathbb{R}^+$.

4. The case of mixed sterile and active states, $m^D \approx m_R^M$ and/or $m^D \approx m_L^M$, wherein the mass eigenstates are composed of significant active and sterile parts.

5. The seesaw limit, $m_R^M \gg m^D$ and $m_R^M \gg m_L^M$, enabling a light, mostly active state, $m_1 = m_L^M - \frac{\left(m^D\right)^2}{m_R^M}$ and a heavy, mainly sterile state, $m_2 \approx m_R^M$. The latter state decouples at low energies.

The seesaw limit is the most interesting scenario in view of the present work since this scenario results in a right-handed or sterile neutrino in the keV energy range which is allowed to decay into three active neutrinos or, via a two-body decay, into one active neutrino and a photon as follows,

$$\nu_{\text{sterile}} \rightarrow \nu_{\text{active}} + \gamma_{\text{X-ray}}, \tag{2.21}$$

whereby ν_{sterile} or ν_R, ν_{active} or ν_L, and $\gamma_{\text{X-ray}}$ or γ denote a sterile neutrino, an active neutrino and a X-ray photon, respectively. Since the latter decay is a two-body decay, the energy of the photon would be half of the rest mass of the initial sterile neutrino, $E_\gamma = m_R^M/2$. The corresponding decay rate of such Majorana sterile neutrinos (89, 90) as a warm dark matter particle of mass $m_{\nu_s} := m_R^M$ is

$$\begin{aligned} \Gamma(\nu_R \rightarrow \gamma\nu_L) = \Gamma_{\nu_s} &= \frac{9\alpha G_{\text{F}}^2}{1024\pi^4} \sin^2(2\Theta) m_{\nu_s}^5 \\ &\approx 1.38 \cdot 10^{-32}\,\text{s}^{-1} \left(\frac{\sin^2(2\Theta)}{10^{-10}}\right) \left(\frac{m_{\nu_s}}{\text{keV}}\right)^5, \end{aligned} \tag{2.22}$$

whereby α and G_{F} denote the fine structure constant and the Fermi constant, respectively. Relative to the decay probability of the two-body decay, the three-body decay,

$$\nu_{\text{sterile}} \rightarrow 3\nu_{\text{active}}, \tag{2.23}$$

dominates the two-body decay by a factor of approximately 128 (92). Furthermore, the masses of the sterile neutrinos are likely above 0.3 keV to 0.5 keV according to a bound calculated by Tremaine & Gunn (85).

2.2.2 Second Dark Matter Particle Model: Axions

The axion belongs to the class of ultra-light and cold weakly interacting slim particles (WISPs) (97, 141). Since the Standard Model of Particle Physics does not provide a link between gravitation and quantum physics or the parameters values of standard particles, like their masses, or the origin of dark matter or dark energy, new solutions are required, wherein WISPs could be such a solution. Weakly interacting particles fulfill all three conditions with respect to dark matter particles (38): They interact mainly on the electroweak scale[1] via mediator bosons as the

[1]The electroweak or Fermi scale is defined via the energy range around an energy value of 246 GeV, whereby this energy value corresponds to the vacuum expectation value $v = \left(G_{\text{F}}\sqrt{2}\right)^{-\frac{1}{2}}$ of the Higgs field.

massive $W_{\pm}$ and Z bosons which results in weak interaction strengths. WISPs could have been thermally produced in the early universe because they were cold due to their high masses in the range of the electroweak scale at the beginning of the structure formation phase. In theory, WISPs can be stabilised by the application of symmetries which conserve their particle number to have life times of the order of the age of the universe. A further option would be an increase of life time by a reduction of the number of decay channels which can be achieved by small phase spaces due to small masses (141).
The axion in Quantumchromodynamics (QCD) or QCD-axion was once introduced to solve the strong CP-problem[2]. The so-called scale decay constant of the QCD-axion is

$$f_a \propto M_I = (M_W M_P)^{0.5}, \tag{2.24}$$

wherein f_a denotes a dimensionless axion decay constant, M_I denotes the so-called intermediate scale defined as the geometric mean of the Planck scale $M_P \approx 10^{12}$ GeV and the weak scale $M_W \approx 100\,\text{GeV}$ (141). The Lagrangian term

$$\mathcal{L}_{\text{CP-violation}} = \frac{\alpha_s}{8\pi}\Theta G^a_{\mu\nu}\tilde{G}^{a,\mu\nu} = \frac{\alpha_s}{8\pi}\Theta\frac{1}{2}\epsilon^{\mu\nu\alpha\beta}G^a_{\mu\nu}G^a_{\alpha\beta}, \tag{2.25}$$

with G as the gluonic field strength, α_s as the strong coupling constant and Θ as a fundamental parameter which has to be determined experimentally. The electric dipole moment of the neutron d_n is a sensitive probe of the parameter Θ because it depends linearly on $\overline{\Theta} := \Theta + \arg(\det(\mathcal{M}_q))$ with $\mathcal{M}_q$ denoting the quark mass matrix. The absolute value of the electric dipole moment of the neutron is proportional to the absolute value of $\overline{\Theta}$, the neutron mass m_n, the light quark mass m_q and the unit electric charge e, via

$$|d_n| \propto \frac{e}{m_n}\left(\frac{m_q}{m_n}\right)|\overline{\Theta}| \approx 10^{-16}|\overline{\Theta}|\,e\,\text{cm}. \tag{2.26}$$

The dipole moment of the neutron has been experimentally limited to

$$|d_n| < 2.9 \cdot 10^{-26}\,e\,\text{cm}, \tag{2.27}$$

so that absolute value of the fundamental parameter $\overline{\Theta}$ turns out to be $|\overline{\Theta}| \leq 10^{-10}$. The strong CP-problem is closely related to the question, why the dimensionless parameter $|\overline{\Theta}|$ is so small (141). Peccei & Quinn (136) introduced the axion field a

[2]Non-conversion of charge and parity under transformations.

as a dynamical $|\overline{\Theta}|$ parameter which can relax spontaneously to zero. It is assumed that the axion field a fulfills a shift symmetry

$$a \to a + \text{const.}, \tag{2.28}$$

which is broken by anomalous coupling terms to gauge bosons, in particular to gluons (141). Its most general low-energy effective Lagrangian below the weak scale, i.e. where the intermediate vector bosons W and Z and the Higgs bosons are integrated out, can be parameterised as (140):

$$\begin{aligned}\mathcal{L} = &\frac{1}{2}\partial_\mu a \partial^\mu a - \frac{\alpha_s}{8\pi}\left(\overline{\Theta} + \frac{a}{f_a}\right) G^b_{\mu\nu}\tilde{G}^{b,\mu\nu} - \frac{\alpha}{8\pi} C_{\alpha\gamma}\frac{a}{f_a} F_{\mu\nu}\tilde{F}^{\mu\nu} \\ &+ \sum_\Psi \left(\overline{\Psi}\gamma^\mu \frac{1}{2}\left(\tilde{\mathcal{X}}_{\psi_R} + \tilde{\mathcal{X}}_{\psi_L}\right)\gamma_5 \Psi + \overline{\Psi}\gamma^\mu \frac{1}{2}\left(\tilde{\mathcal{X}}_{\psi_R} - \tilde{\mathcal{X}}_{\psi_L}\right)\Psi\right)\frac{\partial_\mu a}{f_a}.\end{aligned} \tag{2.29}$$

The electromagnetic field strength is denoted by F, the model dependent dimensionless parameter from the electromagnetic anomaly by $C_{\alpha\gamma}$, the standard model matter fields by Ψ, the strong coupling constant is denoted by α_s, the fine-structure constant is denoted by α and the dimensionless axion decay constant is represented by f_a. The decay constant f_a and the dimensionless couplings $(C, \mathcal{X})$ are expected to be of the order of one. They determine the strength of the interactions of the axion with standard model particles. Therefore, the strong CP-problem can be solved in the following way:

1. The $\overline{\Theta}$ term can be eliminated by absorbing it into the axion field by $a \coloneqq \overline{a} - \overline{\Theta} f_a$.

2. Due to the nontrivial potential of the axion field $\overline{a}$ in view of a topological charge density proportional to $\langle tr(G^{\mu\nu}\tilde{G}_{\mu\nu})\rangle = 0$, induced by topological fluctuations of the gluon fields such as QCD instantons, $\overline{a}$ is minimised at zero expectation value $\langle a\rangle = 0$, cancelling strong CP-violation.

The nontrivial potential around $\langle a\rangle = 0$ supports the elementary particle excitation of the axion field, the axion, to a pseudo Nambu-Goldstone boson (138, 139) with a non-vanishing but small mass. The mass of the axion matches the axion-quark and axion-gluon couplings to the appropriate couplings to mesons and baryons in the low-energy effective chiral Lagrangian and is expressed by

$$m_a = \frac{m_\pi f_\pi}{f_a}\frac{\sqrt{m_u m_d}}{m_u m_d} \approx 0.6\,\text{meV}\left(\frac{10^{10}}{f_a}\right). \tag{2.30}$$

The mass of the axion is dependent on the pion mass m_π, the light quark masses m_u and m_d as well as the pion decay constant f_π. In the case of a large axion decay constant f_a, the axion a is a WISP in the sense of a slim, very light and very weak coupled particle. The part of the Lagrangian describing the coupling of axions to photons, contains the electromagnetic field strength F, the axion field a and in its rewritten form, the $\vec{E}$ and $\vec{B}$ field,

$$\mathcal{L}_{a\gamma\gamma} = -\frac{1}{4} g_{a\gamma\gamma} a F_{\mu\nu} \tilde{F}^{\mu\nu} = g_{a\gamma\gamma} a \vec{E} \cdot \vec{B}. \tag{2.31}$$

The axion-photon coupling $g_{a\gamma}$ is proportional to the model-dependent dimensionless parameter $C_{a\gamma}$ of the electromagnetic anomaly and depends on the masses of the light quarks m_u and m_d as

$$g_{a\gamma} = \frac{\alpha}{2\pi f_a} \left(C_{a\gamma} - \frac{2}{3} \frac{m_u + 4m_d}{m_u m_d} \right) \approx 10^{-13}\,\mathrm{GeV}^{-1} \left(\frac{10^{10}\,\mathrm{GeV}}{f_a} \right). \tag{2.32}$$

It turns out that the axion-photon coupling constant $g_{a\gamma}$ is very small. The present work focuses on the coupling of an axion to two photons with the corresponding Lagrangian

$$\mathcal{L} = \frac{1}{4} g_{a\gamma\gamma} a F^{\mu\nu} \tilde{F}_{\mu\nu}, \tag{2.33}$$

in which pseudoscalar and scalar axions are indistinguishable. An axion with a lifetime of (113)

$$\tau_a = \Gamma_{a\gamma\gamma}^{-1} = \frac{64\pi}{g_{a\gamma\gamma}^2 m_a^3}, \tag{2.34}$$

with a decay constant $\Gamma_{a\gamma\gamma}$ transforms into two photons. If the lifetime of the axion is larger than the lifetime of the Universe, the monochromatic or monoenergetic photons of the axion decays can form an emission line signal which would be a hint to the existence of the axion (97).

2.3 Assumptions

2.3.1 Dark Matter Particle and Distribution Models

In the course of this work, a first assumption was made that dark matter consists of warm dark matter particles according to the first dark matter particle model or

the second dark matter particle model mentioned afore, namely, sterile neutrinos (**Assumption 1a**), or axions (**Assumption 1b**), each having masses in the keV-regime.
A multitude of models describing spatial density distributions or dark matter density profiles have been introduced so far, for example Kerins (21), King (22), Einasto et al. (23), Moore et al. (24), Navarro et al. (25), Burkert (26), Begeman et al. (27), Bertone et al. (28), Bringmann et al. (86), wherein respective column densities are listed in table 2.1 and/or below and are shown in figure 2.1. Two of the above dark matter density profiles were chosen for further analysis to cover the lowest and highest expected dark matter column densities with respect to longitudes and/or latitudes in Galactic coordinates in the vicinity of the Galactic center as observed from the Earth, namely the isothermal sphere or isothermal profile[3] (27),

$$\rho_{\rm ISO}(r) = \frac{\rho_{\rm ISO,0}}{1 + r^2/r^2_{\rm ISO,0}}, \tag{2.35}$$

and the Navarro-Frenk-White profile (18) or NFW profile,

$$\rho_{\rm NFW}(r) = \frac{\rho_{\rm NFW,0}}{(r/r_{\rm NFW,0})\,(1 + r/r_{\rm NFW,0})^2}, \tag{2.36}$$

respectively. The parameters $\rho_{\rm NFW,0}$ and $\rho_{\rm ISO,0}$ are the so-called central densities of the corresponding dark matter density distributions. The central densities correspond to the maximum densities of these profiles. The latter are located at the geometrical centers or the centers of gravity of these distributions. In theory, it is expected that the center of the dark matter density distribution coincides with the center of the Milky Way galaxy. The radii $r_{\rm NFW,0}$ and $r_{\rm ISO,0}$ represent the distance to the center of the dark matter distributions at which the dark matter density is half the corresponding central densities.
Secondly, in the scope of this work it is assumed that the Milky Way Galaxy comprises a dark matter halo consisting of dark matter particles, namely, sterile neutrinos (**Assumption 1a**), or axions (**Assumption 1b**), whose density profiles or spatial density distributions respectively correspond to the isothermal profile (**Assumption 2a**) or the Navarro-Frenk-White profile (**Assumption 2b**). The respective parameters of the isothermal profile and NFW profile were set according

[3] For a derivation of the functional expression of an isothermal profile, please see Appendix A. Isothermal Profile

to Bringmann et al. (86) and Bertone et al. (28) to

$$\rho_{\mathrm{NFW},0} = 0.4\,\frac{\mathrm{GeV}}{c^2}\,\mathrm{cm}^{-3},$$
$$r_{\mathrm{NFW},0} = 21\,\mathrm{kpc}, \tag{2.37}$$

or

$$\rho_{\mathrm{ISO},0} = 1.37\,\frac{\mathrm{GeV}}{c^2}\,\mathrm{cm}^{-3},$$
$$r_{\mathrm{ISO},0} = 3.5\,\mathrm{kpc}. \tag{2.38}$$

The distance $R_\odot$ from the Galactic Center of an observer located on the Earth, which corresponds to the center of the distribution, was set to $8.3\,\mathrm{kpc}$ according to the distance measurements performed by Ghez et al. (16) and Gillessen et al. (17).

The first dark matter particle model and the second dark matter particle model predict at least one monoenergetic spectral emission line due to decays of WISPs, in particular axions, or WDMPs, in particular sterile neutrinos, respectively. Such an emission line is likely to be redshift broadened since it is believed that dark matter particles in a dark matter halo have significant velocities relative to each other and/or to an observer on or close to the Earth. In case of the isothermal profile the mean direction-independent velocity or the mean of the absolute values of the velocities in the dark matter halo is approximately $170\,\mathrm{km\,s^{-1}}$ (169). Furthermore, natural line broadening might have an effect on the emission line (95).

2.3.2 Signal Form

Furthermore, it is assumed in the course of the present work, that the monoenergetic emission line originating from decays of sterile neutrinos (**Assumption 1a**), or axions (**Assumption 1b**), contained in a dark matter halo with a density resembling that of the isothermal profile (**Assumption 2a**), or a NFW profile (**Assumption 2b**), is shaped as a Gaussian function,

$$\mathrm{L}_\gamma(E_\gamma, \sigma_\gamma, F_\gamma) = \frac{F_\gamma}{\sigma_\gamma\sqrt{2\,\pi}}\,\exp\left(\frac{-\,(E - E_\gamma)^2}{2\,\sigma_\gamma^2}\right), \tag{2.39}$$

if observed in X-ray spectra, whereby E, E_γ, F_γ, and σ_γ denote the energy in keV, the mean energy in keV, the flux normalisation as the number of X-ray photons$/\mathrm{cm}^{-2}/$s, and the width of the emission line in keV, respectively.

dark matter density profile	norm density ρ_0	norm radius r_0	reference
	GeV cm^{-3}	kpc	
$\rho_{\mathrm{ISO}}(r) = \frac{\rho_0}{1+\left(\frac{r}{r_0}\right)^2}$	1.37	3.5	(27)
$\rho_{\mathrm{NFW}}(r) = \frac{\rho_0}{\left(\frac{r}{r_0}\right)\left(1+\left(\frac{r}{r_0}\right)\right)^2}$	0.4	21	(28, 86)
$\rho_{\mathrm{EINASTO,KING}}(r) = \rho_0\left(\left(1+\frac{r^2}{r_0^2}\right)^{-1} - \left(1+\frac{r_{\max}^2}{r_0^2}\right)^{-1}\right), \begin{cases} \text{if } r \leqq r_{\max}, \\ 0, \text{elsewhere.} \end{cases}$	0.413	$r_0 = 1.47, r_{\max} = 117$	(22, 23)
$\rho_{\mathrm{KERINS}}(r) = \frac{\rho_0\, r_0^2}{r^2+r_0^2}, \begin{cases} \text{if } r \leqq r_{\max}, \\ 0, \text{elsewhere.} \end{cases}$	0.036	$r_0 = 5, r_{\max} = 100$	(21)
$\rho_{\mathrm{BURKERT}}(r) = \frac{\rho_0}{\left(1+\frac{r}{r_0}\right)\left(1+\left(\frac{r}{r_0}\right)^2\right)}$	0.335	3.43	(26)
$\rho_{\mathrm{MOORE}}(r) = \frac{\rho_0}{\left(\frac{r}{r_0}\right)^{\frac{3}{2}}\left(1+\left(\frac{r}{r_0}\right)^{\frac{3}{2}}\right)}$	$1.43 \cdot 10^{-3}$	17.9	(24)
$\rho_{\mathrm{N04}}(r) = \rho_0 \exp\left(-\frac{2}{\alpha}\left(\frac{r}{r_0}\right)^{\alpha} - 1\right)$	$6.42 \cdot 10^{-3}$	$r_0 = 11.6, \alpha = 0.17$	(25)
$\rho_{\mathrm{ISOCORE}}(r) = \rho_0\left(\frac{r_0^2+r_c^2}{r^2+r_c^2}\right)$	0.43	$r_0 = 8.3, r_c = 2.8$	(27)

Table 2.1: The above table lists functional forms and parameters of the dark matter density profiles shown in figure 2.1.

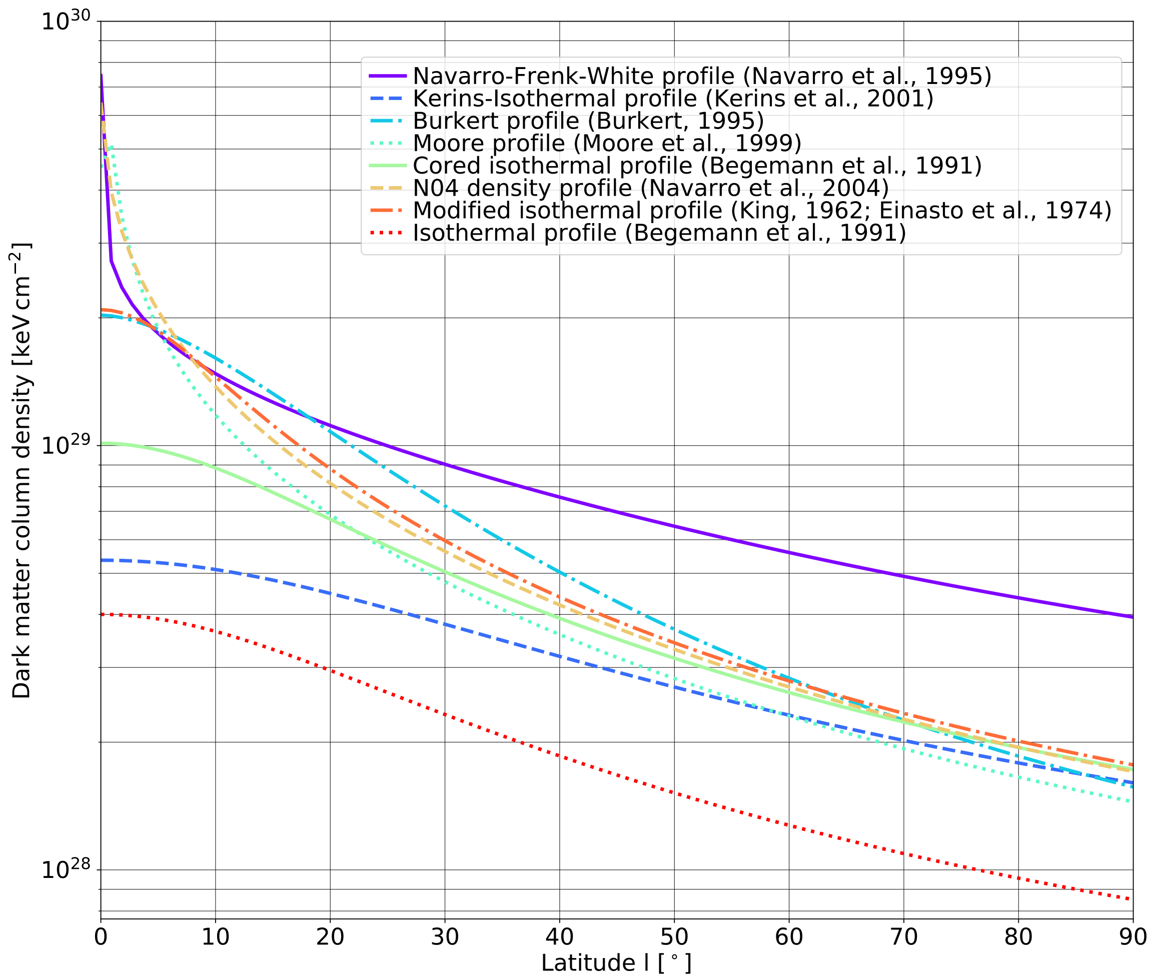

Figure 2.1: The figure shows column densities or dark matter profiles integrated for longitudes l in a range of $0°$ to $90°$ and a latitude b fixed to a value of $0°$ in Galactic coordinates as seen from an observer on Earth, namely a NFW profile (28, 86), a Kerins Isothermal profile (21), a Burkert profile (26), a Moore profile (24), a cored isothermal profile (27), a N04 density profile (25), a modified isothermal profile (22, 23) and an isothermal profile (27). All dark matter density profiles mentioned afore were integrated numerically. The parameters of the above dark matter profiles are listed in table 2.1.

Chapter 3

Instruments and Detectors

3.1 Instrument Selection

The present study investigates several data sets recorded by the EPIC-PN detector of XMM-Newton (41). These data sets were taken into account for further analysis because the EPIC-PN detector provides the largest effective area compared to the two EPIC-MOS[1] detectors as well as the detectors on-board the X-ray satellites Chandra (68) or Suzaku (69, 70). Next to the large effective area, the EPIC-PN detector has the broadest energy bandpass compared to the detectors mentioned afore. It is possible to observe X-ray photons in a an energy interval from $0.38\,\mathrm{keV}$ to approximately $15.0\,\mathrm{keV}$.

3.1.1 The X-ray Telescope XMM-Newton

The X-ray Multi Mirror Mission (XMM) satellite has been proposed in 1982 and became a cornerstone of the Horizon 2000 long-term plan established by the European Space Agency (ESA) in 1985[2] having the objective[3] to explore the Universe in the X-ray regime. XMM was renamed to XMM-Newton shortly after being launched into a $48\,\mathrm{h}$ orbit around the earth by the first commercial Ariane 5 vehicle, V504, on 10. December 1999 (40). With a launch mass of $3764\,\mathrm{kg}$ and a

[1] MOS = metal oxide semiconductor

[2] Please see http://www.esa.int/esapub/br/br114/br114sci.htm

[3] The primary objectives of the mission have been discussed in the scope of an ESA workshop in Lyngby, Denmark, in June of the year 1985. Please see http://www.esa.int/esapub/bulletin/bullet104/lumb104.pdf for further details.

length of approximately $10\,\text{m}$, XMM-Newton was the largest spacecraft ever carried into space until its launch date. The planned mission duration was 2 years but the elapsed mission duration is nearly 18 years as of 2018.
XMM-Newton comprises two payload modules attached to a carbon fiber tube, which together form an optical bench. The assembly in the focal plane of the telescopes on-board XMM-Newton contains five cameras, namely, two Reflection Grating Spectrometer (RGS) read-out cameras (49), one European Photon Imaging Camera (EPIC) incorporating a PN-charged coupled device or PN-CCD (EPIC-PN) (41), as well as two EPIC-MOS imaging detectors (EPIC-MOS) based on MOS-CCDs (48).
The spacecraft service module consists of several sub-systems, an Optical Monitor (OM) (50), and three X-ray mirror modules focusing incoming X-rays towards the focal plane whereby each of the three X-ray mirror modules is assigned to one of the EPIC-PN and EPIC-MOS detectors. The Optical Monitor is a telescope attached to XMM-Newton spacecraft which allows observations in the optical regime as well as in portions of the ultraviolet (UV) regime.
Each one of the three X-ray telescopes provided by one of the three respective X-ray mirror modules consists of 58 Wolter Type I mirrors which are nested in a coaxial and a confocal configuration (46). Such an arrangement allows a large collecting area for X-ray photons over a wide energy band, in particular up to $15\,\text{keV}$. The minor grazing incidence angles range from $17\,\text{arcmin}$ to $42\,\text{arcmin}$, and the focal length of each of the three X-ray telescopes is $7.5\,\text{m}$. The diameter of the largest mirror of each X-ray telescope is $0.7\,\text{m}$. Each of the mirrors comprise a substrate layer consisting of Nickel and a Gold layer which reflects the incoming X-rays by means of grazing incidences. The gold layer is polished to reduce the surface roughness to a minimum. Every assembly composed of the 58 Wolter Type I mirrors is aligned by 16 spokes of a single spider-like structure in the respective entrance aperture (40).
The exit apertures of each of the three X-ray telescopes comprise a low electron deflector providing a circumferential magnetic field. Through this measure, electrons having low energies are deflected away from paths towards the detectors so that false X-ray photon counts triggered through such low energy electrons can be avoided.
The star trackers on-board XMM-Newton serve to determine the position and orientation of the satellite relative to the stars. Their measurement accuracy is $4\,\text{arcsec}$ (half-cone angle, 95% confidence), and the actual resolution ranges from $1\,\text{arcsec}$ to $2\,\text{arcsec}$. The orbit of XMM-Newton corresponds to an ellipse with a perigee of $7000\,\text{km}$, an apogee of $114000\,\text{km}$, and an inclination of approximately

$40°$, relative to the position of the Earth and the Solar plane. These parameters have been chosen to allow high exposures during observation, and to cool the five cameras down to a temperature range from -80°C to -100°C by mere usage of passive radiators. Nevertheless, the observational operation of XMM-Newton is restricted to parts of the orbit equal to or more distant than $60,000$ km from the Earth due to the radiation belt which could otherwise harm the satellite (40).

3.1.2 The EPIC-PN Detector

Since the present work focuses on data recorded by the EPIC-PN detector, some further technical information and features will be given in the following paragraphs.
The EPIC-PN detector consists of a monolithic X-ray CCD array having an extrusion of 6×6 cm^2, featuring a high detection efficiency up to 15 keV with respect to X-ray photons, a low noise level having an read-out noise of approximately $5\,e^-$ and a ultra-fast readout of charges triggered through X-ray photons. Furthermore, the EPIC-PN detector has been developed to provide a high angular resolution, a large collecting area, a wide energy bandpass and a large field of view (FOV). It consists of four separate quadrants each comprising three PN-CCD subunits. Further, each of the PN-CCD subunits again comprises 200×64 pixel which are operated in parallel. In the present context, the term "monolithic“ X-ray CCD array, as stated above, indicates that 12 PN-CCD subunits each having a size of 3×1 cm^2 are applied to a single 4 inch wafer during manufacturing.
The EPIC-PN detector is based on a silicon drift detector proposed in 1983 by Gatti & Rehak (43). First working devices have been manufactured not before 1983. Further technically related large area detectors prepared for space flights were fabricated since 1997 in the semiconductor laboratory of the Max Planck Institute for Extraterrestrial Physics (Max-Planck-Institut für extraterrestrische Physik) in Garching, Germany, for projects XMM and ABRIXAS[4] (A Broad Band Imaging X-ray All-Sky Survey) (44, 45).
It is important to notice, that CCDs have originally been designed to carry out photon intensity imaging by collecting photons over a given exposure time. In contrast, the CCDs incorporated in the EPIC-PN detector are able to count single X-ray photons in a spectroscopic mode (41).

[4]For further information please see http://www.mpe.mpg.de/xray/wave/abrixas/mission/intro.php

At X-ray photon energies of $1.5\,\text{keV}$ and $8.0\,\text{keV}$, the EPIC-PN detector provides a half energy width (HEW) of $15\,\text{arcsec}$ leading to a position resolution of captured X-ray photons in the focal plane of $540\,\mu\text{m}$. In addition, the full width at half maximum (FWHM) of the intrinsic point spread function (PSF) of the EPIC-PN detector is $6.6\,\text{arcsec}$. The energy response of the EPIC-PN detector is above 90% at an energy of $10\,\text{keV}$ mainly because of the large sensitive thickness of the detector of $280\,\mu\text{m}$ to $290\,\mu\text{m}$ (40, 41).
In this context, the EPIC-PN detector is formed from PN-CCDs utilising sideward depletion in a layer of high resistivity silicon of electron-hole pairs triggered through X-ray photons captured in one or more pixels of the PN-CCDs, wherein the average energy to generate an electron-hole pair is $3.7\,\text{eV}$ at a temperature of -90°C. To avoid recombinations of the electron-hole pairs, these are subsequently separated by strong electric fields which are formed between the main surfaces of the respective PN-CCDs. The electrons are then drifted to potential minima by means of the electric fields to be stored beneath transfer registers and are eventually transferred via a total of 768 readout or transfer channels into a storage register for further processing whilst the holes drift to the main surface of the detector opposite the pixels or the main surface through which the photons penetrate the PN-CCDs to be eventually absorbed (41).
Each pixel of the PN-CCDs has a size of $150\,\mu\text{m} \times 150\,\mu\text{m}$ or $4.1\,\text{arcsec} \times 4.1\,\text{arcsec}$ corresponding to a position resolution of $120\,\mu\text{m}$ or to an angular resolution of $3.3\,\text{arcsec}$ in the focal plane. The PN-CCDs inhere a high radiation hardness and a fast transfer of charges or electrons in a depth of more than $10\,\mu\text{m}$ below the main surface opposite the pixels of the detector by avoiding active MOS structures as present in the EPIC-MOS detectors. Advantageously, the EPIC-PN detector shields itself against low-energy photons because the PN-CCDs of the EPIC-PN detector are back-illuminated PN-CCDs such that incoming X-ray or low energy photons have to pass a layer of silicon having a thickness of $280\,\mu\text{m}$ to $290\,\mu\text{m}$. In this regard, low energy photons are so absorbed by the afore-mentioned silicon layer, that these low energy photons are inhibited to interfere with the transfer channels. This consequently suppresses an increase of the charge transfer inefficiency (CTE) which is a measure of charge or electron losses during the transfer of charges or electron via one or more of the transfer channels (41).

Chapter 4

Data Analysis

4.1 Dark Matter Column Density Benchmark

The exposure and the direction of observation are highly relevant to the observation of the dark matter halo of the Milky Way and therefore the optimal choice of data sets. The greater the exposure of a given data set, the higher the expected signal-to-noise ratio of its spectrum being inherent in the given data set. The direction of observation influences the amount of (decaying) dark matter in the field of view of a given detector. Since dark matter density distribution models, e.g. the isothermal profile or the Navarro-Frenk-White profile, do not provide direction-independent or isotropic dark matter column densities to an observer on the Earth but to an observer located at the center of the Milky Way, it is desirable to choose data sets having observation directions providing high dark matter column densities. Therefore, data sets with high individual exposures and dark matter column densities were chosen in the scope of this work whenever possible.
A dark matter column density based on the isothermal profile 2.35 or the NFW profile 2.36 for an ith data set selected from a set of data sets $\mathbf{D}$ is integrated along a line-of-sight s via

$$S^{\mathbf{D},\text{DM-MODEL}}(s, l_i^{\mathbf{D}}, b_i^{\mathbf{D}}) = S_i^{\text{DM-MODEL}} = \int_0^{\infty} \rho_{\text{DM-MODEL}}(s, l_i^{\mathbf{D}}, b_i^{\mathbf{D}})\, ds. \quad (4.1)$$

The estimated or raw exposure $t^{\mathbf{D}}_{\text{exp,est};i}$ and the estimated dark matter column density $S_i^{\mathbf{D},\text{DM-MODEL}}$ of an ith data set according to equation 4.1 were multiplied to account for a benchmark value dependent on the spatial integration length s and the direction of observation in Galactic coordinates $(l_i^{\mathbf{D}}, b_i^{\mathbf{D}})$. Additionally, each of the resulting values $S_i^{\mathbf{D},\text{DM-MODEL}} \cdot t_{\text{exp,est};i}^{\mathbf{D}}$ was normalised through the division of the maximum value,

$$\max_j \left(S_1^{\mathbf{D},\text{DM-MODEL}} \cdot t_{\text{exp,est};1}^{\mathbf{D}}, \ldots, S_j^{\mathbf{D},\text{DM-MODEL}} \cdot t_{\text{exp,est};j}^{\mathbf{D}}, \ldots, S_{\mathbf{N}}^{\mathbf{D},\text{DM-MODEL}} \cdot t_{\text{exp,est};\mathbf{N}}^{\mathbf{D}}\right), \tag{4.2}$$

selected from a sample comprising the multiplicative values of all data sets:

$$b_i^{\mathbf{D},\text{DM-MODEL}} = \frac{S_i^{\mathbf{D},\text{DM-MODEL}} \cdot t_{\text{exp,est};i}^{\mathbf{D}}}{\max_j \left(S_1^{\mathbf{D},\text{DM-MODEL}} \cdot t_{\text{exp,est};1}^{\mathbf{D}}, \ldots, S_j^{\mathbf{D},\text{DM-MODEL}} \cdot t_{\text{exp};j}^{\mathbf{D}}, \ldots, S_{\mathbf{N}}^{\mathbf{D},\text{DM-MODEL}} \cdot t_{\text{exp,est};\mathbf{N}}^{\mathbf{D}}\right)}, \quad i \in \{1, \ldots, \mathbf{N}\}, \tag{4.3}$$

wherein $\mathbf{N_1} = 33$ for $\mathbf{D_1}$ and $\mathbf{N_2} = 23$ for $\mathbf{D_2}$. The term 'DM-MODEL' must be respectively replaced by 'ISO' or 'NFW' if a dark matter column density of the isothermal profile 2.35 or the NFW profile 2.36 was calculated. Unfortunately, the dark matter column density of a NFW profile is not analytically solvable if the observer is not located at the center of the distribution. In consequence the column densities $S_i^{\mathbf{D_1},\text{NFW}}$ and $S_i^{\mathbf{D_2},\text{NFW}}$ and the resulting benchmark values $b_i^{\mathbf{D_1},\text{NFW}}$ and $b_i^{\mathbf{D_2},\text{NFW}}$ were integrated numerically by applying the function *quad* provided by the python package *scipy*[1]. Fortunately, in view of the necessary computational effort, the column densities $S_i^{\mathbf{D_1},\text{ISO}}$ and $S_i^{\mathbf{D_2},\text{ISO}}$ and the resulting benchmark values $b_i^{\mathbf{D_1},\text{ISO}}$ and $b_i^{\mathbf{D_2},\text{ISO}}$ were solved analytically since the respective column densities are integrable by means of analytical methods[2], if an observer is not located at the center of the respective density distribution but in a distance of $R_\odot$ from the center of the distribution, i.e. the Galactic Center, by means of the equation,

$$S^{\text{ISO}}(l,b) = \frac{\rho_{\text{ISO},0} \cdot r_{\text{ISO},0}^2}{\left(r_{\text{ISO},0}^2 + R_\odot^2\left(1 - \cos^2(l)\cos^2(b)\right)\right)^{0.5}} \cdot \left(\frac{\pi}{2} + \arctan\left(\frac{R_\odot \cos(l)\cos(b)}{\left(r_{\text{ISO},0}^2 + R_\odot^2\left(1 - \cos^2(l)\cos^2(b)\right)\right)^{0.5}}\right)\right). \tag{4.4}$$

[1]Python Software Foundation. Python Language Reference, version 2.7. Available at http://www.python.org, as well as Jones E, Oliphant E, Peterson P, et al., SciPy: Open Source Scientific Tools for Python, 2001-, http://www.scipy.org/

[2]Please see Appendix B. Column Density of the Isothermal profile for details

The highly time-varying instrumental and particle backgrounds encountered by XMM-Newton are not covered by this benchmark (62). Despite this disadvantage, the benchmark is acceptable because the most common dark matter distribution models of the dark matter halo of the Milky Way have a comparable spatial and angular shape and a density maximum matching the position of the Galactic center. Furthermore, the focus of this work is set to the presumed dark matter halo of the Milky Way.

4.2 Data Selection

The tables 4.1 and 4.2 show the specifications of two groups of data sets $\mathbf{D} = \mathbf{D_1}$ and $\mathbf{D} = \mathbf{D_2}$, respectively. The observation identities (ObsId), the applied filters[3], the Galactic coordinates in longitude $l_i^{\mathbf{D_1}}$ and latitude $b_i^{\mathbf{D_1}}$, the estimated exposures $t_{\text{exp,est};i}^{\mathbf{D_1}}$, the exposures after filtering (net exposures) $t_{\text{exp,net};i}^{\mathbf{D_1}}$ and the fields of view after filtering (net fov) $\Omega_{\text{fov,net};i}^{\mathbf{D_1}}$, the expected dark matter column densities $S_i^{\mathbf{D_1},\text{ISO}}$ and $S_i^{\mathbf{D_1},\text{NFW}}$ based on the isothermal and the NFW profile, respectively, as well as the corresponding benchmark values $b_i^{\mathbf{D_1},\text{ISO}}$ and $b_i^{\mathbf{D_1},\text{NFW}}$, respectively, are shown in the afore-mentioned tables. The indices i of tables 4.1 and 4.2 are represented by natural numbers. The order of the indices matches the order of both the benchmark values $b_i^{\mathbf{D_1},\text{NFW}}$ and $b_i^{\mathbf{D_1},\text{ISO}}$. A note: The afore-mentioned values are assigned to $\mathbf{D_1}$ and are listed in table 4.1, whereby the corresponding values ($l_i^{\mathbf{D_2}}$,$b_i^{\mathbf{D_2}}$), $t_{\text{exp,est};i}^{\mathbf{D_2}}$, $t_{\text{exp,net};i}^{\mathbf{D_2}}$, $\Omega_{\text{fov,net};i}^{\mathbf{D_2}}$, $S_i^{\mathbf{D_2},\text{ISO}}$, $S_i^{\mathbf{D_2},\text{NFW}}$, $b_i^{\mathbf{D_2},\text{ISO}}$, and $b_i^{\mathbf{D_2},\text{NFW}}$ assigned to $\mathbf{D_2}$ are listed in table 4.2.
A large proportion of the data sets originally taken into account had to be rejected due to strong instrumental background contaminations. These contaminations most likely have their origins in cosmic ray incidents which occur in the body of XMM-Newton (41, 47, 63, 64, 65). Such cosmic ray interactions with the material of the satellite or the detector itself can lead to fluorescence effects and therefore photon emissions. The energies of these fluorescence photons can directly (primary fluorescence photons) or indirectly via further photon-atom processes (secondary fluorescence photons) match the energy bandpass of the EPIC-PN detector. Thus, photons of both groups of fluorescence photons can potentially

[3] Each of the 'Thin1' and 'Medium' filters (41) consist of an aluminum layer having a thickness of 40 nm and 80 nm, respectively, plus a layer of polymide having a thickness of 160 mn.

be detected by the EPIC-PN detector and increase the photon count rate of the corresponding measurement over one or more arbitrary intervals of the exposure.
Furthermore, so-called soft-proton clouds are also a source for high count rates which do not have their origins in the astrophysical object of observation (62). Such soft-proton clouds are nearly indistinguishable from X-ray photons reaching the EPIC-PN detector by reflection or grazing incidence at the mirrors of the telescope. That is, because the soft-protons propagate along paths through the telescope which resemble those of X-ray photons. Soft-proton clouds in the magnetosphere of the Earth have just recently been detected, wherein, unfortunately, the orbit of XMM-Newton intersects the magnetosphere in which the soft-proton clouds propagate along the magnetic field lines (71, 72).
Several data sets of the Chandra Deep Field South and the Canadian Network of Observational Cosmology (CNOC)[4] Field 2 were incorporated into $\mathbf{D_1}$ and $\mathbf{D_2}$, respectively, to account for possible non-spherical dark matter density distributions and/or dark matter density distributions whose centers do not coincide with the Galactic Center (79). The related directions of observation of these data sets as seen from Earth are not located in the vicinity of the direction related to the Galactic center.
The figures 4.1, 4.2, and 4.3, 4.4 show all-sky maps comprising the respective spatial distributions of the observation directions or pointings related to $\mathbf{D_1}$ and $\mathbf{D_2}$ (see tables 4.1 and 4.2), respectively, in Galactic coordinates wherein each colored dot matches a data set. Furthermore, the color of a dot related to the ith data set corresponds to the individual benchmark value $b_i^{\mathbf{D_1},\text{DM-MODEL}}$ or $b_i^{\mathbf{D_2},\text{DM-MODEL}}$, respectively. Figures 4.1 and 4.3 show benchmark values $b_i^{\mathbf{D_1},\text{ISO}}$ or $b_i^{\mathbf{D_2},\text{ISO}}$ calculated for the isothermal profile 2.35 and figures 4.2 and 4.4 show benchmark values $b_i^{\mathbf{D_1},\text{NFW}}$ or $b_i^{\mathbf{D_2},\text{NFW}}$ calculated for the NFW profile 2.36.

[4]Please see http://qold.astro.utoronto.ca/~carlberg/cnoc/

$\mathbf{D_1}$

Index	Object	ObsId	Filter	$l_i^{\mathbf{D_1}}$	$b_i^{\mathbf{D_1}}$	$t_{\text{exp,est};i}^{\mathbf{D_1}}$	$t_{\text{exp,net};i}^{\mathbf{D_1}}$	$\Omega_{\text{fov,net};i}^{\mathbf{D_1}}$	$S_i^{\mathbf{D_1},\text{ISO}}$	$b_i^{\mathbf{D_1},\text{ISO}}$	$S_i^{\mathbf{D_1},\text{NFW}}$	$b_i^{\mathbf{D_1},\text{NFW}}$
i				$\circ$	$\circ$	s	s	10^{-5} str	$10^{27}\ \frac{\text{keV}}{\text{cm}^2}$		$10^{27}\ \frac{\text{keV}}{\text{cm}^2}$	
1	V4046 Sgr	0604860401	Medium	359.66	-7.26	123715.0	82562.7	12.91	38.60	1.00	164.38	1.00
2	V4046 Sgr	0604860301	Medium	359.66	-7.26	123419.0	77397.1	13.32	38.60	0.94	164.38	0.94
3	V4046 Sgr	0604860201	Medium	359.66	-7.26	123316.0	66842.9	13.01	38.60	0.81	164.38	0.81
4	V4633 Sgr	0653550301	Thin1	5.12	-6.26	87320.0	62556.8	13.92	38.18	0.75	158.87	0.73
5	PDS 456	0501580201	Thin1	10.38	11.14	89711.0	64248.3	11.96	33.52	0.68	125.92	0.60
6	PDS 456	0501580101	Thin1	10.38	11.14	92359.0	56316.2	11.77	33.52	0.59	125.92	0.52
7	VV Sco	0555650201	Medium	352.63	19.86	104418.0	53879.3	13.97	29.29	0.50	108.61	0.43
8	VV Sco	0555650301	Medium	352.63	19.86	105375.0	46941.2	13.19	29.29	0.43	108.61	0.38
9	CDFS	0604961101	Thin1	223.61	-54.43	120817.0	77668.3	14.13	7.31	0.18	31.94	0.18
10	CDFS	0555780501	Thin1	223.63	-54.43	113004.0	70312.5	14.09	7.31	0.16	31.94	0.17
11	CDFS	0604961001	Thin1	223.64	-54.44	122515.0	69485.7	14.10	7.31	0.16	31.94	0.16
12	CDFS	0555781001	Thin1	223.65	-54.44	125813.0	69485.4	14.07	7.31	0.16	31.94	0.16
13	CDFS	0555780701	Thin1	223.66	-54.43	118415.0	69399.5	14.05	7.31	0.16	31.94	0.16
14	CNOC2 Field 2	0603590201	Medium	51.38	-42.01	81419.0	40675.6	13.84	12.80	0.16	54.23	0.16
15	CDFS	0604961801	Thin1	223.64	-54.44	125042.0	67660.4	14.11	7.31	0.16	31.94	0.16
16	CNOC2 Field 1	0603590101	Medium	50.98	-42.00	82317.0	39191.1	14.05	12.85	0.16	54.42	0.16
17	XX Cha	0300270201	Medium	297.02	-14.65	128948.0	39875.7	13.65	12.50	0.16	53.13	0.16

To be continued on the next page.

$\mathbf{D_1}$												
Index	Object	ObsId	Filter	$l_i^{\mathbf{D_1}}$	$b_i^{\mathbf{D_1}}$	$t_{\text{exp,est};i}^{\mathbf{D_1}}$	$t_{\text{exp,net};i}^{\mathbf{D_1}}$	$\Omega_{\text{fov,net};i}^{\mathbf{D_1}}$	$S_i^{\mathbf{D_1},\text{ISO}}$	$b_i^{\mathbf{D_1},\text{ISO}}$	$S_i^{\mathbf{D_1},\text{NFW}}$	$b_i^{\mathbf{D_1},\text{NFW}}$
i				$\circ$	$\circ$	s	s	10^{-5} str	$10^{27}\ \frac{\text{keV}}{\text{cm}^2}$		$10^{27}\ \frac{\text{keV}}{\text{cm}^2}$	
18	CDFS	0604961201	Thin1	223.61	-54.44	120718.0	61502.0	14.02	7.31	0.14	31.94	0.14
19	CDFS	0555782301	Thin1	223.65	-54.44	125714.0	60710.0	14.08	7.31	0.14	31.94	0.14
20	CDFS	0555780301	Thin1	223.47	-54.41	123811.0	59349.6	14.09	7.31	0.14	31.92	0.14
21	CDFS	0604960901	Thin1	223.66	-54.44	125344.0	57476.8	14.09	7.31	0.13	31.94	0.14
22	AXAF Ultra Deep F	0108060701	Thin1	223.60	-54.42	94021.0	57495.3	14.01	7.31	0.13	31.93	0.14
23	CDFS	0555780601	Thin1	223.64	-54.43	118413.0	56640.2	14.06	7.31	0.13	31.94	0.13
24	CDFS	0555780801	Thin1	223.62	-54.44	120919.0	55092.0	14.07	7.31	0.13	31.94	0.13
25	CDFS	0555780901	Thin1	223.64	-54.44	121518.0	52361.7	14.07	7.31	0.12	31.94	0.12
26	CDFS	0604960301	Thin1	223.49	-54.40	122302.0	51886.9	14.11	7.31	0.12	31.92	0.12
27	CDFS	0555780201	Thin1	223.48	-54.40	133416.0	51476.4	14.07	7.31	0.12	31.92	0.12
28	CDFS	0604960601	Thin1	223.64	-54.43	125212.0	48253.2	14.08	7.31	0.11	31.94	0.11
29	CDFS	0555780101	Thin1	223.46	-54.40	133118.0	44471.6	14.07	7.31	0.10	31.92	0.10
30	CDFS	0604960201	Thin1	223.47	-54.41	121094.0	40769.4	14.11	7.31	0.09	31.92	0.10
31	CDFS	0604960701	Thin1	223.63	-54.44	120819.0	37520.0	14.09	7.31	0.09	31.94	0.09
32	CDFS	0604960501	Thin1	223.63	-54.43	46983.0	37102.6	14.13	7.31	0.09	31.94	0.09
33	AXAF Ultra Deep F	0108061901	Thin1	223.59	-54.41	54218.0	32848.3	14.03	7.31	0.08	31.93	0.08

Table 4.1: The table lists the observation IDs (ObsId), coordinates and the estimated exposures $t_{\text{exp,est};i}^{\mathbf{D_1}}$ and net exposures $t_{\text{exp,net};i}^{\mathbf{D_1}}$ as well as the net fields of view $\Omega_{\text{fov,net};i}^{\mathbf{D_1}}$ assigned to $\mathbf{D_1}$. The model-dependent, predicted dark matter column densities $S_{\text{ISO};i}^{\mathbf{D_1}}$ and $S_{\text{NFW};i}^{\mathbf{D_1}}$ as well as the final benchmark values $b_i^{\mathbf{D_1},\text{ISO}}$ and $b_i^{\mathbf{D_1},\text{NFW}}$ are also listed in the above table.

$\mathbf{D_2}$

Index	Object	ObsId	Filter	$l_i^{\mathbf{D_2}}$	$b_i^{\mathbf{D_2}}$	$t_{\text{exp,est};i}^{\mathbf{D_2}}$	$t_{\text{exp,net};i}^{\mathbf{D_2}}$	$\Omega_{\text{fov,net};i}^{\mathbf{D_2}}$	$S_i^{\mathbf{D_2},\text{ISO}}$	$b_i^{\mathbf{D_2},\text{ISO}}$	$S_i^{\mathbf{D_2},\text{NFW}}$	$b_i^{\mathbf{D_2},\text{NFW}}$
i				$\circ$	$\circ$	s	s	10^{-5} str	$10^{27}\ \frac{\text{keV}}{\text{cm}^2}$		$10^{27}\ \frac{\text{keV}}{\text{cm}^2}$	
1	V4046 Sgr	0604860301	Medium	359.66	-7.26	123419.0	72761.8	13.78	38.60	1.00	164.38	1.00
2	V4046 Sgr	0604860401	Medium	359.66	-7.26	123715.0	72572.7	13.63	38.60	1.00	164.38	1.00
3	V4046 Sgr	0604860201	Medium	359.66	-7.26	123316.0	62580.4	13.45	38.60	0.86	164.38	0.86
4	V4633 Sgr	0653550301	Thin1	5.12	-6.26	87320.0	56167.0	13.71	38.18	0.76	158.87	0.75
5	MACHO 96 BLG 5	0305970101	Thin1	3.21	-3.10	107012.0	48967.2	12.93	39.80	0.69	189.78	0.78
6	PDS 456	0501580201	Thin1	10.38	11.14	89711.0	62158.3	13.31	33.52	0.74	125.92	0.65
7	PDS 456	0501580101	Thin1	10.38	11.14	92359.0	49372.2	12.46	33.52	0.59	125.92	0.52
8	VV Sco	0555650201	Medium	352.63	19.86	104418.0	48848.0	13.61	29.29	0.51	108.61	0.44
9	OGLE 1999 BUL 32	0152420101	Medium	2.45	-3.53	49940.0	28501.1	12.22	39.86	0.40	191.69	0.46
10	VV Sco	0555650301	Medium	352.63	19.86	105375.0	40931.0	13.60	29.29	0.43	108.61	0.37
11	RXJ2328.8+1453	0502430301	Thin1	94.96	-43.46	104910.0	53772.2	13.53	8.71	0.17	38.07	0.17
12	CDFS	0555780501	Thin1	223.63	-54.43	113004.0	61887.7	13.62	7.31	0.16	31.94	0.17
13	CDFS	0555780701	Thin1	223.66	-54.43	118415.0	59393.9	13.59	7.31	0.15	31.94	0.16

To be continued on the next page.

$\mathbf{D_2}$

Index	Object	ObsId	Filter	$l_i^{\mathbf{D_2}}$	$b_i^{\mathbf{D_2}}$	$t_{\text{exp,est};i}^{\mathbf{D_2}}$	$t_{\text{exp,net};i}^{\mathbf{D_2}}$	$\Omega_{\text{fov,net};i}^{\mathbf{D_2}}$	$S_i^{\mathbf{D_2},\text{ISO}}$	$b_i^{\mathbf{D_2},\text{ISO}}$	$S_i^{\mathbf{D_2},\text{NFW}}$	$b_i^{\mathbf{D_2},\text{NFW}}$
i				$^\circ$	$^\circ$	s	s	10^{-5} str	$10^{27}\ \frac{\text{keV}}{\text{cm}^2}$		$10^{27}\ \frac{\text{keV}}{\text{cm}^2}$	
14	CDFS	0555781001	Thin1	223.65	-54.44	125813.0	58772.7	13.65	7.31	0.15	31.94	0.16
15	CNOC2 Field 1	0603590101	Medium	50.98	-42.00	82317.0	34084.2	13.58	12.85	0.16	54.42	0.16
16	CDFS	0555782301	Thin1	223.65	-54.44	125714.0	51584.6	13.64	7.31	0.13	31.94	0.14
17	CDFS	0555780301	Thin1	223.47	-54.41	123811.0	50978.4	13.54	7.31	0.13	31.92	0.14
18	CDFS	0555780601	Thin1	223.64	-54.43	118413.0	48940.7	13.68	7.31	0.13	31.94	0.13
19	CDFS	0555780801	Thin1	223.62	-54.44	120919.0	47766.2	13.50	7.31	0.12	31.94	0.13
20	CDFS	0555780901	Thin1	223.64	-54.44	121518.0	44934.8	13.52	7.31	0.12	31.94	0.12
21	CDFS	0555780201	Thin1	223.48	-54.40	133416.0	42680.9	13.47	7.31	0.11	31.92	0.11
22	CDFS	0555780101	Thin1	223.46	-54.40	133118.0	34855.0	13.44	7.31	0.09	31.92	0.09
23	LH VLA 2	0554121301	Medium	148.46	51.42	55542.0	22947.6	13.56	6.98	0.06	30.45	0.06

Table 4.2: The table lists the observation IDs (ObsId), coordinates and the estimated exposures $t_{\text{exp,est};i}^{\mathbf{D_2}}$ and net exposures $t_{\text{exp,net};i}^{\mathbf{D_2}}$ as well as the net fields of view $\Omega_{\text{fov,net};i}^{\mathbf{D_2}}$ assigned to $\mathbf{D_2}$. The model-dependent, predicted dark matter column densities $S_{\text{ISO};i}^{\mathbf{D_2}}$ and $S_{\text{NFW};i}^{\mathbf{D_2}}$ as well as the final benchmark values $b_i^{\mathbf{D_2},\text{ISO}}$ and $b_i^{\mathbf{D_2},\text{NFW}}$ are also listed in the above table.

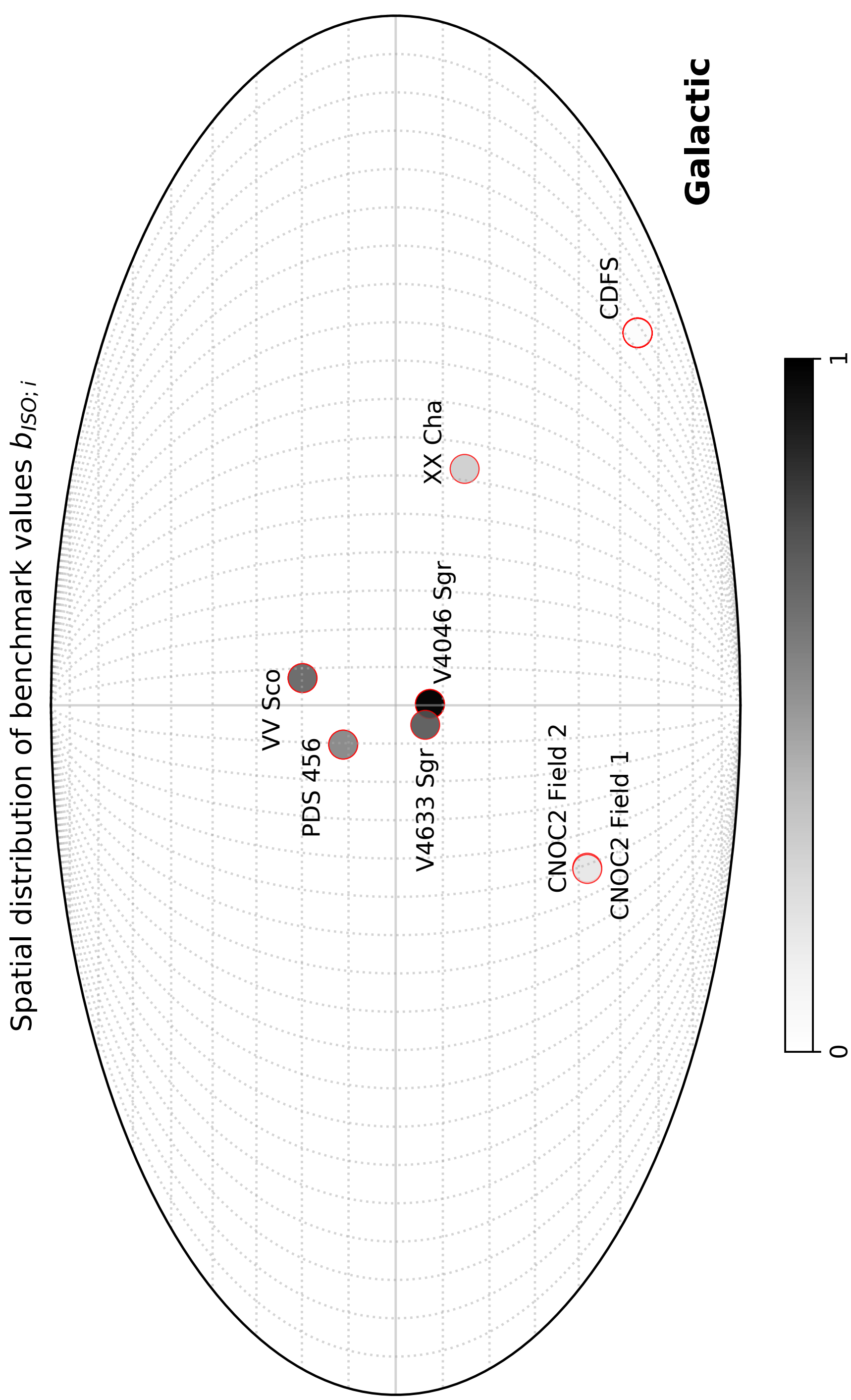

Figure 4.1: The plot shows an all-sky map comprising the spatial distribution of the observation directions or pointings related to $\mathbf{D}_1$ (see table 4.1) in Galactic coordinates wherein each colored dot matches a data set. Furthermore, the color of a dot related to an ith data set corresponds to the individual benchmark value $b_{\mathrm{ISO};i}$.

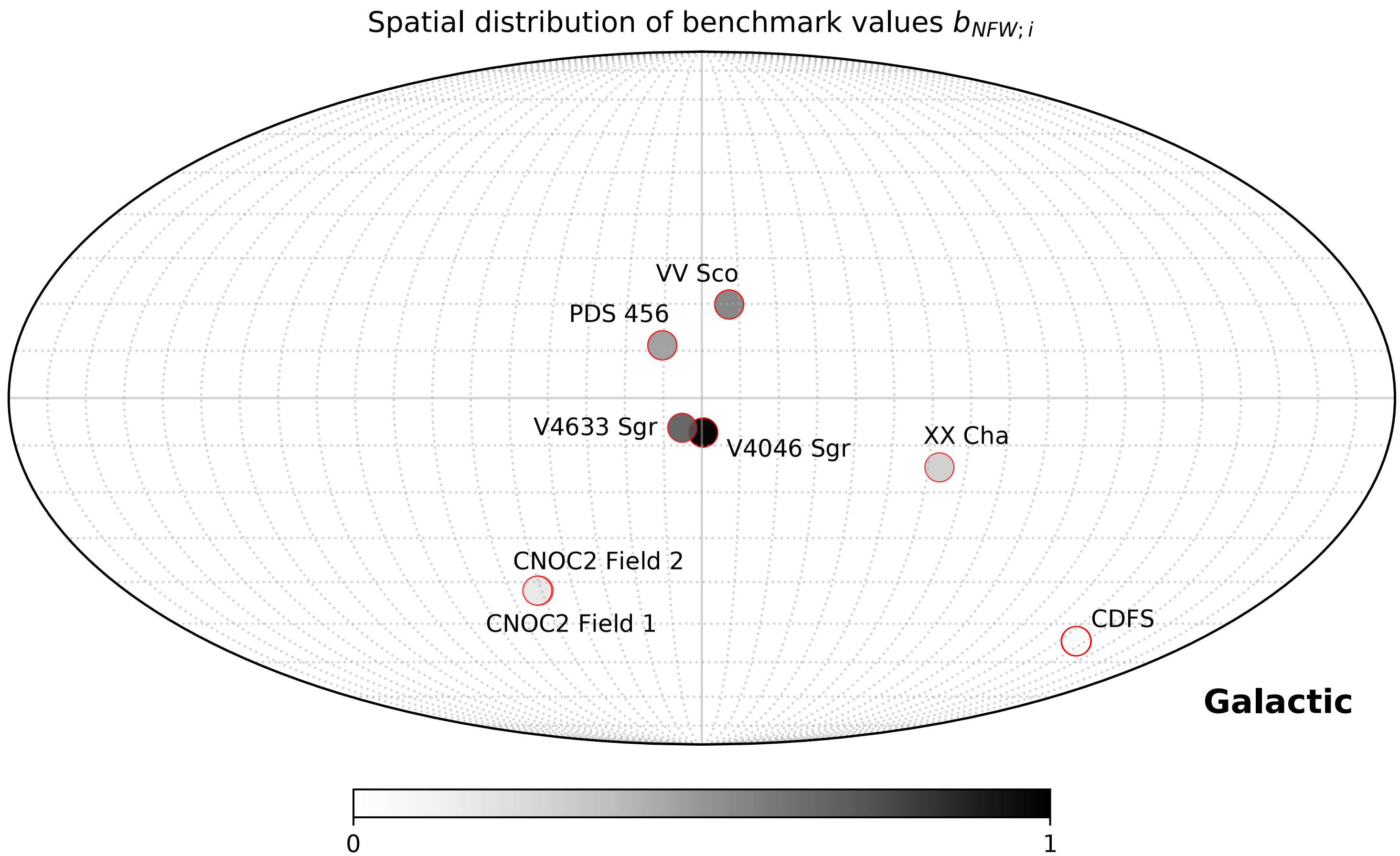

Figure 4.2: The plot shows an all-sky map comprising the spatial distribution of the observation directions or pointings related to $\mathbf{D_1}$ (see table 4.1) in Galactic coordinates wherein each colored dot matches a data set. Furthermore, the color of a dot related to an ith data set corresponds to the individual benchmark value $b_{\mathrm{NFW};i}$.

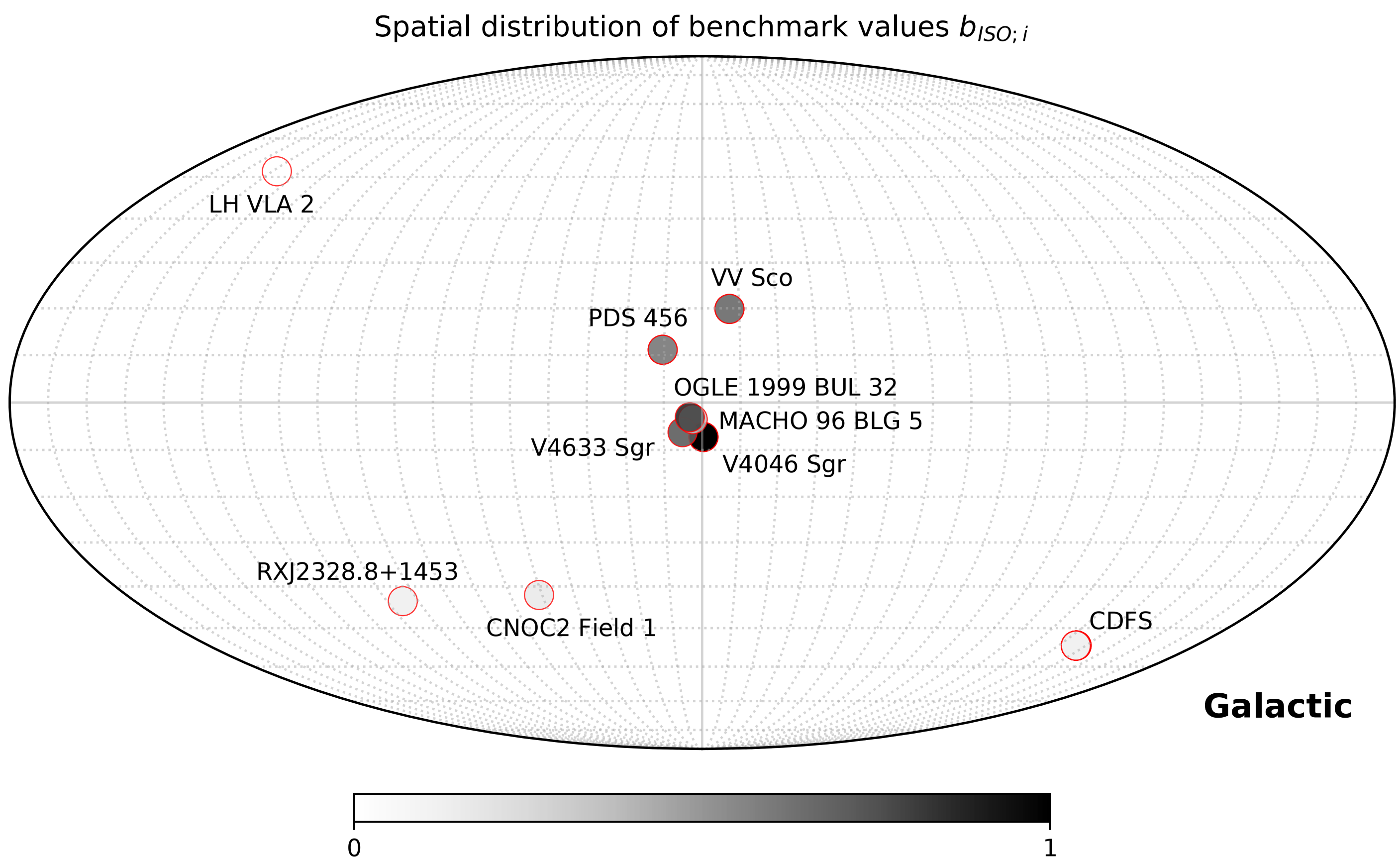

Figure 4.3: The plot shows an all-sky map comprising the spatial distribution of the observation directions or pointings related to $\mathbf{D_2}$ (see table 4.2) in Galactic coordinates wherein each colored dot matches a data set. Furthermore, the color of a dot related to an ith data set corresponds to the individual benchmark value $b_{\mathrm{ISO};i}$.

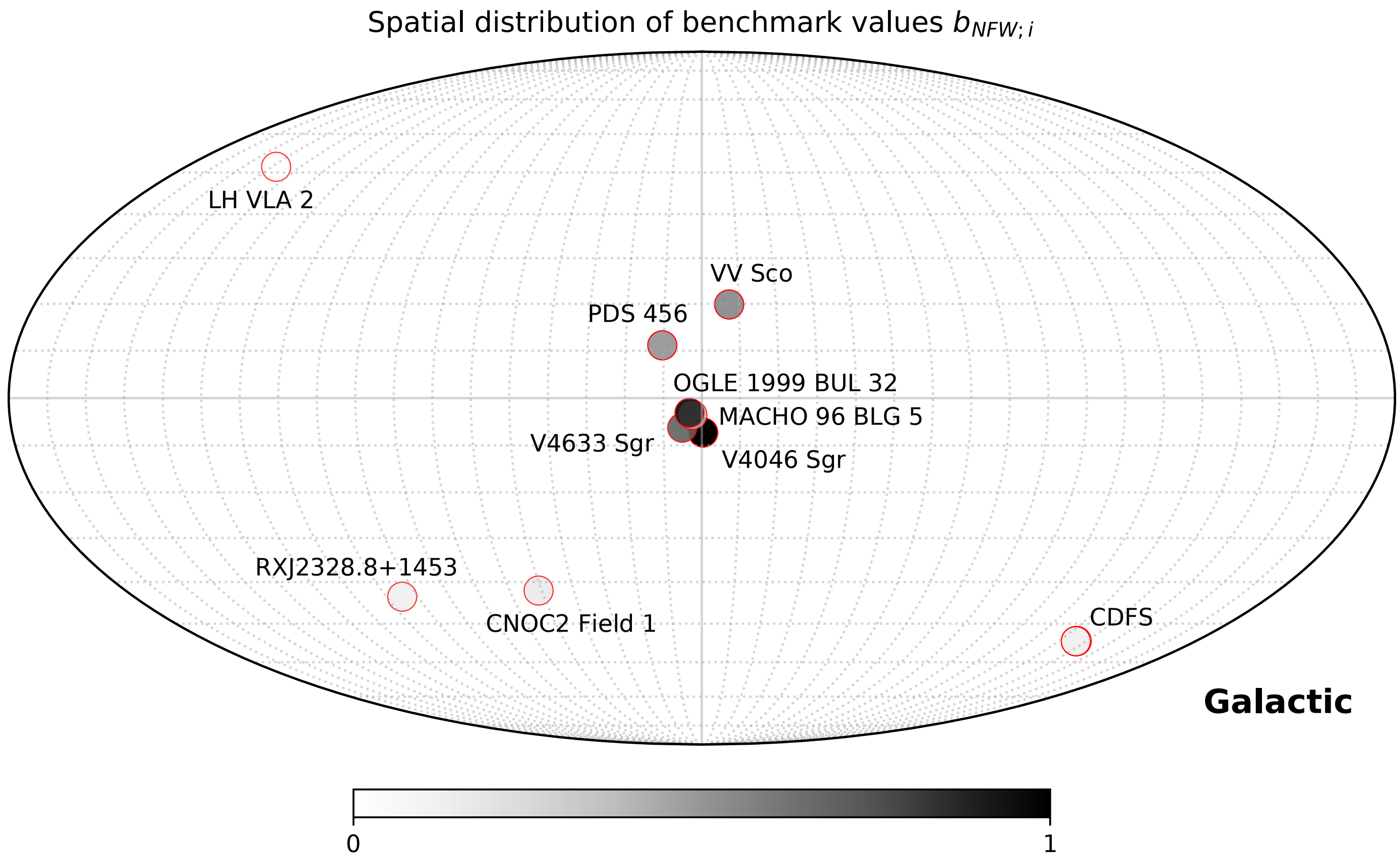

Figure 4.4: The plot shows an all-sky map comprising the spatial distribution of the observation directions or pointings related to $\mathbf{D_2}$ (see table 4.2) in Galactic coordinates wherein each colored dot matches a data set. Furthermore, the color of a dot related to an ith data set corresponds to the individual benchmark value $b_{\mathrm{NFW};i}$.

4.3 Data Reduction

The basic data reduction and analysis up to the generation of count spectra and their companion files were both achieved with the Scientific Analysis System (SAS, version 14.0.0)[5] and the related Current Calibration Files (CCF)[6] provided by the XMM-Newton Science Operations Center (XMM-SOC). The SAS data reduction and analysis can be classified into four major steps, reprocessing, time and spatial filtering, source detection and generation of spectra:

Reprocessing. The reprocessing task, in particular the task *epproc*, was applied with the default adjustments recommended by the SAS-team[7].

Time and spatial filtering. The time and spatial filtering of the data sets was performed by the script *espfilt* from the ESAS[8] software package which filters flares in the light curves by cutting tails of count rate histograms generated from the light curves. The energy range was set from 0.3 keV to 12 keV. For illustration, the light curves of the field of view and the corners of the data set with the observation identification 0604860301 ($i = 2$ from $\mathbf{D_2}$, table 4.2) are plotted in figure 4.5. This figure shows the filtered and unfiltered lightcurves of the field of view $\Omega_{\text{fov,net};i}$ of the EPIC-PN detector and the out-of-fov or corner regions of the PN-CCD, respectively. The light curves of the corner areas of the PN-CCDs show smaller count rate levels than the lightcurves of the field of view $\Omega_{\text{fov,net};i}$ which is mainly a scaling effect proportional to the corresponding detector area. The differences between the raw and filtered light curves originate, inter alia, from flares due to instrumental background processes which have an effect on both the field-of-view (fov) regions and the out-of-fov regions of the PN-CCDs. Furthermore, a spatial filter was applied via the task *evselect* to cut the events contributing to so-called hot columns, bad pixels and/or chip gaps between the PN-CCDs.

[5]"Users Guide to the XMM-Newton Science Analysis System", Issue 11.0, 2014 (ESA: XMM-Newton SOC).

[6]The Current Calibration Files are dated February 3rd, 2015.

[7]Please see https://www.cosmos.esa.int/web/xmm-newton

[8]The XMM-ESAS software package is based on the software used for the background modeling described in (56).

Source detection with respect to $\mathbf{D_2}$. The source detection algorithm *vtpdetect*[9] (57) included in the CIAO analysis software (60) provided by the Chandra X-ray Center (CXC) was applied to each data set of $\mathbf{D_2}$. The *vtpdetect* algorithm determines complex regions following isocontours of the detected sources instead of circular regions as the standard SAS source detection does. This approach results in a reduced contamination by the exclusion of sources. The energy range was set from $0.6\,\mathrm{keV}$ to $1.4\,\mathrm{keV}$ during the source detection to target an energy range in which astrophysical sources or instrumental artifacts can be located and be consequently detected by the means of the *vtpdetect* algorithm. One of the parameters of *vtpdetect* was modified relative to the default setting as follows: The parameter *coarse* defines the lower threshold of events to be interpreted as contributors to real sources and was set to 2 instead of 10. The number of false source events is equal the product of the parameter *limit* $=\ 10^{-6}$ times the number of background events. Note, the choice of parameters prioritises the detection of unresolved sources over the non-detection of misidentified sources.
The SAS source detection procedure was applied to each data set of $\mathbf{D_2}$ in addition to the afore-mentioned source detection algorithm *vtpdetect* to obtain a conservative upper limit of the remaining source photons in the X-ray background, since the source detection algorithm *vtpdetect* only outputs a value of the number of false source events per number of background events which does not allow to compute the individual contributions of the counts to the true source events, the false background events and the true background events in one go. Furthermore, the choice of such an upper limit is justified by the quality of the outcome of the *vtpdetect*-algorithm, which led to more precise result in each of the data sets in contrast to results of the SAS source detection.
The following parameter settings were applied in the course of the SAS source detection procedure: The energy range was constrained from $0.5\,\mathrm{keV}$ to $4\,\mathrm{keV}$ for all tasks involved in the SAS source detection. The task *emask* masks all pixels of the detector which have an exposure below the fraction of the maximum exposure denoted by the parameter *threshold1*. The latter was set to 0.1 instead of the default value of 0.3 to avoid excessive rejections of pixel on the detector and therefore photon counts in the event file. The minimum detection likelihood *likemin* or *mlmin* was decreased to 3 relative to the default value 10 for the tasks *eboxdetect*, *emldetect* and *esensmap*. The number of detection runs *nruns* of the command *eboxdetect* was increased from 3 to 4. This change was necessary to

[9] See "The Detect Reference Manual" (dated December 2006) for further information: `http://cxc.harvard.edu/ciao/download/doc/detect_manual/`

identify very faint or weak sources since the focus of this work lay on the diffuse X-ray background. Furthermore, the source selection radius *scut* and the source cut-out radius *ecut* of the script *emldetect* were adjusted to 0.4 and 0.95, respectively. The latter two parameters represent the encircled energy as a fraction of the point spread function related to the calibration of the EPIC-PN detector and its telescopes.
The column denoted by $N_{\text{source}}^{\text{X-ray}}$ in table 5.1 lists upper limits of the percentage of photons from sources which possibly remained in the filtered background event file and are calculated as

$$N_{\text{source}}^{\text{X-ray}} = \frac{100\,(1 - \mathit{ecut})\,N_{\text{source}}}{N_{\text{background}}} \tag{4.5}$$

for each ith data set of a group of data sets $\mathbf{D}$. This upper limit also applies to the *vtpdetect* results. Exemplary results of the two source detection algorithms applied on the data set corresponding to the observation identifier 0604860301 ($i = 2$, $\mathbf{D_2}$, table 4.2) can be compared in figure 4.7.

Source detection with respect to $\mathbf{D_1}$. The afore-mentioned SAS source detection procedure was applied to $\mathbf{D_1}$ as a source detection. The parameters were set as listed above. The column denoted by $N_{\text{source}}^{\text{X-ray}}$ in table 5.3 also lists upper limits of the percentage of photons from the sources which possibly remained in the filtered background event file for $\mathbf{D_1}$ according to equation 4.5.

Generation of spectra. The spectral analysis was applied with changes in the parameters of the tasks *rmfgen* and *arfgen*: The energy interval was expanded to a range of 0.05 keV to 20.48 keV and the number of energy bins was increased to a range of 30 to 4096 bins to match the spectral resolution of the physical energy channels of the PN-detector. In addition, the parameter *PATTERN* was set to ≤ 4 for $\mathbf{D_1}$ and to 0 for $\mathbf{D_2}$. In the first case, events or photon counts which triggered more than 3 pixel of one of the PN-CCDs (this is the default setting of all preceding tasks) were rejected and, in the latter case, merely events or photon counts which triggered more than one pixel of one of the PN-CCDs were rejected[10].
The figure 4.6 visualises the raw event file (upper left panel) and the outcomes of the three successive analysis steps: the time and particle background filtering

[10]For further details please see `http://xmm-tools.cosmos.esa.int/external/xmm_user_support/documentation/sas_usg/USG/MOSevtlist.html`.

(upper right panel), the spatial filtering (lower left panel) and the source filtering (lower right panel) of the data set corresponding to the observation identifier 0604860301 ($i = 2$, $\mathbf{D_2}$, table 4.2)[11].

[11] Please see Appendix C. Reduction and Filtering of Event Files for corresponding figures of the remaining data sets

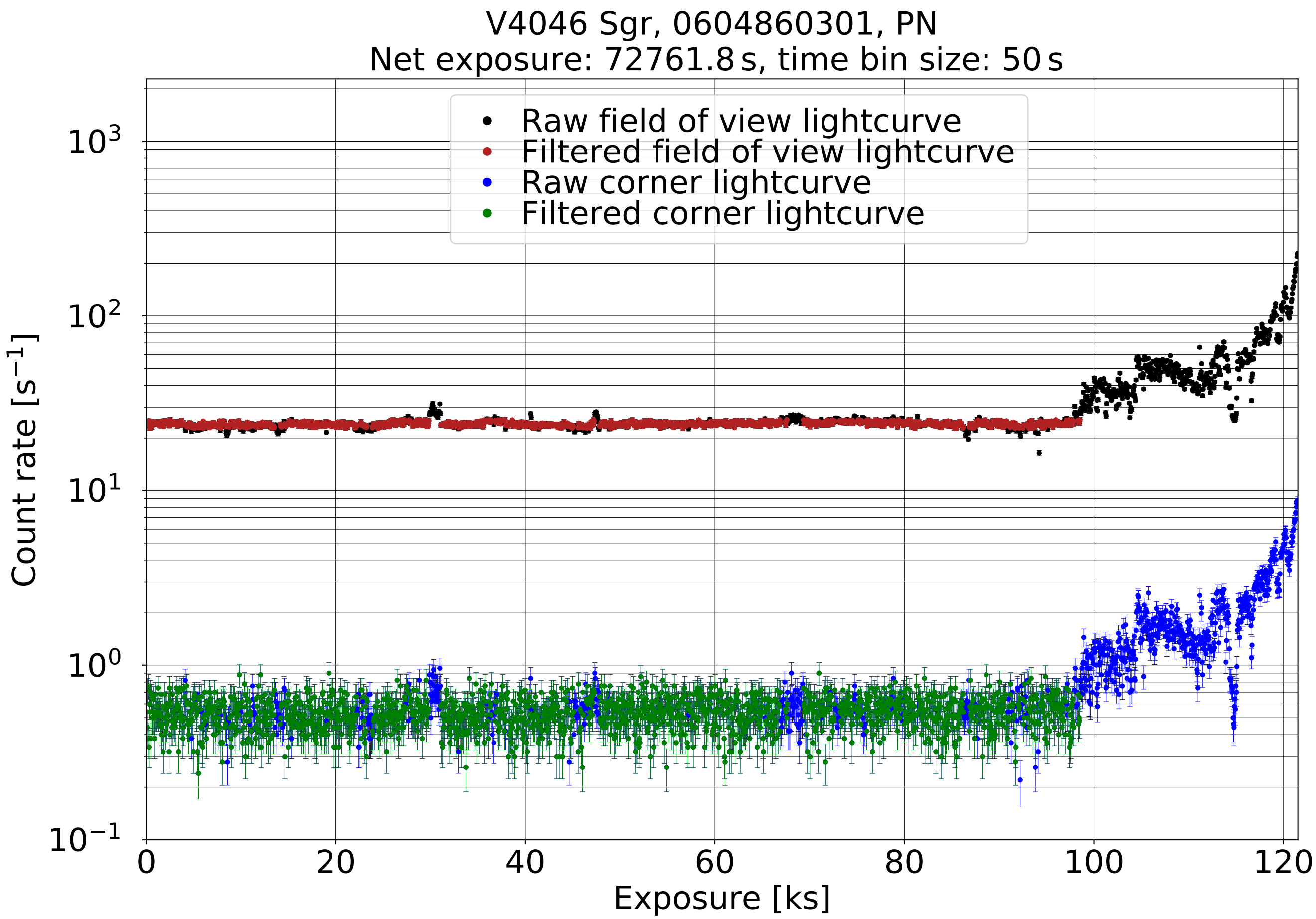

Figure 4.5: The above figure shows lightcurves of the data set 0604860301 ($i = 2$, $\mathbf{D_2}$, table 4.2), selected for the successive analysis. In particular, the red and black error bars represent the filtered lightcurve and the raw lightcurves of the net field of view $\Omega_{\mathrm{fov,net};i=2}$, respectively, while the green and blue error bars represent the filtered lightcurves and the raw lightcurves of the corner fields of view, respectively. The time bin size of the light curves is $50\,\mathrm{s}$.

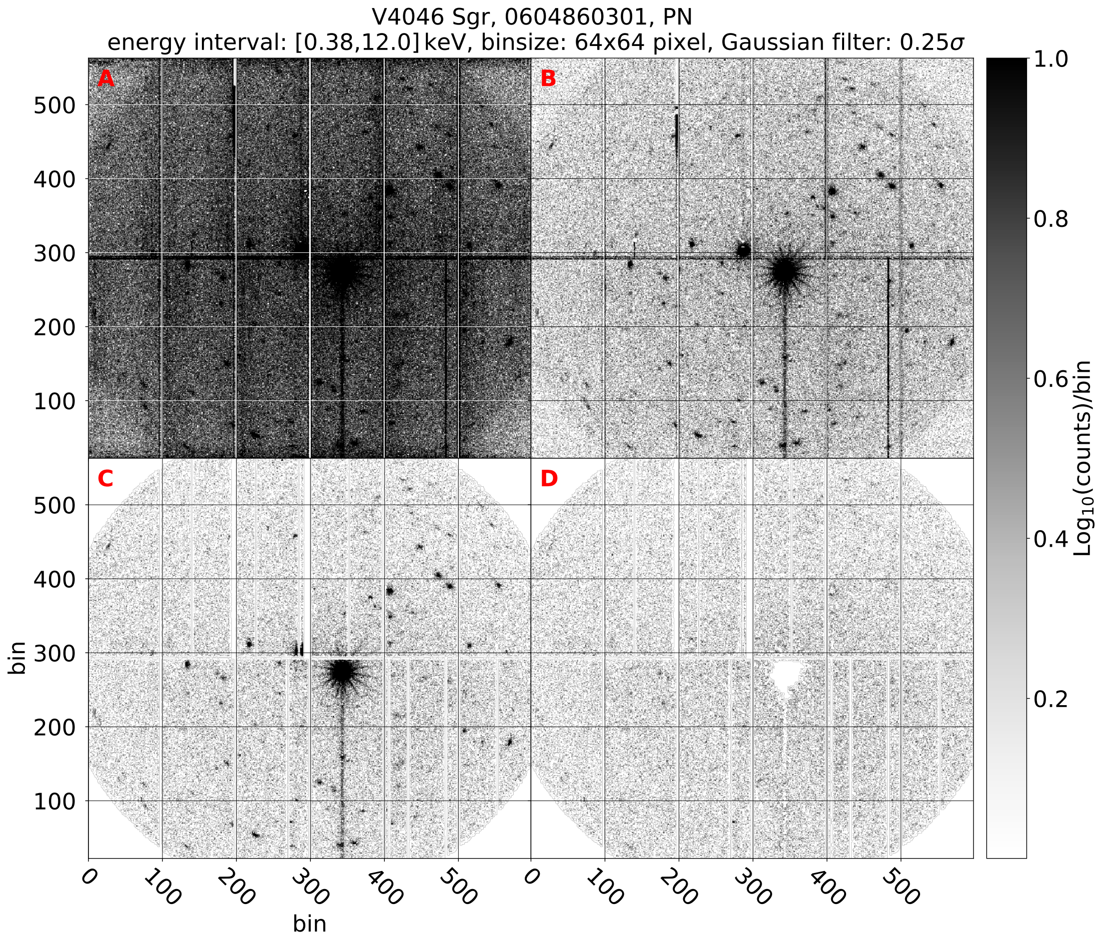

Figure 4.6: All four panels show event files of the data set 0604860301 ($i = 2$, $\mathbf{D_2}$, table 4.2) taken with the EPIC-PN detector in an energy range of $0.38\,\mathrm{keV}$ to $12\,\mathrm{keV}$. The colour coding represents the decadic logarithm of the number of X-ray photons counts per bin. The coordinates X and Y correspond to sky pixel coordinates. The upper left panel (A) shows the unfiltered raw event file and the upper right panel (B) is the time and particle background filtered result. The lower left panel (C) shows the time and particle background filtered result after application of the spatial filter and the lower right panel (D) represents the final source filtered diffuse X-ray background. All four representations of the corresponding event files were smoothed with a Gaussian kernel having a filter width of 0.25σ.

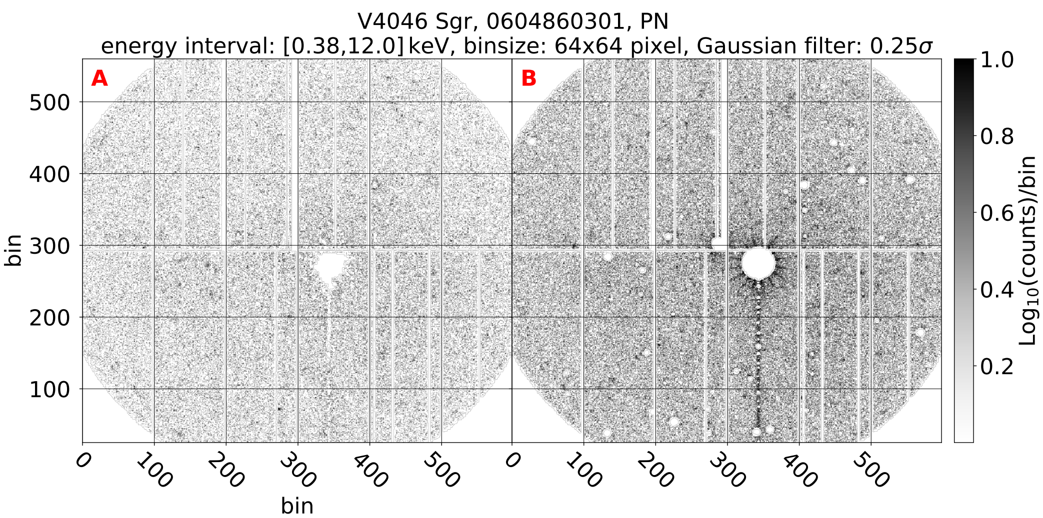

Figure 4.7: The panels show two source-filtered event files of the data set 0604860301 ($i = 2$, $\mathbf{D_2}$, table 4.2) taken with the EPIC-PN detector in an energy range of $0.38\,\mathrm{keV}$ to $12\,\mathrm{keV}$. The colour coding represents the decadic logarithm of the number of X-ray photons counts, per bin. The coordinates X and Y correspond to the sky pixel coordinates. The left panel (A) shows the output of the *vtpdetect* source detection of the CIAO software package and the right panel (B) represents the output of the source filtering routine by the SAS source detection. The two representations of the corresponding event files were smoothed with a Gaussian kernel having a filter width of 0.25σ.

4.4 Instrumental Background Spectra

The data taken with the X-ray telescope XMM-Newton suffer from both non-negligible instrumental and particle background contamination and electronic noise. The satellite is frequently exposed to energetic cosmic radiation, varying in parts systematically and in parts randomly in orbit as well as clouds of low energy protons entering the telescope (62). Figure 4.8 shows a instrumental background spectra applied in the present analysis. The instrumental background spectrum shows emission lines originating from fluorescence effects triggered by cosmic-ray interactions with the support structure of the PN-CCDs and the EPIC-PN detector material itself. The camera housing partially enclosing the EPIC-PN detector consists aluminum (AlZnMgCu1,5) comprising silicon (Si), iron (Fe), copper (Cu), mangan (Mn), magnesium (Mg), chrome (Cr), zirconium (Zn) and titan (Ti) as trace elements which provide $10\,\%$ of the total mass of the camera housing.

Invar support rods[12] which are integrated in the tubes of the telescopes consist of nickel (Ni), magnesium (Mg), silicon (Si), carbon (C), and iron (Fe). A printed circuit board (PC board) close to the EPIC-PN detector contains at least a part of the control electronic of the afore-mentioned detector and consists of molybdenum (Mo) and copper (Cu). Corresponding spectral lines have been detected by Strüder et al. (41), Kendziorra et al. (47), Freyberg (63, 64, 65) through the analysis of in-orbit and/or filter-wheel-closed data.
The filter-wheel-closed event files provided by the XMM-SOC were utilised to generate a spectrum of the instrumental background for the PN-detector. The event file of the instrumental background is a merger of all data taken while the filter-wheel of the telescope was closed[13]. Despite the closed filter wheel, the corresponding light curve shows flares induced by cosmic ray incidents. Therefore, it was time-filtered with the similar time filtering procedure mentioned in section 4.3. This procedure led to a spectrum having a net exposure $t_{\text{exp,inst,net}}$ of $215\,\text{ks}$. The merged and time-filtered instrumental background continuum were fitted[14] simultaneously in the energy intervals,

$$\begin{aligned}&(0.65; 1.10)\,\text{keV}, (1.675; 1.925)\,\text{keV}, (2.325; 4.350)\,\text{keV}, (4.75; 5.15)\,\text{keV},\\&(6.9; 7.15)\,\text{keV}, (9.2; 9.3)\,\text{keV}, (10.00; 13.25)\,\text{keV},\end{aligned} \tag{4.6}$$

with a polynomial of the 7th order,

$$R(E) = \sum_{i=0}^{7} a_i \left(\frac{E}{\text{keV}}\right)^i . \tag{4.7}$$

The above energy intervals were selected to exclude spectral lines having an instrumental origin identified as aluminum Al-K$_\alpha$ ($1.49\,\text{keV}$), nickel Ni-K$_\alpha$ ($7.48\,\text{keV}$), copper Cu-K$_\alpha$ ($8.05\,\text{keV}$ and $8.95\,\text{keV}$), and zirconium Zn-K$_\alpha$ ($8.64\,\text{keV}$ and $9.57\,\text{keV}$) in the fitted energy range. These spectral lines correspond to spectral lines found

[12] Please see https://www.cosmos.esa.int/web/xmm-newton/om-baffle for further details.

[13] The corresponding event file in full-frame mode of the version dated 2013 was taken from the web page of the XMM-SOC: http://xmm2.esac.esa.int/external/xmm_sw_cal/background/filter_closed/pn/index.shtml.
The full frame mode is defined by the following operation parameters of the EPIC-PN detector: Size of pixel area: 398×384 pixel or 27.2×26.2 arcmin; time resolution: 73.3 ms; out of time (OOT) events: 6.2%. Furthermore, the filter applied for capturing filter-wheel-closed data is provided by an aluminum layer with an area density of $270200\,\mu\text{g}\,\text{cm}^{-2}$

[14] The method applied here is alike the fitting procedure used in the software package ESAS (56).

by Strüder et al. (41), Kendziorra et al. (47), Freyberg (63, 64, 65).
The resulting goodness-of-fit is $\chi^2 = 1324.82$ with 1338 degrees of freedom (d.o.f.) with a corresponding probability value or p-value of 0.596 and best-fit coefficients,

$$\begin{aligned}\vec{a} &= (a_1, \ldots, a_i, \ldots, a_7)^{\mathrm{T}} \\ &= (739.57,\ -2.26, 4.79 \cdot 10^{-3},\ -5.86 \cdot 10^{-6},\ 4.29 \cdot 10^{-9}, \\ &\quad - 1.85 \cdot 10^{-12},\ 4.28 \cdot 10^{-16},\ -4.09 \cdot 10^{-20})^{\mathrm{T}}\,\mathrm{s}^{-1}. \end{aligned} \tag{4.8}$$

The final model of the instrumental background continuum spectrum is composed of line-free parts from measurements on the one hand and interpolated over intervals of the measured instrumental spectrum on the other hand, which exhibit strong instrumental emission lines. Figure 4.8 shows a final model of the instrumental background continuum spectrum. The fitted instrumental background spectra were normalised to each ith spectrum of the astrophysical background spectra related to $\mathbf{D_1}$ and $\mathbf{D_2}$ in an energy range of $E = 12.5\,\mathrm{keV}$ to $E = 14\,\mathrm{keV}$, respectively, wherein a significant number of photon or counts having an astrophysical origin is not expected in the afore-mentioned energy range but mainly a contribution of photons or counts having an instrumental origin. The normalisation factor,

$$N_{\text{INST}} = \frac{R_{\text{background}}}{R_{\text{instrumental}}}, \tag{4.9}$$

is composed of a ratio of the sums of the background and the instrumental photon counts $R_\gamma(E)$ in the energy range of $12.5\,\mathrm{keV}$ to $14\,\mathrm{keV}$,

$$R_{r \in \{\text{background,instrumental}\}} = \sum_E \begin{cases} R_\gamma(E), & \text{for } 12.5\,\mathrm{keV} \leq E \leq 14\,\mathrm{keV}, \\ 0, & \text{elsewhere}, \end{cases}$$

and is listed in tables 5.1 and 5.3 for each individual data set of $\mathbf{D_1}$ and $\mathbf{D_2}$, respectively. The effective area is close to zero in this energy regime, so that the fraction of the instrumental background photon counts dominates above $10\,\mathrm{keV}$ for each of the astrophysical background spectra. In a further step, the partially fitted and normalised instrumental background continuum spectrum was subtracted from the astrophysical background spectrum with the software XSPEC (51)[15]. The equation describing the subtraction of photon counts of a channel or spectral energy

[15] The software XSPEC V11 (51) was utilised for the purpose of subtracting the individually scaled instrumental background spectra of the astrophysical spectra and of fitting the remaining spectra with multiplicative and/or additive combinations of predefined spectra.

bin β by instrumental photon counts of the same channel or spectral energy bin β for each ith data set of a group of data sets $\mathbf{D}$ analysed in this work is

$$N^{\mathbf{D}}_{\text{subtracted background},i,\beta} = N^{\mathbf{D}}_{\text{background},i,\beta} - N^{\mathbf{D}}_{\text{inst},i,\beta} \cdot \frac{t^{\mathbf{D}}_{\text{exp,net},i} \cdot \Omega^{\mathbf{D}}_{\text{fov,net},i}}{t^{\mathbf{D}}_{\text{exp, inst, net},i} \cdot \Omega^{\mathbf{D}}_{\text{fov, inst, net},i}} \tag{4.10}$$

with $N^{\mathbf{D}}_{\text{background},i,\beta}$ and $N^{\mathbf{D}}_{\text{inst},i,\beta}$ being the photon counts in the βth channel of the background spectrum and the instrumental background spectrum, respectively, and $t^{\mathbf{D}}_{\text{exp,net},i}$ and $t^{\mathbf{D}}_{\text{exp, inst,net},i}$ are the respective net exposures, while $\Omega^{\mathbf{D}}_{\text{fov,net},i}$ and $\Omega^{\mathbf{D}}_{\text{fov, inst,net},i}$ are the corresponding net fields of view. The errors per bin or channel of an instrumental-background-subtracted spectrum were calculated by means of a standard error propagation under the assumption that the errors of the counts per bin or channel of the initial spectrum and the instrumental background spectrum are individually distributed as Gaussian functions.

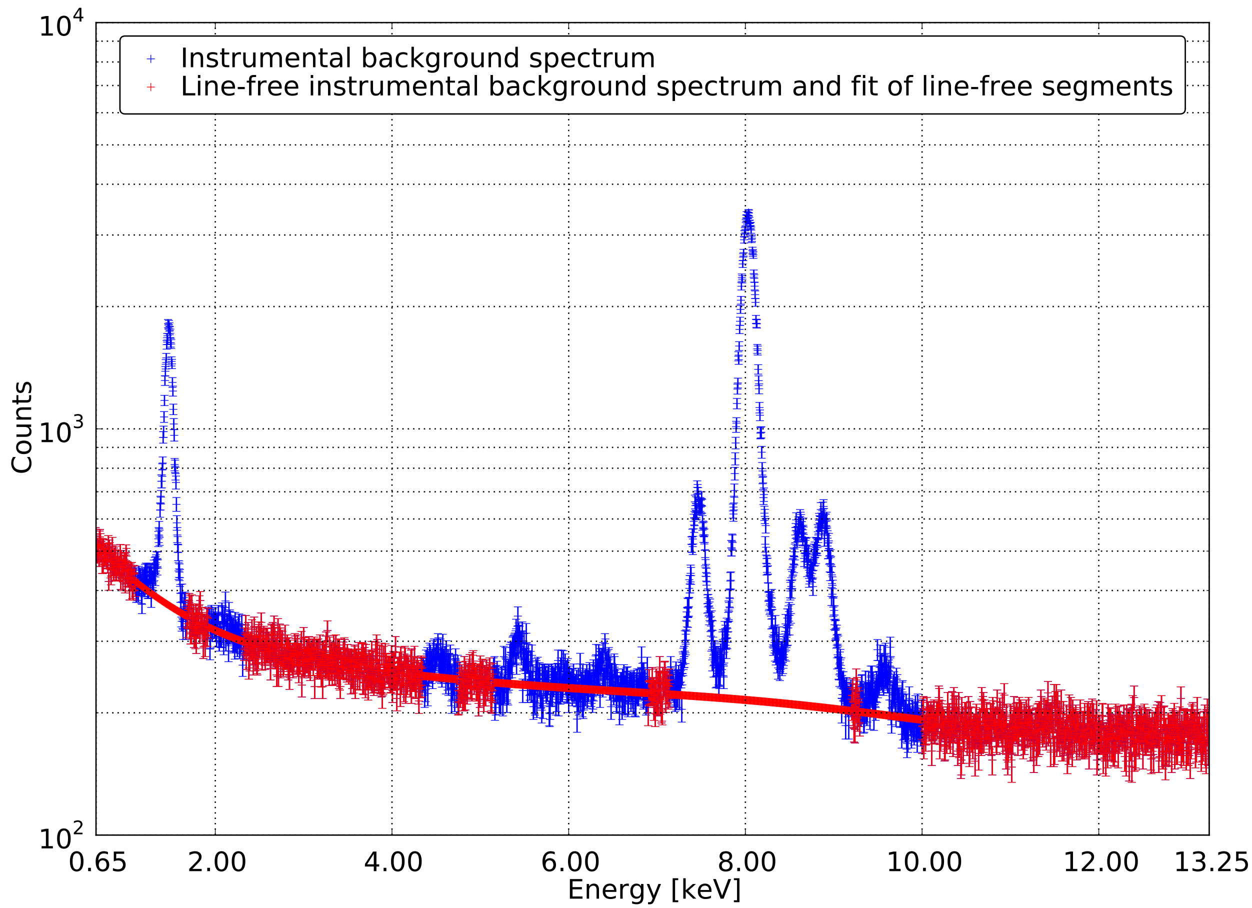

Figure 4.8: The model of the instrumental background continuum corresponding to the data set 0604860301 ($i = 2$, $\mathbf{D_2}$, table 4.2) shows the measured line-free segments (red crosses with error bars) and the fitted gaps (red line segments) which were dominated by spectral lines (blue error bars) in the primary spectrum in an energy range from $0.65\,\mathrm{keV}$ to $13.25\,\mathrm{keV}$. A polynomial of the 7th order (equation 4.7) has been applied to bridge the gaps.

Chapter 5

Statistical Methods

5.1 χ^2-Fit-Statistics

The goodness-of-fit measures the difference between a model and its fit to a data set. Let $y(x_p)$ be a function which is linear in η parameters which is fitted to $\mathcal{N}$ data points (x_p, y_p) as an estimate of the variance S^2 of the data y_p relative to the model fit $m(x_p)$ for each bin denoted by an index p (74),

$$S^2 = \sum_{p=1}^{\mathcal{N}} (y_p - m(x_p))^2. \tag{5.1}$$

The above goodness-of-fit S^2 can be extended to include the weightings of the variances as

$$\hat{S}^2 = \frac{1}{\mathcal{N} - \eta} \frac{\sum_{p=1}^{\mathcal{N}} \left(\left(\frac{1}{\sigma_p^2} \right) (y_p - m(x_p))^2 \right)}{\frac{1}{\mathcal{N}} \sum_{i=p}^{\mathcal{N}} \left(\frac{1}{\sigma_p^2} \right)}, \tag{5.2}$$

with $\mathcal{N} - \eta =: \nu$ being the number of degrees of freedom. The weighting factor for each measurement corresponding to a pth bin is

$$\mathcal{W}_p = \frac{\frac{1}{\sigma_p^2}}{\frac{1}{\mathcal{N}} \sum_{p=1}^{\mathcal{N}} \left(\frac{1}{\sigma_p^2} \right)}, \tag{5.3}$$

and represents the inverse of the variance σ^2, so that a variance-weighted goodness-of-fit χ^2 can be defined as

$$\chi^2 := \sum_{p=1}^{\mathcal{N}} \left(\frac{y_p - m(x_p)}{\sigma_p} \right)^2 . \tag{5.4}$$

A further weighting of the χ^2 by its number of degrees of freedom ν,

$$\chi^2_\nu := \frac{\chi^2}{\nu} = \frac{S^2}{\langle \sigma^2 \rangle}, \tag{5.5}$$

with a mean of the variance defined as

$$\langle \sigma^2 \rangle = \frac{\left(\frac{1}{\mathcal{N}}\right) \sum_{p=1}^{\mathcal{N}} \left(\frac{1}{\sigma_p^2}\, \sigma_p^2\right)}{\left(\frac{1}{\mathcal{N}}\right) \sum_{p=1}^{\mathcal{N}} \left(\frac{1}{\sigma_p^2}\right)}. \tag{5.6}$$

implies that $\chi^2_\nu \approx 1$ indicates a good fit with a model close to the data. The fit is judged as bad in cases of $\chi^2_\nu > 1$, while $\chi^2_\nu < 1$ can lead to the conclusion that the uncertainties, e.g. the values of σ_p are very large,

$$\chi^2_\nu < 1 \quad \Leftrightarrow \quad \chi^2 = \frac{S^2}{\langle \sigma^2 \rangle} = \sum_{p=1}^{\mathcal{N}} \left(\frac{y_p - m(x_p)}{\sigma_p} \right)^2 < 1. \tag{5.7}$$

This situation may indicate a false estimate of the errors of the measured data. The χ^2-distribution or probability density function[1] of χ^2 (73, 74) dependent on the number of degrees of freedom ν is defined as

$$p_\chi(\chi^2; \nu) := \frac{(x^2)^{\frac{1}{2}(\nu-2)} \exp\left(-\frac{x^2}{2}\right)}{2^{\frac{\nu}{2}} \Gamma\left(\frac{\nu}{2}\right)}. \tag{5.8}$$

The integral probability or p-value $P_\chi(\chi^2; \nu)$ from $x^2 = \chi^2$ to $x^2 = \infty = \chi^2$ is the integral over the probability density function $p_\chi(\chi^2; \nu)$,

$$P_\chi(\chi^2; \nu) = \int_{\chi^2}^{\infty} p_\chi(x^2; \nu)\, dx^2. \tag{5.9}$$

[1]The Gamma function $\Gamma(a)$ is defined as $\Gamma(1) = 1$, $\Gamma(\frac{1}{2}) = \sqrt{\pi}$, $\Gamma(a-1) = a\Gamma(a)$ and $\Gamma(a+1) = a!$, $a \in \{0, 1, ...\}$ for integral values and $\Gamma(a+1) = a \cdot (a-1) \cdot (a-2) \cdot ... \cdot \left(\frac{2}{2}\right) \cdot \left(\frac{1}{2}\sqrt{\pi}\right)$, $a \in \{\frac{1}{2}, \frac{3}{2}, \frac{5}{2}, ...\}$ for half-integral values, respectively.

The above integral results in a probability that a random set of data points drawn from the probability density function $p_\chi(\chi^2;\nu)$ would yield a value of χ^2 equal to or greater than a predetermined value. In the words of Protassov et al. (75):

> "*A probability value or p-value is the probability of observing a value of the test statistics (such as χ^2) as extreme or more extreme than the value actually observed given that the null model holds.*"

As a result, small p-values are interpreted as evidence against the null model. A good fit of a model $m(x_p)$ to a data set y_p results, as a rule of thumb, in $\chi^2_\nu \approx 1$ which should translate into a p-value $P_\chi(\chi^2;\nu) \approx 0.5$.

5.2 Bevington-$\mathcal{F}$-Test

The χ^2 goodness-of-fit measures the discrepancy between an estimated function $m(x_p)$ and a corresponding probability density function $p_\chi(\chi^2;\nu)$ as well as the deviation between the data y_p and the corresponding probability density function $p_\chi(\chi^2;\nu)$ at the same time. The $\mathcal{F}$-test provides a separation of this information, wherein the related f-distribution is defined as

$$f := \frac{\chi_0^2/\nu_0}{\chi_1^2/\nu_1} = \frac{S_0^2/\langle\sigma_0^2\rangle/\nu_0}{S_1^2/\langle\sigma_1\rangle/\nu_1}, \tag{5.10}$$

while χ_0^2 and χ_1^2 each follow a χ^2-distribution (73). The corresponding probability density function is defined as

$$p_f(f;\nu_0,\nu_1) := \frac{\Gamma\left(\frac{\nu_0+\nu_1}{2}\right)}{\Gamma\left(\frac{\nu_0}{2}\right)\Gamma\left(\frac{\nu_1}{2}\right)}\left(\frac{\nu_0}{\nu_1}\right)^{\frac{\nu_0}{2}}\frac{f^{\frac{1}{2}(\nu_1-2)}}{\left(1+\frac{\nu_0}{\nu_1}f\right)^{\frac{1}{2}(\nu_0+\nu_1)}}. \tag{5.11}$$

A modified variant of the $\mathcal{F}$-test introduced in Bevington (74) was applied in this work. It is denoted as the Bevington-$\mathcal{F}$-test or $\mathcal{F}_\mathcal{B}$-statistics. Originally, it was defined to test additive model components with one degree of freedom in relation to a nullhypothesis model. The number of degrees of freedom was expanded from one to two for the purpose of the present analysis, wherein a variance-weighted goodness-of-fit χ_0^2 related to a nullhypothesis model $m(x_p) = m_0(\eta; x_p)$ comprising η parameters[2] is defined as

$$\chi_0^2 = \chi_0^2(\eta; m_0(\eta; x_p)) = \sum_{p=1}^{\mathcal{N}} \left(\frac{y_p - m_0(\eta; x_p)}{\sigma_p} \right)^2 , \tag{5.12}$$

having $\nu_0 = \mathcal{N} - \eta$ degrees of freedom, with $\mathcal{N}$ being the number of data points x_p. Bevington (74) describes a test of a nullhypothesis model against an alternative model consisting of the nullhypothesis model plus an additive term or component. The resulting alternative hypothesis model is related to a variance-weighted goodness-of-fit comprising $\eta + 1$ free parameters and $\nu_1 = \mathcal{N} - \eta - 1$ degrees of freedom as introduced by Bevington (74) which was modified as

$$\chi_1^2 = \chi_1^2(\eta + 2; m_1(\eta + 2; x_p)) = \sum_{p=1}^{\mathcal{N}} \left(\frac{y_p - m_1(\eta + 2; x_p)}{\sigma_p^2} \right)^2 \tag{5.13}$$

in the scope of this work, related to a model $y(x_p) = m_1(\eta{+}2; x_p)$, which provides two additional free parameters and $\nu_1 = \mathcal{N} - \eta - 2$ degrees of freedom. The difference of the goodness-of-fits,

$$\Delta\chi^2 := \chi_0^2(\eta; m_0(\eta, x_p)) - \chi_1^2(\eta + 2; m_1(\eta + 2; x_p)) \tag{5.14}$$

should follow a χ^2-distribution with 2 degrees of freedom. Following Bevington (74), equation 11.50, the resulting $\mathcal{F}_{\mathcal{B}}$-test for testing models having a difference of their degrees of freedom $\nu_0 - \nu_1 = 2$ is

$$\mathcal{F}_{\mathcal{B}}(\eta; m_0(\eta, x_p), m_1(\eta + 2; x_p)) = \mathcal{F}_{\mathcal{B}} := \frac{\chi_0^2(\eta) - \chi_1^2(\eta + 2)}{\frac{\chi_1^2(\eta+2)}{\mathcal{N}-\eta-2}} = \frac{\Delta\chi^2}{\chi_{0,\nu}^2(\eta)}, \tag{5.15}$$

having a reduced χ^2 defined as

$$\chi_{0,\nu}^2 := \frac{\chi^2(\eta + 2)}{\mathcal{N} - \eta - 2}. \tag{5.16}$$

The above-defined nullhypothesis model $m_0(\eta; x_p)$ and alternative model $m_1(\eta + 2; x_p)$ belong to the class of so-called finite mixture models which in general have

[2] The subscripts 0 and 1 denote the relations to the nullhypothesis models and the alternative models, respectively.

the following functional forms,

$$m_0(\eta; x_p) \coloneqq \sum_{\eta=1}^{\mathcal{H}_0} a_\eta \, m_{0,\eta}(x_p), \tag{5.17}$$

and

$$\begin{aligned} m_1(\eta+2; x_p) &\coloneqq \left(\sum_{\eta=1}^{\mathcal{H}_1} a_\eta \, m_{1,\eta}(x_p) \right) \\ &= \left(\sum_{\eta=1}^{\mathcal{H}_0} a_\eta \, m_{0,\eta}(x_p) \right) + a_{\eta+1,\eta+2} \, m_{1,\eta+1,\eta+2}(x_p), \end{aligned} \tag{5.18}$$

respectively, with $\mathcal{H}_0$ and $\mathcal{H}_1$ being the respective number of parameters or terms of the nullhypothesis model $m_0(\eta; x_p)$ and the alternative hypothesis model $m_1(\eta+2; x_p)$. The $\mathcal{F}_\mathcal{B}$-test was applied to test if the coefficient $a_{\eta+1,\eta+2}$ of the additional term $a_{\eta+1,t+2} \, f_{\eta+1,\eta+2}(x_p)$ is zero or not. If $\mathcal{F}_\mathcal{B} > \mathcal{F}_\mathcal{B}^{\mathbf{measure}}$, with $\mathcal{F}^{\mathbf{measure}}$ being the respective measured or observed $\mathcal{F}_\mathcal{B}$-value, the additional term of the related alternative hypothesis model will be accepted since it shows confidence that $a_{\eta+1,\eta+2} \neq 0$ is high in such a case.

5.3 Posterior Predictive p-value Analysis

The following analysis applies the $\mathcal{F}_\mathcal{B}$ test statistics (equation 5.15) in combination with the posterior predictive p-value analysis emphasised by Protassov et al. (75). The $\mathcal{F}_\mathcal{B}$ test statistics is expected to follow a χ^2-distribution as reference or parent distribution but it is not the case in general. A (simple) nullhypothesis model will be rejected in favour of a more complex alternative hypothesis model, if the observed or measured test statistics is extreme with respect to the reference distribution, e.g., its p-value is smaller 5% or 1%, etc.. The posterior predictive p-value analysis was chosen to avoid this issue by the generation of reference distributions via a Monte-Carlo method applied to $\mathcal{F}_\mathcal{B}$-values dependent on a nullhypothesis model $m_{0,\eta}$ and an alternative model $m_{1,\eta+2}$. Three mathematical conditions have to be fulfilled to test whether a nullhypothesis model or an alternative hypothesis model consisting of the nullhypothesis model and an additional term is favoured (75):

1. The allowed parameter values of the nullhypothesis model have to be a subset of those parameter values of the alternative hypothesis model or vice versa. In other words: The parameter values of a nullhypothesis model have to be nested in the allowed parameter space of an alternative hypothesis model, which is compared to the nullhypothesis model.

2. The null values of the parameters of the additional component are not allowed to be on the boundary of the set of possible parameter values.

3. The reference distributions related to a chosen test statistics, such as the $\mathcal{F}_{\mathcal{B}}$ test statistics, will only be reliable, if the underlying data sets are sufficiently large.

Protassov et al. (75) demonstrate the failure of condition 2 in case of a likelihood ratio test for an independent sample $(x_p, y_p) = (x_1, ..., x_n, y_1, ..., y_n)$ (for example, (x_p, y_p) can be a set of counts per spectral channel). A parameter element or vector Θ is contained in the set of the possible parameters of the nullhypothesis model Θ_0 which itself is a subset of the parameter space of the alternative model Θ_1 as required by condition 1, listed above. The condition 1 holds true, if a nullhypothesis model consisting of a powerlaw is compared to an alternative hypothesis model consisting of a powerlaw plus a Gaussian emission line, for example, but the second condition 2 is not fulfilled. The flux normalisation of the Gaussian line can have its minimum at $F_{\text{Photon}} = 0$ with $F_{\text{Photon}} \in \Theta_0$ which would be located on the boundary of the allowed parameter space Θ_0 of the nullhypothesis model (in case of a likelihood ratio test, in such a scenario, a supremum being the least upper bound of Θ_0 instead of a maximum would have to be calculated). According to Protassov et al. (75), this results in a scenario outside the bounds of the standard mathematical theory so that the corresponding reference distribution is therefore unknown, uncalibrated and unpredictable. Such a scenario related to a likelihood ratio test can be transfered to a $\mathcal{F}$-test (75), wherein the standard $\mathcal{F}$-statistics (equation 5.11) may notably vary from the nominal tabulated statistics (76, 77, 78).
In the course of the present analysis, the following steps were taken to apply the posterior predictive p-value analysis in combination with the $\mathcal{F}_{\mathcal{B}}$ test statistics as the underlying test statistics:

1. A number of $M^{\mathbf{D}}$ data sets $x_p^{\mathbf{monte-carlo}} = x_p^{\mathbf{mc}}$ are simulated from a nullhypothesis model $m_0^{\mathbf{D}}(\eta; x_p^{\mathbf{measure}})$ dependent on a set of measured data $x_p^{\mathbf{measure}} = x_p^{\mathbf{m}}$, here the diffuse X-ray background spectra, and related to a

group of data sets $\mathbf{D}$ by means of the task *fakeit*[3] in XSPEC while using the original binning, effective areas, response matrices and background models of the corresponding nullhypothesis model. Such an approach via a Monte-Carlo simulation is applied to access the sampling distribution of the $\mathcal{F}_{\mathcal{B}}$ test statistics, wherein the measured value $\mathcal{F}_{\mathcal{B}}^{\mathbf{measure}} = \mathcal{F}_{\mathcal{B}}^{\mathbf{m}}$ comprising the values,

$$\chi_0^{2,\mathbf{m}} = \chi_0^2(\eta; m_0^{\mathbf{D}}(\eta; x_p^{\mathbf{m}}), y_p^{\mathbf{m}}) \tag{5.19}$$

as well as

$$\chi_1^{2,\mathbf{m}} = \chi_1^2(\eta+2; m_1^{\mathbf{D}}(\eta+2; x_p^{\mathbf{m}}), y_p^{\mathbf{m}}), \tag{5.20}$$

is defined as,

$$\begin{aligned}\mathcal{F}_{\mathcal{B}}^{\mathbf{m}} &= \frac{\chi_0^{2,\mathbf{m}} - \chi_1^{2,\mathbf{m}}}{\chi_1^{2,\mathbf{m}}/\nu_1} \\ &= \frac{\chi_0^2(\eta; m_0^{\mathbf{D}}(\eta; x_p^{\mathbf{m}}), y_p^{\mathbf{m}}) - \chi_1^2(\eta+2; m_1^{\mathbf{D}}(\eta+2; x_p^{\mathbf{m}}), y_p^{\mathbf{m}})}{\chi_1^2(\eta+2; m_1^{\mathbf{D}}(\eta+2; x_p^{\mathbf{m}}), y_p^{\mathbf{m}})/\nu_1}. \end{aligned} \tag{5.21}$$

2. A nullhypothesis model $m_0^{\mathbf{D}}$ and an alternative hypothesis model $m_1^{\mathbf{D}}$ are simultaneously fitted to each of the $M^{\mathbf{D}}$ simulated data sets $(x_p^{\mathbf{mc}}, y_p^{\mathbf{mc}})$, wherein the corresponding $\mathcal{F}_{\mathcal{B}}^{\mathbf{monte-carlo}} = \mathcal{F}_{\mathcal{B}}^{\mathbf{mc}}$ values are calculated from the resulting values,

$$\chi_0^{2,\mathbf{mc}} = \chi_0^2(\eta; m_0^{\mathbf{D}}(\eta; x_p^{\mathbf{mc}}), y_p^{\mathbf{mc}}) \tag{5.22}$$

as well as

$$\chi_1^{2,\mathbf{mc}} = \chi_1^2(\eta+2; m_1^{\mathbf{D}}(\eta+2; x_p^{\mathbf{mc}}), y_p^{\mathbf{mc}}), \tag{5.23}$$

[3]Please see Arnaud (51) and/or https://heasarc.gsfc.nasa.gov/docs/xanadu/xspec/manual/XSfakeit.html. The underlying algorithm of the task *fakeit* generates simulated spectra and their corresponding error distributions based on input spectra, in this case the diffuse X-ray background spectra, wherein the algorithm further determines if the input spectra have Poissionian or Gaussian error distributions based on the number of photon counts in a bin or energy channel.

respectively, to generate a respective sampling distribution comprising of $\mathcal{F}_{\mathcal{B}}^{\mathbf{mc}}$ values defined as

$$\begin{aligned}\mathcal{F}_{\mathcal{B}}^{\mathbf{mc}} &= \frac{\chi_0^{2,\mathbf{mc}} - \chi_1^{2,\mathbf{mc}}}{\chi_1^{2,\mathbf{mc}}/\nu_1} \\ &= \frac{\chi_0^2(\eta; m_0^{\mathbf{D}}(\eta; x_p^{\mathbf{mc}}), y_p^{\mathbf{mc}}) - \chi_1^2(\eta+2; m_1^{\mathbf{D}}(\eta+2; x_p^{\mathbf{mc}}), y_p^{\mathbf{mc}})}{\chi_1^2(\eta+2; m_1^{\mathbf{D}}(\eta+2; x_p^{\mathbf{mc}}), y_p^{\mathbf{mc}})/\nu_1},\end{aligned} \tag{5.24}$$

wherein the number of simulated data sets $M^{\mathbf{D}}$ corresponds to the number of $\mathcal{F}_{\mathcal{B}}^{\mathbf{mc}}$ values in the sampling distribution.

3. An approximate p-value is determined by the sum of all $\mathcal{F}_{\mathcal{B}}^{\mathbf{mc}}$ values of the sampled $\mathcal{F}_{\mathcal{B}}^{\mathbf{mc}}$ distributions up to the measured $\mathcal{F}$-value $\mathcal{F}_{\mathcal{B}}^{\mathbf{m}}$ as

$$p = \frac{\sum_{k=1}^{M^{\mathbf{D}}} \mathcal{I}\left(\mathcal{F}_{\mathcal{B}}^{\mathbf{mc};k} > \mathcal{F}_{\mathcal{B}}^{\mathbf{m}}\right)}{M^{\mathbf{D}}}. \tag{5.25}$$

The abbreviation '$\mathcal{I}$' denotes the indicator function

$$\mathcal{I}\left(\mathcal{F}_{\mathcal{B}}^{\mathbf{mc};k} > \mathcal{F}_{\mathcal{B}}^{\mathbf{m}}\right) := \begin{cases} 1, & \text{if} \quad \mathcal{F}_{\mathcal{B}}^{\mathbf{mc};k} > \mathcal{F}_{\mathcal{B}}^{\mathbf{m}}, \\ 0, & \text{if} \quad \mathcal{F}_{\mathcal{B}}^{\mathbf{mc};k} \leq \mathcal{F}_{\mathcal{B}}^{\mathbf{m}}. \end{cases}$$

5.4 Null Hypothesis Models

The present analysis focuses on possible additional emission lines in the diffuse X-ray background, wherein these lines are each shaped as a non-absorbed[4] Gaussian curve (equation 2.39). This leads to nullhypothesis models $m_0^{\mathbf{D}}\left(\eta; x_p^{\mathbf{m}} = E^{\mathbf{D}}\right)$[5] related to a group of data sets $\mathbf{D}$ of a continuum with superposed line emissions, wherein the measured data sets $x_p^{\mathbf{m}}$ equate to the energy axis $E^{\mathbf{D}}$. Further, the nullhypothesis model $m_0^{\mathbf{D_1}}\left(\eta; x_p^{\mathbf{m}} = E^{\mathbf{D_1}}\right)$ related to $\mathbf{D_1}$ consists of a rather non-physical model which fits to the diffuse X-ray background spectra nearly as well as the nullhypothesis model $m_0^{\mathbf{D_2}}\left(\eta; x_p^{\mathbf{m}} = E^{\mathbf{D_2}}\right)$, whereby the approach of latter model was to build a physical model with respect to an assumed composition of the diffuse X-ray background.

[4]For further details, please see Appendix D. Emission and Absorption.

[5]The models are folded with the corresponding response matrices and their auxiliary files during the fitting process to account for instrumental effects, e.g., the spectral energy resolution.

Nullhypothesis model of $\mathbf{D_1}$. The nullhypothesis model which fits the data sets or spectra of $\mathbf{D_1}$ is defined as,

$$m_0^{\mathbf{D_1}}\left(\eta; E^{\mathbf{D_1}}\right) = \tag{5.26}$$

$$m_0^{\mathbf{D_1}}\Bigg(wabs\left(\mathrm{n}_{\mathrm{H};i}^{\mathbf{D_1}}, E^{\mathbf{D_1}}\right), bremss\left(\mathrm{T}_i^{\mathbf{D_1}}, \mathrm{N}_{bremss;i}^{\mathbf{D_1}}, E^{\mathbf{D_1}}\right), pow\left(\Gamma_i^{\mathbf{D_1}}, \mathrm{N}_{pow;i}^{\mathbf{D_1}}, E^{\mathbf{D_1}}\right),$$
$$gauss\left(E_{gauss;ij}^{\mathbf{D_1}}, \sigma_{ij}^{\mathbf{D_1}}, F_{gauss;ij}^{\mathbf{D_1}}, E^{\mathbf{D_1}}\right)\Bigg) =$$
$$\sum_{i=1}^{\mathbf{N_1}}\Bigg(\underbrace{wabs\left(\mathrm{n}_{\mathrm{H};i}^{\mathbf{D_1}}, E^{\mathbf{D_1}}\right)\cdot bremss\left(\mathrm{T}_i^{\mathbf{D_1}}, \mathrm{N}_{bremss;i}^{\mathbf{D_1}}, E^{\mathbf{D_1}}\right) + pow\left(\Gamma_i^{\mathbf{D_1}}, \mathrm{N}_{pow;i}^{\mathbf{D_1}}, E^{\mathbf{D_1}}\right)}_{\text{continuum emission}}$$
$$+ \underbrace{\left(\sum_{l=1}^{\mathbf{L_1}} gauss\left(E_{gauss;il}^{\mathbf{D_1}}, \sigma_{gauss;il}^{\mathbf{D_1}}, F_{gauss;il}^{\mathbf{D_1}}, E^{\mathbf{D_1}}\right)\right)\Bigg)}_{\text{additional component or line emission}}. \tag{5.27}$$

Firstly, the continuum emission[6] of an ith data set of $\mathbf{D_1}$ is modelled as a powerlaw *pow*[7] dependent on a dimensionless photon index $\Gamma_i^{\mathbf{D_1}}$ and a normalisation $\mathrm{N}_{pow;i}^{\mathbf{D_1}}$ as well as a thermal bremsstrahlung spectrum *bremss*[8] dependent on a temperature $\mathrm{T}_i^{\mathbf{D_1}}$ and a normalisation $\mathrm{N}_{bremss;i}^{\mathbf{D_1}}$, wherein the latter component is attenuated by a photoelectric absorption component denoted as *wabs*[9], dependent on a hydrogen column $\mathrm{n}_{\mathrm{H};i}^{\mathbf{D_1}}$. Secondly, the line emission of such an ith data set of $\mathbf{D_1}$ is modelled by the sum of $\mathbf{L_1} = 17$ astrophysical and instrumental emission lines each

[6]Please see Appendix E. Spatial Distribution of Fitted Parameters for a illustration of the spatial distribution related to the parameters of the continuum emission.

[7]Please see Arnaud (51) and/or https://heasarc.nasa.gov/xanadu/xspec/manual/node208.html. The spectral component *powerlaw* is defined as $\mathrm{N}_{pow}^{\mathbf{D}} \cdot \left(E^{\mathbf{D}}\right)^{-\Gamma^{\mathbf{D}}}$.

[8]Please see Arnaud (51) and/or https://heasarc.nasa.gov/xanadu/xspec/manual/XSmodelBremss.html. In essence, *XSPEC* applies a ploynomial fit of a thermal bremsstrahlung spectrum according to Kellogg et al. (54) which is based on numerical values published by Karzas & Latter (55). The normalisation $\mathrm{N}_{bremss}^{\mathbf{D}} = \left(\frac{3.02\cdot 10^{-15}}{4\,\pi\,D^2}\right)\int n_e\, n_I\, dV$ is dependent on an electron density n_e [cm^{-3}], an ion density n_I [cm^{-3}], and a distance to the source of the bremsstrahlung D [cm]. The abundance of helium was set to 0.085 times the abundance of hydrogen.

[9]Please see Arnaud (51) and/or https://heasarc.nasa.gov/xanadu/xspec/manual/node258.html. The photo-electric absorption applied here is described by the functional expression $\exp\left(-\mathrm{n}_{\mathrm{H};i}^{\mathbf{D}}\cdot\sigma\left(E^{\mathbf{D}}\right)\right)$, wherein $\sigma(E)$ denotes a photo-electric cross-section according to Anders & Ebihara (53).

of Gaussian shape *gauss*[10] dependent on the mean energy $E^{\mathbf{D_1}}_{gauss;il}$, the intrinsic line width $\sigma^{\mathbf{D_1}}_{gauss;il}$ and the flux normalisation $F^{\mathbf{D_1}}_{gauss;il}$ of a lth emission line. The respective units of the above values are listed in tables 5.1 and 5.2.
The fitted Gaussian lines accounting for the line emission at energies of 0.58 keV (O VII), 0.67 keV (O VIII), 0.76 keV (Fe XVII and/or O VIII), 0.84 keV (Fe XVII), 0.93 keV (Ne IX), 1.04 keV (Ne IX and/or Ne X) and 1.37 keV (Mg XI) are considered to be of astrophysical origins (12, 14, 15) while Gaussian emission lines fitted at energies of 1.49 keV (Al-K$_\alpha$), 4.54 keV (Ti-K$_\alpha$), 5.43 keV (Cr-K$_\alpha$), 6.42 keV (Fe-K$_\alpha$), 7.48 keV (Ni-K$_\alpha$), 8.04 keV (Cu-K$_\alpha$), 8.08 keV (Cu-K$_\alpha$), 8.63 keV (Cu-K$_\beta$ and/or Zn-K$_\alpha$), 8.90 keV (Cu-K$_\alpha$) and 9.58 keV (Zn-K$_\alpha$) presumably and mainly have instrumental origins (41, 47, 63, 64, 65).
All $\mathbf{N_1} = 33$ data sets listed in table 4.1 were fitted simultaneously in an energy range from 0.38 keV to 16.5 keV by the application of a fitting procedure using the program XSPEC. The quality of the resulting best-fit of the data sets contained in $\mathbf{D_1}$ reaches a goodness-of-fit of

$$\chi^2_0(m^{\mathbf{D_1}}_0) = 105491.6, \tag{5.28}$$

while having 105700 degrees of freedom (d.o.f.) and a p-value $= 0.6743$.

Nullhypothesis model of $\mathbf{D_2}$. The nullhypothesis model which fits the data sets or spectra of $\mathbf{D_2}$ is defined as,

$$m^{\mathbf{D_2}}_0\left(\eta; E^{\mathbf{D_2}}\right) = \tag{5.29}$$

$$m^{\mathbf{D_2}}_0\Bigg(\mathit{wabs}\left(\mathrm{n}^{\mathbf{D_2}}_{\mathrm{H};i}, E^{\mathbf{D_2}}\right), \mathit{pow}\left(\Gamma^{\mathbf{D_2}}_i, \mathrm{N}^{\mathbf{D_2}}_{pow;i}, E^{\mathbf{D_2}}\right), \mathit{bremss}\left(\mathrm{T}^{\mathbf{D_2}}_i, \mathrm{N}^{\mathbf{D_2}}_{bremss;i}, E^{\mathbf{D_2}}\right),$$
$$\mathit{gauss}\left(E^{\mathbf{D_2}}_{gauss;ij}, \sigma^{\mathbf{D_2}}_{ij}, F^{\mathbf{D_2}}_{gauss;ij}, E^{\mathbf{D_2}}\right)\Bigg) =$$
$$\sum_{i=1}^{\mathbf{N}}\Bigg(\underbrace{\mathit{wabs}\left(\mathrm{n}^{\mathbf{D_2}}_{\mathrm{H};i}, E^{\mathbf{D_2}}\right)\cdot\left(\mathit{pow}\left(\Gamma^{\mathbf{D_2}}_i, \mathrm{N}^{\mathbf{D_2}}_{pow;i}, E^{\mathbf{D_2}}\right) + \mathit{bremss}\left(\mathrm{T}^{\mathbf{D_2}}_i, \mathrm{N}^{\mathbf{D_2}}_{bremss;i}, E^{\mathbf{D_2}}\right)\right)}_{\text{continuum emission}}$$
$$+\underbrace{\left(\sum_{l=1}^{\mathbf{L_2}}\mathit{gauss}\left(E^{\mathbf{D_2}}_{gauss;il}, \sigma^{\mathbf{D_2}}_{gauss;il}, F^{\mathbf{D_2}}_{gauss;il}, E^{\mathbf{D_2}}\right)\right)}_{\text{additional component or line emission}}\Bigg). \tag{5.30}$$

[10]Please see Arnaud (51) and/or https://heasarc.nasa.gov/xanadu/xspec/manual/node173.html. The functional expression of the spectral components *gauss* are similar to equations 2.39 or 5.33.

Firstly, the continuum emission[11] of an ith data set of $\mathbf{D_2}$ is modelled as a powerlaw *pow* dependent on a dimensionless photon index $\Gamma_i^{\mathbf{D_2}}$ and a normalisation $\mathrm{N}_{pow;i}^{\mathbf{D_2}}$ as well as a thermal bremsstrahlung spectrum *bremss* dependent on a temperature $\mathrm{T}_i^{\mathbf{D_2}}$ and a normalisation $\mathrm{N}_{bremss;i}^{\mathbf{D_2}}$, both jointly attenuated by a photoelectric absorption component denoted as *wabs*, dependent on a hydrogen column $\mathrm{n}_{\mathrm{H};i}^{\mathbf{D_2}}$. Secondly, the line emission of such an ith data set is modelled by the sum of $\mathbf{L_2} = 19$ astrophysical and instrumental emission lines for $\mathbf{D_2}$, respectively, each of Gaussian shape *gauss* dependent on the mean energy $E_{gauss;il}^{\mathbf{D_2}}$, the intrinsic line width $\sigma_{gauss;il}^{\mathbf{D_2}}$ and the flux normalisation $F_{gauss;il}^{\mathbf{D_2}}$ of a lth emission line. The respective units of the above values are listed in tables 5.3 and 5.4.
The fitted Gaussian lines accounting for the line emission at energies of 0.58 keV (O VII), 0.67 keV (O VIII), 0.75 keV (Fe XVII and/or O VIII), 0.83 keV (Fe XVII), 0.92 keV (Ne IX), 1.03 keV (Ne IX and/or Ne X), 1.38 keV (Mg XI) and 2.35 keV (S_α/S_β) are considered to be of astrophysical origins (12, 13, 14, 15) while the Gaussian emission lines fitted at energies of 1.49 keV (Al-K_α), 1.87 keV (Si-K_α), 4.54 keV (Ti-K_α), 5.42 keV (Cr-K_α), 6.40 keV (Fe-K_α), 7.47 keV (Ni-K_α), 8.03 keV (Cu-K_α), 8.19 keV (Cu-K_α), 8.57 keV (Cu-K_β and/or Zn-K_α), 8.88 keV (Cu-K_α) and 9.57 keV (Zn-K_α) presumably and mainly have instrumental origins (41, 47, 63, 64, 65).
All $\mathbf{N_2} = 23$ data sets listed in table 4.2 were fitted simultaneously in an energy range from 0.38 keV to 12 keV by the application of a fitting procedure using the program XSPEC. The quality of the resulting best-fit of the data sets contained in $\mathbf{D_2}$ reaches a goodness-of-fit of

$$\chi_0^2(m_0^{\mathbf{D_2}}) = 52519.26, \tag{5.31}$$

while having 52529 degrees of freedom (d.o.f.) and a p-value $= 0.5111$.

During the fitting procedure all astrophysical components of the models $m_0^{\mathbf{D_2}}$ were treated independently, wherein any systematical differences by independently fitting the astrophysical parameters even for observations of the same fields of view were investigated. The resulting differences are well consistent with the assumed statistical uncertainties, whereby no additional systematic uncertainties had to be considered.
The above goodness-of-fit values indicate stable and good fits. The intrinsic widths $\sigma_{gauss;il}^{\mathbf{D}}$ of the astrophysical lines enclosed in the spectral models $m_0^{\mathbf{D_1}}$

[11] Please see Appendix E. Spatial Distribution of Fitted Parameters for a illustration of the spatial distribution related to the parameters of the continuum emission.

and $m_0^{\mathbf{D_2}}$ were fixed to zero[12] in contrast to the instrumental Gaussian emission lines. The forward-folding of the model with the related response matrix during the fitting process expands the corresponding line widths $\sigma_{gauss;il}^{\mathbf{D}}$ to the energy-dependent spectral resolutions. Some of the astrophysical lines were not detected in all data sets as listed in tables 5.1, 5.2, 5.3 as well as 5.4.

[12] An unfolded Gaussian line width of zero is interpreted as a width of 0.005 keV related to one energy channel by XSPEC.

$\mathbf{D_1}$

Index	Object	ObsId	$\omega_{\gamma;i}^{\mathbf{D_1},\mathrm{ISO}}$	$\omega_{\gamma;i}^{\mathbf{D_1},\mathrm{NFW}}$	$N_{\mathrm{src};i}^{\mathrm{X\text{-}ray}}$	$N_{\mathrm{INST};i}$	Absorption normalisation	Bremsstr.	Bremsstr. normalisation	Powerlaw	Powerlaw
							$\mathrm{n}_{\mathrm{H},i}^{\mathbf{D_1}}$	$\mathrm{T}_i^{\mathbf{D_1}}$	$\mathrm{N}_{bremss,i}^{\mathbf{D_1}}$	$\Gamma_i^{\mathbf{D_1}}$	$\mathrm{N}_{pow,i}^{\mathbf{D_1}}$
i					%		$10^{21}\ \frac{\mathrm{atoms}}{\mathrm{cm}^2}$	10^{-1} keV	$10^{-4}\ \mathrm{cm}^{-3}$		$\frac{10^{-4}\ \mathrm{photons}}{\mathrm{keV\,cm^2\,s}}$ at 1 keV
1	V4046 Sgr	0604860401	0.11	0.11	1.17	0.13	1.90 ± 0.38	2.71 ± 0.29	36.72 ± 14.96	1.85 ± 0.07	10.77 ± 0.86
2	V4046 Sgr	0604860301	0.10	0.11	1.23	0.18	1.14 ± 0.23	3.29 ± 0.30	10.78 ± 2.90	1.65 ± 0.07	6.38 ± 0.49
3	V4046 Sgr	0604860201	0.09	0.09	1.18	0.15	1.23 ± 0.21	3.23 ± 0.27	29.60 ± 7.55	1.46 ± 0.06	13.51 ± 0.96
4	V4633 Sgr	0653550301	0.09	0.09	0.07	0.09	3.23 ± 0.62	2.78 ± 0.35	90.35 ± 47.53	1.85 ± 0.07	15.75 ± 1.39
5	PDS 456	0501580201	0.07	0.06	2.10	0.13	3.39 ± 1.05	4.31 ± 0.76	4.87 ± 2.42	1.51 ± 0.07	4.54 ± 0.43
6	PDS 456	0501580101	0.06	0.05	3.34	0.08	2.76 ± 0.96	5.13 ± 0.98	3.33 ± 1.33	1.49 ± 0.09	4.61 ± 0.60
7	VV Sco	0555650201	0.06	0.05	0.68	0.08	0.92 ± 0.31	3.78 ± 0.56	10.36 ± 3.82	1.48 ± 0.10	8.69 ± 1.07
8	VV Sco	0555650301	0.05	0.04	0.69	0.11	3.09 ± 1.94	2.22 ± 0.84	–	2.06 ± 0.14	4.83 ± 0.70
9	CDFS	0604961101	0.02	0.02	0.07	0.13	–	0.78 ± 0.19	–	1.83 ± 0.04	5.17 ± 0.09
10	CDFS	0555780501	0.02	0.02	0.12	0.17	–	1.60 ± 0.40	3.93 ± 2.04	1.71 ± 0.06	6.36 ± 0.24
11	CDFS	0604961001	0.02	0.02	0.26	0.17	–	1.47 ± 0.55	2.07 ± 1.79	1.95 ± 0.07	3.20 ± 0.13
12	CDFS	0555781001	0.02	0.02	0.16	0.11	–	1.64 ± 0.41	2.06 ± 1.09	1.62 ± 0.05	3.53 ± 0.12
13	CDFS	0555780701	0.02	0.02	0.26	0.17	–	1.43 ± 0.40	2.73 ± 1.91	1.74 ± 0.05	3.35 ± 0.11
14	CNOC2 Field 2	0603590201	0.02	0.02	0.03	0.06	–	1.85 ± 0.25	3.96 ± 0.94	1.71 ± 0.06	5.01 ± 0.22
15	CDFS	0604961801	0.02	0.02	0.10	0.11	–	0.80 ± 0.17	–	1.74 ± 0.04	3.45 ± 0.06
16	CNOC2 Field 1	0603590101	0.02	0.02	0.61	0.06	–	1.31 ± 0.35	7.47 ± 5.91	1.81 ± 0.06	4.14 ± 0.16
17	XX Cha	0300270201	0.02	0.02	2.13	0.10	–	11.48 ± 7.70	0.51 ± 0.36	1.62 ± 0.09	3.57 ± 0.73

To be continued on the next page.

$\mathbf{D_1}$											
Index	Object	ObsId	$\omega_{\gamma;i}^{\mathbf{D_1},\mathrm{ISO}}$	$\omega_{\gamma;i}^{\mathbf{D_1},\mathrm{NFW}}$	$N_{\mathrm{src}}^{\mathrm{X\text{-}ray}}$	N_{INST}	Absorption normalisation	Bremsstr.	Bremsstr. normalisation	Powerlaw	Powerlaw
							$\mathrm{n}_{\mathrm{H},i}^{\mathbf{D_1}}$	$\mathrm{T}_i^{\mathbf{D_1}}$	$\mathrm{N}_{bremss,i}^{\mathbf{D_1}}$	$\Gamma_i^{\mathbf{D_1}}$	$\mathrm{N}_{pow,i}^{\mathbf{D_1}}$
i					%		$10^{21}\ \frac{\mathrm{atoms}}{\mathrm{cm}^2}$	10^{-1} keV	$10^{-4}\ \mathrm{cm}^{-3}$		$\frac{10^{-4}\ \mathrm{photons}}{\mathrm{keV\ cm^2\ s}}$ at 1 keV
18	CDFS	0604961201	0.02	0.02	0.08	0.10	–	1.00 ± 0.22	10.25 ± 9.00	1.71 ± 0.04	3.37 ± 0.07
19	CDFS	0555782301	0.02	0.02	0.12	0.15	–	1.12 ± 0.33	–	1.75 ± 0.04	3.35 ± 0.08
20	CDFS	0555780301	0.02	0.02	0.14	0.09	–	0.62 ± 0.12	–	1.79 ± 0.04	4.64 ± 0.10
21	CDFS	0604960901	0.02	0.02	0.09	0.14	–	0.93 ± 0.30	–	1.99 ± 0.05	4.12 ± 0.10
22	CDFS	0108060701	0.02	0.02	0.18	0.06	–	1.72 ± 0.24	5.18 ± 1.34	1.88 ± 0.08	3.65 ± 0.20
23	CDFS	0555780601	0.02	0.02	0.11	0.14	–	0.70 ± 0.29	–	1.93 ± 0.04	3.44 ± 0.07
24	CDFS	0555780801	0.01	0.02	0.13	0.08	–	0.52 ± 0.13	–	1.84 ± 0.04	3.02 ± 0.07
25	CDFS	0555780901	0.01	0.01	0.12	0.08	–	1.39 ± 0.40	3.13 ± 2.34	1.69 ± 0.05	3.22 ± 0.11
26	CDFS	0604960301	0.01	0.01	0.11	0.12	–	1.76 ± 0.36	2.23 ± 0.91	1.51 ± 0.04	3.85 ± 0.13
27	CDFS	0555780201	0.01	0.01	0.15	0.13	–	1.17 ± 0.34	6.87 ± 6.58	1.60 ± 0.04	5.01 ± 0.13
28	CDFS	0604960601	0.01	0.01	0.11	0.11	–	1.71 ± 0.49	4.34 ± 2.47	1.66 ± 0.07	7.47 ± 0.34
29	CDFS	0555780101	0.01	0.01	0.17	0.11	–	1.43 ± 0.48	2.48 ± 2.06	1.76 ± 0.06	3.13 ± 0.12
30	CDFS	0604960201	0.01	0.01	0.12	0.07	–	1.71 ± 0.46	3.05 ± 1.68	1.53 ± 0.05	5.56 ± 0.21
31	CDFS	0604960701	0.01	0.01	0.15	0.06	–	0.87 ± 0.23	–	1.71 ± 0.05	3.16 ± 0.10
32	CDFS	0604960501	0.01	0.01	0.11	0.09	–	0.39 ± 0.11	–	2.09 ± 0.06	3.93 ± 0.10
33	CDFS	0108061901	0.01	0.01	0.10	0.03	–	2.38 ± 0.27	2.51 ± 0.35	1.59 ± 0.10	2.66 ± 0.23

Table 5.1: The table above lists the best-fit values of the absorbed bremsstrahlung and the powerlaw components of the nullhypothesis model $m_0^{\mathbf{D_1}}$. The observation identifications (ObsId) and the weightings $\omega_{\gamma;i}^{\mathbf{D_1},\mathrm{ISO}}$ and $\omega_{\gamma;i}^{\mathbf{D_1},\mathrm{NFW}}$ of the additional line with respect to the alternative hypothesis models $m_1^{\mathbf{D_1},\mathrm{ISO}}$ according to equation 5.36 and $m_1^{\mathbf{D_1},\mathrm{NFW}}$ according to equation 5.38 are also listed.

$\mathbf{D_1}$											
						E_{gauss} [keV]	0.58	0.67	0.76	0.84	0.93
						Phys. origin	O VII	O VIII	Fe XVII	Fe XVII	Ne IX
Index	Object	ObsId	$\omega_{\gamma;i}^{\mathbf{D_1},\mathrm{ISO}}$	$\omega_{\gamma;i}^{\mathbf{D_1},\mathrm{NFW}}$	$N_{\mathrm{src}}^{\mathrm{X\text{-}ray}}$	N_{INST}	$F_{gauss}^{\mathbf{D_1}}$	$F_{gauss}^{\mathbf{D_1}}$	$F_{gauss}^{\mathbf{D_1}}$	$F_{gauss}^{\mathbf{D_1}}$	$F_{gauss}^{\mathbf{D_1}}$
i					%		$\frac{10^{-4}}{\mathrm{cm}^2\,\mathrm{s}}$	$\frac{10^{-4}}{\mathrm{cm}^2\,\mathrm{s}}$	$\frac{10^{-4}}{\mathrm{cm}^2\,\mathrm{s}}$	$\frac{10^{-4}}{\mathrm{cm}^2\,\mathrm{s}}$	$\frac{10^{-4}}{\mathrm{cm}^2\,\mathrm{s}}$
1	V4046 Sgr	0604860401	0.11	0.11	1.17	0.13	6.64 ± 0.13	4.69 ± 0.12	3.43 ± 0.12	4.15 ± 0.10	2.60 ± 0.07
2	V4046 Sgr	0604860301	0.10	0.11	1.23	0.18	4.51 ± 0.09	3.27 ± 0.07	2.36 ± 0.07	2.90 ± 0.06	1.83 ± 0.04
3	V4046 Sgr	0604860201	0.09	0.09	1.18	0.15	9.64 ± 0.20	6.88 ± 0.18	4.94 ± 0.16	6.13 ± 0.14	3.93 ± 0.10
4	V4633 Sgr	0653550301	0.09	0.09	0.07	0.09	9.33 ± 0.23	6.73 ± 0.17	6.48 ± 0.17	7.40 ± 0.17	4.52 ± 0.12
5	PDS 456	0501580201	0.07	0.06	2.10	0.13	1.44 ± 0.07	1.30 ± 0.06	1.25 ± 0.05	1.44 ± 0.04	0.90 ± 0.03
6	PDS 456	0501580101	0.06	0.05	3.34	0.08	1.43 ± 0.07	1.28 ± 0.06	1.23 ± 0.05	1.48 ± 0.04	0.86 ± 0.03
7	VV Sco	0555650201	0.06	0.05	0.68	0.08	6.83 ± 0.18	5.74 ± 0.16	4.18 ± 0.14	4.25 ± 0.12	2.56 ± 0.09
8	VV Sco	0555650301	0.05	0.04	0.69	0.11	2.91 ± 0.10	2.37 ± 0.08	1.64 ± 0.10	1.66 ± 0.09	1.01 ± 0.05
9	CDFS	0604961101	0.02	0.02	0.07	0.13	1.19 ± 0.09	0.33 ± 0.05	–	0.04 ± 0.03	–
10	CDFS	0555780501	0.02	0.02	0.12	0.17	1.40 ± 0.10	0.19 ± 0.07	–	–	0.05 ± 0.04
11	CDFS	0604961001	0.02	0.02	0.26	0.17	0.87 ± 0.06	0.38 ± 0.05	–	0.06 ± 0.02	0.06 ± 0.02
12	CDFS	0555781001	0.02	0.02	0.16	0.11	0.79 ± 0.06	0.07 ± 0.04	–	–	0.02 ± 0.02
13	CDFS	0555780701	0.02	0.02	0.26	0.17	0.69 ± 0.06	0.12 ± 0.04	–	0.04 ± 0.02	0.02 ± 0.02
14	CNOC2 Field 2	0603590201	0.02	0.02	0.03	0.06	2.04 ± 0.09	0.41 ± 0.06	–	–	0.08 ± 0.03
15	CDFS	0604961801	0.02	0.02	0.10	0.11	0.82 ± 0.06	0.19 ± 0.03	–	0.05 ± 0.02	–
16	CNOC2 Field 1	0603590101	0.02	0.02	0.61	0.06	1.83 ± 0.13	0.42 ± 0.08	0.06 ± 0.05	–	0.08 ± 0.03
17	XX Cha	0300270201	0.02	0.02	2.13	0.10	0.98 ± 0.09	0.41 ± 0.09	0.17 ± 0.07	0.29 ± 0.06	0.28 ± 0.05

To be continued on the next page.

$\mathbf{D_1}$

						E_{gauss} [keV]	0.58	0.67	0.76	0.84	0.93
						Phys. origin	O VII	O VIII	Fe XVII	Fe XVII	Ne IX
Index	Object	ObsId	$\omega_{\gamma;i}^{\mathbf{D_1},\mathrm{ISO}}$	$\omega_{\gamma;i}^{\mathbf{D_1},\mathrm{NFW}}$	$N_{\mathrm{src}}^{\text{X-ray}}$	N_{INST}	$F_{gauss}^{\mathbf{D_1}}$	$F_{gauss}^{\mathbf{D_1}}$	$F_{gauss}^{\mathbf{D_1}}$	$F_{gauss}^{\mathbf{D_1}}$	$F_{gauss}^{\mathbf{D_1}}$
i					%		$\frac{10^{-4}}{\mathrm{cm}^2\,\mathrm{s}}$	$\frac{10^{-4}}{\mathrm{cm}^2\,\mathrm{s}}$	$\frac{10^{-4}}{\mathrm{cm}^2\,\mathrm{s}}$	$\frac{10^{-4}}{\mathrm{cm}^2\,\mathrm{s}}$	$\frac{10^{-4}}{\mathrm{cm}^2\,\mathrm{s}}$
18	CDFS	0604961201	0.02	0.02	0.08	0.10	0.81 ± 0.06	0.17 ± 0.04	–	0.06 ± 0.02	–
19	CDFS	0555782301	0.02	0.02	0.12	0.15	0.73 ± 0.07	0.15 ± 0.04	–	0.06 ± 0.02	–
20	CDFS	0555780301	0.02	0.02	0.14	0.09	1.03 ± 0.07	0.23 ± 0.05	–	0.04 ± 0.03	–
21	CDFS	0604960901	0.02	0.02	0.09	0.14	1.13 ± 0.08	0.35 ± 0.05	–	0.07 ± 0.03	0.04 ± 0.02
22	CDFS	0108060701	0.02	0.02	0.18	0.06	1.48 ± 0.08	0.22 ± 0.06	–	0.10 ± 0.03	–
23	CDFS	0555780601	0.02	0.02	0.11	0.14	0.74 ± 0.06	0.16 ± 0.04	–	–	0.03 ± 0.02
24	CDFS	0555780801	0.01	0.02	0.13	0.08	0.73 ± 0.05	0.14 ± 0.03	–	0.03 ± 0.02	–
25	CDFS	0555780901	0.01	0.01	0.12	0.08	0.79 ± 0.07	0.17 ± 0.05	–	0.03 ± 0.03	0.05 ± 0.02
26	CDFS	0604960301	0.01	0.01	0.11	0.12	0.70 ± 0.06	–	–	0.04 ± 0.03	0.03 ± 0.02
27	CDFS	0555780201	0.01	0.01	0.15	0.13	0.94 ± 0.09	0.22 ± 0.06	–	0.07 ± 0.03	0.05 ± 0.03
28	CDFS	0604960601	0.01	0.01	0.11	0.11	1.44 ± 0.14	0.20 ± 0.11	–	–	–
29	CDFS	0555780101	0.01	0.01	0.17	0.11	0.66 ± 0.07	0.07 ± 0.05	–	0.06 ± 0.03	0.03 ± 0.02
30	CDFS	0604960201	0.01	0.01	0.12	0.07	1.05 ± 0.10	–	–	0.09 ± 0.05	–
31	CDFS	0604960701	0.01	0.01	0.15	0.06	0.85 ± 0.08	0.22 ± 0.05	–	0.06 ± 0.03	0.10 ± 0.03
32	CDFS	0604960501	0.01	0.01	0.11	0.09	1.33 ± 0.08	0.19 ± 0.06	–	–	–
33	CDFS	0108061901	0.01	0.01	0.10	0.03	1.46 ± 0.07	0.22 ± 0.05	–	–	–

To be continued on the next page.

$\mathbf{D_1}$

						E_{gauss} [keV]	1.04	1.37	1.49	4.54	5.43
						Phys. origin	Ne IX	Mg XI	Al-K$_\alpha$	Si-K$_\alpha$	Cr-K$_\alpha$
Index	Object	ObsId	$\omega_{\gamma;i}^{\mathbf{D_1},\mathrm{ISO}}$	$\omega_{\gamma;i}^{\mathbf{D_1},\mathrm{NFW}}$	$N_{\mathrm{src}}^{\text{X-ray}}$	N_{INST}	$F_{gauss}^{\mathbf{D_1}}$	$F_{gauss}^{\mathbf{D_1}}$	$F_{gauss}^{\mathbf{D_1}}$	$F_{gauss}^{\mathbf{D_1}}$	$F_{gauss}^{\mathbf{D_1}}$
i					%		$\frac{10^{-4}}{\mathrm{cm^2\,s}}$	$\frac{10^{-4}}{\mathrm{cm^2\,s}}$	$\frac{10^{-4}}{\mathrm{cm^2\,s}}$	$\frac{10^{-4}}{\mathrm{cm^2\,s}}$	$\frac{10^{-4}}{\mathrm{cm^2\,s}}$
1	V4046 Sgr	0604860401	0.11	0.11	1.17	0.13	1.04 ± 0.05	0.29 ± 0.03	2.78 ± 0.03	0.09 ± 0.02	0.28 ± 0.02
2	V4046 Sgr	0604860301	0.10	0.11	1.23	0.18	0.73 ± 0.03	0.18 ± 0.02	1.75 ± 0.02	0.06 ± 0.01	0.16 ± 0.02
3	V4046 Sgr	0604860201	0.09	0.09	1.18	0.15	1.54 ± 0.08	0.32 ± 0.04	3.86 ± 0.05	0.10 ± 0.04	0.49 ± 0.04
4	V4633 Sgr	0653550301	0.09	0.09	0.07	0.09	2.06 ± 0.10	0.34 ± 0.05	3.27 ± 0.06	0.12 ± 0.03	0.38 ± 0.04
5	PDS 456	0501580201	0.07	0.06	2.10	0.13	0.32 ± 0.03	0.09 ± 0.02	1.37 ± 0.02	–	0.14 ± 0.01
6	PDS 456	0501580101	0.06	0.05	3.34	0.08	0.33 ± 0.03	0.09 ± 0.02	1.36 ± 0.02	0.06 ± 0.01	0.14 ± 0.02
7	VV Sco	0555650201	0.06	0.05	0.68	0.08	0.83 ± 0.07	0.29 ± 0.04	3.43 ± 0.05	0.08 ± 0.03	0.37 ± 0.04
8	VV Sco	0555650301	0.05	0.04	0.69	0.11	0.32 ± 0.04	0.15 ± 0.02	1.55 ± 0.02	0.07 ± 0.02	0.18 ± 0.02
9	CDFS	0604961101	0.02	0.02	0.07	0.13	–	0.18 ± 0.02	2.94 ± 0.03	0.10 ± 0.02	0.32 ± 0.02
10	CDFS	0555780501	0.02	0.02	0.12	0.17	–	0.18 ± 0.03	3.42 ± 0.04	0.18 ± 0.03	0.40 ± 0.04
11	CDFS	0604961001	0.02	0.02	0.26	0.17	–	0.11 ± 0.01	1.82 ± 0.02	0.04 ± 0.02	0.21 ± 0.02
12	CDFS	0555781001	0.02	0.02	0.16	0.11	–	0.09 ± 0.01	1.83 ± 0.02	0.09 ± 0.02	0.18 ± 0.02
13	CDFS	0555780701	0.02	0.02	0.26	0.17	–	0.09 ± 0.01	1.80 ± 0.02	0.08 ± 0.01	0.16 ± 0.02
14	CNOC2 Field 2	0603590201	0.02	0.02	0.03	0.06	–	0.13 ± 0.02	2.03 ± 0.03	0.06 ± 0.02	0.21 ± 0.02
15	CDFS	0604961801	0.02	0.02	0.10	0.11	–	0.08 ± 0.01	1.76 ± 0.02	0.06 ± 0.02	0.20 ± 0.02
16	CNOC2 Field 1	0603590101	0.02	0.02	0.61	0.06	–	0.09 ± 0.02	1.63 ± 0.03	0.06 ± 0.02	0.14 ± 0.02
17	XX Cha	0300270201	0.02	0.02	2.13	0.10	0.18 ± 0.04	0.08 ± 0.02	1.37 ± 0.03	0.06 ± 0.02	0.17 ± 0.02

To be continued on the next page.

$\mathbf{D_1}$											
						E_{gauss} [keV]	1.04	1.37	1.49	4.54	5.43
						Phys. origin	Ne IX	Mg XI	Al-K$_\alpha$	Si-K$_\alpha$	Cr-K$_\alpha$
Index	Object	ObsId	$\omega_{\gamma;i}^{\mathbf{D_1},\mathrm{ISO}}$	$\omega_{\gamma;i}^{\mathbf{D_1},\mathrm{NFW}}$	$N_{\mathrm{src}}^{\mathrm{X\text{-}ray}}$	N_{INST}	$F_{gauss}^{\mathbf{D_1}}$	$F_{gauss}^{\mathbf{D_1}}$	$F_{gauss}^{\mathbf{D_1}}$	$F_{gauss}^{\mathbf{D_1}}$	$F_{gauss}^{\mathbf{D_1}}$
i					%		$\frac{10^{-4}}{\mathrm{cm^2\,s}}$	$\frac{10^{-4}}{\mathrm{cm^2\,s}}$	$\frac{10^{-4}}{\mathrm{cm^2\,s}}$	$\frac{10^{-4}}{\mathrm{cm^2\,s}}$	$\frac{10^{-4}}{\mathrm{cm^2\,s}}$
18	CDFS	0604961201	0.02	0.02	0.08	0.10	–	0.08 ± 0.01	1.76 ± 0.02	0.06 ± 0.01	0.19 ± 0.02
19	CDFS	0555782301	0.02	0.02	0.12	0.15	–	0.08 ± 0.01	1.78 ± 0.02	0.08 ± 0.02	0.19 ± 0.02
20	CDFS	0555780301	0.02	0.02	0.14	0.09	–	0.13 ± 0.02	2.23 ± 0.03	0.11 ± 0.02	0.21 ± 0.02
21	CDFS	0604960901	0.02	0.02	0.09	0.14	–	0.12 ± 0.02	2.12 ± 0.03	0.06 ± 0.02	0.21 ± 0.02
22	CDFS	0108060701	0.02	0.02	0.18	0.06	–	0.12 ± 0.02	1.30 ± 0.03	0.05 ± 0.02	0.24 ± 0.02
23	CDFS	0555780601	0.02	0.02	0.11	0.14	–	0.09 ± 0.02	1.84 ± 0.02	0.06 ± 0.02	0.19 ± 0.02
24	CDFS	0555780801	0.01	0.02	0.13	0.08	–	0.07 ± 0.01	1.60 ± 0.02	0.07 ± 0.01	0.17 ± 0.02
25	CDFS	0555780901	0.01	0.01	0.12	0.08	–	0.09 ± 0.02	1.75 ± 0.02	0.09 ± 0.02	0.18 ± 0.02
26	CDFS	0604960301	0.01	0.01	0.11	0.12	–	0.08 ± 0.02	1.73 ± 0.02	0.05 ± 0.02	0.18 ± 0.02
27	CDFS	0555780201	0.01	0.01	0.15	0.13	–	0.11 ± 0.02	2.15 ± 0.03	0.09 ± 0.02	0.21 ± 0.02
28	CDFS	0604960601	0.01	0.01	0.11	0.11	–	0.20 ± 0.04	4.15 ± 0.06	0.15 ± 0.05	0.49 ± 0.05
29	CDFS	0555780101	0.01	0.01	0.17	0.11	–	0.07 ± 0.02	1.52 ± 0.02	0.04 ± 0.02	0.15 ± 0.02
30	CDFS	0604960201	0.01	0.01	0.12	0.07	–	0.12 ± 0.03	2.72 ± 0.04	0.07 ± 0.03	0.26 ± 0.03
31	CDFS	0604960701	0.01	0.01	0.15	0.06	–	0.10 ± 0.02	1.87 ± 0.03	0.06 ± 0.02	0.22 ± 0.02
32	CDFS	0604960501	0.01	0.01	0.11	0.09	–	0.12 ± 0.02	2.39 ± 0.03	0.07 ± 0.02	0.21 ± 0.03
33	CDFS	0108061901	0.01	0.01	0.10	0.03	–	0.10 ± 0.02	0.91 ± 0.02	0.04 ± 0.02	0.14 ± 0.02

To be continued on the next page.

$\mathbf{D_1}$											
						E_{gauss} [keV]	6.42	7.48	8.04	8.08	8.63
						Phys. origin	Fe-K$_\alpha$	Ni-K$_\alpha$	Cu-K$_\alpha$	Cu-K$_\alpha$	Cu-K$_\beta$/Zn-K$_\alpha$
Index	Object	ObsId	$\omega_{\gamma;i}^{\mathbf{D_1},\mathrm{ISO}}$	$\omega_{\gamma;i}^{\mathbf{D_1},\mathrm{NFW}}$	$N_{\mathrm{src}}^{\mathrm{X\text{-}ray}}$	N_{INST}	$F_{gauss}^{\mathbf{D_1}}$	$F_{gauss}^{\mathbf{D_1}}$	$F_{gauss}^{\mathbf{D_1}}$	$F_{gauss}^{\mathbf{D_1}}$	$F_{gauss}^{\mathbf{D_1}}$
i					%		$\frac{10^{-4}}{\mathrm{cm}^2\,\mathrm{s}}$	$\frac{10^{-4}}{\mathrm{cm}^2\,\mathrm{s}}$	$\frac{10^{-4}}{\mathrm{cm}^2\,\mathrm{s}}$	$\frac{10^{-4}}{\mathrm{cm}^2\,\mathrm{s}}$	$\frac{10^{-4}}{\mathrm{cm}^2\,\mathrm{s}}$
1	V4046 Sgr	0604860401	0.11	0.11	1.17	0.13	0.18 ± 0.03	3.43 ± 0.05	22.17 ± 0.24	7.30 ± 0.24	4.12 ± 0.10
2	V4046 Sgr	0604860301	0.10	0.11	1.23	0.18	0.13 ± 0.02	2.04 ± 0.03	13.97 ± 0.16	4.97 ± 0.16	2.66 ± 0.07
3	V4046 Sgr	0604860201	0.09	0.09	1.18	0.15	0.19 ± 0.05	5.21 ± 0.09	34.04 ± 0.40	12.01 ± 0.40	6.36 ± 0.16
4	V4633 Sgr	0653550301	0.09	0.09	0.07	0.09	0.25 ± 0.04	4.03 ± 0.07	25.99 ± 0.34	10.23 ± 0.34	5.08 ± 0.14
5	PDS 456	0501580201	0.07	0.06	2.10	0.13	0.10 ± 0.01	1.65 ± 0.03	11.22 ± 0.13	3.46 ± 0.13	2.07 ± 0.05
6	PDS 456	0501580101	0.06	0.05	3.34	0.08	0.09 ± 0.02	1.67 ± 0.03	11.29 ± 0.13	3.15 ± 0.13	2.05 ± 0.06
7	VV Sco	0555650201	0.06	0.05	0.68	0.08	0.24 ± 0.04	3.80 ± 0.07	25.81 ± 0.33	8.65 ± 0.33	4.89 ± 0.14
8	VV Sco	0555650301	0.05	0.04	0.69	0.11	0.10 ± 0.02	1.71 ± 0.03	11.80 ± 0.15	3.42 ± 0.15	2.18 ± 0.06
9	CDFS	0604961101	0.02	0.02	0.07	0.13	0.16 ± 0.02	3.13 ± 0.05	21.29 ± 0.24	7.70 ± 0.24	4.03 ± 0.10
10	CDFS	0555780501	0.02	0.02	0.12	0.17	0.24 ± 0.04	4.45 ± 0.07	29.91 ± 0.34	9.37 ± 0.34	5.74 ± 0.14
11	CDFS	0604961001	0.02	0.02	0.26	0.17	0.10 ± 0.02	1.98 ± 0.03	13.75 ± 0.17	5.03 ± 0.17	2.60 ± 0.07
12	CDFS	0555781001	0.02	0.02	0.16	0.11	0.12 ± 0.02	1.99 ± 0.03	14.47 ± 0.16	4.64 ± 0.16	2.70 ± 0.07
13	CDFS	0555780701	0.02	0.02	0.26	0.17	0.10 ± 0.02	2.00 ± 0.03	13.92 ± 0.16	4.43 ± 0.16	2.62 ± 0.07
14	CNOC2 Field 2	0603590201	0.02	0.02	0.03	0.06	0.11 ± 0.02	2.21 ± 0.05	15.32 ± 0.21	5.00 ± 0.21	2.91 ± 0.09
15	CDFS	0604961801	0.02	0.02	0.10	0.11	0.12 ± 0.02	2.01 ± 0.03	13.90 ± 0.17	5.14 ± 0.17	2.68 ± 0.07
16	CNOC2 Field 1	0603590101	0.02	0.02	0.61	0.06	0.08 ± 0.02	1.79 ± 0.04	12.05 ± 0.17	4.05 ± 0.17	2.25 ± 0.07
17	XX Cha	0300270201	0.02	0.02	2.13	0.10	0.08 ± 0.02	1.57 ± 0.04	11.60 ± 0.17	2.81 ± 0.18	2.15 ± 0.07

To be continued on the next page.

$\mathbf{D_1}$

						E_{gauss} [keV]	6.42	7.48	8.04	8.08	8.63
						Phys. origin	Fe-K$_\alpha$	Ni-K$_\alpha$	Cu-K$_\alpha$	Cu-K$_\alpha$	Cu-K$_\beta$/Zn-K$_\alpha$
Index	Object	ObsId	$\omega_{\gamma;i}^{\mathbf{D_1},\mathrm{ISO}}$	$\omega_{\gamma;i}^{\mathbf{D_1},\mathrm{NFW}}$	$N_{\mathrm{src}}^{\mathrm{X\text{-}ray}}$	N_{INST}	$F_{gauss}^{\mathbf{D_1}}$	$F_{gauss}^{\mathbf{D_1}}$	$F_{gauss}^{\mathbf{D_1}}$	$F_{gauss}^{\mathbf{D_1}}$	$F_{gauss}^{\mathbf{D_1}}$
i					%		$\frac{10^{-4}}{\mathrm{cm}^2\,\mathrm{s}}$	$\frac{10^{-4}}{\mathrm{cm}^2\,\mathrm{s}}$	$\frac{10^{-4}}{\mathrm{cm}^2\,\mathrm{s}}$	$\frac{10^{-4}}{\mathrm{cm}^2\,\mathrm{s}}$	$\frac{10^{-4}}{\mathrm{cm}^2\,\mathrm{s}}$
18	CDFS	0604961201	0.02	0.02	0.08	0.10	0.09 ± 0.02	1.95 ± 0.03	13.48 ± 0.16	4.47 ± 0.16	2.48 ± 0.06
19	CDFS	0555782301	0.02	0.02	0.12	0.15	0.11 ± 0.02	2.01 ± 0.04	14.25 ± 0.17	4.54 ± 0.17	2.80 ± 0.07
20	CDFS	0555780301	0.02	0.02	0.14	0.09	0.14 ± 0.02	2.30 ± 0.04	16.93 ± 0.20	4.72 ± 0.20	3.12 ± 0.08
21	CDFS	0604960901	0.02	0.02	0.09	0.14	0.15 ± 0.02	2.35 ± 0.04	16.19 ± 0.20	5.58 ± 0.20	3.15 ± 0.08
22	CDFS	0108060701	0.02	0.02	0.18	0.06	0.09 ± 0.02	1.71 ± 0.04	13.31 ± 0.17	1.46 ± 0.17	2.29 ± 0.08
23	CDFS	0555780601	0.02	0.02	0.11	0.14	0.09 ± 0.02	1.97 ± 0.04	13.73 ± 0.17	4.57 ± 0.17	2.68 ± 0.07
24	CDFS	0555780801	0.01	0.02	0.13	0.08	0.12 ± 0.02	1.75 ± 0.03	12.12 ± 0.15	3.74 ± 0.15	2.32 ± 0.06
25	CDFS	0555780901	0.01	0.01	0.12	0.08	0.09 ± 0.02	2.00 ± 0.04	13.67 ± 0.17	4.33 ± 0.17	2.74 ± 0.07
26	CDFS	0604960301	0.01	0.01	0.11	0.12	0.06 ± 0.02	1.91 ± 0.04	12.74 ± 0.16	4.40 ± 0.16	2.47 ± 0.07
27	CDFS	0555780201	0.01	0.01	0.15	0.13	0.11 ± 0.02	2.39 ± 0.05	16.26 ± 0.20	5.14 ± 0.21	2.97 ± 0.08
28	CDFS	0604960601	0.01	0.01	0.11	0.11	0.24 ± 0.05	5.38 ± 0.10	35.26 ± 0.45	12.03 ± 0.45	6.77 ± 0.18
29	CDFS	0555780101	0.01	0.01	0.17	0.11	0.08 ± 0.02	1.61 ± 0.03	11.51 ± 0.15	3.16 ± 0.15	2.08 ± 0.06
30	CDFS	0604960201	0.01	0.01	0.12	0.07	0.09 ± 0.03	2.87 ± 0.06	19.99 ± 0.26	6.51 ± 0.27	3.65 ± 0.11
31	CDFS	0604960701	0.01	0.01	0.15	0.06	0.11 ± 0.02	2.05 ± 0.05	14.15 ± 0.20	4.83 ± 0.20	2.70 ± 0.08
32	CDFS	0604960501	0.01	0.01	0.11	0.09	0.15 ± 0.03	2.41 ± 0.05	17.27 ± 0.24	5.89 ± 0.24	3.31 ± 0.10
33	CDFS	0108061901	0.01	0.01	0.10	0.03	0.08 ± 0.02	1.10 ± 0.04	9.04 ± 0.14	0.97 ± 0.14	1.49 ± 0.06

To be continued on the next page.

$\mathbf{D_1}$								
						E_{gauss} [keV]	8.90	9.58
						Phys. origin	Cu-K$_\alpha$	Zn-K$_\alpha$
Index	Object	ObsId	$\omega_{\gamma;i}^{\mathbf{D_1},\mathrm{ISO}}$	$\omega_{\gamma;i}^{\mathbf{D_1},\mathrm{NFW}}$	$N_{\mathrm{src}}^{\mathrm{X\text{-}ray}}$	N_{INST}	$F_{gauss}^{\mathbf{D_1}}$	$F_{gauss}^{\mathbf{D_1}}$
i					%		$\frac{10^{-4}}{\mathrm{cm^2\,s}}$	$\frac{10^{-4}}{\mathrm{cm^2\,s}}$
1	V4046 Sgr	0604860401	0.11	0.11	1.17	0.13	5.09 ± 0.10	0.94 ± 0.08
2	V4046 Sgr	0604860301	0.10	0.11	1.23	0.18	3.27 ± 0.07	0.65 ± 0.05
3	V4046 Sgr	0604860201	0.09	0.09	1.18	0.15	7.70 ± 0.17	1.72 ± 0.13
4	V4633 Sgr	0653550301	0.09	0.09	0.07	0.09	6.52 ± 0.15	0.96 ± 0.11
5	PDS 456	0501580201	0.07	0.06	2.10	0.13	2.51 ± 0.06	0.58 ± 0.04
6	PDS 456	0501580101	0.06	0.05	3.34	0.08	2.45 ± 0.06	0.47 ± 0.05
7	VV Sco	0555650201	0.06	0.05	0.68	0.08	6.08 ± 0.14	1.14 ± 0.11
8	VV Sco	0555650301	0.05	0.04	0.69	0.11	2.41 ± 0.06	0.41 ± 0.05
9	CDFS	0604961101	0.02	0.02	0.07	0.13	5.12 ± 0.10	0.97 ± 0.08
10	CDFS	0555780501	0.02	0.02	0.12	0.17	6.71 ± 0.15	1.48 ± 0.11
11	CDFS	0604961001	0.02	0.02	0.26	0.17	3.29 ± 0.07	0.62 ± 0.06
12	CDFS	0555781001	0.02	0.02	0.16	0.11	3.35 ± 0.07	0.67 ± 0.06
13	CDFS	0555780701	0.02	0.02	0.26	0.17	3.16 ± 0.07	0.62 ± 0.05
14	CNOC2 Field 2	0603590201	0.02	0.02	0.03	0.06	3.52 ± 0.09	0.75 ± 0.08
15	CDFS	0604961801	0.02	0.02	0.10	0.11	3.28 ± 0.07	0.59 ± 0.06
16	CNOC2 Field 1	0603590101	0.02	0.02	0.61	0.06	2.65 ± 0.07	0.51 ± 0.06
17	XX Cha	0300270201	0.02	0.02	2.13	0.10	2.53 ± 0.08	0.56 ± 0.07

To be continued on the next page.

$\mathbf{D_1}$								
						E_{gauss} [keV]	8.90	9.58
						Phys. origin	Cu-K$_\alpha$	Zn-K$_\alpha$
Index	Object	ObsId	$\omega_{\gamma;i}^{\mathbf{D_1},\mathrm{ISO}}$	$\omega_{\gamma;i}^{\mathbf{D_1},\mathrm{NFW}}$	$N_{\mathrm{src}}^{\text{X-ray}}$	N_{INST}	$F_{gauss}^{\mathbf{D_1}}$	$F_{gauss}^{\mathbf{D_1}}$
i					%		$\frac{10^{-4}}{\mathrm{cm}^2\,\mathrm{s}}$	$\frac{10^{-4}}{\mathrm{cm}^2\,\mathrm{s}}$
18	CDFS	0604961201	0.02	0.02	0.08	0.10	3.04 ± 0.07	0.56 ± 0.05
19	CDFS	0555782301	0.02	0.02	0.12	0.15	3.23 ± 0.07	0.60 ± 0.06
20	CDFS	0555780301	0.02	0.02	0.14	0.09	3.74 ± 0.09	0.58 ± 0.07
21	CDFS	0604960901	0.02	0.02	0.09	0.14	3.78 ± 0.09	0.59 ± 0.07
22	CDFS	0108060701	0.02	0.02	0.18	0.06	2.48 ± 0.08	0.55 ± 0.07
23	CDFS	0555780601	0.02	0.02	0.11	0.14	3.06 ± 0.07	0.49 ± 0.06
24	CDFS	0555780801	0.01	0.02	0.13	0.08	2.68 ± 0.06	0.56 ± 0.05
25	CDFS	0555780901	0.01	0.01	0.12	0.08	3.13 ± 0.08	0.62 ± 0.06
26	CDFS	0604960301	0.01	0.01	0.11	0.12	2.88 ± 0.07	0.55 ± 0.05
27	CDFS	0555780201	0.01	0.01	0.15	0.13	3.70 ± 0.09	0.78 ± 0.07
28	CDFS	0604960601	0.01	0.01	0.11	0.11	7.79 ± 0.19	1.33 ± 0.15
29	CDFS	0555780101	0.01	0.01	0.17	0.11	2.54 ± 0.07	0.47 ± 0.05
30	CDFS	0604960201	0.01	0.01	0.12	0.07	4.31 ± 0.11	0.63 ± 0.09
31	CDFS	0604960701	0.01	0.01	0.15	0.06	3.24 ± 0.09	0.63 ± 0.07
32	CDFS	0604960501	0.01	0.01	0.11	0.09	3.98 ± 0.10	0.67 ± 0.08
33	CDFS	0108061901	0.01	0.01	0.10	0.03	1.70 ± 0.07	0.31 ± 0.06

Table 5.2: This table shows the best-fit values of the normalisations $F_{gauss}^{\mathbf{D_1}}$ of spectral emission lines of the nullhypothesis model $m_0^{\mathbf{D_1}}$. The mean energies E_{gauss} of the spectral lines with Gaussian shape as well as their physical origins are presented in the first two rows. The observation identifications (ObsId) and the weightings $\omega_{\gamma;i}^{\mathbf{D_1},\mathrm{ISO}}$ and $\omega_{\gamma;i}^{\mathbf{D_1},\mathrm{NFW}}$ of the additional line with respect to the alternative hypothesis models $m_1^{\mathbf{D_1},\mathrm{ISO}}$ according to equation 5.36 and $m_1^{\mathbf{D_1},\mathrm{NFW}}$ according to equation 5.38 are also listed.

$\mathbf{D_2}$

Index	Object	ObsId	$\omega_{\gamma;i}^{\mathbf{D_2},\mathrm{ISO}}$	$\omega_{\gamma;i}^{\mathbf{D_2},\mathrm{NFW}}$	$N_{\mathrm{src}}^{\text{X-ray}}$	N_{INST}	Absorption	Bremsstr.	Bremsstr. normalisation	Powerlaw	Powerlaw normalisation
i							$\mathrm{n}_{\mathrm{H},i}^{\mathbf{D_2}}$	$\mathrm{T}_i^{\mathbf{D_2}}$	$\mathrm{N}_{bremss,i}^{\mathbf{D_2}}$	$\Gamma_i^{\mathbf{D_2}}$	$\mathrm{N}_{pow,i}^{\mathbf{D_2}}$
					$\%$		$10^{21}\ \frac{\mathrm{atoms}}{\mathrm{cm}^2}$	$10^{-1}\,\mathrm{keV}$	$10^{-4}\,\mathrm{cm}^{-3}$		$\frac{10^{-4}\ \mathrm{photons}}{\mathrm{keV\,cm^2\,s}}$ at $1\,\mathrm{keV}$
1	V4046 Sgr	0604860201	0.10	0.10	1.18	0.19	1.59 ± 0.17	2.78 ± 0.15	60.80 ± 14.11	1.01 ± 0.04	14.66 ± 0.64
2	V4046 Sgr	0604860301	0.12	0.12	1.23	0.23	1.59 ± 0.16	2.78 ± 0.14	61.66 ± 13.45	1.04 ± 0.03	14.66 ± 0.63
3	V4046 Sgr	0604860401	0.12	0.12	1.17	0.22	1.60 ± 0.16	2.79 ± 0.15	59.81 ± 13.24	1.09 ± 0.04	13.75 ± 0.64
4	V4633 Sgr	0653550301	0.09	0.09	0.07	0.15	2.11 ± 0.19	3.02 ± 0.20	66.22 ± 16.90	1.19 ± 0.05	14.90 ± 0.97
5	PDS 456	0501580201	0.09	0.08	2.10	0.18	2.26 ± 0.30	3.43 ± 0.40	24.65 ± 9.84	1.05 ± 0.05	13.04 ± 0.97
6	PDS 456	0501580101	0.06	0.06	3.34	0.14	2.30 ± 0.33	3.47 ± 0.47	28.03 ± 12.77	1.11 ± 0.06	15.99 ± 1.37
7	VV Sco	0555650301	0.05	0.04	0.69	0.12	2.26 ± 0.30	2.41 ± 0.18	104.94 ± 40.87	1.00 ± 0.06	11.55 ± 0.81
8	VV Sco	0555650201	0.06	0.05	0.68	0.14	2.02 ± 0.27	2.44 ± 0.18	85.49 ± 31.04	1.03 ± 0.05	13.96 ± 0.80
9	CNOC2 Field 1	0603590101	0.02	0.02	0.61	0.10	0.56 ± 0.28	2.15 ± 0.21	24.04 ± 11.25	0.92 ± 0.05	14.68 ± 0.87
10	OGLE 1999 BUL 32	0152420101	0.04	0.05	0.02	0.05	2.59 ± 0.32	2.69 ± 0.26	98.80 ± 43.47	1.82 ± 0.06	32.09 ± 2.38
11	MACHO 96 BLG 5	0305970101	0.08	0.09	0.07	0.10	2.58 ± 0.19	3.12 ± 0.22	86.07 ± 22.45	1.55 ± 0.05	33.02 ± 1.94
12	LH VLA 2	0554121301	0.01	0.01	0.11	0.07	1.66 ± 0.49	1.83 ± 0.21	54.99 ± 39.35	1.09 ± 0.08	14.40 ± 1.32
13	RXJ2328.8+1453	0502430301	0.02	0.02	0.06	0.13	1.01 ± 0.31	2.63 ± 0.31	13.13 ± 6.39	0.80 ± 0.05	10.77 ± 0.65

To be continued on the next page.

$\mathbf{D_2}$											
Index	Object	ObsId	$\omega_{\gamma;i}^{\mathbf{D_2},\mathrm{ISO}}$	$\omega_{\gamma;i}^{\mathbf{D_2},\mathrm{NFW}}$	$N_{\mathrm{src}}^{\text{X-ray}}$	N_{INST}	Absorption	Bremsstr.	Bremsstr. normalisation	Powerlaw	Powerlaw normalisation
i							$\mathrm{n}_{\mathrm{H},i}^{\mathbf{D_2}}$	$\mathrm{T}_i^{\mathbf{D_2}}$	$\mathrm{N}_{bremss,i}^{\mathbf{D_2}}$	$\Gamma_i^{\mathbf{D_2}}$	$\mathrm{N}_{pow,i}^{\mathbf{D_2}}$
					%		$10^{21}\ \frac{\text{atoms}}{\text{cm}^2}$	10^{-1} keV	$10^{-4}\ \text{cm}^{-3}$		$\frac{10^{-4}\ \text{photons}}{\text{keV cm}^2\ \text{s}}$ at 1 keV
14	CDFS	0555780101	0.01	0.01	0.17	0.10	1.09 ± 0.37	2.41 ± 0.34	18.23 ± 10.93	1.00 ± 0.07	11.20 ± 0.93
15	CDFS	0555780201	0.01	0.01	0.15	0.12	0.94 ± 0.32	2.46 ± 0.30	16.00 ± 8.25	0.91 ± 0.05	12.71 ± 0.82
16	CDFS	0555780301	0.02	0.02	0.14	0.14	0.87 ± 0.29	2.71 ± 0.33	13.04 ± 5.96	0.77 ± 0.05	10.76 ± 0.67
17	CDFS	0555780501	0.02	0.02	0.12	0.18	0.92 ± 0.26	2.89 ± 0.33	11.83 ± 4.81	0.70 ± 0.05	10.00 ± 0.61
18	CDFS	0555780601	0.02	0.02	0.11	0.14	1.33 ± 0.29	2.47 ± 0.26	22.52 ± 10.00	0.81 ± 0.05	11.24 ± 0.74
19	CDFS	0555780701	0.02	0.02	0.26	0.17	1.07 ± 0.26	2.49 ± 0.24	18.19 ± 7.40	0.79 ± 0.05	11.24 ± 0.63
20	CDFS	0555780801	0.01	0.02	0.13	0.14	1.21 ± 0.31	2.53 ± 0.28	19.10 ± 9.00	0.80 ± 0.05	11.23 ± 0.74
21	CDFS	0555780901	0.01	0.01	0.12	0.13	1.17 ± 0.33	2.21 ± 0.24	23.95 ± 12.35	0.93 ± 0.05	12.73 ± 0.82
22	CDFS	0555781001	0.02	0.02	0.16	0.17	1.08 ± 0.27	2.55 ± 0.27	17.51 ± 7.51	0.84 ± 0.05	12.77 ± 0.71
23	CDFS	0555782301	0.02	0.02	0.12	0.15	1.10 ± 0.29	2.51 ± 0.26	17.91 ± 7.86	0.78 ± 0.05	11.53 ± 0.69

Table 5.3: The table above lists the best-fit values of the absorbed bremsstrahlung and the powerlaw components of the nullhypothesis model $m_0^{\mathbf{D_2}}$. The observation identification (ObsId) and the weightings $\omega_{\gamma;i}^{\mathbf{D_2},\mathrm{ISO}}$ and $\omega_{\gamma;i}^{\mathbf{D_2},\mathrm{NFW}}$ of the additional line with respect to the alternative hypothesis models $m_1^{\mathbf{D_2},\mathrm{ISO}}$ according to equation 5.40 and $m_1^{\mathbf{D_2},\mathrm{ISO}}$ according to equation 5.42 are also listed.

$\mathbf{D_2}$											
						E_{gauss} [keV]	0.58	0.67	0.75	0.83	0.92
						Phys. origin	O VII	O VIII	Fe XVII	Fe XVII	Ne IX
Index	Object	ObsId	$\omega_{\gamma;i}^{\mathbf{D_2},\mathrm{ISO}}$	$\omega_{\gamma;i}^{\mathbf{D_2},\mathrm{NFW}}$	$N_{\mathrm{src}}^{\mathrm{X\text{-}ray}}$	N_{INST}	$F_{gauss}^{\mathbf{D_2}}$	$F_{gauss}^{\mathbf{D_2}}$	$F_{gauss}^{\mathbf{D_2}}$	$F_{gauss}^{\mathbf{D_2}}$	$F_{gauss}^{\mathbf{D_2}}$
i					%		$\frac{10^{-4}}{\mathrm{cm}^2\,\mathrm{s}}$	$\frac{10^{-4}}{\mathrm{cm}^2\,\mathrm{s}}$	$\frac{10^{-4}}{\mathrm{cm}^2\,\mathrm{s}}$	$\frac{10^{-4}}{\mathrm{cm}^2\,\mathrm{s}}$	$\frac{10^{-4}}{\mathrm{cm}^2\,\mathrm{s}}$
1	V4046 Sgr	0604860201	0.10	0.10	1.18	0.19	10.26 ± 0.24	6.44 ± 0.26	4.08 ± 0.25	5.39 ± 0.24	3.65 ± 0.15
2	V4046 Sgr	0604860301	0.12	0.12	1.23	0.23	10.72 ± 0.23	6.63 ± 0.25	4.10 ± 0.24	5.64 ± 0.23	3.60 ± 0.14
3	V4046 Sgr	0604860401	0.12	0.12	1.17	0.22	10.15 ± 0.22	6.28 ± 0.25	4.00 ± 0.24	5.39 ± 0.23	3.55 ± 0.15
4	V4633 Sgr	0653550301	0.09	0.09	0.07	0.15	9.59 ± 0.23	6.04 ± 0.29	5.32 ± 0.28	6.57 ± 0.25	4.09 ± 0.17
5	PDS 456	0501580201	0.09	0.08	2.10	0.18	3.85 ± 0.15	2.73 ± 0.19	2.30 ± 0.19	3.16 ± 0.18	2.08 ± 0.12
6	PDS 456	0501580101	0.06	0.06	3.34	0.14	4.47 ± 0.21	3.10 ± 0.23	2.90 ± 0.23	3.88 ± 0.20	2.26 ± 0.15
7	VV Sco	0555650301	0.05	0.04	0.69	0.12	8.46 ± 0.31	5.16 ± 0.38	3.44 ± 0.37	4.15 ± 0.36	2.89 ± 0.19
8	VV Sco	0555650201	0.06	0.05	0.68	0.14	9.68 ± 0.28	6.47 ± 0.36	3.99 ± 0.34	4.38 ± 0.32	3.08 ± 0.19
9	CNOC2 Field 1	0603590101	0.02	0.02	0.61	0.10	6.96 ± 0.31	1.14 ± 0.21	–	–	0.52 ± 0.12
10	OGLE 1999 BUL 32	0152420101	0.04	0.05	0.02	0.05	7.82 ± 0.30	4.07 ± 0.35	2.53 ± 0.42	4.96 ± 0.45	4.01 ± 0.23
11	MACHO 96 BLG 5	0305970101	0.08	0.09	0.07	0.10	8.09 ± 0.23	3.77 ± 0.28	3.70 ± 0.28	6.59 ± 0.26	4.57 ± 0.18
12	LH VLA 2	0554121301	0.01	0.01	0.11	0.07	3.83 ± 0.30	–	–	–	–
13	RXJ2328.8+1453	0502430301	0.02	0.02	0.06	0.13	2.95 ± 0.24	0.77 ± 0.23	–	–	0.15 ± 0.08

To be continued on the next page.

$\mathbf{D_2}$

						E_{gauss} [keV]	0.58	0.67	0.75	0.83	0.92
						Phys. origin	O VII	O VIII	Fe XVII	Fe XVII	Ne IX
Index	Object	ObsId	$\omega_{\gamma;i}^{\mathbf{D_2},\mathrm{ISO}}$	$\omega_{\gamma;i}^{\mathbf{D_2},\mathrm{NFW}}$	$N_{\mathrm{src}}^{\text{X-ray}}$	N_{INST}	$F_{gauss}^{\mathbf{D_2}}$	$F_{gauss}^{\mathbf{D_2}}$	$F_{gauss}^{\mathbf{D_2}}$	$F_{gauss}^{\mathbf{D_2}}$	$F_{gauss}^{\mathbf{D_2}}$
i					%		$\frac{10^{-4}}{\mathrm{cm^2\,s}}$	$\frac{10^{-4}}{\mathrm{cm^2\,s}}$	$\frac{10^{-4}}{\mathrm{cm^2\,s}}$	$\frac{10^{-4}}{\mathrm{cm^2\,s}}$	$\frac{10^{-4}}{\mathrm{cm^2\,s}}$
14	CDFS	0555780101	0.01	0.01	0.17	0.10	2.90 ± 0.23	–	–	–	–
15	CDFS	0555780201	0.01	0.01	0.15	0.12	2.60 ± 0.20	–	–	–	0.15 ± 0.09
16	CDFS	0555780301	0.02	0.02	0.14	0.14	2.78 ± 0.19	–	–	–	–
17	CDFS	0555780501	0.02	0.02	0.12	0.18	2.96 ± 0.17	–	–	–	–
18	CDFS	0555780601	0.02	0.02	0.11	0.14	2.91 ± 0.19	–	–	–	0.17 ± 0.09
19	CDFS	0555780701	0.02	0.02	0.26	0.17	2.92 ± 0.18	–	–	–	0.13 ± 0.08
20	CDFS	0555780801	0.01	0.02	0.13	0.14	3.20 ± 0.20	–	–	–	0.24 ± 0.10
21	CDFS	0555780901	0.01	0.01	0.12	0.13	3.49 ± 0.21	–	–	–	0.25 ± 0.09
22	CDFS	0555781001	0.02	0.02	0.16	0.17	3.41 ± 0.19	–	–	–	0.12 ± 0.08
23	CDFS	0555782301	0.02	0.02	0.12	0.15	2.99 ± 0.19	–	–	–	0.17 ± 0.09

To be continued on the next page.

$\mathbf{D_2}$

						E_{gauss} [keV]	1.03	1.38	1.49	1.87	2.35
						Phys. origin	Ne IX	Mg XI	Al-K$_\alpha$	Si-K$_\alpha$	S$_\alpha$/S$_\beta$
Index	Object	ObsId	$\omega_{\gamma;i}^{\mathbf{D_2},\mathrm{ISO}}$	$\omega_{\gamma;i}^{\mathbf{D_2},\mathrm{NFW}}$	$N_{\mathrm{src}}^{\mathrm{X\text{-}ray}}$	N_{INST}	$F_{gauss}^{\mathbf{D_2}}$	$F_{gauss}^{\mathbf{D_2}}$	$F_{gauss}^{\mathbf{D_2}}$	$F_{gauss}^{\mathbf{D_2}}$	$F_{gauss}^{\mathbf{D_2}}$
i					%		$\frac{10^{-4}}{\mathrm{cm^2\,s}}$	$\frac{10^{-4}}{\mathrm{cm^2\,s}}$	$\frac{10^{-4}}{\mathrm{cm^2\,s}}$	$\frac{10^{-4}}{\mathrm{cm^2\,s}}$	$\frac{10^{-4}}{\mathrm{cm^2\,s}}$
1	V4046 Sgr	0604860201	0.10	0.10	1.18	0.19	1.39 ± 0.09	0.40 ± 0.06	3.90 ± 0.08	–	–
2	V4046 Sgr	0604860301	0.12	0.12	1.23	0.23	1.44 ± 0.09	0.48 ± 0.05	3.89 ± 0.08	–	–
3	V4046 Sgr	0604860401	0.12	0.12	1.17	0.22	1.45 ± 0.09	0.44 ± 0.06	3.98 ± 0.08	–	–
4	V4633 Sgr	0653550301	0.09	0.09	0.07	0.15	1.91 ± 0.11	0.35 ± 0.06	3.28 ± 0.07	–	–
5	PDS 456	0501580201	0.09	0.08	2.10	0.18	0.78 ± 0.08	0.30 ± 0.06	3.37 ± 0.09	–	0.32 ± 0.05
6	PDS 456	0501580101	0.06	0.06	3.34	0.14	0.78 ± 0.10	0.28 ± 0.10	3.78 ± 0.09	–	0.25 ± 0.07
7	VV Sco	0555650301	0.05	0.04	0.69	0.12	0.77 ± 0.11	0.48 ± 0.10	4.61 ± 0.10	–	–
8	VV Sco	0555650201	0.06	0.05	0.68	0.14	0.97 ± 0.12	0.44 ± 0.07	4.52 ± 0.09	–	–
9	CNOC2 Field 1	0603590101	0.02	0.02	0.61	0.10	–	1.61 ± 0.35	4.89 ± 0.38	–	–
10	OGLE 1999 BUL 32	0152420101	0.04	0.05	0.02	0.05	2.51 ± 0.15	0.41 ± 0.08	1.72 ± 0.08	0.43 ± 0.07	–
11	MACHO 96 BLG 5	0305970101	0.08	0.09	0.07	0.10	2.80 ± 0.12	0.46 ± 0.07	2.29 ± 0.07	0.48 ± 0.06	–
12	LH VLA 2	0554121301	0.01	0.01	0.11	0.07	–	–	6.03 ± 1.01	–	–
13	RXJ2328.8+1453	0502430301	0.02	0.02	0.06	0.13	–	–	5.66 ± 0.10	–	–

To be continued on the next page.

$\mathbf{D_2}$

						E_{gauss} [keV]	1.03	1.38	1.49	1.87	2.35
						Phys. origin	Ne IX	Mg XI	Al-K$_\alpha$	Si-K$_\alpha$	S$_\alpha$/S$_\beta$
Index	Object	ObsId	$\omega_{\gamma;i}^{\mathbf{D_2},\mathrm{ISO}}$	$\omega_{\gamma;i}^{\mathbf{D_2},\mathrm{NFW}}$	$N_{\mathrm{src}}^{\text{X-ray}}$	N_{INST}	$F_{gauss}^{\mathbf{D_2}}$	$F_{gauss}^{\mathbf{D_2}}$	$F_{gauss}^{\mathbf{D_2}}$	$F_{gauss}^{\mathbf{D_2}}$	$F_{gauss}^{\mathbf{D_2}}$
i					%		$\frac{10^{-4}}{\mathrm{cm^2\,s}}$	$\frac{10^{-4}}{\mathrm{cm^2\,s}}$	$\frac{10^{-4}}{\mathrm{cm^2\,s}}$	$\frac{10^{-4}}{\mathrm{cm^2\,s}}$	$\frac{10^{-4}}{\mathrm{cm^2\,s}}$
14	CDFS	0555780101	0.01	0.01	0.17	0.10	–	0.31 ± 0.13	5.78 ± 0.16	–	0.26 ± 0.11
15	CDFS	0555780201	0.01	0.01	0.15	0.12	–	0.30 ± 0.12	5.78 ± 0.15	–	0.37 ± 0.10
16	CDFS	0555780301	0.02	0.02	0.14	0.14	–	0.44 ± 0.09	5.76 ± 0.11	–	0.27 ± 0.09
17	CDFS	0555780501	0.02	0.02	0.12	0.18	–	0.31 ± 0.07	6.01 ± 0.10	–	0.14 ± 0.08
18	CDFS	0555780601	0.02	0.02	0.11	0.14	–	0.41 ± 0.09	6.20 ± 0.12	–	0.25 ± 0.09
19	CDFS	0555780701	0.02	0.02	0.26	0.17	–	0.34 ± 0.07	6.15 ± 0.10	–	0.29 ± 0.09
20	CDFS	0555780801	0.01	0.02	0.13	0.14	–	0.24 ± 0.07	6.52 ± 0.11	–	0.47 ± 0.10
21	CDFS	0555780901	0.01	0.01	0.12	0.13	–	0.52 ± 0.14	6.03 ± 0.17	–	0.22 ± 0.10
22	CDFS	0555781001	0.02	0.02	0.16	0.17	–	0.51 ± 0.11	6.42 ± 0.13	–	0.34 ± 0.09
23	CDFS	0555782301	0.02	0.02	0.12	0.15	–	0.40 ± 0.13	6.26 ± 0.15	–	0.12 ± 0.09

To be continued on the next page.

$\mathbf{D_2}$

						E_{gauss} [keV]	4.52	5.42	6.40	7.47
						Phys. origin	Ti-K$_\alpha$	Cr-K$_\alpha$	Fe-K$_\alpha$	Ni-K$_\alpha$
Index	Object	ObsId	$\omega_{\gamma;i}^{\mathbf{D_2},\mathrm{ISO}}$	$\omega_{\gamma;i}^{\mathbf{D_2},\mathrm{NFW}}$	$N_{\mathrm{src}}^{\mathrm{X\text{-}ray}}$	N_{INST}	$F_{gauss}^{\mathbf{D_2}}$	$F_{gauss}^{\mathbf{D_2}}$	$F_{gauss}^{\mathbf{D_2}}$	$F_{gauss}^{\mathbf{D_2}}$
i					%		$\frac{10^{-4}}{\mathrm{cm}^2\,\mathrm{s}}$	$\frac{10^{-4}}{\mathrm{cm}^2\,\mathrm{s}}$	$\frac{10^{-4}}{\mathrm{cm}^2\,\mathrm{s}}$	$\frac{10^{-4}}{\mathrm{cm}^2\,\mathrm{s}}$
1	V4046 Sgr	0604860201	0.10	0.10	1.18	0.19	0.08 ± 0.05	0.45 ± 0.05	0.22 ± 0.06	6.07 ± 0.19
2	V4046 Sgr	0604860301	0.12	0.12	1.23	0.23	0.10 ± 0.04	0.32 ± 0.05	0.29 ± 0.06	5.99 ± 0.17
3	V4046 Sgr	0604860401	0.12	0.12	1.17	0.22	0.11 ± 0.04	0.41 ± 0.05	0.28 ± 0.06	6.47 ± 0.18
4	V4633 Sgr	0653550301	0.09	0.09	0.07	0.15	0.20 ± 0.05	0.46 ± 0.05	0.31 ± 0.06	5.22 ± 0.17
5	PDS 456	0501580201	0.09	0.08	2.10	0.18	–	0.37 ± 0.05	0.33 ± 0.06	5.39 ± 0.16
6	PDS 456	0501580101	0.06	0.06	3.34	0.14	–	0.46 ± 0.06	0.25 ± 0.07	5.98 ± 0.27
7	VV Sco	0555650301	0.05	0.04	0.69	0.12	0.17 ± 0.06	0.52 ± 0.07	0.25 ± 0.09	6.98 ± 0.22
8	VV Sco	0555650201	0.06	0.05	0.68	0.14	0.14 ± 0.06	0.56 ± 0.07	0.28 ± 0.08	7.06 ± 0.23
9	CNOC2 Field 1	0603590101	0.02	0.02	0.61	0.10	0.33 ± 0.09	0.67 ± 0.10	0.37 ± 0.12	9.63 ± 0.37
10	OGLE 1999 BUL 32	0152420101	0.04	0.05	0.02	0.05	–	0.23 ± 0.05	0.08 ± 0.06	2.66 ± 0.15
11	MACHO 96 BLG 5	0305970101	0.08	0.09	0.07	0.10	0.08 ± 0.04	0.27 ± 0.05	0.30 ± 0.06	3.52 ± 0.13
12	LH VLA 2	0554121301	0.01	0.01	0.11	0.07	0.43 ± 0.12	0.86 ± 0.13	0.60 ± 0.15	9.36 ± 0.41
13	RXJ2328.8+1453	0502430301	0.02	0.02	0.06	0.13	0.21 ± 0.07	0.48 ± 0.08	0.30 ± 0.09	8.48 ± 0.24

To be continued on the next page.

$\mathbf{D_2}$										
						E_{gauss} [keV]	4.52	5.42	6.40	7.47
						Phys. origin	Ti-K$_\alpha$	Cr-K$_\alpha$	Fe-K$_\alpha$	Ni-K$_\alpha$
Index	Object	ObsId	$\omega_{\gamma;i}^{\mathbf{D_2},\mathrm{ISO}}$	$\omega_{\gamma;i}^{\mathbf{D_2},\mathrm{NFW}}$	$N_{\mathrm{src}}^{\mathrm{X\text{-}ray}}$	N_{INST}	$F_{gauss}^{\mathbf{D_2}}$	$F_{gauss}^{\mathbf{D_2}}$	$F_{gauss}^{\mathbf{D_2}}$	$F_{gauss}^{\mathbf{D_2}}$
i					%		$\frac{10^{-4}}{\mathrm{cm^2\,s}}$	$\frac{10^{-4}}{\mathrm{cm^2\,s}}$	$\frac{10^{-4}}{\mathrm{cm^2\,s}}$	$\frac{10^{-4}}{\mathrm{cm^2\,s}}$
14	CDFS	0555780101	0.01	0.01	0.17	0.10	0.24 ± 0.09	0.70 ± 0.10	0.27 ± 0.12	8.81 ± 0.32
15	CDFS	0555780201	0.01	0.01	0.15	0.12	0.31 ± 0.09	0.68 ± 0.10	0.25 ± 0.11	8.35 ± 0.31
16	CDFS	0555780301	0.02	0.02	0.14	0.14	0.21 ± 0.08	0.55 ± 0.09	0.33 ± 0.10	8.22 ± 0.29
17	CDFS	0555780501	0.02	0.02	0.12	0.18	0.24 ± 0.07	0.59 ± 0.08	0.53 ± 0.10	9.05 ± 0.27
18	CDFS	0555780601	0.02	0.02	0.11	0.14	0.23 ± 0.08	0.68 ± 0.09	0.39 ± 0.11	8.80 ± 0.30
19	CDFS	0555780701	0.02	0.02	0.26	0.17	0.26 ± 0.07	0.60 ± 0.08	0.40 ± 0.10	9.17 ± 0.30
20	CDFS	0555780801	0.01	0.02	0.13	0.14	0.33 ± 0.08	0.82 ± 0.10	0.55 ± 0.11	9.64 ± 0.33
21	CDFS	0555780901	0.01	0.01	0.12	0.13	0.35 ± 0.09	0.86 ± 0.10	0.59 ± 0.11	9.24 ± 0.33
22	CDFS	0555781001	0.02	0.02	0.16	0.17	0.38 ± 0.08	0.80 ± 0.09	0.49 ± 0.10	9.41 ± 0.27
23	CDFS	0555782301	0.02	0.02	0.12	0.15	0.26 ± 0.08	0.80 ± 0.09	0.51 ± 0.11	9.26 ± 0.31

To be continued on the next page.

$\mathbf{D_2}$

Index	Object	ObsId	$\omega_{\gamma;i}^{\mathbf{D_2},\mathrm{ISO}}$	$\omega_{\gamma;i}^{\mathbf{D_2},\mathrm{NFW}}$	$N_{\mathrm{src}}^{\text{X-ray}}$	N_{INST}	$F_{gauss}^{\mathbf{D_2}}$	$F_{gauss}^{\mathbf{D_2}}$	$F_{gauss}^{\mathbf{D_2}}$	$F_{gauss}^{\mathbf{D_2}}$	$F_{gauss}^{\mathbf{D_2}}$
						E_{gauss} [keV]	8.03	8.19	8.57	8.88	9.57
						Phys. origin	Cu-K$_\alpha$	Cu-K$_\alpha$	Cu-K$_\beta$/Zn-K$_\alpha$	Cu-K$_\alpha$	Zn-K$_\alpha$
i					%		$\frac{10^{-4}}{\mathrm{cm^2\,s}}$	$\frac{10^{-4}}{\mathrm{cm^2\,s}}$	$\frac{10^{-4}}{\mathrm{cm^2\,s}}$	$\frac{10^{-4}}{\mathrm{cm^2\,s}}$	$\frac{10^{-4}}{\mathrm{cm^2\,s}}$
1	V4046 Sgr	0604860201	0.10	0.10	1.18	0.19	51.25 ± 0.53	7.98 ± 0.51	7.36 ± 0.56	10.38 ± 0.32	4.22 ± 0.37
2	V4046 Sgr	0604860301	0.12	0.12	1.23	0.23	52.76 ± 0.50	7.91 ± 0.53	7.24 ± 0.33	10.82 ± 0.37	3.69 ± 0.33
3	V4046 Sgr	0604860401	0.12	0.12	1.17	0.22	53.19 ± 0.47	7.43 ± 0.69	7.63 ± 0.36	11.05 ± 0.37	3.10 ± 0.29
4	V4633 Sgr	0653550301	0.09	0.09	0.07	0.15	45.64 ± 0.41	6.76 ± 1.05	6.10 ± 0.52	9.21 ± 0.49	1.87 ± 0.27
5	PDS 456	0501580201	0.09	0.08	2.10	0.18	46.28 ± 0.48	6.50 ± 0.59	6.68 ± 0.54	8.93 ± 0.31	3.36 ± 0.31
6	PDS 456	0501580101	0.06	0.06	3.34	0.14	52.92 ± 0.54	7.10 ± 0.52	7.38 ± 1.05	10.13 ± 0.56	2.54 ± 0.35
7	VV Sco	0555650301	0.05	0.04	0.69	0.12	58.81 ± 0.90	7.87 ± 0.63	9.00 ± 0.60	11.28 ± 0.40	2.89 ± 0.43
8	VV Sco	0555650201	0.06	0.05	0.68	0.14	61.09 ± 0.84	8.16 ± 0.65	9.54 ± 0.92	12.05 ± 0.51	3.06 ± 0.38
9	CNOC2 Field 1	0603590101	0.02	0.02	0.61	0.10	78.99 ± 1.07	11.31 ± 0.91	11.21 ± 0.61	15.99 ± 0.55	4.64 ± 0.59
10	OGLE 1999 BUL 32	0152420101	0.04	0.05	0.02	0.05	23.88 ± 0.46	3.71 ± 0.38	2.92 ± 0.22	4.71 ± 0.22	0.70 ± 0.20
11	MACHO 96 BLG 5	0305970101	0.08	0.09	0.07	0.10	32.85 ± 0.31	5.92 ± 0.64	3.76 ± 0.20	6.15 ± 0.24	1.26 ± 0.20
12	LH VLA 2	0554121301	0.01	0.01	0.11	0.07	84.08 ± 1.03	12.89 ± 1.95	9.60 ± 0.77	15.98 ± 0.92	1.77 ± 0.55
13	RXJ2328.8+1453	0502430301	0.02	0.02	0.06	0.13	71.93 ± 0.79	7.52 ± 0.63	10.48 ± 0.43	13.83 ± 0.39	2.93 ± 0.33

To be continued on the next page.

$\mathbf{D_2}$											
						E_{gauss} [keV]	8.03	8.19	8.57	8.88	9.57
						Phys. origin	Cu-K$_\alpha$	Cu-K$_\alpha$	Cu-K$_\beta$/Zn-K$_\alpha$	Cu-K$_\alpha$	Zn-K$_\alpha$
Index	Object	ObsId	$\omega_{\gamma;i}^{\mathbf{D_2},\mathrm{ISO}}$	$\omega_{\gamma;i}^{\mathbf{D_2},\mathrm{NFW}}$	$N_{\mathrm{src}}^{\mathrm{X\text{-}ray}}$	N_{INST}	$F_{gauss}^{\mathbf{D_2}}$	$F_{gauss}^{\mathbf{D_2}}$	$F_{gauss}^{\mathbf{D_2}}$	$F_{gauss}^{\mathbf{D_2}}$	$F_{gauss}^{\mathbf{D_2}}$
i					%		$\frac{10^{-4}}{\mathrm{cm^2\,s}}$	$\frac{10^{-4}}{\mathrm{cm^2\,s}}$	$\frac{10^{-4}}{\mathrm{cm^2\,s}}$	$\frac{10^{-4}}{\mathrm{cm^2\,s}}$	$\frac{10^{-4}}{\mathrm{cm^2\,s}}$
15	CDFS	0555780201	0.01	0.01	0.15	0.12	78.29 ± 0.75	13.70 ± 1.28	9.61 ± 0.58	15.29 ± 0.62	3.48 ± 0.40
16	CDFS	0555780301	0.02	0.02	0.14	0.14	77.36 ± 0.70	11.92 ± 1.23	9.82 ± 0.58	15.27 ± 0.60	3.25 ± 0.36
17	CDFS	0555780501	0.02	0.02	0.12	0.18	80.90 ± 0.67	11.07 ± 1.10	10.71 ± 0.55	15.89 ± 0.54	4.30 ± 0.35
18	CDFS	0555780601	0.02	0.02	0.11	0.14	83.02 ± 0.73	13.74 ± 1.35	10.34 ± 0.60	15.76 ± 0.65	3.14 ± 0.39
19	CDFS	0555780701	0.02	0.02	0.26	0.17	81.31 ± 0.75	11.71 ± 0.97	10.51 ± 0.56	16.36 ± 0.51	4.01 ± 0.35
20	CDFS	0555780801	0.01	0.02	0.13	0.14	87.24 ± 0.83	11.75 ± 1.27	10.78 ± 0.67	16.81 ± 0.65	3.76 ± 0.40
21	CDFS	0555780901	0.01	0.01	0.12	0.13	81.84 ± 0.81	12.51 ± 1.28	11.22 ± 0.66	16.49 ± 0.63	3.89 ± 0.41
22	CDFS	0555781001	0.02	0.02	0.16	0.17	84.51 ± 0.76	11.56 ± 1.12	10.63 ± 0.67	16.12 ± 0.59	3.74 ± 0.37
23	CDFS	0555782301	0.02	0.02	0.12	0.15	85.00 ± 0.77	11.66 ± 1.12	11.82 ± 0.60	16.59 ± 0.58	3.09 ± 0.38

Table 5.4: This table shows the best-fit values of the normalisations $F_{gauss}^{\mathbf{D_2}}$ of spectral emission lines of the nullhypothesis model $m_0^{\mathbf{D_2}}$. The mean energies E_{gauss} of the spectral lines with Gaussian shape as well as their physical origins are presented in the first two rows. The observation identification (ObsId) and the weightings $\omega_{\gamma;i}^{\mathbf{D_2},\mathrm{ISO}}$ and $\omega_{\gamma;i}^{\mathbf{D_2},\mathrm{NFW}}$ of the additional line with respect to the alternative hypothesis models $m_1^{\mathbf{D_2},\mathrm{ISO}}$ according to equation 5.40 and $m_1^{\mathbf{D_2},\mathrm{ISO}}$ according to equation 5.42 are also listed.

The resulting fitted values of the continuum components of the respective nullhypothesis models $m_0^{\mathbf{D_1}}$ and $m_0^{\mathbf{D_2}}$ are listed in tables 5.1 and 5.3, wherein tables 5.2 and 5.4 contain the normalisations $F_{gauss}^{\mathbf{D_1}}$ and $F_{gauss}^{\mathbf{D_2}}$ of the $\mathbf{L_1} = 17$ and $\mathbf{L_2} = 19$ astrophysical and instrumental Gaussian emission lines denoted as *gauss* within the nullhypothesis models $m_0^{\mathbf{D_1}}$ and $m_0^{\mathbf{D_2}}$.
Normalisations were ignored (denoted by "-" in tables 5.1 and 5.3 as well as tables 5.2 and 5.4) if the square root of the diagonal elements contained in the covariance matrix of the Levenberg-Marquardt routine[13] applied by *XSPEC* as a fitting algorithm were equal or higher than their central value.
The absorption is given by the hydrogen columns $n_{\mathrm{H}}^{\mathbf{D_1}}$ and $n_{\mathrm{H}}^{\mathbf{D_2}}$ and was applied to the respective bremsstrahlung component in case of $m_0^{\mathbf{D_1}}$ or the respective powerlaw and bremsstrahlung components $m_0^{\mathbf{D_2}}$. The powerlaw components are represented as the dimensionless photon indices $\Gamma^{\mathbf{D_1}}$ as well as $\Gamma^{\mathbf{D_2}}$, wherein their respective normalisations are $\mathrm{N}_{pow}^{\mathbf{D_1}}$ and $\mathrm{N}_{pow}^{\mathbf{D_2}}$. The bremsstrahlung components are denoted by the temperatures $\mathrm{T}^{\mathbf{D_1}}$ and $\mathrm{T}^{\mathbf{D_2}}$ as well as the corresponding normalisations $\mathrm{N}_{bremss}^{\mathbf{D_1}}$ and $\mathrm{N}_{bremss}^{\mathbf{D_2}}$, respectively. In addition, tables 5.2 and 5.4 contain the mean energies E_{gauss} and the respective normalisation values $F_{gauss}^{\mathbf{D_1}}$ and $F_{gauss}^{\mathbf{D_2}}$ of all $\mathbf{L_1} = 17$ and $\mathbf{L_2} = 19$ Gaussian-shaped spectral emission lines with astrophysical or instrumental origin, respectively. The line energies are given as mean values since their variations are in the order of $\mathcal{O}(eV)$. The flux normalisations or normalisations F_{gauss} of the instrumental emission lines are consistent with the overall activation of the telescope and its detectors by cosmic rays and soft proton clouds.
The instrumental background subtracted spectrum, the related best-fit model $m_0^{\mathbf{D_1}}$ or $m_0^{\mathbf{D_2}}$, the normalised instrumental background continuum spectrum and the spectrum of the detected sources, all related to the data set having the observation identifier 0604860301 ($i = 2$, $\mathbf{D_1}$ and $\mathbf{D_2}$) are exemplary shown in panels A and C of figures 5.1 and 5.2, respectively[14]. The x-axis represents the energy scale in keV and the y-axis indicates the photon counts. Panels B and D show the residuals among the respective models $m_0^{\mathbf{D_1}}$ and $m_0^{\mathbf{D_2}}$ and the data in units of $\chi = \mathrm{sgn}(\mathrm{Data} - \mathrm{Model})\sqrt{(\mathrm{Data} - \mathrm{Model})^2}$.

[13] *XSPEC* applies a Levenberg-Marquardt routine to minimise a predetermined fit statistic and thus find a set of best-fit parameters of a given (spectral) model, wherein the Levenberg-Marquardt routine of *XSPEC* is based on the *CURFIT* algorithm disclosed by Bevington (74). Please also see https://heasarc.nasa.gov/xanadu/xspec/manual/node12.html for further reference.

[14] Please see Appendix F. Spectral Models for the corresponding spectra of the remaining data sets.

The best-fit models $m_0^{\mathbf{D_1}}$ and $m_0^{\mathbf{D_2}}$ of all respective $\mathbf{N_1} = 33$ and $\mathbf{N_2} = 23$ data sets are plotted in figures 5.3 and 5.4. Panels A and B show the modelled counts per bin of the astrophysical background spectra in energy ranges from $0.38\,$keV to $2\,$keV as well as from $2\,$keV to $12\,$keV or from $2\,$keV to $16.5\,$keV, respectively.
The residuals distributions per energy bin shown in panels A and B of figures 5.5 and 5.6 as well as the accumulated residual distributions of all energy bins presented in panel C of figures 5.5 and 5.6 show a recognisable shift of their means towards positive values. This bias of the residuals,

$$\chi = \mathrm{sgn}(\mathrm{Data} - \mathrm{Model})\sqrt{(\mathrm{Data} - \mathrm{Model})^2}, \tag{5.32}$$

can be explained by a non-vanishing contribution of photon counts from astrophysical sources in the normalisation range among the instrumental background model and the astrophysical spectra contrary to the assumption made in section 4.4.

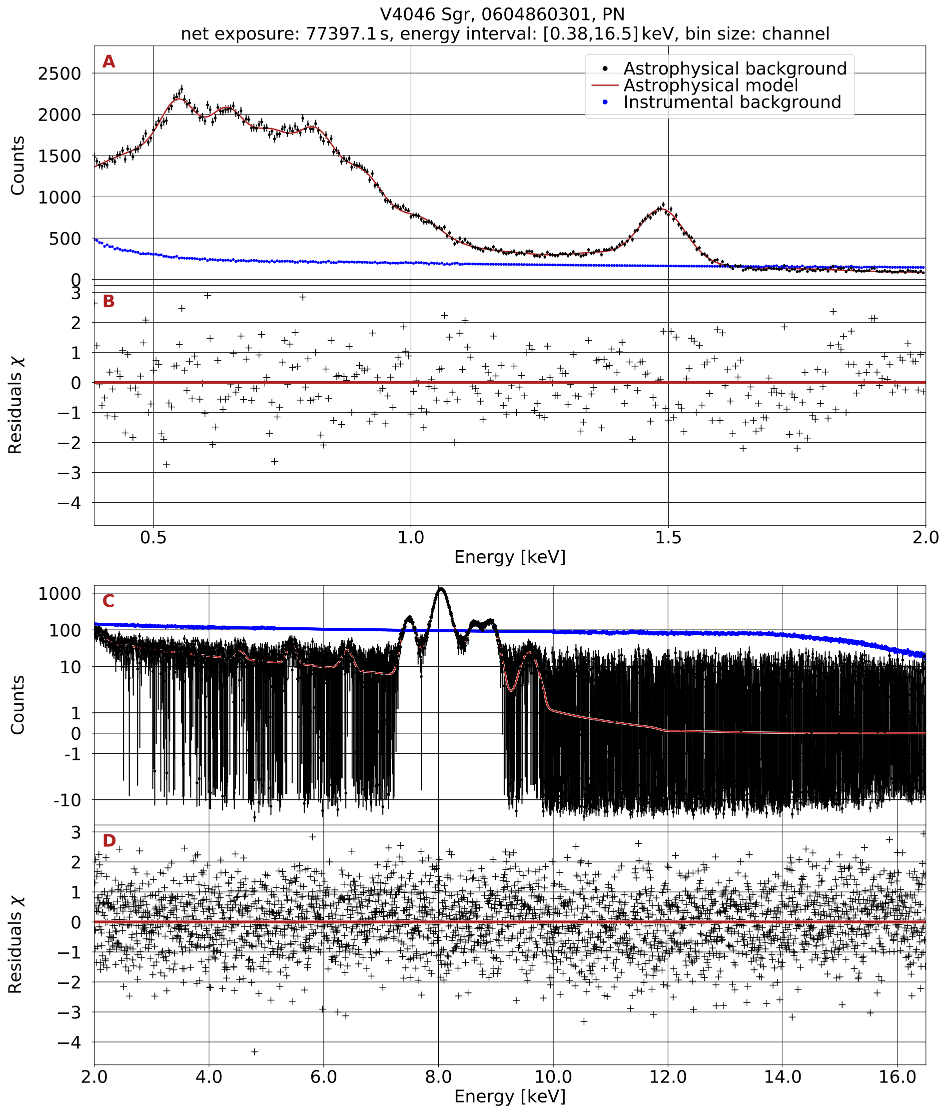

Figure 5.1: The panels A and C show the measured spectrum of an individual data set (Table 4.1, observation identifier: 0604860301, $i = 2$, $\mathbf{D_1}$) as black error bars and its fitted nullhypothesis model $m_0^{\mathbf{D_1}}$ in an energy range from 0.38 keV to 2 keV (panels A and B) and from 2 keV to 16.5 keV (panels C and D) as red lines, respectively, while the blue error bars show the instrumental background model. The fitted model is composed of two continuum components consisting of a bremsstrahlung component *bremss* and a powerlaw component *pow*, wherein the bremsstrahlung component is attenuated by an absorption component *wabs*, plus $\mathbf{L_1} = 17$ instrumental and astrophysical Gaussian emission lines *gauss*. The best-fit values are specified in tables 5.1 and 5.2. The panels B and D show the residuals per energy bin in values of $\chi = \text{sgn}(\text{Data} - \text{Model})\,\sqrt{(\text{Data} - \text{Model})^2}$.

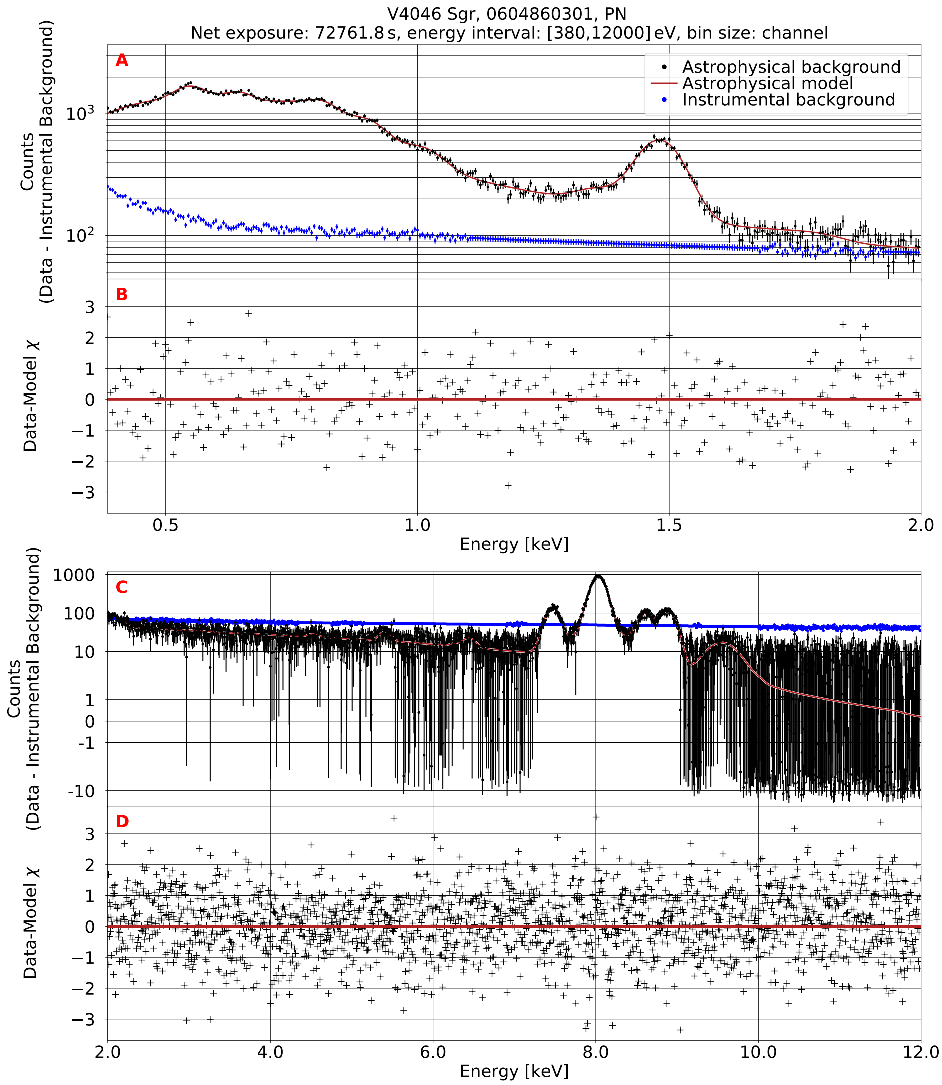

Figure 5.2: The panels A and C show the measured spectrum of an individual data set (Table 4.2, observation identifier: 0604860301, $i = 2$, $\mathbf{D_2}$) as black error bars and its fitted nullhypothesis model $m_0^{\mathbf{D_2}}$ in an energy range from 0.38 keV to 2 keV (panel A and B) and from 2 keV to 12 keV (panel C and D) as red lines, respectively, while the blue error bars show the instrumental background model. The fitted model is composed of two continuum components consisting of a bremsstrahlung component *bremss* and a powerlaw component *pow*, both attenuated by an absorption component *wabs*, plus $\mathbf{L_2} = 19$ instrumental and astrophysical Gaussian emission lines *gauss*. The best-fit values are specified in tables 5.3 and 5.4. The panels B and D show the residuals per energy bin in values of $\chi = \mathrm{sgn}(\mathrm{Data} - \mathrm{Model})\sqrt{(\mathrm{Data} - \mathrm{Model})^2}$.

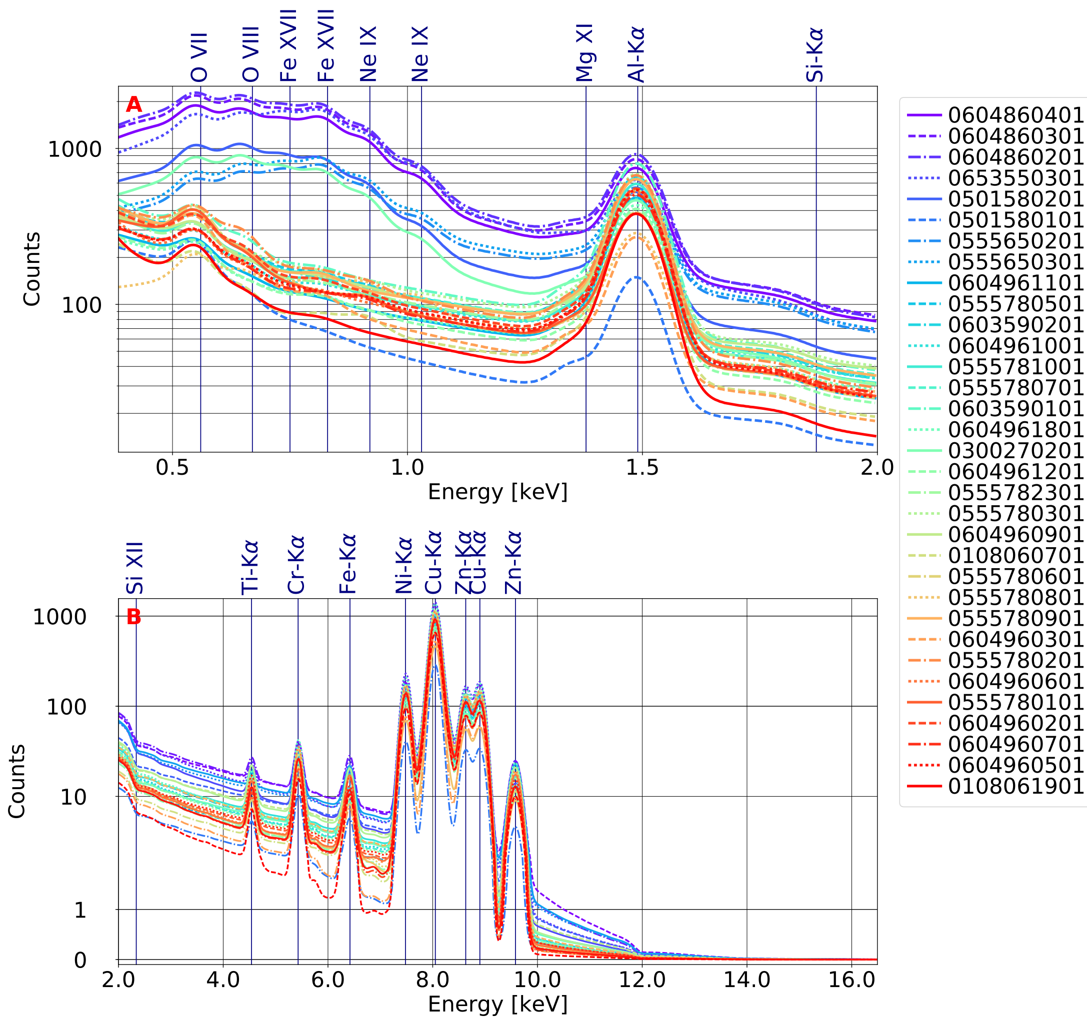

Figure 5.3: The panels A and B show the fitted nullhypothesis model $m_0^{\mathbf{D_1}}$ of each data set of $\mathbf{D_1}$ in energy ranges of 0.38 keV to 2 keV (panel A) and of 2 keV to 16.5 keV (panel B), respectively. The fitted model consists of two continuum components consisting of a powerlaw component *pow* and a bremsstrahlung component *bremss*, the latter component attenuated by an absorption component *wabs*, plus $\mathbf{L_1} = 17$ instrumental and astrophysical Gaussian emission lines *gauss*. The best-fit values are specified in tables 5.1 and 5.2.

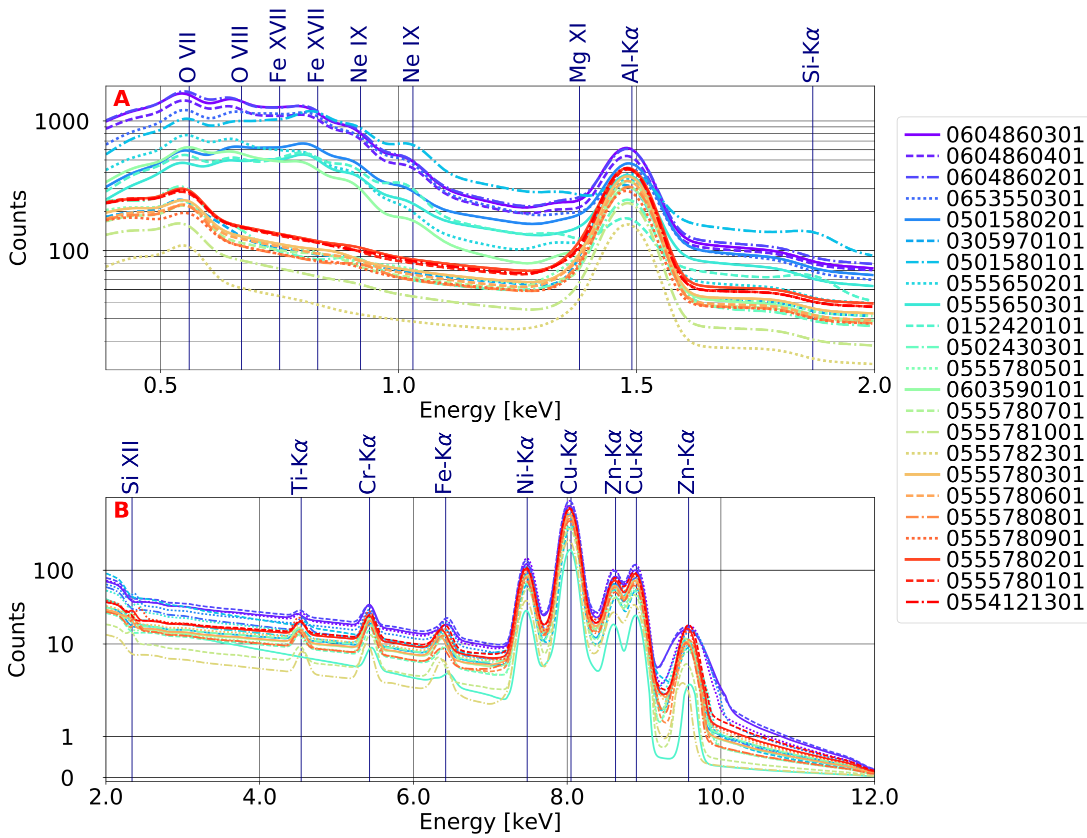

Figure 5.4: The panels A and B show the fitted nullhypothesis model $m_0^{\mathbf{D_2}}$ of each data set of $\mathbf{D_2}$ in energy ranges of $0.38\,\mathrm{keV}$ to $2\,\mathrm{keV}$ (panel A) and of $2\,\mathrm{keV}$ to $12\,\mathrm{keV}$ (panel B), respectively. The fitted model consists of two continuum components consisting of a powerlaw component *pow* and a bremsstrahlung component *bremss*, both attenuated by an absorption component *wabs*, plus $\mathbf{L_2} = 19$ instrumental and astrophysical Gaussian emission lines *gauss*. The best-fit values are specified in tables 5.3 and 5.4.

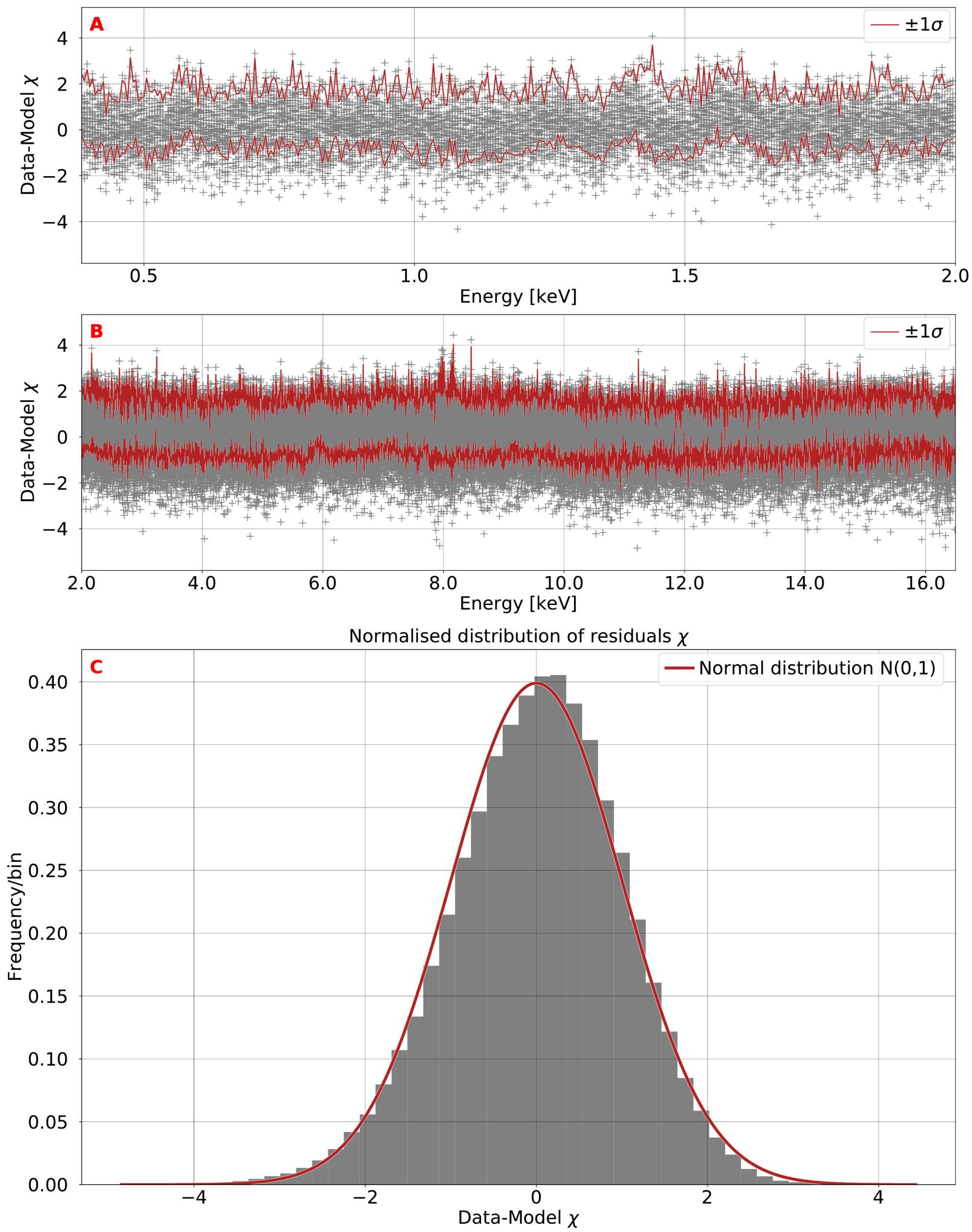

Figure 5.5: The panels A and B show the residuals χ among the best-fit model $m_0^{\mathbf{D_1}}$ and the corresponding data sets of $\mathbf{D_1}$ in energy regimes of $0.38\,\mathrm{keV}$ to $2\,\mathrm{keV}$ (panel A) and $2\,\mathrm{keV}$ to $16.5\,\mathrm{keV}$ (panel B), respectively. The red curves indicate the $\pm 1\sigma$ levels of the residual distributions in each energy bin. The panel C presents the accumulated residual distribution of all energy bins. A normal distribution is also plotted for comparison.

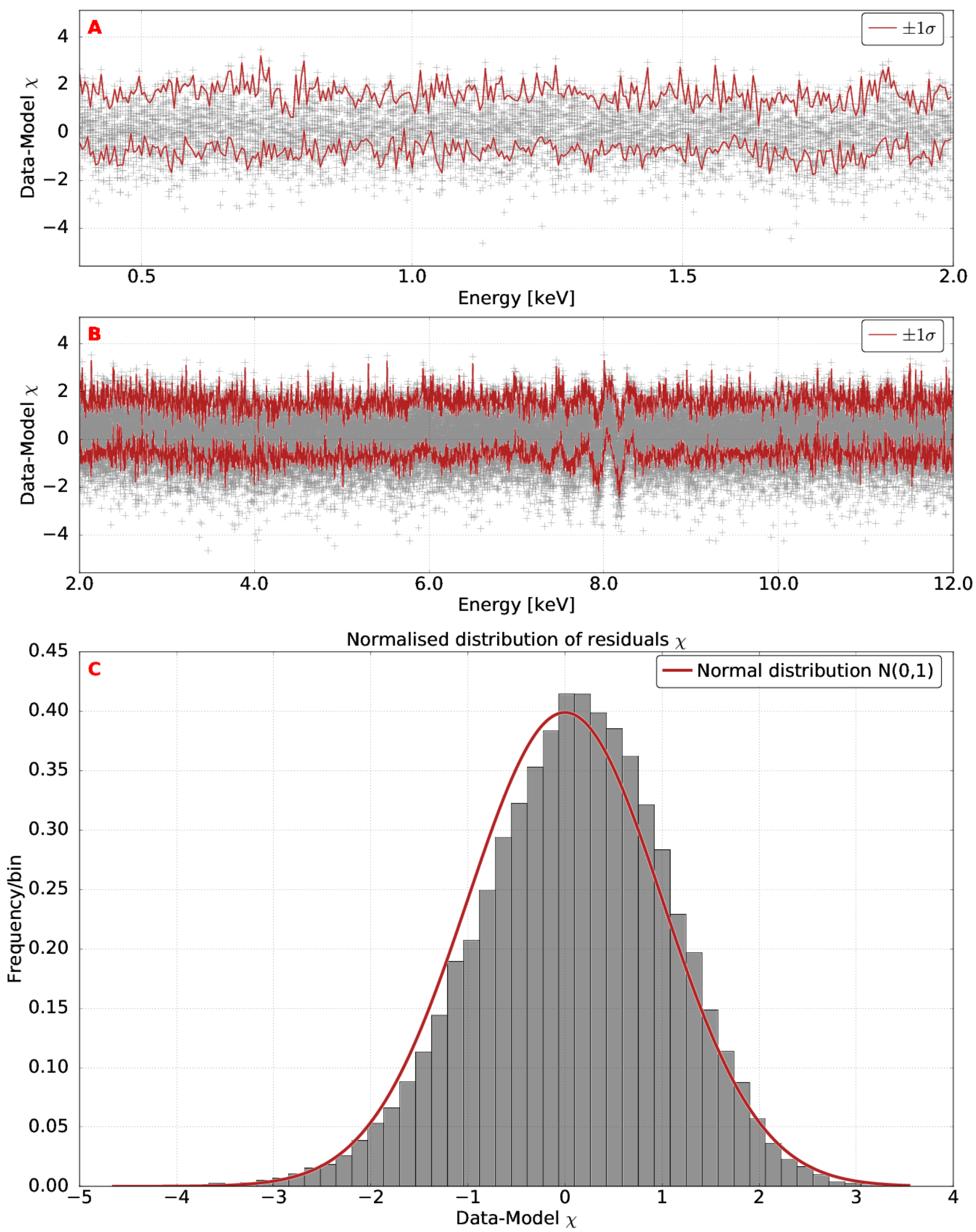

Figure 5.6: The panels A and B show the residuals χ among the best-fit model $m_0^{\mathbf{D_2}}$ and the corresponding data sets of $\mathbf{D_2}$ in energy regimes of $0.38\,\mathrm{keV}$ to $2\,\mathrm{keV}$ (panel A) and $2\,\mathrm{keV}$ to $12\,\mathrm{keV}$ (panel B), respectively. The red curves indicate the $\pm1\sigma$ levels of the residual distributions in each energy bin. The panel C presents the accumulated residual distribution of all energy bins. A normal distribution is also plotted for comparison.

5.5 Alternative Hypothesis Models

Additional component. An alternative hypothesis model $m_1^{\mathbf{D}}$ to test whether the coefficient $a_{\eta+1,\eta+2}$ enclosed in the additional term $a_{\eta+1,t+2}\, f_{\eta+1,\eta+2}(x_p)$ is zero or not (section 5.2), was basically defined on a corresponding nullhypothesis model $m_0^{\mathbf{D}}$, wherein the additional component $a_{\eta+1,t+2}\, f_{\eta+1,\eta+2}(x_p)$ (equation 5.18) was defined as a Gaussian emission line L_γ according to equation 2.39,

$$\begin{aligned} a_{\eta+1,\eta+2}\, m_{1,\,\eta+1,\eta+2}(x_p) &:= \mathrm{L}_\gamma^{\mathbf{D}}\left(E_\gamma^{\mathbf{D}}, \sigma_\gamma^{\mathbf{D}}, \omega_{\gamma;i}^{\mathbf{D},\text{DM-MODEL}} \cdot F_\gamma^{\mathbf{D}}\right) \\ &= \frac{\omega_{\gamma;i}^{\mathbf{D},\text{DM-MODEL}} \cdot F_\gamma^{\mathbf{D}}}{\sigma_\gamma^{\mathbf{D}}\sqrt{2\,\pi}} \exp\left(\frac{-\left(E^{\mathbf{D}} - E_\gamma^{\mathbf{D}}\right)^2}{2\left(\sigma_\gamma^{\mathbf{D}}\right)^2}\right), \end{aligned} \tag{5.33}$$

dependent on a mean energy $E_\gamma^{\mathbf{D}}$, a line width $\sigma_\gamma^{\mathbf{D}}$ and a flux normalisation $F_\gamma^{\mathbf{D}}$ weighted by a factor $\omega_{\gamma;i}^{\mathbf{D},\text{DM-MODEL}}$ dependent on a spatial dark matter distribution of the Milky Way and dark matter model, respectively.

Basic weighting factor. With respect to the weighting factor, the respective expected contributions of the flux normalisations $F_\gamma^{\mathbf{D}}$ of the additional emission line $\mathrm{L}_\gamma^{\mathbf{D}}$ is thereby distributed over each data set of a group of data sets $\mathbf{D}$, so that the flux normalisation $F_{\gamma;i}^{\mathbf{D}}$ corresponding to an ith data set of $\mathbf{D}$ is multiplied by the weighting factor

$$\omega_{\gamma;i}^{\mathbf{D},\text{DM-MODEL}} = \frac{S_i^{\mathbf{D},\text{DM-MODEL}} \cdot t_{\text{exp};i}^{\mathbf{D}} \cdot \Omega_{\text{fov};i}^{\mathbf{D}}}{\sum_{k=1}^{\mathbf{N}}\left(S_k^{\mathbf{D},\text{DM-MODEL}} \cdot t_{\text{exp};k}^{\mathbf{D}} \cdot \Omega_{\text{fov};k}^{\mathbf{D}}\right)}, \quad \sum_{i=1}^{\mathbf{N}} \omega_{\gamma;i}^{\mathbf{D},\text{DM-MODEL}} = 1, \tag{5.34}$$

to take the dark matter model-dependent dark matter column density $S_{\text{NFW};j}$, the field of view $\Omega_{\text{fov};i}^{\mathbf{D}} = \Omega_{\text{fov,net};i}^{\mathbf{D}}$ and the net exposure $t_{\text{exp};i}^{\mathbf{D}} = t_{\text{exp,net};i}^{\mathbf{D}}$ of each ith individual observation into account.

Basic alternative hypothesis model. Hence, a basic alternative hypothesis model incorporating a Gaussian emission line $\mathrm{L}_\gamma^{\mathbf{D}}$ as an additional term or component is defined as

$$
\begin{aligned}
& m_1^{\mathbf{D},\text{DM-MODEL}}\left(\eta; E^{\mathbf{D}}\right) \\
&= m_1^{\mathbf{D},\text{DM-MODEL}}\left(\mathrm{n}_{\mathrm{H};i}, \Gamma_i, \mathrm{N}_{pow;i}, \mathrm{T}_i, \mathrm{N}_{bremss;i}, E_{gauss;ij}, \sigma_{ij}, F_{gauss;ij}, E_\gamma, \sigma_\gamma, F_\gamma\right) \\
&= m_0^{\mathbf{D}}\left(\eta; E^{\mathbf{D}}\right) + \underbrace{\sum_{i=1}^{\mathbf{N}} \mathrm{L}_\gamma^{\mathbf{D}}\left(E_\gamma^{\mathbf{D}}, \sigma_\gamma^{\mathbf{D}}, \omega_{\gamma;i}^{\mathbf{D},\text{DM-MODEL}} \cdot F_\gamma^{\mathbf{D}}\right)}_{\text{additional emission line}}.
\end{aligned}
\tag{5.35}
$$

Dark matter distribution-dependent alternative hypothesis models. A total of four alternative models were tested in the course of the present analysis in dependence of the model- and direction-dependent dark matter column densities, fields of view and net exposures. Two of these models are corresponding to the nullhypothesis model $m_0^{\mathbf{D_1}}\left(\eta; E^{\mathbf{D_1}}\right)$ related to $\mathbf{D_1}$, wherein each of them is dependent on a different dark matter distribution model, namely the isothermal profile according to equation 2.35 and the NFW profile according to equation 2.36,

$$
\begin{aligned}
& m_1^{\mathbf{D_1},\text{ISO}}\left(\eta; E^{\mathbf{D_1}}, \omega_{\gamma;i}^{\mathbf{D_1},\text{ISO}} \cdot F_\gamma^{\mathbf{D_1}}\right) = \\
& m_0^{\mathbf{D_1}}\left(\eta; E^{\mathbf{D_1}}\right) + \underbrace{\sum_{i=1}^{\mathbf{N_1}} \mathrm{L}_\gamma^{\mathbf{D_1}}\left(E_\gamma^{\mathbf{D_1}}, \sigma_\gamma^{\mathbf{D_1}}, \omega_{\gamma;i}^{\mathbf{D_1},\text{ISO}} \cdot F_\gamma^{\mathbf{D_1}}\right)}_{\text{additional emission line}},
\end{aligned}
\tag{5.36}
$$

having a dark-matter-model-dependent weighting factor

$$
\omega_{\gamma;i}^{\mathbf{D_1},\text{ISO}} = \frac{S_i^{\mathbf{D_1},\text{ISO}} \cdot t_{\text{exp};i}^{\mathbf{D_1}} \cdot \Omega_{\text{fov};i}^{\mathbf{D_1}}}{\sum_{j=1}^{\mathbf{N_1}}\left(S_j^{\mathbf{D_1},\text{ISO}} \cdot t_{\text{exp};j}^{\mathbf{D_1}} \cdot \Omega_{\text{fov};j}^{\mathbf{D_1}}\right)}, \quad i \in \{1, \ldots, \mathbf{N_1}\}, \tag{5.37}
$$

as well as

$$
\begin{aligned}
& m_1^{\mathbf{D_1},\text{NFW}}\left(\eta; E^{\mathbf{D_1}}, \omega_{\gamma;i}^{\mathbf{D_1},\text{NFW}} \cdot F_\gamma^{\mathbf{D_1}}\right) = \\
& m_0^{\mathbf{D_1}}\left(\eta; E^{\mathbf{D_1}}\right) + \underbrace{\sum_{i=1}^{\mathbf{N_1}} \mathrm{L}_\gamma^{\mathbf{D_1}}\left(E_\gamma^{\mathbf{D_1}}, \sigma_\gamma^{\mathbf{D_1}}, \omega_{\gamma;i}^{\mathbf{D_1},\text{NFW}} \cdot F_\gamma^{\mathbf{D_1}}\right)}_{\text{additional emission line}},
\end{aligned}
\tag{5.38}
$$

having a dark-matter-model-dependent weighting factor

$$
\omega_{\gamma;i}^{\mathbf{D_1},\text{NFW}} = \frac{S_i^{\mathbf{D_1},\text{NFW}} \cdot t_{\text{exp};i}^{\mathbf{D_1}} \cdot \Omega_{\text{fov};i}^{\mathbf{D_1}}}{\sum_{j=1}^{\mathbf{N_1}}\left(S_j^{\mathbf{D_1},\text{NFW}} \cdot t_{\text{exp};j}^{\mathbf{D_1}} \cdot \Omega_{\text{fov};j}^{\mathbf{D_1}}\right)}, \quad i \in \{1, \ldots, \mathbf{N_1}\}, \tag{5.39}
$$

respectively. The same applies to the remaining two alternative models dependent on the afore-mentioned dark matter distribution models corresponding to the nullhypothesis model $m_0^{\mathbf{D_2}}\left(\eta; E^{\mathbf{D_2}}\right)$ which is related to $\mathbf{D_2}$,

$$\begin{aligned} &m_1^{\mathbf{D_2},\mathrm{ISO}}\left(\eta; E^{\mathbf{D_2}}, \omega_{\gamma;i}^{\mathbf{D_2},\mathrm{ISO}} \cdot F_\gamma^{\mathbf{D_2}}\right) = \\ &m_0^{\mathbf{D_2}}\left(\eta; E^{\mathbf{D_2}}\right) + \underbrace{\sum_{i=1}^{\mathbf{N_2}} \mathrm{L}_\gamma^{\mathbf{D_2}}\left(E_\gamma^{\mathbf{D_2}}, \sigma_\gamma^{\mathbf{D_2}}, \omega_{\gamma;i}^{\mathbf{D_2},\mathrm{ISO}} \cdot F_\gamma^{\mathbf{D_2}}\right)}_{\text{additional emission line}}, \end{aligned} \tag{5.40}$$

having a dark-matter-model-dependent weighting factor

$$\omega_{\gamma;i}^{\mathbf{D_2},\mathrm{ISO}} = \frac{S_i^{\mathbf{D_2},\mathrm{ISO}} \cdot t_{\mathrm{exp};i}^{\mathbf{D_2}} \cdot \Omega_{\mathrm{fov};i}^{\mathbf{D_2}}}{\sum_{j=1}^{\mathbf{N_2}}\left(S_j^{\mathbf{D_2},\mathrm{ISO}} \cdot t_{\mathrm{exp};j}^{\mathbf{D_2}} \cdot \Omega_{\mathrm{fov};j}^{\mathbf{D_2}}\right)}, \quad i \in \{1, \ldots, \mathbf{N_2}\}, \tag{5.41}$$

as well as

$$\begin{aligned} &m_1^{\mathbf{D_2},\mathrm{NFW}}\left(\eta; E^{\mathbf{D_2}}, \omega_{\gamma;i}^{\mathbf{D_2},\mathrm{NFW}} \cdot F_\gamma^{\mathbf{D_2}}\right) = \\ &m_0^{\mathbf{D_2}}\left(\eta; E^{\mathbf{D_2}}\right) + \underbrace{\sum_{i=1}^{\mathbf{N_2}} \mathrm{L}_\gamma^{\mathbf{D_2}}\left(E_\gamma^{\mathbf{D_2}}, \sigma_\gamma^{\mathbf{D_2}}, \omega_{\gamma;i}^{\mathbf{D_2},\mathrm{NFW}} \cdot F_\gamma^{\mathbf{D_2}}\right)}_{\text{additional emission line}}, \end{aligned} \tag{5.42}$$

having a dark-matter-model-dependent weighting factor

$$\omega_{\gamma;i}^{\mathbf{D_2},\mathrm{NFW}} = \frac{S_i^{\mathbf{D_2},\mathrm{NFW}} \cdot t_{\mathrm{exp};i}^{\mathbf{D_2}} \cdot \Omega_{\mathrm{fov};i}^{\mathbf{D_2}}}{\sum_{j=1}^{\mathbf{N_2}}\left(S_j^{\mathbf{D_2},\mathrm{NFW}} \cdot t_{\mathrm{exp};j}^{\mathbf{D_2}} \cdot \Omega_{\mathrm{fov};j}^{\mathbf{D_2}}\right)}, \quad i \in \{1, \ldots, \mathbf{N_2}\}, \tag{5.43}$$

respectively. The respective weightings $\omega_{\gamma;i}^{\mathbf{D_1},\mathrm{ISO}}$, $\omega_{\gamma;i}^{\mathbf{D_1},\mathrm{NFW}}$, $\omega_{\gamma;i}^{\mathbf{D_2},\mathrm{ISO}}$ and $\omega_{\gamma;i}^{\mathbf{D_2},\mathrm{NFW}}$ are listed in tables 5.1 and 5.3 as well as tables 5.2 and 5.4.

Additional component on a parameter grid. Each of the above four alternative hypothesis models were fitted to all points $(E_{\gamma;n}^{\mathbf{D}}, F_{\gamma;m}^{\mathbf{D}})$ in a two-dimensional parameter grid,

$$\mathrm{G}_2^{\mathbf{D}}\left(E_{\gamma;n}^{\mathbf{D}}, F_{\gamma;m}^{\mathbf{D}}\right) = \begin{pmatrix} \left(E_{\gamma;1}^{\mathbf{D}}, F_{\gamma;m_{\max}^{\mathbf{D}}}^{\mathbf{D}}\right) & \ldots & \left(E_{\gamma;n_{\max}^{\mathbf{D}}}^{\mathbf{D}}, F_{\gamma;m_{\max}^{\mathbf{D}}}^{\mathbf{D}}\right) \\ \vdots & \iddots & \vdots \\ \left(E_{\gamma;1}^{\mathbf{D}}, F_{\gamma;1}^{\mathbf{D}}\right) & \ldots & \left(E_{\gamma;n_{\max}^{\mathbf{D}}}^{\mathbf{D}}, F_{\gamma;1}^{\mathbf{D}}\right) \end{pmatrix}, \tag{5.44}$$

respectively, which is spanned by discrete values of the line energies $E^{\mathbf{D}}_{\gamma;n}$ and the flux normalisations $F^{\mathbf{D}}_{\gamma;m}$ of the additional Gaussian emission line

$$\mathrm{L}_\gamma\left(E^{\mathbf{D}}_\gamma, \sigma^{\mathbf{D}}_\gamma, \omega^{\mathbf{D},\text{DM-MODEL}}_{\gamma;i} \cdot F^{\mathbf{D}}_\gamma\right) = \mathrm{L}_\gamma\left(E^{\mathbf{D}}_{\gamma;n}, \sigma^{\mathbf{D}}_\gamma, \omega^{\mathbf{D},\text{DM-MODEL}}_{\gamma;i} \cdot F^{\mathbf{D}}_{\gamma;m}\right) \quad (5.45)$$

while the widths $\sigma^{\mathbf{D}}_\gamma$ were fixed at zero. Each point $(E^{\mathbf{D}}_{\gamma;n}, F^{\mathbf{D}}_{\gamma;m})$ in a parameter grid is associated with its individual simulated sampling distribution $\mathcal{F}^{\mathbf{mc}}_{\mathcal{B}}$ and its individual measured $\mathcal{F}^{\mathbf{m}}_{\mathcal{B}}$ value. The size of the parameter grid ranges from $E^{\mathbf{D_1}} = 0.38\,\text{keV}$ to $E^{\mathbf{D_1}} = 16.5\,\text{keV}$ for $\mathbf{D_1}$ and from $E^{\mathbf{D_2}} = 0.38\,\text{keV}$ to $E^{\mathbf{D_2}} = 12.0\,\text{keV}$ for $\mathbf{D_2}$ on a linear energy axis and from a total flux of $10^{-9}\,\text{photons}\,\text{cm}^{-2}\,\text{s}^{-1}$ to $10^{3}\,\text{photons}\,\text{cm}^{-2}\,\text{s}^{-1}$ on a logarithmic normalisation axis for each $\mathbf{D_1}$ and $\mathbf{D_2}$, respectively. The resolution is $n^{\mathbf{D_1}}_{\text{max}} = 201$ times $m^{\mathbf{D_1}}_{\text{max}} = 201$ points for $\mathbf{D_1}$ and $n^{\mathbf{D_2}}_{\text{max}} = 151$ times $m^{\mathbf{D_2}}_{\text{max}} = 151$ points for $\mathbf{D_2}$ in the corresponding parameter grids $\mathrm{G}^{\mathbf{D_1}}_2$ and $\mathrm{G}^{\mathbf{D_2}}_2$, respectively, wherein the resulting energy resolutions are approximately 80.6 eV for $\mathbf{D_1}$ and approximately 76.95 eV for $\mathbf{D_2}$. Consequently, grids of measured $\mathcal{F}^{\mathbf{m}}_{\mathcal{B}}$-values,

$$\mathcal{F}^{\mathbf{m}}_{\mathcal{B}}\left(\mathrm{G}^{\mathbf{D}}_2\left(E^{\mathbf{D}}_{\gamma;n}, F^{\mathbf{D}}_{\gamma;m}\right)\right) = \mathcal{F}^{\mathbf{m}}_{\mathcal{B}}\begin{pmatrix} \left(E^{\mathbf{D}}_{\gamma;1}, F^{\mathbf{D}}_{\gamma;m^{\mathbf{D}}_{\text{max}}}\right) & \dots & \left(E^{\mathbf{D}}_{\gamma;n^{\mathbf{D}}_{\text{max}}}, F^{\mathbf{D}}_{\gamma;m^{\mathbf{D}}_{\text{max}}}\right) \\ \vdots & \iddots & \vdots \\ \left(E^{\mathbf{D}}_{\gamma;1}, F^{\mathbf{D}}_{\gamma;1}\right) & \dots & \left(E^{\mathbf{D}}_{\gamma;n^{\mathbf{D}}_{\text{max}}}, F^{\mathbf{D}}_{\gamma;1}\right) \end{pmatrix}, \quad (5.46)$$

were calculated according to equation 5.21 for $\mathbf{D} = \mathbf{D_1}$ and for $\mathbf{D} = \mathbf{D_2}$, respectively, and therefore for each of the four alternative models $m_1^{\mathbf{D_1},\text{ISO}}$ and $m_1^{\mathbf{D_1},\text{NFW}}$ as well as $m_1^{\mathbf{D_2},\text{ISO}}$ and $m_1^{\mathbf{D_2},\text{NFW}}$ mentioned afore in combination with the respective nullhypothesis models $m_0^{\mathbf{D_1}}$ and $m_0^{\mathbf{D_2}}$. For each model $1 \times 201 \times 201 = 40,401$ $\mathcal{F}^{\mathbf{m}}_{\mathcal{B}}$-values or $1 \times 151 \times 151 = 22,801$ $\mathcal{F}^{\mathbf{m}}_{\mathcal{B}}$-values were computed for $\mathbf{D_1}$ and $\mathbf{D_2}$, respectively. The same calculations were performed for each of the $M^{\mathbf{D}} = M^{\mathbf{D_1}} = 500$ and $M^{\mathbf{D}} = M^{\mathbf{D_2}} = 500$ sampled $\mathcal{F}^{\mathbf{mc}}_{\mathcal{B}}$-values to obtain one corresponding sampling distribution per pair of parameters $(E^{\mathbf{D}}_{\gamma;n}, F^{\mathbf{D}}_{\gamma;m})$ in a grid according to equation 5.24,

$$\mathcal{F}^{\mathbf{mc}}_{\mathcal{B}}\left(\mathrm{G}^{\mathbf{D}}_2\left(E^{\mathbf{D}}_{\gamma;n}, F^{\mathbf{D}}_{\gamma;m}\right)\right) = \mathcal{F}^{\mathbf{mc}}_{\mathcal{B}}\begin{pmatrix} \left(E^{\mathbf{D}}_{\gamma;1}, F^{\mathbf{D}}_{\gamma;m^{\mathbf{D}}_{\text{max}}}\right) & \dots & \left(E^{\mathbf{D}}_{\gamma;n^{\mathbf{D}}_{\text{max}}}, F^{\mathbf{D}}_{\gamma;m^{\mathbf{D}}_{\text{max}}}\right) \\ \vdots & \iddots & \vdots \\ \left(E^{\mathbf{D}}_{\gamma;1}, F^{\mathbf{D}}_{\gamma;1}\right) & \dots & \left(E^{\mathbf{D}}_{\gamma;n^{\mathbf{D}}_{\text{max}}}, F^{\mathbf{D}}_{\gamma;1}\right) \end{pmatrix}. \quad (5.47)$$

For each model $500 \times 201 \times 201 = 20,200,500$ or $500 \times 151 \times 151 = 11,400,500$ $\mathcal{F}_{\mathcal{B}}^{\mathbf{mc}}$-values were computed for $\mathbf{D_1}$ and $\mathbf{D_2}$, respectively. The above grid of measured $\mathcal{F}_{\mathcal{B}}^{\mathbf{m}}$-values (equation 5.46) and the above grids of sampled $\mathcal{F}_{\mathcal{B}}^{\mathbf{mc}}$-values (equation 5.47) were applied to calculate corresponding p-values according to equation 5.25,

$$p\left(\mathrm{G}_2^{\mathbf{D}}\left(E_{\gamma;n}^{\mathbf{D}}, F_{\gamma;m}^{\mathbf{D}}\right)\right) = \begin{pmatrix} p(E_{\gamma;1}, F_{\gamma;m_{\max}^{\mathbf{D}}}) & \dots & p(E_{\gamma;n_{\max}^{\mathbf{D}}}, F_{\gamma;m_{\max}^{\mathbf{D}}}) \\ \vdots & \iddots & \vdots \\ p(E_{\gamma;1}, F_{\gamma;1}) & \dots & p(E_{\gamma;n_{\max}^{\mathbf{D}}}, F_{\gamma;1}) \end{pmatrix}, \tag{5.48}$$

or q-values, wherein the latter are defined as $q \coloneqq 1 - p$,

$$q\left(\mathrm{G}_2^{\mathbf{D}}\left(E_{\gamma;n}^{\mathbf{D}}, F_{\gamma;m}^{\mathbf{D}}\right)\right) = 1 - p\left(\mathrm{G}_2^{\mathbf{D}}\left(E_{\gamma;n}^{\mathbf{D}}, F_{\gamma;m}^{\mathbf{D}}\right)\right). \tag{5.49}$$

Confidence regions $\mathrm{R}_l^{q>0.99}$ in the energy-normalisation parameter space corresponding to a q-value of

$$q_{0.99} \coloneqq q(E_{\gamma;n}, F_{\gamma;m}) > 0.99^{15} \tag{5.50}$$

were chosen to discriminate the parameter space of an additional emission line into regions in which the nullhypothesis model $m_0^{\mathbf{D}}$ is favoured, ($q \leq 0.99$), and in which the alternative hypothesis model $m_1^{\mathbf{D}}$ is preferred, ($q > 0.99$).

5.6 Upper Limits and Errors based on $\Delta\chi^2$-Statistics

Upper Limits. A value $\Delta\chi^2$ defined as the difference between a given χ^2-value and a local minimum in a χ^2-space can be calculated to generate upper limits or confidence limits on the parameters $E_{\gamma;n}^{\mathbf{D}}$ and/or $F_{\gamma,m}^{\mathbf{D}}$. The following confidence limits were calculated in the scope of this work with respect to the goodness-of-fit values 5.28 and 5.31 which should be absolute minima in an ideal scenario,

$$\Delta\chi^2_{90\%}(E_{\gamma;n}^{\mathbf{D}}, F_{\gamma;m}^{\mathbf{D}}) \coloneqq \chi^2(E_{\gamma;n}^{\mathbf{D}}, F_{\gamma;m}^{\mathbf{D}}) - \chi^2_0(m_0^{\mathbf{D}}) = 4.605, \tag{5.51}$$

$$\Delta\chi^2_{95\%}(E_{\gamma;n}^{\mathbf{D}}, F_{\gamma;m}^{\mathbf{D}}) \coloneqq \chi^2(E_{\gamma;n}^{\mathbf{D}}, F_{\gamma;m}^{\mathbf{D}}) - \chi^2_0(m_0^{\mathbf{D}}) = 5.992, \tag{5.52}$$

$$\Delta\chi^2_{99\%}(E_{\gamma;n}^{\mathbf{D}}, F_{\gamma;m}^{\mathbf{D}}) \coloneqq \chi^2(E_{\gamma;n}^{\mathbf{D}}, F_{\gamma;m}^{\mathbf{D}}) - \chi^2_0(m_0^{\mathbf{D}}) = 9.211. \tag{5.53}$$

Further, for the purpose of visualising the results shown in the next chapter, levels of $\Delta\chi^2$ having values of -9.211, -5.992, -4.605 and 0.0 were computed.

[15] $q = 1 - \frac{1}{M^D} = 1 - \frac{1}{500} = 0.998 > 0.99$ with M^D being the number of simulated data sets or spectra.

Errors. The basic hypothesis which allows the application of the $\Delta\chi^2$-statistics is the existence of an additional component or an emission line L_γ or, with other words, the acceptance of the alternative hypothesis model $m_1^{\mathbf{D}}$ formulated in section 5.5, wherein the flux normalisation $F_\gamma^{\mathbf{D}}$ of the corresponding additional emission line L_γ has to be greater zero.
In this case, the value of $\Delta\chi^2$ is defined as the difference between a given χ^2-value and a local minimum in the χ^2-space, both contained in a lth region of a number N_l, $l \in \{1, ..., N_l\}$ of closed regions $\mathrm{R}_l^{q>0.99}(E_{\gamma;n}^{\mathbf{D}}, F_{\gamma;m}^{\mathbf{D}})$ fulfilling the condition $q > 0.99$ in which the nullhypothesis model $m_0^{\mathbf{D}}$ is rejected according to the posterior predictive p-value analysis. Further, a 95% or a 99% confidence level (for $\eta + 2 - \eta = 2$ degrees of freedom) has to fulfill one of the respective conditions[16],

$$\begin{aligned}\Delta\chi_{l;95\%}^{2;q>0.99}(E_{\gamma;n}^{\mathbf{D}}, F_{\gamma;m}^{\mathbf{D}}) &:= \chi_l^{2;q>0.99}(E_{\gamma;n}^{\mathbf{D}}, F_{\gamma;m}^{\mathbf{D}}) - \min_{\mathrm{R}_l^{q>0.99}} \left(\chi_l^{2;q>0.99}(E_{\gamma;n}^{\mathbf{D}}, F_{\gamma,m}^{\mathbf{D}})\right) \\ &= 5.992, \end{aligned} \tag{5.54}$$

$$\begin{aligned}\Delta\chi_{l;99\%}^{2;q>0.99}(E_{\gamma;n}^{\mathbf{D}}, F_{\gamma;m}^{\mathbf{D}}) &:= \chi_l^{2;q>0.99}(E_{\gamma;n}^{\mathbf{D}}, F_{\gamma;m}^{\mathbf{D}}) - \min_{\mathrm{R}_l^{q>0.99}} \left(\chi_l^{2;q>0.99}(E_{\gamma;n}^{\mathbf{D}}, F_{\gamma,m}^{\mathbf{D}})\right) \\ &= 9.211, \end{aligned} \tag{5.55}$$

wherein $\min_{\mathrm{R}_l^{q>0.99}}(\chi_l^{2;q>0.99}(E_{\gamma;n}^{\mathbf{D}}, F_{\gamma,m}^{\mathbf{D}}))$ represents a global or local minimum of a corresponding region $\mathrm{R}_l^{q>0.99}$ in the χ^2-space.
Eventually, the resulting set of $\Delta\chi^2_{l;95\%}$-values and $\Delta\chi^2_{l;99\%}$-values was evaluated to determine the respective 95%-errors and 99%-errors of the parameters $E_{\gamma;n}$ and $F_{\gamma,m}$ related to minima located in the corresponding closed regions R_l in which the nullhypothesis model was rejected.

5.7 Combined Model-dependent Upper Limits

The dark matter models introduced in section 2.3.1 propose particles having a mass m_{dm}. Further, these particles are theoretically allowed to undergo two-body-decays to generate X-ray photons with an energy of $E_\gamma = \frac{m_{\mathrm{dm}}}{2}$ in natural units (88, 89, 91). The decay measure of such a process contains the decay width Γ_{dm}

[16] Please see the Xspec Manual: https://heasarc.gsfc.nasa.gov/docs/xanadu/xspec/manual/XspecSpectralFitting.html or Avni (52).

as the inverse of the decay time and is defined as

$$\epsilon_{\text{dm}} = \frac{1}{4\pi}\frac{E_\gamma \Gamma_{\text{dm}}}{m_{\text{dm}}}. \tag{5.56}$$

The expected intensity I_{dm} is the product of the decay measure and the model-dependent dark matter column density S_{dm} which, moreover, is an integral of a dark matter density distribution ρ_{dm} over the line-of-sight s (see also equation 4.1 for a comparison):

$$I_{\text{dm}}(s) = \epsilon_{\text{dm}} S_{\text{dm}}(s) = \frac{\Gamma_{\text{dm}}}{8\pi}\int_0^\infty \rho_{\text{dm}}(s)\, ds. \tag{5.57}$$

The upper limits of the flux of both statistical methods applied in this work were used to constrain the parameter spaces of two theoretically proposed dark matter particles, the sterile neutrino and the axion. Both particles are theoretically allowed to decay into X-ray photons. The decay rate of the Majorana sterile neutrino (89, 90) as a warm dark matter particle of mass m_{ν_s} into a photon and an active neutrino is

$$\begin{aligned}&\Gamma(\nu_R \to \gamma\nu_L) = \\ &\Gamma_{\nu_s} = \frac{9\alpha G_{\text{F}}^2}{1024\pi^4}\sin^2(2\Theta) m_{\nu_s}^5 \approx 1.38\cdot 10^{-32}\,\text{s}^{-1}\left(\frac{\sin^2(2\Theta)}{10^{-10}}\right)\left(\frac{m_{\nu_s}}{\text{keV}}\right)^5,\end{aligned} \tag{5.58}$$

with α being the fine structure constant, G_{F} denotes the Fermi constant and Θ is defined as the mixing angle between sterile neutrinos and photons. The Dirac sterile neutrino would have half the decay rate of the Majorana sterile neutrino. The decay rate of an axion, which would be a cold dark matter particle (97, 113) with mass m_ϕ, with respect to decays into two photons, is

$$\Gamma(a \to \gamma\gamma) = \Gamma_{a\gamma\gamma} = \frac{64\pi}{g_{a\gamma\gamma}^2\, m_a^3} \approx 7.69\cdot 10^{-26}\,\text{s}^{-1}\left(\frac{g_{a\gamma\gamma}}{10^{-10}\,\text{GeV}^{-1}}\right)^2\left(\frac{m_a}{\text{eV}}\right)^3. \tag{5.59}$$

The intensity I_{dm} is composed of the normalisation F_γ divided by a field of view Ω_{fov} while the energy flux is the product of the normalisation F_γ (photons per cm^2 per s) of an additional emission line L_γ and the mean energy of the additional emission line E_γ,

$$I_{\text{dm}} = E_\gamma \cdot F_\gamma \cdot \left(\Omega_{\text{fov}}^{\text{net}}\right)^{-1}. \tag{5.60}$$

The upper limits for the mixing $\sin^2(2\Theta)$ of the sterile neutrinos are constrained via the mixing,

$$\sin^2(2\Theta) \leq \left(\frac{E_\gamma \cdot F_\gamma}{6.9 \cdot 10^4\,\mathrm{keV\,cm^{-2}\,s^{-1}}}\right)\left(\frac{S_{\mathrm{dm}}}{10^{27}\,\mathrm{keV\,cm^{-2}}} \cdot \frac{\Omega_{\mathrm{fov}}^{\mathrm{net}}}{4\pi\,\mathrm{str}}\right)^{-1}\left(\frac{m_{\nu_s}}{\mathrm{keV}}\right)^{-5}. \tag{5.61}$$

The coupling of the axion is constrained by

$$g_{a\gamma\gamma} \leq \left(\left(\frac{E_\gamma \cdot F_\gamma}{3.8 \cdot 10^{30}\,\mathrm{keV\,cm^{-2}\,s^{-1}}}\right)\left(\frac{S_{\mathrm{dm}}}{10^{27}\,\mathrm{keV\,cm^{-2}}} \cdot \frac{\Omega_{\mathrm{fov}}^{\mathrm{net}}}{4\pi\,\mathrm{str}}\right)^{-1}\left(\frac{m_a}{\mathrm{keV}}\right)^{-3}\right)^{0.5}\mathrm{GeV}^{-1}. \tag{5.62}$$

The combined upper limits of the mixing $\sin^2(2\Theta)$ can be calculated from the combined upper limits of the flux normalisations $F_\gamma^{\mathbf{D}}$. The total mixing between sterile neutrinos and photons related to $\mathbf{N}$ data sets of a group of data sets $\mathbf{D}$ dependent on a pair of parameters $\left(E_{\gamma;n}^{\mathbf{D}}, F_{\gamma,m}^{\mathbf{D}}\right)$ contained in a parameter grid $\mathrm{G}_2\left(E_{\gamma;n}^{\mathbf{D}}, F_{\gamma,m}^{\mathbf{D}}\right)$ according to equation 5.44 is

$$\begin{aligned}&\sin^2(2\Theta)_{\mathrm{total}}^{\mathbf{D}}\left(E_{\gamma;n}^{\mathbf{D}}, F_{\gamma;m}^{\mathbf{D}}\right) = \\ &\sum_{i=1}^{\mathbf{N}}\left(\frac{E_{\gamma;n}^{\mathbf{D}} \cdot \omega_{\gamma,i}^{\mathbf{D},\mathrm{DM\text{-}MODEL}} \cdot F_{\gamma;mi}^{\mathbf{D}}}{6.9 \cdot 10^{4}\,\mathrm{keV\,cm^{-2}\,s^{-1}}}\right) \cdot \\ &\left(\sum_{p=1}^{\mathbf{N}}\left(\frac{S_p^{\mathbf{D},\mathrm{DM\text{-}MODEL}}}{10^{27}\,\mathrm{keV\,cm^{-2}}} \cdot \frac{\Omega_{\mathrm{fov};p}^{\mathbf{D}}}{4\pi\,\mathrm{str}}\right)\right)^{-1}\left(\frac{2E_{\gamma;n}^{\mathbf{D}}}{\mathrm{keV}}\right)^{-5}.\end{aligned} \tag{5.63}$$

The very same procedure leads to the combined upper limit of the coupling of axions and photons,

$$\begin{aligned}&g_{a\gamma\gamma,\mathrm{total}}^{\mathbf{D}}\left(E_{\gamma;n}^{\mathbf{D}}, F_{\gamma;m}^{\mathbf{D}}\right) = \\ &\sum_{i=1}^{\mathbf{N}}\left(\left(\frac{E_{\gamma;n}^{\mathbf{D}} \cdot \omega_{\gamma,i}^{\mathbf{D},\mathrm{DM\text{-}MODEL}} \cdot F_{\gamma;mi}^{\mathbf{D}}}{3.8 \cdot 10^{30}\,\mathrm{keV\,cm^{-2}\,s^{-1}}}\right) \cdot \right. \\ &\left.\left(\sum_{p=1}^{\mathbf{N}}\left(\frac{S_p^{\mathbf{D},\mathrm{DM\text{-}MODEL}}}{10^{27}\,\mathrm{keV\,cm^{-2}}} \cdot \frac{\Omega_{\mathrm{fov};p}^{\mathbf{D}}}{4\pi\,\mathrm{str}}\right)\right)^{-1}\left(\frac{2E_{\gamma;n}^{\mathbf{D}}}{\mathrm{keV}}\right)^{-3}\right)^{0.5}\mathrm{GeV}^{-1}.\end{aligned} \tag{5.64}$$

Chapter 6

Results

6.1 Constraints on F_γ

Each of the figures 6.1, 6.2, 6.3 and 6.4 shows results of the posterior predictive p-value analysis and the $\Delta\chi^2_{99\%}$-statistics comprising $q(E^{\mathbf{D}}_{\gamma;n}, F^{\mathbf{D}}_{\gamma;m})$-values as well as $q_{0.99}$-confidence regions calculated by equations 5.48, 5.49 and 5.50 for every pair of parameters $(E^{\mathbf{D}}_{\gamma;n}, F^{\mathbf{D}}_{\gamma;m})$ of the normalisation F_γ (in units of [photons cm^{-2} s^{-1}]) of the additional emission line L_γ. Furthermore, these figures show $\Delta\chi^2_{99\%}$-contours, $\Delta\chi^2_{95\%}$-contours, and $\Delta\chi^2_{90\%}$-contours according to the respective equations 5.51, 5.52, and 5.53 as well as contours based on $\Delta\chi^2 = -9.211$, $\Delta\chi^2 = -5.992$, $\Delta\chi^2 = -4.605$, and $\Delta\chi^2 = 0.0$ for the purpose of visualising the results. Further, figures 6.1, 6.2, 6.3 and 6.4 correspond to the models $m_1^{\mathbf{D_1},\mathrm{ISO}}$, $m_1^{\mathbf{D_1},\mathrm{NFW}}$, $m_1^{\mathbf{D_2},\mathrm{ISO}}$ and $m_1^{\mathbf{D_2},\mathrm{NFW}}$, respectively, for every pair of values $(E^{\mathbf{D}}_{\gamma;n}, F^{\mathbf{D}}_{\gamma;m})$ in the corresponding two-dimensional grids $\mathrm{G}_2^{\mathbf{D_1}}$ and $\mathrm{G}_2^{\mathbf{D_2}}$. The emission line claimed by Bulbul et al. (154) at an energy of $3.51 \pm 0.03\,\mathrm{keV}$ and a normalisation of $3.9\,^{+0.6}_{-1.0} \cdot 10^{-6}\,\mathrm{cm}^{-2}\,\mathrm{s}^{-1}$ is also shown in the figures mentioned afore.

Figure 6.5 shows a Monte-Carlo-$\mathcal{F}^{\mathbf{mc}}_{\mathcal{B}}$-distribution represented in form of a histogram for grid parameters,

$$\mathrm{G}_2^{\mathbf{D}}\left(E^{\mathbf{D}}_{\gamma;n}, F^{\mathbf{D}}_{\gamma;m}\right) = \mathrm{G}_2^{\mathbf{D_1}}\left(E^{\mathbf{D_1}}_{\gamma;n=69} = 5.94\,\mathrm{keV}, F^{\mathbf{D_1}}_{\gamma;m=109} = 34.67 \cdot 10^{-4}\,\mathrm{cm}^{-2}\,\mathrm{s}^{-1}\right), \tag{6.1}$$

according to equation 5.47 and a sample size of $M^{\mathbf{D_1}} = 500$ as well as a measured $\mathcal{F}_{\mathcal{B}}$-value,

$$\mathcal{F}_{\mathcal{B}}^{\mathbf{m}}\left(\mathrm{G}_2^{\mathbf{D_1}}\left(E_{\gamma;n=69}^{\mathbf{D_1}} = 5.94\,\mathrm{keV}, F_{\gamma;m=109}^{\mathbf{D_1}} = 34.67\cdot 10^{-4}\,\mathrm{cm}^{-2}\,\mathrm{s}^{-1}\right)\right) = 8.016, \tag{6.2}$$

as an example. The related nullhypothesis model $m_0^{\mathbf{D_1},\mathrm{NFW}}$ is rejected in this case. This, since the pair of parameters,

$$(E_{\gamma;n=69}^{\mathbf{D_1}}, F_{\gamma;m=109}^{\mathbf{D_1}}) = (5.94\,\mathrm{keV}, 34.67\cdot 10^{-4}\,\mathrm{cm}^{-2}\,\mathrm{s}^{-1}), \tag{6.3}$$

which is related to a q-value,

$$q = 1 - p\left(\mathrm{G}_2^{\mathbf{D_1}}\left(E_{\gamma;n=69}^{\mathbf{D_1}} = 5.94\,\mathrm{keV}, F_{\gamma;m=109}^{\mathbf{D_1}} = 34.67\cdot 10^{-4}\,\mathrm{cm}^{-2}\,\mathrm{s}^{-1}\right)\right) = 1.0, \tag{6.4}$$

according to equations 5.48 and 5.49 is located in a $q_{0.99}$-confidence region $\mathrm{R}_l^{q>0.99}$ according to equation 5.50 (please see figure 6.2 or tables 6.3 and 6.4, in particular the $\mathrm{R}_{l=14}^{q>0.99}$-region) such that the alternative hypothesis model $m_1^{\mathbf{D_1},\mathrm{NFW}}$ is favoured in this case in view of the pair of parameters mentioned afore.

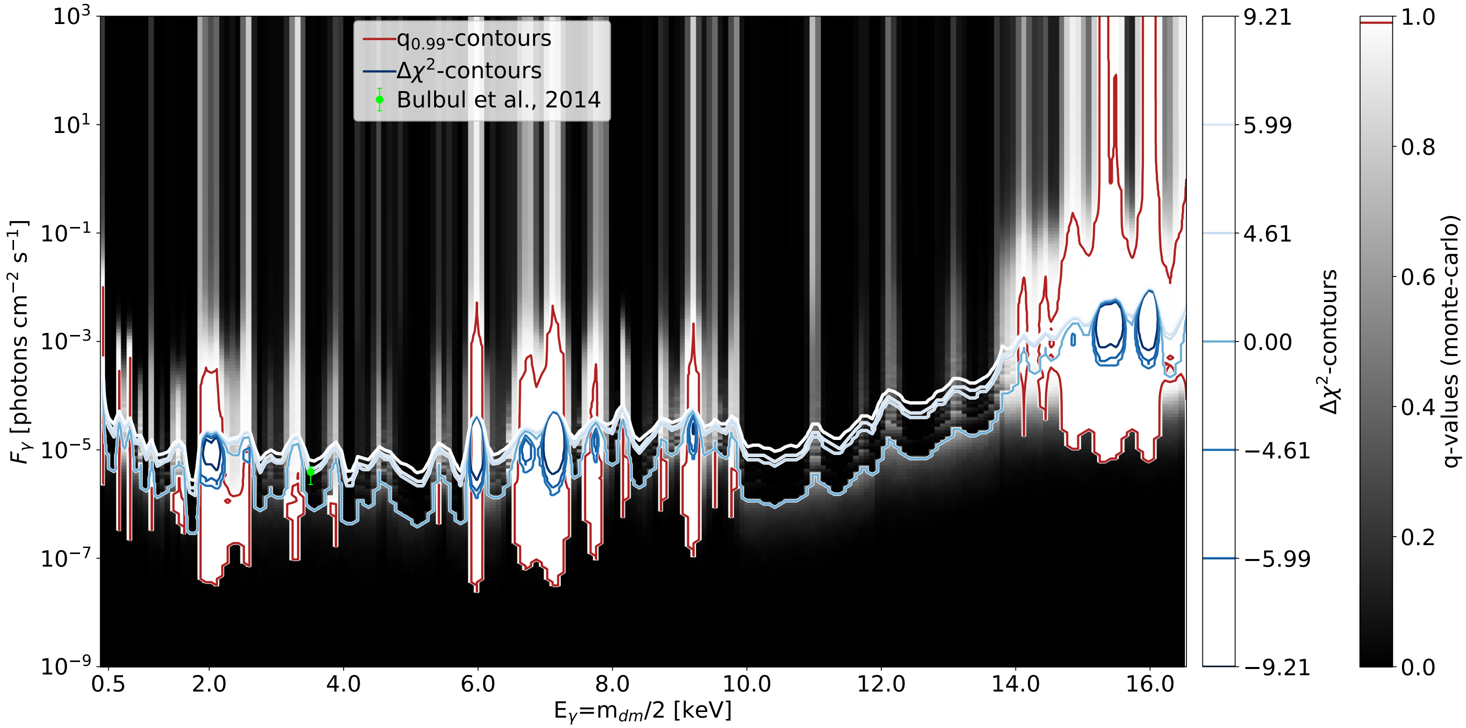

Figure 6.1: The figure shows the resulting $q(E_{\gamma;n}^{\mathbf{D_1}}, F_{\gamma;m}^{\mathbf{D_1}})$-values (white to black colour gradient represented by the colour bar) and the combined $q_{0.99}$-confidence regions (red solid lines) on the grid $\mathrm{G}_2^{\mathbf{D_1}}\left(E_{\gamma;n}^{\mathbf{D_1}}, F_{\gamma;m}^{\mathbf{D_1}}\right)$ related to the additional Gaussian emission line L_γ based on the model $m_1^{\mathbf{D_1},\mathrm{ISO}}$. The energy regime ranges from $0.38\,\mathrm{keV}$ to $16.5\,\mathrm{keV}$ and the flux normalisation regime ranges from 10^{-9} photons cm^{-2} s^{-1} to 10^{3} photons cm^{-2} s^{-1}. $\Delta\chi^2_{99\%}$-contours, $\Delta\chi^2_{95\%}$-contours, and $\Delta\chi^2_{90\%}$-contours as well as contours based on $\Delta\chi^2 = -9.211$, $\Delta\chi^2 = -5.992$, $\Delta\chi^2 = -4.605$, and $\Delta\chi^2 = 0.0$ for the purpose of visualising the results are shown for a comparison (lines having a white to dark blue colour gradient). The emission line claimed by Bulbul et al. (154) at an energy of $3.51 \pm 0.03\,\mathrm{keV}$ and a normalisation of $3.9^{+0.6}_{-1.0} \cdot 10^{-6}\,\mathrm{cm}^{-2}\,\mathrm{s}^{-1}$ is indicated by an orange error bar.

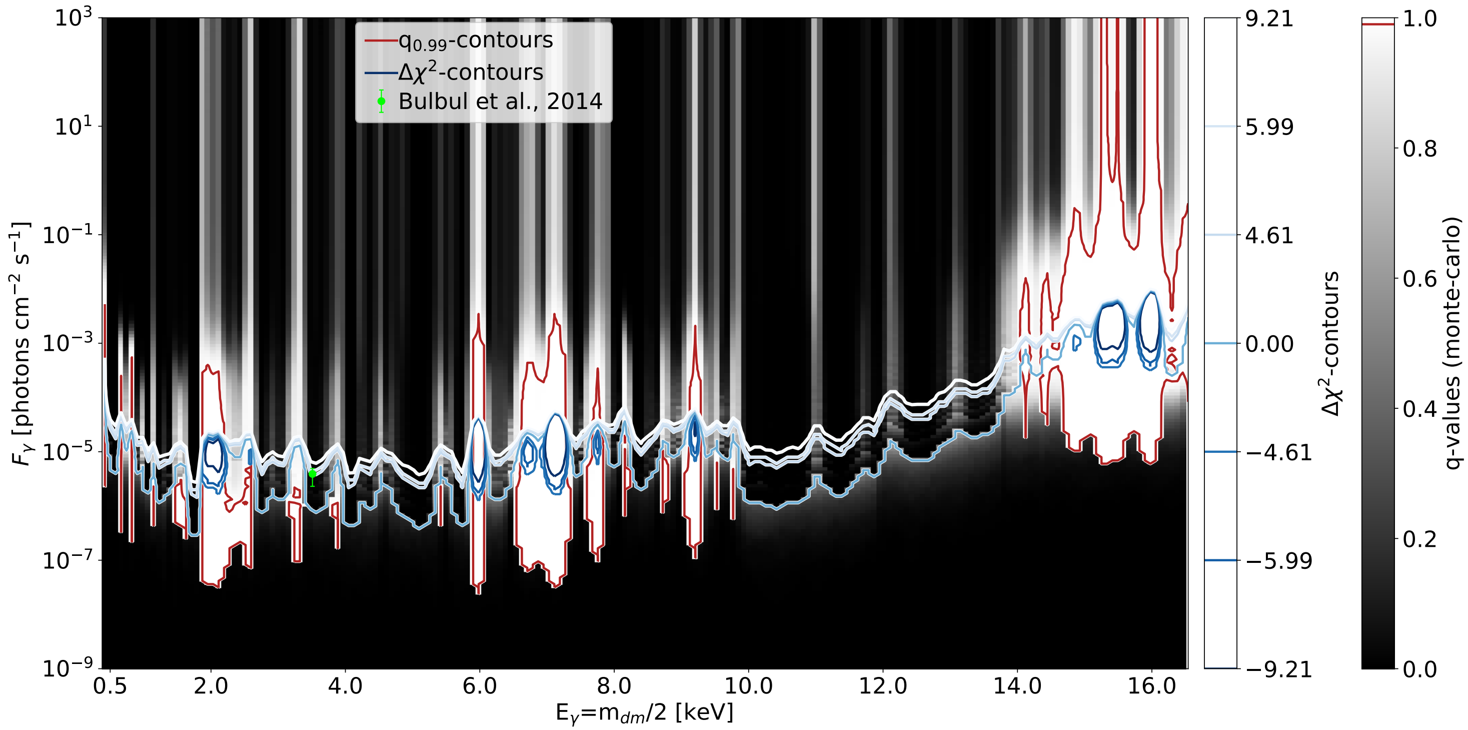

Figure 6.2: The figure shows the resulting $q(E^{\mathbf{D_1}}_{\gamma;n}, F^{\mathbf{D_1}}_{\gamma;m})$-values (white to black colour gradient represented by the colour bar) and the combined $q_{0.99}$-confidence regions (red solid lines) on the grid $\mathrm{G}_2^{\mathbf{D_1}}\left(E^{\mathbf{D_1}}_{\gamma;n}, F^{\mathbf{D_1}}_{\gamma;m}\right)$ related to the additional Gaussian emission line L_γ based on the model $m_1^{\mathbf{D_1},\mathrm{NFW}}$. The energy regime ranges from $0.38\,\mathrm{keV}$ to $16.5\,\mathrm{keV}$ and the flux normalisation regime ranges from 10^{-9} photons $\mathrm{cm}^{-2}\,\mathrm{s}^{-1}$ to 10^{3} photons $\mathrm{cm}^{-2}\,\mathrm{s}^{-1}$. $\Delta\chi^2_{99\%}$-contours, $\Delta\chi^2_{95\%}$-contours, and $\Delta\chi^2_{90\%}$-contours as well as contours based on $\Delta\chi^2 = -9.211$, $\Delta\chi^2 = -5.992$, $\Delta\chi^2 = -4.605$, and $\Delta\chi^2 = 0.0$ for the purpose of visualising the results are shown for a comparison (lines having a white to dark blue colour gradient). The emission line claimed by Bulbul et al. (154) at an energy of $3.51 \pm 0.03\,\mathrm{keV}$ and a normalisation of $3.9^{+0.6}_{-1.0} \cdot 10^{-6}\,\mathrm{cm}^{-2}\,\mathrm{s}^{-1}$ is indicated by an orange error bar.

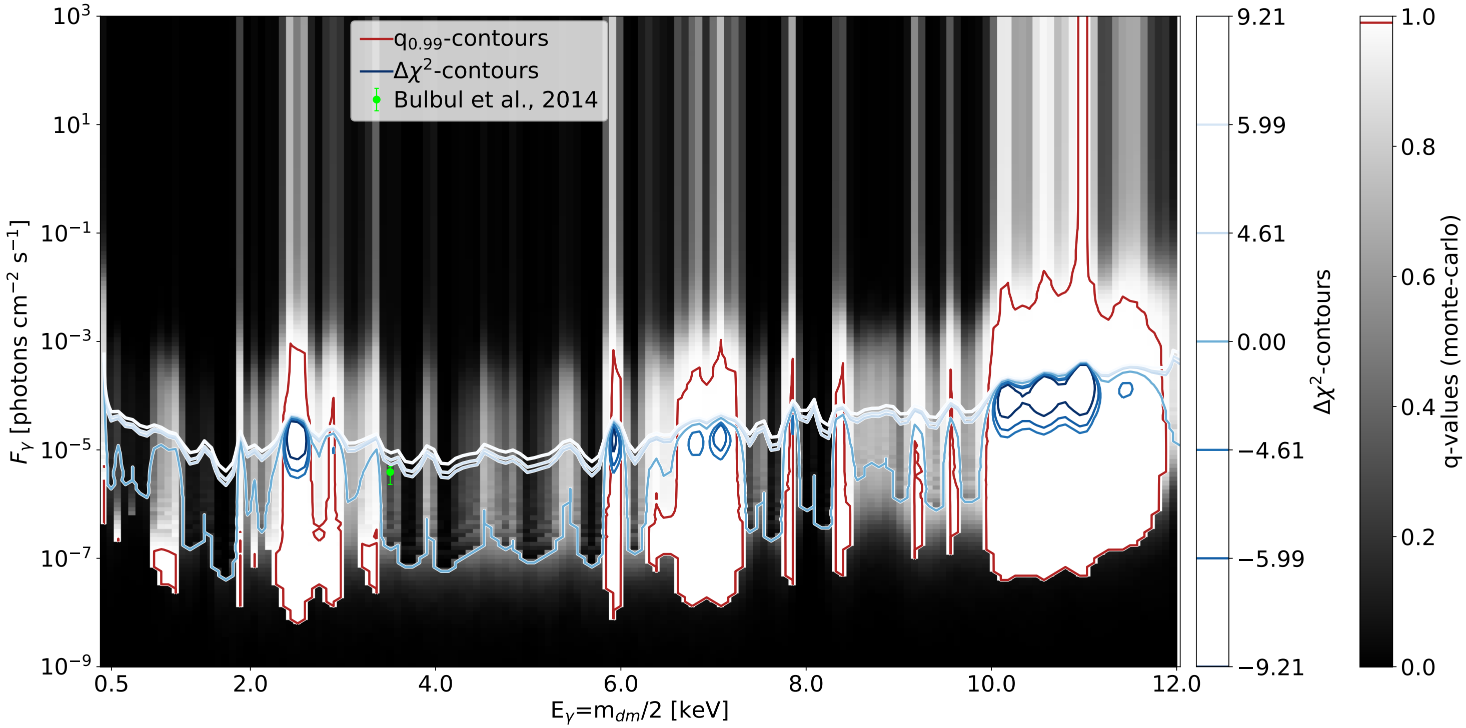

Figure 6.3: The figure shows the resulting $q(E^{\mathbf{D_2}}_{\gamma;n}, F^{\mathbf{D_2}}_{\gamma;m})$-values (white to black colour gradient represented by the colour bar) and the combined $q_{0.99}$-confidence regions (red solid lines) on the grid $\mathrm{G}_2^{\mathbf{D_2}}\left(E^{\mathbf{D_2}}_{\gamma;n}, F^{\mathbf{D_2}}_{\gamma;m}\right)$ related to the additional Gaussian emission line L_γ based on the model $m_1^{\mathbf{D_2},\mathrm{ISO}}$. The energy regime ranges from $0.38\,\mathrm{keV}$ to $12\,\mathrm{keV}$ and the flux normalisation regime ranges from $10^{-9}\,\mathrm{photons\,cm^{-2}\,s^{-1}}$ to $10^{3}\,\mathrm{photons\,cm^{-2}\,s^{-1}}$. $\Delta\chi^2_{99\%}$-contours, $\Delta\chi^2_{95\%}$-contours, and $\Delta\chi^2_{90\%}$-contours as well as contours based on $\Delta\chi^2 = -9.211$, $\Delta\chi^2 = -5.992$, $\Delta\chi^2 = -4.605$, and $\Delta\chi^2 = 0.0$ for the purpose of visualising the results are shown for a comparison (lines having a white to dark blue colour gradient). The emission line claimed by Bulbul et al. (154) at an energy of $3.51 \pm 0.03\,\mathrm{keV}$ and a normalisation of $3.9^{+0.6}_{-1.0} \cdot 10^{-6}\,\mathrm{cm^{-2}\,s^{-1}}$ is indicated by an orange error bar.

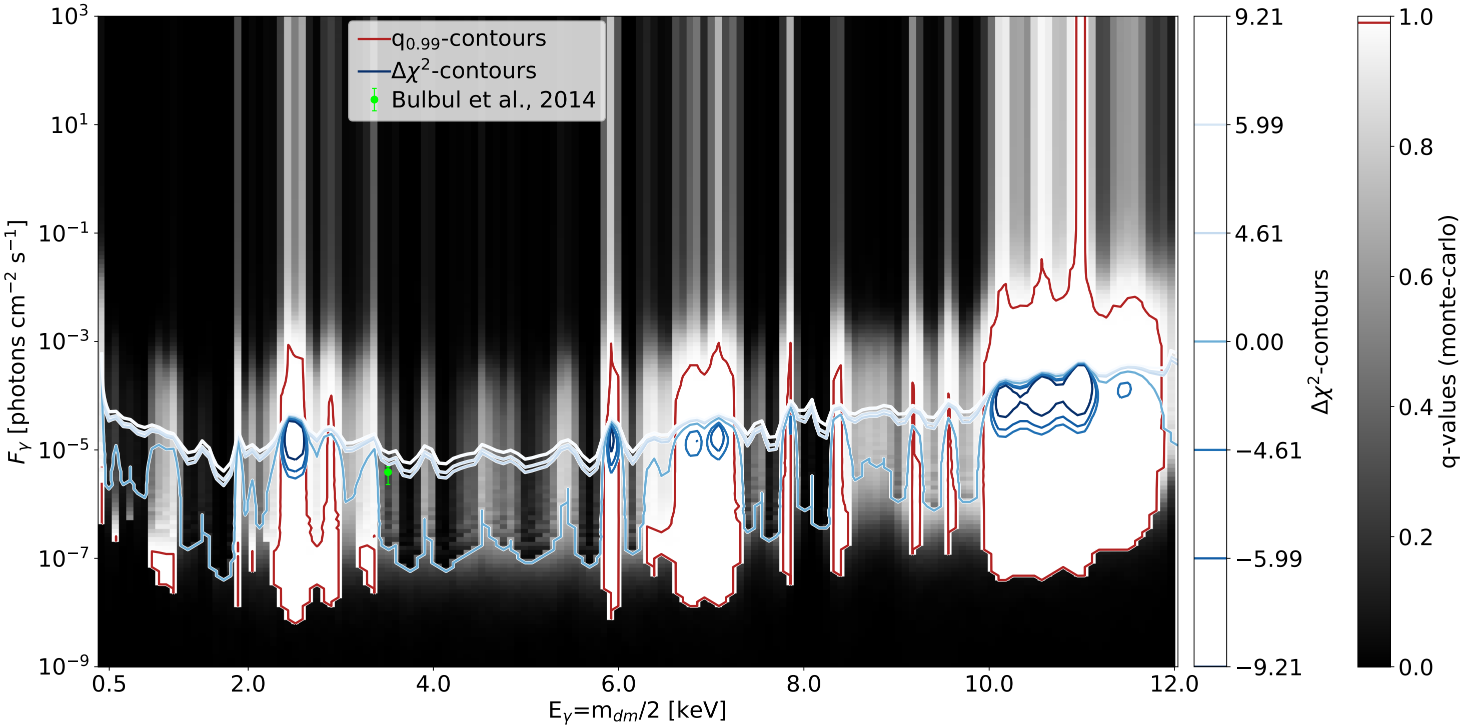

Figure 6.4: The figure shows the resulting $q(E^{\mathbf{D_2}}_{\gamma;n}, F^{\mathbf{D_2}}_{\gamma;m})$-values (white to black colour gradient represented by the colour bar) and the combined $q_{0.99}$-confidence regions (red solid lines) on the grid $\mathrm{G}_2^{\mathbf{D_2}}\left(E^{\mathbf{D_2}}_{\gamma;n}, F^{\mathbf{D_2}}_{\gamma;m}\right)$ related to the additional Gaussian emission line L_γ based on the model $m_1^{\mathbf{D_2},\mathrm{NFW}}$. The energy regime ranges from $0.38\,\mathrm{keV}$ to $12\,\mathrm{keV}$ and the flux normalisation regime ranges from 10^{-9} photons $\mathrm{cm}^{-2}\,\mathrm{s}^{-1}$ to 10^{3} photons $\mathrm{cm}^{-2}\,\mathrm{s}^{-1}$. $\Delta\chi^2_{99\%}$-contours, $\Delta\chi^2_{95\%}$-contours, and $\Delta\chi^2_{90\%}$-contours as well as contours based on $\Delta\chi^2 = -9.211$, $\Delta\chi^2 = -5.992$, $\Delta\chi^2 = -4.605$, and $\Delta\chi^2 = 0.0$ for the purpose of visualising the results are shown for a comparison (lines having a white to dark blue colour gradient). The emission line claimed by Bulbul et al. (154) at an energy of $3.51 \pm 0.03\,\mathrm{keV}$ and a normalisation of $3.9\,^{+0.6}_{-1.0} \cdot 10^{-6}\,\mathrm{cm}^{-2}\,\mathrm{s}^{-1}$ is indicated by an orange error bar.

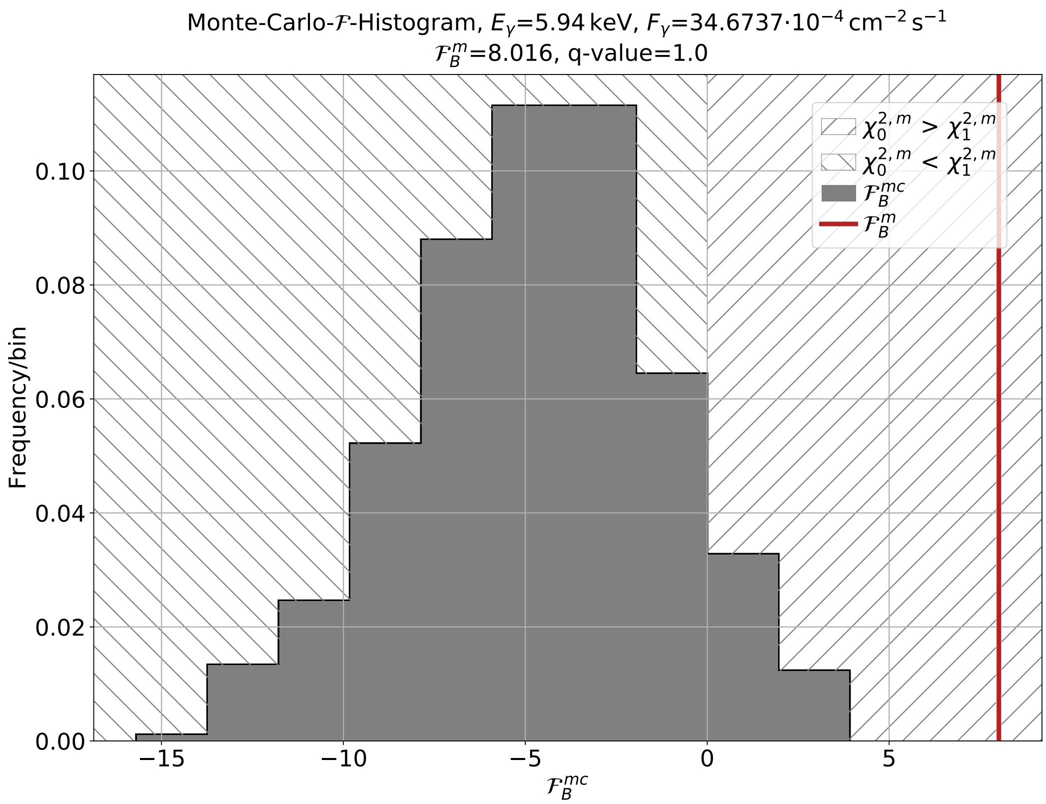

Figure 6.5: The above figure shows a Monte-Carlo-$\mathcal{F}_{\mathcal{B}}^{\mathbf{mc}}$-distribution, $\mathcal{F}_{\mathcal{B}}^{\mathbf{mc}}\left(\mathrm{G}_2^{\mathbf{D}}\left(E_{\gamma;n}^{\mathbf{D}}, F_{\gamma;m}^{\mathbf{D}}\right)\right)$, represented in form of a histogram (grey bars) for parameters $\left(E_{\gamma;n}^{\mathbf{D}}, F_{\gamma;m}^{\mathbf{D}}\right) = \left(E_{\gamma;n=69}^{\mathbf{D_1}} = 5.94\,\mathrm{keV}, F_{\gamma;m=109}^{\mathbf{D_1}} = 34.67 \cdot 10^{-4}\,\mathrm{cm}^{-2}\,\mathrm{s}^{-1}\right)$ and a sample size of $M^{\mathbf{D_1}} = 500$ as well as a measured $\mathcal{F}_{\mathcal{B}}$-value, $\mathcal{F}_{\mathcal{B}}^{\mathbf{m}}\left(\mathrm{G}_2^{\mathbf{D_1}}\left(E_{\gamma;n=69}^{\mathbf{D_1}} = 5.94\,\mathrm{keV}, F_{\gamma;m=109}^{\mathbf{D_1}} = 34.67 \cdot 10^{-4}\,\mathrm{cm}^{-2}\,\mathrm{s}^{-1}\right)\right) = 8.016$ (dark red line), wherein the corresponding q-value is equal to 1.0. The related nullhypothesis model $m_0^{\mathbf{D_1},\mathrm{NFW}}$ is rejected in this case since the pair of parameters $(E_{\gamma;n=69}^{\mathbf{D_1}}, F_{\gamma;m=109}^{\mathbf{D_1}}) = (5.94\,\mathrm{keV}, 34.67 \cdot 10^{-4}\,\mathrm{cm}^{-2}\,\mathrm{s}^{-1})$ is located in a $q_{0.99}$-confidence region $\mathrm{R}_l^{q>0.99}$ (please see figure 6.2 or tables 6.3 and 6.4, in particular the $\mathrm{R}_{l=14}^{q>0.99}$-region). Two regions which fulfill the conditions $\chi_0^{2,\mathbf{m}} > \chi_1^{2,\mathbf{m}}$ and $\chi_0^{2,\mathbf{m}} < \chi_1^{2,\mathbf{m}}$, respectively, are represented by grid-like grey lines each having different orientations.

6.2 Constraints on $\sin^2(2\Theta)$ and $g_{a\gamma\gamma}$

Each of the figures 6.6, 6.7, 6.8, 6.9 as well as each of the figures 6.10, 6.11, 6.12, 6.13 show the respective $q(E^{\mathbf{D}}_{\gamma;n}, F^{\mathbf{D}}_{\gamma;m})$-values, $q_{0.99}$-confidence regions, and $\Delta\chi^2_{99\%}(E_{\gamma;n}, F_{\gamma;m})$-contours as well as contours fulfilling the condition,

$$\Delta\chi^2(E_{\gamma;n}, F_{\gamma;m}) = -9.211, \tag{6.5}$$

shown in figures 6.1, 6.2, 6.3 and 6.4 except that all values and contours based on the pairs of values $\left(E^{\mathbf{D}}_{\gamma;n}, F^{\mathbf{D}}_{\gamma;m}\right)$ were recalculated to the mixing between sterile neutrinos and photons, $\sin^2(2\Theta)^{\mathbf{D}}_{\text{total}}\left(E^{\mathbf{D}}_{\gamma;n}, F^{\mathbf{D}}_{\gamma;m}\right)$ according to equation 5.63, as well as the couplings between axions and photons, $g^{2,\mathbf{D}}_{a\gamma\gamma,\text{total}}\left(E^{\mathbf{D}}_{\gamma;n}, F^{\mathbf{D}}_{\gamma;m}\right)$ according to equation 5.64, respectively.
The figures 6.6, 6.7, 6.8, 6.9 as well as the figures 6.10, 6.11, 6.12, 6.13 relate to the models $m_1^{\mathbf{D_1},\text{ISO}}$, $m_1^{\mathbf{D_1},\text{NFW}}$, $m_1^{\mathbf{D_2},\text{ISO}}$ and $m_1^{\mathbf{D_2},\text{NFW}}$, respectively, for every pair of values $(E^{\mathbf{D}}_{\gamma;n}, F^{\mathbf{D}}_{\gamma;m})$ in the corresponding two-dimensional grids $\text{G}_2^{\mathbf{D_1}}$ and $\text{G}_2^{\mathbf{D_2}}$.
The mixing of sterile neutrinos and photons corresponding to the emission line claimed by Bulbul et al. (154) at an energy of $3.51 \pm 0.03\,\text{keV}$ and a normalisation of $3.9^{+0.6}_{-1.0} \cdot 10^{-6}\,\text{cm}^{-2}\,\text{s}^{-1}$ was recalculated to a sterile neutrino-photon mixing of $\sin^2(2\Theta)_{\text{Bulbul}} = 6.7^{+1.7}_{-1.0} \cdot 10^{-11}\,\text{cm}^{-2}\,\text{s}^{-1}$ and an axion-photon coupling of $g_{a\gamma\gamma;\,\text{Bulbul}} = 6.5^{+0.57}_{-0.97} \cdot 10^{-18}\,\text{GeV}^{-1}$, respectively.
The upper limits of the publications Watson et al. (168), Malyshev et al. (149), and Horiuchi et al. (165), represent a 95% confidence level with regard to a Monte-Carlo-generated distribution, a 90% confidence level, and a 90% confidence level ($\Delta\chi^2_{90\%} = 4.605$), respectively. The plotted upper limits of Abazajian et al. (91) and Adhikari et al. (96) are a net upper limit composed of several upper limits which have specifically been taken from the publications Boyarsky et al. (169), Nevalainen et al. (171), Watson et al. (172), Boyarsky et al. (173, 176), Abazajian et al. (177), Dolgov et al. (178), K. Abazajian et al. (179), Abazajian et al. (180), Riemer-Sorensen et al. (181), Malyshev et al. (182), Loewenstein et al. (183, 184), Boyarsky et al. (185) and Malyshev et al. (149), Horiuchi et al. (165), Watson et al. (168), Boyarsky et al. (169, 170), Nevalainen et al. (171), Watson et al. (172), Boyarsky et al. (173, 176), Abazajian et al. (180), Malyshev et al. (182), Loewenstein et al. (183, 184), Boyarsky et al. (186), Riemer-Sorensen et al. (187), Mirabal et al. (188), Mirabal (189), Loewenstein et al. (190), Riemer-Sorensen et al. (191), Yuksel et al. (192), Boyarsky et al. (193), Borriello et al.

(194), Iakubovskyi (195), Ng et al. (196), respectively[1]. Further, each of the figures 6.6, 6.7, 6.8, 6.9 show two parameter exclusion regions based on cosmological contraints (91). The upper regions denoted by $\Omega_{\nu_s} > \Omega_{DM}$ result from the condition that the proportion of sterile neutrinos in the dark matter content of the Universe should not exceed 100% whereby the lower regions denoted by $\Omega_{\nu_s} > \Omega_{DM}$ result in constraints related to the production of sterile neutrinos during a primordial or big bang nucleosynthesis (BBN) derived from the results of the KARMEN experiment (83, 84). Both upper and lower regions were extrapolated for energies in a range from 0.5 keV to 1.0 keV.

[1]It is important to note that the upper limits published in Adhikari et al. (96) have been smoothed and, furthermore, divided by 2 according to the corresponding authors to take influences of potential uncertainties of dark matter distributions to the upper limits into account. Such an approach would have tighten the upper limits, whereby it is more likely that the upper limits have been divided by 0.5 or multiplied by 2 to achieve more conservative upper limits instead of tighter upper limits. Therefore, the upper limits were divided by 2 in the scope of this work.

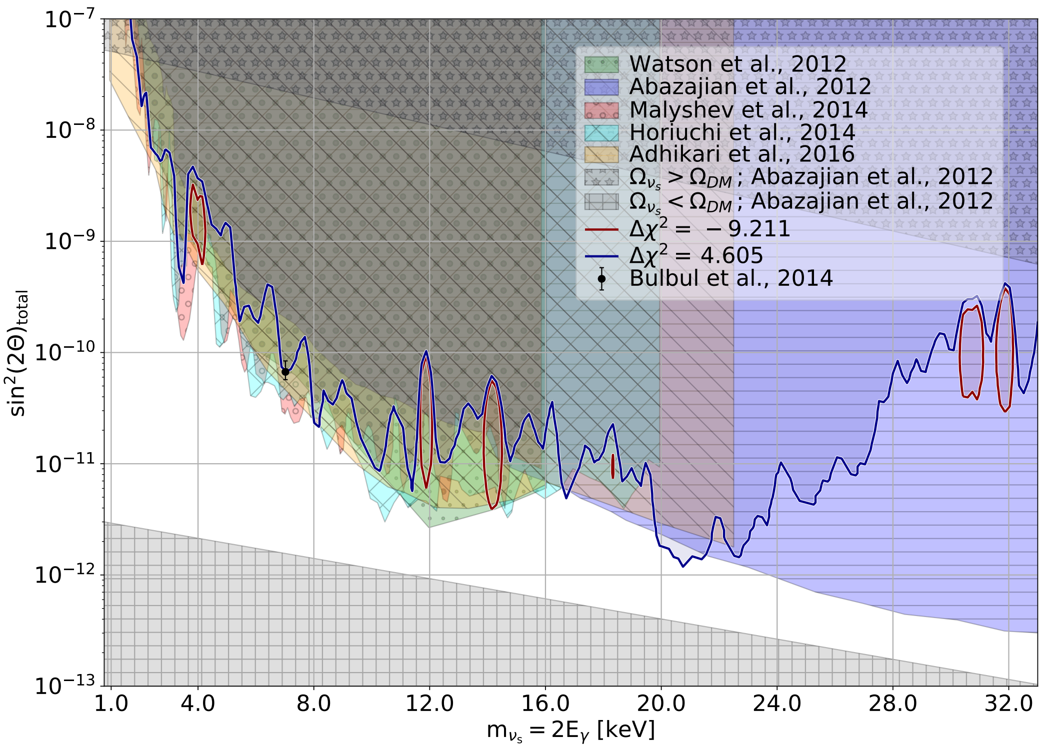

Figure 6.6: The above figure shows the $\Delta\chi^2_{95\%} = 4.605$ contours (dark blue lines) as well as the $\Delta\chi^2 = -9.211$ contours (dark red lines) of the sterile neutrino-photon mixing $\sin^2(2\Theta)^{\mathbf{D_1}}_{\mathrm{total}}\left(E^{\mathbf{D_1}}_{\gamma;n}, F^{\mathbf{D_1}}_{\gamma;m}\right)$ calculated from the total flux normalisation F_γ in a sterile neutrino mass regime from $0.76\,\mathrm{keV}$ to $33\,\mathrm{keV}$ based on the model $m_1^{\mathbf{D_1},\mathrm{ISO}}$. The results of this work are compared to the upper limit results of the publications Abazajian et al. (91), Adhikari et al. (96), Malyshev et al. (149), Horiuchi et al. (165), Watson et al. (168) as well as the claimed emission line in Bulbul et al. (154). The shaded regions are excluded. The emission line claimed by Bulbul et al. (154) at an energy of $3.51 \pm 0.03\,\mathrm{keV}$ and corresponding to a sterile neutrino-photon mixing of $\sin^2(2\Theta)_{\mathrm{Bulbul}} = 6.7^{+1.7}_{-1.0} \cdot 10^{-11}\,\mathrm{cm}^{-2}\,\mathrm{s}^{-1}$ is indicated by a black error bar.

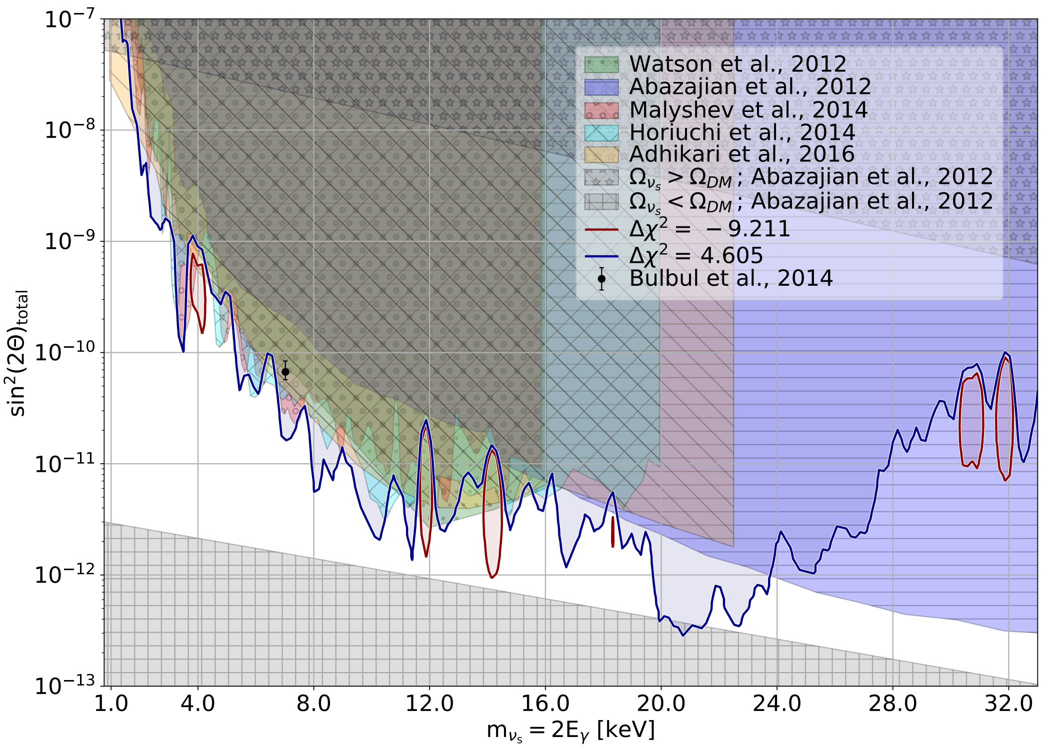

Figure 6.7: The above figure shows the $\Delta\chi^2_{95\%} = 4.605$ contours (dark blue lines) as well as the $\Delta\chi^2 = -9.211$ contours (dark red lines) of the sterile neutrino-photon mixing $\sin^2(2\Theta)^{\mathbf{D_1}}_{\text{total}}\left(E^{\mathbf{D_1}}_{\gamma;n}, F^{\mathbf{D_1}}_{\gamma;m}\right)$ calculated from the total flux normalisation F_γ in a sterile neutrino mass regime from $0.76\,\text{keV}$ to $33\,\text{keV}$ based on the model $m_1^{\mathbf{D_1},\text{NFW}}$. The results of this work are compared to the upper limit results of the publications Abazajian et al. (91), Adhikari et al. (96), Malyshev et al. (149), Horiuchi et al. (165), Watson et al. (168) as well as the claimed emission line in Bulbul et al. (154). The shaded regions are excluded. The emission line claimed by Bulbul et al. (154) at an energy of $3.51 \pm 0.03\,\text{keV}$ and corresponding to a sterile neutrino-photon mixing of $\sin^2(2\Theta)_{\text{Bulbul}} = 6.7^{+1.7}_{-1.0} \cdot 10^{-11}\,\text{cm}^{-2}\,\text{s}^{-1}$ is indicated by a black error bar.

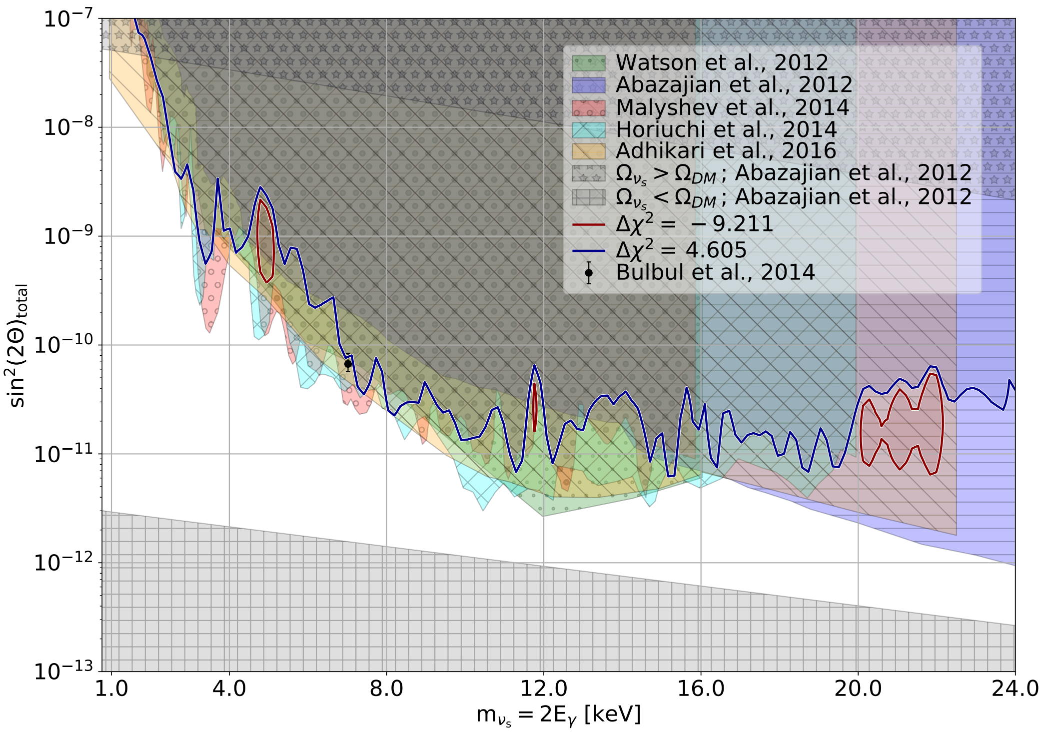

Figure 6.8: The above figure shows the $\Delta\chi^2_{95\%} = 4.605$ contours (dark blue lines) as well as the $\Delta\chi^2 = -9.211$ contours (dark red lines) of the sterile neutrino-photon mixing $\sin^2(2\Theta)^{\mathbf{D_2}}_{\text{total}}\left(E^{\mathbf{D_2}}_{\gamma;n}, F^{\mathbf{D_2}}_{\gamma;m}\right)$ calculated from the total flux normalisation F_γ in a sterile neutrino mass regime from $0.76\,\text{keV}$ to $24\,\text{keV}$ based on the model $m_1^{\mathbf{D_2},\text{ISO}}$. The results of this work are compared to the upper limit results of the publications Watson et al. (168), Abazajian et al. (91), Malyshev et al. (149), Horiuchi et al. (165) and Adhikari et al. (96) as well as the claimed emission line by Bulbul et al. (154). The shaded regions are excluded. The emission line claimed by Bulbul et al. (154) at an energy of $3.51 \pm 0.03\,\text{keV}$ and corresponding to a sterile neutrino-photon mixing of $\sin^2(2\Theta)_{\text{Bulbul}} = 6.7^{+1.7}_{-1.0} \cdot 10^{-11}\,\text{cm}^{-2}\,\text{s}^{-1}$ is indicated by a black error bar.

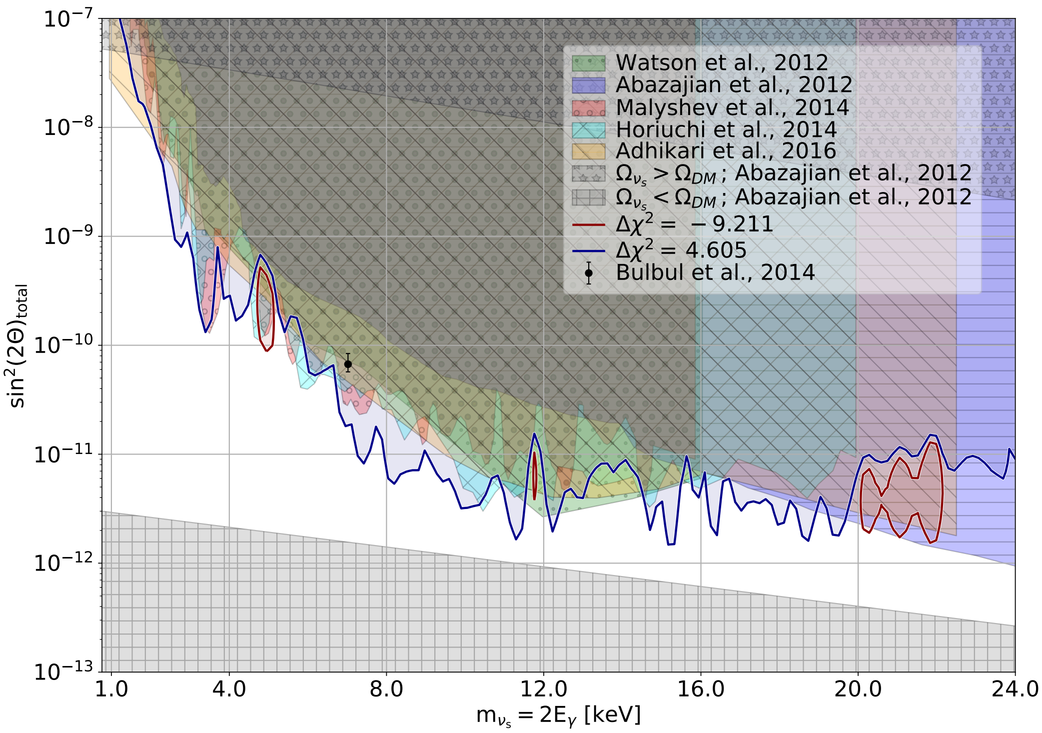

Figure 6.9: The above figure shows the $\Delta\chi^2_{95\%} = 4.605$ contours (dark blue lines) as well as the $\Delta\chi^2 = -9.211$ contours (dark red lines) of the sterile neutrino-photon mixing $\sin^2(2\Theta)^{\mathbf{D_2}}_{\text{total}}\left(E^{\mathbf{D_2}}_{\gamma;n}, F^{\mathbf{D_2}}_{\gamma;m}\right)$ calculated from the total flux normalisation F_γ in a sterile neutrino mass regime from $0.76\,\text{keV}$ to $24\,\text{keV}$ based on the model $m_1^{\mathbf{D_2},\text{NFW}}$. The results of this work are compared to the upper limit results of the publications Watson et al. (168), Abazajian et al. (91), Malyshev et al. (149), Horiuchi et al. (165) and Adhikari et al. (96) as well as the claimed emission line by Bulbul et al. (154). The shaded regions are excluded. The emission line claimed by Bulbul et al. (154) at an energy of $3.51 \pm 0.03\,\text{keV}$ and corresponding to a sterile neutrino-photon mixing of $\sin^2(2\Theta)_{\text{Bulbul}} = 6.7^{+1.7}_{-1.0} \cdot 10^{-11}\,\text{cm}^{-2}\,\text{s}^{-1}$ is indicated by a black error bar.

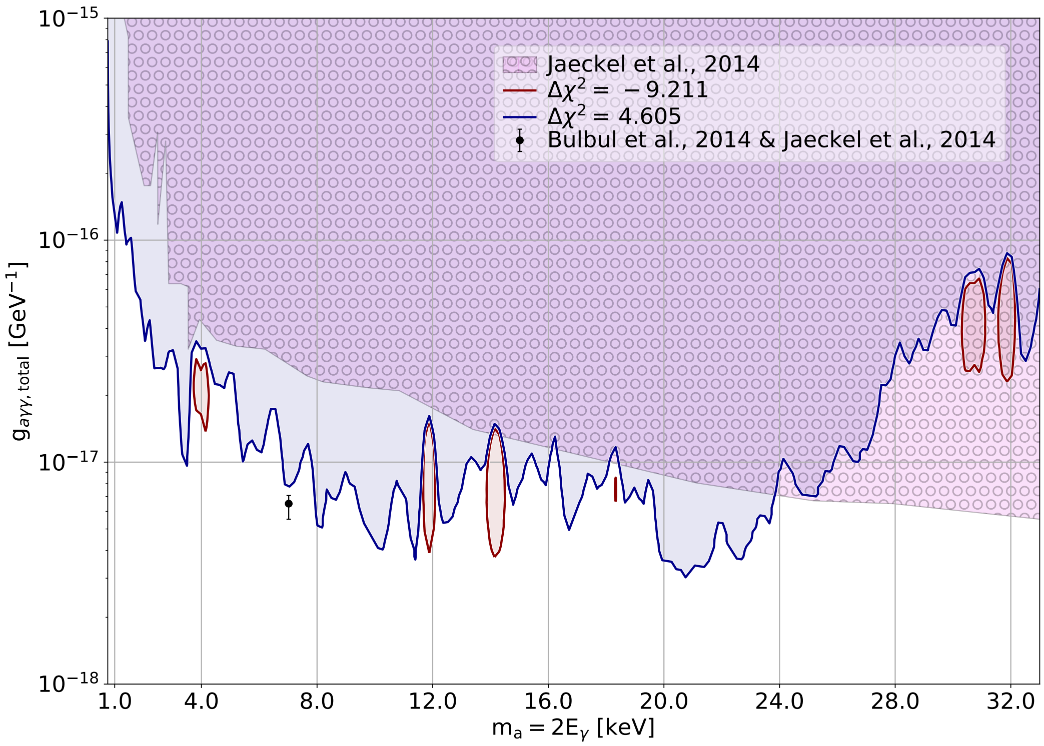

Figure 6.10: The above figure shows the $\Delta\chi^2_{95\%} = 4.605$ contours (dark blue lines) as well as the $\Delta\chi^2 = -9.211$ contours (dark red lines) of the axion-photon coupling $g^{\mathbf{D_1}}_{a\gamma\gamma,\text{total}}\left(E^{\mathbf{D_1}}_{\gamma;n}, F^{\mathbf{D_1}}_{\gamma;m}\right)$ calculated from the upper limits of the total flux normalisation in an axion mass regime from $0.76\,\text{keV}$ to $33\,\text{keV}$ based on the model $m_1^{\mathbf{D_1},\text{ISO}}$. The results of this work are compared to the upper limit results of the publication Jaeckel et al. (113) as well as the claimed emission line by Bulbul et al. (154). The shaded regions are excluded. The emission line claimed by Bulbul et al. (154) at an energy of $3.51 \pm 0.03\,\text{keV}$ and corresponding to an axion-photon coupling of $g_{a\gamma\gamma;\,\text{Bulbul}} = 6.5\,^{+0.57}_{-0.97} \cdot 10^{-18}\,\text{GeV}^{-1}$ is indicated by a black error bar.

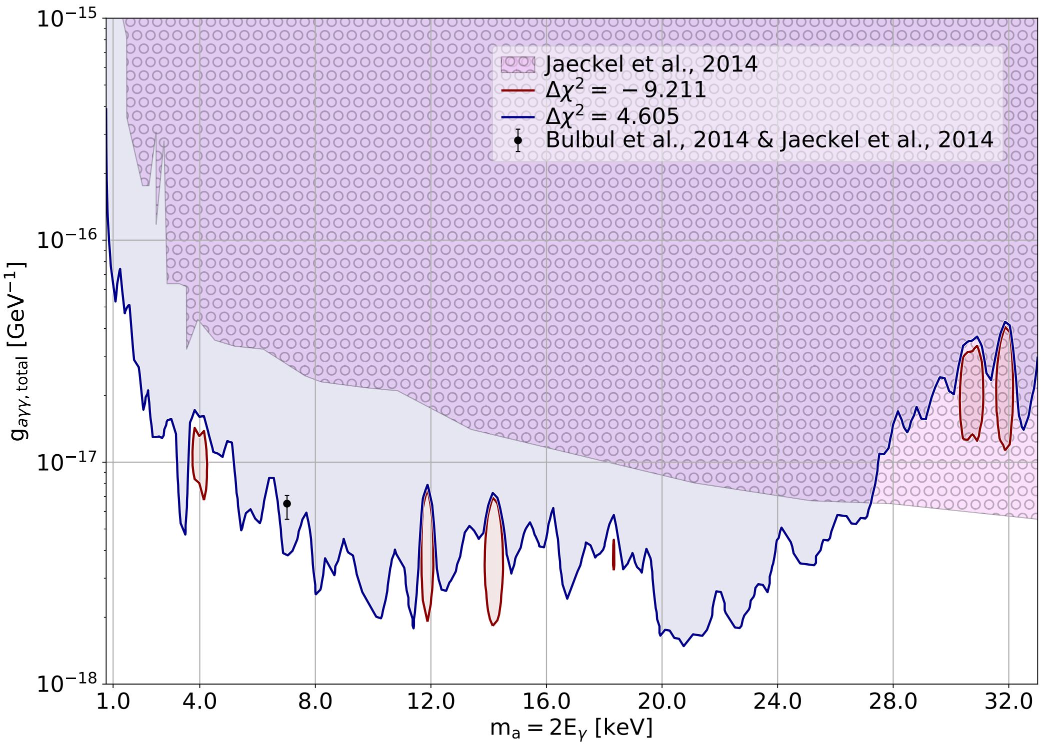

Figure 6.11: The above figure shows the $\Delta\chi^2_{95\%} = 4.605$ contours (dark blue lines) as well as the $\Delta\chi^2 = -9.211$ contours (dark red lines) of the axion-photon coupling $g^{\mathbf{D_1}}_{a\gamma\gamma,\mathrm{total}}\left(E^{\mathbf{D_1}}_{\gamma;n}, F^{\mathbf{D_1}}_{\gamma;m}\right)$ calculated from the upper limits of the total flux normalisation in an axion mass regime from $0.76\,\mathrm{keV}$ to $33\,\mathrm{keV}$ based on the model $m_1^{\mathbf{D_1},\mathrm{NFW}}$. The results of this work are compared to the upper limit results of the publication Jaeckel et al. (113) as well as the claimed emission line by Bulbul et al. (154). The shaded regions are excluded. The emission line claimed by Bulbul et al. (154) at an energy of $3.51\pm0.03\,\mathrm{keV}$ and corresponding to an axion-photon coupling of $g_{a\gamma\gamma;\,\mathrm{Bulbul}} = 6.5^{+0.57}_{-0.97}\cdot 10^{-18}\,\mathrm{GeV}^{-1}$ is indicated by a black error bar.

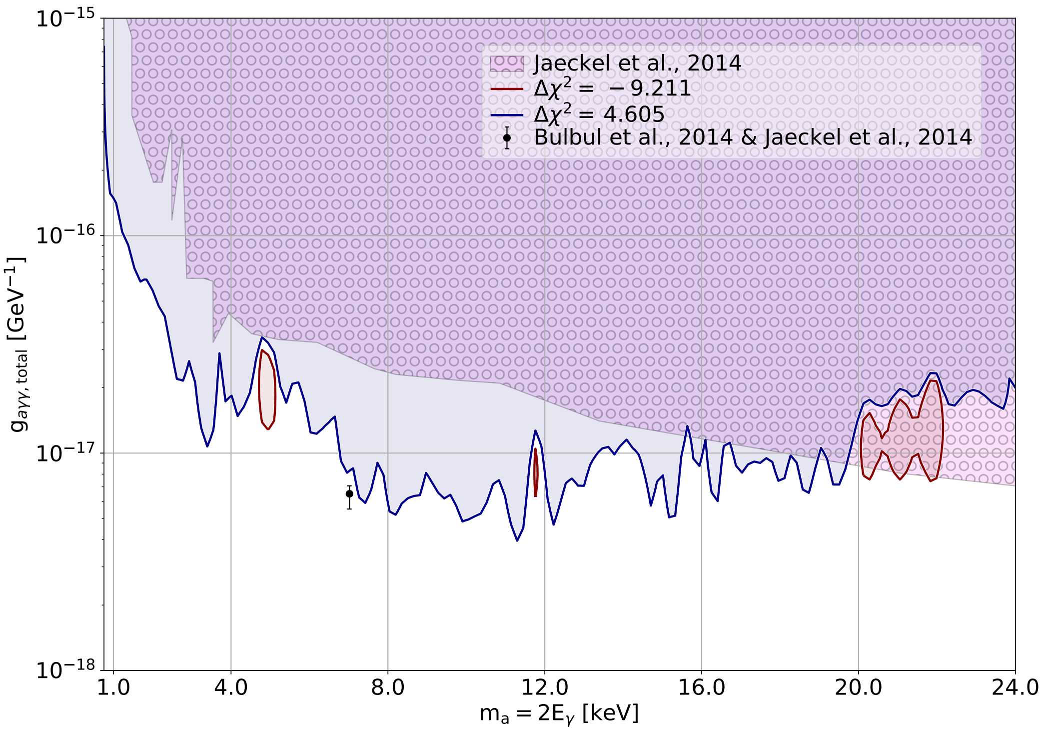

Figure 6.12: The above figure shows the $\Delta\chi^2_{95\%} = 4.605$ contours (dark blue lines) as well as the $\Delta\chi^2 = -9.211$ contours (dark red lines) of the axion-photon coupling $g^{\mathbf{D_2}}_{a\gamma\gamma,\mathrm{total}}\left(E^{\mathbf{D_2}}_{\gamma;n}, F^{\mathbf{D_2}}_{\gamma;m}\right)$ calculated from the upper limits of the total flux normalisation in an axion mass regime from $0.76\,\mathrm{keV}$ to $24\,\mathrm{keV}$ based on the model $m_1^{\mathbf{D_2},\mathrm{ISO}}$. The results of this work are compared to the upper limit results of the publication Jaeckel et al. (113) as well as the claimed emission line by Bulbul et al. (154). The shaded regions are excluded. The emission line claimed by Bulbul et al. (154) at an energy of $3.51 \pm 0.03\,\mathrm{keV}$ and corresponding to an axion-photon coupling of $g_{a\gamma\gamma;\,\mathrm{Bulbul}} = 6.5^{+0.57}_{-0.97} \cdot 10^{-18}\,\mathrm{GeV}^{-1}$ is indicated by a black error bar.

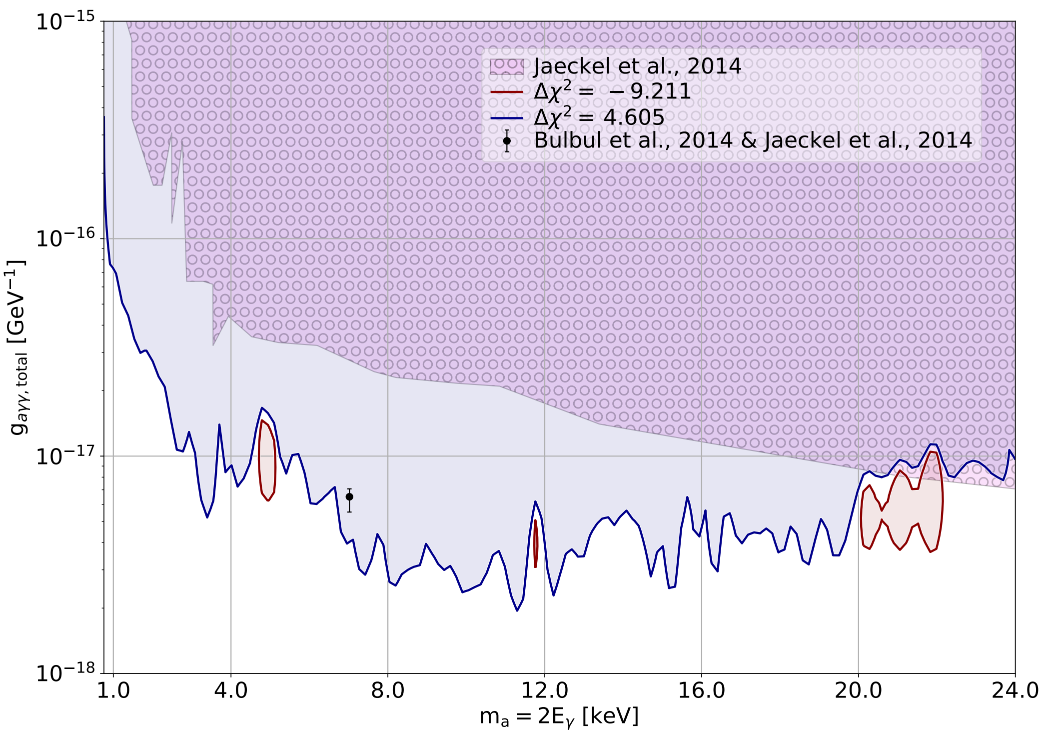

Figure 6.13: The above figure shows the $\Delta\chi^2_{95\%} = 4.605$ contours (dark blue lines) as well as the $\Delta\chi^2 = -9.211$ contours (dark red lines) of the axion-photon coupling $g^{\mathbf{D_2}}_{a\gamma\gamma,\mathrm{total}}\left(E^{\mathbf{D_2}}_{\gamma;n}, F^{\mathbf{D_2}}_{\gamma;m}\right)$ calculated from the upper limits of the total flux normalisation in an axion mass regime from $0.76\,\mathrm{keV}$ to $24\,\mathrm{keV}$ based on the model $m_1^{\mathbf{D_2},\mathrm{NFW}}$. The results of this work are compared to the upper limit results of the publication Jaeckel et al. (113) as well as the claimed emission line by Bulbul et al. (154). The shaded regions are excluded. The emission line claimed by Bulbul et al. (154) at an energy of $3.51 \pm 0.03\,\mathrm{keV}$ and corresponding to an axion-photon coupling of $g_{a\gamma\gamma;\,\mathrm{Bulbul}} = 6.5^{+0.57}_{-0.97} \cdot 10^{-18}\,\mathrm{GeV}^{-1}$ is indicated by a black error bar.

6.3 Additional Emission Lines in the Diffuse X-ray Background

The most dominant contour features have centroids in the areas closed by the $q_{0.99}$-confidence regions $\mathrm{R}_l^{q>0.99}$ with energies and normalisations presented in tables 6.1, 6.3, 6.5, 6.7 and 6.2, 6.4, 6.6, 6.8. The most-likely physical origins are also listed in these tables. A part of the $\mathrm{R}_l^{q>0.99}$-regions up to energies of $0.45\,\mathrm{keV}$ and above $10\,\mathrm{keV}$ shown in figures 6.1, 6.2, 6.3 and 6.4 are not closed but extent to flux normalisations $F_{\gamma;m}^{\mathbf{D_1}}$ and $F_{\gamma;m}^{\mathbf{D_2}}$ greater than $10^3\,\mathrm{cm}^{-2}\,\mathrm{s}^{-1}$ which can be a consequence of bad constrains of the fitted models because of low effective areas and/or a bad scaling of the instrumental background spectrum in these energy regimes. Therefore all emission lines in these energy regimes will be ignored in the scope of this work.

The authors of Bulbul et al. (154) claim an emission line at a photon energy of $3.51 \pm 0.03\,\mathrm{keV}$ and a respective flux normalisation of $3.9\,^{+0.6}_{-1.0} \cdot 10^{-6}\,\mathrm{cm}^{-2}\,\mathrm{s}^{-1}$ in case of a non-frozen energy parameter during their fitting procedure and a normalisation of $2.5\,^{+0.6}_{-0.7} \cdot 10^{-6}\,\mathrm{cm}^{-2}\,\mathrm{s}^{-1}$ for a fixed energy at $3.57\,\mathrm{keV}$. The emission line is located in a region in which the condition $q \leq 0.99$ holds as shown in figures 6.6, 6.7, 6.8 and 6.9.

In addition, the energy and the normalisation of the emission line claimed by Bulbul et al. (154) is located in regions of the parameter spaces investigated with respect to the data set $\mathbf{D_1}$ fulfilling the condition $\Delta\chi^2 \leq 4.61$ (please see figures 6.6 and 6.7). This is not the case in view of the parameter spaces related to the data set $\mathbf{D_2}$ since here the paramater values of the claimed emission line are located in the regions fulfilling the condition $0 \leq \Delta\chi^2 \leq 4.61$ (please see figures 6.8 and 6.9).

The centroids of $N_l^{\mathbf{D_1},\mathrm{ISO}} = 20$, $N_l^{\mathbf{D_1},\mathrm{NFW}} = 23$, $N_l^{\mathbf{D_2},\mathrm{ISO}} = 21$ and $N_l^{\mathbf{D_2},\mathrm{NFW}} = 16$ closed $\mathrm{R}_l^{q>0.99}$-regions which were found within the present analysis (see tables 6.1, 6.3, 6.5, 6.7 and 6.2, 6.4, 6.6, 6.8) are located at energies and normalisations which can be matched to classical physical origins (12, 13, 14, 15), wherein corresponding possible classical physical origins are also listed in tables 6.1, 6.3, 6.5, 6.7 and 6.2, 6.4, 6.6, 6.8, respectively.

The $\mathrm{R}_l^{q>0.99}$-regions, in which the respective null hypothesis models $m_0^{\mathbf{D_1}}$ and $m_0^{\mathbf{D_2}}$ are rejected according to the posterior predictive p-value analysis, mostly overlap with the corresponding regions enclosed by the $\Delta\chi^2 = -9.211$-contours in which at least one minimum,

$$\min_{\mathrm{R}_l^{q>0.99}} \left(\chi_l^{2;q>0.99} (E_{\gamma;n}^{\mathbf{D}}, F_{\gamma,m}^{\mathbf{D}}) \right), \tag{6.6}$$

was found.
The centroids of the found $\mathrm{R}_l^{q>0.99}$-regions corresponding to

$$(E_{\gamma;n}^{\mathbf{D}}, F_{\gamma,m}^{\mathbf{D}}) = (E_{\gamma;l}^{\text{centroid}}, F_{\gamma;l}^{\text{centroid}}), \tag{6.7}$$

as well as the respective minima $(E_{\gamma;l}^{\text{min}}, F_{\gamma;l}^{\text{min}})$ and maxima $(E_{\gamma;l}^{\text{max}}, F_{\gamma;l}^{\text{max}})$ related to the respective minimal and maximal extensions of the $\mathrm{R}_l^{q>0.99}$-regions along the respective axes spanned by $E_{\gamma;n}^{\mathbf{D}}$ and $F_{\gamma;m}^{\mathbf{D}}$ are listed in tables 6.1, 6.3, 6.5, and 6.7.
The minima in the found $\mathrm{R}_l^{q>0.99}$-regions,

$$\Delta\chi^2_{\text{min}} \coloneqq \min_{\mathrm{R}_l^{q>0.99}} \left(\chi_l^{2;q>0.99} (E_{\gamma;n}^{\mathbf{D}}, F_{\gamma,m}^{\mathbf{D}}) \right), \tag{6.8}$$

according to equation 5.55, located at parameter values

$$(E_{\gamma;n}^{\mathbf{D}}, F_{\gamma,m}^{\mathbf{D}}) = (E_{\gamma;min}^{99\%}, F_{\gamma;min}^{99\%}) \tag{6.9}$$

in the investigated parameter spaces as well as the respective $\Delta\chi_{l;95\%}^{2;q>0.99}$-errors and the $\Delta\chi_{l;99\%}^{2;q>0.99}$-errors are listed in tables 6.2, 6.4, 6.6, and 6.8.
An additional emission line at an energy of 5.9 keV was identified in all investigated scenarios related to data sets $\mathbf{D_1}$ and $\mathbf{D_2}$ (tables 6.2, 6.4, 6.6, and 6.8). This emission line can be explained by an influence of the internal calibration source of XMM-Newton at 5.9 keV (65).
The emission line identified at an energy of approximately 2.47 keV for all investigated scenarios related to data set $\mathbf{D_2}$ (tables 6.6, 6.8) can have an origin in the instrumental Aurum Au-M edge related to the gold-coated mirrors of XMM-Newton (65). The emission line at an energy of approximately 1.9 keV was identified in all investigated scenarios related to data set $\mathbf{D_1}$ (tables 6.2, 6.4). This emission line can be a residual feature of the instrumental Silicon Si-K edge at 1.84 keV[2] (63, 64). The emission line identified at an energy of approximately 2.07 keV for all investigated scenarios related to data set $\mathbf{D_1}$ can have Aluminum Al XIII and/or the Silicon Si XIV as an astrophysical and/or instrumental origin

[2]For further details in view of the instrumental background of XMM-Newton and its detectors, please see http://xmm2.esac.esa.int/docs/documents/CAL-TN-0016-2-0.ps.gz

(tables 6.2, 6.4). An influence of the Iron K-edge at an energy of $7.04\,\text{keV}$ for all investigated scenarios related to data set $\mathbf{D_1}$ can be an explanation of the emission line identified at an energy of approximately $7.07\,\text{keV}$ (tables 6.2, 6.4). Further, the emission line identified at an energy of $9.17\,\text{keV}$ for all investigated scenarios related to data sets of $\mathbf{D_1}$ can be explained by an influence of the instrumental Zirconium Zn and/or Aurum Au emission lines (63, 64) (tables 6.2, 6.4).

$\mathbf{D_1}$							
Posterior predictive p-value, $\mathrm{R}_l^{q>0.99}$							
Index	$E_{\gamma;l}^{\mathrm{min}}$	$E_{\gamma;l}^{\mathrm{centroid}}$	$E_{\gamma;l}^{\mathrm{max}}$	$F_{\gamma;l}^{\mathrm{min}}$	$F_{\gamma;l}^{\mathrm{centroid}}$	$F_{\gamma;l}^{\mathrm{max}}$	Possible origin
$l^{\mathbf{D_1},\mathrm{ISO}}$	keV	keV	keV	$\frac{10^{-4}}{\mathrm{cm}^2\,\mathrm{s}}$	$\frac{10^{-4}}{\mathrm{cm}^2\,\mathrm{s}}$	$\frac{10^{-4}}{\mathrm{cm}^2\,\mathrm{s}}$	
1	0.4203	0.4210	0.4215	0.0229	12.8788	104.7130	-
2	0.6613	0.6627	0.6685	0.0033	0.4137	2.8840	-
3	0.8154	0.8228	0.8248	0.0022	0.6317	5.0119	-
4	1.1447	1.1457	1.1467	0.0033	0.0087	0.0200	-
5	1.4671	1.5672	1.6302	0.0029	0.0117	0.0303	-
6	1.8702	2.1952	2.5978	0.0003	0.3173	3.3113	Al XIII and/or Si XIV
7	2.2338	2.2741	2.3144	0.0103	0.0112	0.0123	-
8	2.5562	2.5885	2.5968	0.0912	0.1024	0.1202	-
9	3.1598	3.2860	3.4035	0.0010	0.0076	0.0240	Ar XVIII at 3.31 keV
10	3.3112	3.3200	3.3226	0.0283	0.0319	0.0372	Ar XVIII at 3.31 keV
11	3.8046	3.8710	3.8870	0.0017	0.0048	0.0104	-
12	5.4162	5.4174	5.4185	0.0044	0.0113	0.0229	-
13	5.8990	5.9810	6.0656	0.0002	4.2078	52.4807	Mn, inst.
14	6.5449	6.9820	7.3528	0.0003	3.5604	45.7088	Iron K-edge at 7.04 keV
15	7.5926	7.7297	7.8367	0.0010	0.4268	3.8019	Ni XXVII at 7.79 keV
16	8.1559	8.1768	8.2395	0.0057	0.0808	0.3318	Resi. of Zn-K$_\alpha$ and Cu-K$_\alpha$, inst.
17	8.7208	8.7472	8.8040	0.0076	0.0381	0.1053	-
18	9.0436	9.1921	9.2894	0.0011	2.1917	21.4306	Au, inst
19	9.5267	9.5281	9.5298	0.0087	0.0360	0.0913	Zn-K$_\alpha$, resi., inst
20	9.7690	9.7884	9.8520	0.0057	0.0188	0.0457	-

Table 6.1: The table lists the minimal, centroidal and maximal energies $E_{\gamma;l}^{\mathrm{min}}$, $E_{\gamma;l}^{\mathrm{centroid}}$ and $E_{\gamma;l}^{\mathrm{max}}$ as well as the minimal, centroidal and maximal normalisations $F_{\gamma;l}^{\mathrm{min}}$, $F_{\gamma;l}^{\mathrm{centroid}}$ and $F_{\gamma;l}^{\mathrm{max}}$ of the found $\mathrm{R}_l^{q>0.99}$-regions as well as possible physical origins with respect to the model $m_1^{\mathbf{D_1},\mathrm{ISO}}$. The abbreviations "inst." and "resi." stand for "instrumental" and "residual", respectively.

$\mathbf{D_1}$				
		$\Delta\chi^2$		
Index	$E^{99\%}_{\gamma;min}$	$F^{99\%}_{\gamma;min}$	$\Delta\chi^2_{\mathrm{min}}$	Possible origin
$l^{\mathbf{D_1},\mathrm{ISO}}$	keV	$\frac{10^{-4}}{\mathrm{cm}^2\,\mathrm{s}}$		
6	$1.911^{+0.239}_{-0.074}\,(^{+0.292}_{-0.088})$	$0.091^{+0.079}_{-0.054}\,(^{+0.105}_{-0.081})$	-12.0	Si-K, instrumental
6	$1.911^{+0.228}_{-0.062}\,(^{+0.280}_{-0.086})$	$0.105^{+0.066}_{-0.068}\,(^{+0.091}_{-0.095})$	-12.0	Si-K, instrumental
6	$2.073^{+0.046}_{-0.196}\,(^{+0.098}_{-0.244})$	$0.105^{+0.063}_{-0.063}\,(^{+0.087}_{-0.085})$	-14.0	Al XIII and/or Si XIV
13	$5.941^{+0.017}_{-0.020}\,(^{+0.034}_{-0.038})$	$0.209^{+0.093}_{-0.062}\,(^{+0.125}_{-0.095})$	-38.0	Mn, instrumental
14	$7.070^{+0.053}_{-0.019}\,(^{+0.091}_{-0.037})$	$0.275^{+0.092}_{-0.101}\,(^{+0.127}_{-0.139})$	-38.0	Influence of Iron K-edge at $7.04\,$keV
18	$9.165^{+0.044}_{-0.074}\,(^{+0.085}_{-0.130})$	$0.240^{+0.189}_{-0.156}\,(^{+0.270}_{-0.239})$	-10.0	Au, instrumental

Table 6.2: The table lists the minimum values ($E^{99\%}_{\gamma;min}, F^{99\%}_{\gamma;min}$) of the regions enclosed by the found $\Delta\chi^2 = -9.211$-contours overlapping with the found $\mathrm{R}_l^{q>0.99}$-regions and the $\Delta\chi^{2;q>0.99}_{l;95\%}$-errors ($\Delta\chi^{2;q>0.99}_{l;99\%}$-errors in brackets) as well as possible physical origins with respect to the model $m_1^{\mathbf{D_1},\mathrm{ISO}}$. Merely regions with $\Delta\chi^2$-values equal or lower than $\Delta\chi^2 = -9.211$ were taken into account.

$\mathbf{D_1}$							
	Posterior predictive p-value, $\mathrm{R}_l^{q>0.99}$						
Index	$E_{\gamma;l}^{\text{min}}$	$E_{\gamma;l}^{\text{centroid}}$	$E_{\gamma;l}^{\text{max}}$	$F_{\gamma;l}^{\text{min}}$	$F_{\gamma;l}^{\text{centroid}}$	$F_{\gamma;l}^{\text{max}}$	Possible origin
$l^{\mathbf{D_1},\text{NFW}}$	keV	keV	keV	$\frac{10^{-4}}{\text{cm}^2\,\text{s}}$	$\frac{10^{-4}}{\text{cm}^2\,\text{s}}$	$\frac{10^{-4}}{\text{cm}^2\,\text{s}}$	
1	0.4203	0.4210	0.4215	0.0229	7.0100	52.4807	-
2	0.6612	0.6625	0.6662	0.0033	0.3675	2.5119	-
3	0.8179	0.8229	0.8247	0.0022	0.7108	5.5069	-
4	1.1447	1.1457	1.1467	0.0044	0.0104	0.0229	-
5	1.4671	1.5633	1.6301	0.0025	0.0112	0.0303	-
6	1.8703	2.1729	2.5976	0.0003	0.3765	3.9896	Al XIII and/or Si XIV
7	2.4756	2.5124	2.5389	0.0105	0.0112	0.0120	S XV at 2.45 keV
8	2.5141	2.5665	2.5970	0.0347	0.0428	0.0525	-
9	2.5696	2.5912	2.5970	0.0525	0.0589	0.0692	-
10	3.1597	3.2654	3.3353	0.0010	0.0045	0.0119	Ar XVIII at 3.31 keV
11	3.2234	3.2739	3.3228	0.0144	0.0172	0.0219	Ar XVIII at 3.31 keV
12	3.8046	3.8715	3.8871	0.0017	0.0050	0.0115	-
13	5.4161	5.4174	5.4186	0.0044	0.0113	0.0229	-
14	5.8991	5.9811	6.0654	0.0002	2.8758	34.6737	Mn, inst. line
15	6.5450	6.9822	7.3528	0.0003	2.7853	34.6737	Iron K-edge at 7.04 keV
16	7.5928	7.7395	7.8370	0.0010	0.4264	3.4340	Ni XXVII at 7.79 keV
17	8.1577	8.1580	8.1584	0.2754	0.3015	0.3240	Zn-K$_\alpha$ and Cu-K$_\alpha$, resi., inst.
18	8.1572	8.1583	8.1605	0.1421	0.1661	0.1974	Zn-K$_\alpha$ and Cu-K$_\alpha$, resi., inst.
19	8.1570	8.1717	8.2395	0.0066	0.0368	0.1125	Zn-K$_\alpha$ and Cu-K$_\alpha$, resi., inst.
20	8.7206	8.7480	8.8037	0.0076	0.0380	0.1054	-
21	9.0436	9.1959	9.2896	0.0011	2.1960	20.9380	Au, inst.
22	9.5269	9.5281	9.5291	0.0087	0.0272	0.0632	Zn-K$_\alpha$, resi., inst.
23	9.7689	9.7700	9.7715	0.0057	0.0197	0.0482	-

Table 6.3: The table lists the minimal, centroidal and maximal energies $E_{\gamma;l}^{\text{min}}$, $E_{\gamma;l}^{\text{centroid}}$ and $E_{\gamma;l}^{\text{max}}$ as well as the minimal, centroidal and maximal normalisations $F_{\gamma;l}^{\text{min}}$, $F_{\gamma;l}^{\text{centroid}}$ and $F_{\gamma;l}^{\text{max}}$ of the found $\mathrm{R}_l^{q>0.99}$-regions as well as possible physical origins with respect to the model $m_1^{\mathbf{D_1},\text{NFW}}$. The abbreviations "inst." and "resi." stand for "instrumental" and "residual", respectively.

$\mathbf{D_1}$				
		$\Delta\chi^2$		
Index	$E^{99\%}_{\gamma;min}$	$F^{99\%}_{\gamma;min}$	$\Delta\chi^2_{\text{min}}$	Possible origin
$l^{\mathbf{D_1},\text{NFW}}$	keV	$\frac{10^{-4}}{\text{cm}^2\,\text{s}}$		
6	$1.911^{+0.234}_{-0.053}\,(^{+0.280}_{-0.085})$	$0.105^{+0.063}_{-0.068}\,(^{+0.089}_{-0.095})$	-12.0	Si-K, instrumental
6	$2.073^{+0.052}_{-0.192}\,(^{+0.098}_{-0.242})$	$0.105^{+0.066}_{-0.063}\,(^{+0.091}_{-0.088})$	-14.0	Al XIII and/or Si XIV
14	$5.941^{+0.017}_{-0.020}\,(^{+0.034}_{-0.040})$	$0.209^{+0.102}_{-0.067}\,(^{+0.131}_{-0.098})$	-37.0	Mn, instrumental
15	$7.070^{+0.049}_{-0.019}\,(^{+0.087}_{-0.037})$	$0.275^{+0.081}_{-0.099}\,(^{+0.120}_{-0.139})$	-37.9	Influence of Iron K-edge at $7.04\,$keV
21	$9.165^{+0.044}_{-0.074}\,(^{+0.085}_{-0.130})$	$0.240^{+0.209}_{-0.156}\,(^{+0.284}_{-0.239})$	-10.0	Au, instrumental
21	$9.165^{+0.038}_{-0.063}\,(^{+0.076}_{-0.116})$	$0.275^{+0.174}_{-0.192}\,(^{+0.248}_{-0.274})$	-10.0	Au, instrumental

Table 6.4: The table lists the minimum values $(E^{99\%}_{\gamma;min}, F^{99\%}_{\gamma;min})$ of the regions enclosed by the found $\Delta\chi^2 = -9.211$-contours overlapping with the found $\text{R}_l^{q>0.99}$-regions and the $\Delta\chi^{2;q>0.99}_{l;95\%}$-errors ($\Delta\chi^{2;q>0.99}_{l;99\%}$-errors in brackets) as well as possible physical origins with respect to the model $m_1^{\mathbf{D_1},\text{NFW}}$. Merely regions with $\Delta\chi^2$-values equal or lower than $\Delta\chi^2 = -9.211$ were taken into account.

$\mathbf{D_2}$							
Posterior predictive p-value, $\mathrm{R}_l^{q>0.99}$							
Index	$E_{\gamma;l}^{\min}$	$E_{\gamma;l}^{\text{centroid}}$	$E_{\gamma;l}^{\max}$	$F_{\gamma;l}^{\min}$	$F_{\gamma;l}^{\text{centroid}}$	$F_{\gamma;l}^{\max}$	Possible origin
$l^{\mathbf{D_2},\mathrm{ISO}}$	keV	keV	keV	$\frac{10^{-4}}{\mathrm{cm}^2\,\mathrm{s}}$	$\frac{10^{-4}}{\mathrm{cm}^2\,\mathrm{s}}$	$\frac{10^{-4}}{\mathrm{cm}^2\,\mathrm{s}}$	
1	0.4187	0.4190	0.4196	0.0465	0.0489	0.0523	-
2	0.4187	0.4194	0.4197	0.0044	0.0134	0.0282	-
3	0.5730	0.5737	0.5743	0.0021	0.0021	0.0023	-
4	0.9602	1.1030	1.1943	0.0002	0.0007	0.0015	Ne IX/Na-K$_\alpha$, resi.
5	1.8896	1.8906	1.8916	0.0001	0.0004	0.0011	Si-K, inst.
6	1.8904	1.8906	1.8909	0.0030	0.0030	0.0031	Si-K, inst.
7	1.8897	1.8907	1.8919	0.0013	0.0017	0.0021	Si-K, inst.
8	2.0446	2.0455	2.0465	0.0007	0.0008	0.0012	Al XIII and/or Si XIV
9	2.2769	2.6520	2.9769	0.0001	0.5987	9.1588	S XV at 2.45 keV
10	2.6789	2.7423	2.7998	0.0021	0.0027	0.0036	-
11	3.2062	3.3055	3.3641	0.0002	0.0009	0.0019	Ar XVIII at 3.31 keV
12	3.3348	3.3571	3.3636	0.0023	0.0027	0.0034	-
13	5.8400	5.9317	6.0004	0.0001	0.5737	6.9183	Mn, inst.
14	6.3781	6.3835	6.3885	0.0121	0.0133	0.0158	-
15	6.3037	6.8692	7.3148	0.0001	0.8986	10.6742	Fe XXV at 6.7 keV
16	7.7767	7.8321	7.8566	0.0003	0.4782	4.7863	Ni XXVII at 7.79 keV
17	8.3193	8.3764	8.4765	0.0005	0.4208	3.9811	Resi. of Zn-K$_\alpha$ and Cu-K$_\alpha$, inst.
18	9.1717	9.1775	9.1983	0.1000	0.1170	0.1445	Au, inst.
19	9.1701	9.1903	9.2499	0.0331	0.0586	0.1000	Au, inst.
20	9.1686	9.2046	9.2543	0.0010	0.0087	0.0331	Au, inst.
21	9.5515	9.5748	9.6403	0.0012	0.3974	3.0328	Zn-K$_\alpha$, resi., inst.

Table 6.5: The table lists the minimal, centroidal and maximal energies $E_{\gamma;l}^{\min}$, $E_{\gamma;l}^{\text{centroid}}$ and $E_{\gamma;l}^{\max}$ as well as the minimal, centroidal and maximal normalisations $F_{\gamma;l}^{\min}$, $F_{\gamma;l}^{\text{centroid}}$ and $F_{\gamma;l}^{\max}$ of the found $\mathrm{R}_l^{q>0.99}$-regions as well as possible physical origins with respect to the model $m_1^{\mathbf{D_2},\mathrm{ISO}}$. The abbreviations "inst." and "resi." stand for "instrumental" and "residual", respectively.

$\mathbf{D_2}$				
		$\Delta\chi^2$		
Index	$E^{99\%}_{\gamma;min}$	$F^{99\%}_{\gamma;min}$	$\Delta\chi^2_{\text{min}}$	Possible origin
$l^{\mathbf{D_2},\text{ISO}}$	keV	$\frac{10^{-4}}{\text{cm}^2\,\text{s}}$		
9	$2.472^{+0.072}_{-0.099}\,(^{+0.099}_{-0.121})$	$0.209^{+0.095}_{-0.117}\,(^{+0.136}_{-0.160})$	-16.3	S XV at $2.45\,$keV
13	$5.880^{+0.047}_{-0.022}\,(^{+0.083}_{-0.044})$	$0.174^{+0.101}_{-0.109}\,(^{+0.146}_{-0.153})$	-11.9	Mn, instrumental line

Table 6.6: The table lists the minimum values $(E^{99\%}_{\gamma;min}, F^{99\%}_{\gamma;min})$ of the regions enclosed by the found $\Delta\chi^2 = -9.211$-contours overlapping with the found $\text{R}_l^{q>0.99}$-regions and the $\Delta\chi^{2;q>0.99}_{l;95\%}$-errors ($\Delta\chi^{2;q>0.99}_{l;99\%}$-errors in brackets) as well as possible physical origins with respect to the model $m_1^{\mathbf{D_2},\text{ISO}}$. Merely regions with $\Delta\chi^2$-values equal or lower than $\Delta\chi^2 = -9.211$ were taken into account.

$\mathbf{D_2}$							
			Posterior predictive p-value, $\mathrm{R}_l^{q>0.99}$				
Index	$E_{\gamma;l}^{\text{min}}$	$E_{\gamma;l}^{\text{centroid}}$	$E_{\gamma;l}^{\text{max}}$	$F_{\gamma;l}^{\text{min}}$	$F_{\gamma;l}^{\text{centroid}}$	$F_{\gamma;l}^{\text{max}}$	Possible origin
$l^{\mathbf{D_2},\text{NFW}}$	keV	keV	keV	$\frac{10^{-4}}{\text{cm}^2\,\text{s}}$	$\frac{10^{-4}}{\text{cm}^2\,\text{s}}$	$\frac{10^{-4}}{\text{cm}^2\,\text{s}}$	
1	0.4187	0.4188	0.4189	0.0475	0.0482	0.0492	-
2	0.4187	0.4194	0.4197	0.0044	0.0120	0.0248	-
3	0.5732	0.5737	0.5741	0.0021	0.0023	0.0026	-
4	0.9602	1.1049	1.1943	0.0002	0.0006	0.0013	Ne IX/Na-K$_\alpha$, resi.
5	1.8897	1.8906	1.8915	0.0001	0.0004	0.0011	Si-K, inst.
6	1.8901	1.8907	1.8914	0.0013	0.0016	0.0019	Si-K, inst.
7	2.0445	2.0456	2.0466	0.0006	0.0009	0.0014	Al XIII and/or Si XIV
8	2.2769	2.6549	2.9769	0.0001	0.5394	8.6541	S XV at 2.45 keV
9	3.2062	3.3071	3.3637	0.0002	0.0007	0.0017	Ar XVIII at 3.31 keV
10	3.3560	3.3612	3.3627	0.0025	0.0025	0.0026	-
11	5.8400	5.9275	5.9996	0.0001	0.8123	9.1588	Mn, inst.
12	6.3040	6.8722	7.3146	0.0001	0.8105	9.4392	Fe XXV at 6.7 keV
13	7.7767	7.8299	7.8570	0.0003	0.9261	9.4392	Ni XXVII at 7.79 keV
14	8.3194	8.3747	8.4766	0.0005	0.4136	3.6462	Resi. of Zn-K$_\alpha$ and Cu-K$_\alpha$, inst.
15	9.1685	9.1959	9.2543	0.0012	0.2450	1.7452	Au, inst.
16	9.5531	9.5765	9.6396	0.0012	0.1513	1.0965	Zn-K$_\alpha$, resi., inst.

Table 6.7: The table lists the minimal, centroidal and maximal energies $E_{\gamma;l}^{\text{min}}$, $E_{\gamma;l}^{\text{centroid}}$ and $E_{\gamma;l}^{\text{max}}$ as well as the minimal, centroidal and maximal normalisations $F_{\gamma;l}^{\text{min}}$, $F_{\gamma;l}^{\text{centroid}}$ and $F_{\gamma;l}^{\text{max}}$ of the found $\mathrm{R}_l^{q>0.99}$-regions as well as possible physical origins with respect to the model $m_1^{\mathbf{D_2},\text{NFW}}$. The abbreviations "inst." and "resi." stand for "instrumental" and "residual", respectively.

$\mathbf{D_2}$				
		$\Delta\chi^2$		
Index	$E^{99\%}_{\gamma;min}$	$F^{99\%}_{\gamma;min}$	$\Delta\chi^2_{\text{min}}$	Possible origin
$l^{\mathbf{D_2},\text{NFW}}$	keV	$\frac{10^{-4}}{\text{cm}^2\,\text{s}}$		
8	$2.472^{+0.072}_{-0.098}\,(^{+0.095}_{-0.121})$	$0.209^{+0.097}_{-0.115}\,(^{+0.138}_{-0.158})$	-16.6	S XV at $2.45\,$keV
11	$5.880^{+0.047}_{-0.022}\,(^{+0.083}_{-0.044})$	$0.174^{+0.100}_{-0.109}\,(^{+0.146}_{-0.154})$	-11.8	Mn, instrumental line

Table 6.8: The table lists the minimum values $(E^{99\%}_{\gamma;min}, F^{99\%}_{\gamma;min})$ of the regions enclosed by the found $\Delta\chi^2 = -9.211$-contours overlapping with the found $\text{R}_l^{q>0.99}$-regions and the $\Delta\chi^{2;q>0.99}_{l;95\%}$-errors ($\Delta\chi^{2;q>0.99}_{l;99\%}$-errors in brackets) as well as possible physical origins with respect to the model $m_1^{\mathbf{D_2},\text{NFW}}$. Merely regions with $\Delta\chi^2$-values equal or lower than $\Delta\chi^2 = -9.211$ were taken into account.

Chapter 7

Discussion, Conclusion and Outlook

7.1 Discussion

A new type of analysis of diffuse X-ray background spectra was carried out to search for unknown astrophysical or dark-matter-dependent emission lines. The application of a more rigorous statistical method, the posterior predictive p-value analysis, was adapted to the needs of the analysis in the present work.
The instrumental background continuum model was built of a merger of a multitude of single filter-wheel-closed (FWC) data sets recorded by to the EPIC-PN detector from observation dates distributed over the operating duration of the satellite XMM-Newton up to the year 2013. The resulting merged instrumental background continuum model was scaled and subtracted from each of the analysed astrophysical spectra. Therefore, the utilised FWC spectrum represents a time average of the energy distribution of the instrumental background. Unfortunately, the subtraction of the instrumental background spectrum carried out in the present work has its drawback in increasing the errors of the counts per energy bin of the resulting spectrum because of the unavoidable propagation of errors which has to be considered. The corner spectra were not taken into account due to low numbers of counts in view of the small chip area involved as well as instrumental emission lines which are present in the corner areas of the PN-CCDs but not in areas of the PN-CCDs related to the typical fields of view in case of astrophysical observations. An alternative method would have been the combined fitting of the spectra by astrophysical and instrumental models in a single step. It is important to note that the instrumental model would not be allowed to be folded by the response matrix during the fitting process in such an alternative method.

Furthermore, two nullhypothesis models $m_0^{\mathbf{D_1}}$ and $m_0^{\mathbf{D_2}}$ were found in the scope of the present work which were flexibly and simultaneously fitted to a multitude of spectra of the astrophysical diffuse X-ray background related to observations with pointings indiscriminately distributed over the sky.
The results presented here were also achieved by the posterior predictive p-value analysis proposed by Protassov et al. (75) which is well fitted to find confidence regions in parameter spaces of additional model components by the exertion of an hypothesis test. This allowed to probe the parameter space of additive components which had the potential to reveal hithero unknown or unexpected signals. Several confidence regions in the energy-flux-normalisation parameter space of an additional line were found, firstly, under the assumption of one or the other of two popular dark matter models, namely, the sterile neutrino or the axion, respectively, secondly, under the assumption of one or the other of a NFW or an isothermal dark matter halo distribution and, thirdly, under the assumption that the signal form of the additive component features the form of a Gaussian function.
The application of the posterior predictive p-value analysis as an hypothesis test to find regions in the parameter space which favour the respective alternative models, $m_1^{\mathbf{D_1},\mathrm{ISO}}$, $m_1^{\mathbf{D_1},\mathrm{NFW}}$, $m_1^{\mathbf{D_2},\mathrm{ISO}}$ or $m_1^{\mathbf{D_2},\mathrm{NFW}}$, unveiled several regions favoring the alternative models over the nullhypothesis models $m_0^{\mathbf{D_1}}$ or $m_0^{\mathbf{D_2}}$, respectively. Most of the emission lines can be related to astrophysical or instrumental origins.
Unfortunately, it is not directly possible to resolve the photon flux normalisations of the found centroids into the individual contributions of the data sets of $\mathbf{D_1}$ or $\mathbf{D_2}$ investigated in the scope of the present analysis because of the joint fitting and the consequential unified statistical handling of the data sets.
The combined application of the posterior predictive p-value analysis as a hypothesis test for additional emission lines and, in case of a rejection of the nullhypothesis model $m_0^{\mathbf{D}}$, the successive determination of flux normalisation limits with help of the $\Delta\chi^2$-statistics, proved to be a powerful tool to uncover spectral emission lines.
Moreover, the present results do not show any hints towards the existence of a spectral emission line at an energy of $3.55\,\mathrm{keV}$ as claimed by Bulbul et al. (154). The energy and flux normalisation of the emission line claimed by Bulbul et al. (154) is contained in a region fulfilling the condition $\Delta\chi^2 \leq 4.61$ of the parameter spaces investigated with respect to the data set $\mathbf{D_1}$. This is not the case in regard to the parameter spaces related to the data set $\mathbf{D_2}$ since the paramater values of the claimed emission line are located in a region fulfilling the condition $0 \leq \Delta\chi^2 \leq 4.61$.

7.2 Conclusion

In summary the present search for unknown emission lines in the diffuse X-ray background exceeds previous searches. Unknown emission lines having a high significance were not found in the scope of the present work, in particular the famous 3.55 keV line was not identified. Notably, it was shown that the posterior predictive p-value analysis can be successfully applied to scan parameter spaces of alternative hypothesis models incorporating additive components. The application of this method is not restricted to the X-ray regime but quite the contrary. Future applications of this method have the potential to efficiently uncover parameter regions of additional components worthy to be the target of further searches.

7.3 Outlook

In the future, the incorporation of further data sets of additional astrophysical objects, such as Galaxy Clusters, which are expected to be embedded in dark matter halos which could provide high expected dark matter column densities, should be undertaken to gain more confidence in the exclusion of parameter spaces of dark matter models. Moreover, future X-ray missions as eRosita (66) and Athena (67) could lead to further exclusions of the parameter space of dark matter particle models or could unveil further information with respect to the claimed emission line at an energy of 3.55 keV (154) or so far unknown signals that could possibly lead to the origin of the dark matter problem. Independent of the afore-mentioned, an expansion of the present analysis to other or broader energy regimes and/or data taken by other instruments could not only be of interest in view of the search for dark matter but also for astrophysical signals. Further, the nullhypothesis models applied to the diffuse X-ray background should be deeper investigated in view of a "classical" astrophysical perspective. The fitted astrophysical bremsstrahlung components as well as the fitted emission lines could disclose interesting new information about the environments of the astrophysical objects originally in focus of the data sets analysed in this work.

Chapter 8

Appendices

8.1 Appendix A. Isothermal Profile

The functional expression related to an isothermal profile can be derived with the following Ansatz according to Dipankar Bhattacharya[1], wherein a polytropic equation $p = K\rho^\gamma$ is combined with a gravitational potential ϕ via an hydrostatic equation,

$$\frac{dp}{dr} = -\rho\frac{d\phi}{dr} = \gamma K\rho^{\gamma-1}\frac{d\rho}{dr} \tag{A.1}$$

$$\Rightarrow \frac{d\phi}{dr} = -\gamma K\rho^{\gamma-2}\frac{d\rho}{dr}. \tag{A.2}$$

The integration of the last equation unfolds ϕ,

$$\int \frac{d\phi}{dr}dr = \phi = -\gamma K \int \rho^{\gamma-2}\frac{d\rho}{dr}dr. \tag{A.3}$$

[1]Inter-University Centre for Astronomy and Astrophysics (IUCAA), Pune, India, http://www.iucaa.in/~dipankar/ph217/isothsph.pdf

The isothermal condition is $\gamma = 1$ and $p \propto \rho$,

$$\begin{aligned}
\Rightarrow \qquad \phi &= -K \int_{\rho_0}^{\rho} \frac{1}{\rho'} \frac{d\rho'}{dr} dr && \text{(A.4)}\\
&= -K \int_{\rho_0}^{\rho} \frac{d \ln(\rho')}{dr} dr && \text{(A.5)}\\
&= -K \left(\ln(\rho) - \ln(\rho_0)\right) && \text{(A.6)}\\
&= -K \ln\left(\frac{\rho}{\rho_0}\right) && \text{(A.7)}\\
\Leftrightarrow \qquad \rho &= \rho_0 \exp\left(-\frac{\phi}{K}\right). && \text{(A.8)}
\end{aligned}$$

The last equation is a solution to the Poisson equation in polar coordinates in which the integration constant ρ_0 vanishes,

$$\Delta\phi = \frac{d^2\phi}{dr^2} + \frac{2}{r}\frac{d\phi}{dr} = -4\pi G\rho = -4\pi G\rho_0 \exp\left(-\frac{\phi}{K}\right), \tag{A.9}$$

$$\begin{aligned}
\Leftrightarrow \qquad \frac{d^2}{dr^2}\ln(\rho) + \frac{2}{r}\frac{d}{dr}\ln(\rho) &= \frac{-4\pi G\rho}{K} && \text{(A.10)}\\
\Leftrightarrow \qquad \frac{1}{r^2}\left(r^2\frac{d^2}{dr^2}\ln(\rho) + 2r\frac{d}{dr}\ln(\rho)\right) &= \frac{-4\pi G\rho}{K} && \text{(A.11)}\\
\Leftrightarrow \qquad \frac{1}{r^2}\frac{d}{dr}\left(r^2\frac{d}{dr}\ln(\rho)\right) &= \frac{-4\pi G\rho}{K}. && \text{(A.12)}
\end{aligned}$$

The equation $\rho(r) = \frac{K}{2\pi G r^2}$ is an exact solution to the above equation,

$$\begin{aligned}
\frac{1}{r^2}\frac{d}{dr}\left(r^2\frac{d}{dr}\ln\left(\frac{K}{2\pi G r^2}\right)\right) = -2 &= \frac{-4\pi G\rho}{K} && \text{(A.13)}\\
\Leftrightarrow \qquad \rho(r) &= \frac{K}{2\pi G r^2}. && \text{(A.14)}
\end{aligned}$$

There are additional boundary conditions necessary for the non-singular solutions of isothermal spheres,

$$\frac{d^2w}{dz^2} + \frac{2}{z}\frac{dw}{dz} = \exp(-w) \quad \text{with} \quad z = Ar,\ A^2 = \frac{4\pi G\rho_0}{K},\ w = \frac{\phi}{K}. \tag{A.15}$$

The boundary condition at $z = 0$ are $w = w' = 0$. The corresponding solution can be found numerically. The functional behavior of w around $z = 0$ can be approximated by the relation $w \propto z^2$,

$$\rho(w) = \frac{\rho_0}{\exp(w)} \approx \frac{\rho_0}{1 + \left(\frac{z}{z_0}\right)^2} = \frac{\rho_0}{1 + \left(\frac{r}{r_0}\right)^2} \quad \text{with} \quad r_0 := \frac{z_0}{A} = \left(\frac{9K}{4\pi G \rho_0}\right)^{\frac{1}{2}}. \tag{A.16}$$

The value r_0 is named as the core or King radius. The constant ρ_0 can be resolved by the assumption of a circular orbit of all particles in the density distribution with a velocity v_0 which is related to the gravitational potential by $v_0^2 = \frac{GM}{r}$,

$$v_0^2 := \langle v^2 \rangle = \frac{GM}{r} = \frac{4\pi\rho_0 G r_0^2}{r}\left(r - r_0 \arctan\left(\frac{r}{r_0}\right)\right) \tag{A.17}$$

$$= 4\pi\rho_0 r_0^2 \underbrace{\left(1 - \frac{r_0}{r}\arctan\left(\frac{r}{r_0}\right)\right)}_{\begin{cases} = 0, & \text{for} \quad r \to \infty \\ = 0, & \text{for} \quad r \to 0 \end{cases}} \tag{A.18}$$

$$\approx 4\pi\rho_0 r_0^2 G, \tag{A.19}$$

$$\Leftrightarrow \qquad \rho_0 = \frac{v_0^2}{4\pi G r_0^2}. \tag{A.20}$$

8.2 Appendix B. Column Density of the Isothermal profile

To calculate a dark matter column density related to an isothermal profile 2.35, a substitution has to be applied to start the integration at the position of the Earth which appears as an equation build up by the combination of the sine rule and solutions of triangles,

$$s(x,l,b) := (x^2 - 2xR_\odot \cos(l)\cos(b) + R_\odot^2)^{0.5}, \tag{B.21}$$

with $R_\odot = 8.3\,\mathrm{kpc}$ as the distance between the observer on the Earth and the Galactic center (16, 17). The column density integral is:

$$\begin{aligned} S_{\mathrm{ISO}}\,(l,b) &= \int_0^\infty \rho_{\mathrm{ISO}}(s(x,l,b))\,dr & \text{(B.22)}\\ &= \int_0^\infty \frac{\rho_{\mathrm{ISO,0}}}{1 + r^2(x,l,b)/r^2_{\mathrm{ISO,0}}}\,dr & \text{(B.23)}\\ &= \rho_{\mathrm{ISO,0}} \cdot r^2_{\mathrm{ISO,0}} \int_0^\infty \frac{dx}{x^2 - 2xR_\odot\cos(l)\cos(b) + R_\odot^2 + r^2_{\mathrm{ISO,0}}} & \text{(B.24)} \end{aligned}$$

The following equation (I. N. Bronstein, K. A. Semendjajew, G. Musiol, H. Mühlig, "Taschenbuch der Mathematik" (2000), 5. Auflage, S.1051, 21.5.1.2.40) was taken to resolve the above substituted integral,

$$X = ax^2 + bx + c; \quad \Delta = 4ac - b^2 \tag{B.25}$$

$$\int \frac{dx}{X} = \frac{2}{\sqrt{\Delta}} \arctan\left(\frac{2ax + b}{\sqrt{\Delta}}\right) \quad \text{if } \Delta > 0. \tag{B.26}$$

This results in the analytical expression with regard to $\arctan(-y) = -\arctan(y)$ as well as $\lim_{y\to\infty} \arctan(y) = \pi/2$,

$$\begin{aligned} S^{\mathrm{ISO}}(l,b) = &\frac{\rho_{\mathrm{ISO,0}}\, r^2_{\mathrm{ISO,0}}}{\left(r^2_{\mathrm{ISO,0}} + R_\odot^2\,(1 - \cos^2(l)\cos^2(b))\right)^{0.5}}\\ &\cdot \left(\frac{\pi}{2} + \arctan\left(\frac{R_\odot \cos(l)\cos(b)}{\left(r^2_{\mathrm{ISO,0}} + R_\odot^2\,(1 - \cos^2(l)\cos^2(b))\right)^{0.5}}\right)\right). \end{aligned} \tag{B.27}$$

8.3 Appendix C. Reduction and Filtering of Event Files

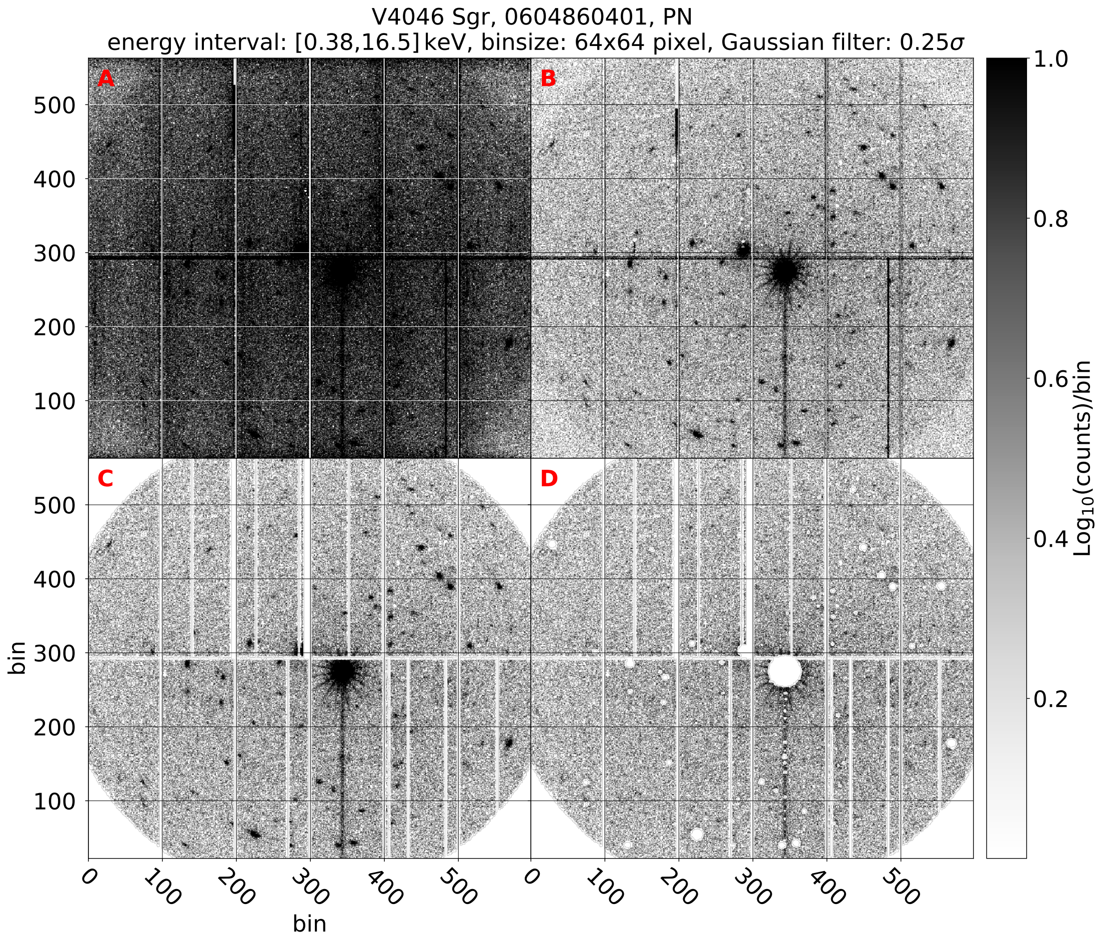

Figure C.1: All four panels show event files of the data set 0604860401 ($i = 1$, $\mathbf{D_1}$, table 4.1) taken with the EPIC-PN detector in an energy range of 0.38 keV to 16.5 keV. The colour coding represents the decadic logarithm of the number of X-ray photons counts per bin. The coordinates X and Y correspond to sky pixel coordinates. The upper left panel (A) shows the unfiltered raw event file and the upper right panel (B) is the time and particle background filtered result. The lower left panel (C) shows the time and particle background filtered result after application of the spatial filter and the lower right panel (D) represents the final source filtered diffuse X-ray background. All four representations of the corresponding event files have been smoothed with a Gaussian kernel having a filter width of 0.25σ.

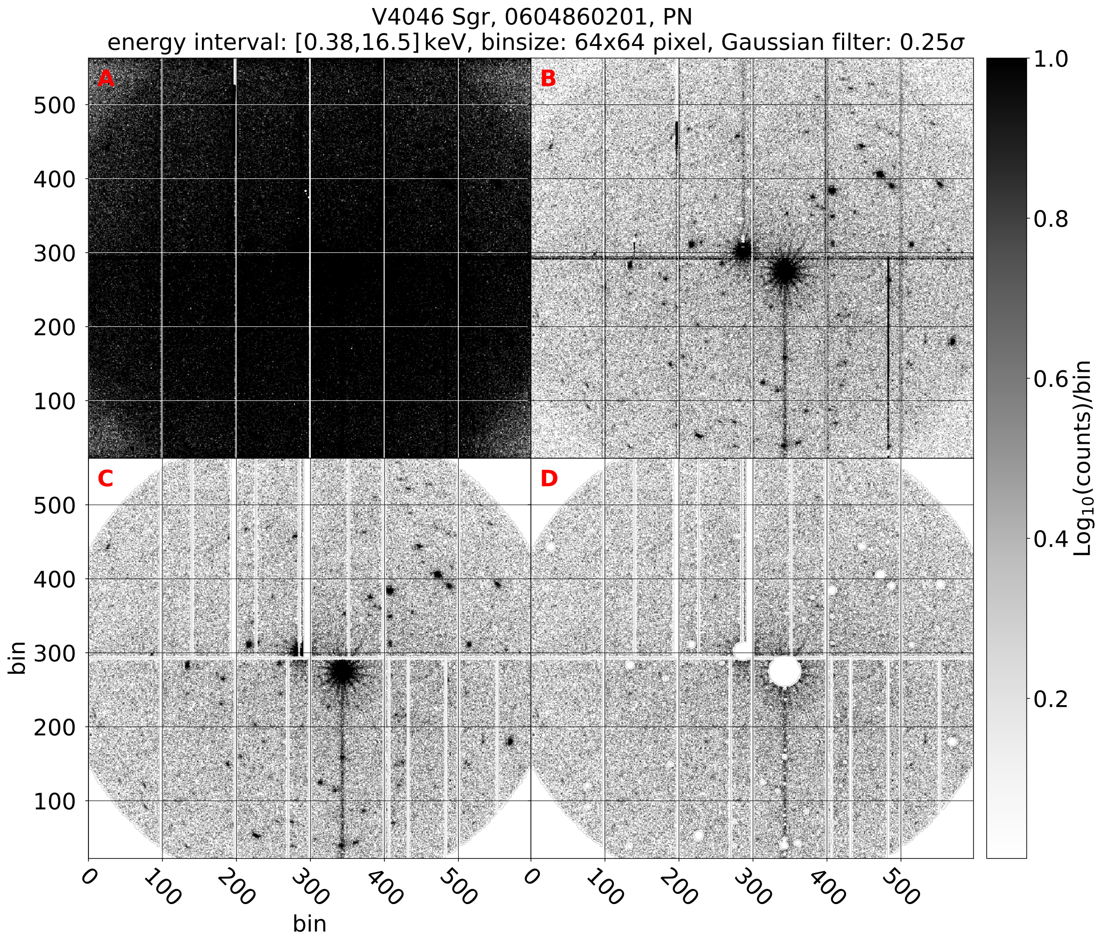

Figure C.2: All four panels show event files of the data set 0604860201 ($i = 3$, $\mathbf{D_1}$, table 4.1) taken with the EPIC-PN detector in an energy range of 0.38 keV to 16.5 keV. The colour coding represents the decadic logarithm of the number of X-ray photons counts per bin. The coordinates X and Y correspond to sky pixel coordinates. The upper left panel (A) shows the unfiltered raw event file and the upper right panel (B) is the time and particle background filtered result. The lower left panel (C) shows the time and particle background filtered result after application of the spatial filter and the lower right panel (D) represents the final source filtered diffuse X-ray background. All four representations of the corresponding event files have been smoothed with a Gaussian kernel having a filter width of 0.25σ.

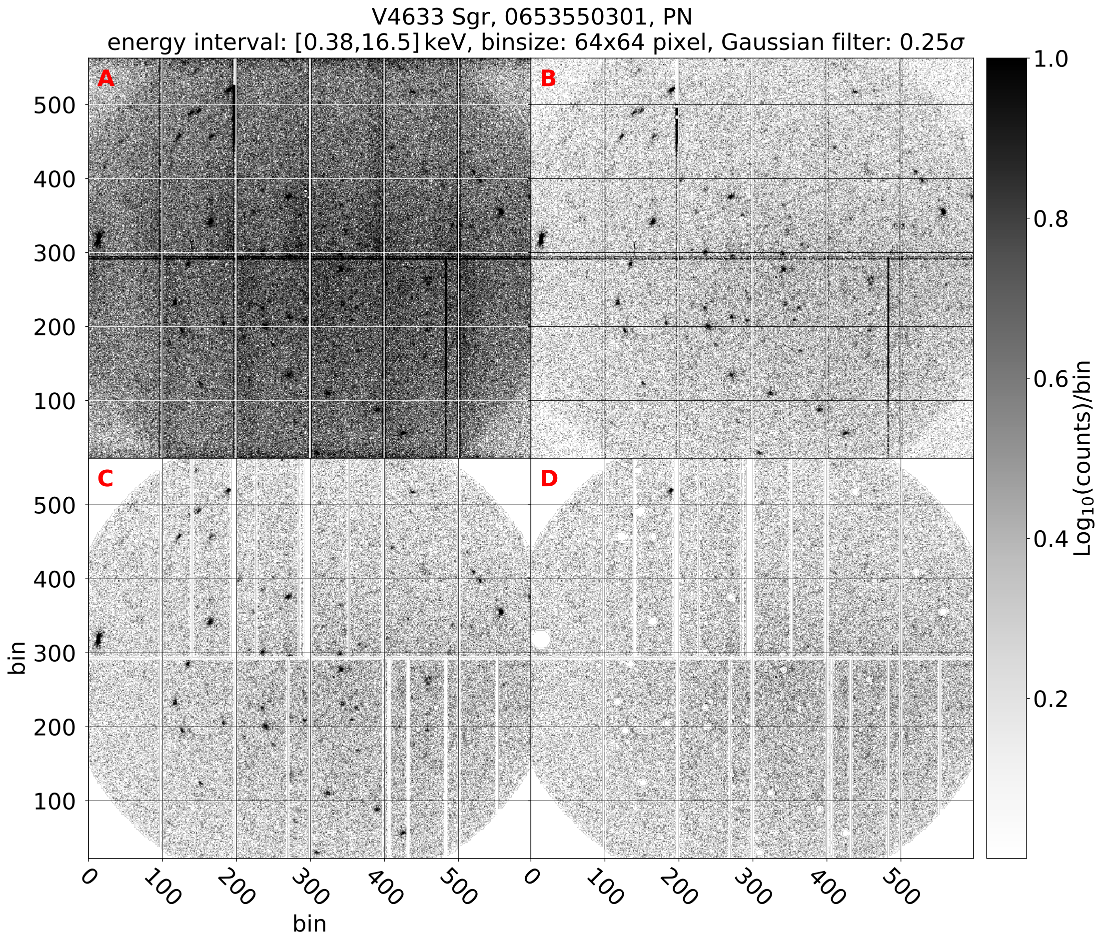

Figure C.3: All four panels show event files of the data set 0653550301 ($i = 4$, $\mathbf{D_1}$, table 4.1) taken with the EPIC-PN detector in an energy range of $0.38\,\mathrm{keV}$ to $16.5\,\mathrm{keV}$. The colour coding represents the decadic logarithm of the number of X-ray photons counts per bin. The coordinates X and Y correspond to sky pixel coordinates. The upper left panel (A) shows the unfiltered raw event file and the upper right panel (B) is the time and particle background filtered result. The lower left panel (C) shows the time and particle background filtered result after application of the spatial filter and the lower right panel (D) represents the final source filtered diffuse X-ray background. All four representations of the corresponding event files have been smoothed with a Gaussian kernel having a filter width of 0.25σ.

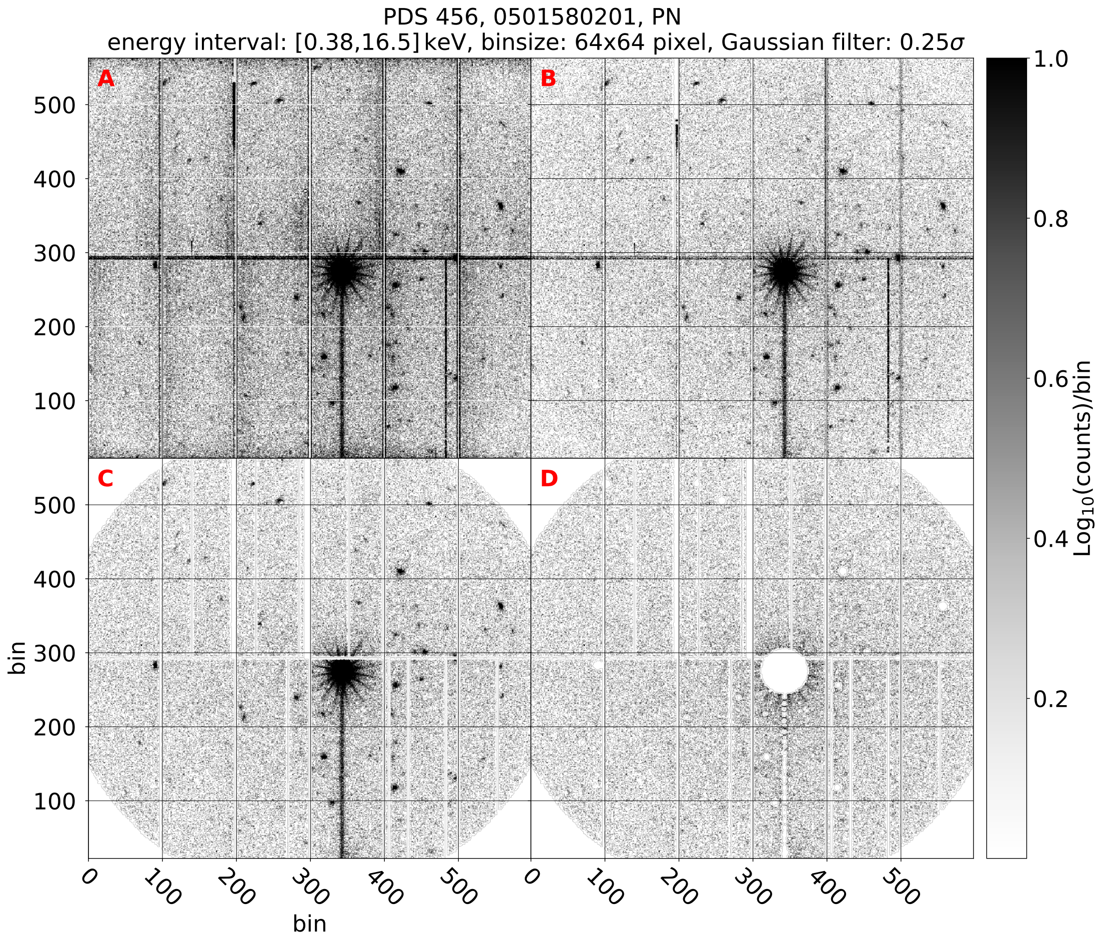

Figure C.4: All four panels show event files of the data set 0501580201 ($i = 5$, $\mathbf{D_1}$, table 4.1) taken with the EPIC-PN detector in an energy range of 0.38 keV to 16.5 keV. The colour coding represents the decadic logarithm of the number of X-ray photons counts per bin. The coordinates X and Y correspond to sky pixel coordinates. The upper left panel (A) shows the unfiltered raw event file and the upper right panel (B) is the time and particle background filtered result. The lower left panel (C) shows the time and particle background filtered result after application of the spatial filter and the lower right panel (D) represents the final source filtered diffuse X-ray background. All four representations of the corresponding event files have been smoothed with a Gaussian kernel having a filter width of 0.25σ.

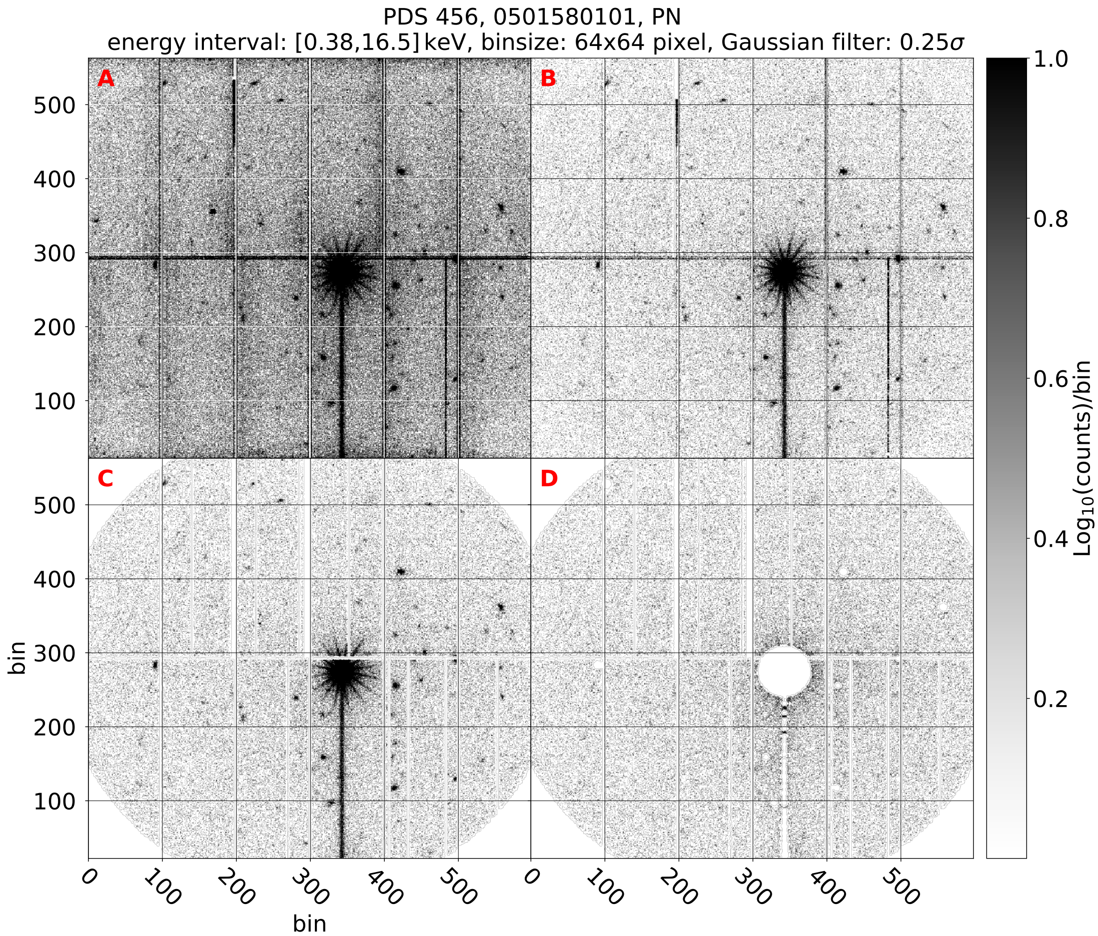

Figure C.5: All four panels show event files of the data set 0501580101 ($i = 6$, $\mathbf{D_1}$, table 4.1) taken with the EPIC-PN detector in an energy range of $0.38\,\mathrm{keV}$ to $16.5\,\mathrm{keV}$. The colour coding represents the decadic logarithm of the number of X-ray photons counts per bin. The coordinates X and Y correspond to sky pixel coordinates. The upper left panel (A) shows the unfiltered raw event file and the upper right panel (B) is the time and particle background filtered result. The lower left panel (C) shows the time and particle background filtered result after application of the spatial filter and the lower right panel (D) represents the final source filtered diffuse X-ray background. All four representations of the corresponding event files have been smoothed with a Gaussian kernel having a filter width of 0.25σ.

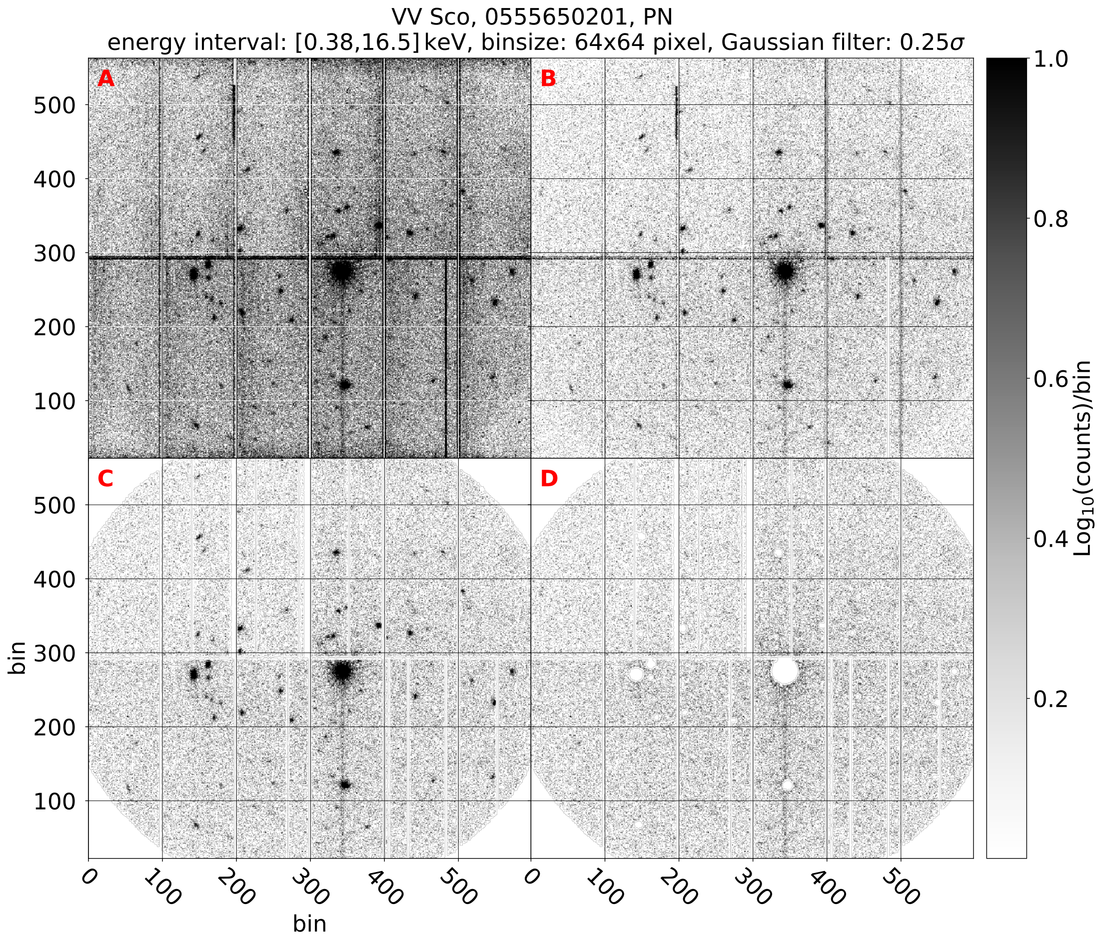

Figure C.6: All four panels show event files of the data set 0555650201 ($i = 7$, $\mathbf{D_1}$, table 4.1) taken with the EPIC-PN detector in an energy range of $0.38\,$keV to $16.5\,$keV. The colour coding represents the decadic logarithm of the number of X-ray photons counts per bin. The coordinates X and Y correspond to sky pixel coordinates. The upper left panel (A) shows the unfiltered raw event file and the upper right panel (B) is the time and particle background filtered result. The lower left panel (C) shows the time and particle background filtered result after application of the spatial filter and the lower right panel (D) represents the final source filtered diffuse X-ray background. All four representations of the corresponding event files have been smoothed with a Gaussian kernel having a filter width of 0.25σ.

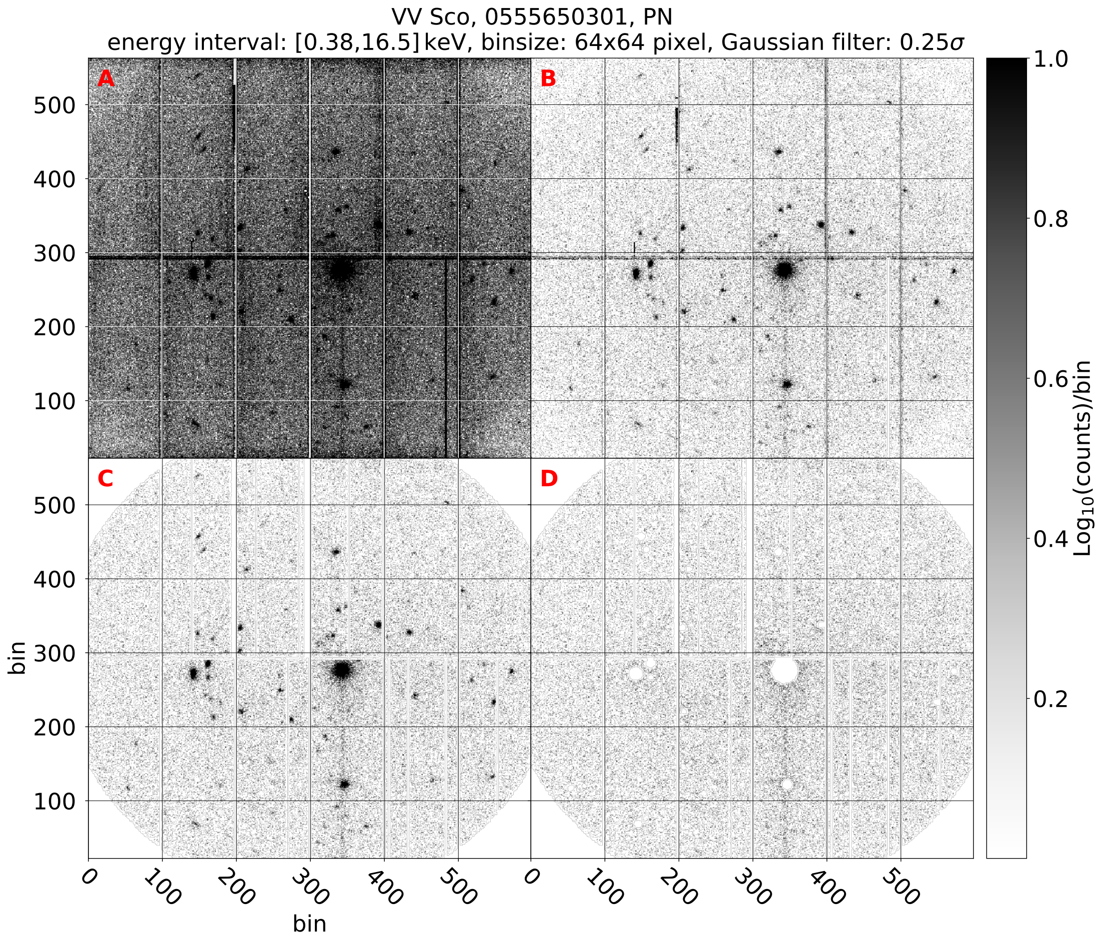

Figure C.7: All four panels show event files of the data set 0555650301 ($i = 8$, $\mathbf{D_1}$, table 4.1) taken with the EPIC-PN detector in an energy range of $0.38\,\mathrm{keV}$ to $16.5\,\mathrm{keV}$. The colour coding represents the decadic logarithm of the number of X-ray photons counts per bin. The coordinates X and Y correspond to sky pixel coordinates. The upper left panel (A) shows the unfiltered raw event file and the upper right panel (B) is the time and particle background filtered result. The lower left panel (C) shows the time and particle background filtered result after application of the spatial filter and the lower right panel (D) represents the final source filtered diffuse X-ray background. All four representations of the corresponding event files have been smoothed with a Gaussian kernel having a filter width of 0.25σ.

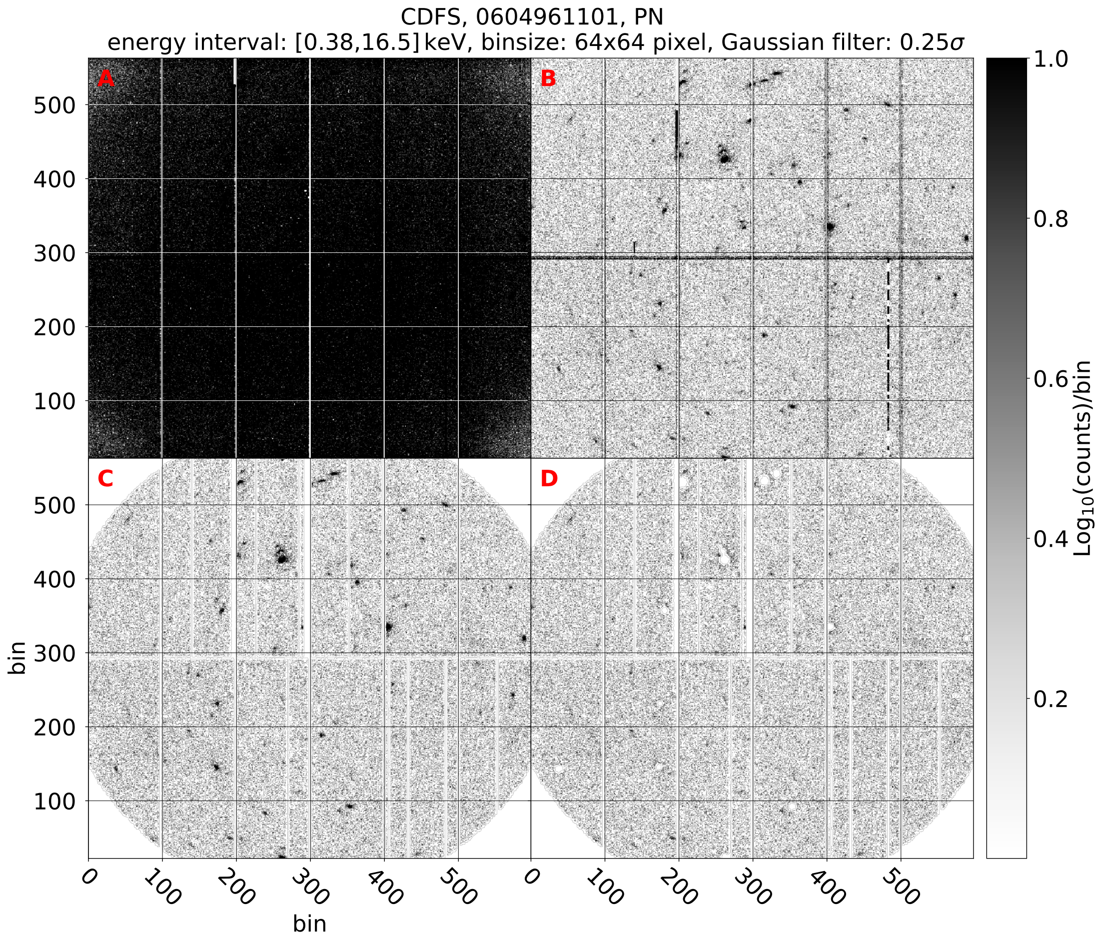

Figure C.8: All four panels show event files of the data set 0604961101 ($i = 9$, $\mathbf{D_1}$, table 4.1) taken with the EPIC-PN detector in an energy range of 0.38 keV to 16.5 keV. The colour coding represents the decadic logarithm of the number of X-ray photons counts per bin. The coordinates X and Y correspond to sky pixel coordinates. The upper left panel (A) shows the unfiltered raw event file and the upper right panel (B) is the time and particle background filtered result. The lower left panel (C) shows the time and particle background filtered result after application of the spatial filter and the lower right panel (D) represents the final source filtered diffuse X-ray background. All four representations of the corresponding event files have been smoothed with a Gaussian kernel having a filter width of 0.25σ.

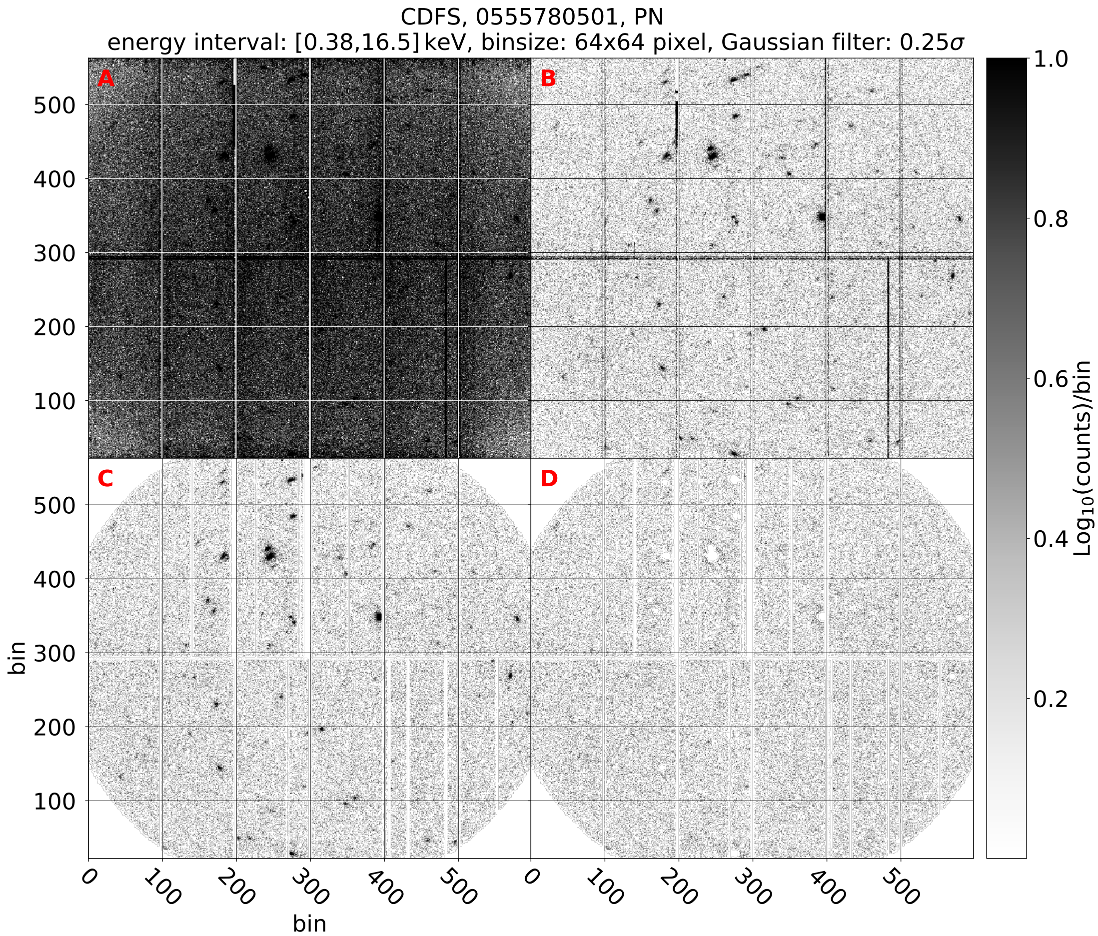

Figure C.9: All four panels show event files of the data set 0555780501 ($i = 10$, $\mathbf{D_1}$, table 4.1) taken with the EPIC-PN detector in an energy range of $0.38\,\mathrm{keV}$ to $16.5\,\mathrm{keV}$. The colour coding represents the decadic logarithm of the number of X-ray photons counts per bin. The coordinates X and Y correspond to sky pixel coordinates. The upper left panel (A) shows the unfiltered raw event file and the upper right panel (B) is the time and particle background filtered result. The lower left panel (C) shows the time and particle background filtered result after application of the spatial filter and the lower right panel (D) represents the final source filtered diffuse X-ray background. All four representations of the corresponding event files have been smoothed with a Gaussian kernel having a filter width of 0.25σ.

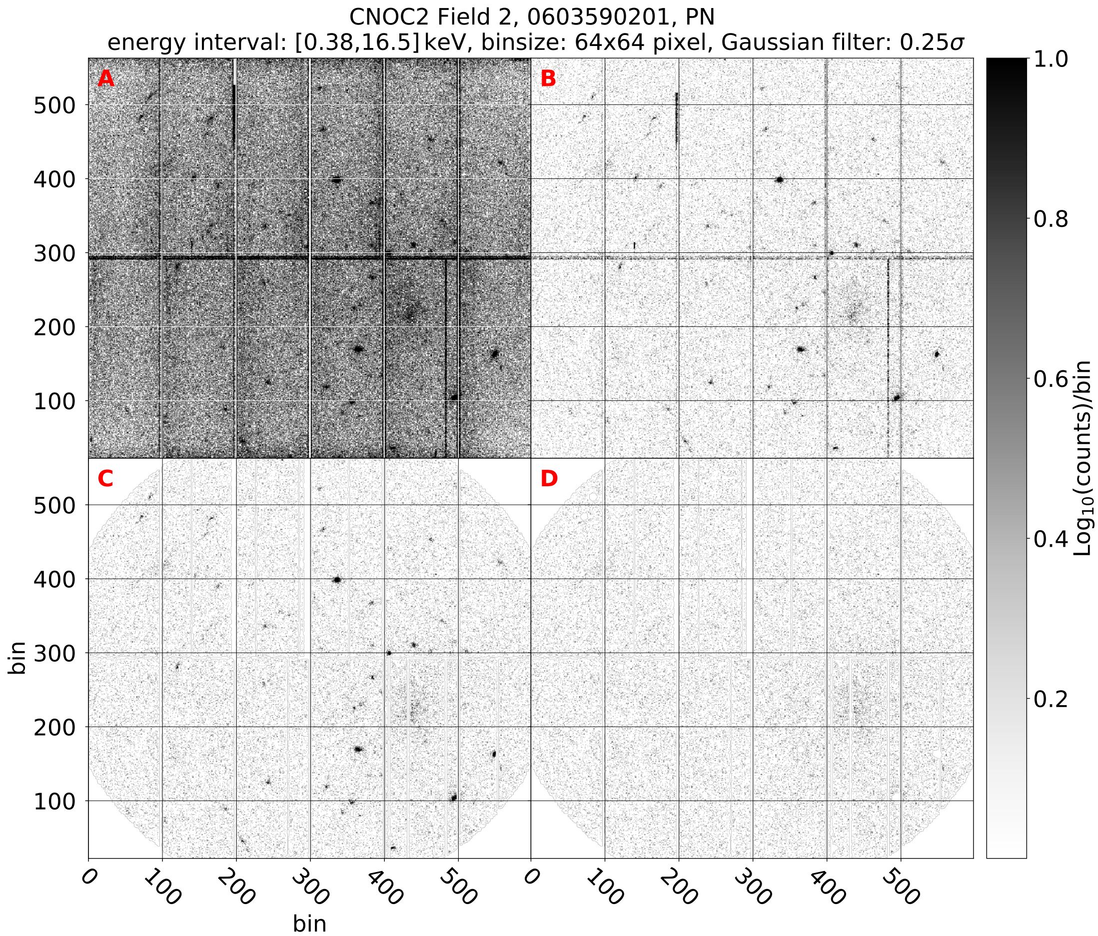

Figure C.10: All four panels show event files of the data set 0603590201 ($i = 14$, $\mathbf{D_1}$, table 4.1) taken with the EPIC-PN detector in an energy range of $0.38\,\mathrm{keV}$ to $16.5\,\mathrm{keV}$. The colour coding represents the decadic logarithm of the number of X-ray photons counts per bin. The coordinates X and Y correspond to sky pixel coordinates. The upper left panel (A) shows the unfiltered raw event file and the upper right panel (B) is the time and particle background filtered result. The lower left panel (C) shows the time and particle background filtered result after application of the spatial filter and the lower right panel (D) represents the final source filtered diffuse X-ray background. All four representations of the corresponding event files have been smoothed with a Gaussian kernel having a filter width of 0.25σ.

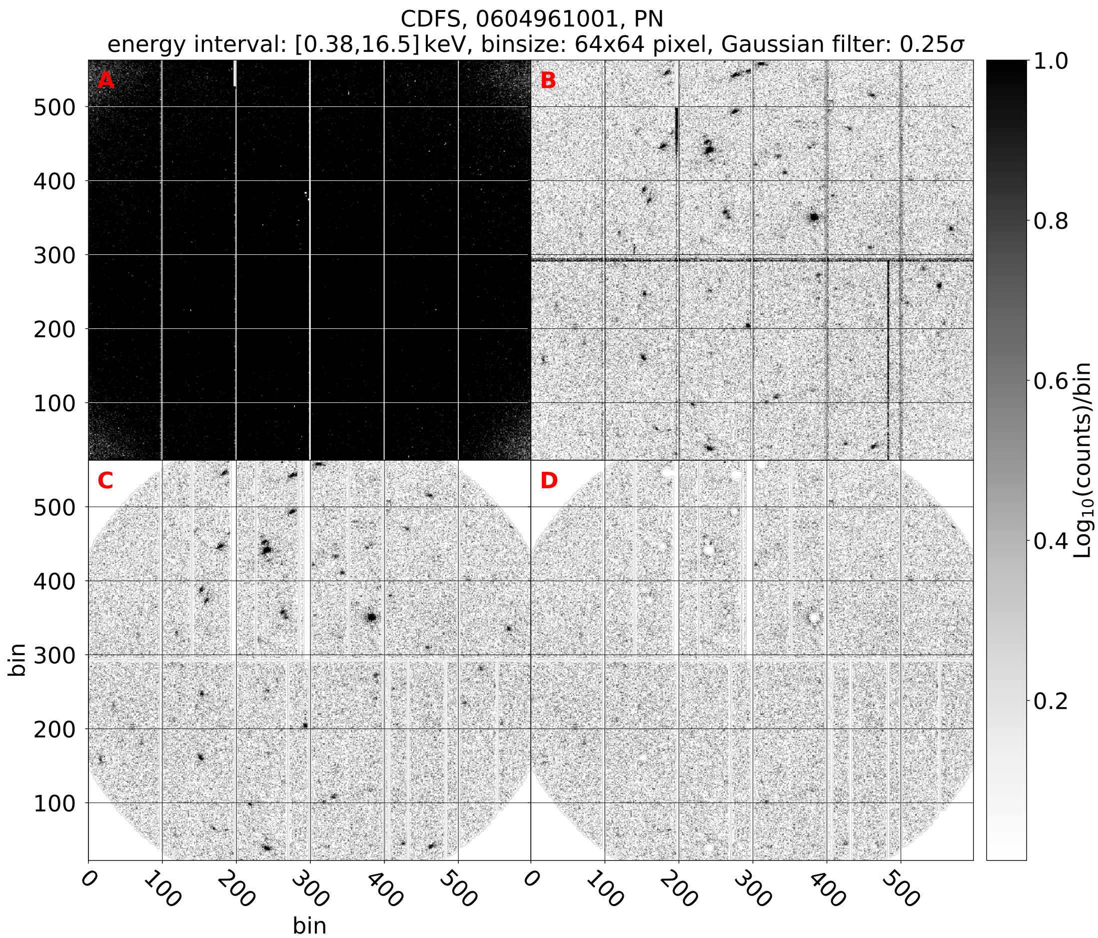

Figure C.11: All four panels show event files of the data set 0604961001 ($i = 11$, $\mathbf{D_1}$, table 4.1) taken with the EPIC-PN detector in an energy range of $0.38\,\mathrm{keV}$ to $16.5\,\mathrm{keV}$. The colour coding represents the decadic logarithm of the number of X-ray photons counts per bin. The coordinates X and Y correspond to sky pixel coordinates. The upper left panel (A) shows the unfiltered raw event file and the upper right panel (B) is the time and particle background filtered result. The lower left panel (C) shows the time and particle background filtered result after application of the spatial filter and the lower right panel (D) represents the final source filtered diffuse X-ray background. All four representations of the corresponding event files have been smoothed with a Gaussian kernel having a filter width of 0.25σ.

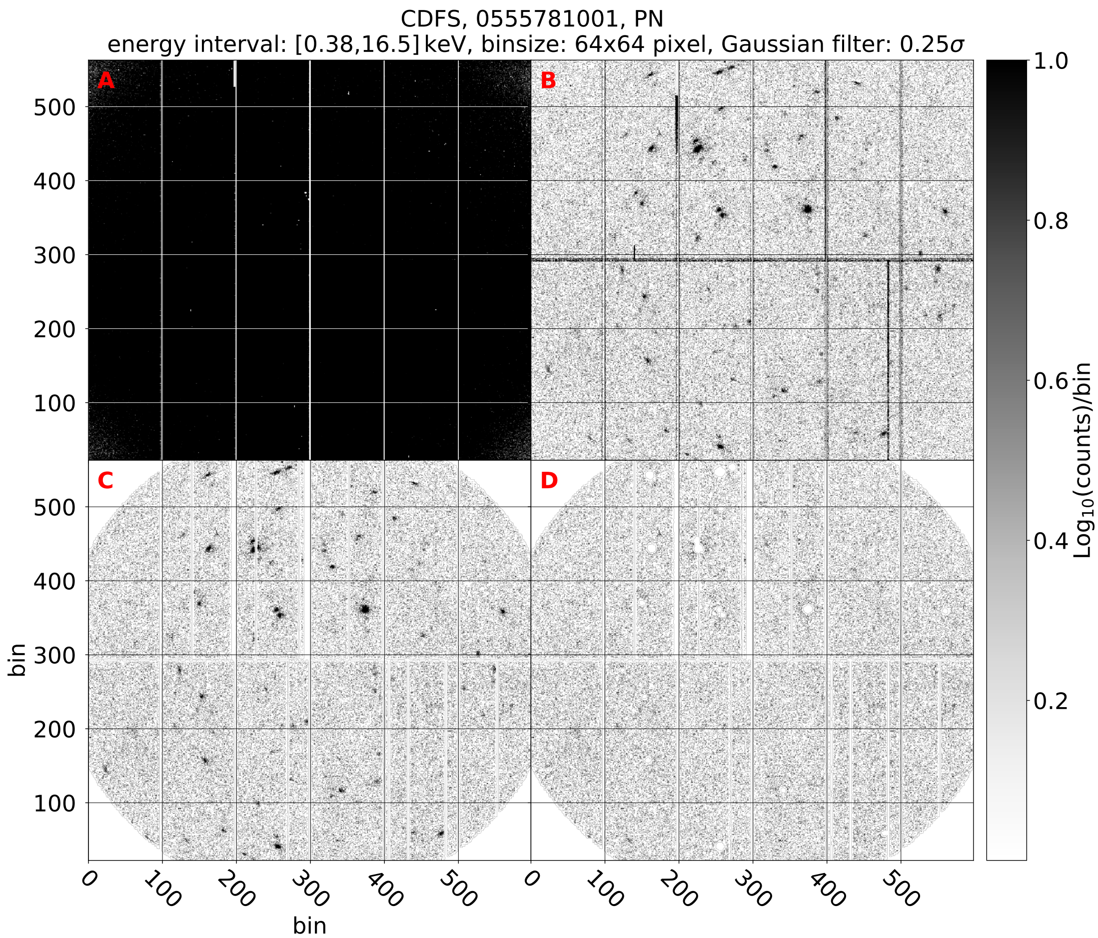

Figure C.12: All four panels show event files of the data set 0555781001 ($i = 12$, $\mathbf{D_1}$, table 4.1) taken with the EPIC-PN detector in an energy range of $0.38\,\mathrm{keV}$ to $16.5\,\mathrm{keV}$. The colour coding represents the decadic logarithm of the number of X-ray photons counts per bin. The coordinates X and Y correspond to sky pixel coordinates. The upper left panel (A) shows the unfiltered raw event file and the upper right panel (B) is the time and particle background filtered result. The lower left panel (C) shows the time and particle background filtered result after application of the spatial filter and the lower right panel (D) represents the final source filtered diffuse X-ray background. All four representations of the corresponding event files have been smoothed with a Gaussian kernel having a filter width of 0.25σ.

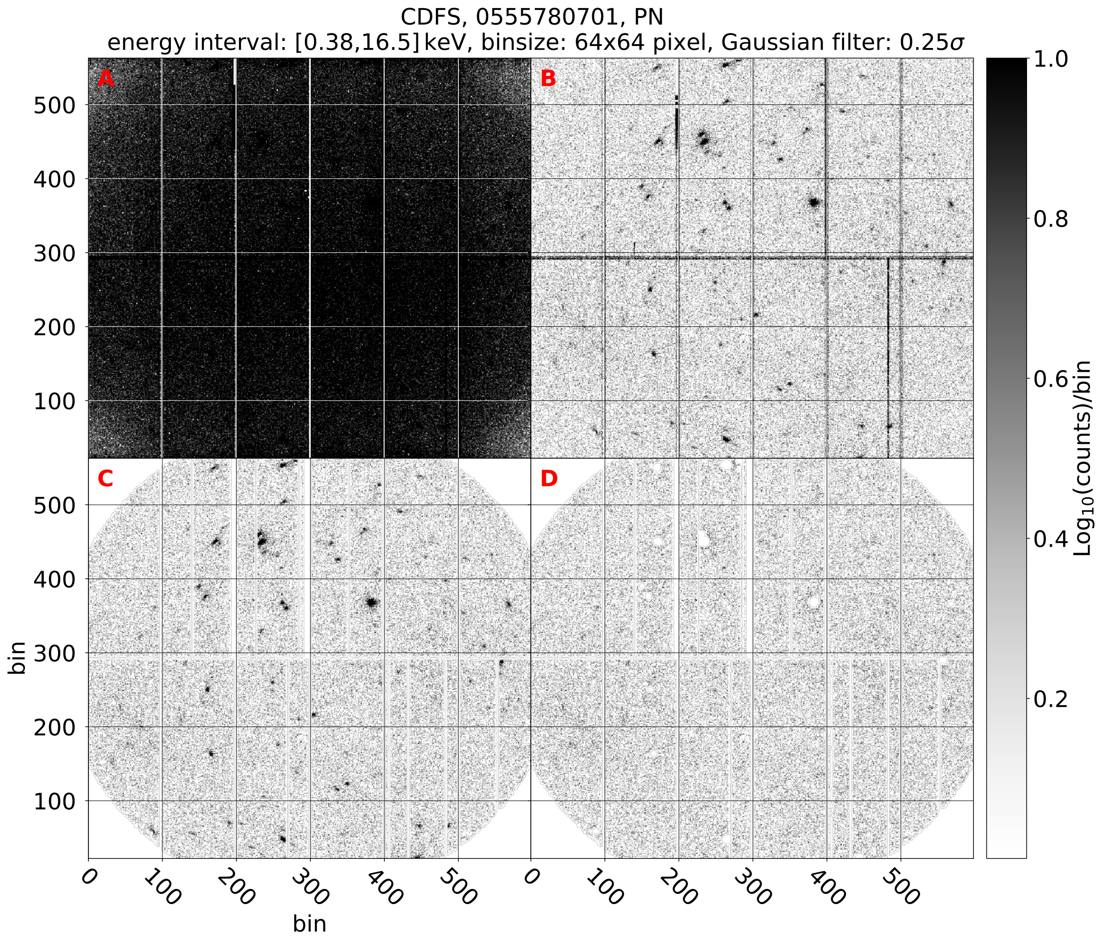

Figure C.13: All four panels show event files of the data set 0555780701 ($i = 13$, $\mathbf{D_1}$, table 4.1) taken with the EPIC-PN detector in an energy range of $0.38\,\mathrm{keV}$ to $16.5\,\mathrm{keV}$. The colour coding represents the decadic logarithm of the number of X-ray photons counts per bin. The coordinates X and Y correspond to sky pixel coordinates. The upper left panel (A) shows the unfiltered raw event file and the upper right panel (B) is the time and particle background filtered result. The lower left panel (C) shows the time and particle background filtered result after application of the spatial filter and the lower right panel (D) represents the final source filtered diffuse X-ray background. All four representations of the corresponding event files have been smoothed with a Gaussian kernel having a filter width of 0.25σ.

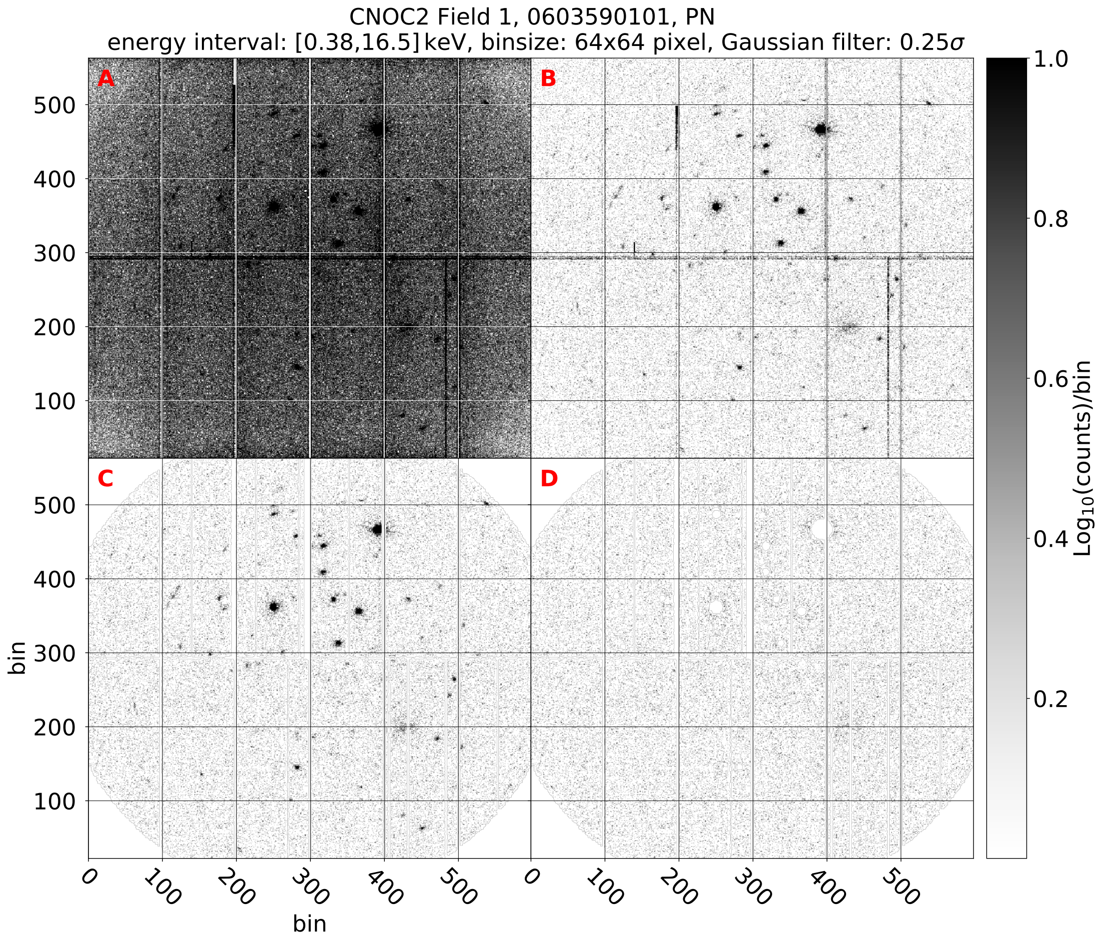

Figure C.14: All four panels show event files of the data set 0603590101 ($i = 16$, $\mathbf{D_1}$, table 4.1) taken with the EPIC-PN detector in an energy range of $0.38\,\mathrm{keV}$ to $16.5\,\mathrm{keV}$. The colour coding represents the decadic logarithm of the number of X-ray photons counts per bin. The coordinates X and Y correspond to sky pixel coordinates. The upper left panel (A) shows the unfiltered raw event file and the upper right panel (B) is the time and particle background filtered result. The lower left panel (C) shows the time and particle background filtered result after application of the spatial filter and the lower right panel (D) represents the final source filtered diffuse X-ray background. All four representations of the corresponding event files have been smoothed with a Gaussian kernel having a filter width of 0.25σ.

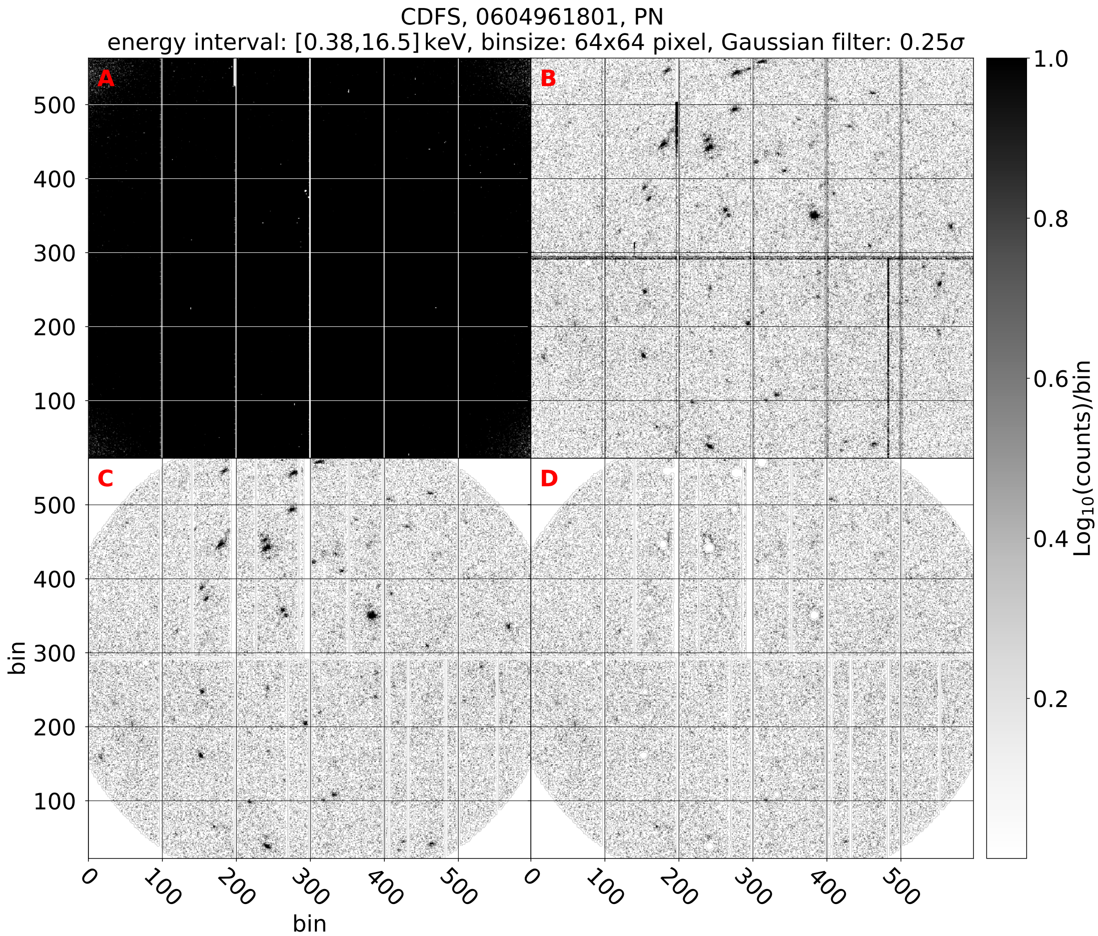

Figure C.15: All four panels show event files of the data set 0604961801 ($i = 15$, $\mathbf{D_1}$, table 4.1) taken with the EPIC-PN detector in an energy range of 0.38 keV to 16.5 keV. The colour coding represents the decadic logarithm of the number of X-ray photons counts per bin. The coordinates X and Y correspond to sky pixel coordinates. The upper left panel (A) shows the unfiltered raw event file and the upper right panel (B) is the time and particle background filtered result. The lower left panel (C) shows the time and particle background filtered result after application of the spatial filter and the lower right panel (D) represents the final source filtered diffuse X-ray background. All four representations of the corresponding event files have been smoothed with a Gaussian kernel having a filter width of 0.25σ.

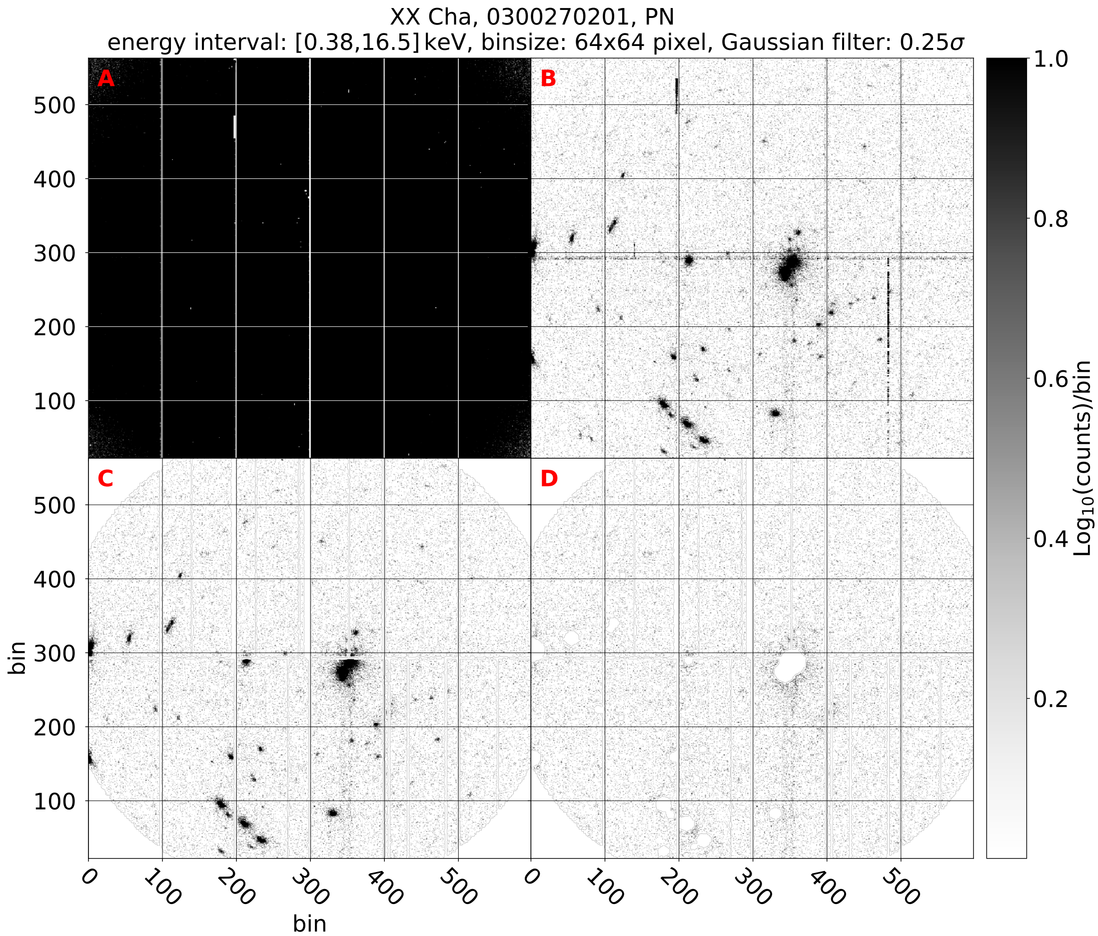

Figure C.16: All four panels show event files of the data set 0300270201 ($i = 17$, $\mathbf{D_1}$, table 4.1) taken with the EPIC-PN detector in an energy range of 0.38 keV to 16.5 keV. The colour coding represents the decadic logarithm of the number of X-ray photons counts per bin. The coordinates X and Y correspond to sky pixel coordinates. The upper left panel (A) shows the unfiltered raw event file and the upper right panel (B) is the time and particle background filtered result. The lower left panel (C) shows the time and particle background filtered result after application of the spatial filter and the lower right panel (D) represents the final source filtered diffuse X-ray background. All four representations of the corresponding event files have been smoothed with a Gaussian kernel having a filter width of 0.25σ.

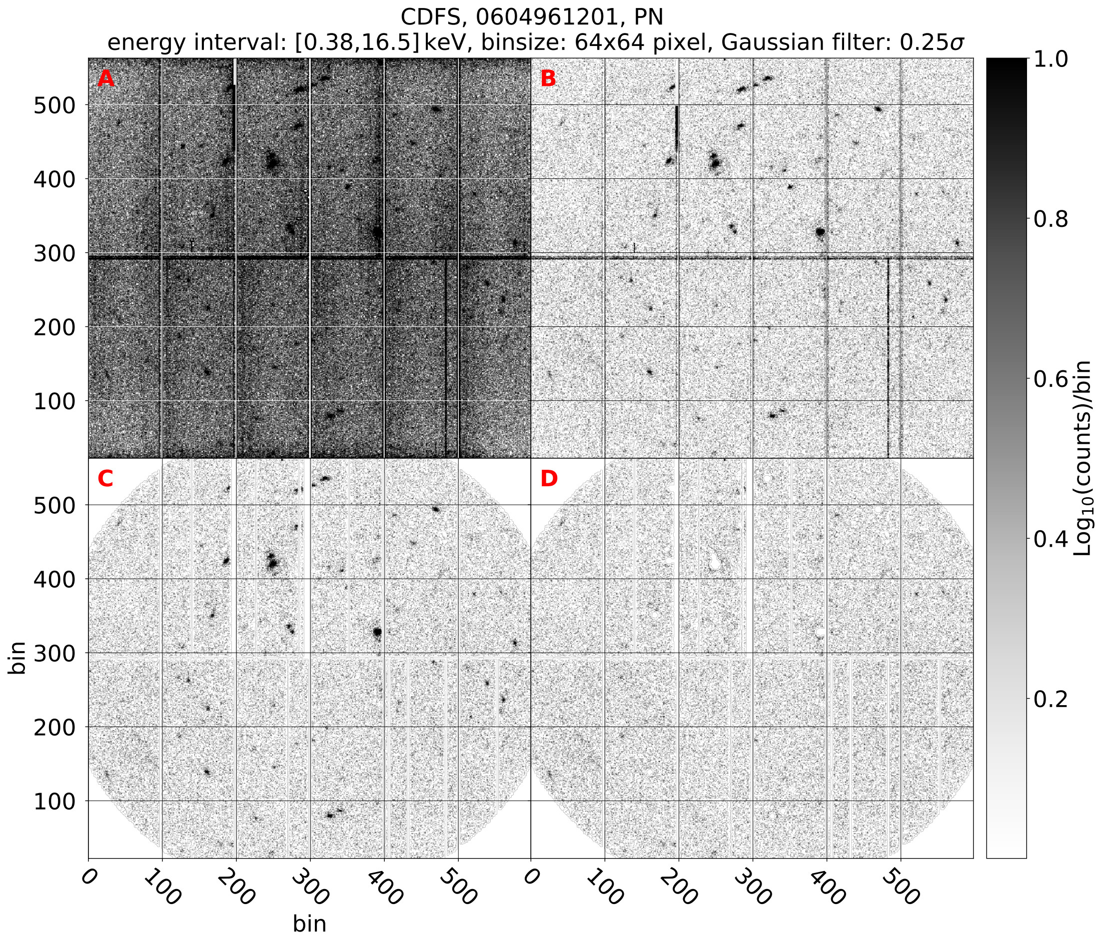

Figure C.17: All four panels show event files of the data set 0604961201 ($i = 18$, $\mathbf{D_1}$, table 4.1) taken with the EPIC-PN detector in an energy range of $0.38\,\mathrm{keV}$ to $16.5\,\mathrm{keV}$. The colour coding represents the decadic logarithm of the number of X-ray photons counts per bin. The coordinates X and Y correspond to sky pixel coordinates. The upper left panel (A) shows the unfiltered raw event file and the upper right panel (B) is the time and particle background filtered result. The lower left panel (C) shows the time and particle background filtered result after application of the spatial filter and the lower right panel (D) represents the final source filtered diffuse X-ray background. All four representations of the corresponding event files have been smoothed with a Gaussian kernel having a filter width of 0.25σ.

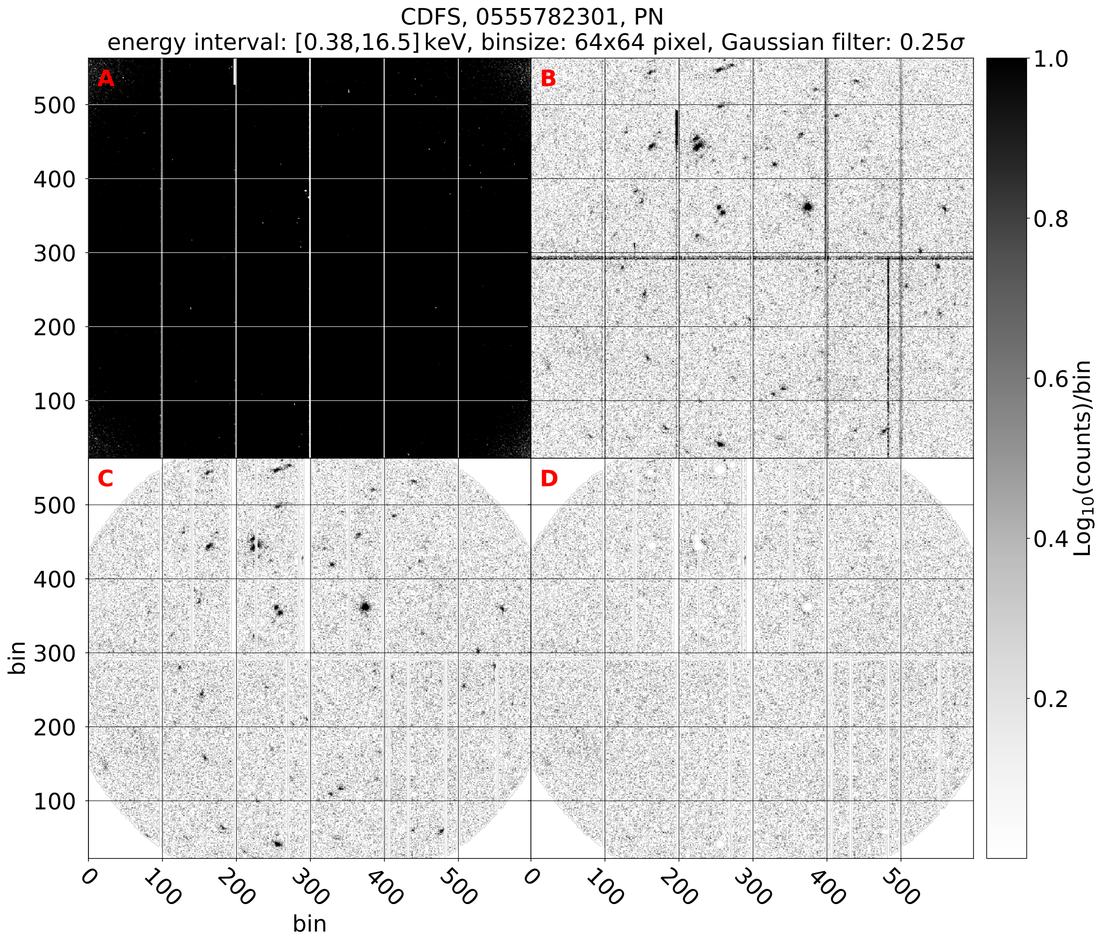

Figure C.18: All four panels show event files of the data set 0555782301 ($i = 19$, $\mathbf{D_1}$, table 4.1) taken with the EPIC-PN detector in an energy range of $0.38\,\mathrm{keV}$ to $16.5\,\mathrm{keV}$. The colour coding represents the decadic logarithm of the number of X-ray photons counts per bin. The coordinates X and Y correspond to sky pixel coordinates. The upper left panel (A) shows the unfiltered raw event file and the upper right panel (B) is the time and particle background filtered result. The lower left panel (C) shows the time and particle background filtered result after application of the spatial filter and the lower right panel (D) represents the final source filtered diffuse X-ray background. All four representations of the corresponding event files have been smoothed with a Gaussian kernel having a filter width of 0.25σ.

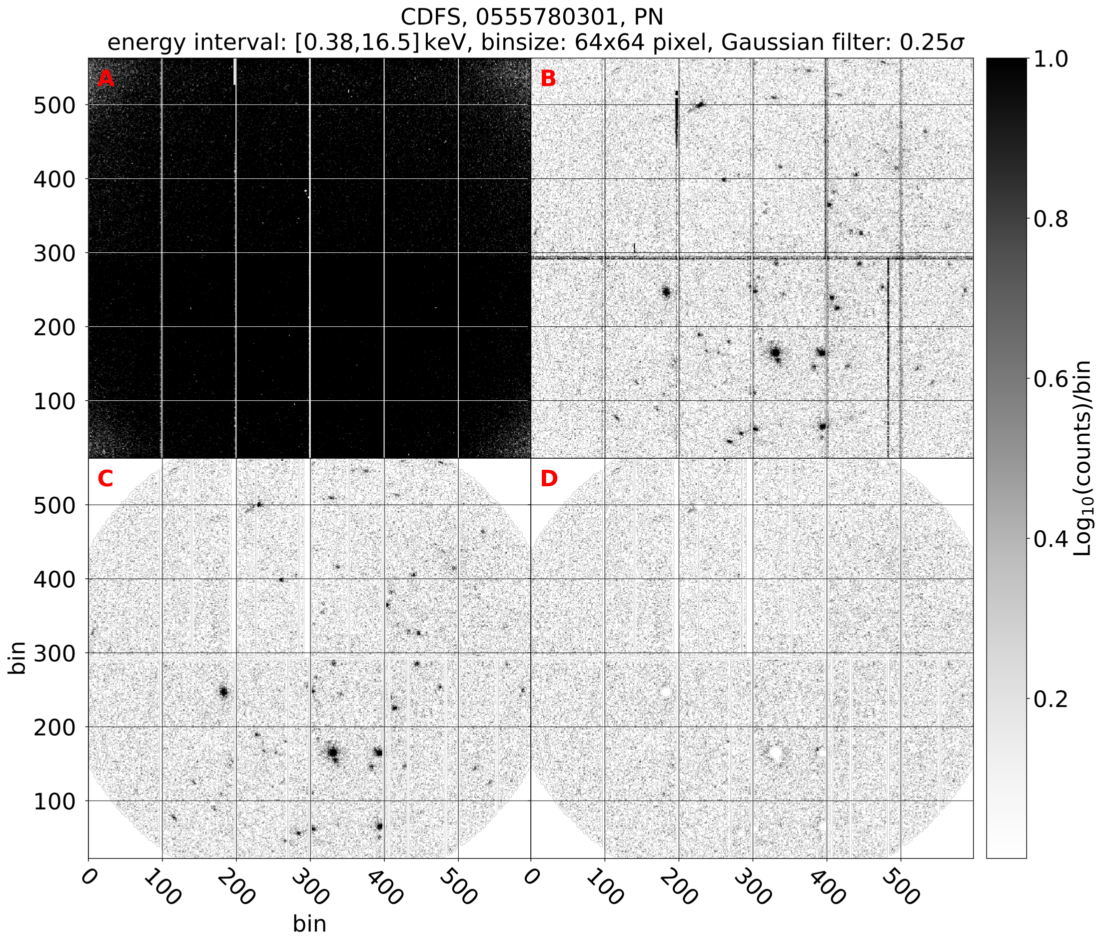

Figure C.19: All four panels show event files of the data set 0555780301 ($i = 20$, $\mathbf{D_1}$, table 4.1) taken with the EPIC-PN detector in an energy range of 0.38 keV to 16.5 keV. The colour coding represents the decadic logarithm of the number of X-ray photons counts per bin. The coordinates X and Y correspond to sky pixel coordinates. The upper left panel (A) shows the unfiltered raw event file and the upper right panel (B) is the time and particle background filtered result. The lower left panel (C) shows the time and particle background filtered result after application of the spatial filter and the lower right panel (D) represents the final source filtered diffuse X-ray background. All four representations of the corresponding event files have been smoothed with a Gaussian kernel having a filter width of 0.25σ.

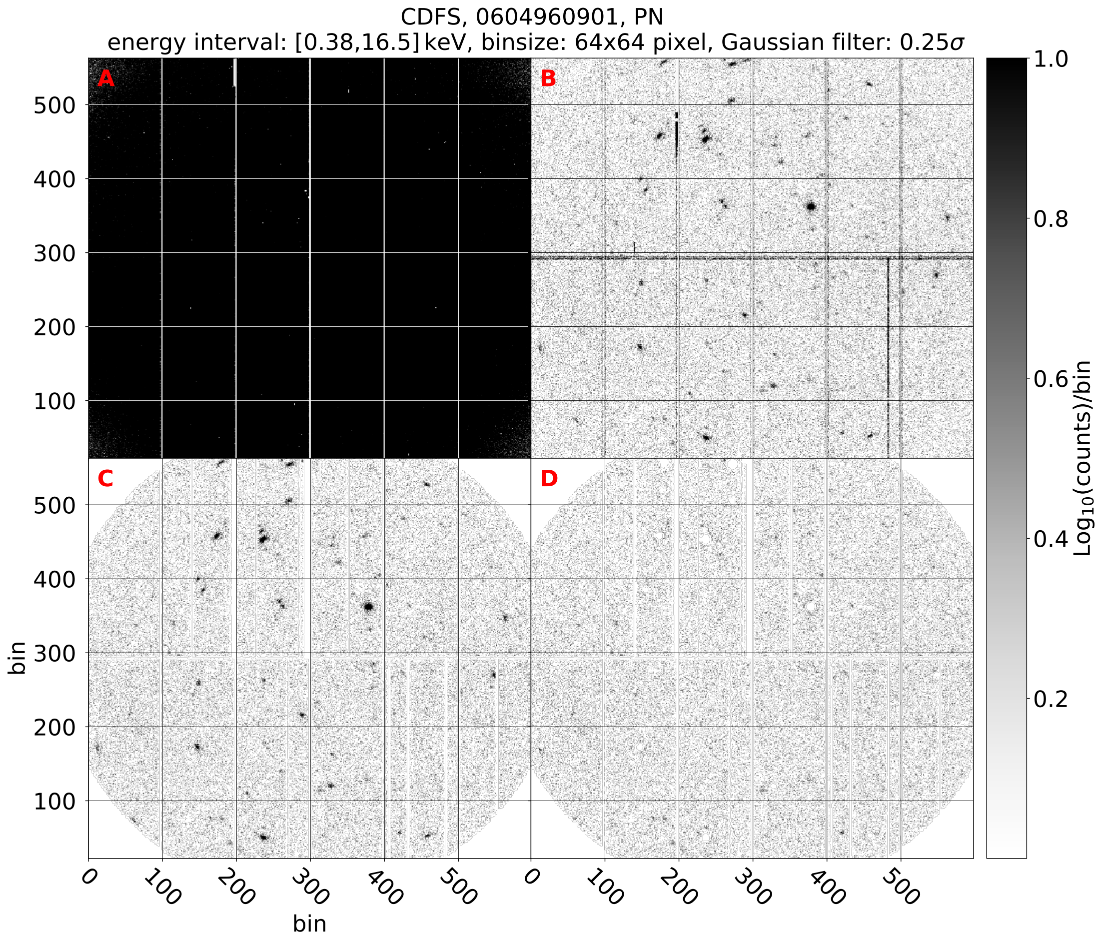

Figure C.20: All four panels show event files of the data set 0604960901 ($i = 21$, $\mathbf{D_1}$, table 4.1) taken with the EPIC-PN detector in an energy range of $0.38\,\mathrm{keV}$ to $16.5\,\mathrm{keV}$. The colour coding represents the decadic logarithm of the number of X-ray photons counts per bin. The coordinates X and Y correspond to sky pixel coordinates. The upper left panel (A) shows the unfiltered raw event file and the upper right panel (B) is the time and particle background filtered result. The lower left panel (C) shows the time and particle background filtered result after application of the spatial filter and the lower right panel (D) represents the final source filtered diffuse X-ray background. All four representations of the corresponding event files have been smoothed with a Gaussian kernel having a filter width of 0.25σ.

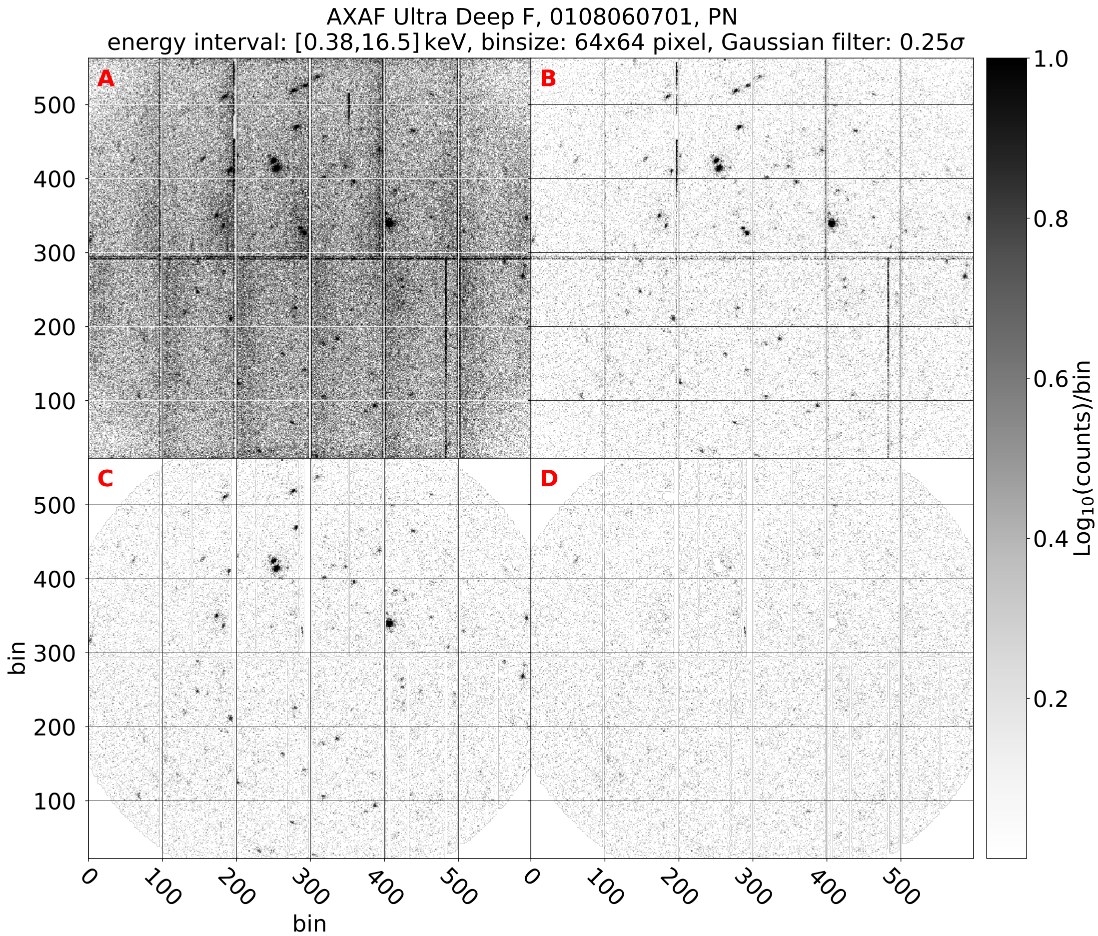

Figure C.21: All four panels show event files of the data set 0108060701 ($i = 22$, $\mathbf{D_1}$, table 4.1) taken with the EPIC-PN detector in an energy range of 0.38 keV to 16.5 keV. The colour coding represents the decadic logarithm of the number of X-ray photons counts per bin. The coordinates X and Y correspond to sky pixel coordinates. The upper left panel (A) shows the unfiltered raw event file and the upper right panel (B) is the time and particle background filtered result. The lower left panel (C) shows the time and particle background filtered result after application of the spatial filter and the lower right panel (D) represents the final source filtered diffuse X-ray background. All four representations of the corresponding event files have been smoothed with a Gaussian kernel having a filter width of 0.25σ.

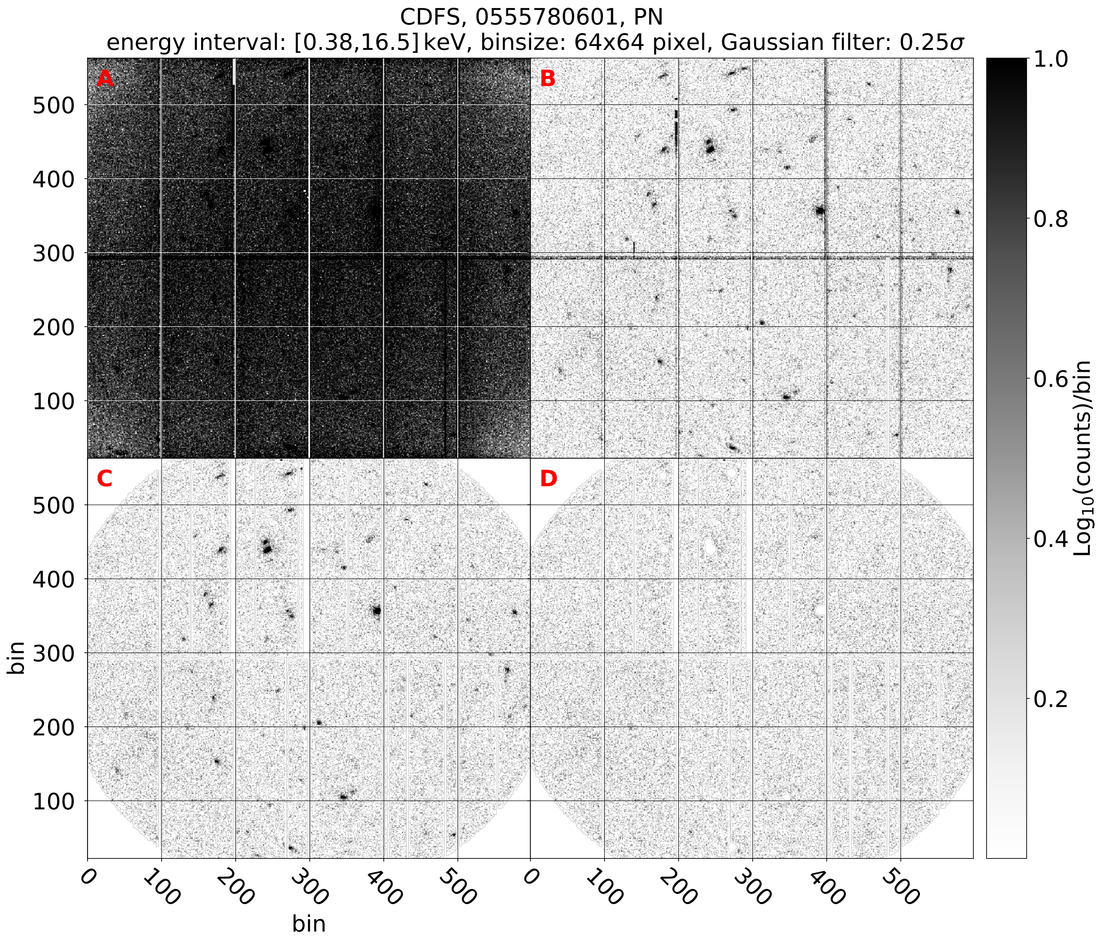

Figure C.22: All four panels show event files of the data set 0555780601 ($i = 23$, $\mathbf{D_1}$, table 4.1) taken with the EPIC-PN detector in an energy range of $0.38\,\mathrm{keV}$ to $16.5\,\mathrm{keV}$. The colour coding represents the decadic logarithm of the number of X-ray photons counts per bin. The coordinates X and Y correspond to sky pixel coordinates. The upper left panel (A) shows the unfiltered raw event file and the upper right panel (B) is the time and particle background filtered result. The lower left panel (C) shows the time and particle background filtered result after application of the spatial filter and the lower right panel (D) represents the final source filtered diffuse X-ray background. All four representations of the corresponding event files have been smoothed with a Gaussian kernel having a filter width of 0.25σ.

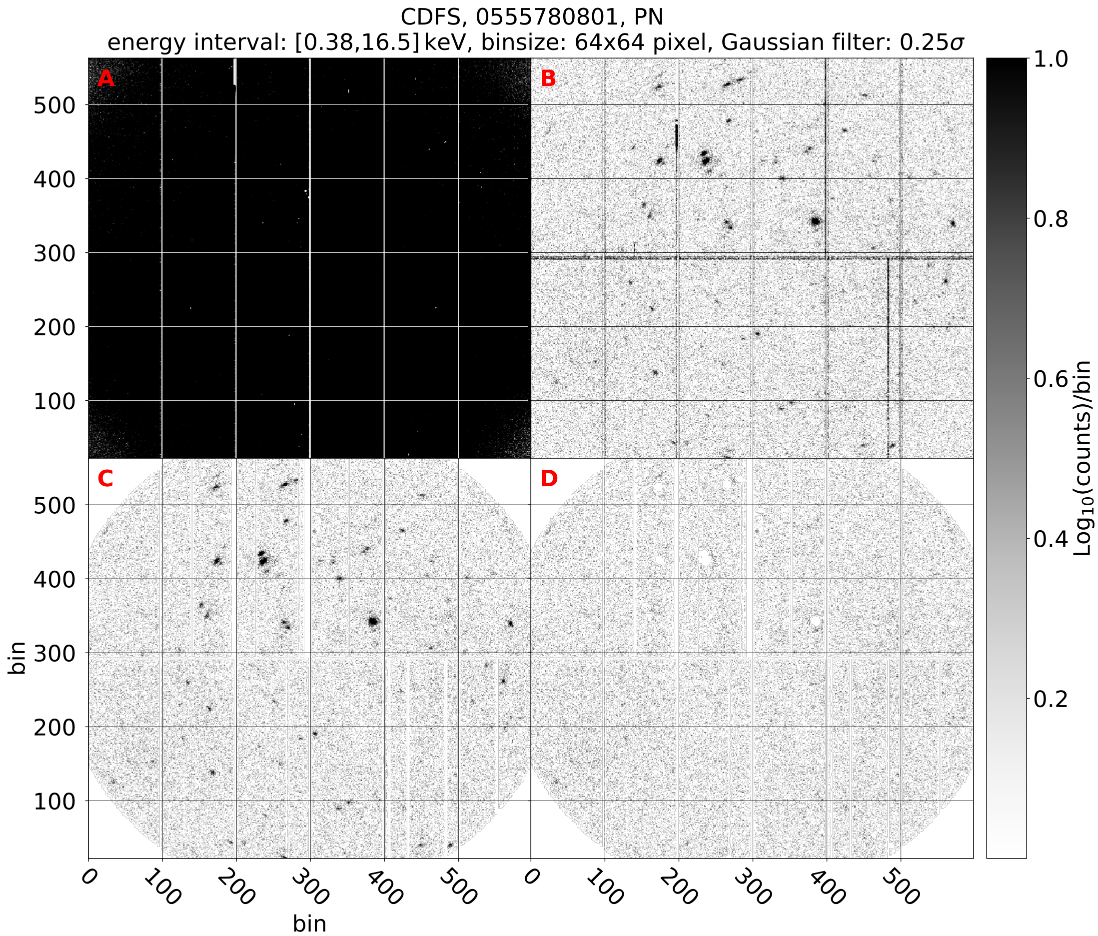

Figure C.23: All four panels show event files of the data set 0555780801 ($i = 24$, $\mathbf{D_1}$, table 4.1) taken with the EPIC-PN detector in an energy range of 0.38 keV to 16.5 keV. The colour coding represents the decadic logarithm of the number of X-ray photons counts per bin. The coordinates X and Y correspond to sky pixel coordinates. The upper left panel (A) shows the unfiltered raw event file and the upper right panel (B) is the time and particle background filtered result. The lower left panel (C) shows the time and particle background filtered result after application of the spatial filter and the lower right panel (D) represents the final source filtered diffuse X-ray background. All four representations of the corresponding event files have been smoothed with a Gaussian kernel having a filter width of 0.25σ.

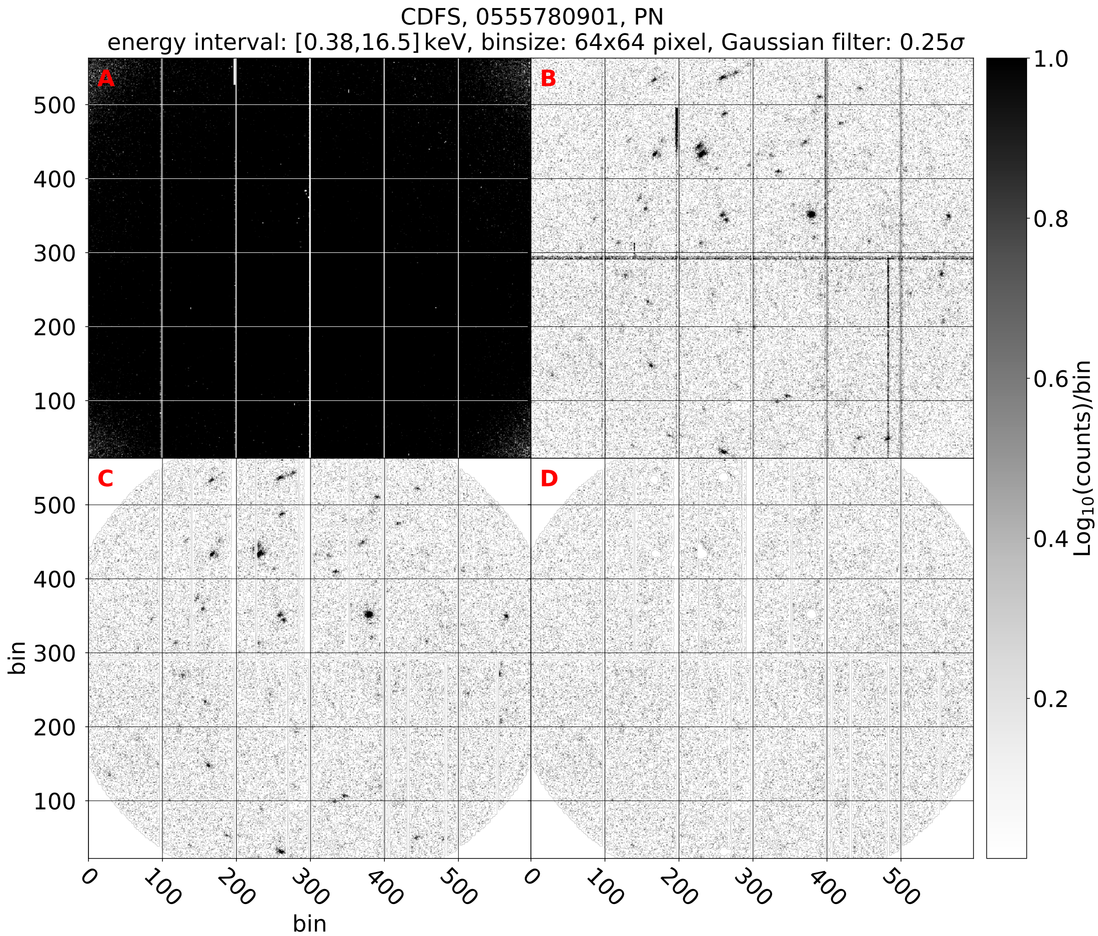

Figure C.24: All four panels show event files of the data set 0555780901 ($i = 25$, $\mathbf{D_1}$, table 4.1) taken with the EPIC-PN detector in an energy range of $0.38\,\mathrm{keV}$ to $16.5\,\mathrm{keV}$. The colour coding represents the decadic logarithm of the number of X-ray photons counts per bin. The coordinates X and Y correspond to sky pixel coordinates. The upper left panel (A) shows the unfiltered raw event file and the upper right panel (B) is the time and particle background filtered result. The lower left panel (C) shows the time and particle background filtered result after application of the spatial filter and the lower right panel (D) represents the final source filtered diffuse X-ray background. All four representations of the corresponding event files have been smoothed with a Gaussian kernel having a filter width of 0.25σ.

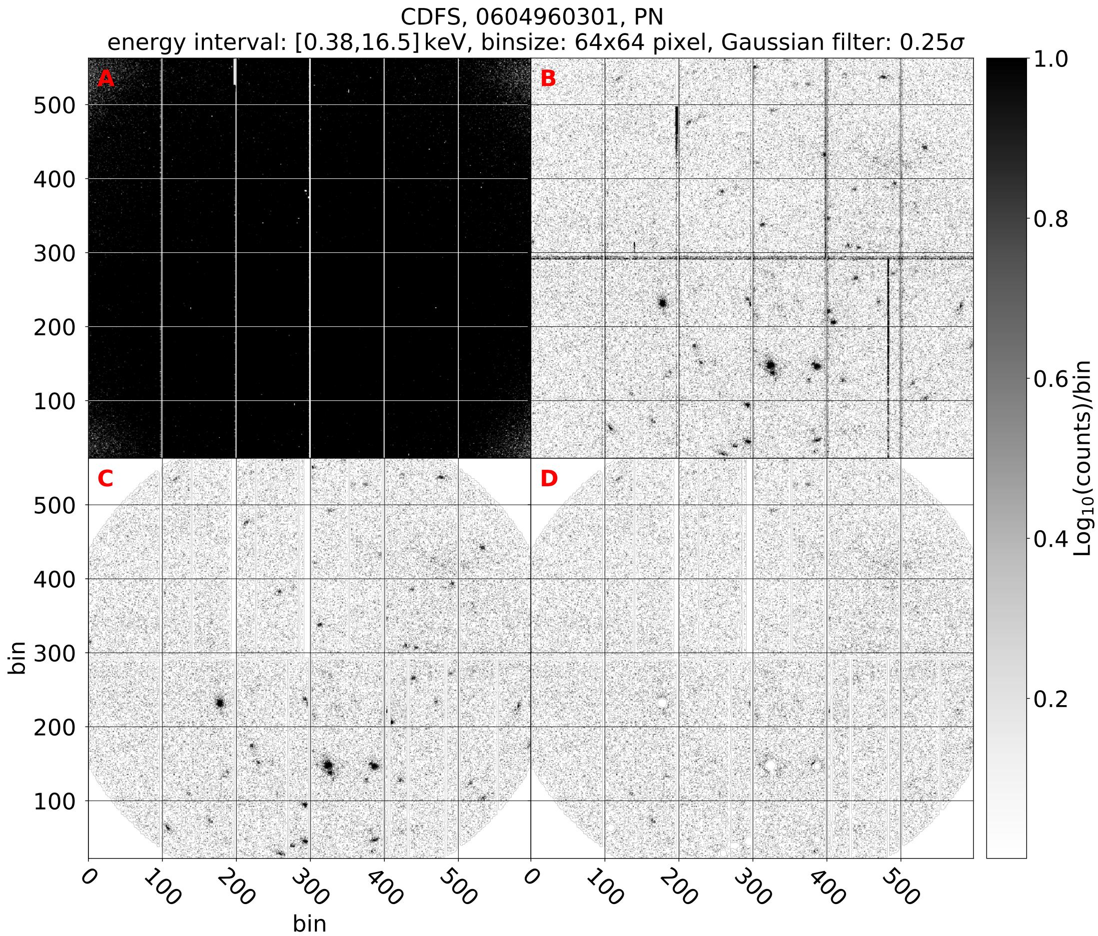

Figure C.25: All four panels show event files of the data set 0604960301 ($i = 26$, $\mathbf{D_1}$, table 4.1) taken with the EPIC-PN detector in an energy range of $0.38\,\text{keV}$ to $16.5\,\text{keV}$. The colour coding represents the decadic logarithm of the number of X-ray photons counts per bin. The coordinates X and Y correspond to sky pixel coordinates. The upper left panel (A) shows the unfiltered raw event file and the upper right panel (B) is the time and particle background filtered result. The lower left panel (C) shows the time and particle background filtered result after application of the spatial filter and the lower right panel (D) represents the final source filtered diffuse X-ray background. All four representations of the corresponding event files have been smoothed with a Gaussian kernel having a filter width of 0.25σ.

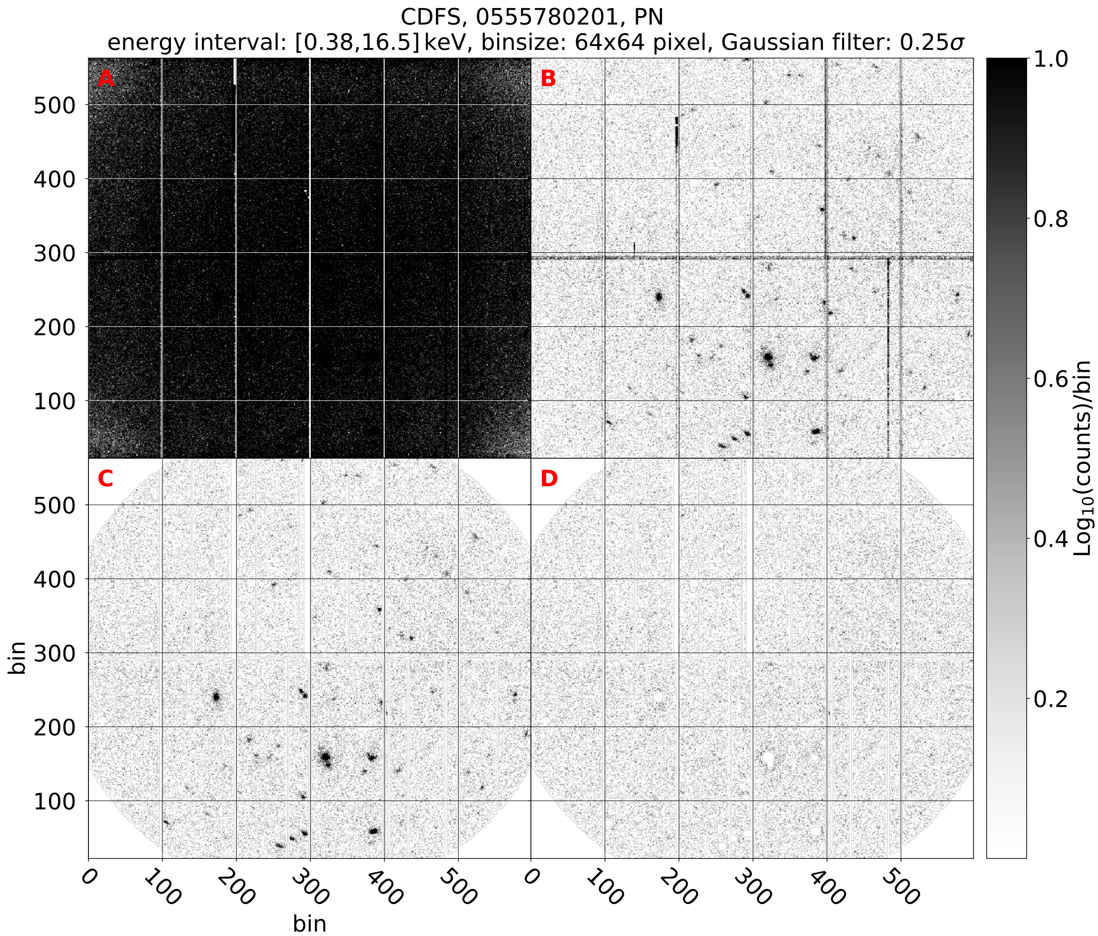

Figure C.26: All four panels show event files of the data set 0555780201 ($i = 27$, $\mathbf{D_1}$, table 4.1) taken with the EPIC-PN detector in an energy range of 0.38 keV to 16.5 keV. The colour coding represents the decadic logarithm of the number of X-ray photons counts per bin. The coordinates X and Y correspond to sky pixel coordinates. The upper left panel (A) shows the unfiltered raw event file and the upper right panel (B) is the time and particle background filtered result. The lower left panel (C) shows the time and particle background filtered result after application of the spatial filter and the lower right panel (D) represents the final source filtered diffuse X-ray background. All four representations of the corresponding event files have been smoothed with a Gaussian kernel having a filter width of 0.25σ.

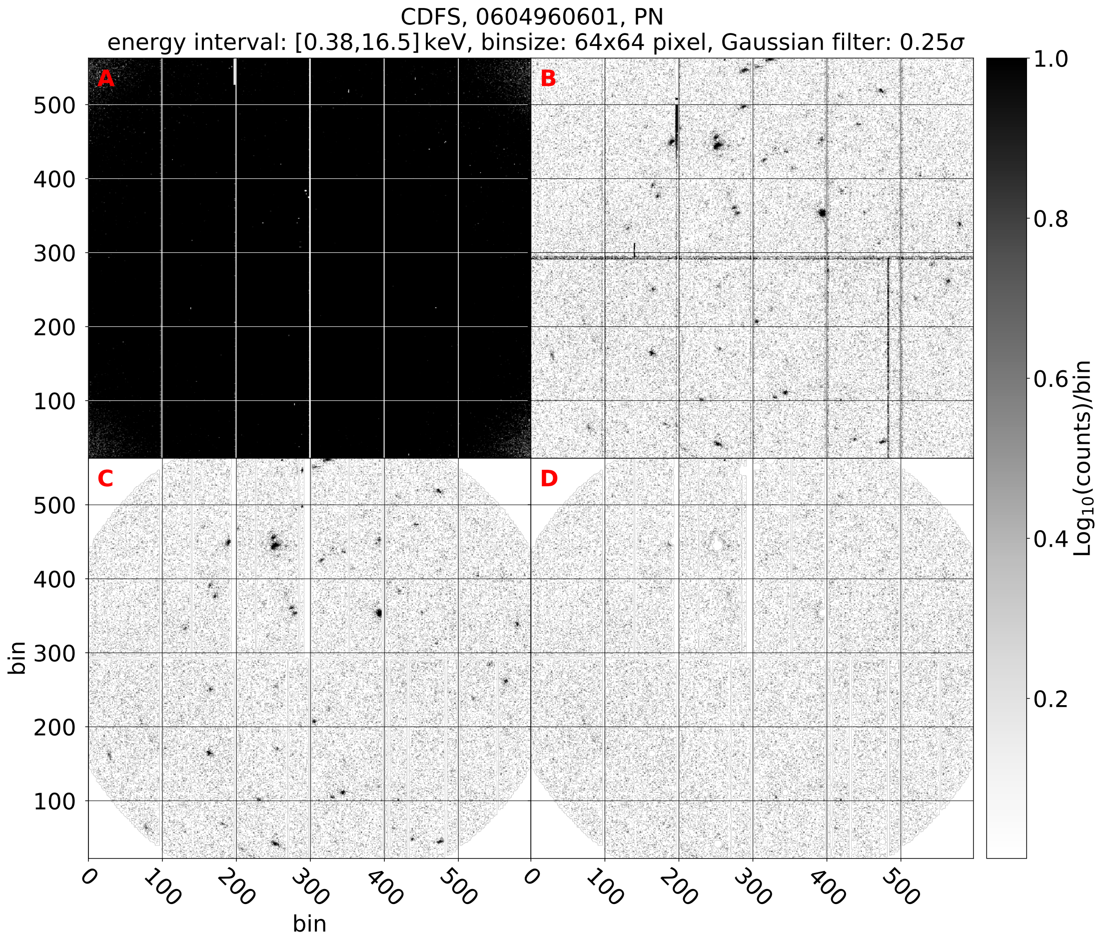

Figure C.27: All four panels show event files of the data set 0604960601 ($i = 28$, $\mathbf{D_1}$, table 4.1) taken with the EPIC-PN detector in an energy range of $0.38\,\mathrm{keV}$ to $16.5\,\mathrm{keV}$. The colour coding represents the decadic logarithm of the number of X-ray photons counts per bin. The coordinates X and Y correspond to sky pixel coordinates. The upper left panel (A) shows the unfiltered raw event file and the upper right panel (B) is the time and particle background filtered result. The lower left panel (C) shows the time and particle background filtered result after application of the spatial filter and the lower right panel (D) represents the final source filtered diffuse X-ray background. All four representations of the corresponding event files have been smoothed with a Gaussian kernel having a filter width of 0.25σ.

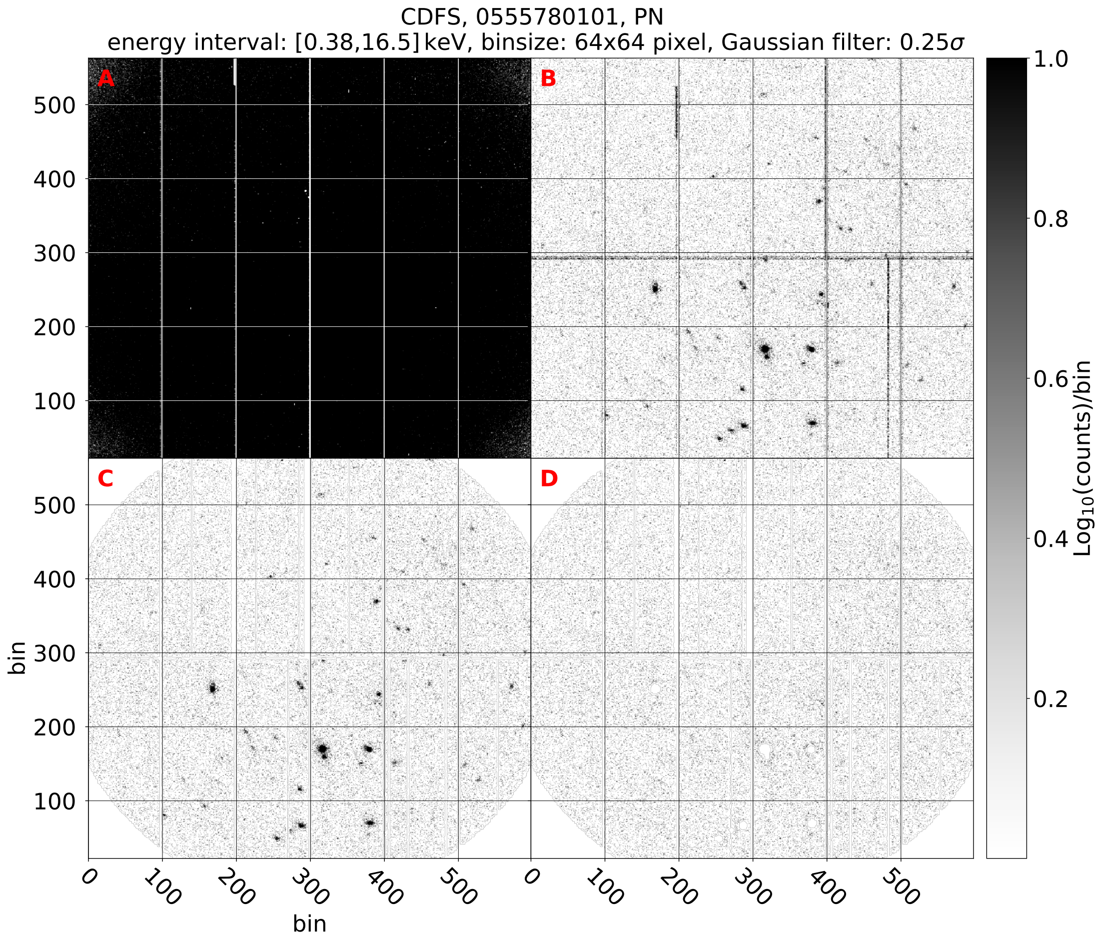

Figure C.28: All four panels show event files of the data set 0555780101 ($i = 29$, $\mathbf{D_1}$, table 4.1) taken with the EPIC-PN detector in an energy range of 0.38 keV to 16.5 keV. The colour coding represents the decadic logarithm of the number of X-ray photons counts per bin. The coordinates X and Y correspond to sky pixel coordinates. The upper left panel (A) shows the unfiltered raw event file and the upper right panel (B) is the time and particle background filtered result. The lower left panel (C) shows the time and particle background filtered result after application of the spatial filter and the lower right panel (D) represents the final source filtered diffuse X-ray background. All four representations of the corresponding event files have been smoothed with a Gaussian kernel having a filter width of 0.25σ.

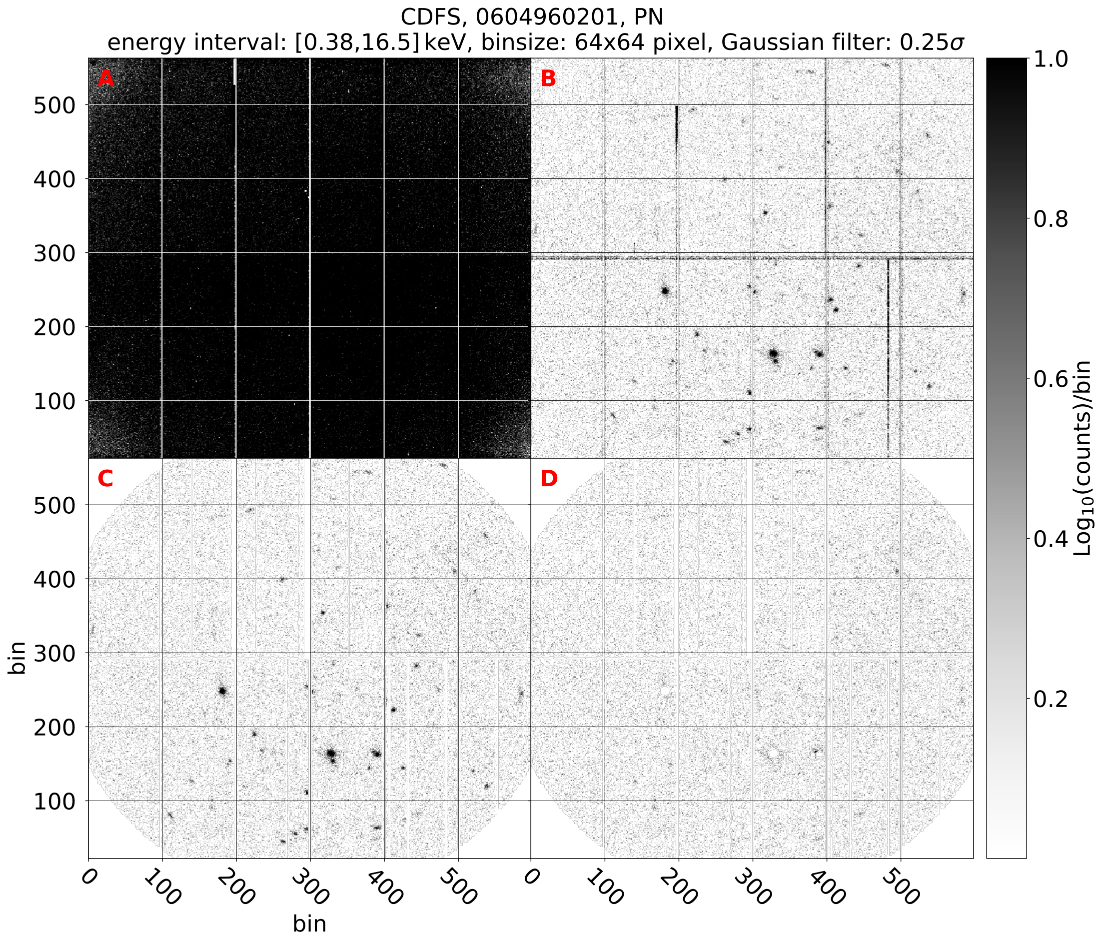

Figure C.29: All four panels show event files of the data set 0604960201 ($i = 30$, $\mathbf{D_1}$, table 4.1) taken with the EPIC-PN detector in an energy range of $0.38\,$keV to $16.5\,$keV. The colour coding represents the decadic logarithm of the number of X-ray photons counts per bin. The coordinates X and Y correspond to sky pixel coordinates. The upper left panel (A) shows the unfiltered raw event file and the upper right panel (B) is the time and particle background filtered result. The lower left panel (C) shows the time and particle background filtered result after application of the spatial filter and the lower right panel (D) represents the final source filtered diffuse X-ray background. All four representations of the corresponding event files have been smoothed with a Gaussian kernel having a filter width of 0.25σ.

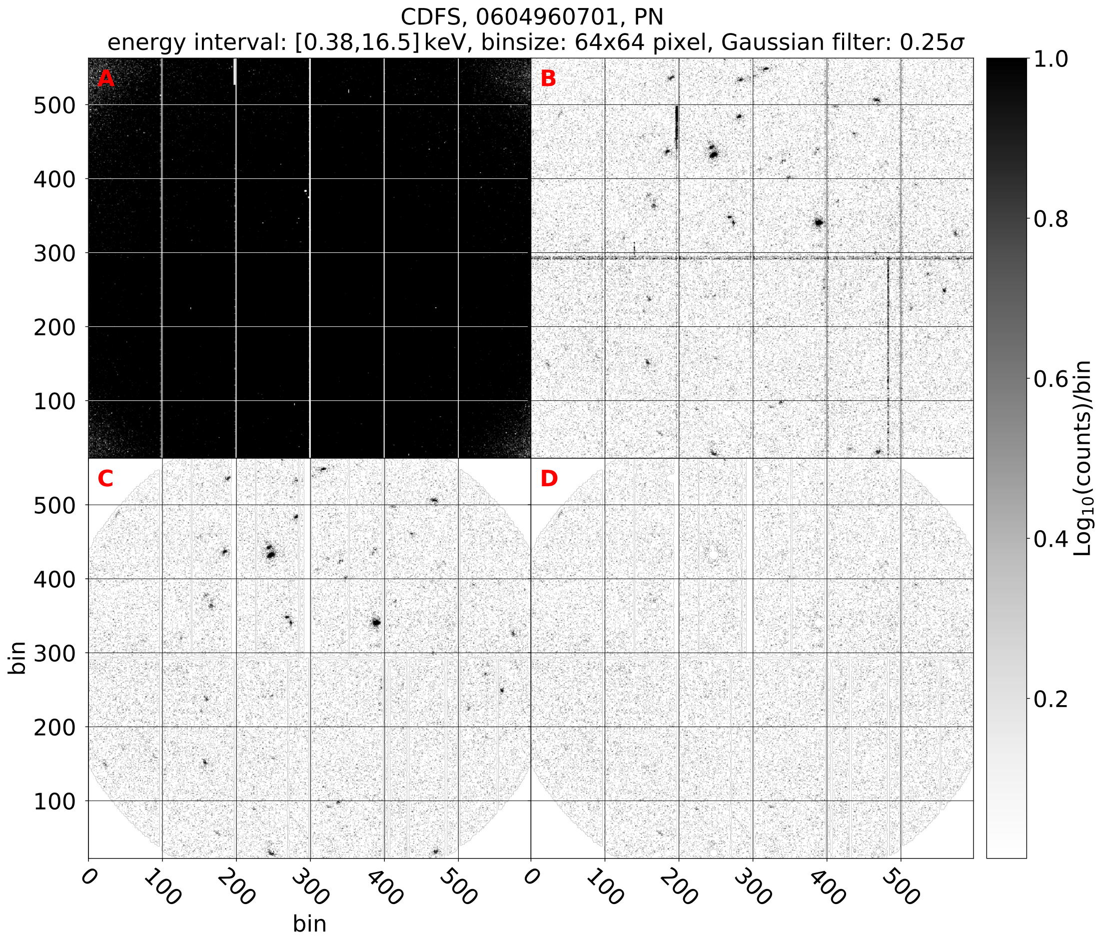

Figure C.30: All four panels show event files of the data set 0604960701 ($i = 31$, $\mathbf{D_1}$, table 4.1) taken with the EPIC-PN detector in an energy range of $0.38\,\text{keV}$ to $16.5\,\text{keV}$. The colour coding represents the decadic logarithm of the number of X-ray photons counts per bin. The coordinates X and Y correspond to sky pixel coordinates. The upper left panel (A) shows the unfiltered raw event file and the upper right panel (B) is the time and particle background filtered result. The lower left panel (C) shows the time and particle background filtered result after application of the spatial filter and the lower right panel (D) represents the final source filtered diffuse X-ray background. All four representations of the corresponding event files have been smoothed with a Gaussian kernel having a filter width of 0.25σ.

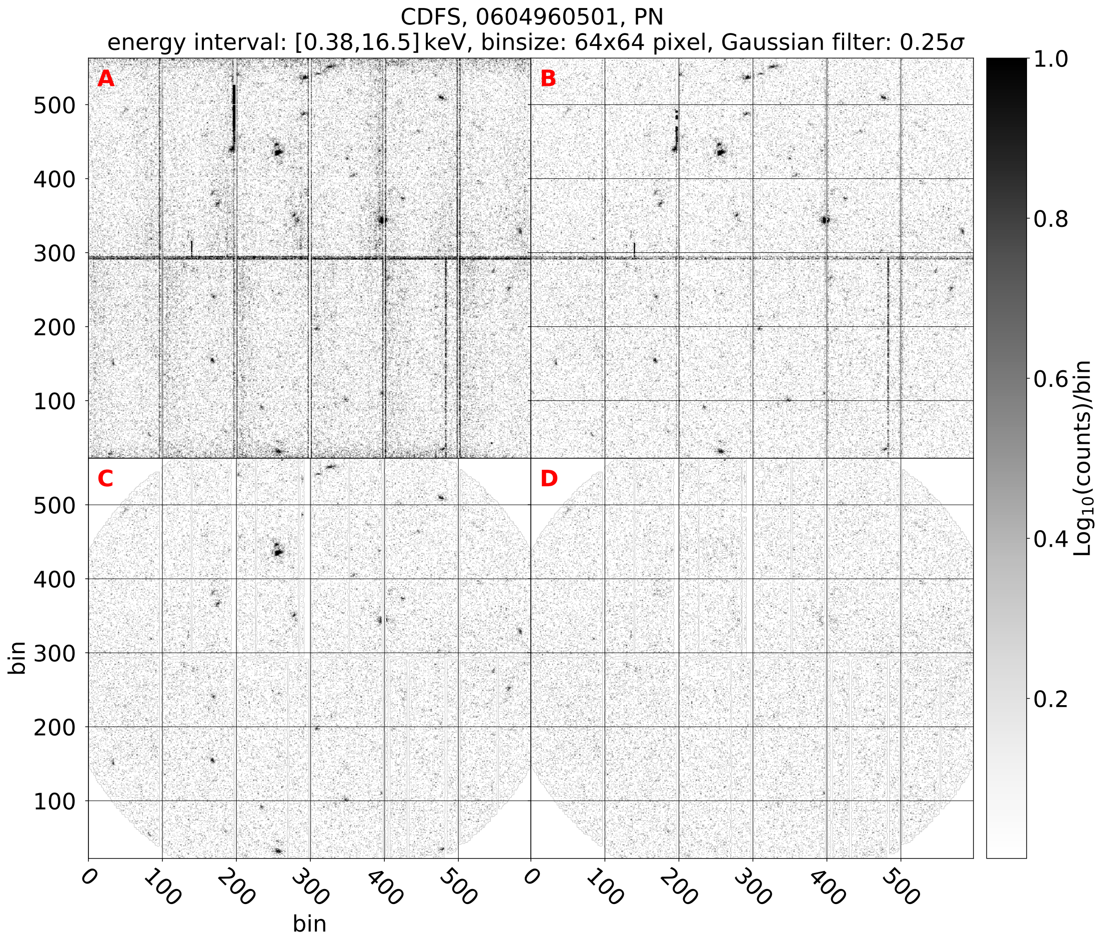

Figure C.31: All four panels show event files of the data set 0604960501 ($i = 32$, $\mathbf{D_1}$, table 4.1) taken with the EPIC-PN detector in an energy range of $0.38\,\mathrm{keV}$ to $16.5\,\mathrm{keV}$. The colour coding represents the decadic logarithm of the number of X-ray photons counts per bin. The coordinates X and Y correspond to sky pixel coordinates. The upper left panel (A) shows the unfiltered raw event file and the upper right panel (B) is the time and particle background filtered result. The lower left panel (C) shows the time and particle background filtered result after application of the spatial filter and the lower right panel (D) represents the final source filtered diffuse X-ray background. All four representations of the corresponding event files have been smoothed with a Gaussian kernel having a filter width of 0.25σ.

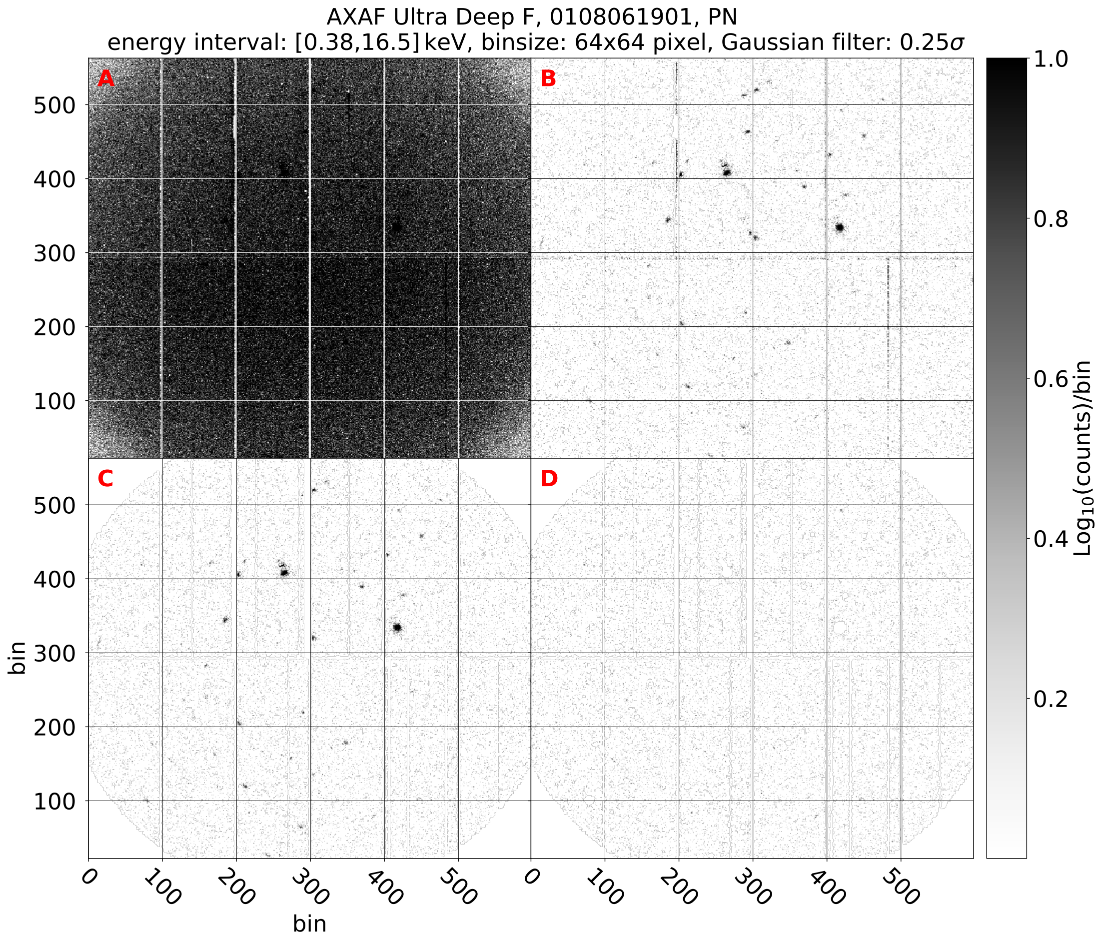

Figure C.32: All four panels show event files of the data set 0108061901 ($i = 33$, $\mathbf{D_1}$, table 4.1) taken with the EPIC-PN detector in an energy range of $0.38\,\mathrm{keV}$ to $16.5\,\mathrm{keV}$. The colour coding represents the decadic logarithm of the number of X-ray photons counts per bin. The coordinates X and Y correspond to sky pixel coordinates. The upper left panel (A) shows the unfiltered raw event file and the upper right panel (B) is the time and particle background filtered result. The lower left panel (C) shows the time and particle background filtered result after application of the spatial filter and the lower right panel (D) represents the final source filtered diffuse X-ray background. All four representations of the corresponding event files have been smoothed with a Gaussian kernel having a filter width of 0.25σ.

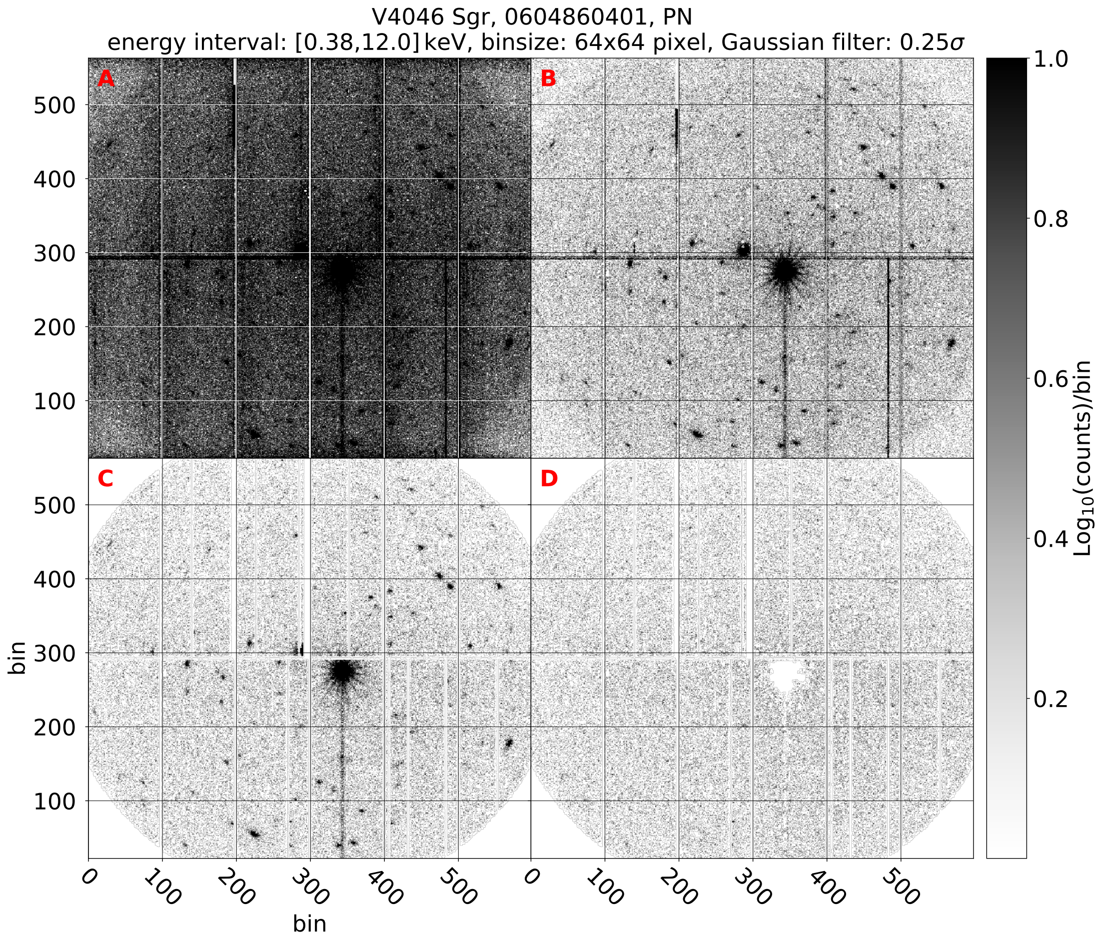

Figure C.33: All four panels show event files of the data set 0604860401 ($i = 2$, $\mathbf{D_2}$, table 4.2) taken with the EPIC-PN detector in an energy range of 0.38 keV to 12 keV. The colour coding represents the decadic logarithm of the number of X-ray photons counts per bin. The coordinates X and Y correspond to sky pixel coordinates. The upper left panel (A) shows the unfiltered raw event file and the upper right panel (B) is the time and particle background filtered result. The lower left panel (C) shows the time and particle background filtered result after application of the spatial filter and the lower right panel (D) represents the final source filtered diffuse X-ray background. All four representations of the corresponding event files have been smoothed with a Gaussian kernel having a filter width of 0.25σ.

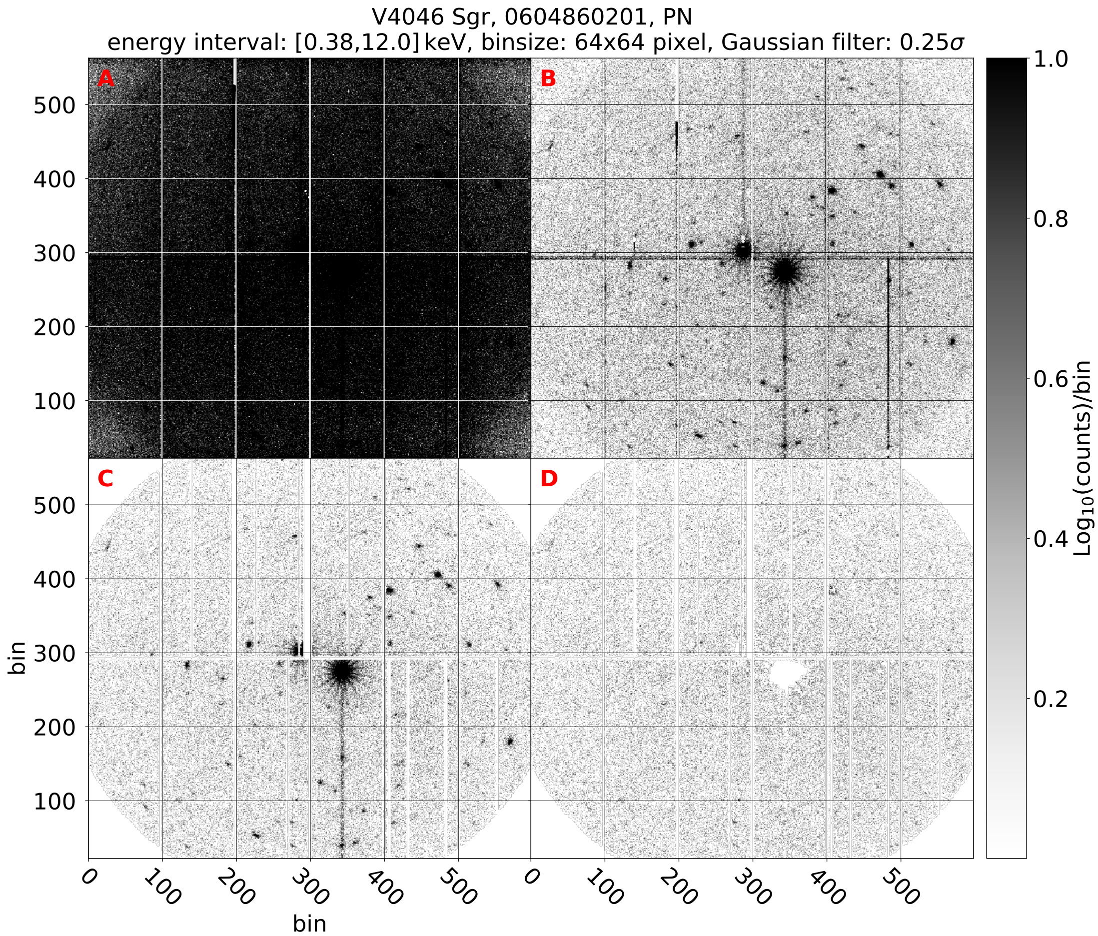

Figure C.34: All four panels show event files of the data set 0604860201 ($i = 3$, $\mathbf{D_2}$, table 4.2) taken with the EPIC-PN detector in an energy range of 0.38 keV to 12 keV. The colour coding represents the decadic logarithm of the number of X-ray photons counts per bin. The coordinates X and Y correspond to sky pixel coordinates. The upper left panel (A) shows the unfiltered raw event file and the upper right panel (B) is the time and particle background filtered result. The lower left panel (C) shows the time and particle background filtered result after application of the spatial filter and the lower right panel (D) represents the final source filtered diffuse X-ray background. All four representations of the corresponding event files have been smoothed with a Gaussian kernel having a filter width of 0.25σ.

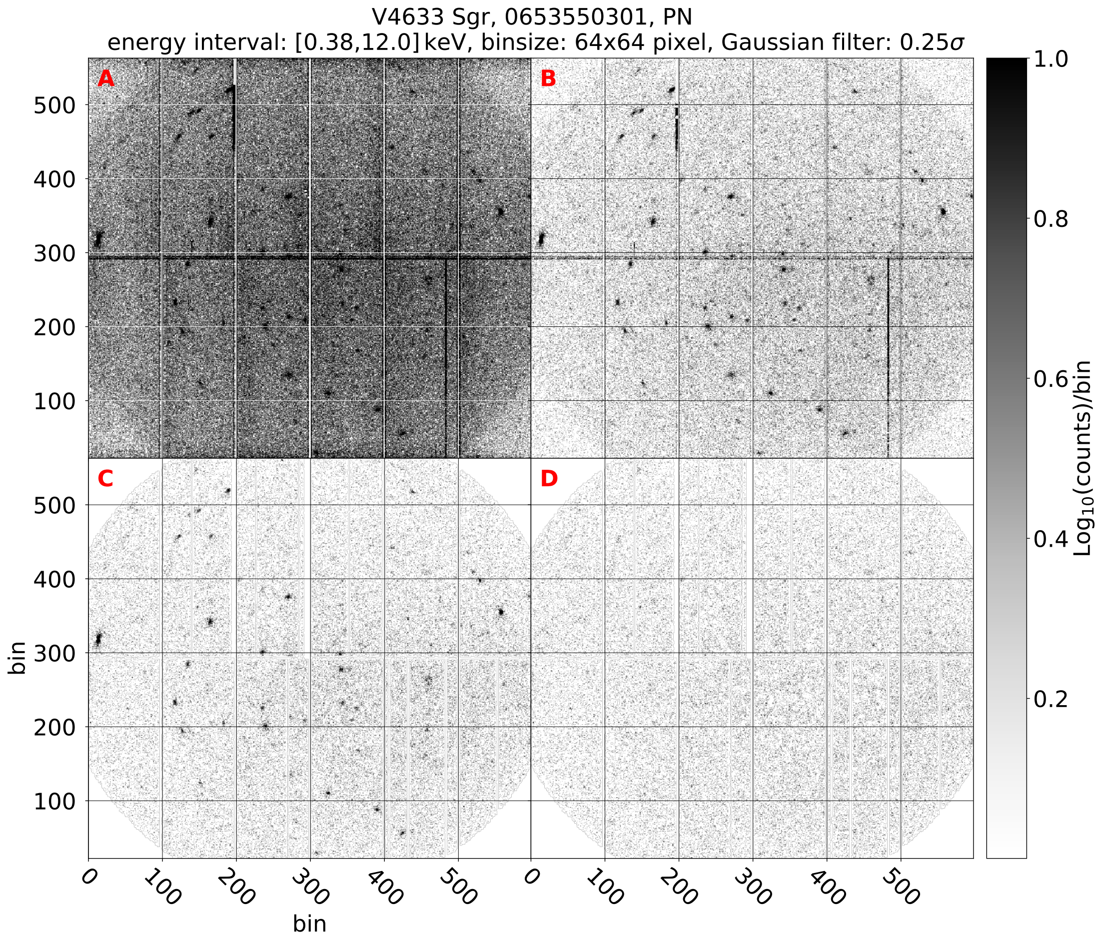

Figure C.35: All four panels show event files of the data set 0653550301 ($i = 4$, $\mathbf{D_2}$, table 4.2) taken with the EPIC-PN detector in an energy range of 0.38 keV to 12 keV. The colour coding represents the decadic logarithm of the number of X-ray photons counts per bin. The coordinates X and Y correspond to sky pixel coordinates. The upper left panel (A) shows the unfiltered raw event file and the upper right panel (B) is the time and particle background filtered result. The lower left panel (C) shows the time and particle background filtered result after application of the spatial filter and the lower right panel (D) represents the final source filtered diffuse X-ray background. All four representations of the corresponding event files have been smoothed with a Gaussian kernel having a filter width of 0.25σ.

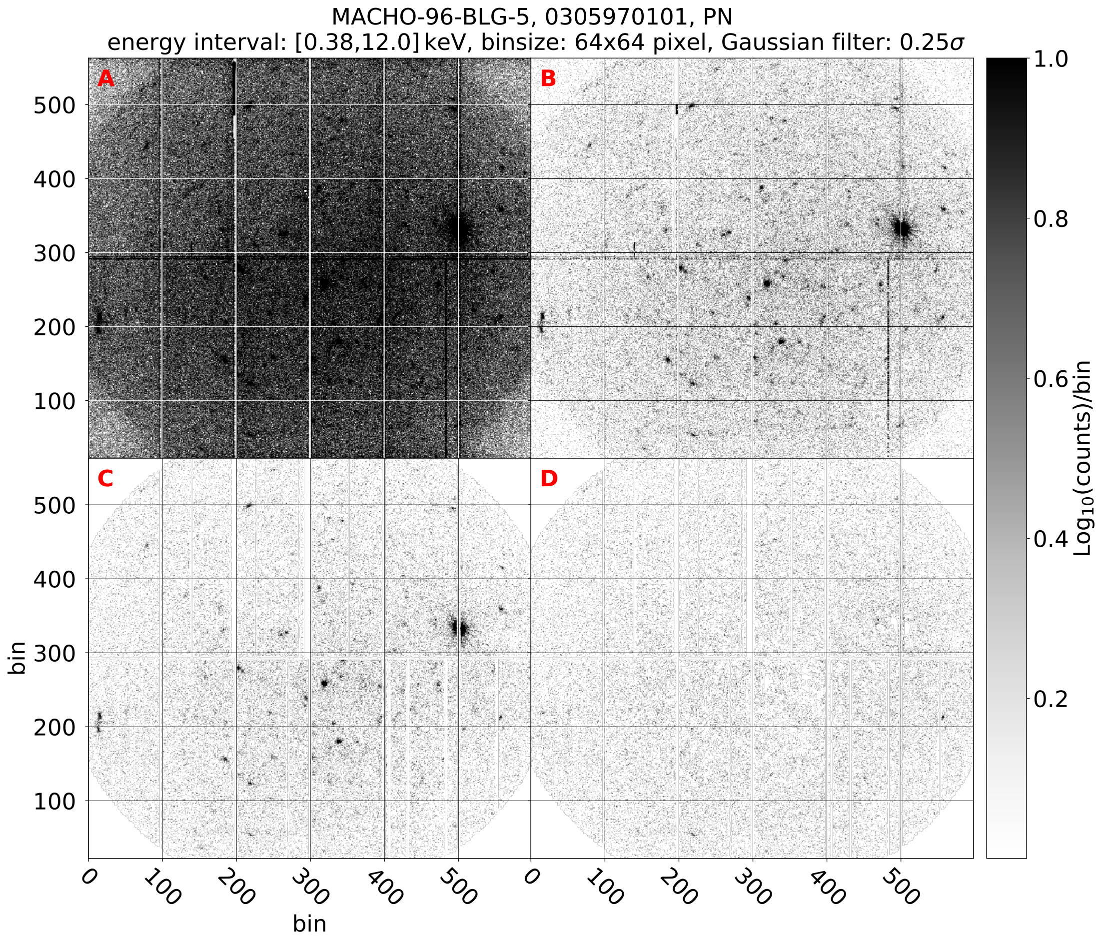

Figure C.36: All four panels show event files of the data set 0305970101 ($i = 5$, $\mathbf{D_2}$, table 4.2) taken with the EPIC-PN detector in an energy range of 0.38 keV to 12 keV. The colour coding represents the decadic logarithm of the number of X-ray photons counts per bin. The coordinates X and Y correspond to sky pixel coordinates. The upper left panel (A) shows the unfiltered raw event file and the upper right panel (B) is the time and particle background filtered result. The lower left panel (C) shows the time and particle background filtered result after application of the spatial filter and the lower right panel (D) represents the final source filtered diffuse X-ray background. All four representations of the corresponding event files have been smoothed with a Gaussian kernel having a filter width of 0.25σ.

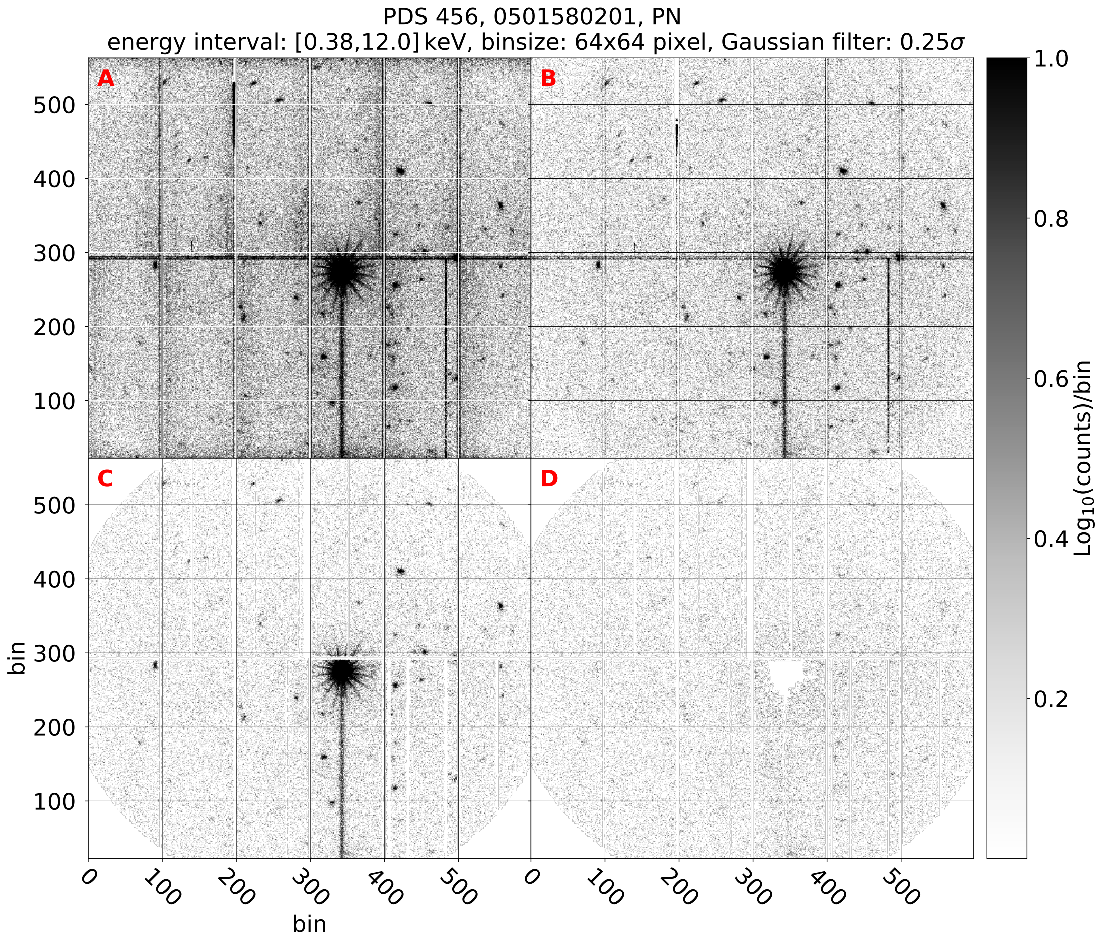

Figure C.37: All four panels show event files of the data set 0501580201 ($i = 6$, $\mathbf{D_2}$, table 4.2) taken with the EPIC-PN detector in an energy range of $0.38\,\mathrm{keV}$ to $12\,\mathrm{keV}$. The colour coding represents the decadic logarithm of the number of X-ray photons counts per bin. The coordinates X and Y correspond to sky pixel coordinates. The upper left panel (A) shows the unfiltered raw event file and the upper right panel (B) is the time and particle background filtered result. The lower left panel (C) shows the time and particle background filtered result after application of the spatial filter and the lower right panel (D) represents the final source filtered diffuse X-ray background. All four representations of the corresponding event files have been smoothed with a Gaussian kernel having a filter width of 0.25σ.

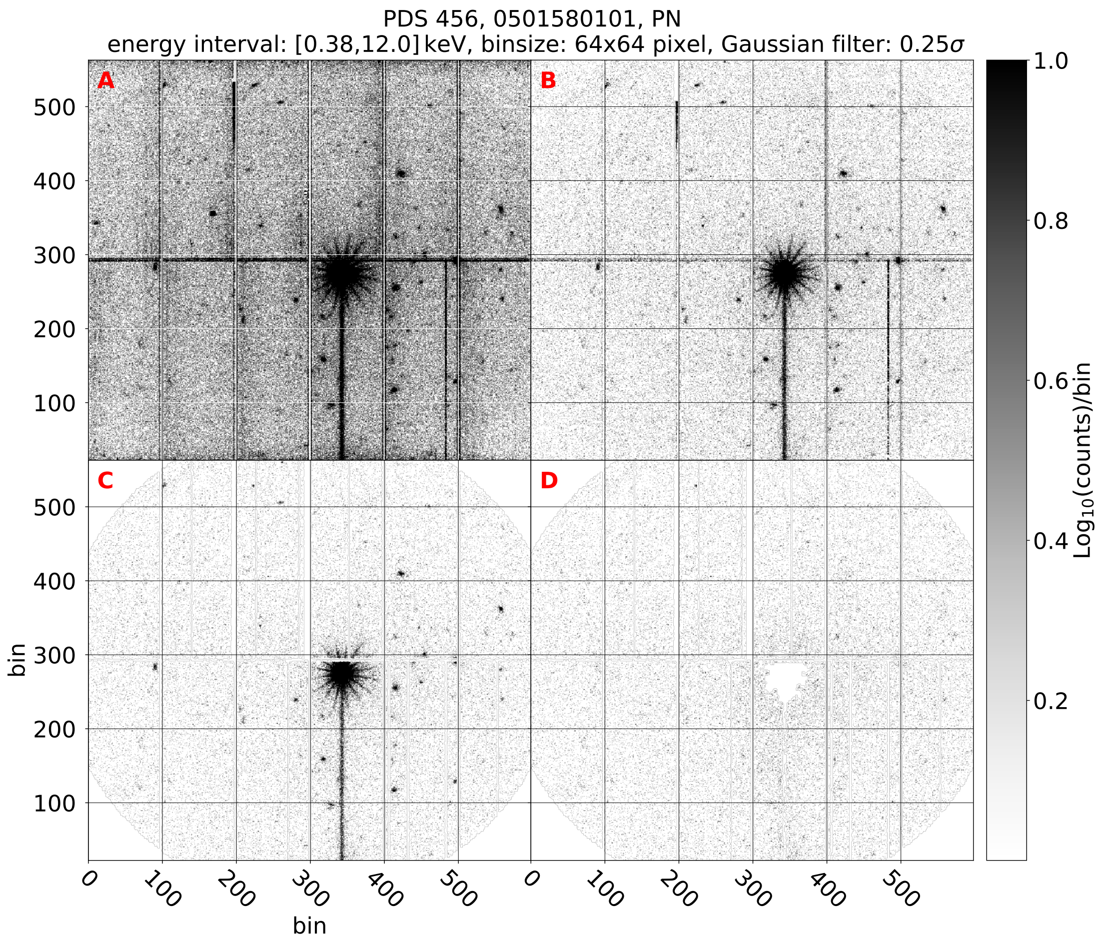

Figure C.38: All four panels show event files of the data set 0501580101 ($i = 7$, $\mathbf{D_2}$, table 4.2) taken with the EPIC-PN detector in an energy range of $0.38\,\mathrm{keV}$ to $12\,\mathrm{keV}$. The colour coding represents the decadic logarithm of the number of X-ray photons counts per bin. The coordinates X and Y correspond to sky pixel coordinates. The upper left panel (A) shows the unfiltered raw event file and the upper right panel (B) is the time and particle background filtered result. The lower left panel (C) shows the time and particle background filtered result after application of the spatial filter and the lower right panel (D) represents the final source filtered diffuse X-ray background. All four representations of the corresponding event files have been smoothed with a Gaussian kernel having a filter width of 0.25σ.

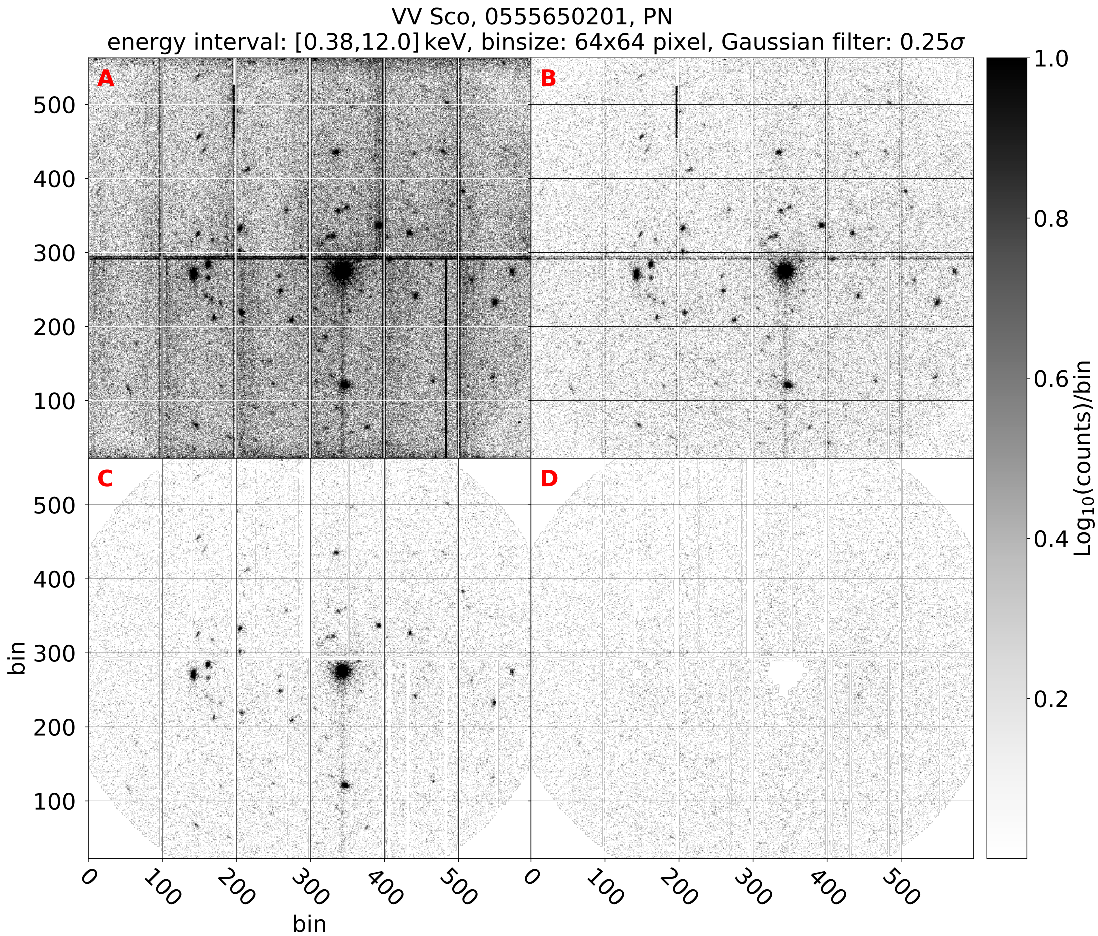

Figure C.39: All four panels show event files of the data set 0555650201 ($i = 8$, $\mathbf{D_2}$, table 4.2) taken with the EPIC-PN detector in an energy range of 0.38 keV to 12 keV. The colour coding represents the decadic logarithm of the number of X-ray photons counts per bin. The coordinates X and Y correspond to sky pixel coordinates. The upper left panel (A) shows the unfiltered raw event file and the upper right panel (B) is the time and particle background filtered result. The lower left panel (C) shows the time and particle background filtered result after application of the spatial filter and the lower right panel (D) represents the final source filtered diffuse X-ray background. All four representations of the corresponding event files have been smoothed with a Gaussian kernel having a filter width of 0.25σ.

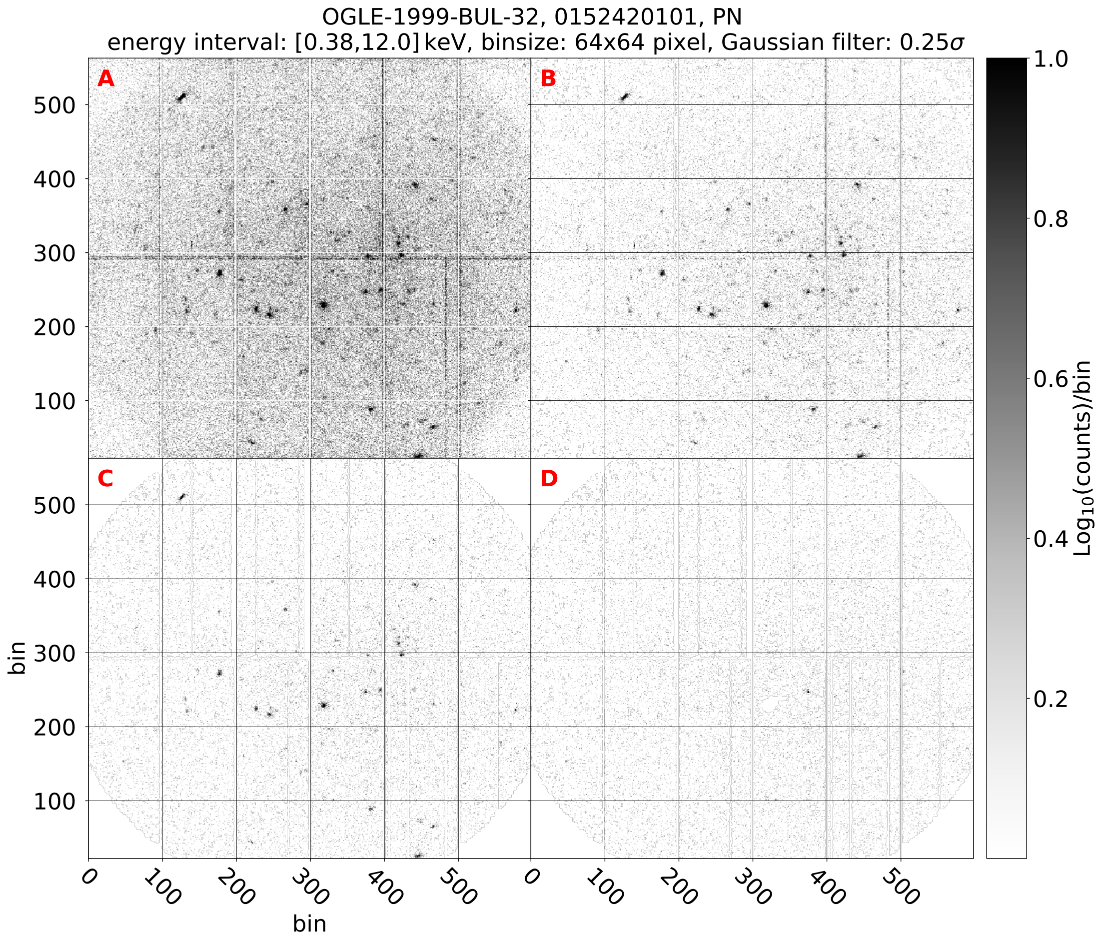

Figure C.40: All four panels show event files of the data set 0152420101 ($i = 9$, $\mathbf{D_2}$, table 4.2) taken with the EPIC-PN detector in an energy range of 0.38 keV to 12 keV. The colour coding represents the decadic logarithm of the number of X-ray photons counts per bin. The coordinates X and Y correspond to sky pixel coordinates. The upper left panel (A) shows the unfiltered raw event file and the upper right panel (B) is the time and particle background filtered result. The lower left panel (C) shows the time and particle background filtered result after application of the spatial filter and the lower right panel (D) represents the final source filtered diffuse X-ray background. All four representations of the corresponding event files have been smoothed with a Gaussian kernel having a filter width of 0.25σ.

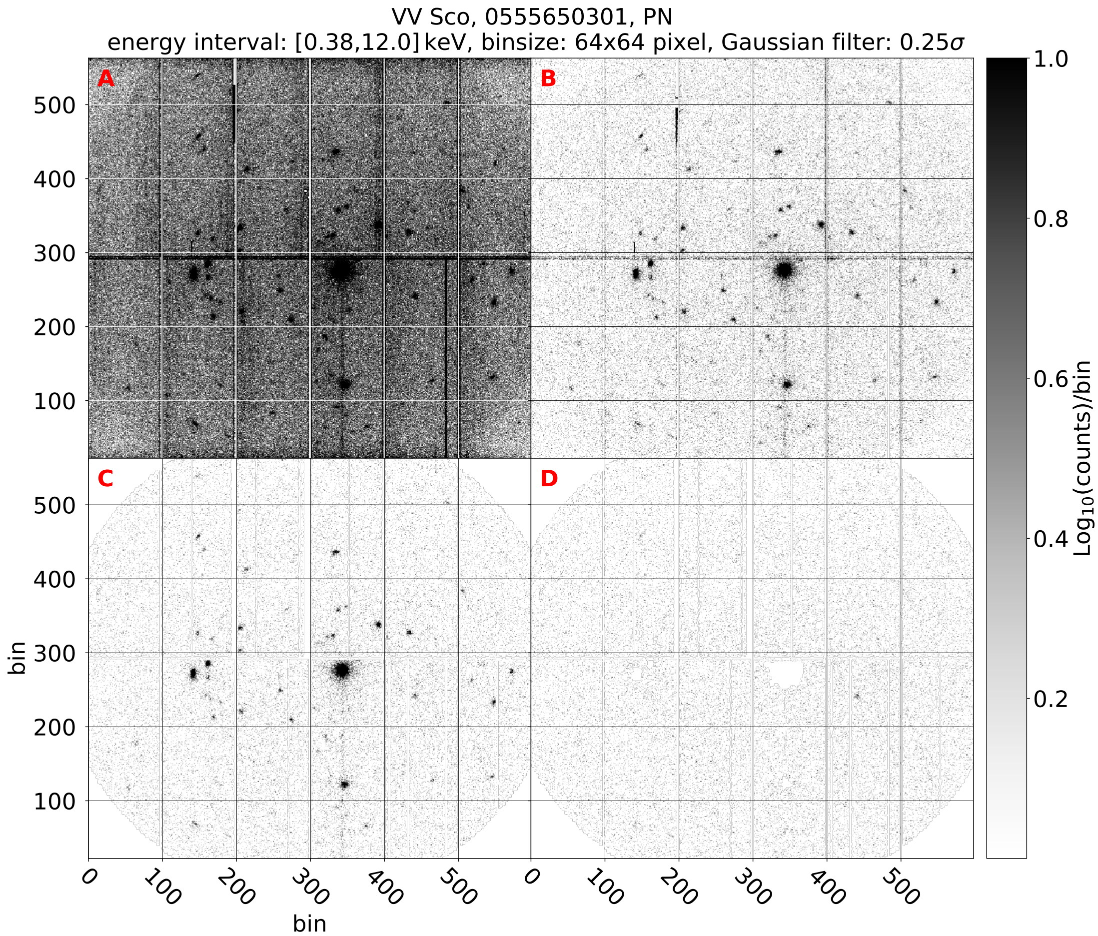

Figure C.41: All four panels show event files of the data set 0555650301 ($i = 10$, $\mathbf{D_2}$, table 4.2) taken with the EPIC-PN detector in an energy range of 0.38 keV to 12 keV. The colour coding represents the decadic logarithm of the number of X-ray photons counts per bin. The coordinates X and Y correspond to sky pixel coordinates. The upper left panel (A) shows the unfiltered raw event file and the upper right panel (B) is the time and particle background filtered result. The lower left panel (C) shows the time and particle background filtered result after application of the spatial filter and the lower right panel (D) represents the final source filtered diffuse X-ray background. All four representations of the corresponding event files have been smoothed with a Gaussian kernel having a filter width of 0.25σ.

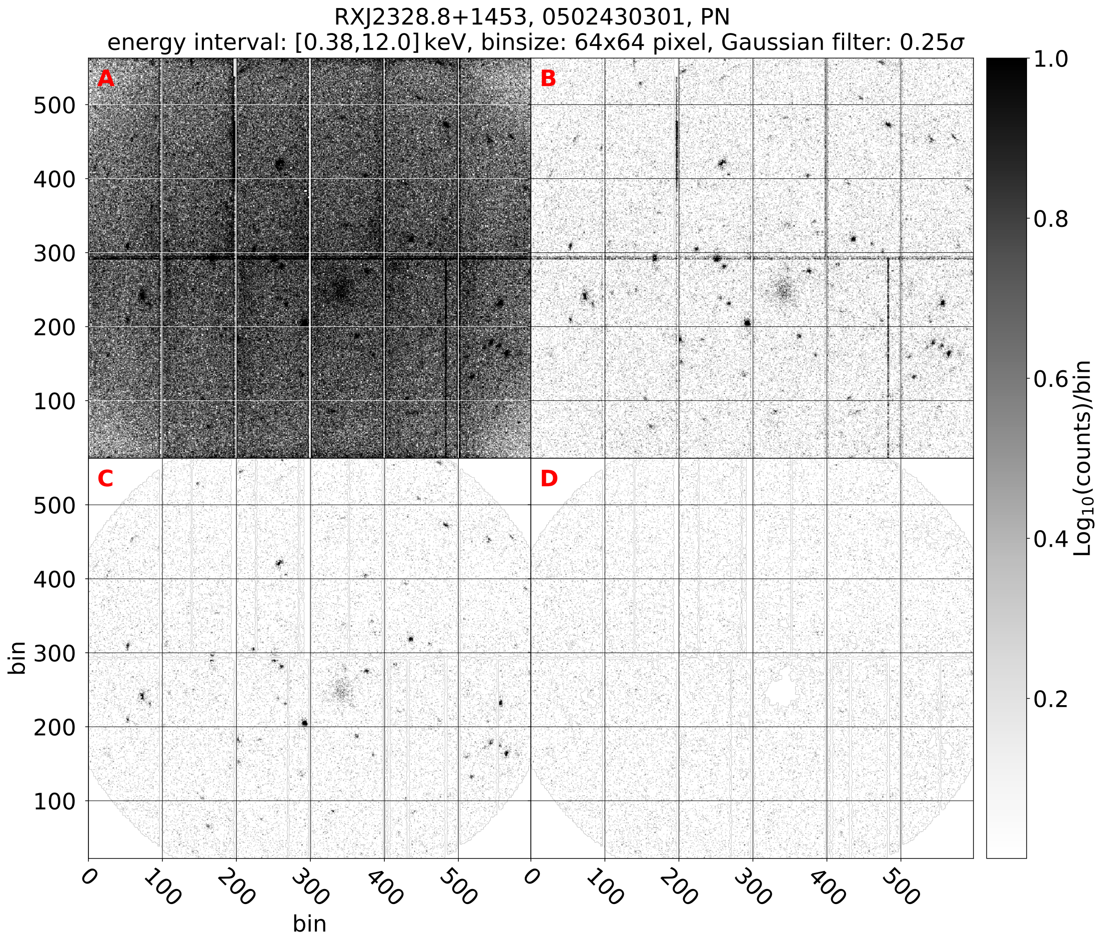

Figure C.42: All four panels show event files of the data set 0502430301 ($i = 11$, $\mathbf{D_2}$, table 4.2) taken with the EPIC-PN detector in an energy range of $0.38\,\text{keV}$ to $12\,\text{keV}$. The colour coding represents the decadic logarithm of the number of X-ray photons counts per bin. The coordinates X and Y correspond to sky pixel coordinates. The upper left panel (A) shows the unfiltered raw event file and the upper right panel (B) is the time and particle background filtered result. The lower left panel (C) shows the time and particle background filtered result after application of the spatial filter and the lower right panel (D) represents the final source filtered diffuse X-ray background. All four representations of the corresponding event files have been smoothed with a Gaussian kernel having a filter width of 0.25σ.

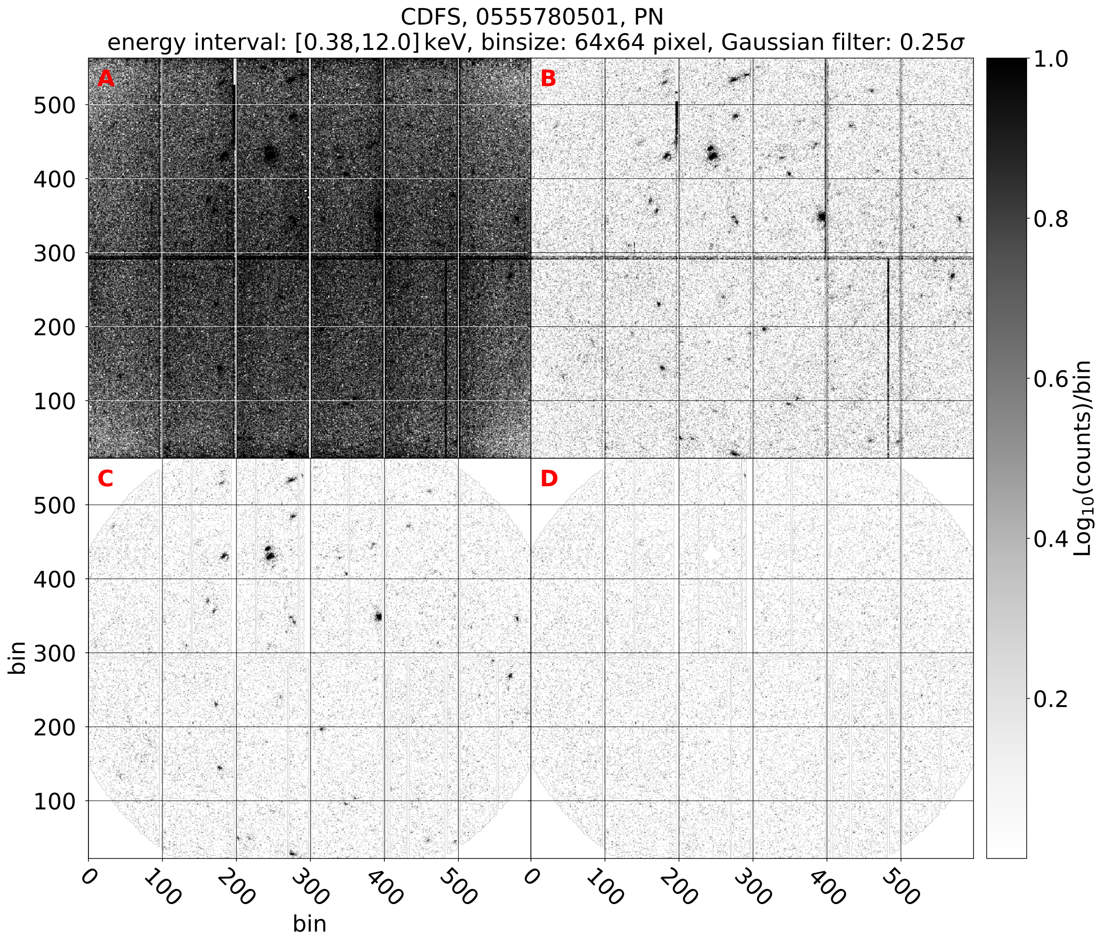

Figure C.43: All four panels show event files of the data set 0555780501 ($i = 12$, $\mathbf{D_2}$, table 4.2) taken with the EPIC-PN detector in an energy range of 0.38 keV to 12 keV. The colour coding represents the decadic logarithm of the number of X-ray photons counts per bin. The coordinates X and Y correspond to sky pixel coordinates. The upper left panel (A) shows the unfiltered raw event file and the upper right panel (B) is the time and particle background filtered result. The lower left panel (C) shows the time and particle background filtered result after application of the spatial filter and the lower right panel (D) represents the final source filtered diffuse X-ray background. All four representations of the corresponding event files have been smoothed with a Gaussian kernel having a filter width of 0.25σ.

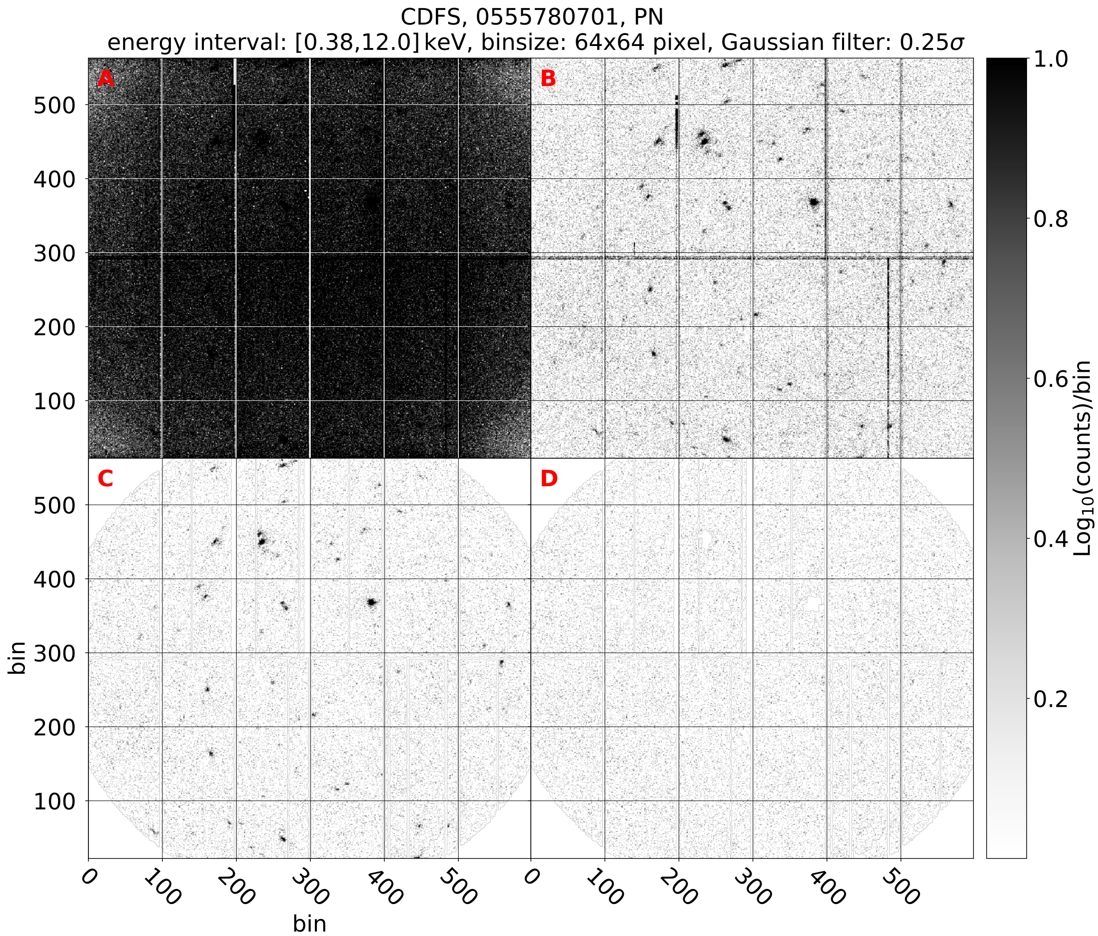

Figure C.44: All four panels show event files of the data set 0555780701 ($i = 13$, $\mathbf{D_2}$, table 4.2) taken with the EPIC-PN detector in an energy range of 0.38 keV to 12 keV. The colour coding represents the decadic logarithm of the number of X-ray photons counts per bin. The coordinates X and Y correspond to sky pixel coordinates. The upper left panel (A) shows the unfiltered raw event file and the upper right panel (B) is the time and particle background filtered result. The lower left panel (C) shows the time and particle background filtered result after application of the spatial filter and the lower right panel (D) represents the final source filtered diffuse X-ray background. All four representations of the corresponding event files have been smoothed with a Gaussian kernel having a filter width of 0.25σ.

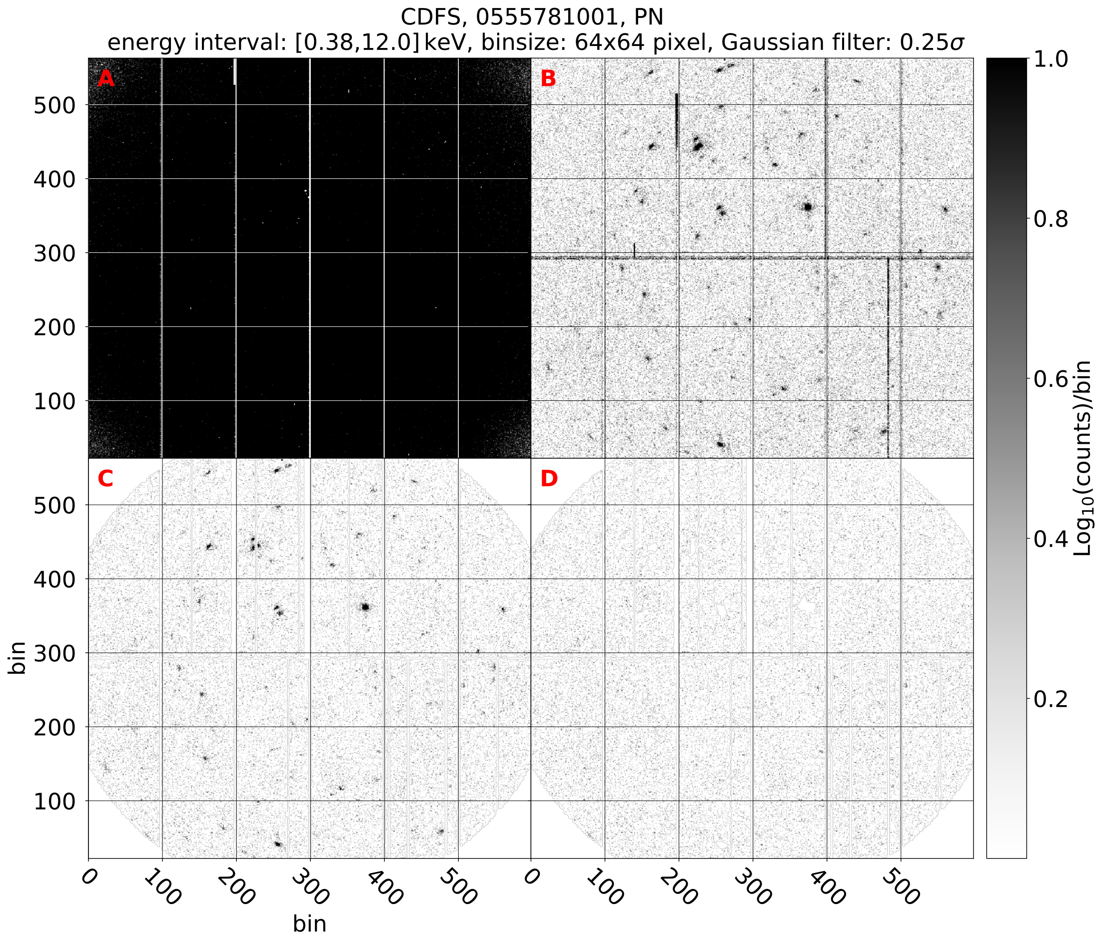

Figure C.45: All four panels show event files of the data set 0555781001 ($i = 14$, $\mathbf{D_2}$, table 4.2) taken with the EPIC-PN detector in an energy range of 0.38 keV to 12 keV. The colour coding represents the decadic logarithm of the number of X-ray photons counts per bin. The coordinates X and Y correspond to sky pixel coordinates. The upper left panel (A) shows the unfiltered raw event file and the upper right panel (B) is the time and particle background filtered result. The lower left panel (C) shows the time and particle background filtered result after application of the spatial filter and the lower right panel (D) represents the final source filtered diffuse X-ray background. All four representations of the corresponding event files have been smoothed with a Gaussian kernel having a filter width of 0.25σ.

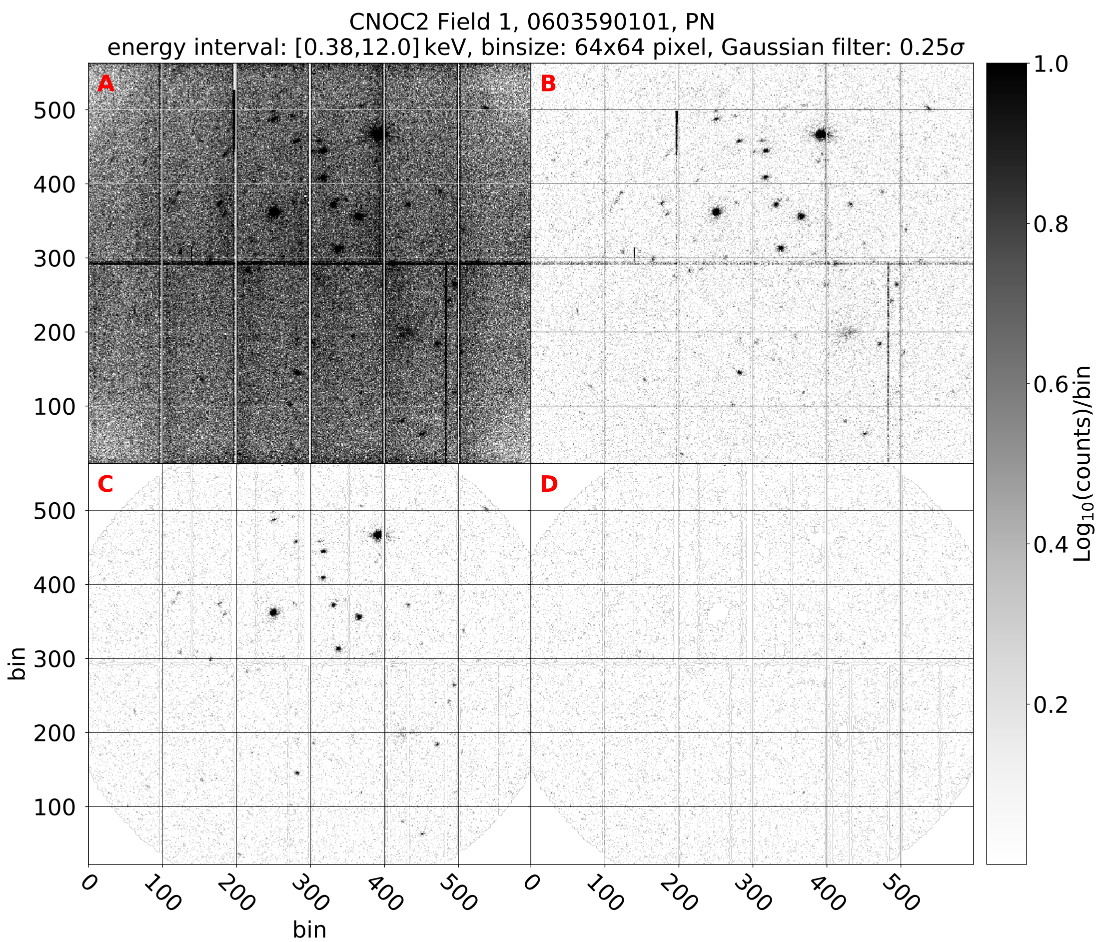

Figure C.46: All four panels show event files of the data set 0603590101 ($i = 15$, $\mathbf{D_2}$, table 4.2) taken with the EPIC-PN detector in an energy range of $0.38\,\mathrm{keV}$ to $12\,\mathrm{keV}$. The colour coding represents the decadic logarithm of the number of X-ray photons counts per bin. The coordinates X and Y correspond to sky pixel coordinates. The upper left panel (A) shows the unfiltered raw event file and the upper right panel (B) is the time and particle background filtered result. The lower left panel (C) shows the time and particle background filtered result after application of the spatial filter and the lower right panel (D) represents the final source filtered diffuse X-ray background. All four representations of the corresponding event files have been smoothed with a Gaussian kernel having a filter width of 0.25σ.

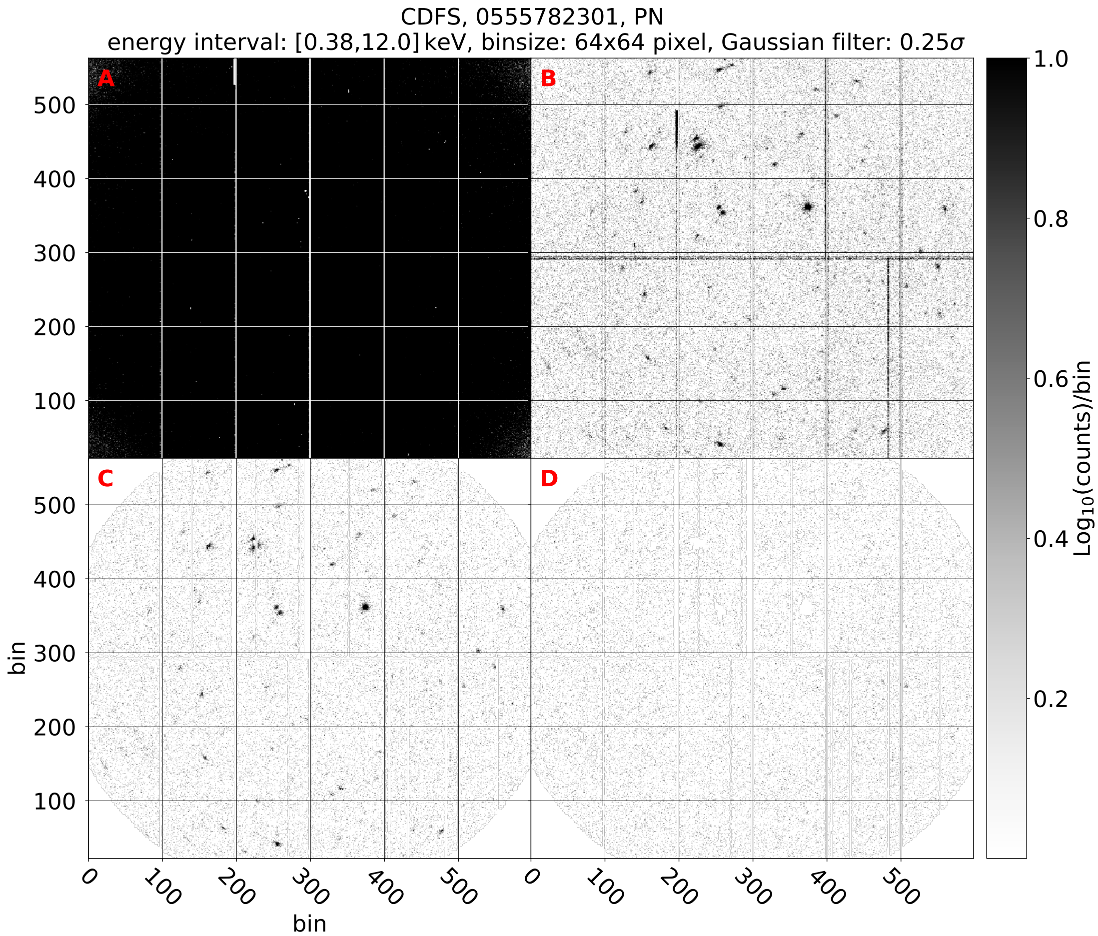

Figure C.47: All four panels show event files of the data set 0555782301 ($i = 16$, $\mathbf{D_2}$, table 4.2) taken with the EPIC-PN detector in an energy range of 0.38 keV to 12 keV. The colour coding represents the decadic logarithm of the number of X-ray photons counts per bin. The coordinates X and Y correspond to sky pixel coordinates. The upper left panel (A) shows the unfiltered raw event file and the upper right panel (B) is the time and particle background filtered result. The lower left panel (C) shows the time and particle background filtered result after application of the spatial filter and the lower right panel (D) represents the final source filtered diffuse X-ray background. All four representations of the corresponding event files have been smoothed with a Gaussian kernel having a filter width of 0.25σ.

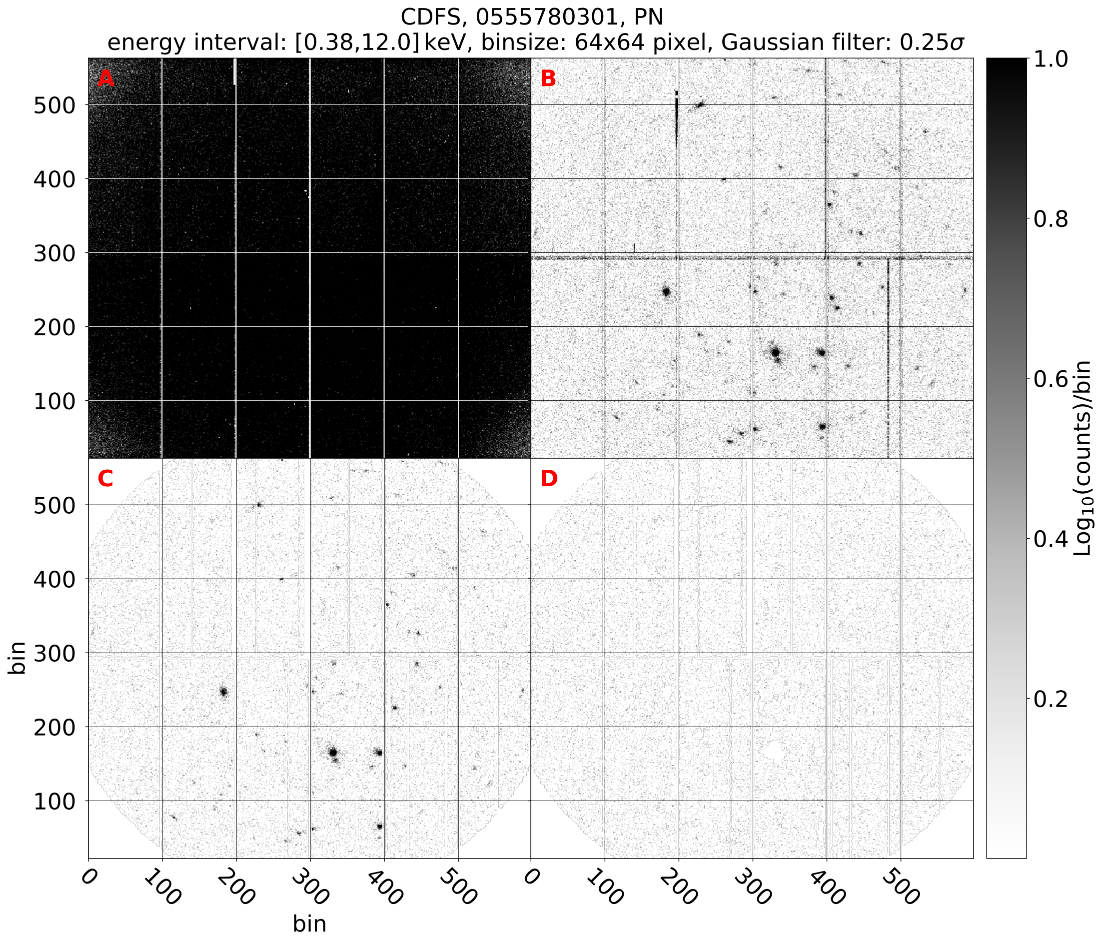

Figure C.48: All four panels show event files of the data set 0555780301 ($i = 17$, $\mathbf{D_2}$, table 4.2) taken with the EPIC-PN detector in an energy range of 0.38 keV to 12 keV. The colour coding represents the decadic logarithm of the number of X-ray photons counts per bin. The coordinates X and Y correspond to sky pixel coordinates. The upper left panel (A) shows the unfiltered raw event file and the upper right panel (B) is the time and particle background filtered result. The lower left panel (C) shows the time and particle background filtered result after application of the spatial filter and the lower right panel (D) represents the final source filtered diffuse X-ray background. All four representations of the corresponding event files have been smoothed with a Gaussian kernel having a filter width of 0.25σ.

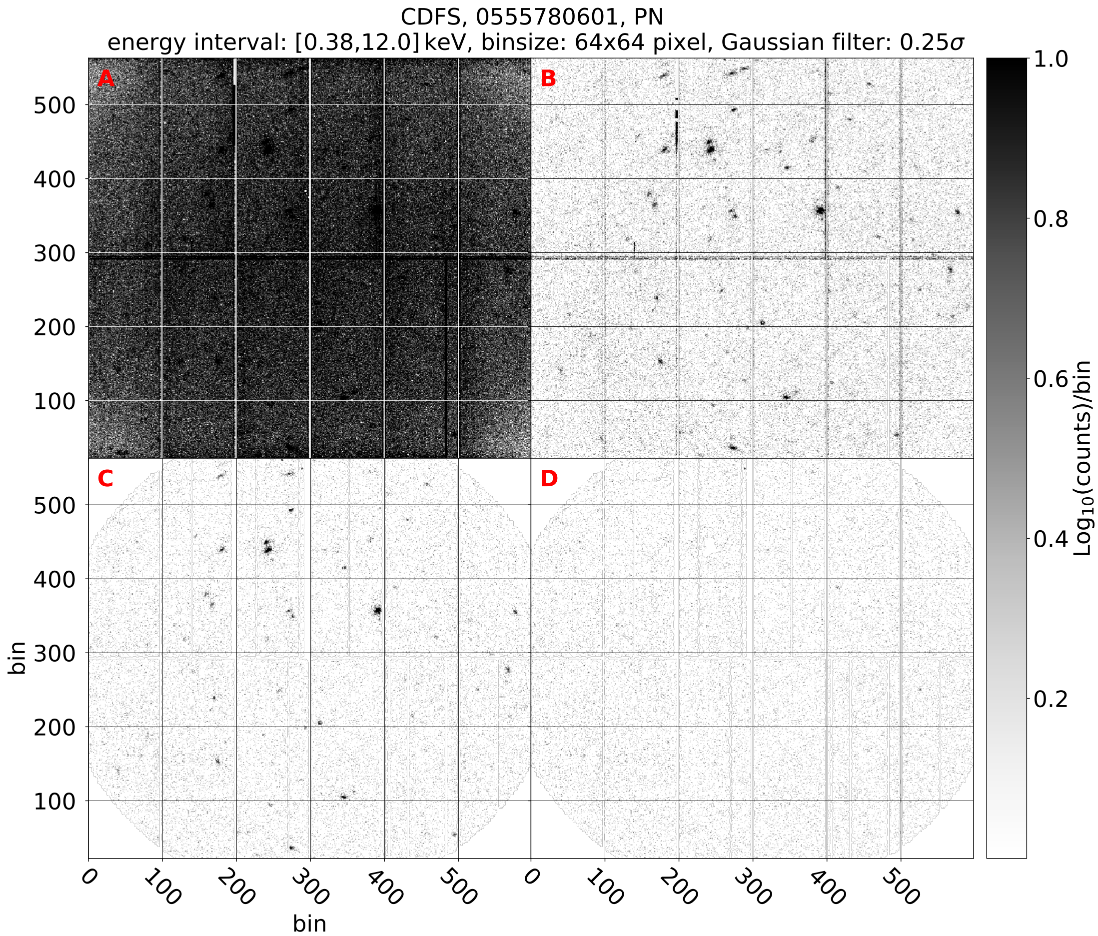

Figure C.49: All four panels show event files of the data set 0555780601 ($i = 18$, $\mathbf{D_2}$, table 4.2) taken with the EPIC-PN detector in an energy range of 0.38 keV to 12 keV. The colour coding represents the decadic logarithm of the number of X-ray photons counts per bin. The coordinates X and Y correspond to sky pixel coordinates. The upper left panel (A) shows the unfiltered raw event file and the upper right panel (B) is the time and particle background filtered result. The lower left panel (C) shows the time and particle background filtered result after application of the spatial filter and the lower right panel (D) represents the final source filtered diffuse X-ray background. All four representations of the corresponding event files have been smoothed with a Gaussian kernel having a filter width of 0.25σ.

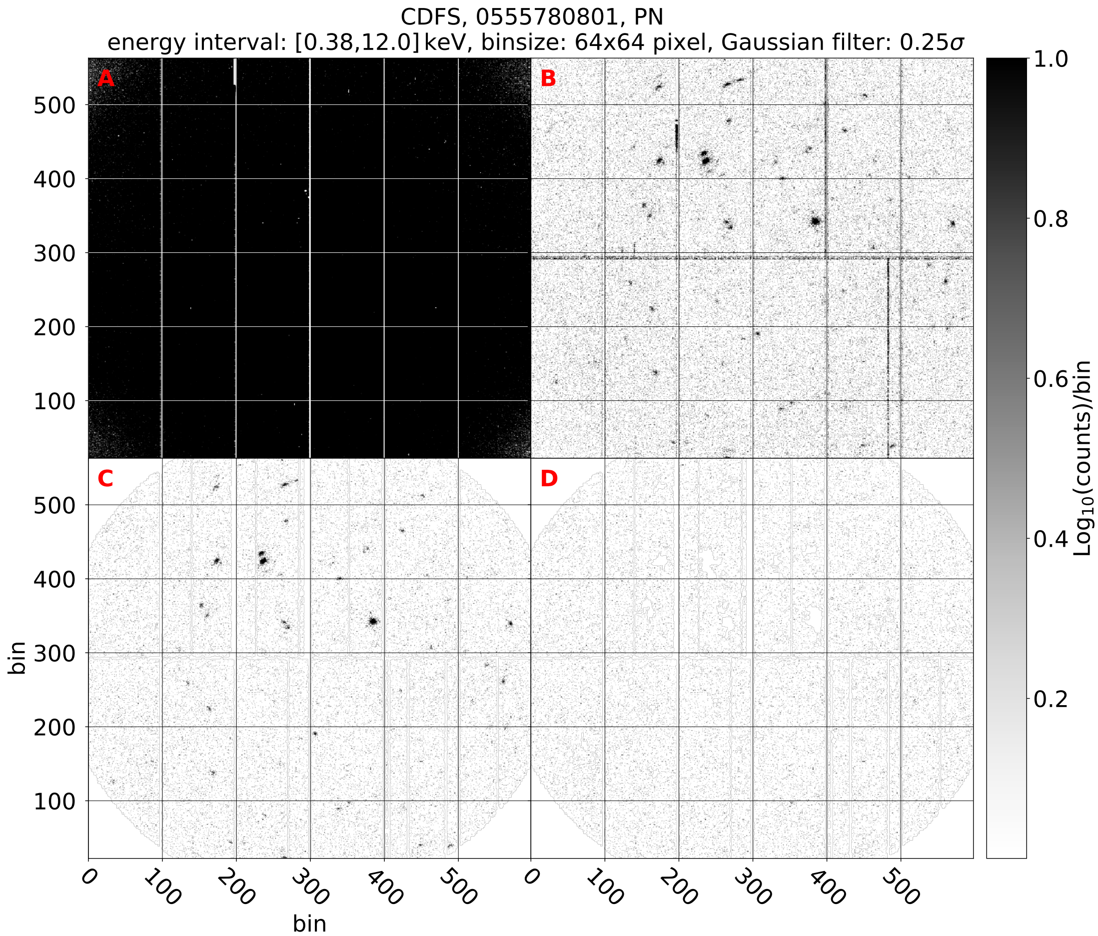

Figure C.50: All four panels show event files of the data set 0555780801 ($i = 19$, $\mathbf{D_2}$, table 4.2) taken with the EPIC-PN detector in an energy range of 0.38 keV to 12 keV. The colour coding represents the decadic logarithm of the number of X-ray photons counts per bin. The coordinates X and Y correspond to sky pixel coordinates. The upper left panel (A) shows the unfiltered raw event file and the upper right panel (B) is the time and particle background filtered result. The lower left panel (C) shows the time and particle background filtered result after application of the spatial filter and the lower right panel (D) represents the final source filtered diffuse X-ray background. All four representations of the corresponding event files have been smoothed with a Gaussian kernel having a filter width of 0.25σ.

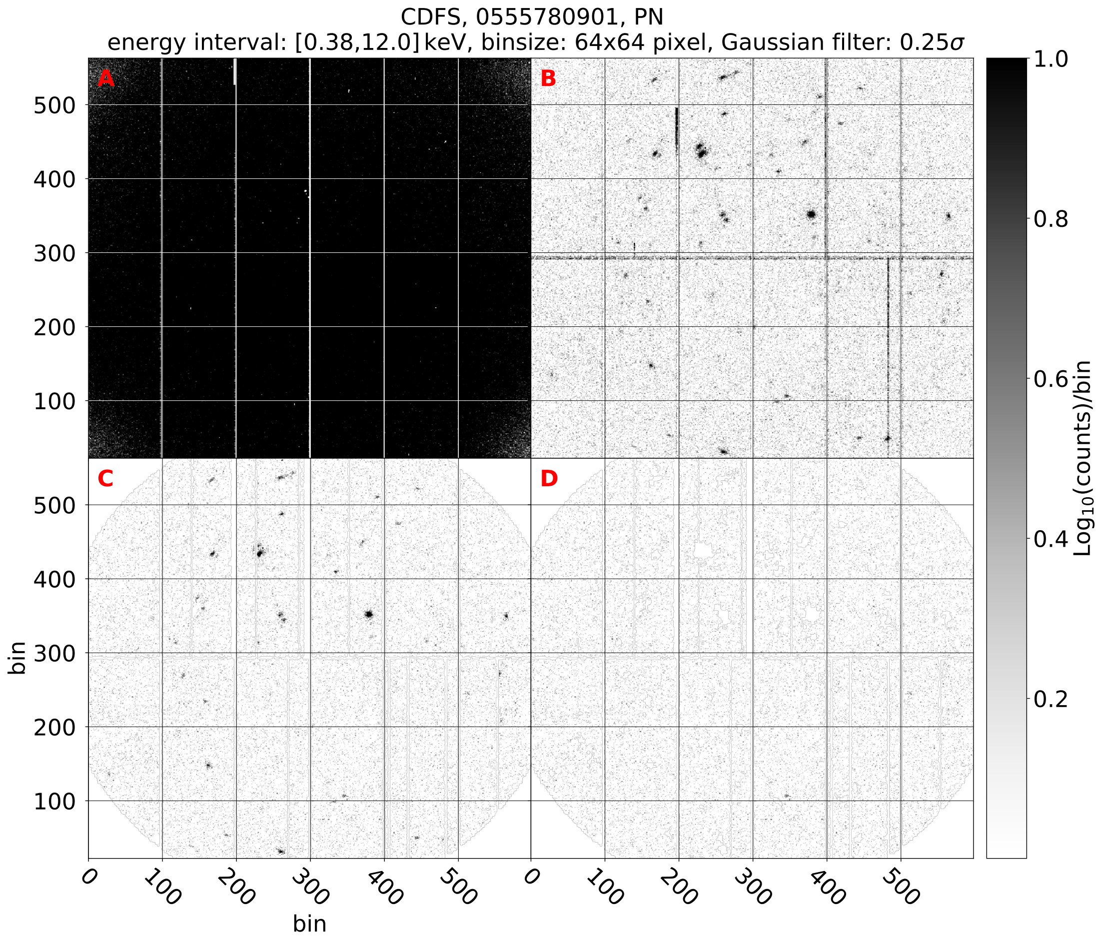

Figure C.51: All four panels show event files of the data set 0555780901 ($i = 20$, $\mathbf{D_2}$, table 4.2) taken with the EPIC-PN detector in an energy range of $0.38\,\mathrm{keV}$ to $12\,\mathrm{keV}$. The colour coding represents the decadic logarithm of the number of X-ray photons counts per bin. The coordinates X and Y correspond to sky pixel coordinates. The upper left panel (A) shows the unfiltered raw event file and the upper right panel (B) is the time and particle background filtered result. The lower left panel (C) shows the time and particle background filtered result after application of the spatial filter and the lower right panel (D) represents the final source filtered diffuse X-ray background. All four representations of the corresponding event files have been smoothed with a Gaussian kernel having a filter width of 0.25σ.

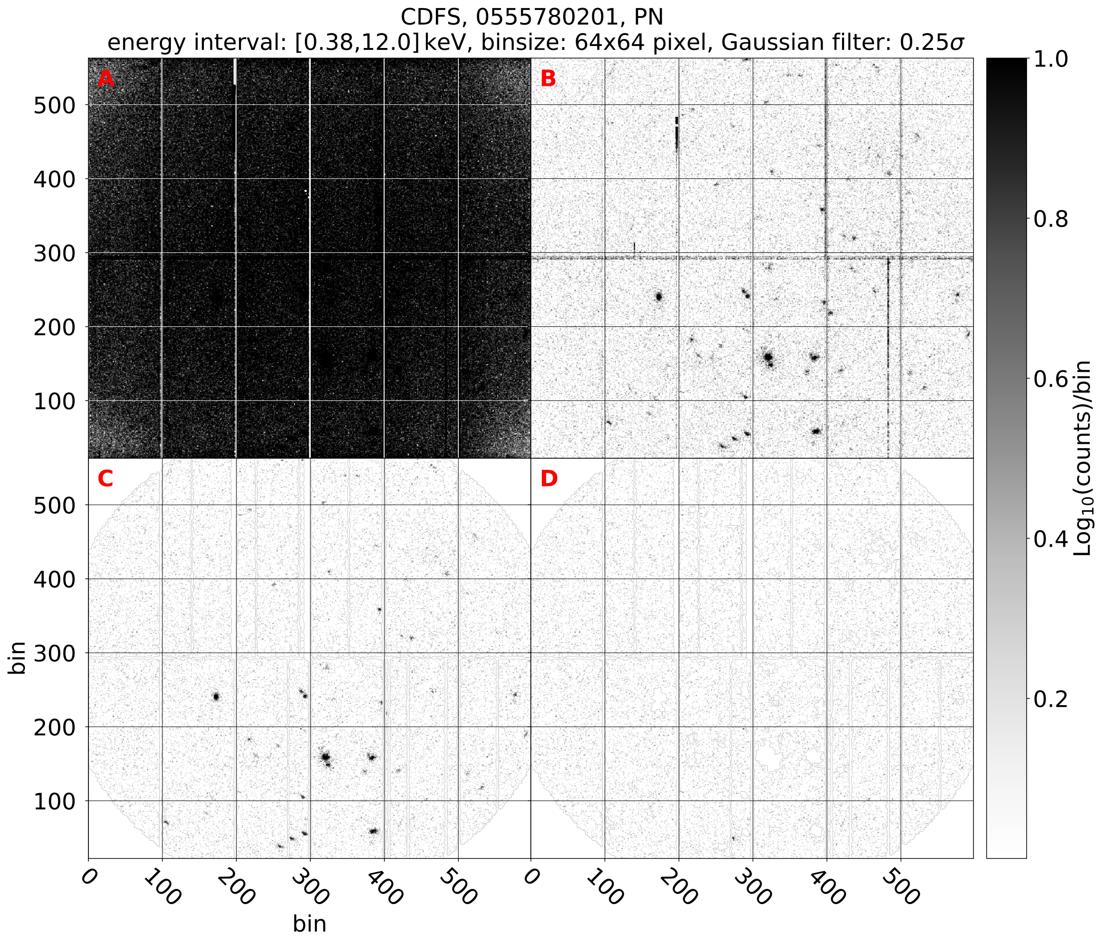

Figure C.52: All four panels show event files of the data set 0555780201 ($i = 21$, $\mathbf{D_2}$, table 4.2) taken with the EPIC-PN detector in an energy range of $0.38\,\mathrm{keV}$ to $12\,\mathrm{keV}$. The colour coding represents the decadic logarithm of the number of X-ray photons counts per bin. The coordinates X and Y correspond to sky pixel coordinates. The upper left panel (A) shows the unfiltered raw event file and the upper right panel (B) is the time and particle background filtered result. The lower left panel (C) shows the time and particle background filtered result after application of the spatial filter and the lower right panel (D) represents the final source filtered diffuse X-ray background. All four representations of the corresponding event files have been smoothed with a Gaussian kernel having a filter width of 0.25σ.

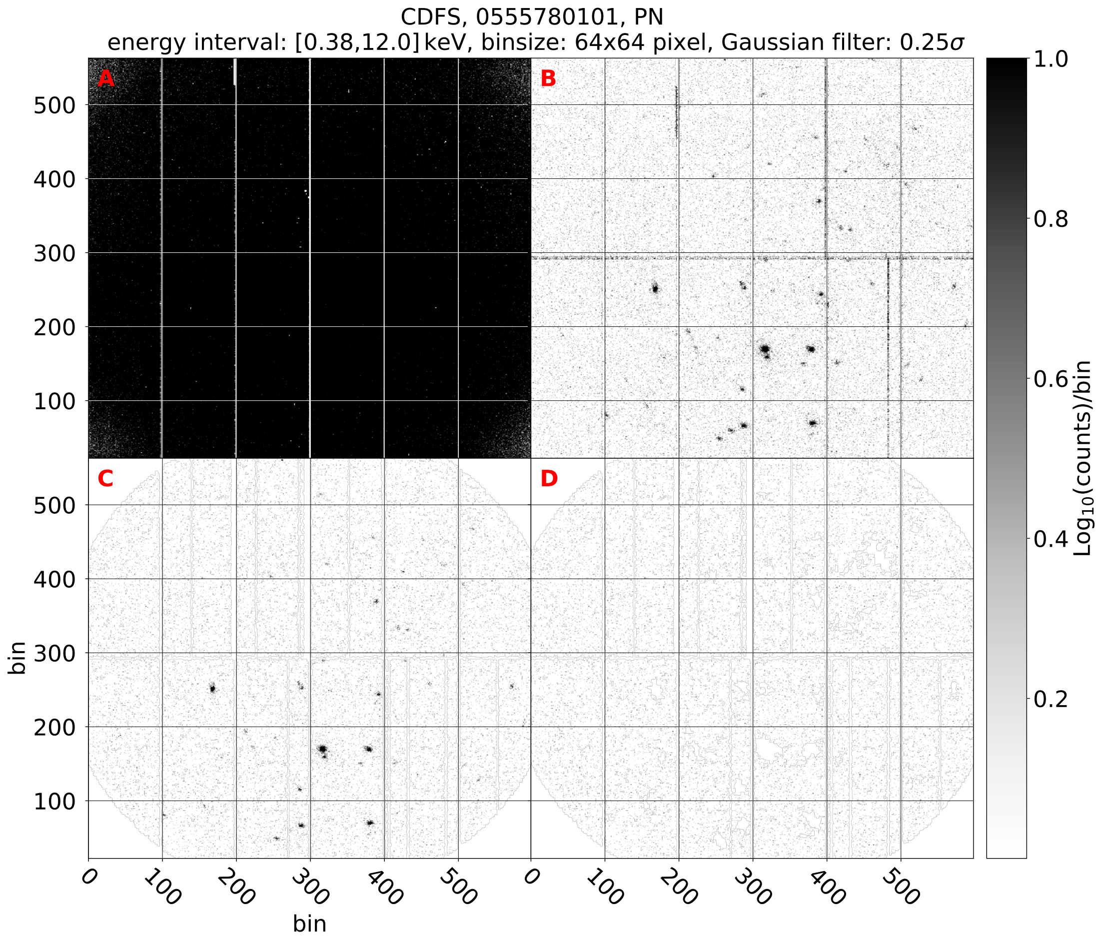

Figure C.53: All four panels show event files of the data set 0555780101 ($i = 22$, $\mathbf{D_2}$, table 4.2) taken with the EPIC-PN detector in an energy range of 0.38 keV to 12 keV. The colour coding represents the decadic logarithm of the number of X-ray photons counts per bin. The coordinates X and Y correspond to sky pixel coordinates. The upper left panel (A) shows the unfiltered raw event file and the upper right panel (B) is the time and particle background filtered result. The lower left panel (C) shows the time and particle background filtered result after application of the spatial filter and the lower right panel (D) represents the final source filtered diffuse X-ray background. All four representations of the corresponding event files have been smoothed with a Gaussian kernel having a filter width of 0.25σ.

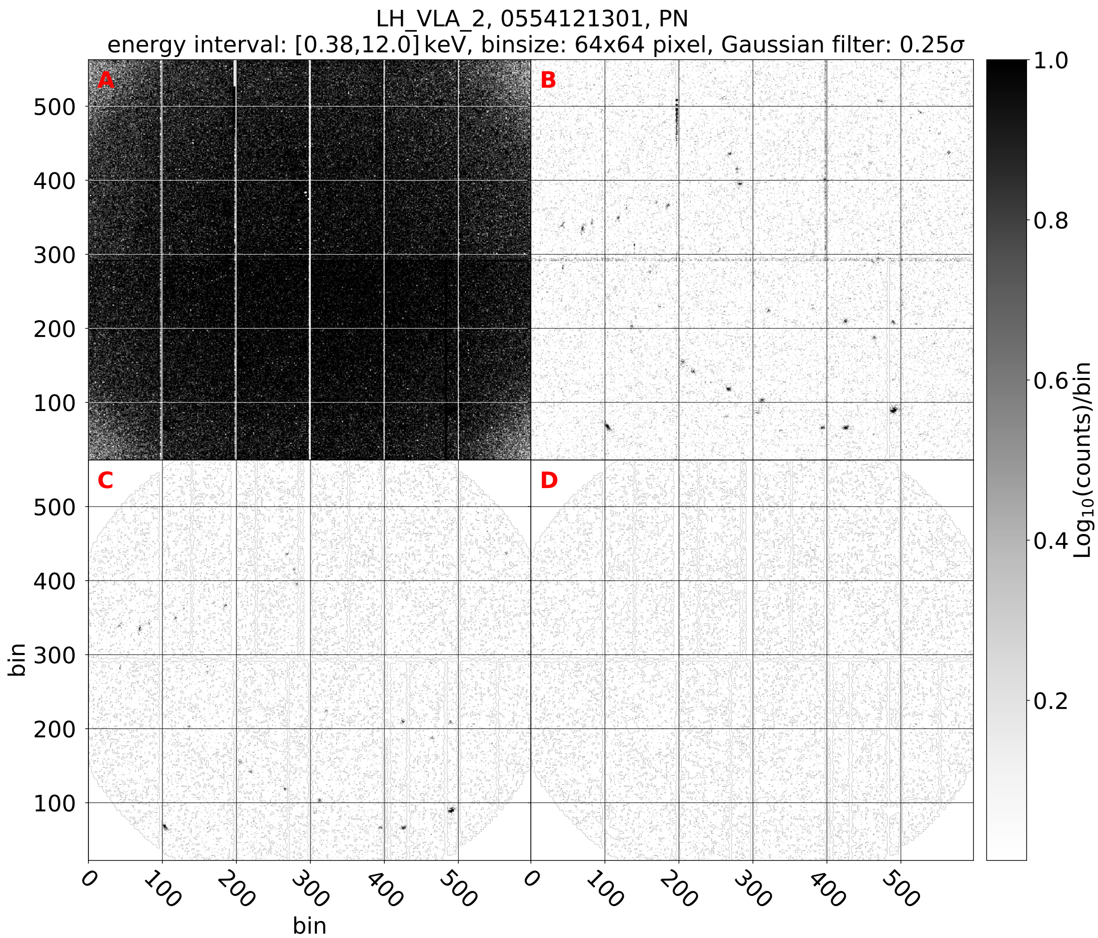

Figure C.54: All four panels show event files of the data set 0554121301 ($i = 23$, $\mathbf{D_2}$, table 4.2) taken with the EPIC-PN detector in an energy range of $0.38\,\mathrm{keV}$ to $12\,\mathrm{keV}$. The colour coding represents the decadic logarithm of the number of X-ray photons counts per bin. The coordinates X and Y correspond to sky pixel coordinates. The upper left panel (A) shows the unfiltered raw event file and the upper right panel (B) is the time and particle background filtered result. The lower left panel (C) shows the time and particle background filtered result after application of the spatial filter and the lower right panel (D) represents the final source filtered diffuse X-ray background. All four representations of the corresponding event files have been smoothed with a Gaussian kernel having a filter width of 0.25σ.

8.4 Appendix D. Emission and Absorption

The specific intensity I_ν according to Chandrasekhar (11) can be defined as

$$dE_\nu = I_\nu \cos(\theta) d\nu dA d\Omega dt. \tag{D.28}$$

The integrated intensity I is the intensity I_ν integrated over all frequencies,

$$I = \int_0^\infty I_\nu \, d\nu. \tag{D.29}$$

The average intensity J_ν is the integrated intensity weighted by the full solid angle Ω of absolute value 4π,

$$J_\nu = \frac{1}{4\pi} \int I_\nu \, d\Omega. \tag{D.30}$$

This part will treat the absorption of X-ray photons generated by decays of dark matter particles by hydrogen atoms of the interstellar medium. Such a scenario can be modeled by two surfaces exchanging radiant energy with flux directions parallel to normal vectors of the surfaces in a frequency range $(\nu, \nu + d\nu)$, a time interval dt and a confinement to a solid angle element $d\Omega$. The absorption measure can be defined as

$$\kappa_\nu \rho_{\mathrm{H}} I_\nu ds d\Omega dA dt d\nu, \tag{D.31}$$

wherein κ denotes an absorption coefficient, ds a line-of-sight element, I an intensity, and dA represents an infinitesimal area element. The emission measure can be defined as

$$j_\nu \rho_{\mathrm{dm}} ds d\Omega dA dt d\nu, \tag{D.32}$$

and features an emission coefficient j_ν and a dark matter density ρ_{dm}. The ratio between the emission coefficient and the absorption coefficient is a so-called source function $\mathcal{J}_\nu$, (11):

$$\mathcal{J}_\nu = \frac{j_\nu}{\kappa_\nu}. \tag{D.33}$$

The difference between the two afore-mentioned equations is equivalent to the amount of radiant energy in a frequency interval $(\nu, \nu+d\nu)$ which perpendicularly propagates relative to the two surfaces with respect to a time interval dt and to a solid angle $d\Omega$:

$$\frac{dI_\nu}{ds} ds d_\nu d_A d_\Omega dt = j_\nu \rho_{\rm dm} dA ds d\Omega dt d\nu - \kappa_\nu \rho_{\rm H} I_\nu ds d\Omega dA dt d\nu \tag{D.34}$$

$$\Leftrightarrow \qquad \frac{dI_\nu}{ds} = j_\nu \rho_{\rm dm} - \kappa_\nu \rho_{\rm H} I_\nu \tag{D.35}$$

$$\Leftrightarrow \qquad -\frac{dI_\nu}{\kappa \rho_{\rm H} ds} = -\frac{j_\nu}{\kappa_\nu} \frac{\rho_{\rm dm}(s,E)}{\rho_{\rm H}(E)} + I_\nu. \tag{D.36}$$

The last equation comprises a dark matter density distribution $\rho_{\rm dm}$ and the source function

$$\mathcal{J} := \frac{j_\nu}{\kappa_\nu} \frac{\rho_{\rm dm}}{\rho_{\rm H}}, \tag{D.37}$$

and leads to a so-called transfer equation

$$-\frac{dI_\nu}{\kappa_\nu \rho_{\rm H} ds} = -\mathcal{J}(s) + I_\nu. \tag{D.38}$$

The formal solution of this differential equation can be written as

$$I(E,s) = I(0)\exp(-\tau(s,0)) + \int_0^s \mathcal{J}(s')\kappa_{\rm H}\rho_{\rm H} \exp(-\tau(s,s'))\, ds' \tag{D.39}$$

$$= \int_0^s j_\nu \rho_{\rm dm}(s') \exp\left(-\int_{s'}^s \kappa_{\rm H}(E)\rho_{\rm H}(E)\, ds\right) ds', \tag{D.40}$$

for $I(0) = 0$ and an optical depth

$$\tau(s,s') = \int_{s'}^s \kappa_{\rm H}\rho_{\rm H}\, ds. \tag{D.41}$$

The isotropic emissivity ϵ_ν is defined as the as the energy emitted per unit frequency per unit time per unit mass into the full solid angle. The emission measure j_ν is defined as the emissivity times the mass density as $\frac{\epsilon_\nu \rho_{\rm dm}}{4\pi}$. In the case of two-body decays of the sterile neutrino $\left(E_\gamma = \frac{m_{\nu_s}}{2}\right)$ into photons, the emissivity can be written as

$$\epsilon_{\nu,DM} = \frac{1}{4\pi} \frac{E_\gamma \Gamma_s}{m_{\nu_s}} = \frac{1}{8\pi \tau_{\nu_s}}. \tag{D.42}$$

The foregoing equations join together into a final transfer equation for different distributions of the emitting and the absorbing medium with $j_\nu = \epsilon_{\nu,DM}\rho_{\text{dm}}$,

$$I(s,E) = \int_0^s \frac{\rho_{\text{dm}}(s')}{8\pi\tau_{\nu,s}} \exp\left(-\int_{s'}^s \kappa_{\text{H}}(E)\rho_{\text{H}}(E)\,ds\right) ds'. \tag{D.43}$$

The preceding equation for a vanishing absorption measure κ_ν results in an integral over the emission measure times the dark matter density distribution,

$$I(s) = \int_0^s j_\nu \rho_{\text{dm}}(s')\; ds' \tag{D.44}$$

$$= \int_0^s \frac{\rho_{\text{dm}}(s')}{8\pi\tau_{\nu,s}}\, ds' \tag{D.45}$$

$$= (8\pi\tau_{\nu_s})^{-1} S_{\text{dm}}(s), \tag{D.46}$$

wherein the dark matter column density is defined as

$$S_{\text{dm}}(s) := \int_0^s \rho_{\text{dm}}(s')\, ds', \tag{D.47}$$

in the case of a lack of absorption and

$$S_{\text{dm}}^{abs}(s,E) = \int_0^s \rho_{\text{dm}}(s') \exp\left(-\int_{s'}^s \kappa_{\text{H}}(E)\rho_{\text{H}}(E)\,ds\right) ds', \tag{D.48}$$

comprising a contribution by an absorbing medium (hydrogen, for example). As a measure for the energy per unit area and per unit time, the flux is defined as the intensity integrated over the solid angle according to Rybicki et al. (10),

$$F = \int I\cos(\theta)\, d\Omega, \tag{D.49}$$

wherein θ is the angle between the normal vector of the area dA and the propagation direction of the radiation passing this area. For small angles or $\theta \to 0$ the cosine of θ is close to 1 such that the preceding equation simplifies to

$$F = \int I\, d\Omega, \tag{D.50}$$

or in the case of an intensity independent of the direction of the corresponding solid angle,

$$F = I\int d\Omega = I\Delta\Omega. \tag{D.51}$$

The field of view of the X-ray satellite XMM-Newton is roughly $2\theta = 30'$ or $\theta \approx 8.73 \cdot 10^{-3}$ rad in diameter so that a cosine of this number would result in $\cos(\theta) \approx 0.99996$ which is close enough to 1 to justify the approximation stated before. A further helpful value is the average intensity (10) which is defined as

$$\langle I \rangle = \frac{\int I \cos(\theta)\, d\Omega}{\int d\Omega} = \frac{F}{\Delta\Omega}. \tag{D.52}$$

A photoelectric absorption model provided by Morrison et al. (9) was investigated in the scope of the present analysis. Morrison et al. (9) disclose a function describing an effective absorption cross section per hydrogen atom in an energy range of $E \in [0.03, 10]$ keV in the interstellar medium,

$$\sigma_{\mathrm{H}} = (c_0 + c_1 E + c_2 E^2) E^{-3} \cdot 10^{-24}\,\mathrm{keV\,cm^2} \quad (E \text{ in keV}). \tag{D.53}$$

Since the effect of absorption in view of the above model is dominating in an energy regime lower than $2\,$keV, such an absorption model was not applied to the additive component or emission line in the course of the present work. This was also necessary to keep the required computational time in a suitable frame.

8.5 Appendix E. Spatial Distribution of Fitted Parameters

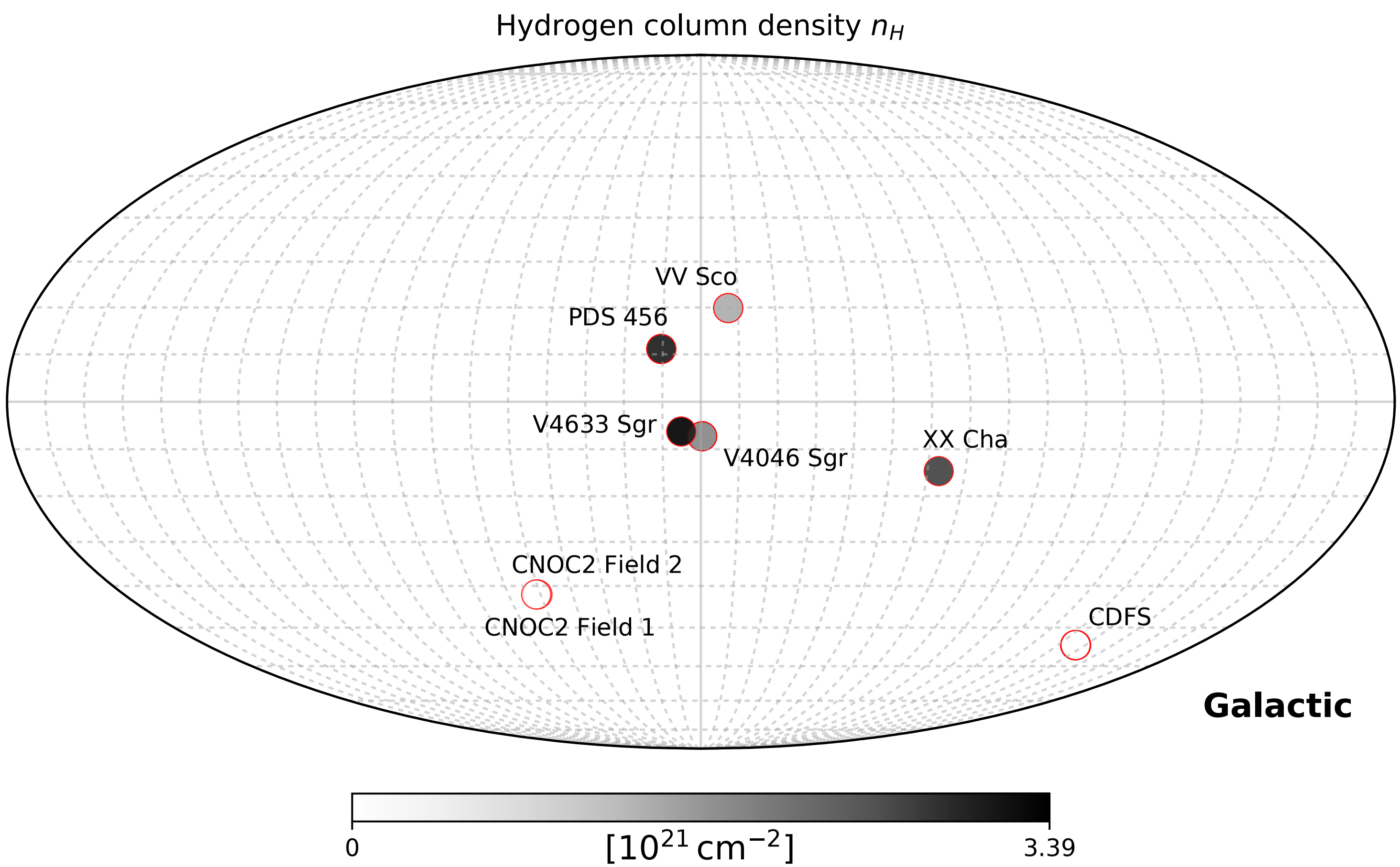

Figure E.1: The plot shows an all-sky map comprising the spatial distribution of the fitted hydrogen column densities $\mathrm{n}_{\mathrm{H},i}^{\mathbf{D_1}}$ corresponding to pointings of $\mathbf{D_1}$ (see tables 4.1 and 5.1) wherein each colored dot matches the Galactic coordinates corresponding to a data set. Furthermore, the color of a dot related to an ith data set corresponds to the individual fitted hydrogen column densities $\mathrm{n}_{\mathrm{H},i}^{\mathbf{D_1}}$.

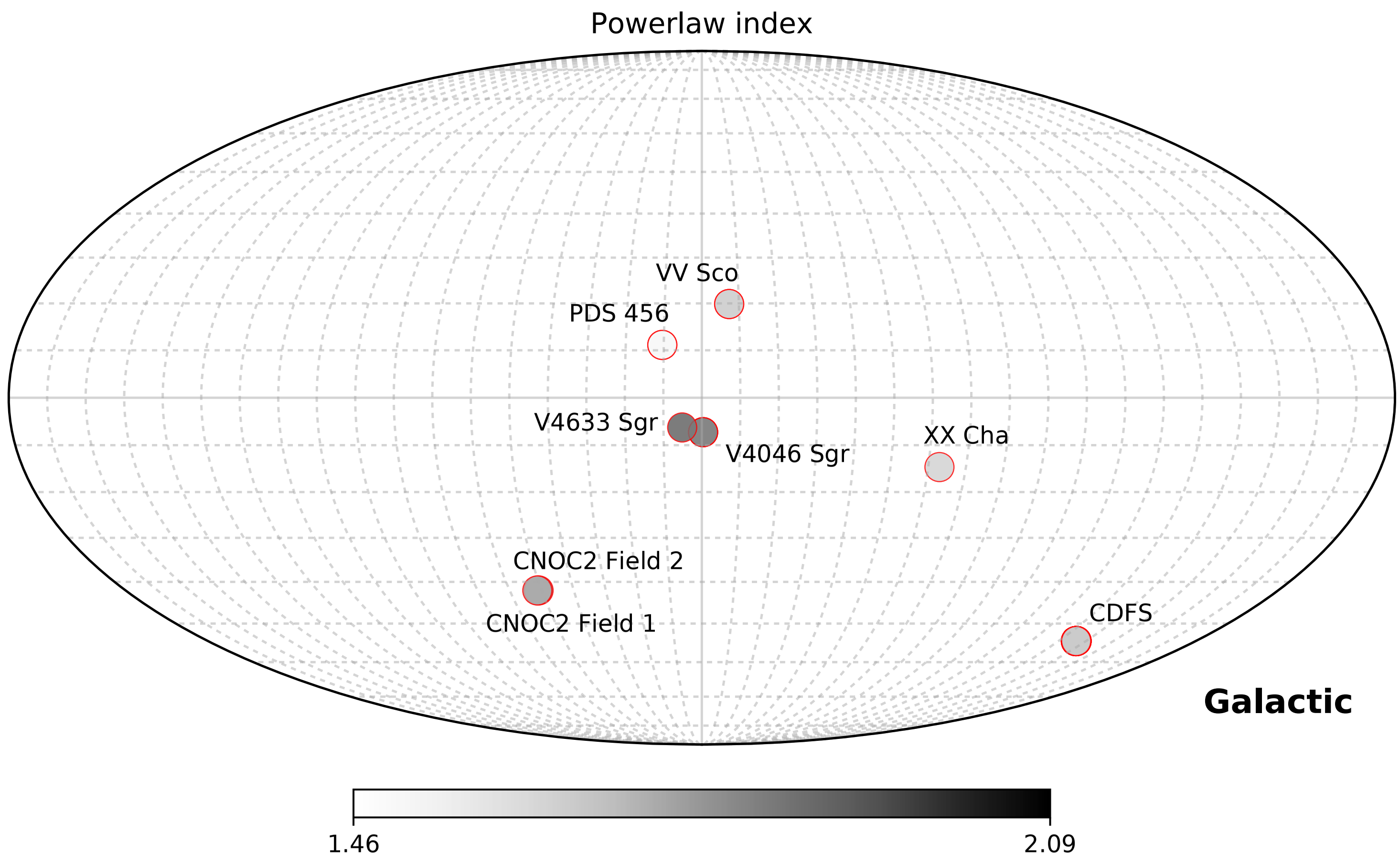

Figure E.2: The plot shows an all-sky map comprising the spatial distribution of the fitted dimensionless photon indices $\Gamma_i^{\mathbf{D_1}}$ of related powerlaw components corresponding to pointings of $\mathbf{D_1}$ (see tables 4.1 and 5.1) wherein each colored dot matches the Galactic coordinates corresponding to a data set. Furthermore, the color of a dot related to an ith data set corresponds to the individual fitted dimensionless photon indices $\Gamma_i^{\mathbf{D_1}}$.

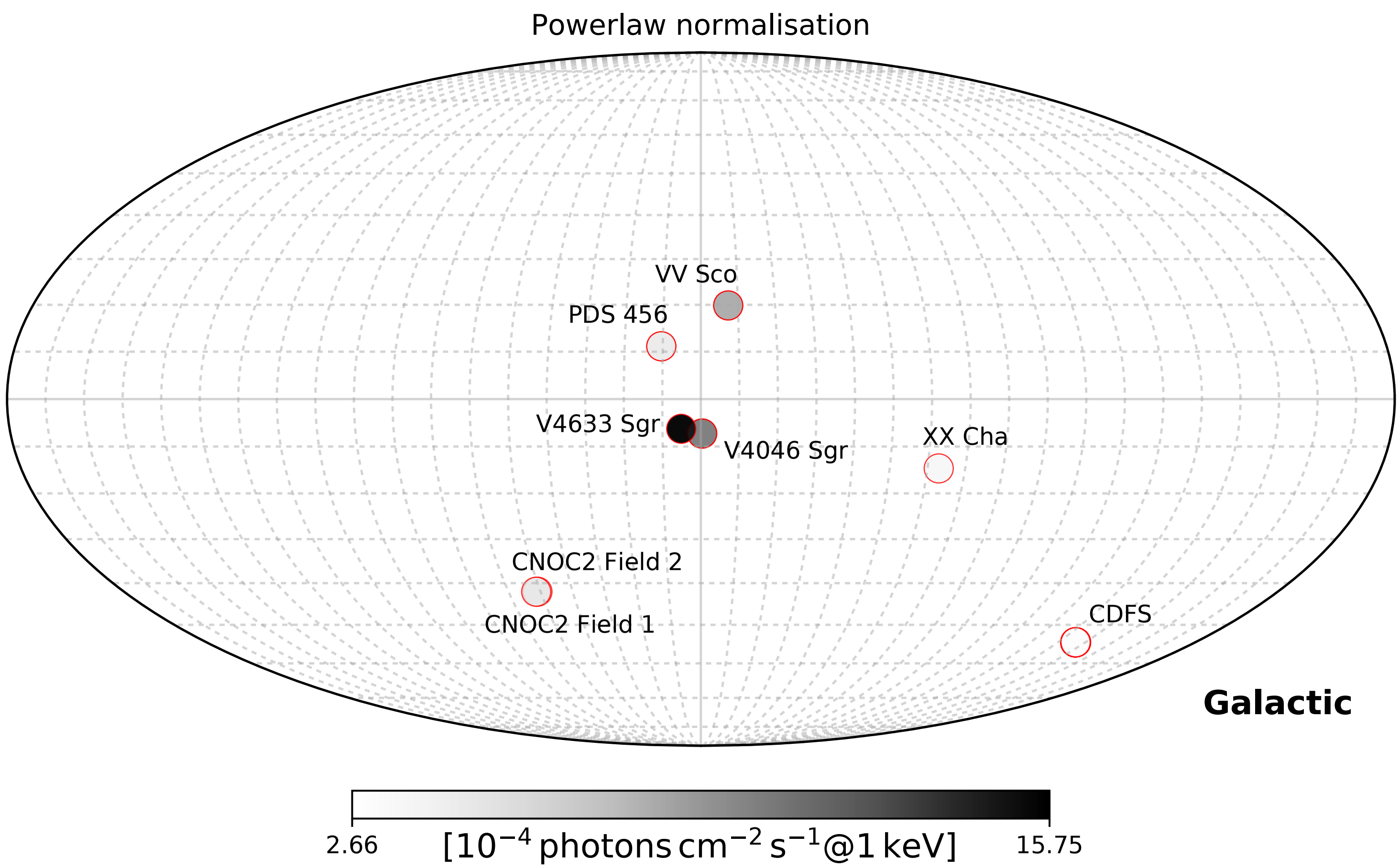

Figure E.3: The plot shows an all-sky map comprising the spatial distribution of the fitted normalisations $\mathrm{N}_{pow;i}^{\mathbf{D_1}}$ of related powerlaw components corresponding to pointings of $\mathbf{D_1}$ (see tables 4.1 and 5.1) wherein each colored dot matches the Galactic coordinates corresponding to a data set. Furthermore, the color of a dot related to an ith data set corresponds to the individual fitted normalisations $\mathrm{N}_{pow;i}^{\mathbf{D_1}}$.

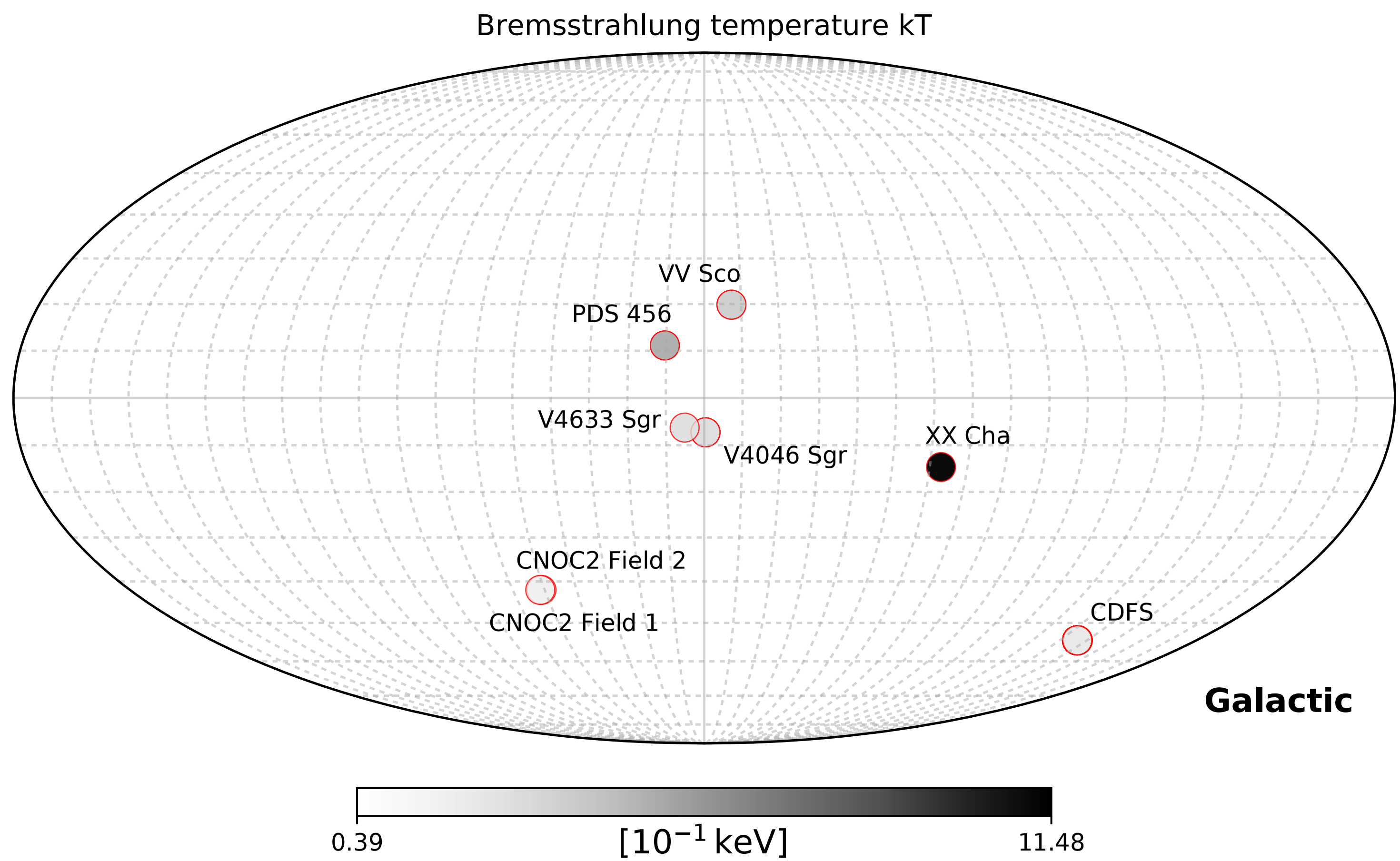

Figure E.4: The plot shows an all-sky map comprising the spatial distribution of the fitted temperatures $\mathrm{T}_i^{\mathbf{D_1}}$ of thermal bremsstrahlung components corresponding to pointings of $\mathbf{D_1}$ (see tables 4.1 and 5.1) wherein each colored dot matches the Galactic coordinates corresponding to a data set. Furthermore, the color of a dot related to an ith data set corresponds to the individual fitted temperatures $\mathrm{T}_i^{\mathbf{D_1}}$.

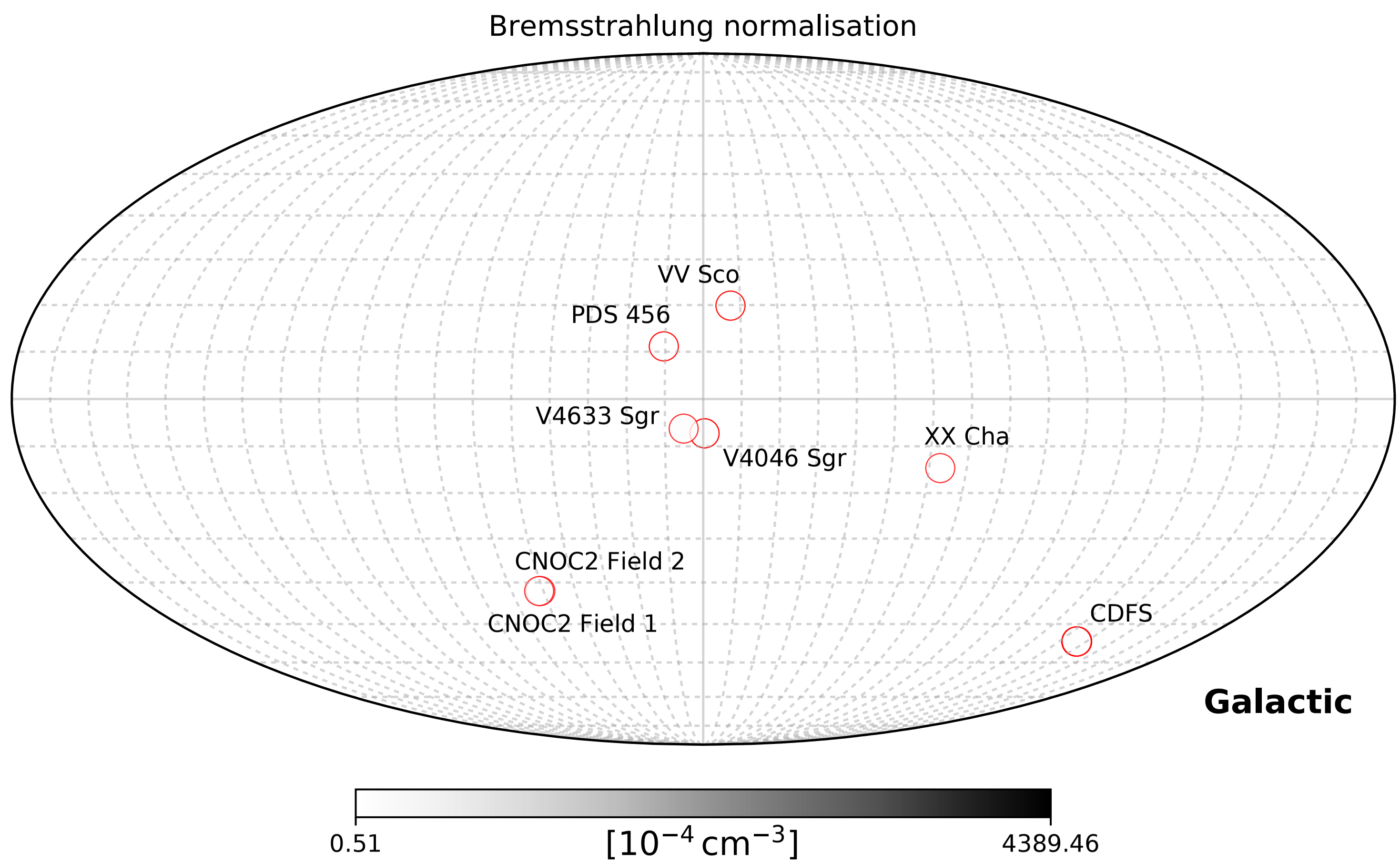

Figure E.5: The plot shows an all-sky map comprising the spatial distribution of the fitted normalisation $\mathrm{N}_{bremss;i}^{\mathbf{D_1}}$ of thermal bremsstrahlung components corresponding to pointings of $\mathbf{D_1}$ (see tables 4.1 and 5.1) wherein each colored dot matches the Galactic coordinates corresponding to a data set. Furthermore, the color of a dot related to an ith data set corresponds to the individual fitted normalisations $\mathrm{N}_{bremss;i}^{\mathbf{D_1}}$.

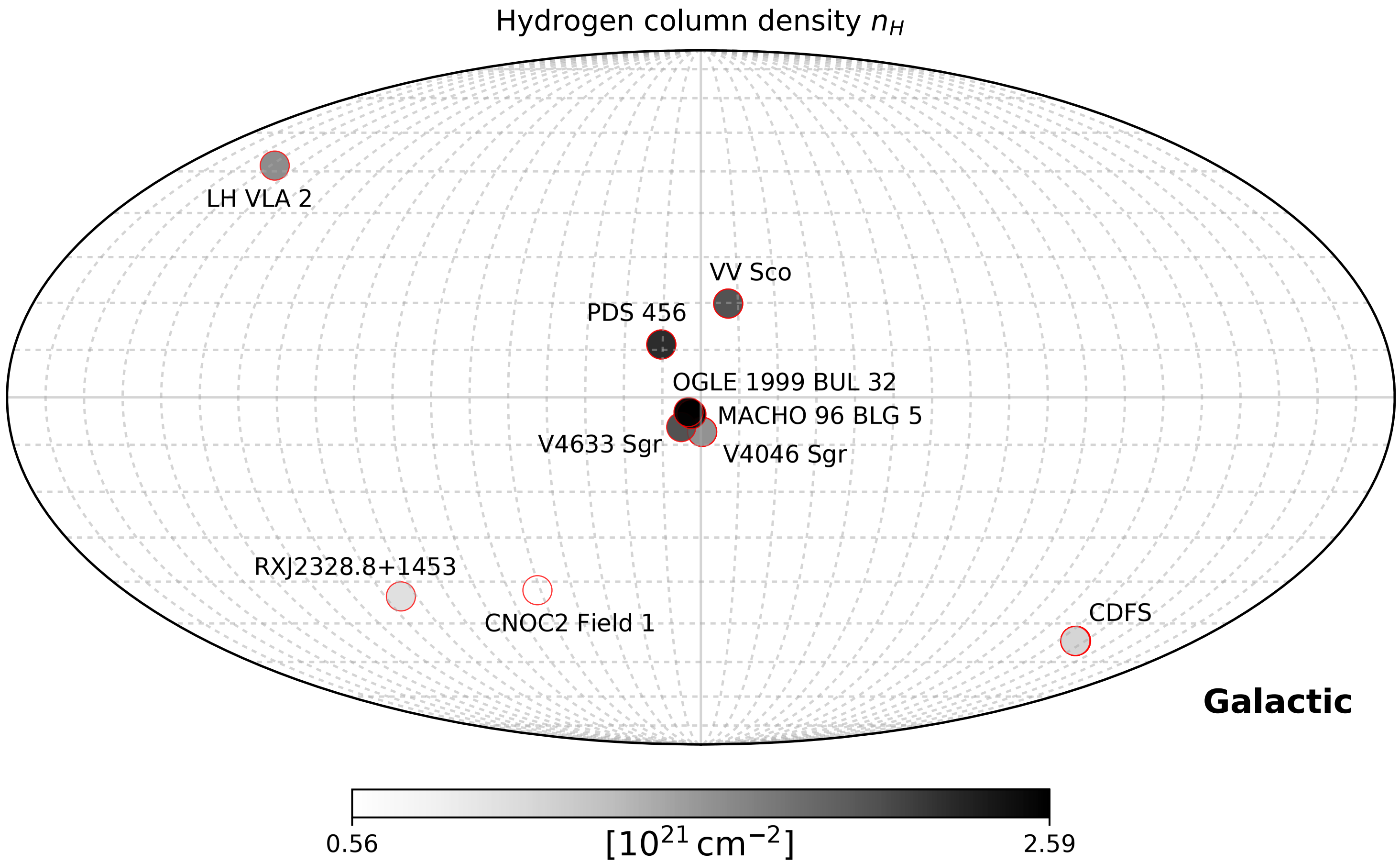

Figure E.6: The plot shows an all-sky map comprising the spatial distribution of the fitted hydrogen column densities $n_{H,i}^{\mathbf{D_2}}$ corresponding to pointings of $\mathbf{D_2}$ (see tables 4.2 and 5.3) wherein each colored dot matches the Galactic coordinates corresponding to a data set. Furthermore, the color of a dot related to an ith data set corresponds to the individual fitted hydrogen column densities $n_{H,i}^{\mathbf{D_2}}$.

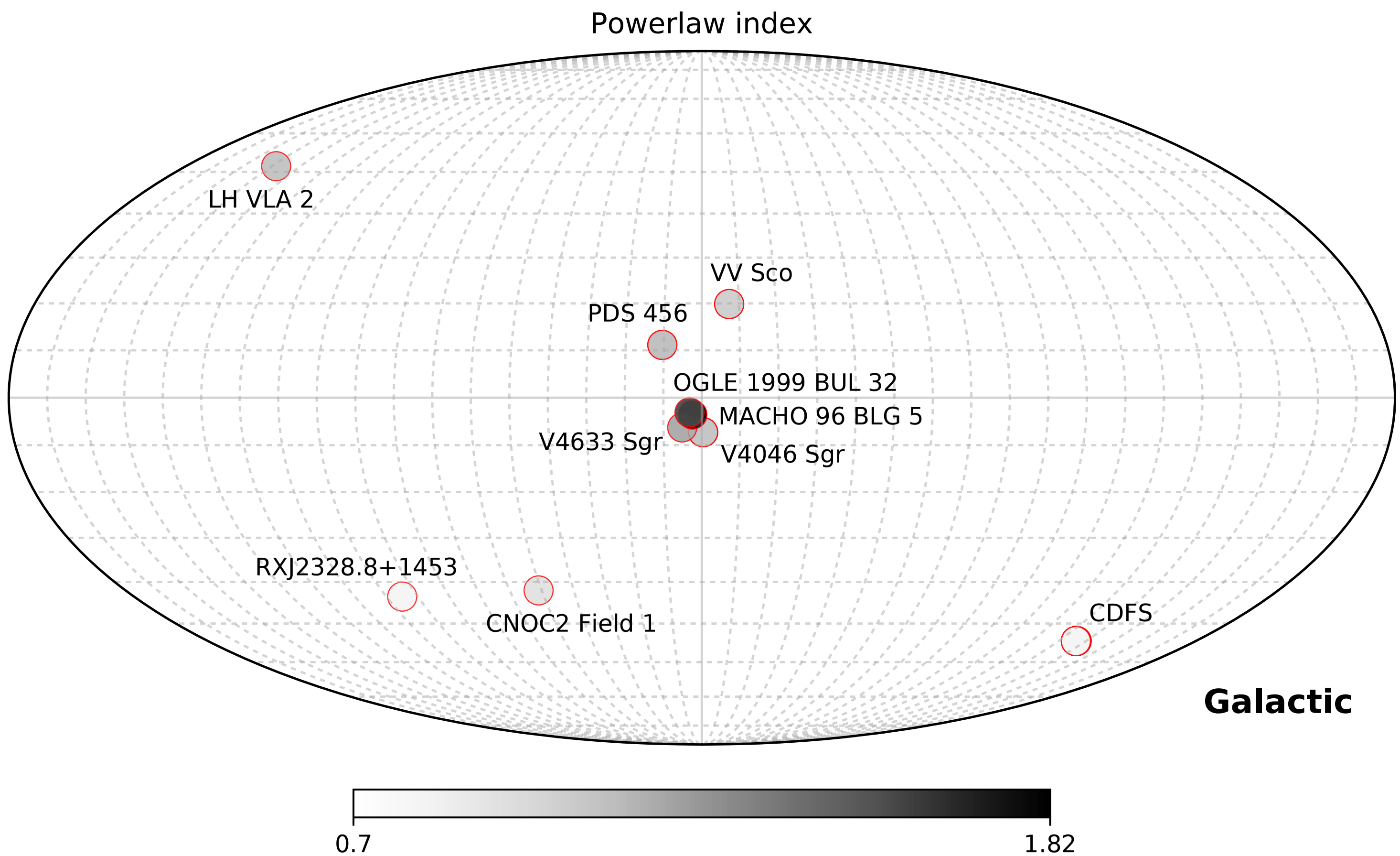

Figure E.7: The plot shows an all-sky map comprising the spatial distribution of the fitted dimensionless photon indices $\Gamma_i^{\mathbf{D_2}}$ of related powerlaw components corresponding to pointings of $\mathbf{D_2}$ (see tables 4.2 and 5.3) wherein each colored dot matches the Galactic coordinates corresponding to a data set. Furthermore, the color of a dot related to an ith data set corresponds to the individual fitted dimensionless photon indices $\Gamma_i^{\mathbf{D_2}}$.

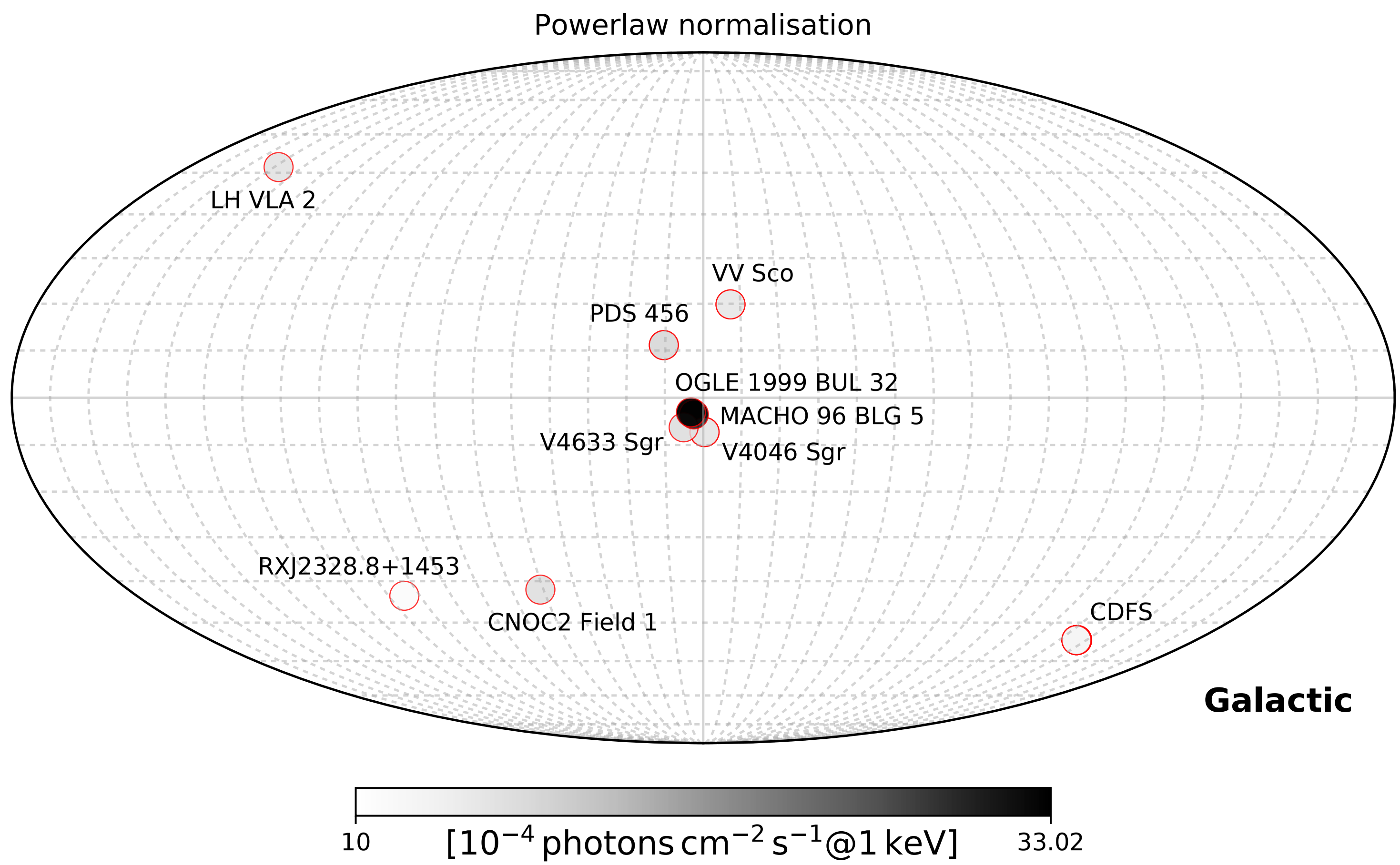

Figure E.8: The plot shows an all-sky map comprising the spatial distribution of the fitted normalisations $N^{\mathbf{D_2}}_{pow;i}$ of related powerlaw components corresponding to pointings of $\mathbf{D_2}$ (see tables 4.2 and 5.3) wherein each colored dot matches the Galactic coordinates corresponding to a data set. Furthermore, the color of a dot related to an ith data set corresponds to the individual fitted normalisations $N^{\mathbf{D_2}}_{pow;i}$.

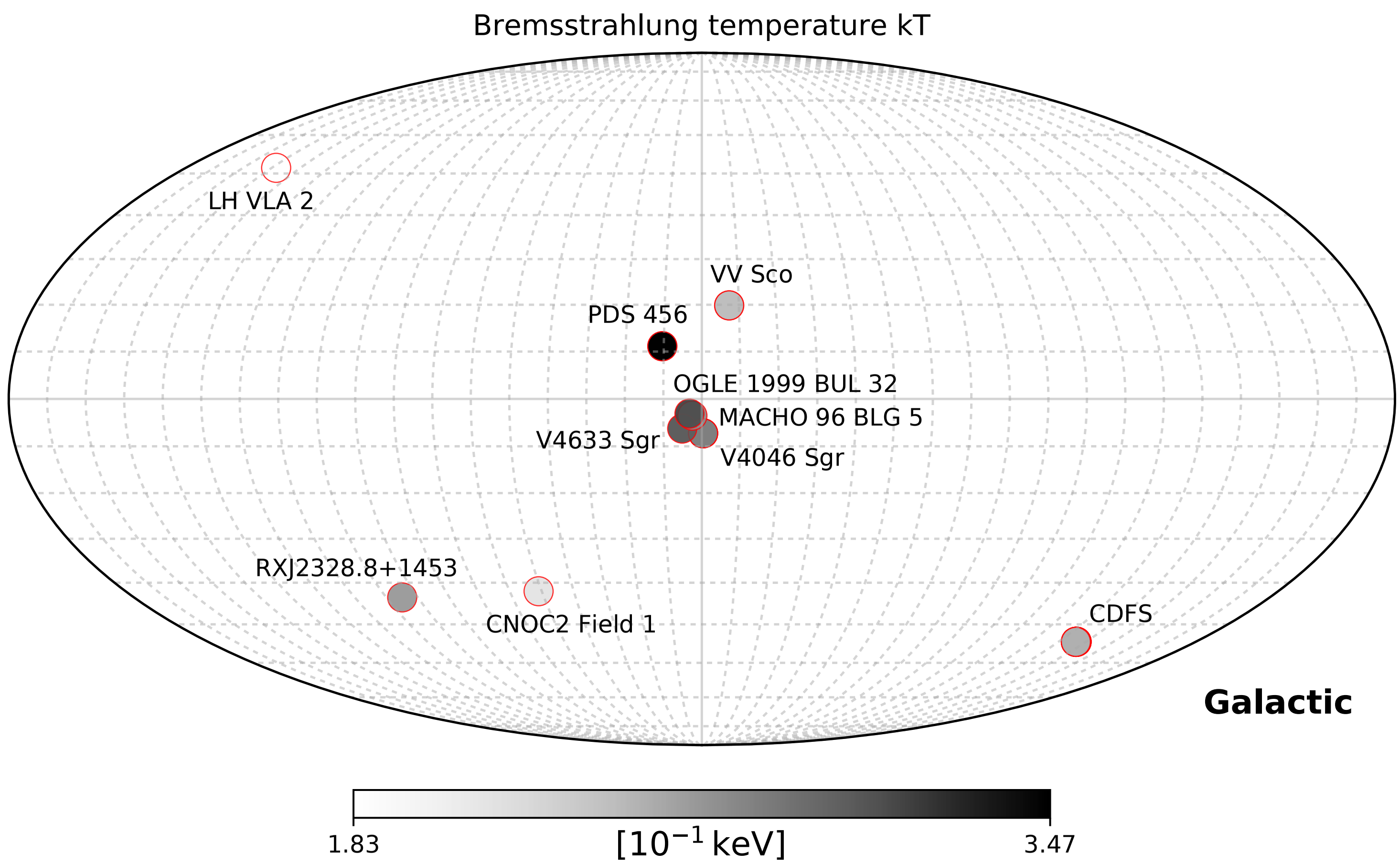

Figure E.9: The plot shows an all-sky map comprising the spatial distribution of the fitted temperatures $T_i^{\mathbf{D_2}}$ of thermal bremsstrahlung components corresponding to pointings of $\mathbf{D_2}$ (see tables 4.2 and 5.3) wherein each colored dot matches the Galactic coordinates corresponding to a data set. Furthermore, the color of a dot related to an ith data set corresponds to the individual fitted temperatures $T_i^{\mathbf{D_2}}$.

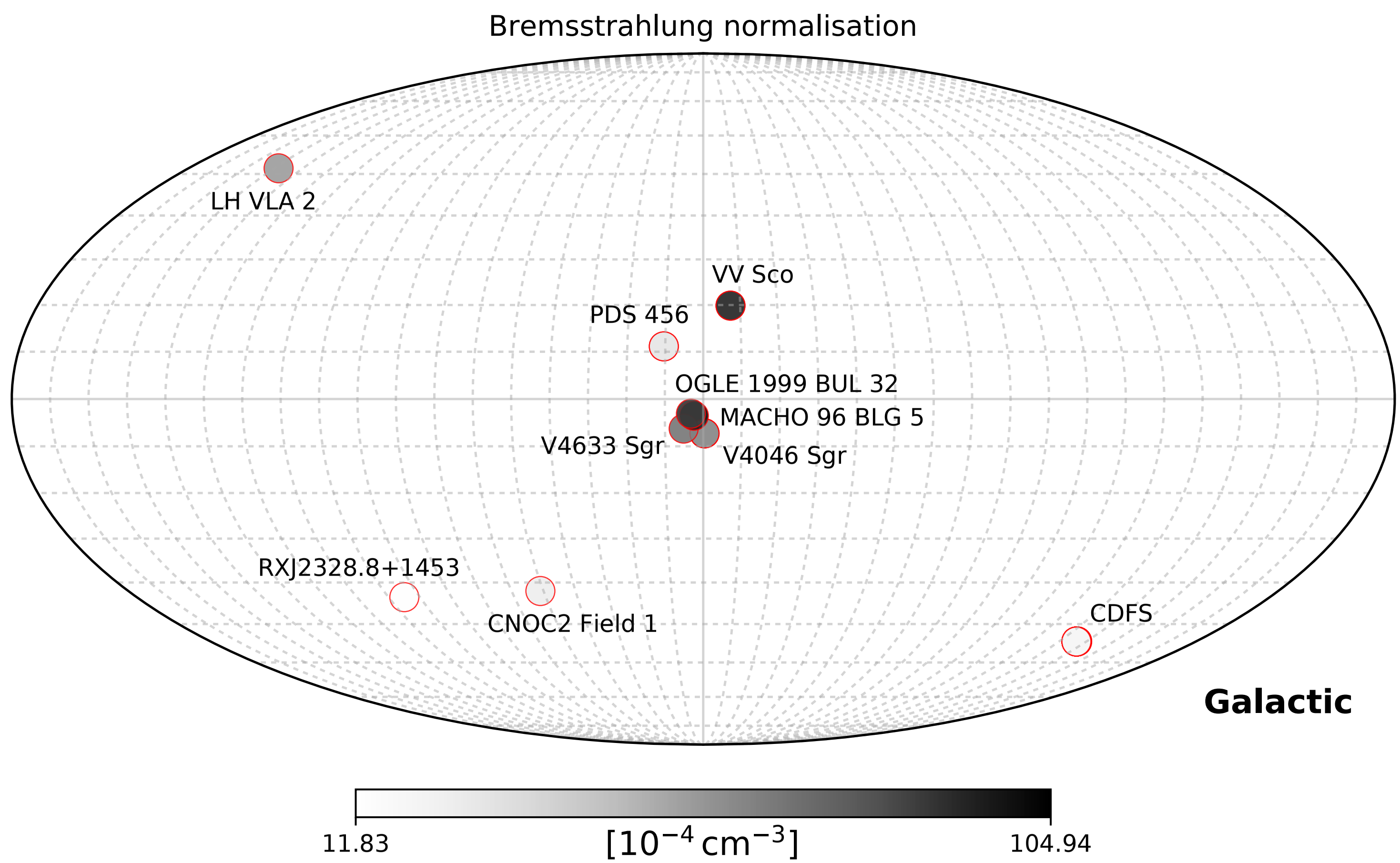

Figure E.10: The plot shows an all-sky map comprising the spatial distribution of the fitted normalisation $N^{\mathbf{D_2}}_{bremss;i}$ of thermal bremsstrahlung components corresponding to pointings of $\mathbf{D_2}$ (see tables 4.2 and 5.3) wherein each colored dot matches the Galactic coordinates corresponding to a data set. Furthermore, the color of a dot related to an ith data set corresponds to the individual fitted normalisations $N^{\mathbf{D_2}}_{bremss;i}$.

8.6 Appendix F. Spectral Models

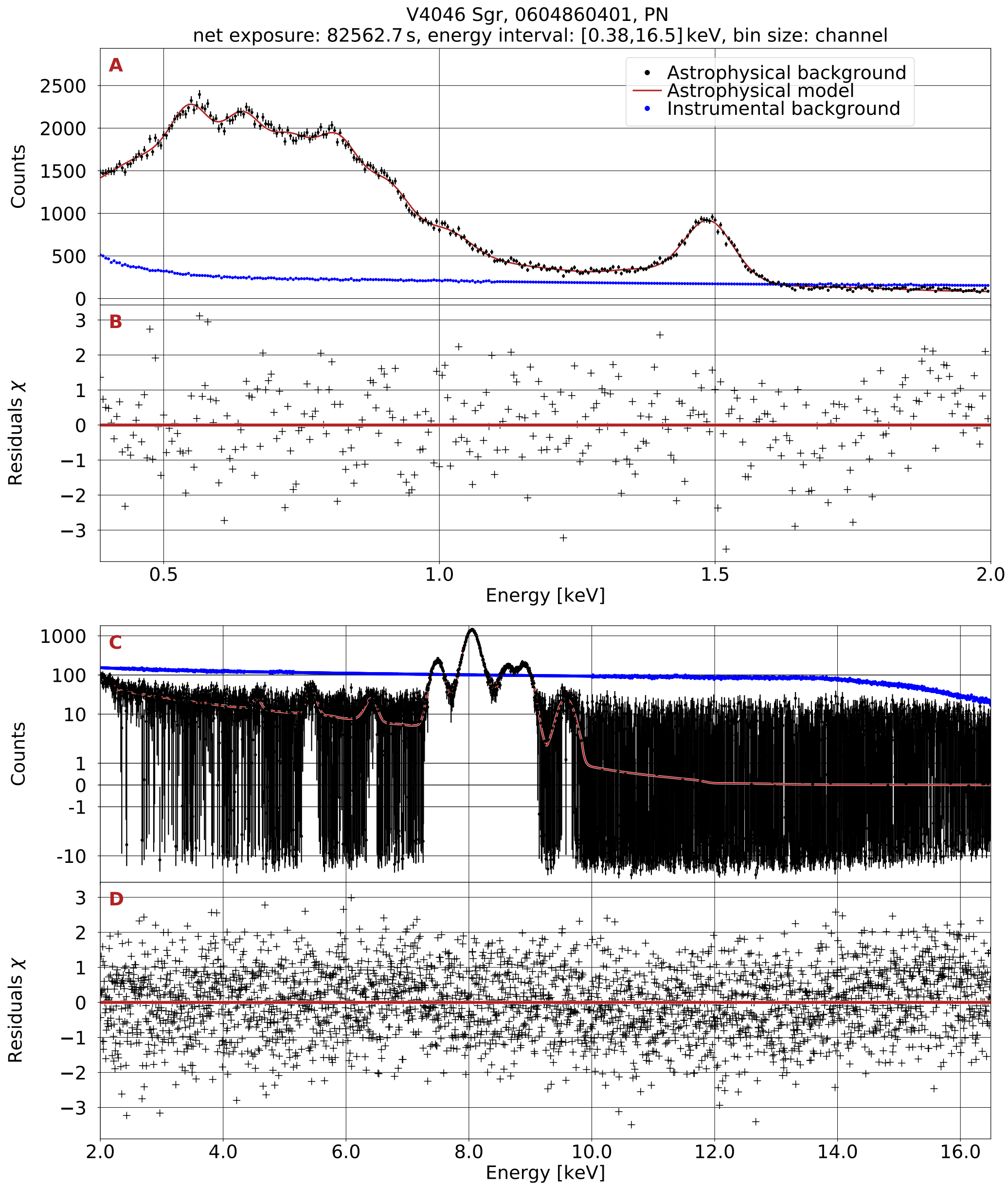

Figure F.1: The panels A and C show the measured spectrum of the data set 0604860401 ($i = 1$, $\mathbf{D_1}$, table 4.1) as black error bars and its fitted null hypothesis model $m_0^{\mathbf{D_1}}$ in an energy range from 0.38 keV to 2 keV (panels A and B) and from 2 keV to 16.5 keV (panels C and D) as red lines, respectively, while the blue error bars show the instrumental background model. The best-fit values are specified in tables 5.1 and 5.2. The panels B and D show the residuals per energy bin in values of $\chi = \mathrm{sgn}(\mathrm{Data} - \mathrm{Model})\sqrt{(\mathrm{Data} - \mathrm{Model})^2}$.

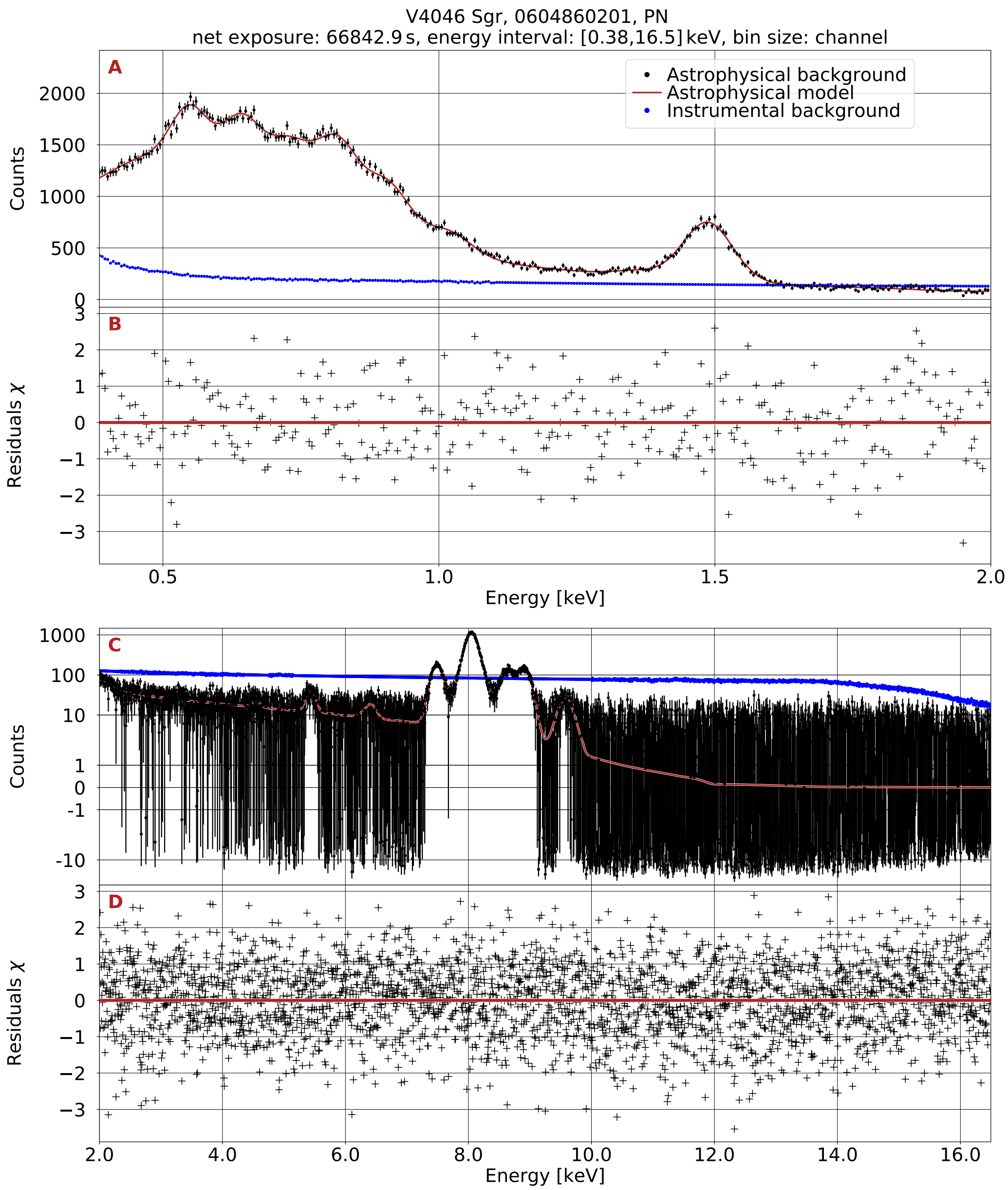

Figure F.2: The panels A and C show the measured spectrum of the data set 0604860201 ($i = 3$, $\mathbf{D_1}$, table 4.1) as black error bars and its fitted null hypothesis model $m_0^{\mathbf{D_1}}$ in an energy range from $0.38\,\mathrm{keV}$ to $2\,\mathrm{keV}$ (panels A and B) and from $2\,\mathrm{keV}$ to $16.5\,\mathrm{keV}$ (panels C and D) as red lines, respectively, while the blue error bars show the instrumental background model. The best-fit values are specified in tables 5.1 and 5.2. The panels B and D show the residuals per energy bin in values of $\chi = \mathrm{sgn}(\mathrm{Data} - \mathrm{Model})\sqrt{(\mathrm{Data} - \mathrm{Model})^2}$.

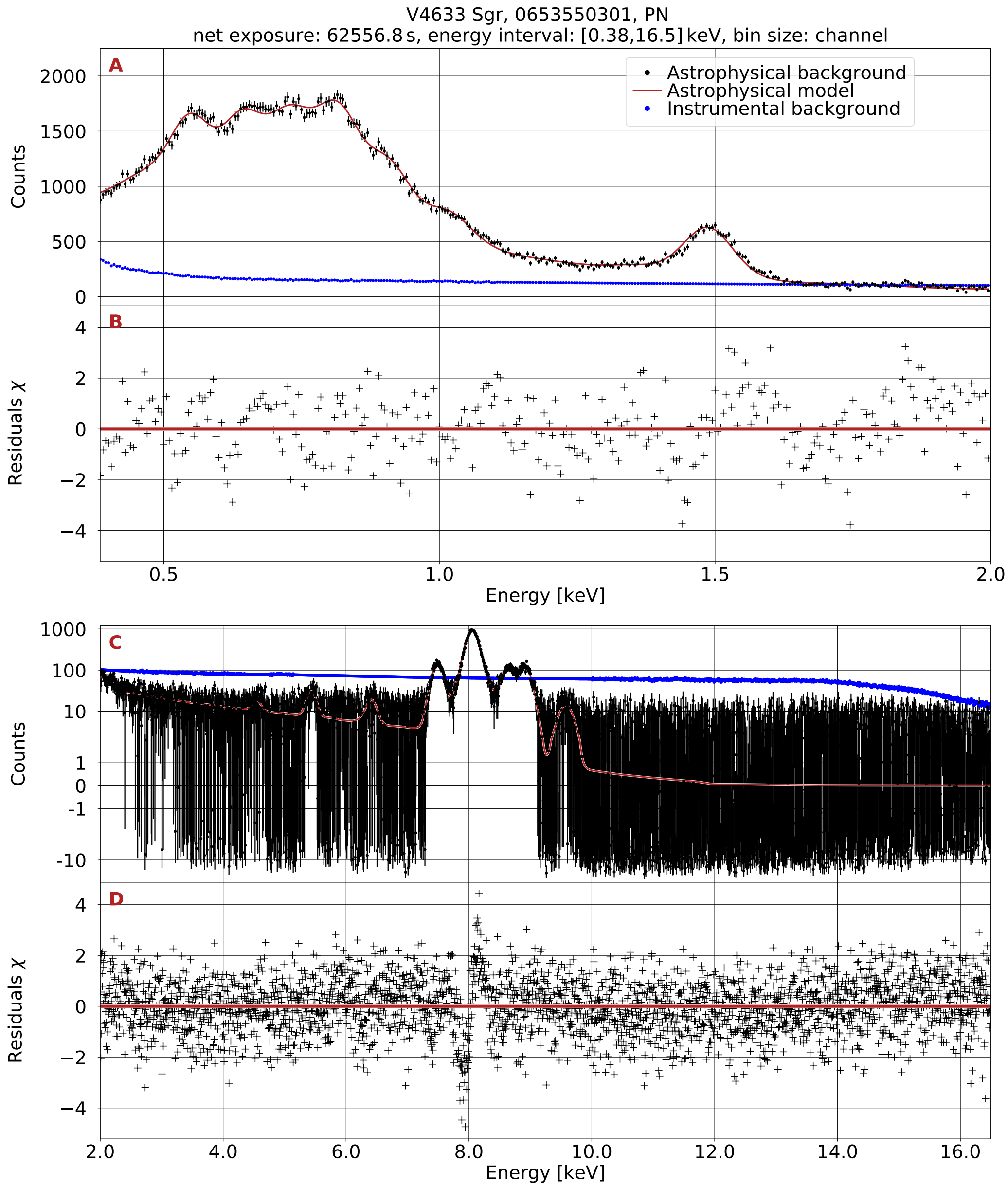

Figure F.3: The panels A and C show the measured spectrum of the data set 0653550301 (i = 4, $\mathbf{D_1}$, table 4.1) as black error bars and its fitted null hypothesis model $m_0^{\mathbf{D_1}}$ in an energy range from 0.38 keV to 2 keV (panels A and B) and from 2 keV to 16.5 keV (panels C and D) as red lines, respectively, while the blue error bars show the instrumental background model. The best-fit values are specified in tables 5.1 and 5.2. The panels B and D show the residuals per energy bin in values of $\chi = \mathrm{sgn}(\mathrm{Data} - \mathrm{Model})\sqrt{(\mathrm{Data} - \mathrm{Model})^2}$.

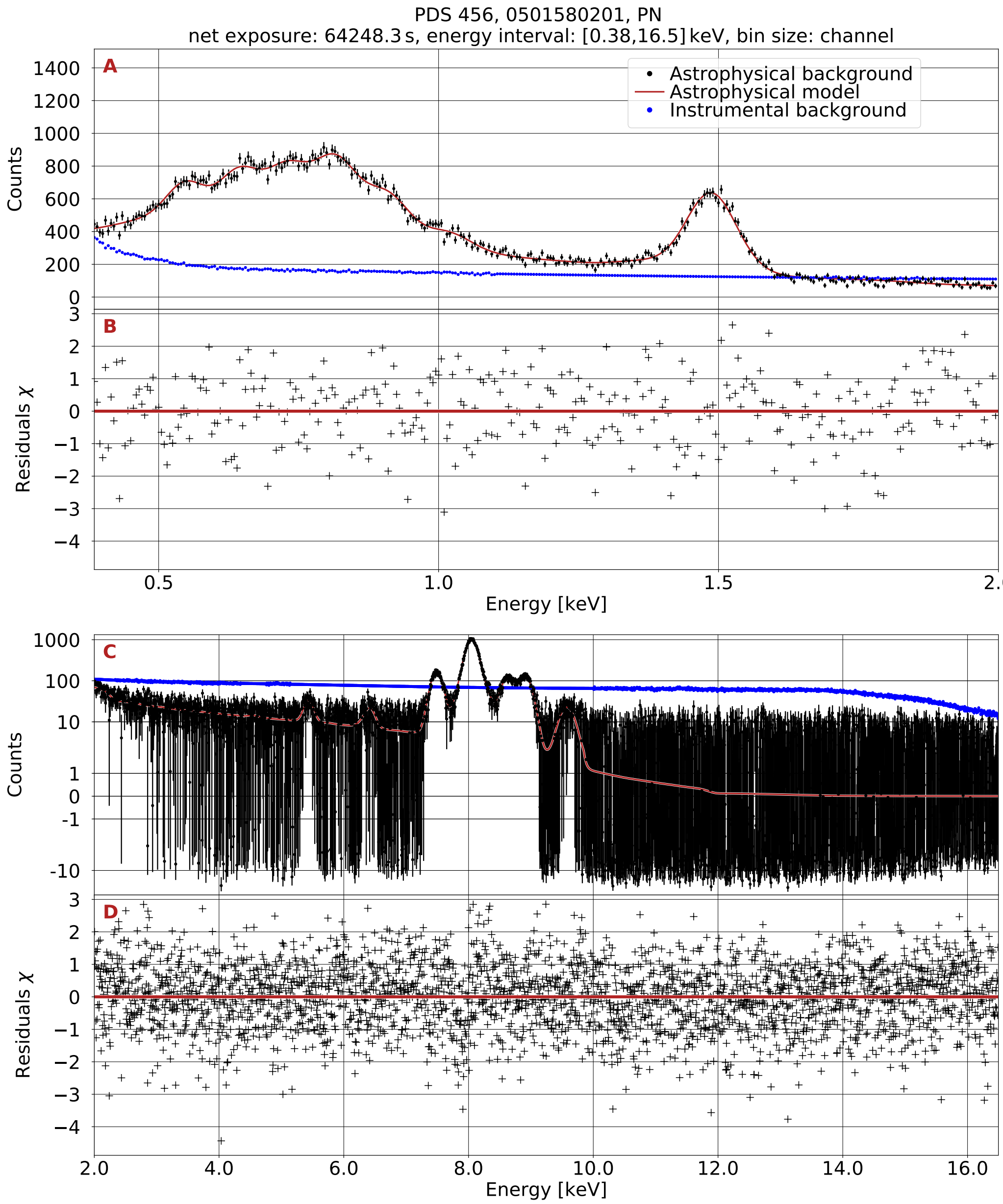

Figure F.4: The panels A and C show the measured spectrum of the data set 0501580201 ($i = 5$, $\mathbf{D_1}$, table 4.1) as black error bars and its fitted null hypothesis model $m_0^{\mathbf{D_1}}$ in an energy range from $0.38\,\mathrm{keV}$ to $2\,\mathrm{keV}$ (panels A and B) and from $2\,\mathrm{keV}$ to $16.5\,\mathrm{keV}$ (panels C and D) as red lines, respectively, while the blue error bars show the instrumental background model. The best-fit values are specified in tables 5.1 and 5.2. The panels B and D show the residuals per energy bin in values of $\chi = \mathrm{sgn}(\mathrm{Data} - \mathrm{Model})\,\sqrt{(\mathrm{Data} - \mathrm{Model})^2}$.

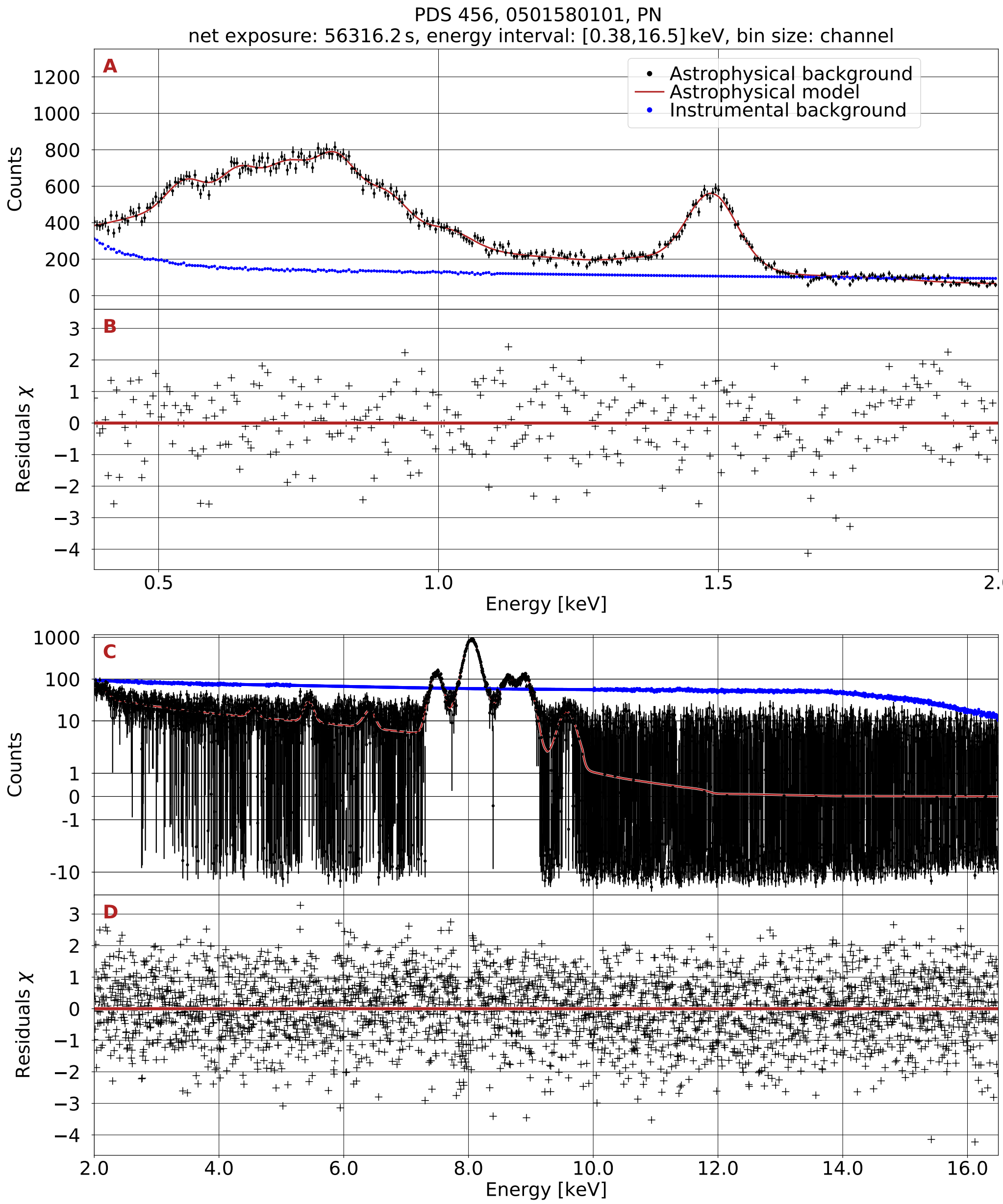

Figure F.5: The panels A and C show the measured spectrum of the data set 0501580101 ($i = 6$, $\mathbf{D_1}$, table 4.1) as black error bars and its fitted null hypothesis model $m_0^{\mathbf{D_1}}$ in an energy range from $0.38\,\mathrm{keV}$ to $2\,\mathrm{keV}$ (panels A and B) and from $2\,\mathrm{keV}$ to $16.5\,\mathrm{keV}$ (panels C and D) as red lines, respectively, while the blue error bars show the instrumental background model. The best-fit values are specified in tables 5.1 and 5.2. The panels B and D show the residuals per energy bin in values of $\chi = \mathrm{sgn}(\mathrm{Data} - \mathrm{Model})\,\sqrt{(\mathrm{Data} - \mathrm{Model})^2}$.

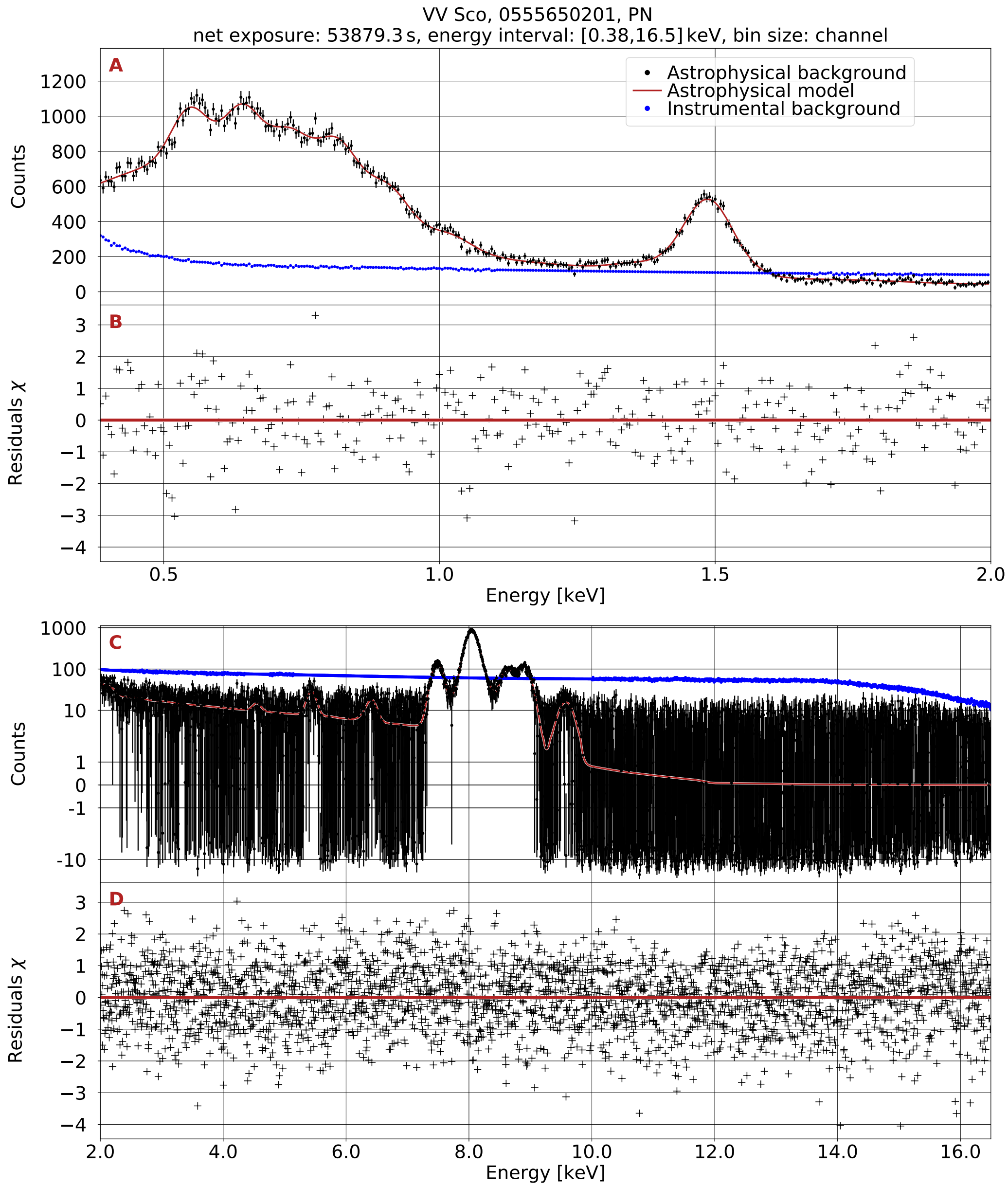

Figure F.6: The panels A and C show the measured spectrum of the data set 0555650201 ($i = 7$, $\mathbf{D_1}$, table 4.1) as black error bars and its fitted null hypothesis model $m_0^{\mathbf{D_1}}$ in an energy range from 0.38 keV to 2 keV (panels A and B) and from 2 keV to 16.5 keV (panels C and D) as red lines, respectively, while the blue error bars show the instrumental background model. The best-fit values are specified in tables 5.1 and 5.2. The panels B and D show the residuals per energy bin in values of $\chi = \mathrm{sgn}(\mathrm{Data} - \mathrm{Model})\sqrt{(\mathrm{Data} - \mathrm{Model})^2}$.

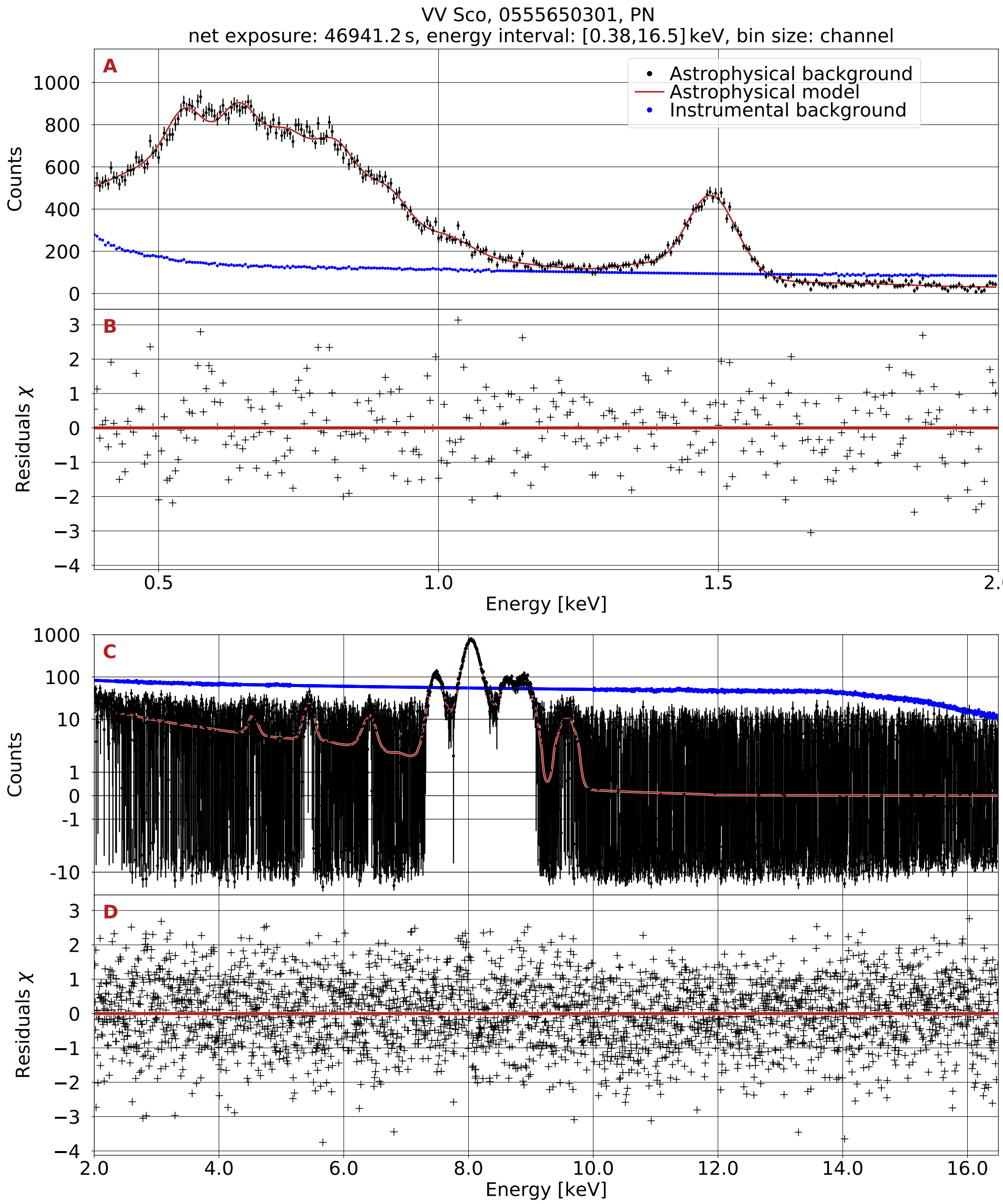

Figure F.7: The panels A and C show the measured spectrum of the data set 0555650301 ($i = 8$, $\mathbf{D_1}$, table 4.1) as black error bars and its fitted null hypothesis model $m_0^{\mathbf{D_1}}$ in an energy range from $0.38\,\text{keV}$ to $2\,\text{keV}$ (panels A and B) and from $2\,\text{keV}$ to $16.5\,\text{keV}$ (panels C and D) as red lines, respectively, while the blue error bars show the instrumental background model. The best-fit values are specified in tables 5.1 and 5.2. The panels B and D show the residuals per energy bin in values of $\chi = \text{sgn}(\text{Data} - \text{Model})\,\sqrt{(\text{Data} - \text{Model})^2}$.

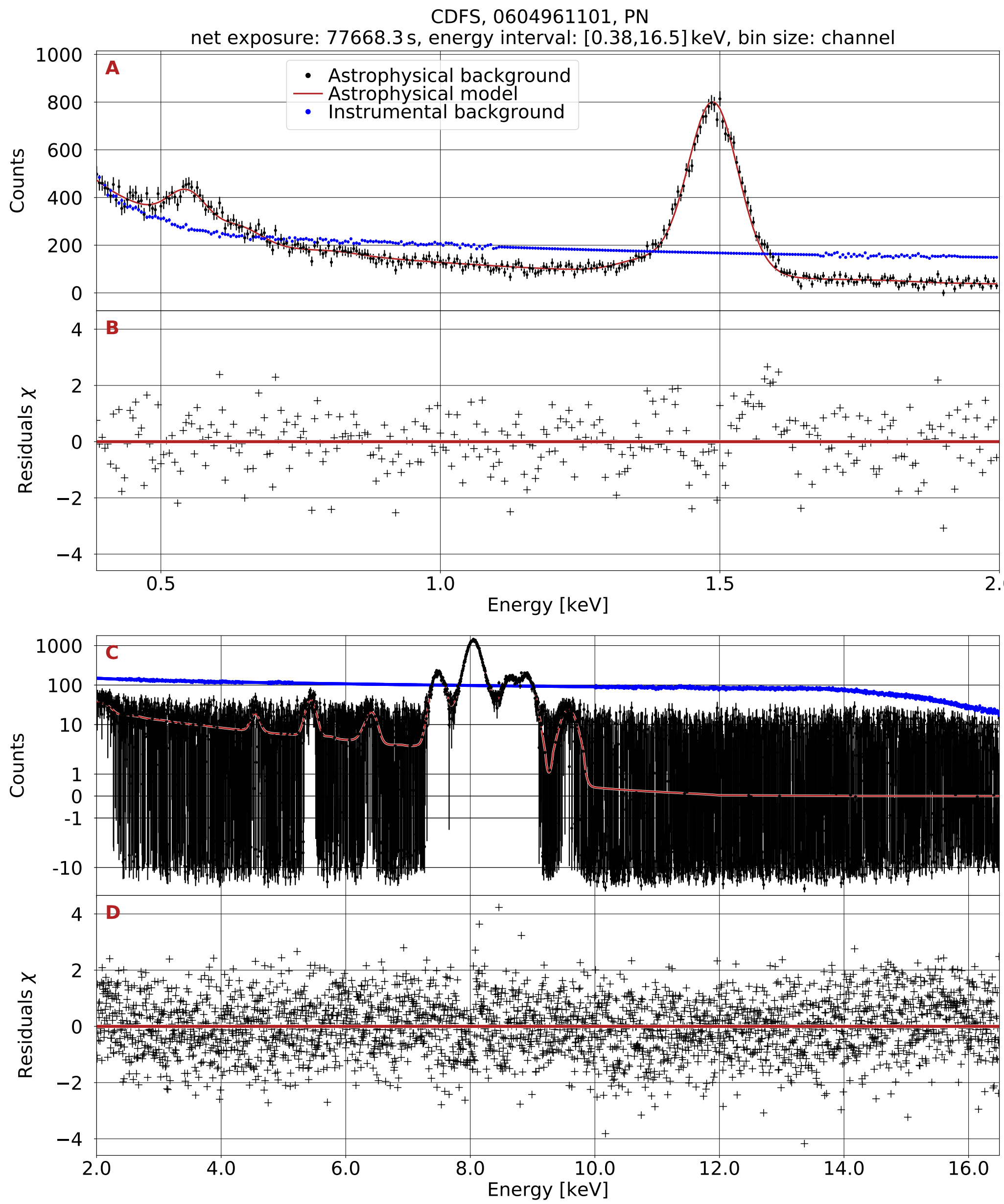

Figure F.8: The panels A and C show the measured spectrum of the data set 0604961101 ($i = 9$, $\mathbf{D_1}$, table 4.1) as black error bars and its fitted null hypothesis model $m_0^{\mathbf{D_1}}$ in an energy range from $0.38\,\mathrm{keV}$ to $2\,\mathrm{keV}$ (panels A and B) and from $2\,\mathrm{keV}$ to $16.5\,\mathrm{keV}$ (panels C and D) as red lines, respectively, while the blue error bars show the instrumental background model. The best-fit values are specified in tables 5.1 and 5.2. The panels B and D show the residuals per energy bin in values of $\chi = \mathrm{sgn}(\mathrm{Data} - \mathrm{Model})\sqrt{(\mathrm{Data} - \mathrm{Model})^2}$.

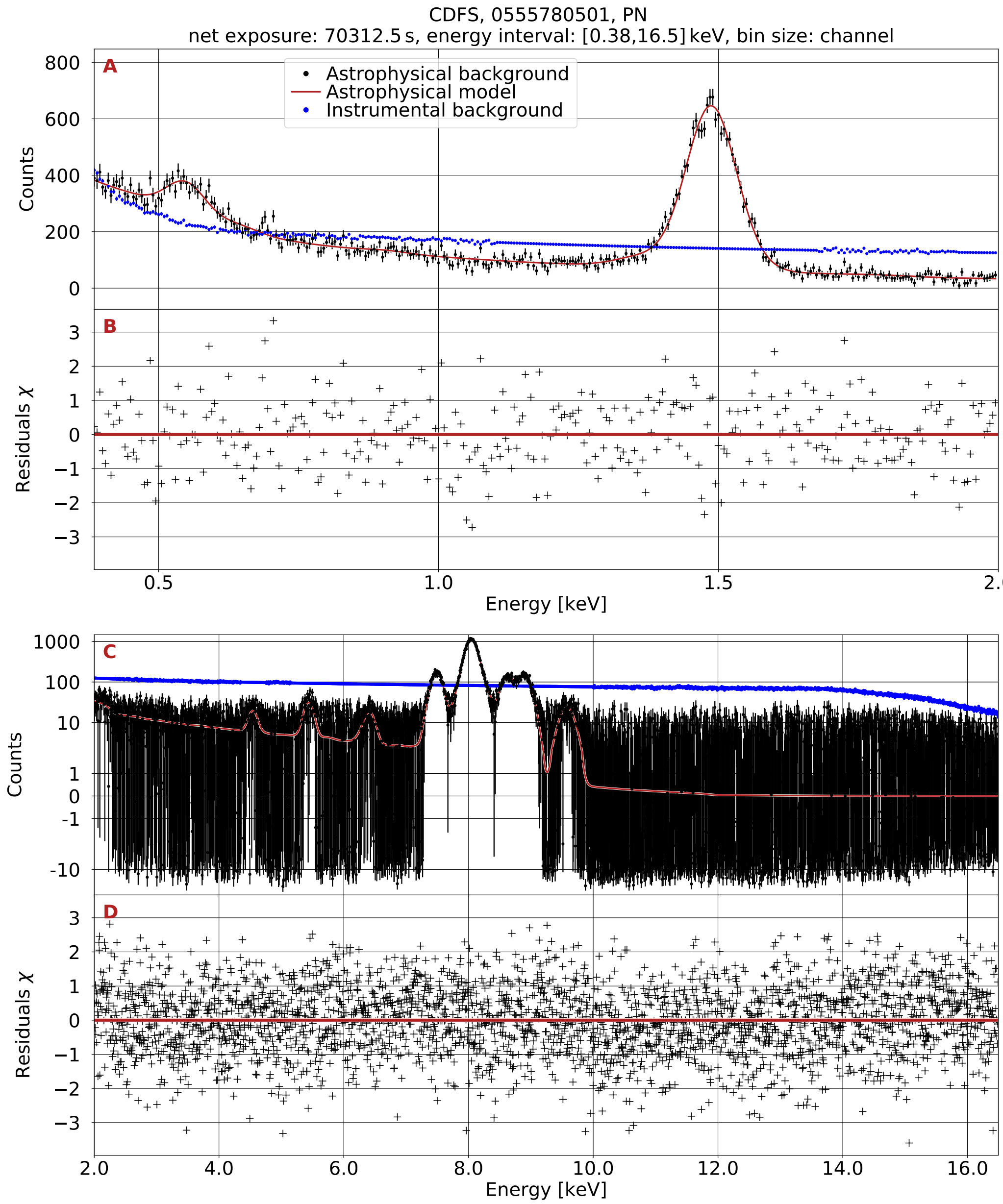

Figure F.9: The panels A and C show the measured spectrum of the data set 0555780501 ($i = 10$, $\mathbf{D_1}$, table 4.1) as black error bars and its fitted null hypothesis model $m_0^{\mathbf{D_1}}$ in an energy range from $0.38\,\mathrm{keV}$ to $2\,\mathrm{keV}$ (panels A and B) and from $2\,\mathrm{keV}$ to $16.5\,\mathrm{keV}$ (panels C and D) as red lines, respectively, while the blue error bars show the instrumental background model. The best-fit values are specified in tables 5.1 and 5.2. The panels B and D show the residuals per energy bin in values of $\chi = \mathrm{sgn}(\mathrm{Data} - \mathrm{Model})\,\sqrt{(\mathrm{Data} - \mathrm{Model})^2}$.

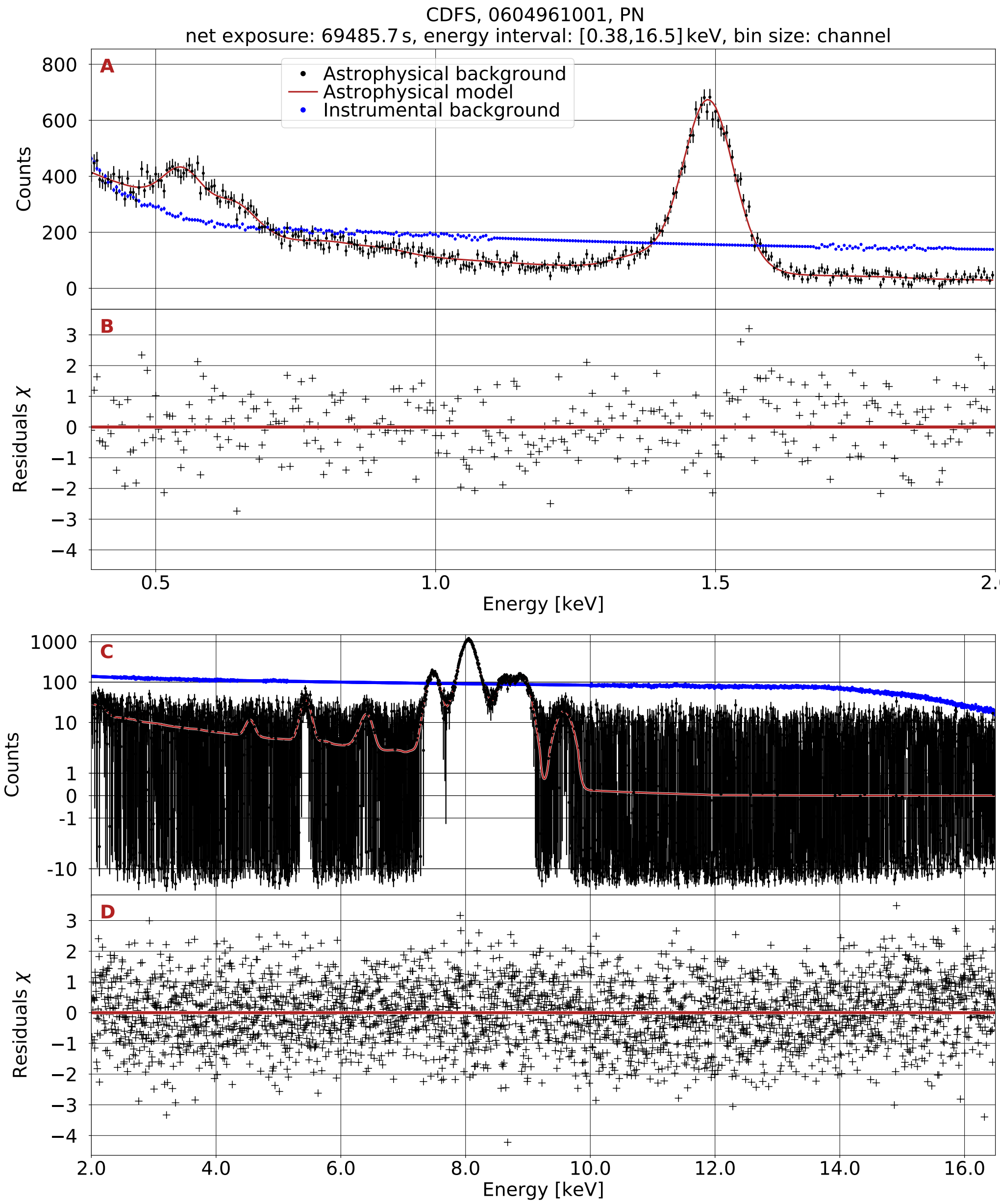

Figure F.10: The panels A and C show the measured spectrum of the data set 0604961001 ($i = 11$, $\mathbf{D_1}$, table 4.1) as black error bars and its fitted null hypothesis model $m_0^{\mathbf{D_1}}$ in an energy range from 0.38 keV to 2 keV (panels A and B) and from 2 keV to 16.5 keV (panels C and D) as red lines, respectively, while the blue error bars show the instrumental background model. The best-fit values are specified in tables 5.1 and 5.2. The panels B and D show the residuals per energy bin in values of $\chi = \mathrm{sgn}(\mathrm{Data} - \mathrm{Model})\sqrt{(\mathrm{Data} - \mathrm{Model})^2}$.

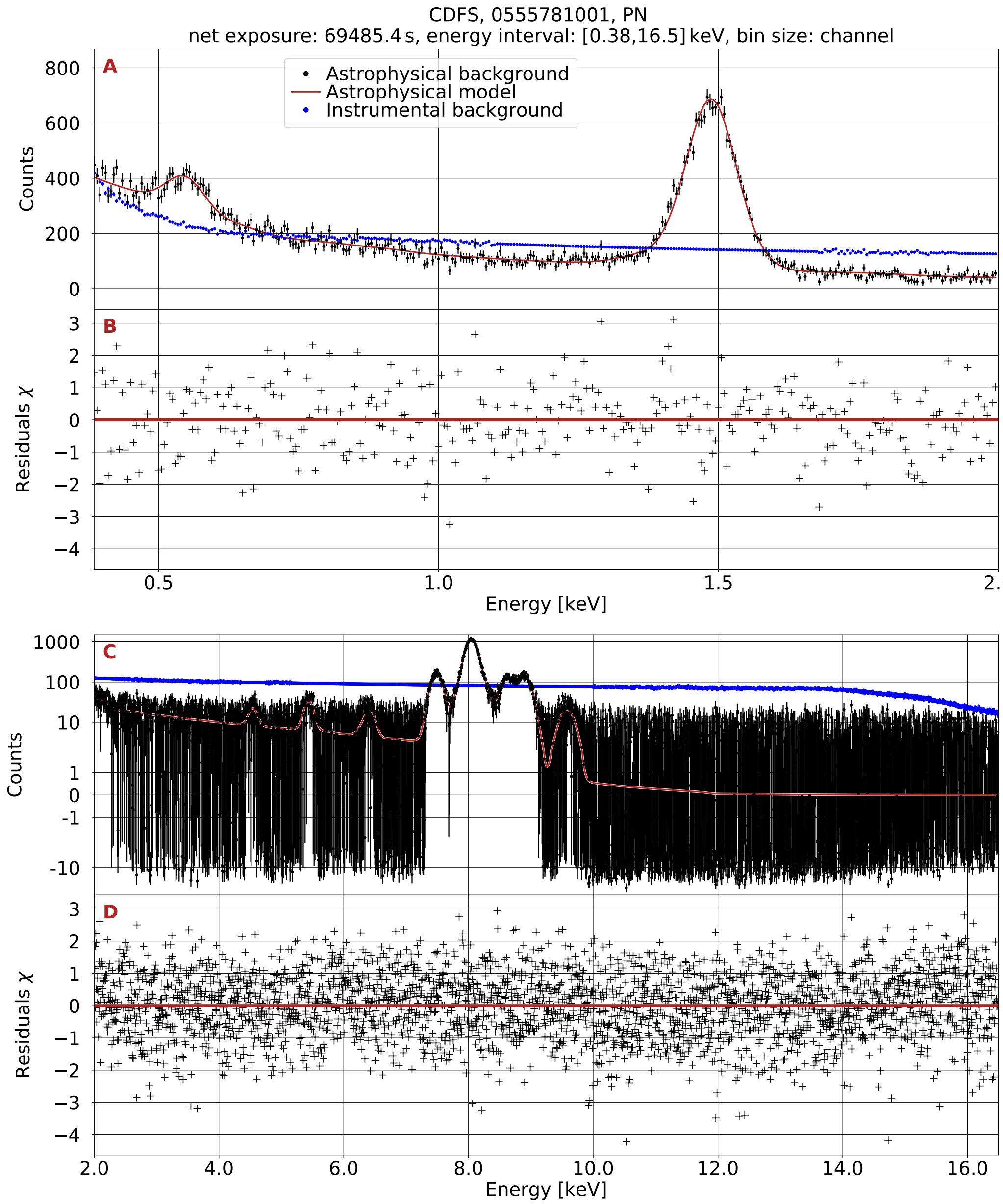

Figure F.11: The panels A and C show the measured spectrum of the data set 0555781001 (i = 12, $\mathbf{D_1}$, table 4.1) as black error bars and its fitted null hypothesis model $m_0^{\mathbf{D_1}}$ in an energy range from 0.38 keV to 2 keV (panels A and B) and from 2 keV to 16.5 keV (panels C and D) as red lines, respectively, while the blue error bars show the instrumental background model. The best-fit values are specified in tables 5.1 and 5.2. The panels B and D show the residuals per energy bin in values of $\chi = \mathrm{sgn}(\mathrm{Data} - \mathrm{Model})\sqrt{(\mathrm{Data} - \mathrm{Model})^2}$.

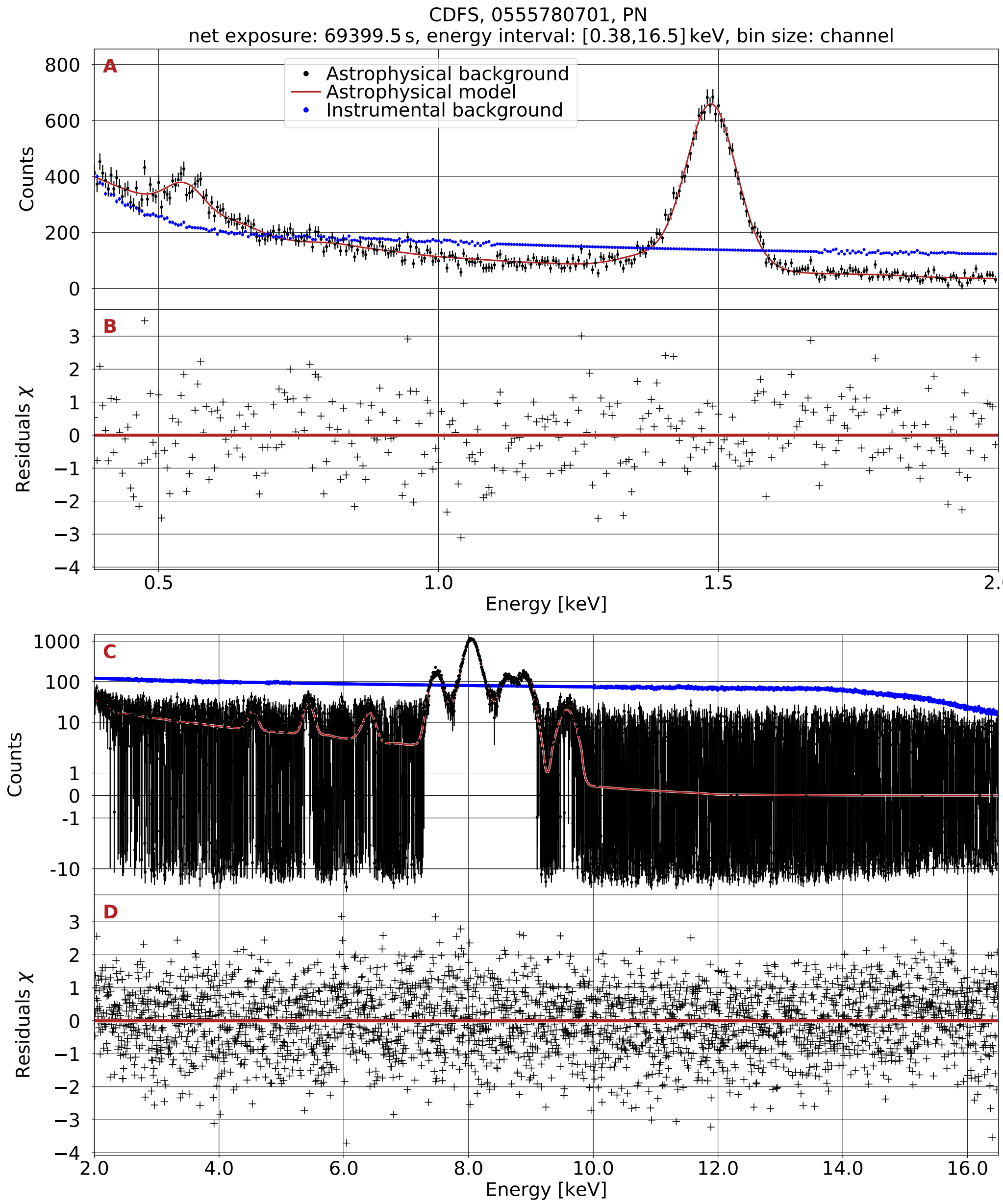

Figure F.12: The panels A and C show the measured spectrum of the data set 0555780701 ($i = 13$, $\mathbf{D_1}$, table 4.1) as black error bars and its fitted null hypothesis model $m_0^{\mathbf{D_1}}$ in an energy range from $0.38\,\text{keV}$ to $2\,\text{keV}$ (panels A and B) and from $2\,\text{keV}$ to $16.5\,\text{keV}$ (panels C and D) as red lines, respectively, while the blue error bars show the instrumental background model. The best-fit values are specified in tables 5.1 and 5.2. The panels B and D show the residuals per energy bin in values of $\chi = \text{sgn}(\text{Data} - \text{Model})\sqrt{(\text{Data} - \text{Model})^2}$.

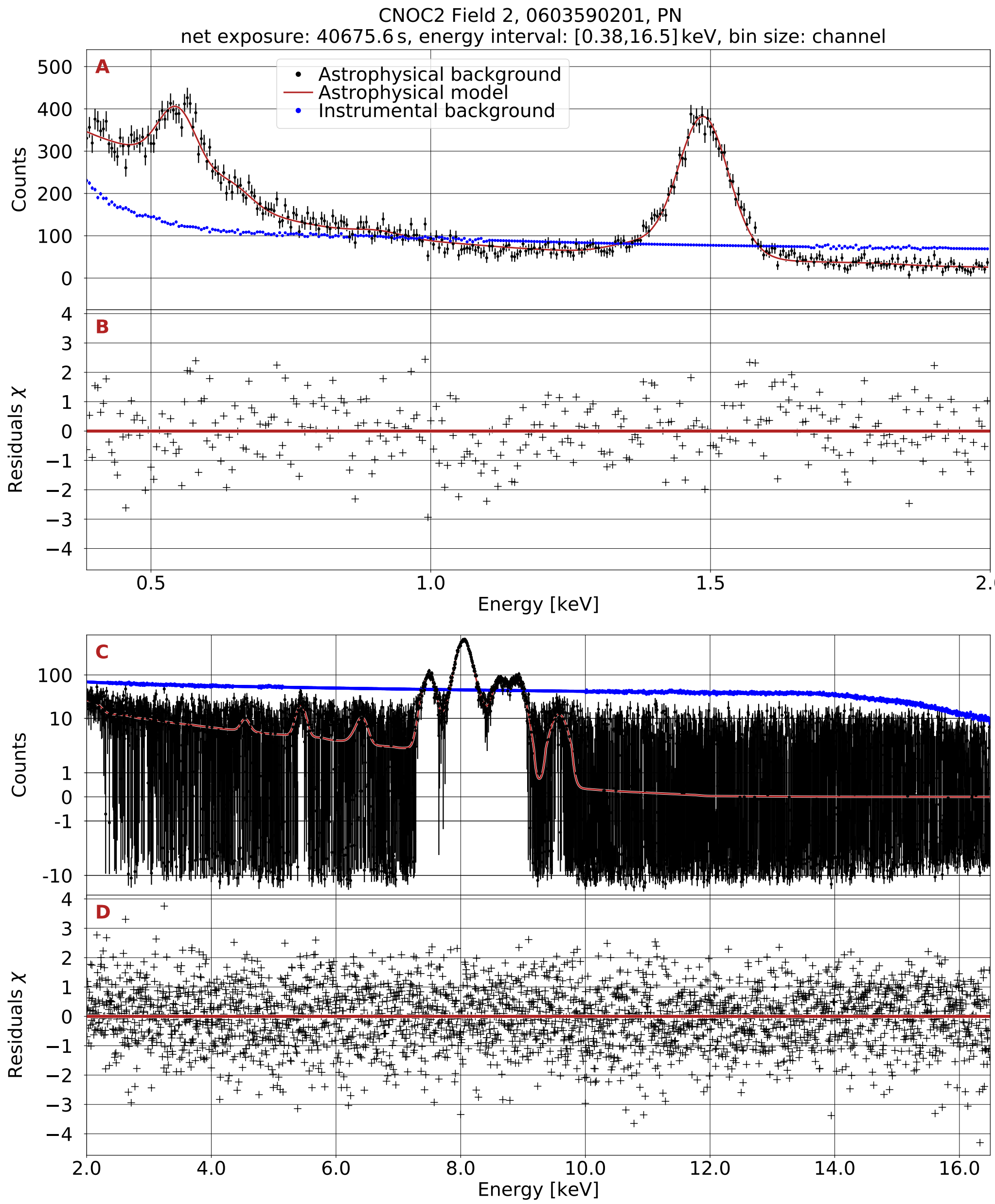

Figure F.13: The panels A and C show the measured spectrum of the data set 0603590201 ($i = 14$, $\mathbf{D_1}$, table 4.1) as black error bars and its fitted null hypothesis model $m_0^{\mathbf{D_1}}$ in an energy range from $0.38\,\mathrm{keV}$ to $2\,\mathrm{keV}$ (panels A and B) and from $2\,\mathrm{keV}$ to $16.5\,\mathrm{keV}$ (panels C and D) as red lines, respectively, while the blue error bars show the instrumental background model. The best-fit values are specified in tables 5.1 and 5.2. The panels B and D show the residuals per energy bin in values of $\chi = \mathrm{sgn}(\mathrm{Data} - \mathrm{Model})\sqrt{(\mathrm{Data} - \mathrm{Model})^2}$.

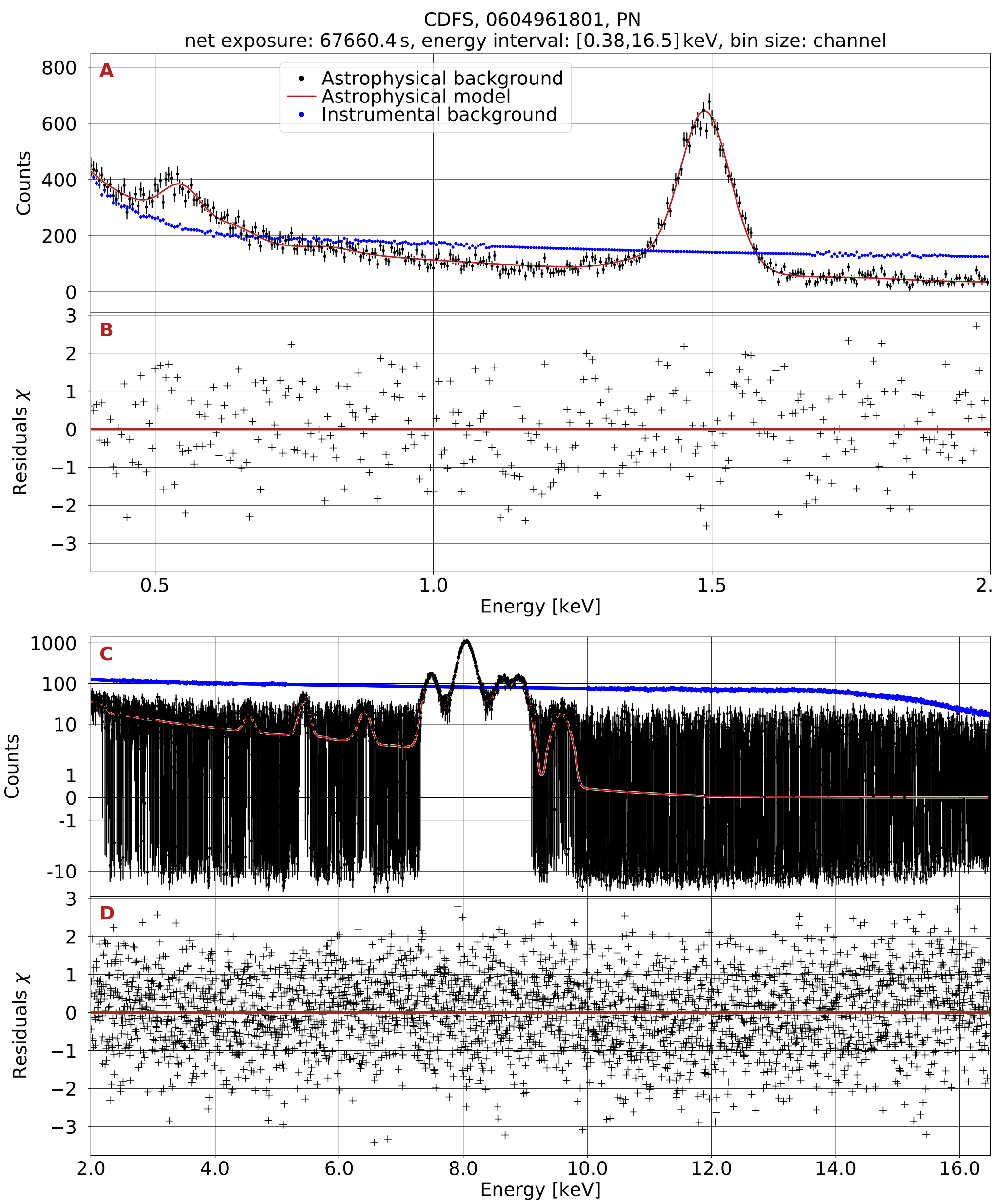

Figure F.14: The panels A and C show the measured spectrum of the data set 0604961801 ($i = 15$, $\mathbf{D_1}$, table 4.1) as black error bars and its fitted null hypothesis model $m_0^{\mathbf{D_1}}$ in an energy range from 0.38 keV to 2 keV (panels A and B) and from 2 keV to 16.5 keV (panels C and D) as red lines, respectively, while the blue error bars show the instrumental background model. The best-fit values are specified in tables 5.1 and 5.2. The panels B and D show the residuals per energy bin in values of $\chi = \mathrm{sgn}(\mathrm{Data} - \mathrm{Model})\sqrt{(\mathrm{Data} - \mathrm{Model})^2}$.

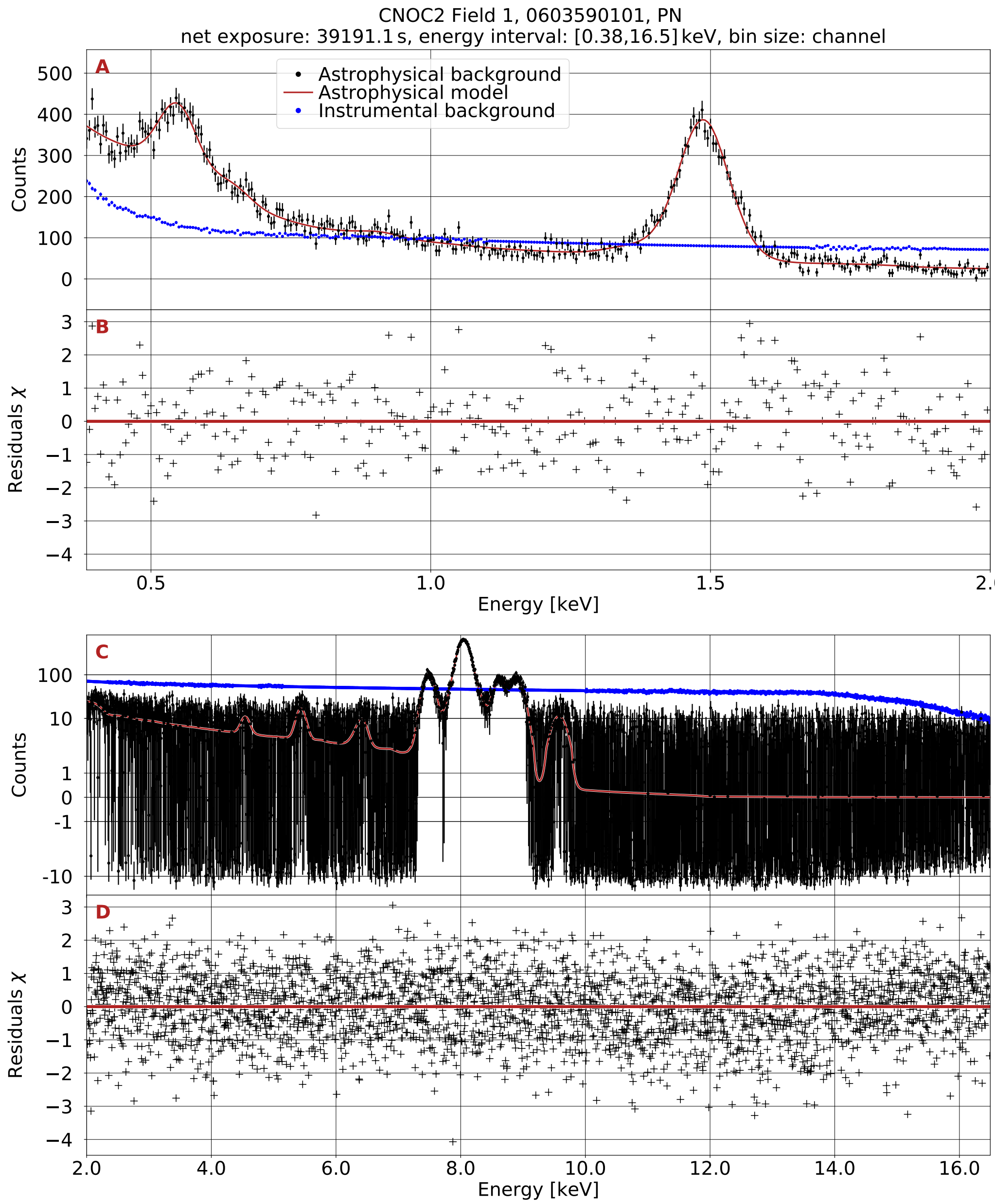

Figure F.15: The panels A and C show the measured spectrum of the data set 0603590101 ($i = 16$, $\mathbf{D_1}$, table 4.1) as black error bars and its fitted null hypothesis model $m_0^{\mathbf{D_1}}$ in an energy range from $0.38\,\mathrm{keV}$ to $2\,\mathrm{keV}$ (panels A and B) and from $2\,\mathrm{keV}$ to $16.5\,\mathrm{keV}$ (panels C and D) as red lines, respectively, while the blue error bars show the instrumental background model. The best-fit values are specified in tables 5.1 and 5.2. The panels B and D show the residuals per energy bin in values of $\chi = \mathrm{sgn}(\mathrm{Data} - \mathrm{Model})\,\sqrt{(\mathrm{Data} - \mathrm{Model})^2}$.

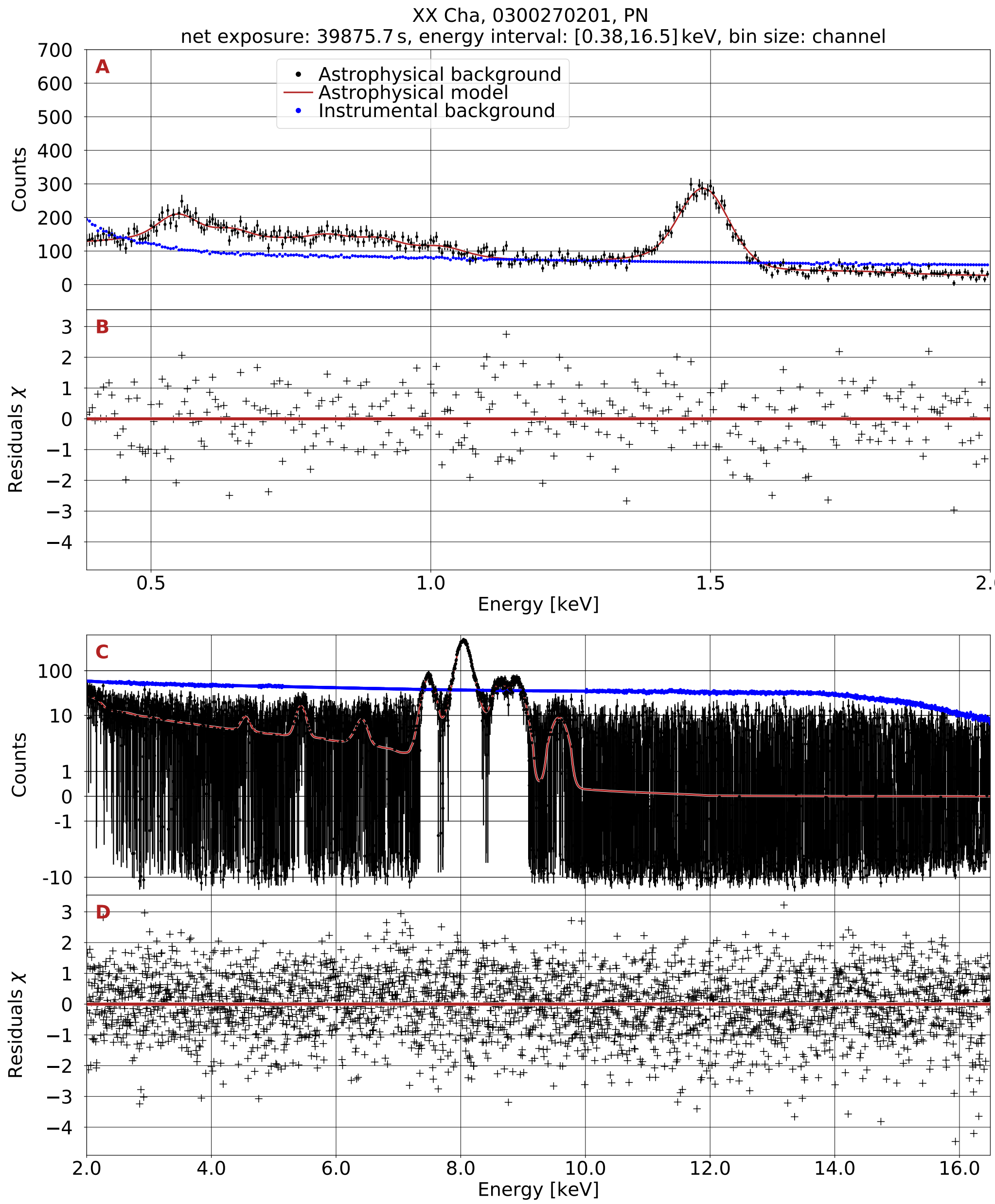

Figure F.16: The panels A and C show the measured spectrum of the data set 0300270201 ($i = 17$, $\mathbf{D_1}$, table 4.1) as black error bars and its fitted null hypothesis model $m_0^{\mathbf{D_1}}$ in an energy range from 0.38 keV to 2 keV (panels A and B) and from 2 keV to 16.5 keV (panels C and D) as red lines, respectively, while the blue error bars show the instrumental background model. The best-fit values are specified in tables 5.1 and 5.2. The panels B and D show the residuals per energy bin in values of $\chi = \mathrm{sgn}(\mathrm{Data} - \mathrm{Model})\sqrt{(\mathrm{Data} - \mathrm{Model})^2}$.

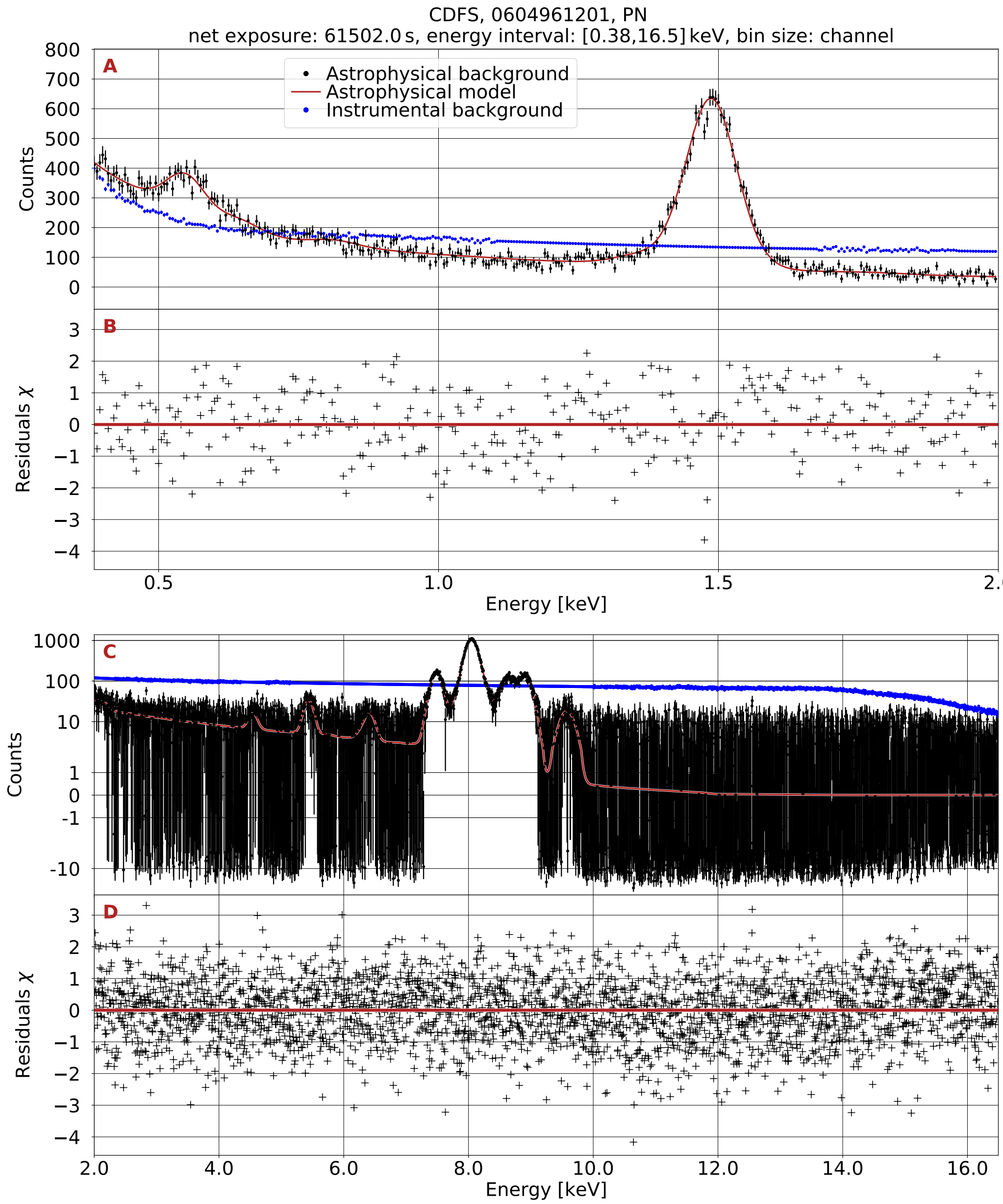

Figure F.17: The panels A and C show the measured spectrum of the data set 0604961201 ($i = 18$, $\mathbf{D_1}$, table 4.1) as black error bars and its fitted null hypothesis model $m_0^{\mathbf{D_1}}$ in an energy range from $0.38\,\mathrm{keV}$ to $2\,\mathrm{keV}$ (panels A and B) and from $2\,\mathrm{keV}$ to $16.5\,\mathrm{keV}$ (panels C and D) as red lines, respectively, while the blue error bars show the instrumental background model. The best-fit values are specified in tables 5.1 and 5.2. The panels B and D show the residuals per energy bin in values of $\chi = \mathrm{sgn}(\mathrm{Data} - \mathrm{Model})\,\sqrt{(\mathrm{Data} - \mathrm{Model})^2}$.

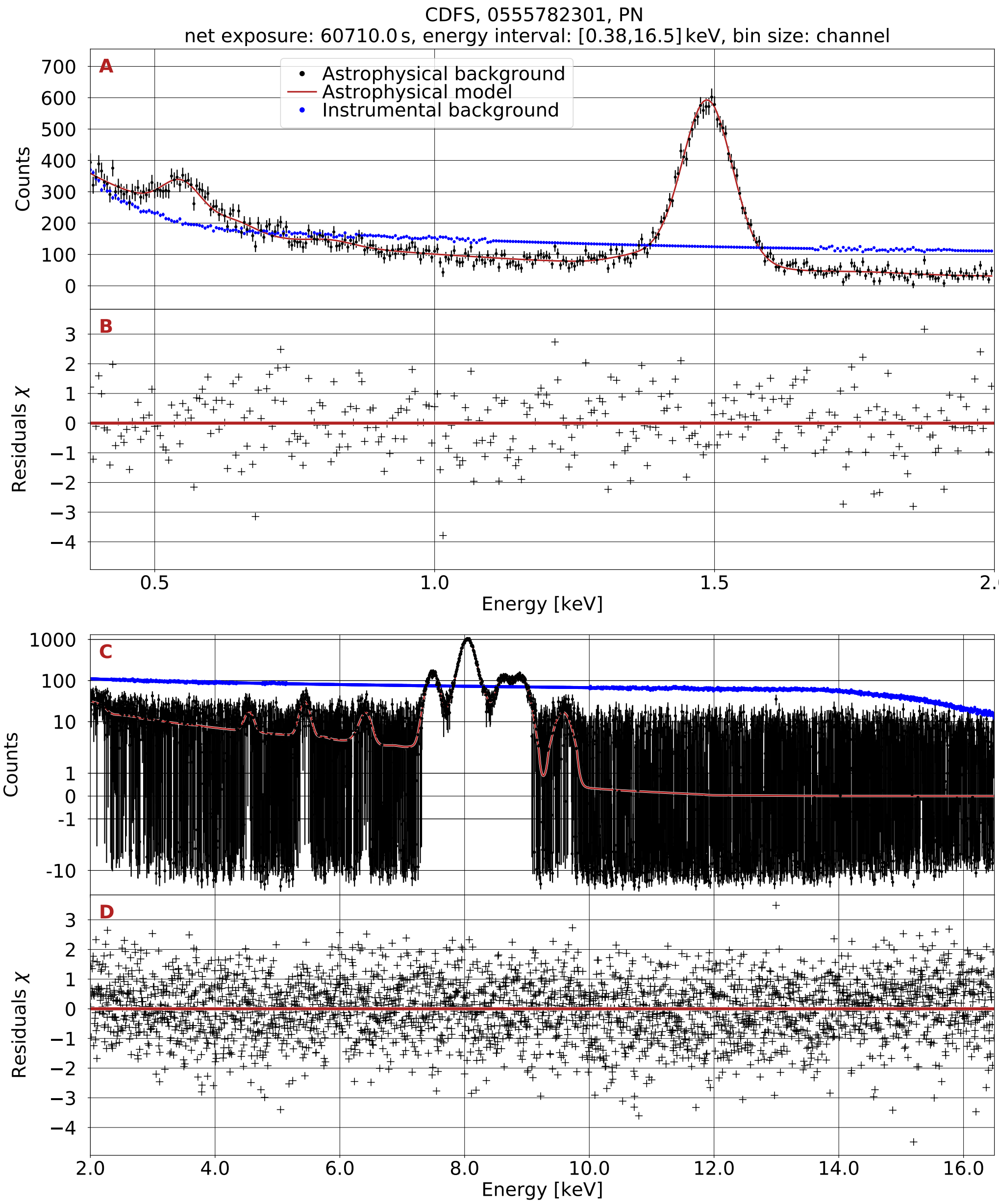

Figure F.18: The panels A and C show the measured spectrum of the data set 0555782301 ($i = 19$, $\mathbf{D_1}$, table 4.1) as black error bars and its fitted null hypothesis model $m_0^{\mathbf{D_1}}$ in an energy range from 0.38 keV to 2 keV (panels A and B) and from 2 keV to 16.5 keV (panels C and D) as red lines, respectively, while the blue error bars show the instrumental background model. The best-fit values are specified in tables 5.1 and 5.2. The panels B and D show the residuals per energy bin in values of $\chi = \mathrm{sgn}(\mathrm{Data} - \mathrm{Model})\sqrt{(\mathrm{Data} - \mathrm{Model})^2}$.

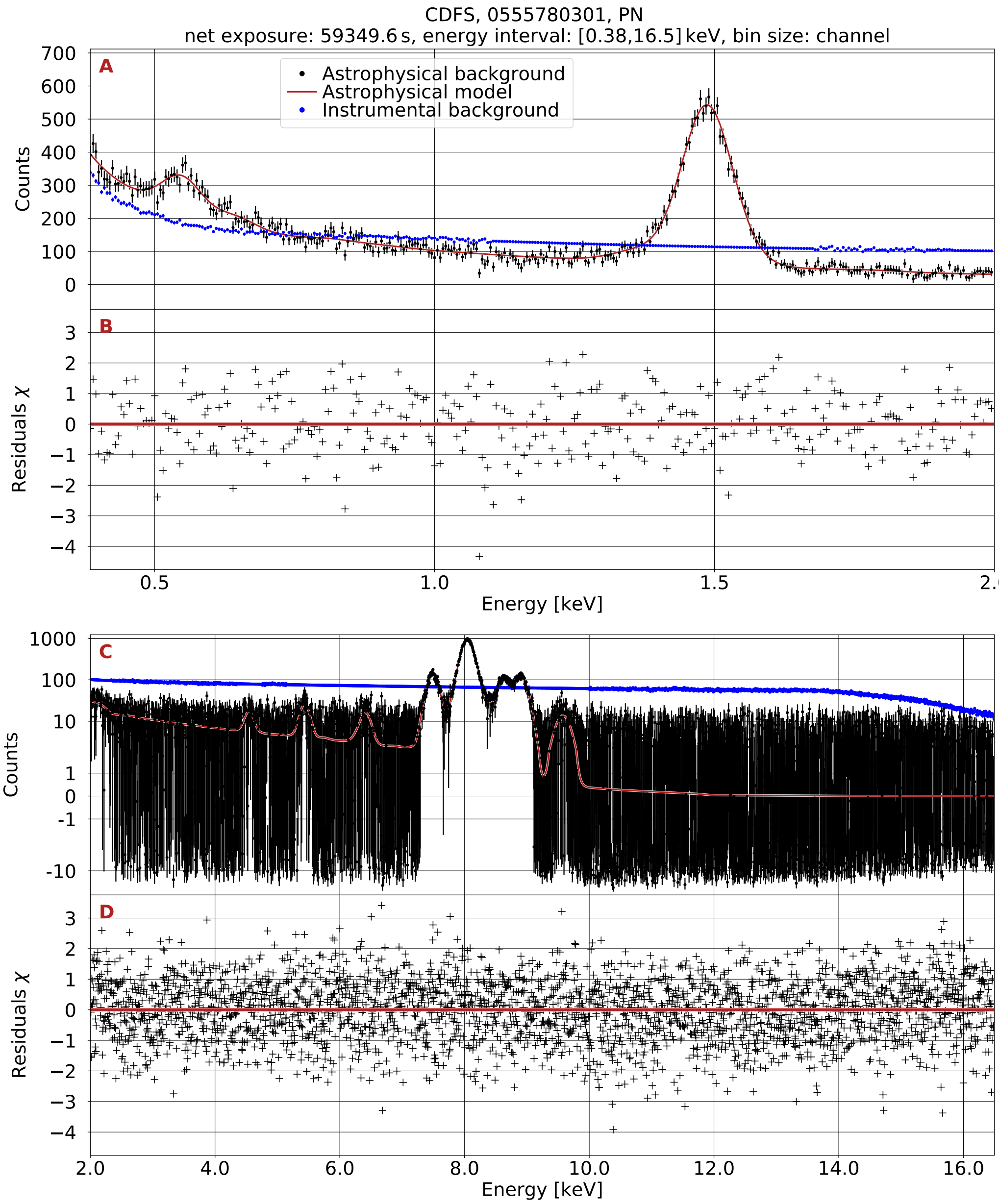

Figure F.19: The panels A and C show the measured spectrum of the data set 0555780301 (i = 20, $\mathbf{D_1}$, table 4.1) as black error bars and its fitted null hypothesis model $m_0^{\mathbf{D_1}}$ in an energy range from 0.38 keV to 2 keV (panels A and B) and from 2 keV to 16.5 keV (panels C and D) as red lines, respectively, while the blue error bars show the instrumental background model. The best-fit values are specified in tables 5.1 and 5.2. The panels B and D show the residuals per energy bin in values of $\chi = \mathrm{sgn}(\mathrm{Data} - \mathrm{Model})\sqrt{(\mathrm{Data} - \mathrm{Model})^2}$.

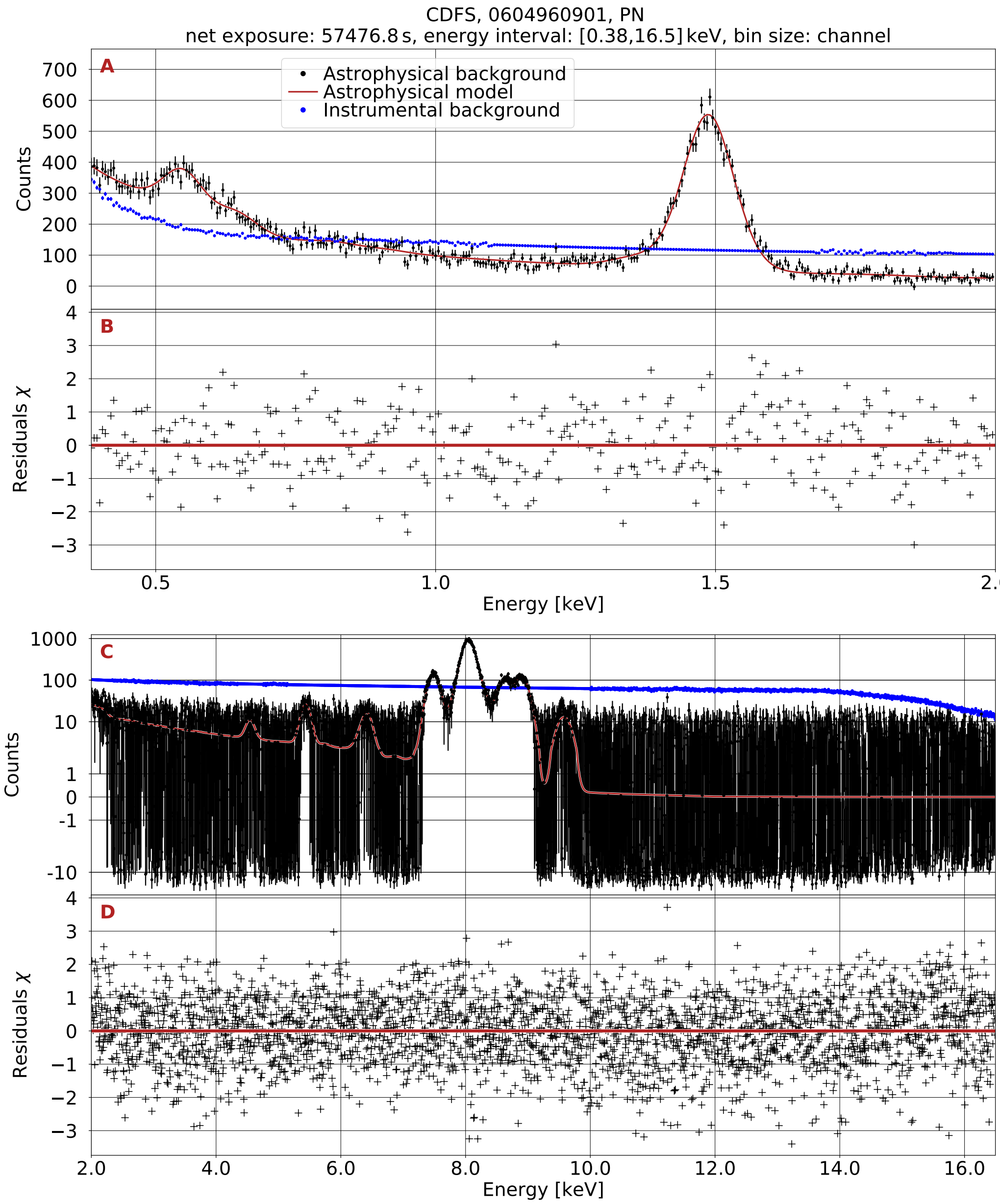

Figure F.20: The panels A and C show the measured spectrum of the data set 0604960901 ($i = 21$, $\mathbf{D_1}$, table 4.1) as black error bars and its fitted null hypothesis model $m_0^{\mathbf{D_1}}$ in an energy range from $0.38\,\mathrm{keV}$ to $2\,\mathrm{keV}$ (panels A and B) and from $2\,\mathrm{keV}$ to $16.5\,\mathrm{keV}$ (panels C and D) as red lines, respectively, while the blue error bars show the instrumental background model. The best-fit values are specified in tables 5.1 and 5.2. The panels B and D show the residuals per energy bin in values of $\chi = \mathrm{sgn}(\mathrm{Data} - \mathrm{Model})\sqrt{(\mathrm{Data} - \mathrm{Model})^2}$.

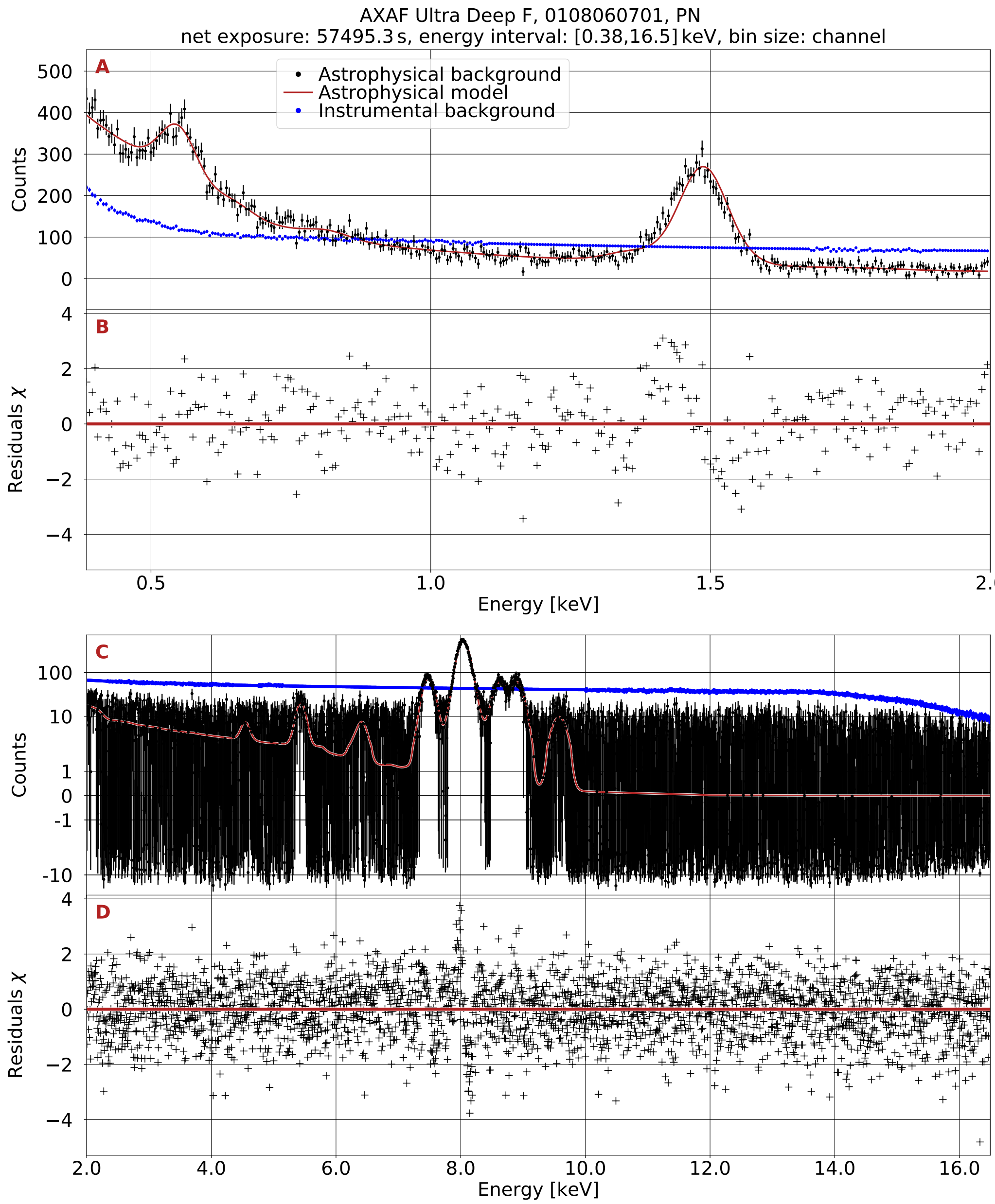

Figure F.21: The panels A and C show the measured spectrum of the data set 0108060701 ($i = 22$, $\mathbf{D_1}$, table 4.1) as black error bars and its fitted null hypothesis model $m_0^{\mathbf{D_1}}$ in an energy range from $0.38\,\mathrm{keV}$ to $2\,\mathrm{keV}$ (panels A and B) and from $2\,\mathrm{keV}$ to $16.5\,\mathrm{keV}$ (panels C and D) as red lines, respectively, while the blue error bars show the instrumental background model. The best-fit values are specified in tables 5.1 and 5.2. The panels B and D show the residuals per energy bin in values of $\chi = \mathrm{sgn}(\mathrm{Data} - \mathrm{Model})\,\sqrt{(\mathrm{Data} - \mathrm{Model})^2}$.

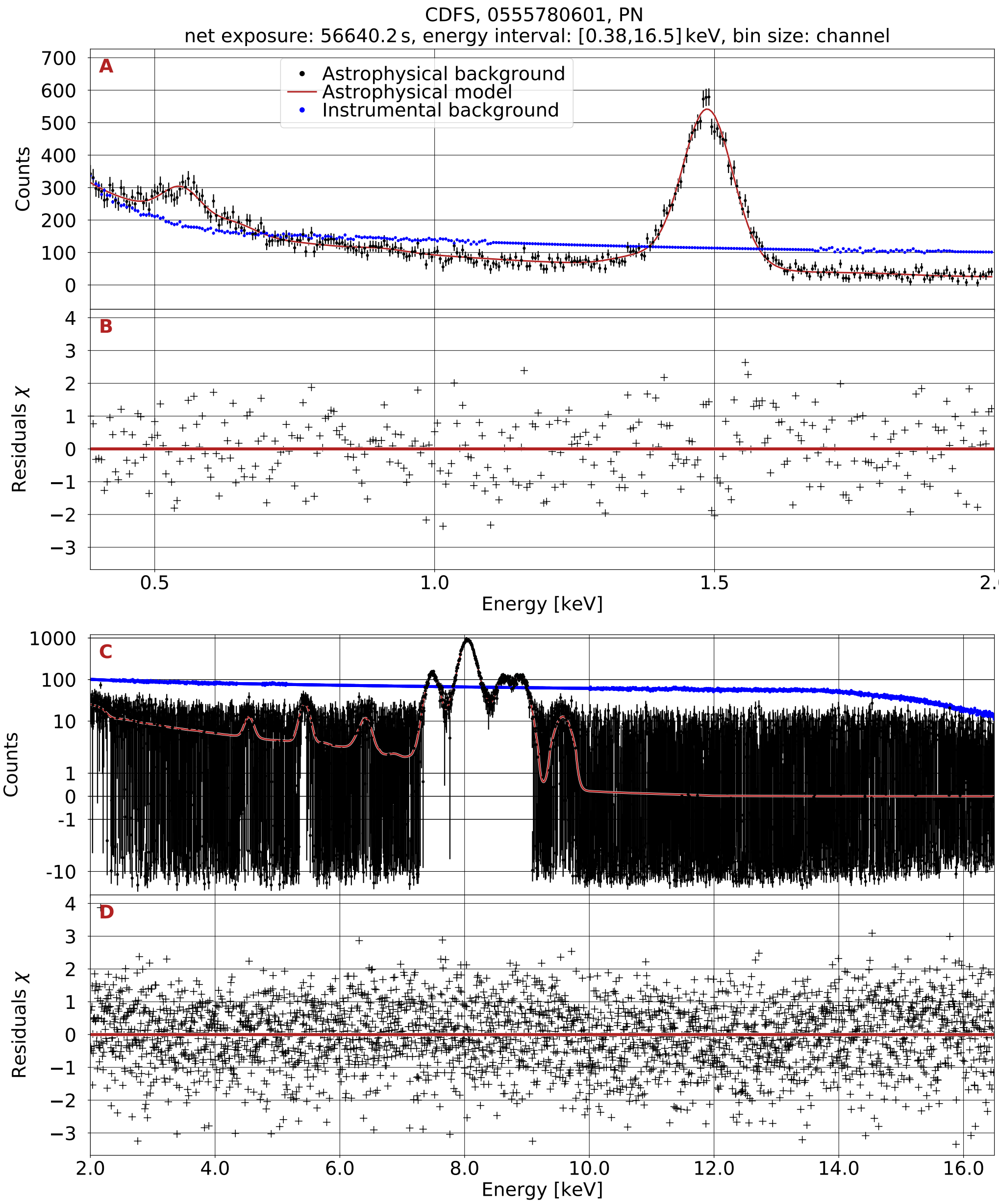

Figure F.22: The panels A and C show the measured spectrum of the data set 0555780601 ($i = 23$, $\mathbf{D_1}$, table 4.1) as black error bars and its fitted null hypothesis model $m_0^{\mathbf{D_1}}$ in an energy range from $0.38\,\mathrm{keV}$ to $2\,\mathrm{keV}$ (panels A and B) and from $2\,\mathrm{keV}$ to $16.5\,\mathrm{keV}$ (panels C and D) as red lines, respectively, while the blue error bars show the instrumental background model. The best-fit values are specified in tables 5.1 and 5.2. The panels B and D show the residuals per energy bin in values of $\chi = \mathrm{sgn}(\mathrm{Data} - \mathrm{Model})\sqrt{(\mathrm{Data} - \mathrm{Model})^2}$.

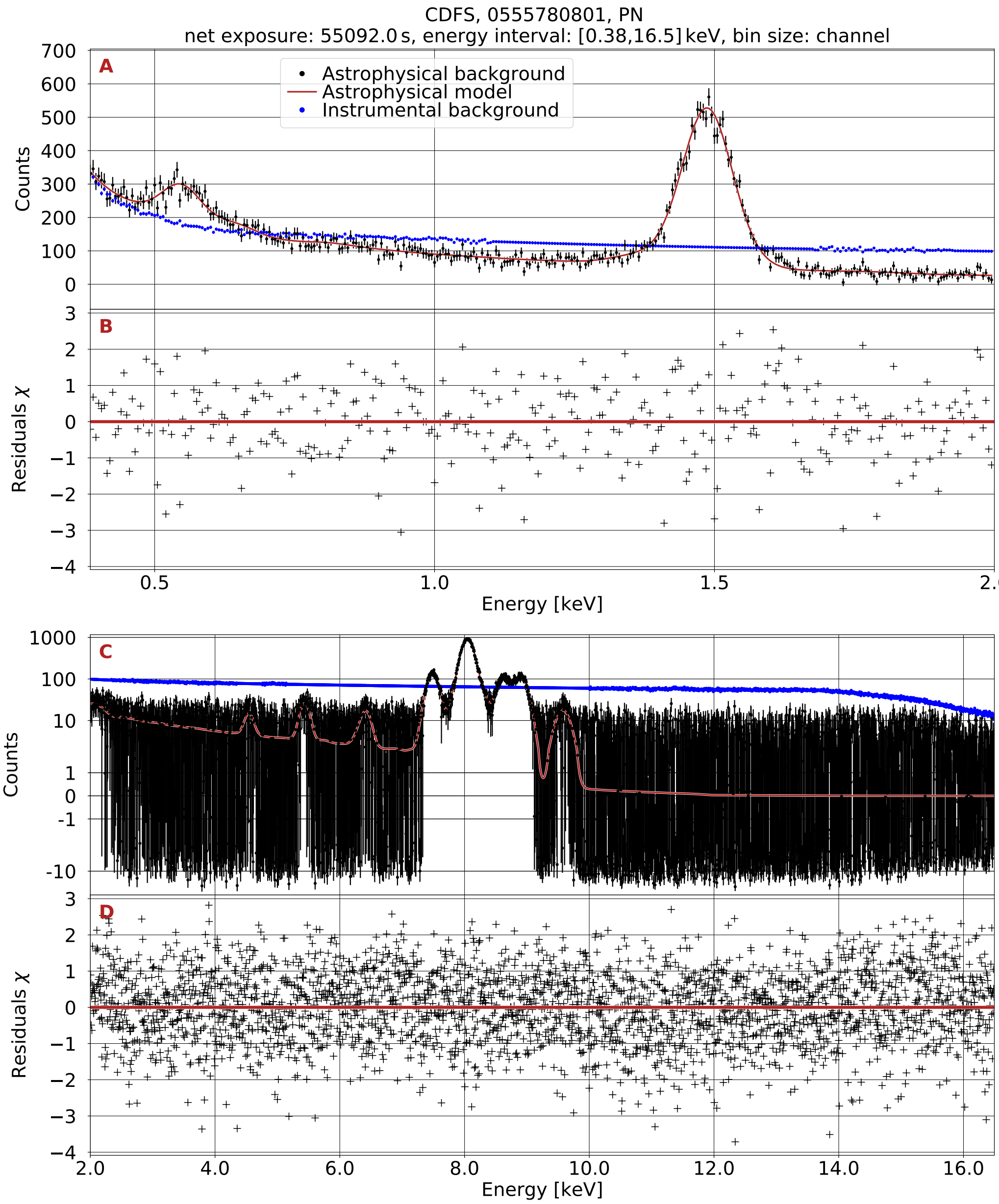

Figure F.23: The panels A and C show the measured spectrum of the data set 0555780801 ($i = 24$, $\mathbf{D_1}$, table 4.1) as black error bars and its fitted null hypothesis model $m_0^{\mathbf{D_1}}$ in an energy range from 0.38 keV to 2 keV (panels A and B) and from 2 keV to 16.5 keV (panels C and D) as red lines, respectively, while the blue error bars show the instrumental background model. The best-fit values are specified in tables 5.1 and 5.2. The panels B and D show the residuals per energy bin in values of $\chi = \mathrm{sgn}(\mathrm{Data} - \mathrm{Model})\sqrt{(\mathrm{Data} - \mathrm{Model})^2}$.

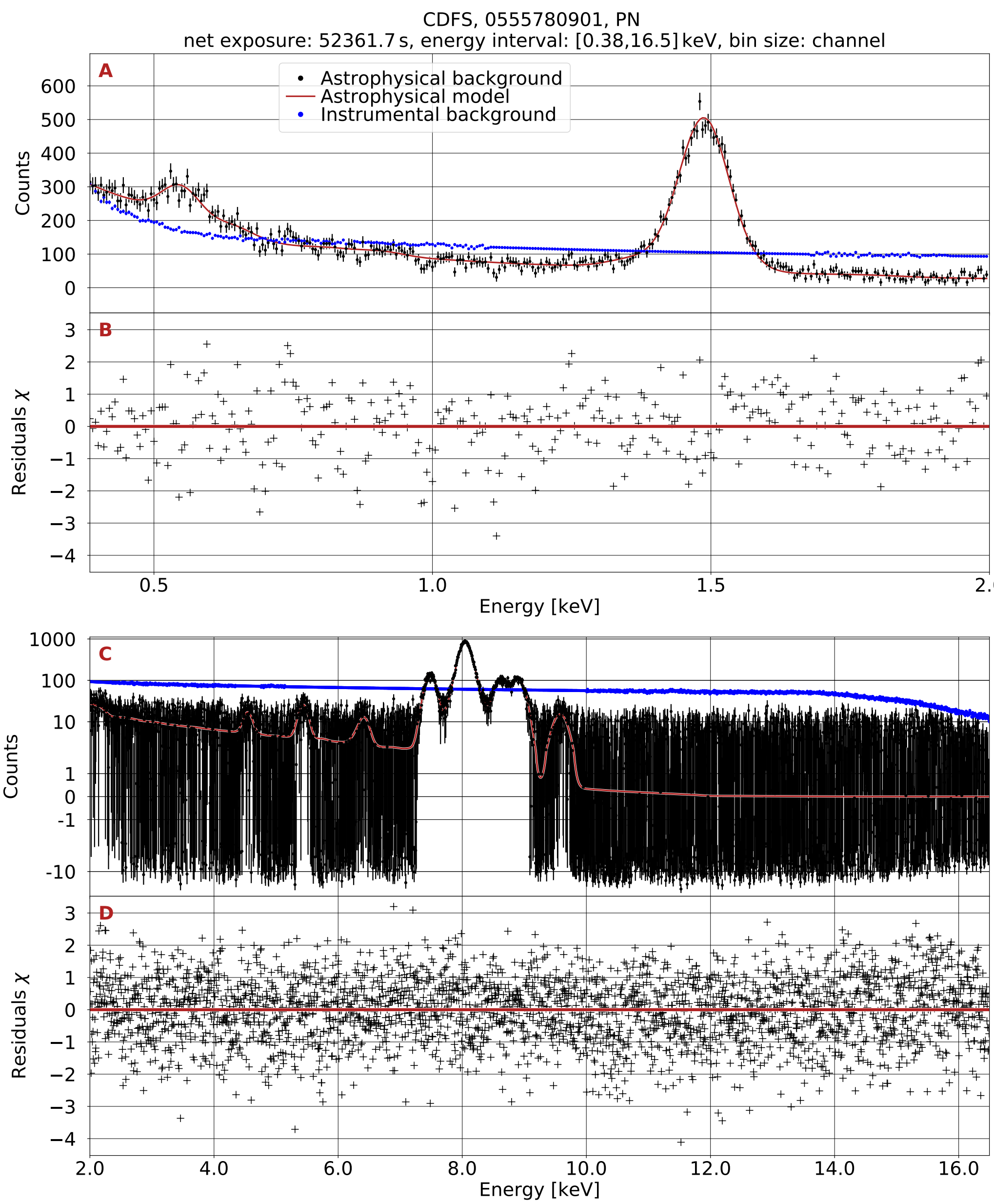

Figure F.24: The panels A and C show the measured spectrum of the data set 0555780901 ($i = 25$, $\mathbf{D_1}$, table 4.1) as black error bars and its fitted null hypothesis model $m_0^{\mathbf{D_1}}$ in an energy range from 0.38 keV to 2 keV (panels A and B) and from 2 keV to 16.5 keV (panels C and D) as red lines, respectively, while the blue error bars show the instrumental background model. The best-fit values are specified in tables 5.1 and 5.2. The panels B and D show the residuals per energy bin in values of $\chi = \mathrm{sgn}(\mathrm{Data} - \mathrm{Model})\sqrt{(\mathrm{Data} - \mathrm{Model})^2}$.

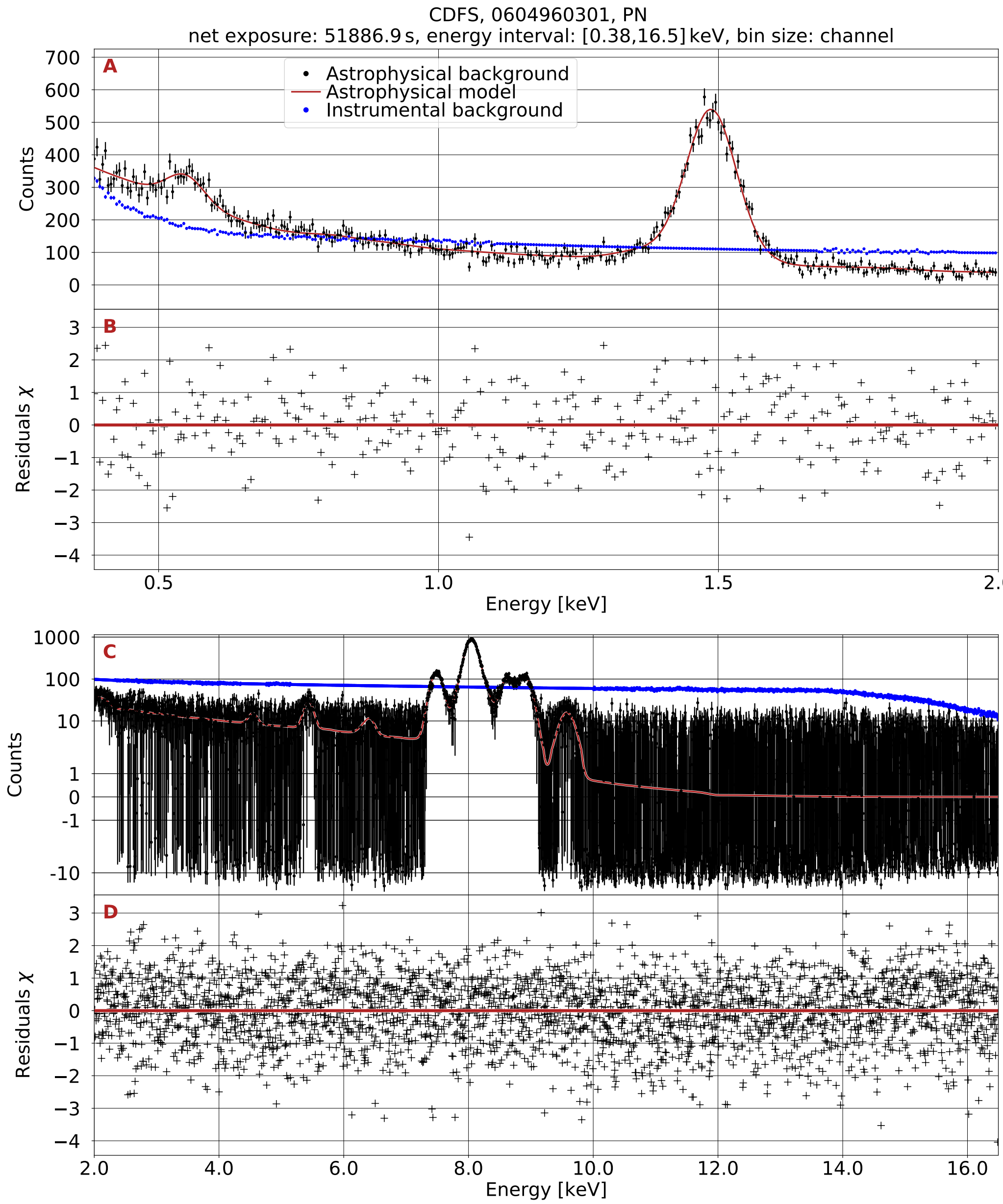

Figure F.25: The panels A and C show the measured spectrum of the data set 0604960301 ($i = 26$, $\mathbf{D_1}$, table 4.1) as black error bars and its fitted null hypothesis model $m_0^{\mathbf{D_1}}$ in an energy range from $0.38\,\mathrm{keV}$ to $2\,\mathrm{keV}$ (panels A and B) and from $2\,\mathrm{keV}$ to $16.5\,\mathrm{keV}$ (panels C and D) as red lines, respectively, while the blue error bars show the instrumental background model. The best-fit values are specified in tables 5.1 and 5.2. The panels B and D show the residuals per energy bin in values of $\chi = \mathrm{sgn}(\mathrm{Data} - \mathrm{Model})\,\sqrt{(\mathrm{Data} - \mathrm{Model})^2}$.

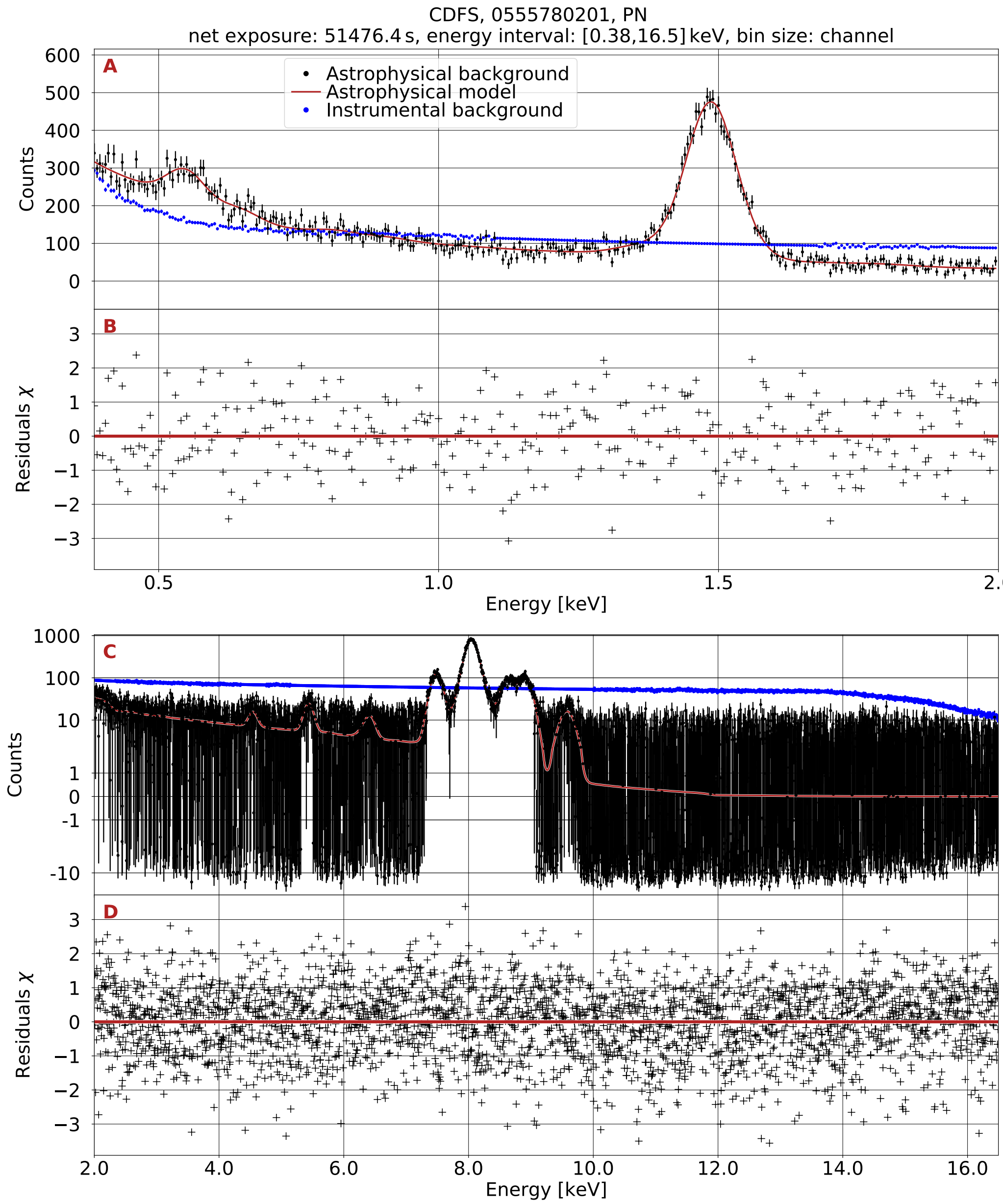

Figure F.26: The panels A and C show the measured spectrum of the data set 0555780201 ($i = 27$, $\mathbf{D_1}$, table 4.1) as black error bars and its fitted null hypothesis model $m_0^{\mathbf{D_1}}$ in an energy range from $0.38\,\text{keV}$ to $2\,\text{keV}$ (panels A and B) and from $2\,\text{keV}$ to $16.5\,\text{keV}$ (panels C and D) as red lines, respectively, while the blue error bars show the instrumental background model. The best-fit values are specified in tables 5.1 and 5.2. The panels B and D show the residuals per energy bin in values of $\chi = \text{sgn}(\text{Data} - \text{Model})\,\sqrt{(\text{Data} - \text{Model})^2}$.

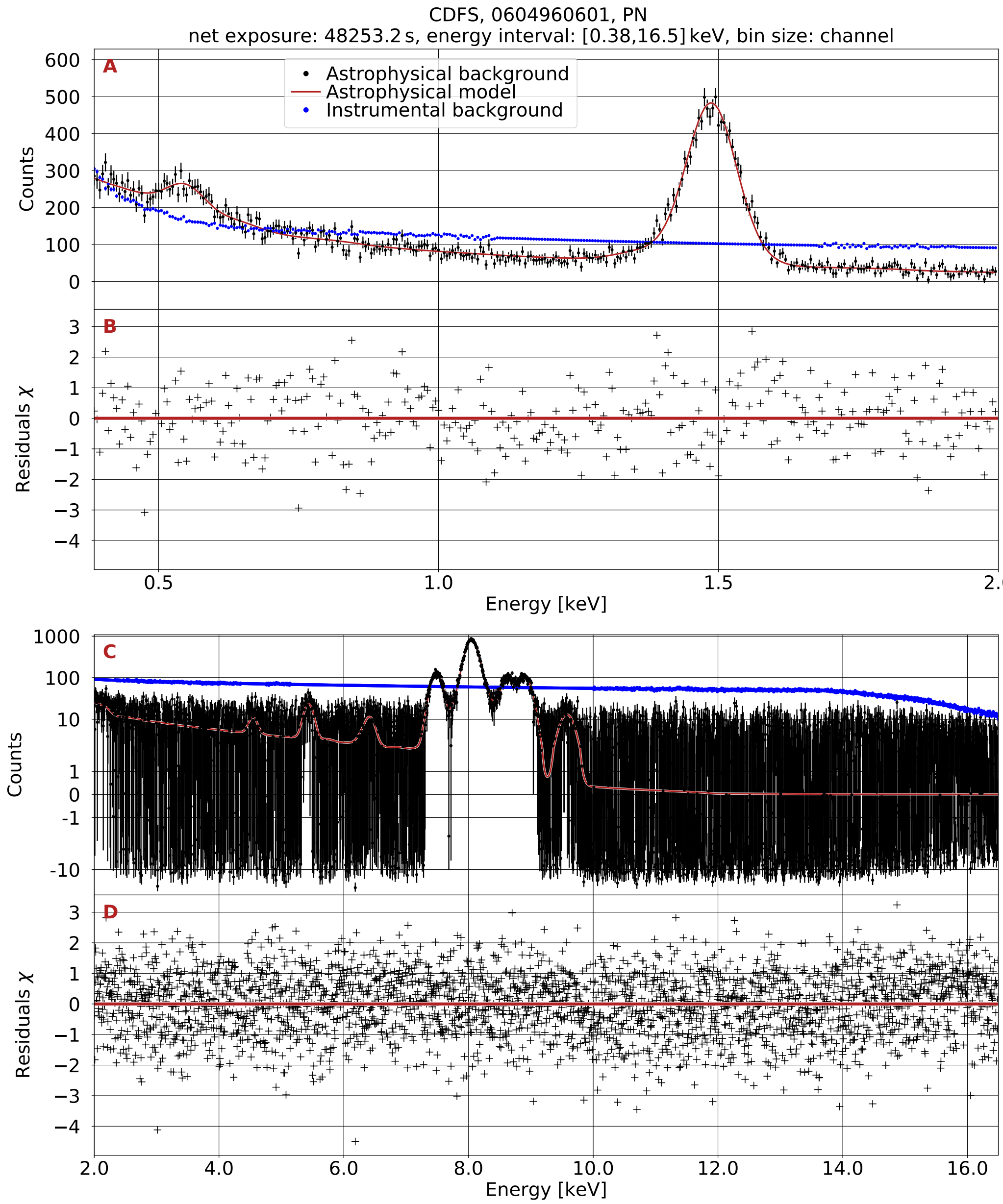

Figure F.27: The panels A and C show the measured spectrum of the data set 0604960601 (i = 28, $\mathbf{D_1}$, table 4.1) as black error bars and its fitted null hypothesis model $m_0^{\mathbf{D_1}}$ in an energy range from 0.38 keV to 2 keV (panels A and B) and from 2 keV to 16.5 keV (panels C and D) as red lines, respectively, while the blue error bars show the instrumental background model. The best-fit values are specified in tables 5.1 and 5.2. The panels B and D show the residuals per energy bin in values of $\chi = \mathrm{sgn}(\mathrm{Data} - \mathrm{Model})\sqrt{(\mathrm{Data} - \mathrm{Model})^2}$.

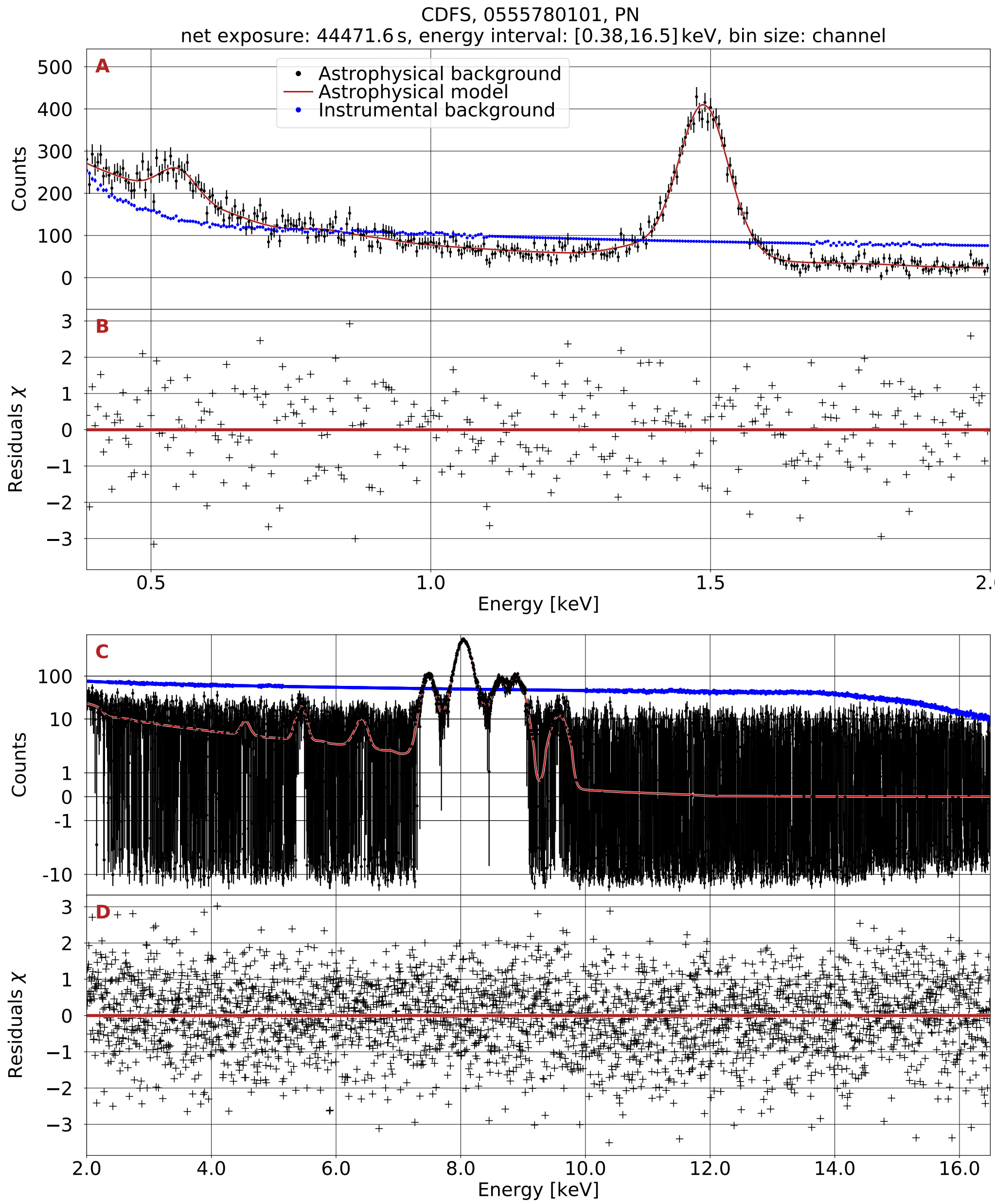

Figure F.28: The panels A and C show the measured spectrum of the data set 0555780101 ($i = 29$, $\mathbf{D_1}$, table 4.1) as black error bars and its fitted null hypothesis model $m_0^{\mathbf{D_1}}$ in an energy range from $0.38\,\text{keV}$ to $2\,\text{keV}$ (panels A and B) and from $2\,\text{keV}$ to $16.5\,\text{keV}$ (panels C and D) as red lines, respectively, while the blue error bars show the instrumental background model. The best-fit values are specified in tables 5.1 and 5.2. The panels B and D show the residuals per energy bin in values of $\chi = \text{sgn}(\text{Data} - \text{Model})\,\sqrt{(\text{Data} - \text{Model})^2}$.

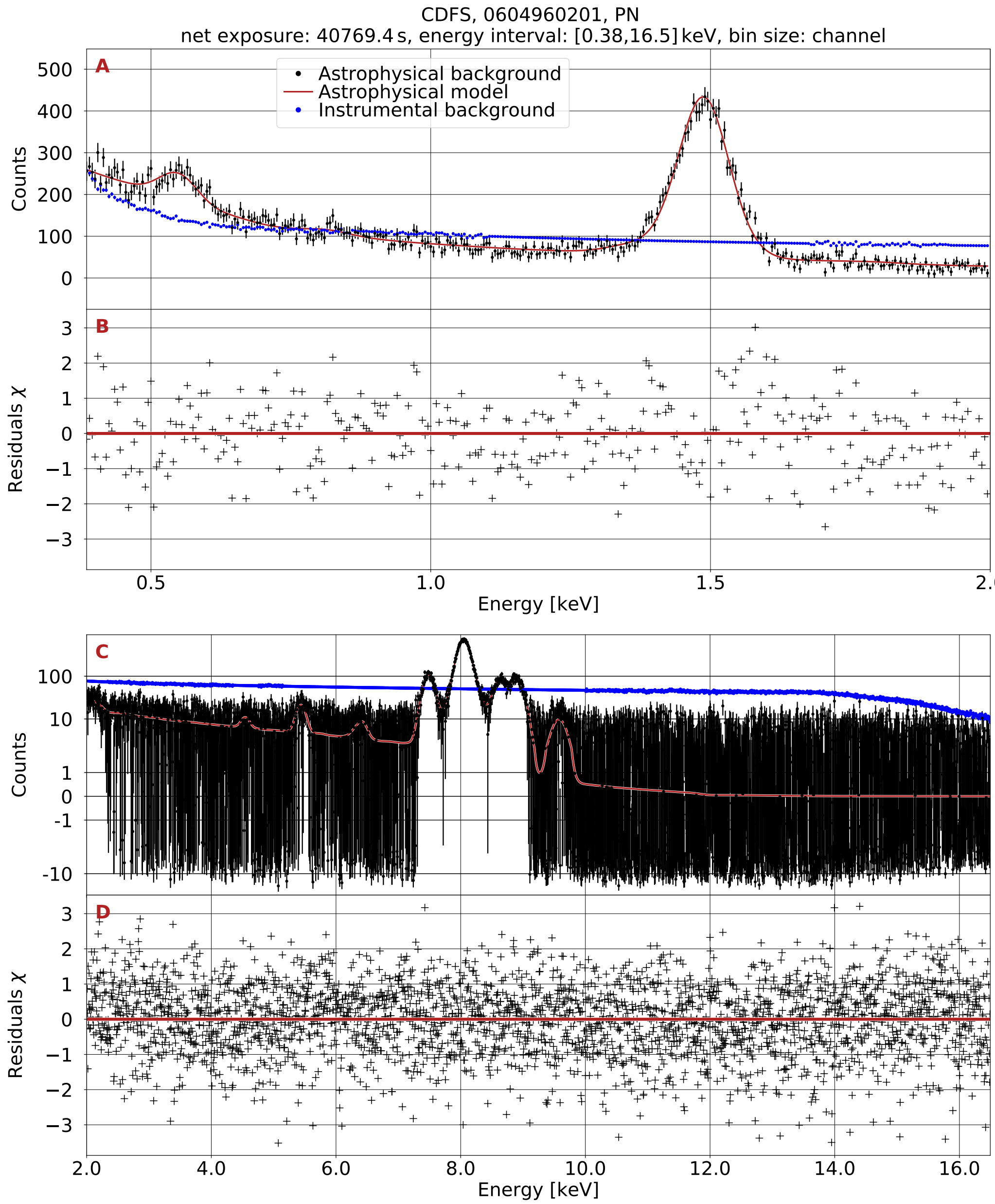

Figure F.29: The panels A and C show the measured spectrum of the data set 0604960201 ($i = 30$, $\mathbf{D_1}$, table 4.1) as black error bars and its fitted null hypothesis model $m_0^{\mathbf{D_1}}$ in an energy range from $0.38\,\mathrm{keV}$ to $2\,\mathrm{keV}$ (panels A and B) and from $2\,\mathrm{keV}$ to $16.5\,\mathrm{keV}$ (panels C and D) as red lines, respectively, while the blue error bars show the instrumental background model. The best-fit values are specified in tables 5.1 and 5.2. The panels B and D show the residuals per energy bin in values of $\chi = \mathrm{sgn}(\mathrm{Data} - \mathrm{Model})\sqrt{(\mathrm{Data} - \mathrm{Model})^2}$.

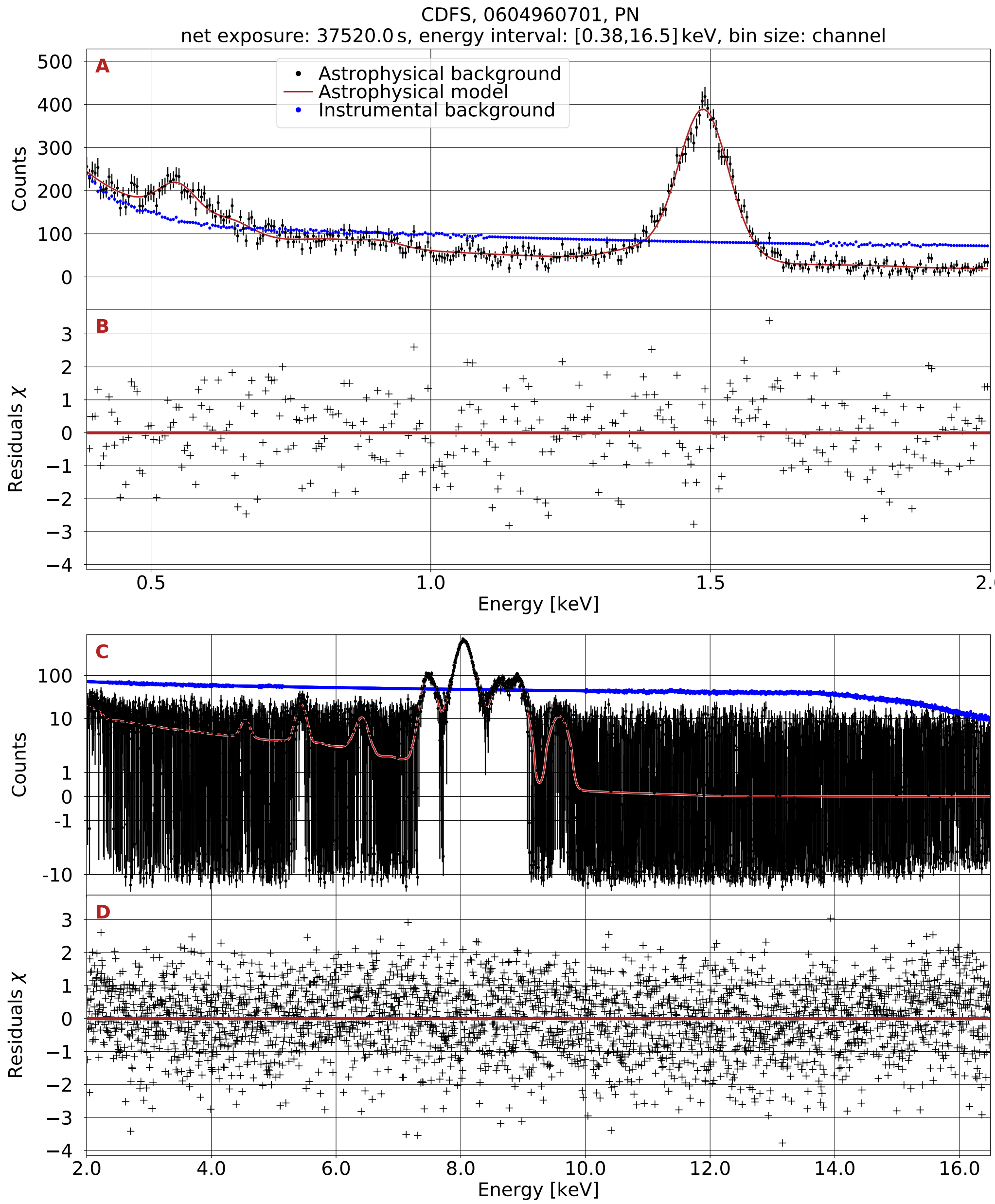

Figure F.30: The panels A and C show the measured spectrum of the data set 0604960701 ($i = 31$, $\mathbf{D_1}$, table 4.1) as black error bars and its fitted null hypothesis model $m_0^{\mathbf{D_1}}$ in an energy range from $0.38\,\text{keV}$ to $2\,\text{keV}$ (panels A and B) and from $2\,\text{keV}$ to $16.5\,\text{keV}$ (panels C and D) as red lines, respectively, while the blue error bars show the instrumental background model. The best-fit values are specified in tables 5.1 and 5.2. The panels B and D show the residuals per energy bin in values of $\chi = \text{sgn}(\text{Data} - \text{Model})\sqrt{(\text{Data} - \text{Model})^2}$.

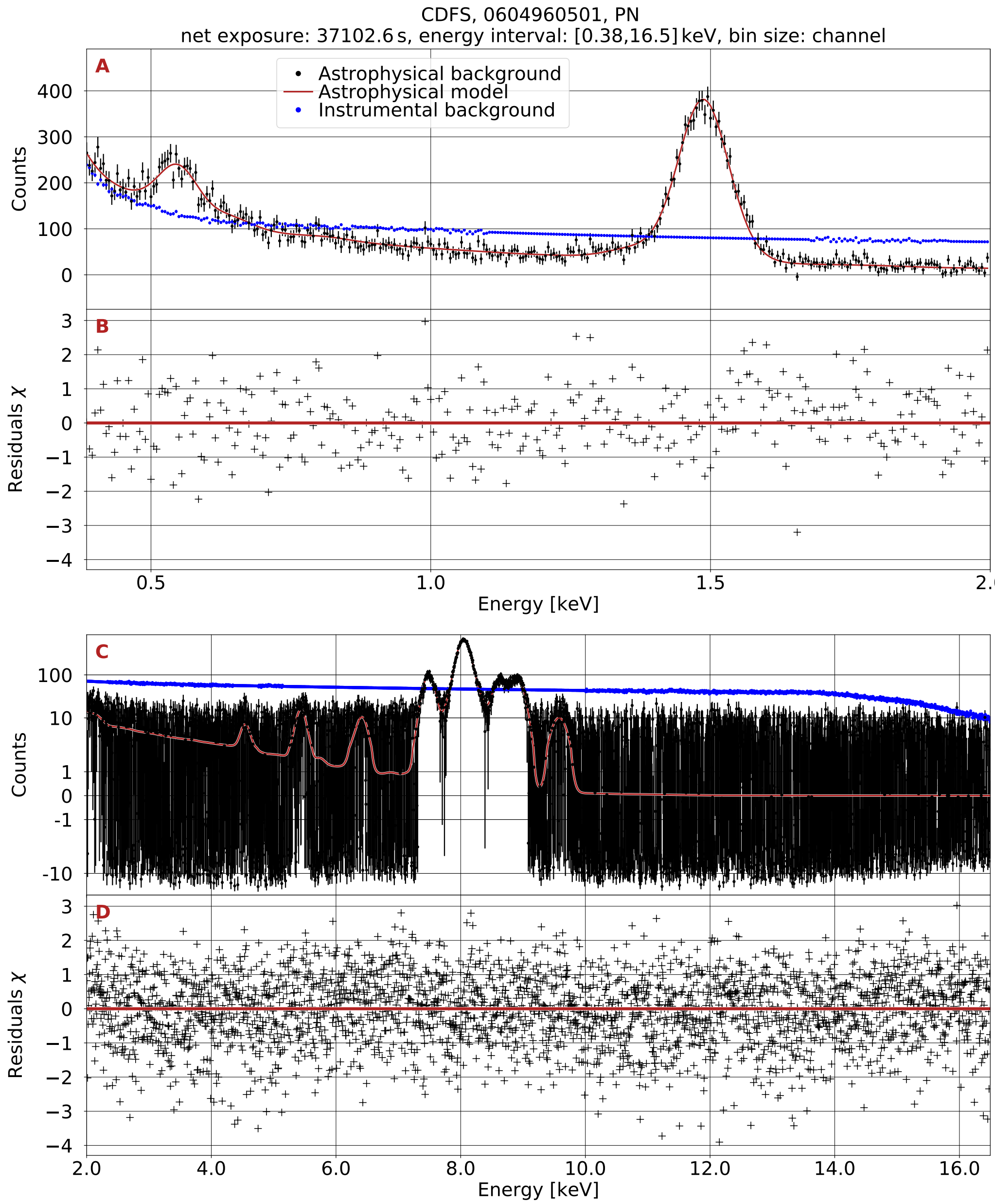

Figure F.31: The panels A and C show the measured spectrum of the data set 0604960501 ($i = 32$, $\mathbf{D_1}$, table 4.1) as black error bars and its fitted null hypothesis model $m_0^{\mathbf{D_1}}$ in an energy range from $0.38\,\mathrm{keV}$ to $2\,\mathrm{keV}$ (panels A and B) and from $2\,\mathrm{keV}$ to $16.5\,\mathrm{keV}$ (panels C and D) as red lines, respectively, while the blue error bars show the instrumental background model. The best-fit values are specified in tables 5.1 and 5.2. The panels B and D show the residuals per energy bin in values of $\chi = \mathrm{sgn}(\mathrm{Data} - \mathrm{Model})\sqrt{(\mathrm{Data} - \mathrm{Model})^2}$.

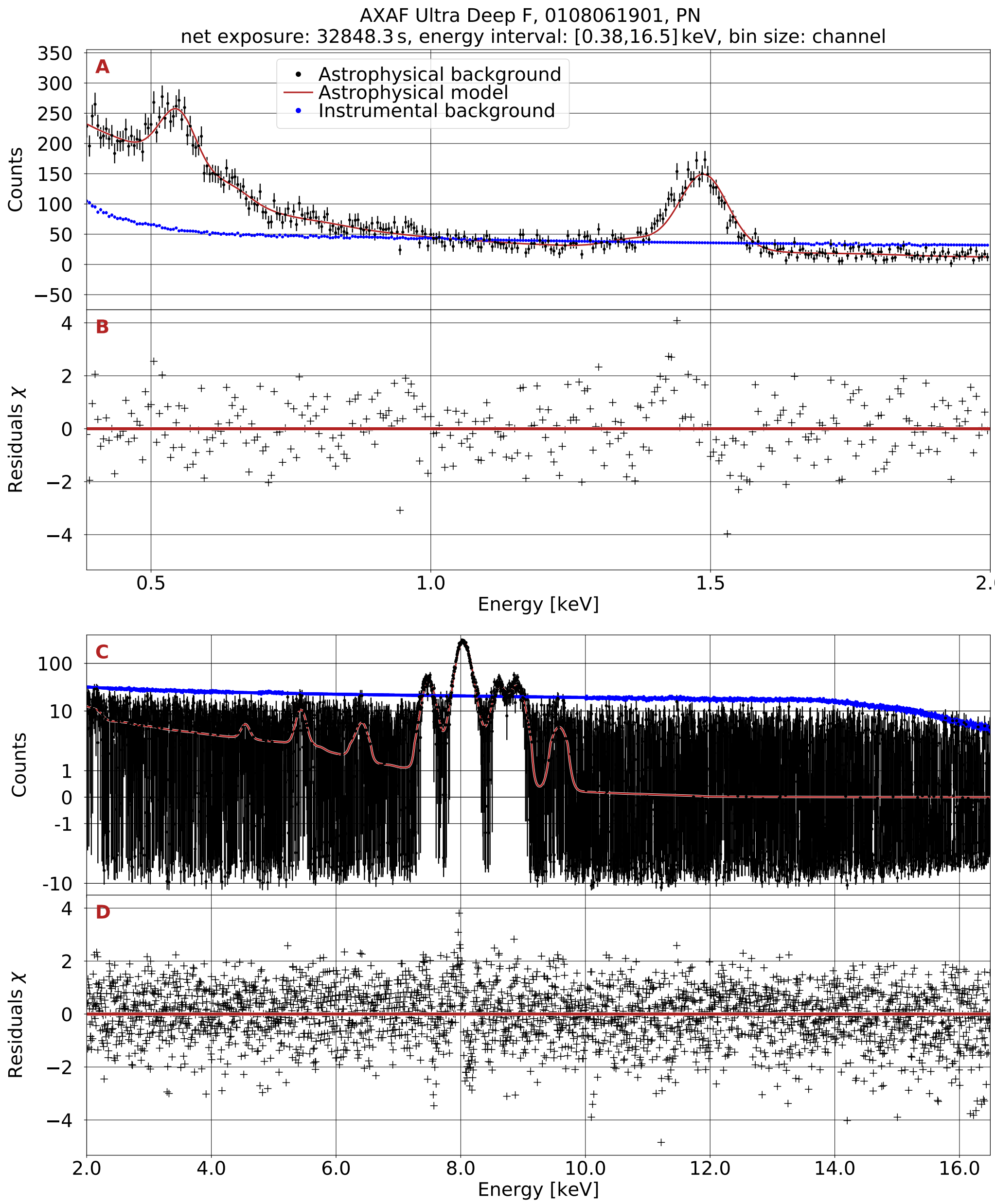

Figure F.32: The panels A and C show the measured spectrum of the data set 0108061901 ($i = 33$, $\mathbf{D_1}$, table 4.1) as black error bars and its fitted null hypothesis model $m_0^{\mathbf{D_1}}$ in an energy range from 0.38 keV to 2 keV (panels A and B) and from 2 keV to 16.5 keV (panels C and D) as red lines, respectively, while the blue error bars show the instrumental background model. The best-fit values are specified in tables 5.1 and 5.2. The panels B and D show the residuals per energy bin in values of $\chi = \mathrm{sgn}(\mathrm{Data} - \mathrm{Model})\sqrt{(\mathrm{Data} - \mathrm{Model})^2}$.

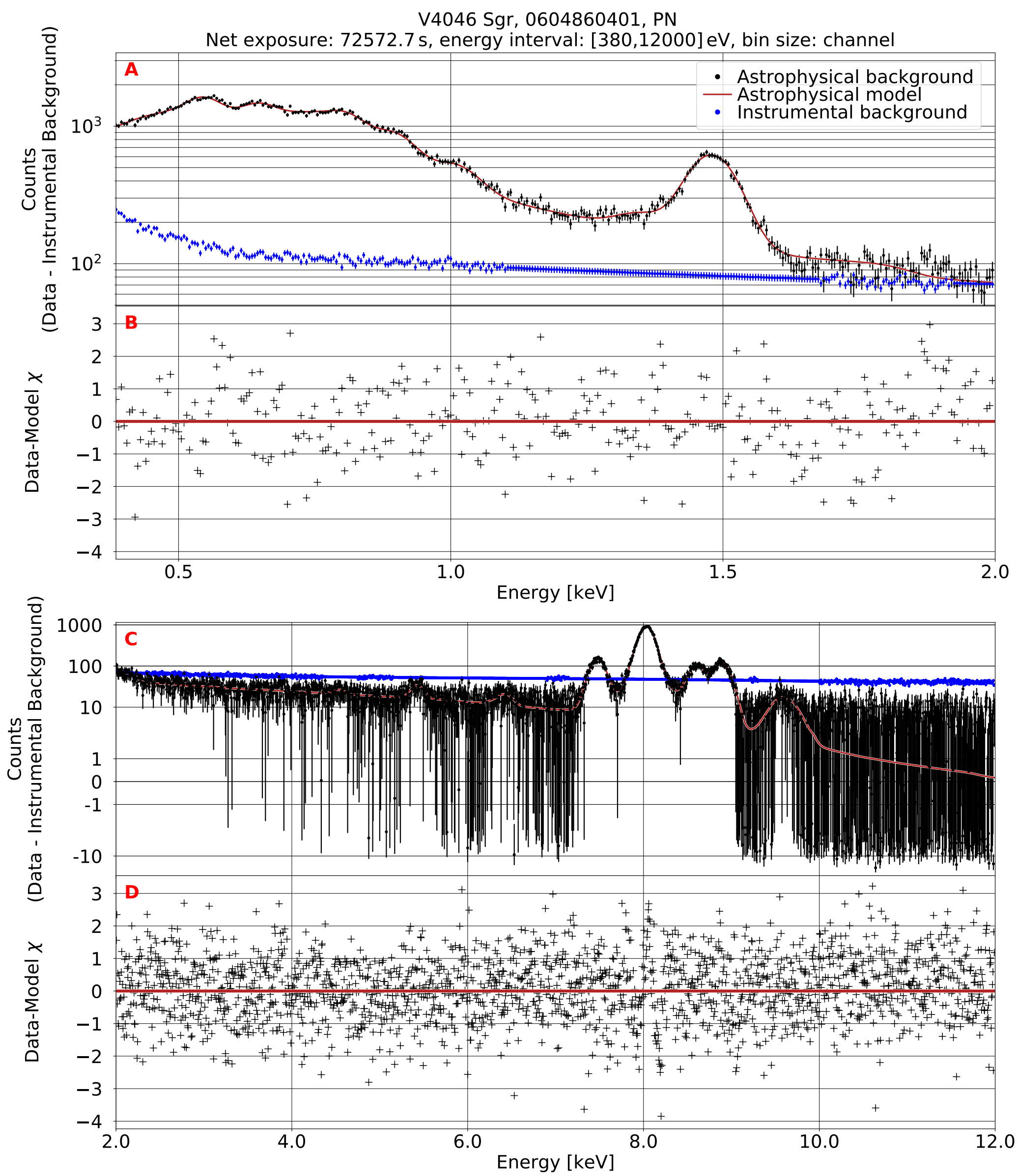

Figure F.33: The panels A and C show the measured spectrum of the data set 0604860401, ($i = 2$, $\mathbf{D_2}$, table 4.2) as black error bars and its fitted null hypothesis model $m_0^{\mathbf{D_2}}$ in an energy range from $0.38\,\mathrm{keV}$ to $2\,\mathrm{keV}$ (panels A and B) and from $2\,\mathrm{keV}$ to $12\,\mathrm{keV}$ (panels C and D) as red lines, respectively, while the blue error bars show the instrumental background model. The best-fit values are specified in tables 5.3 and 5.4. The panels B and D show the residuals per energy bin in values of $\chi = \mathrm{sgn}(\mathrm{Data} - \mathrm{Model})\sqrt{(\mathrm{Data} - \mathrm{Model})^2}$.

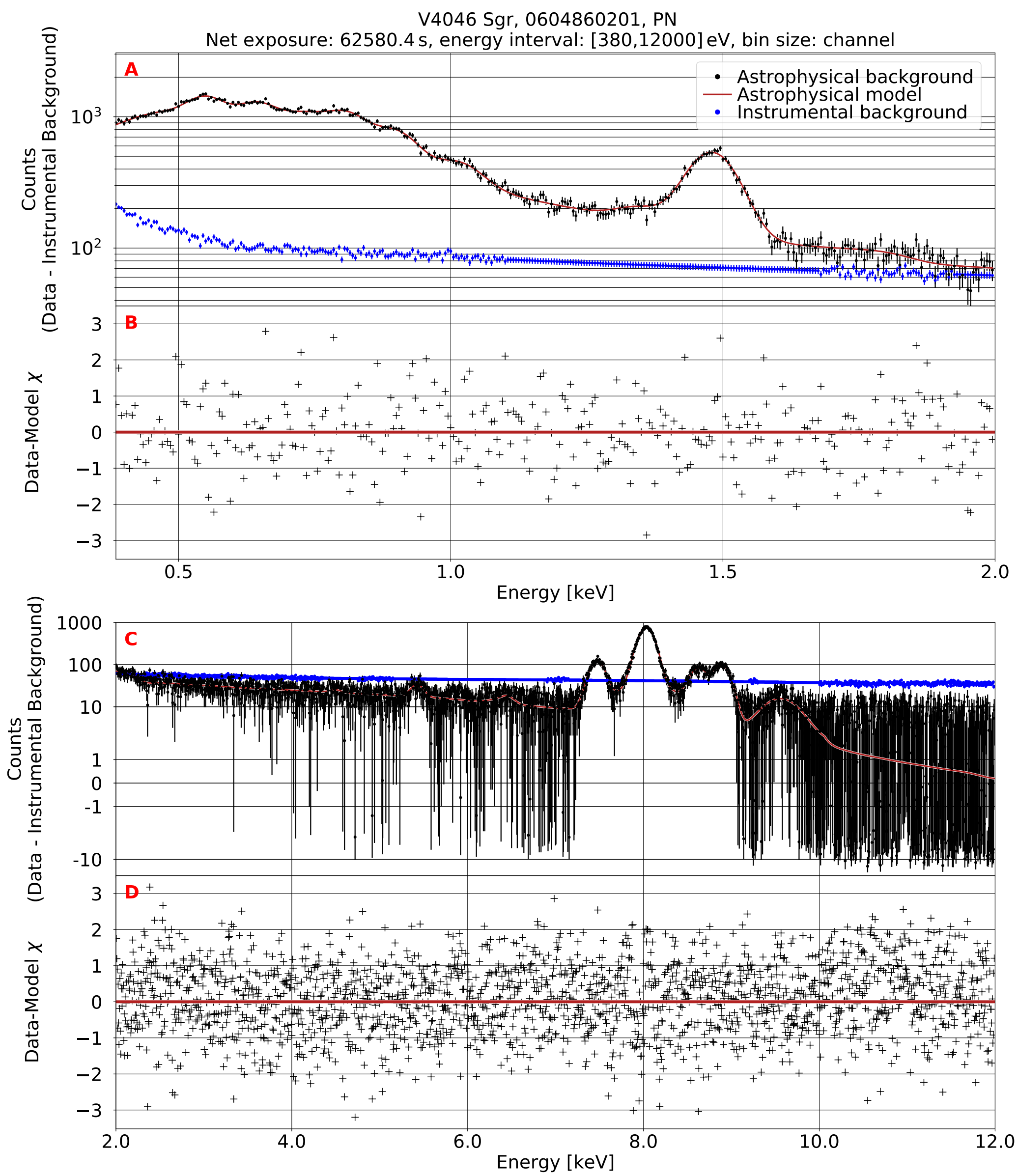

Figure F.34: The panels A and C show the measured spectrum of the data set 0604860201, ($i = 3$, $\mathbf{D_2}$, table 4.2) as black error bars and its fitted null hypothesis model $m_0^{\mathbf{D_2}}$ in an energy range from $0.38\,\mathrm{keV}$ to $2\,\mathrm{keV}$ (panels A and B) and from $2\,\mathrm{keV}$ to $12\,\mathrm{keV}$ (panels C and D) as red lines, respectively, while the blue error bars show the instrumental background model. The best-fit values are specified in tables 5.3 and 5.4. The panels B and D show the residuals per energy bin in values of $\chi = \mathrm{sgn}(\mathrm{Data} - \mathrm{Model})\,\sqrt{(\mathrm{Data} - \mathrm{Model})^2}$.

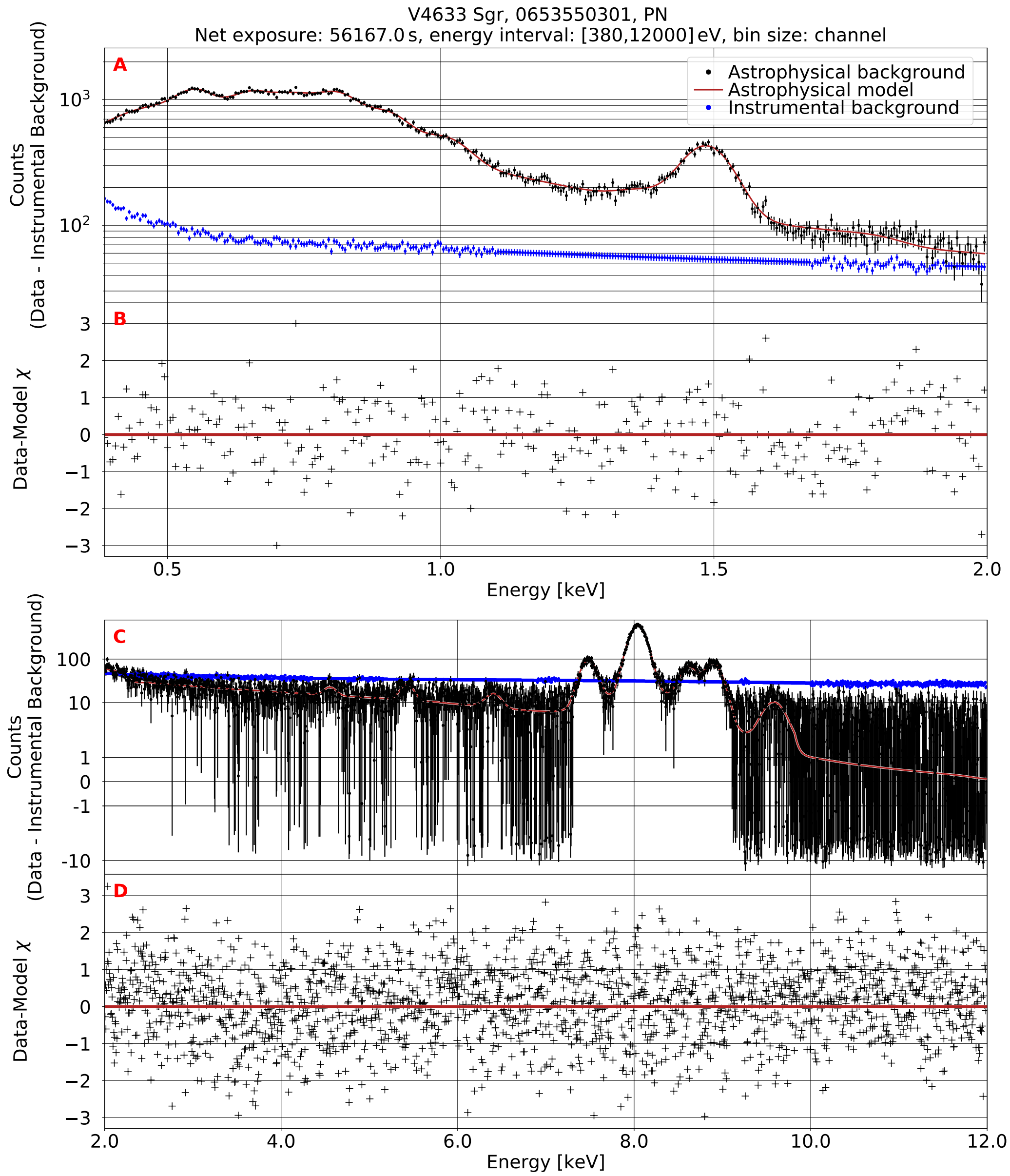

Figure F.35: The panels A and C show the measured spectrum of the data set 0653550301, ($i = 4$, $\mathbf{D_2}$, table 4.2) as black error bars and its fitted null hypothesis model $m_0^{\mathbf{D_2}}$ in an energy range from $0.38\,\mathrm{keV}$ to $2\,\mathrm{keV}$ (panels A and B) and from $2\,\mathrm{keV}$ to $12\,\mathrm{keV}$ (panels C and D) as red lines, respectively, while the blue error bars show the instrumental background model. The best-fit values are specified in tables 5.3 and 5.4. The panels B and D show the residuals per energy bin in values of $\chi = \mathrm{sgn}(\mathrm{Data} - \mathrm{Model})\sqrt{(\mathrm{Data} - \mathrm{Model})^2}$.

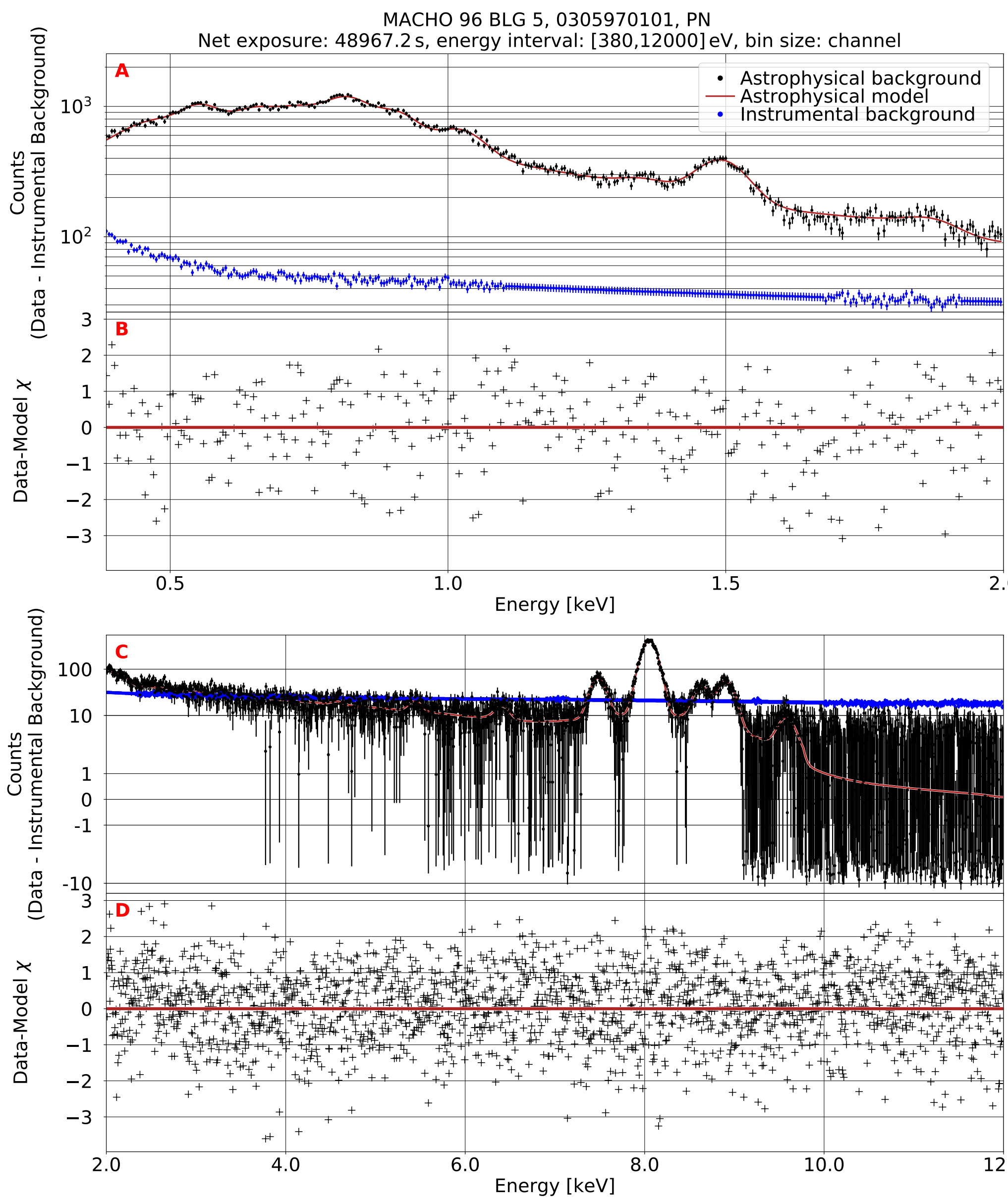

Figure F.36: The panels A and C show the measured spectrum of the data set 0305970101, ($i = 5$, $\mathbf{D_2}$, table 4.2) as black error bars and its fitted null hypothesis model $m_0^{\mathbf{D_2}}$ in an energy range from $0.38\,\mathrm{keV}$ to $2\,\mathrm{keV}$ (panels A and B) and from $2\,\mathrm{keV}$ to $12\,\mathrm{keV}$ (panels C and D) as red lines, respectively, while the blue error bars show the instrumental background model. The best-fit values are specified in tables 5.3 and 5.4. The panels B and D show the residuals per energy bin in values of $\chi = \mathrm{sgn}(\mathrm{Data} - \mathrm{Model})\,\sqrt{(\mathrm{Data} - \mathrm{Model})^2}$.

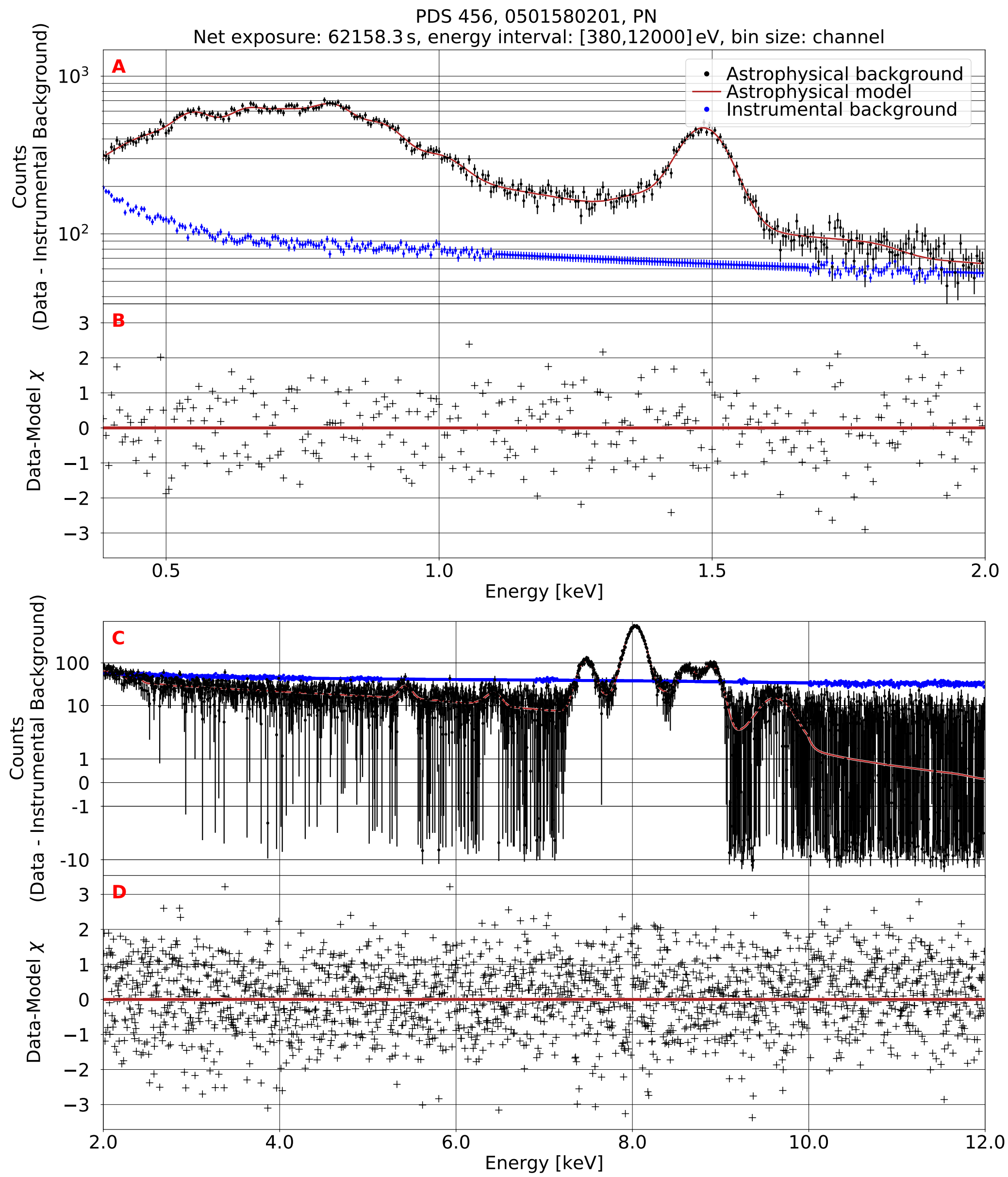

Figure F.37: The panels A and C show the measured spectrum of the data set 0501580201, ($i = 6$, $\mathbf{D_2}$, table 4.2) as black error bars and its fitted null hypothesis model $m_0^{\mathbf{D_2}}$ in an energy range from $0.38\,\mathrm{keV}$ to $2\,\mathrm{keV}$ (panels A and B) and from $2\,\mathrm{keV}$ to $12\,\mathrm{keV}$ (panels C and D) as red lines, respectively, while the blue error bars show the instrumental background model. The best-fit values are specified in tables 5.3 and 5.4. The panels B and D show the residuals per energy bin in values of $\chi = \mathrm{sgn}(\mathrm{Data} - \mathrm{Model})\sqrt{(\mathrm{Data} - \mathrm{Model})^2}$.

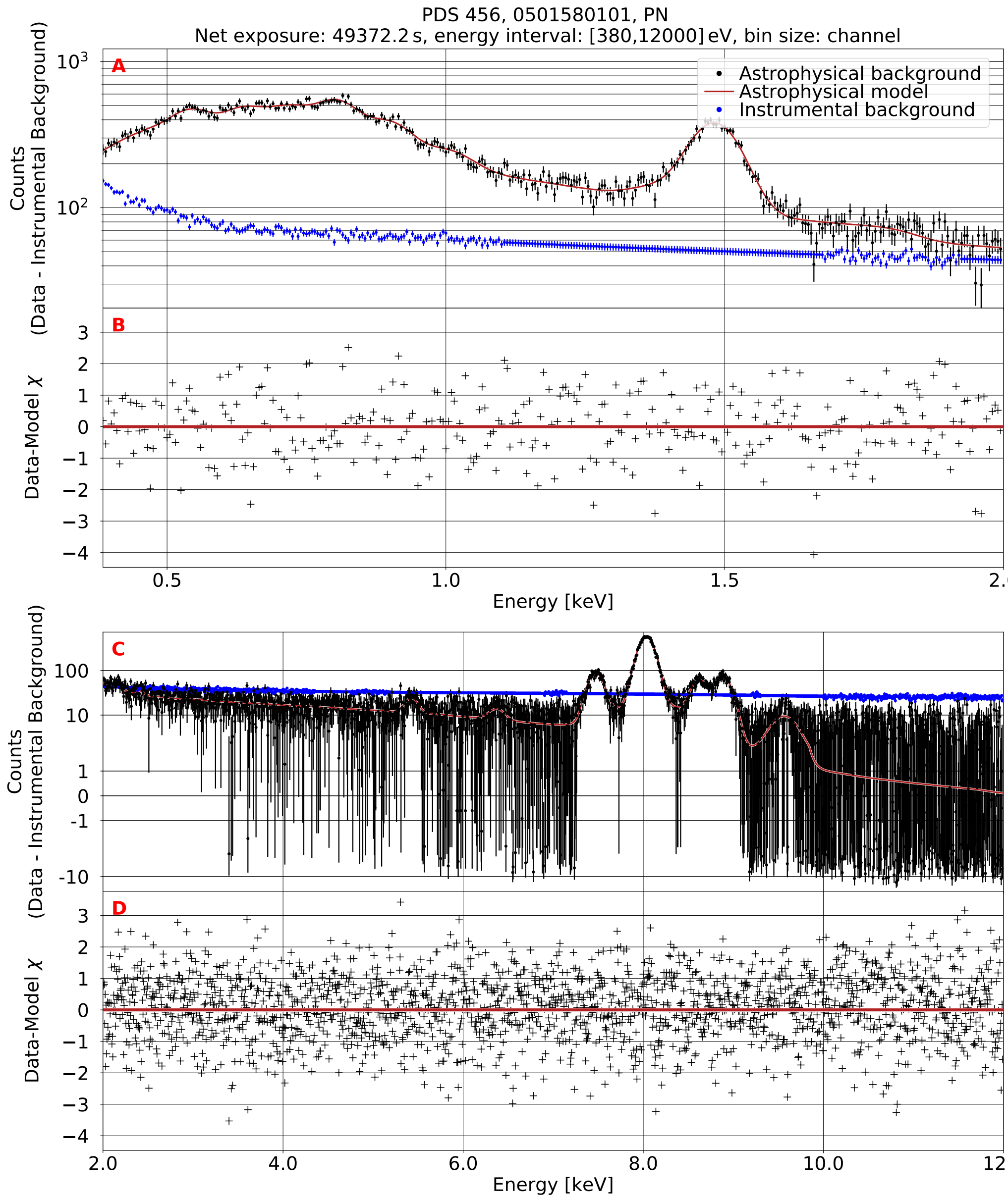

Figure F.38: The panels A and C show the measured spectrum of the data set 0604860301, (i = 7, $\mathbf{D_2}$, table 4.2) as black error bars and its fitted null hypothesis model $m_0^{\mathbf{D_2}}$ in an energy range from 0.38 keV to 2 keV (panels A and B) and from 2 keV to 12 keV (panels C and D) as red lines, respectively, while the blue error bars show the instrumental background model. The best-fit values are specified in tables 5.3 and 5.4. The panels B and D show the residuals per energy bin in values of $\chi = \mathrm{sgn}(\mathrm{Data} - \mathrm{Model})\sqrt{(\mathrm{Data} - \mathrm{Model})^2}$.

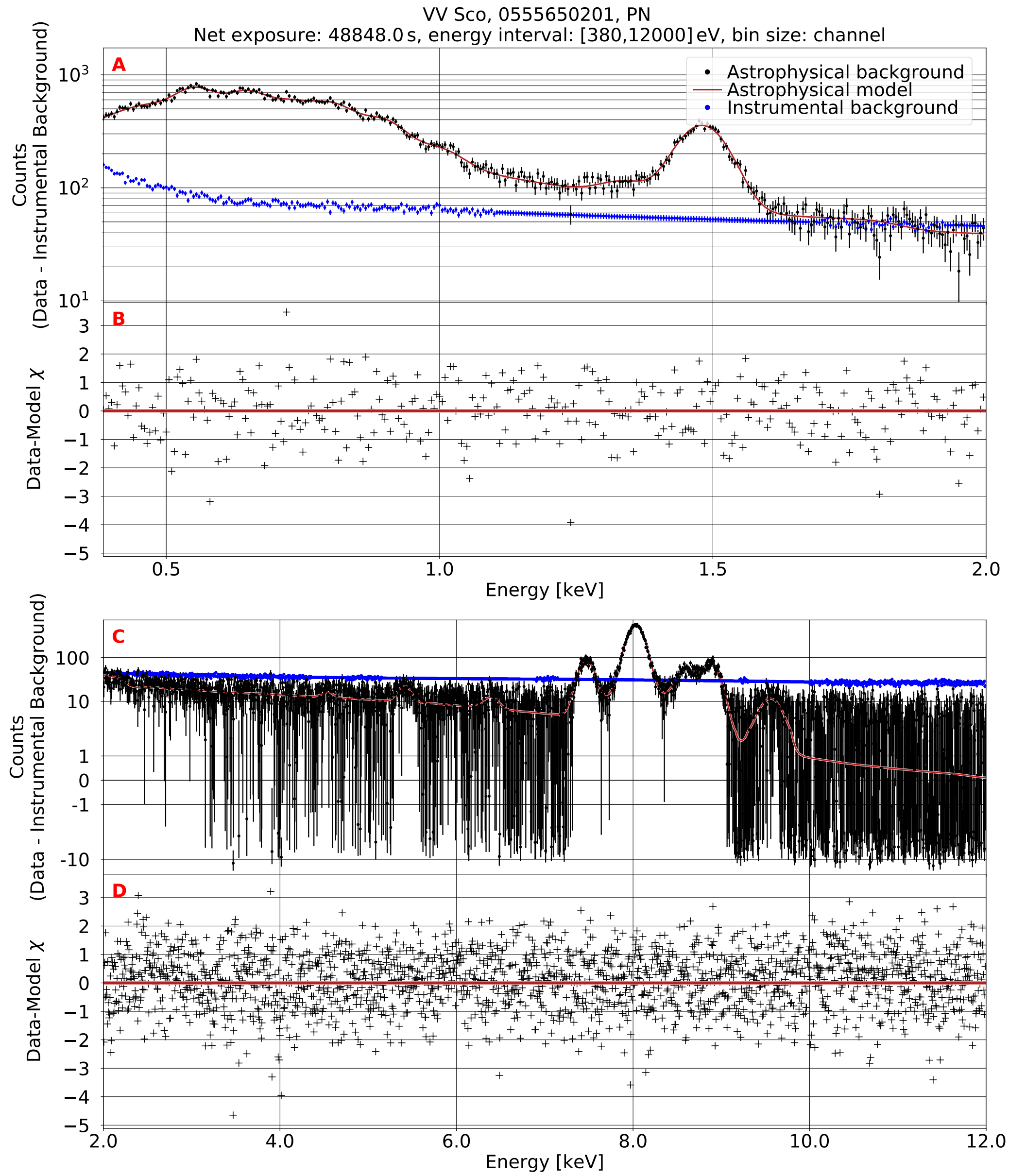

Figure F.39: The panels A and C show the measured spectrum of the data set 0555650201, ($i = 8$, $\mathbf{D_2}$, table 4.2) as black error bars and its fitted null hypothesis model $m_0^{\mathbf{D_2}}$ in an energy range from $0.38\,\text{keV}$ to $2\,\text{keV}$ (panels A and B) and from $2\,\text{keV}$ to $12\,\text{keV}$ (panels C and D) as red lines, respectively, while the blue error bars show the instrumental background model. The best-fit values are specified in tables 5.3 and 5.4. The panels B and D show the residuals per energy bin in values of $\chi = \text{sgn}(\text{Data} - \text{Model})\sqrt{(\text{Data} - \text{Model})^2}$.

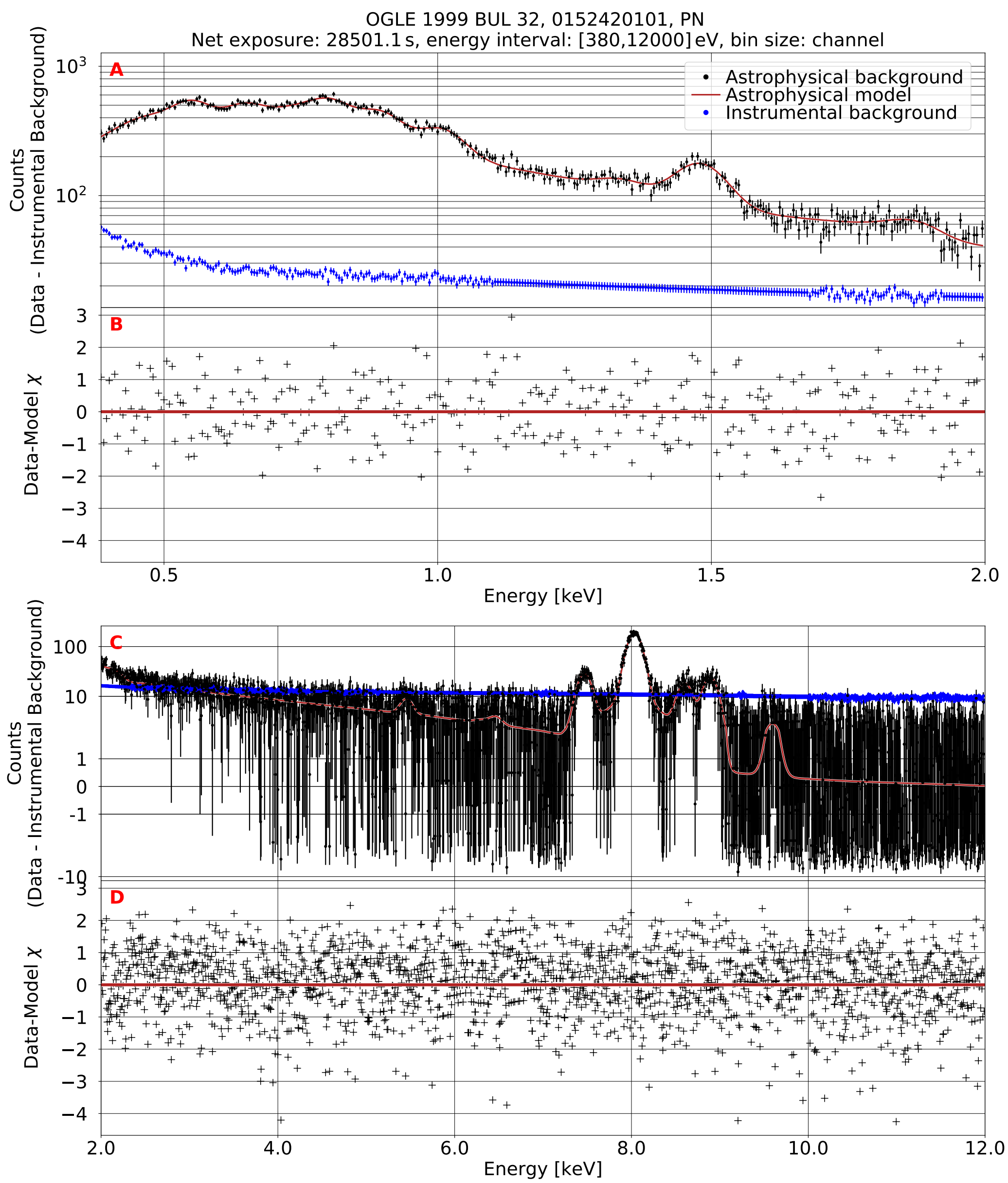

Figure F.40: The panels A and C show the measured spectrum of the data set 0152420101, ($i = 9$, $\mathbf{D_2}$, table 4.2) as black error bars and its fitted null hypothesis model $m_0^{\mathbf{D_2}}$ in an energy range from 0.38 keV to 2 keV (panels A and B) and from 2 keV to 12 keV (panels C and D) as red lines, respectively, while the blue error bars show the instrumental background model. The best-fit values are specified in tables 5.3 and 5.4. The panels B and D show the residuals per energy bin in values of $\chi = \mathrm{sgn}(\mathrm{Data} - \mathrm{Model})\sqrt{(\mathrm{Data} - \mathrm{Model})^2}$.

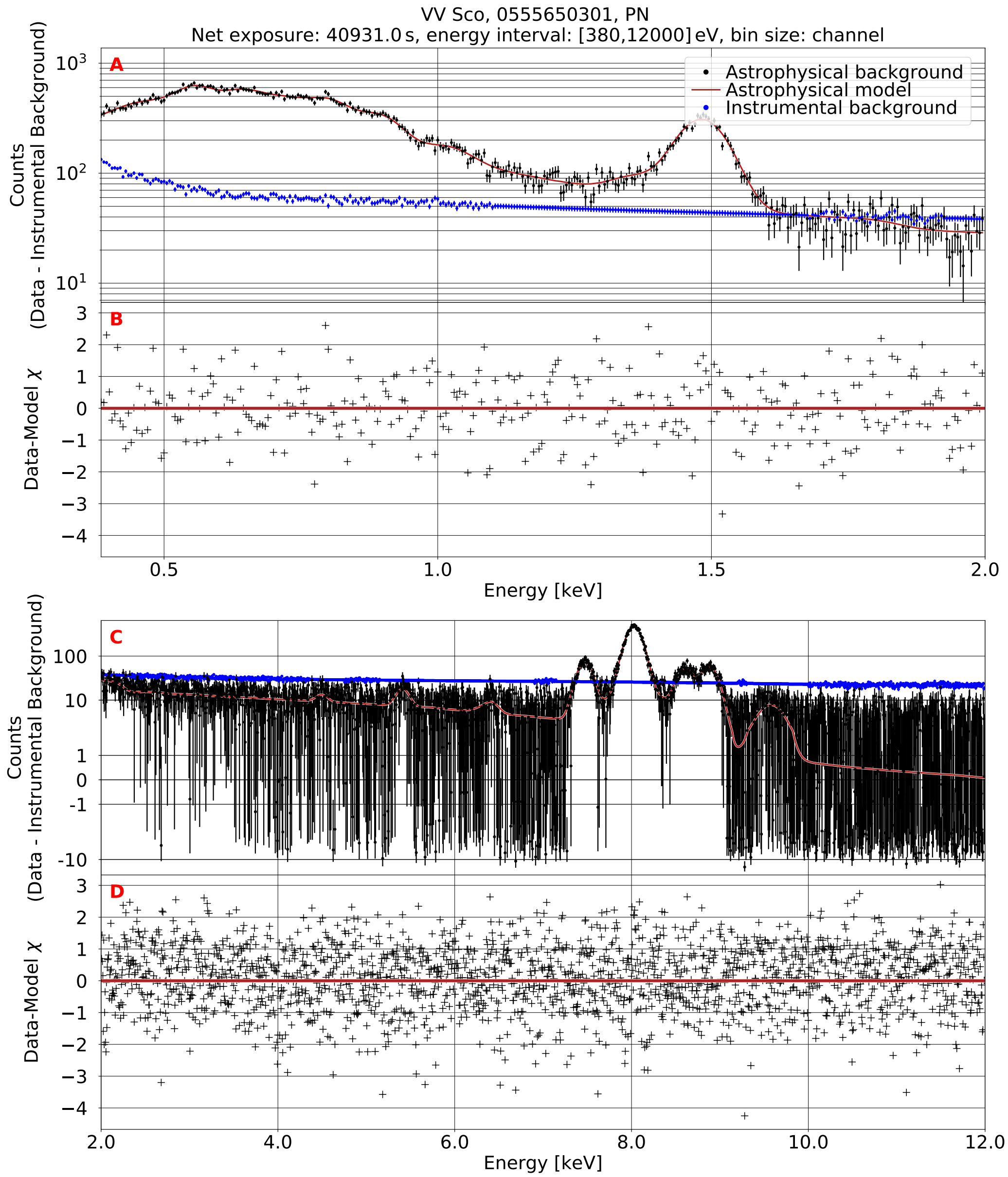

Figure F.41: The panels A and C show the measured spectrum of the data set 0555650301, ($i = 10$, $\mathbf{D_2}$, table 4.2) as black error bars and its fitted null hypothesis model $m_0^{\mathbf{D_2}}$ in an energy range from $0.38\,\mathrm{keV}$ to $2\,\mathrm{keV}$ (panels A and B) and from $2\,\mathrm{keV}$ to $12\,\mathrm{keV}$ (panels C and D) as red lines, respectively, while the blue error bars show the instrumental background model. The best-fit values are specified in tables 5.3 and 5.4. The panels B and D show the residuals per energy bin in values of $\chi = \mathrm{sgn}(\mathrm{Data} - \mathrm{Model})\sqrt{(\mathrm{Data} - \mathrm{Model})^2}$.

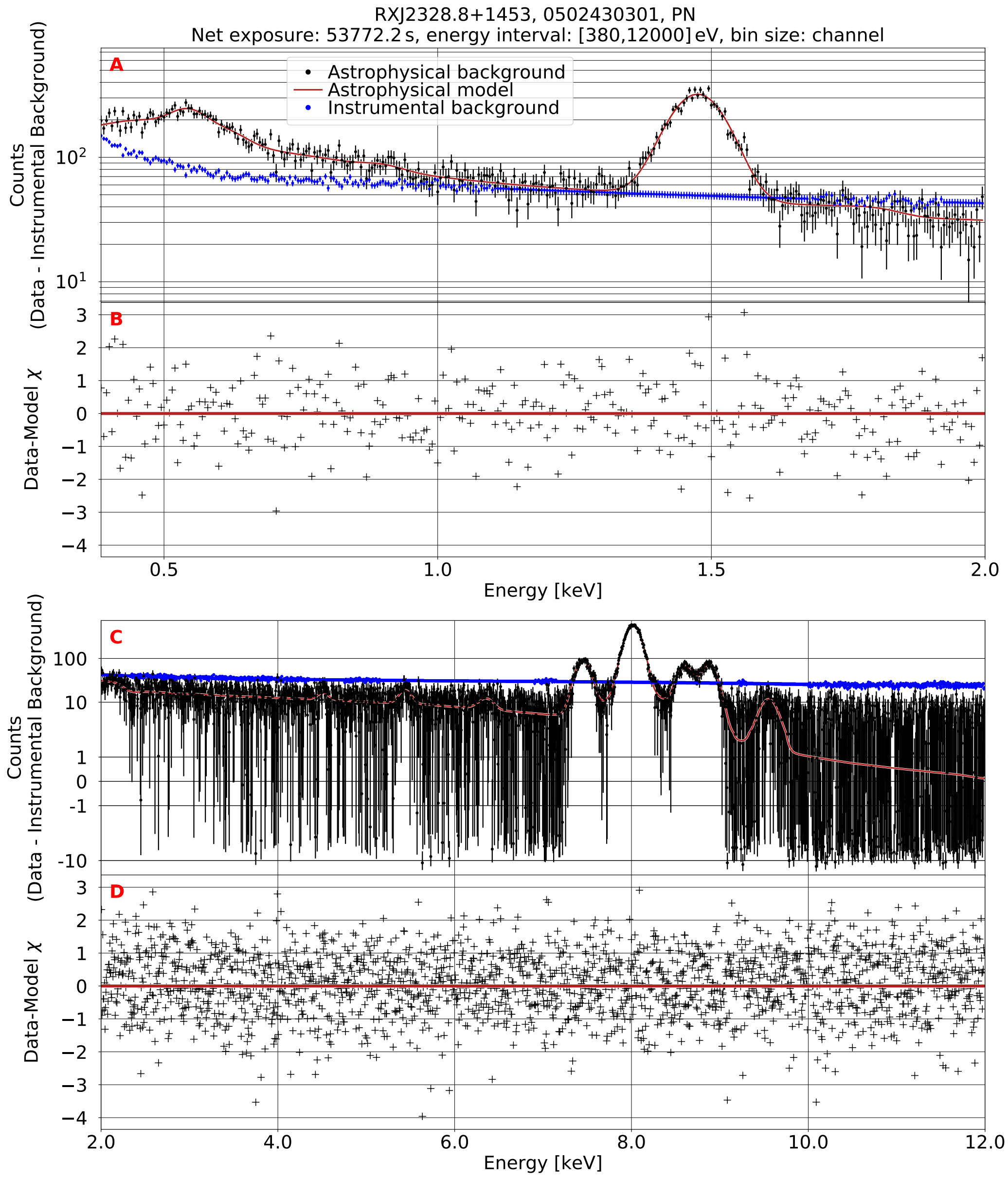

Figure F.42: The panels A and C show the measured spectrum of the data set 0502430301, (i = 11, $\mathbf{D_2}$, table 4.2) as black error bars and its fitted null hypothesis model $m_0^{\mathbf{D_2}}$ in an energy range from 0.38 keV to 2 keV (panels A and B) and from 2 keV to 12 keV (panels C and D) as red lines, respectively, while the blue error bars show the instrumental background model. The best-fit values are specified in tables 5.3 and 5.4. The panels B and D show the residuals per energy bin in values of $\chi = \mathrm{sgn}(\mathrm{Data} - \mathrm{Model})\sqrt{(\mathrm{Data} - \mathrm{Model})^2}$.

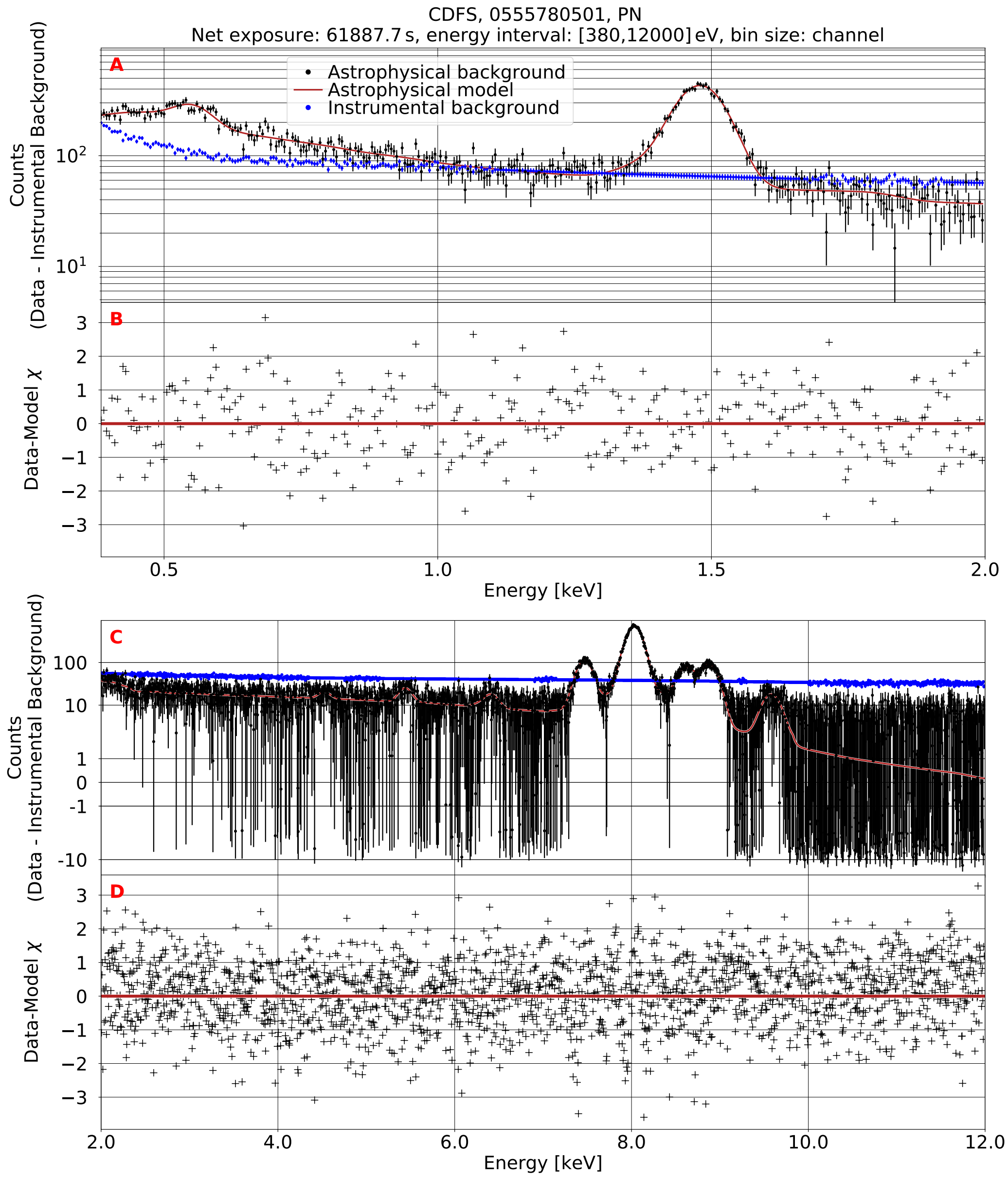

Figure F.43: The panels A and C show the measured spectrum of the data set 0555780501, ($i = 12$, $\mathbf{D_2}$, table 4.2) as black error bars and its fitted null hypothesis model $m_0^{\mathbf{D_2}}$ in an energy range from $0.38\,\mathrm{keV}$ to $2\,\mathrm{keV}$ (panels A and B) and from $2\,\mathrm{keV}$ to $12\,\mathrm{keV}$ (panels C and D) as red lines, respectively, while the blue error bars show the instrumental background model. The best-fit values are specified in tables 5.3 and 5.4. The panels B and D show the residuals per energy bin in values of $\chi = \mathrm{sgn}(\mathrm{Data} - \mathrm{Model})\sqrt{(\mathrm{Data} - \mathrm{Model})^2}$.

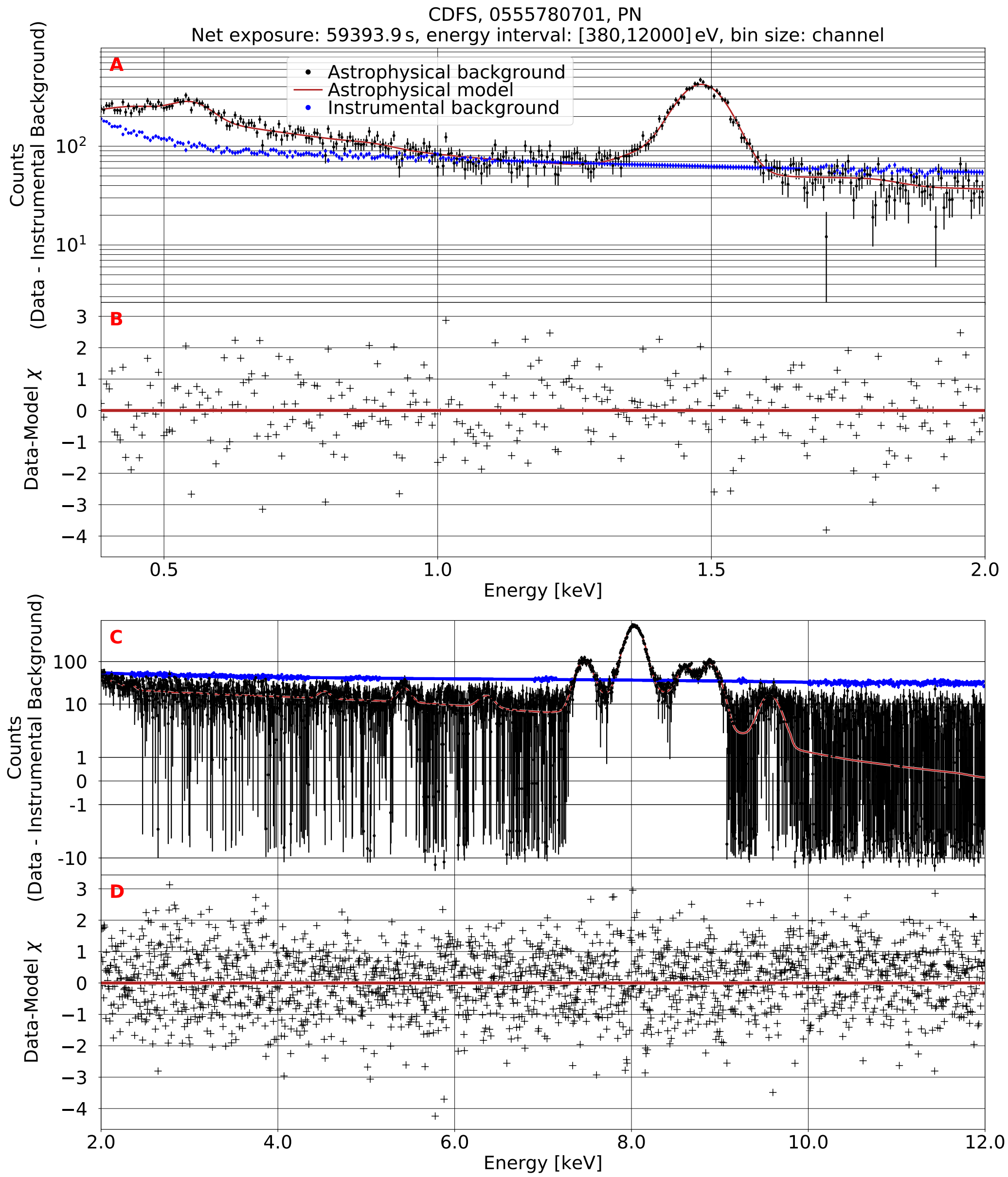

Figure F.44: The panels A and C show the measured spectrum of the data set 0555780701, (i = 13, $\mathbf{D_2}$, table 4.2) as black error bars and its fitted null hypothesis model $m_0^{\mathbf{D_2}}$ in an energy range from 0.38 keV to 2 keV (panels A and B) and from 2 keV to 12 keV (panels C and D) as red lines, respectively, while the blue error bars show the instrumental background model. The best-fit values are specified in tables 5.3 and 5.4. The panels B and D show the residuals per energy bin in values of $\chi = \mathrm{sgn}(\mathrm{Data} - \mathrm{Model})\,\sqrt{(\mathrm{Data} - \mathrm{Model})^2}$.

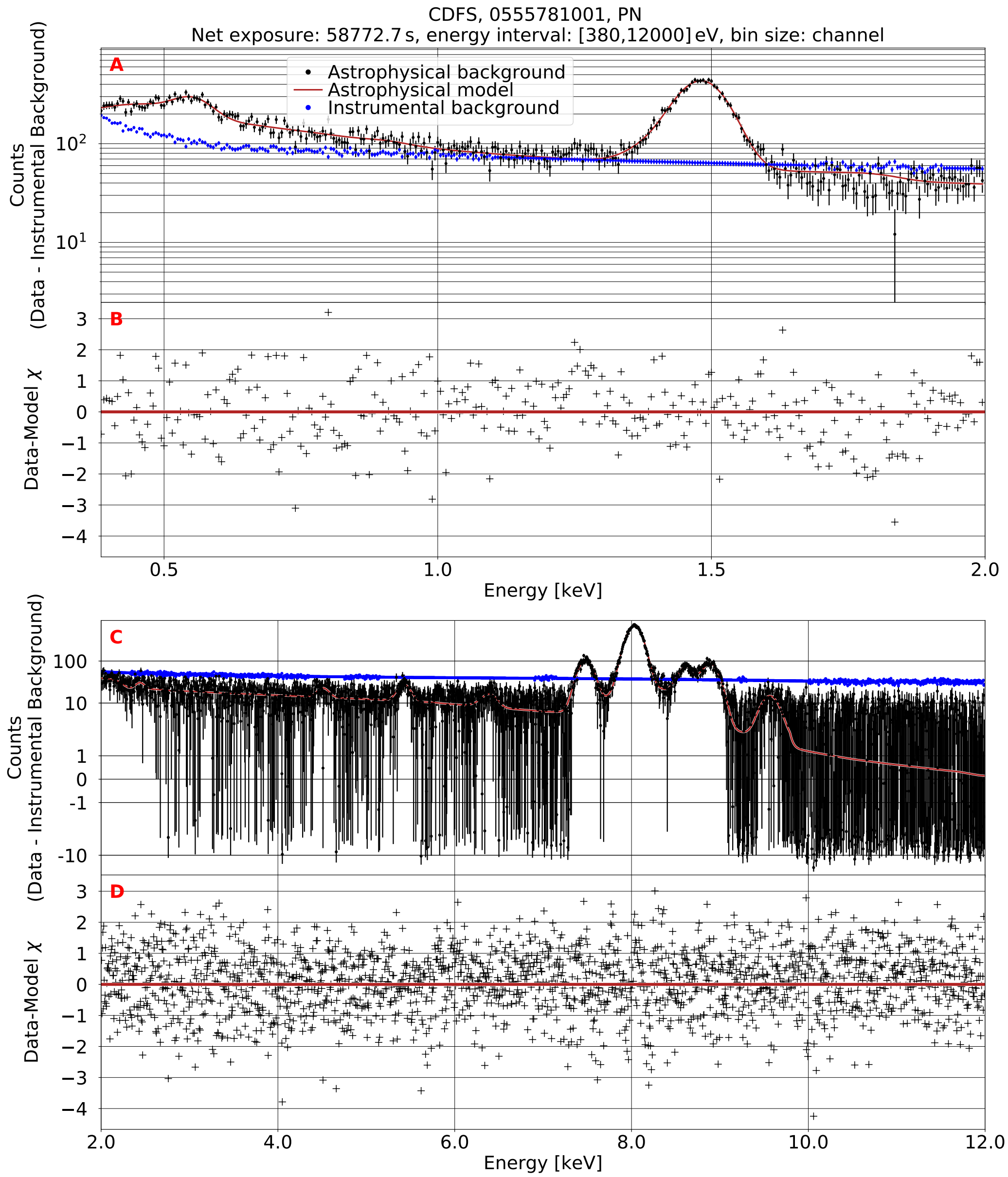

Figure F.45: The panels A and C show the measured spectrum of the data set 0555781001, (i = 14, $\mathbf{D_2}$, table 4.2) as black error bars and its fitted null hypothesis model $m_0^{\mathbf{D_2}}$ in an energy range from 0.38 keV to 2 keV (panels A and B) and from 2 keV to 12 keV (panels C and D) as red lines, respectively, while the blue error bars show the instrumental background model. The best-fit values are specified in tables 5.3 and 5.4. The panels B and D show the residuals per energy bin in values of $\chi = \text{sgn}(\text{Data} - \text{Model})\sqrt{(\text{Data} - \text{Model})^2}$.

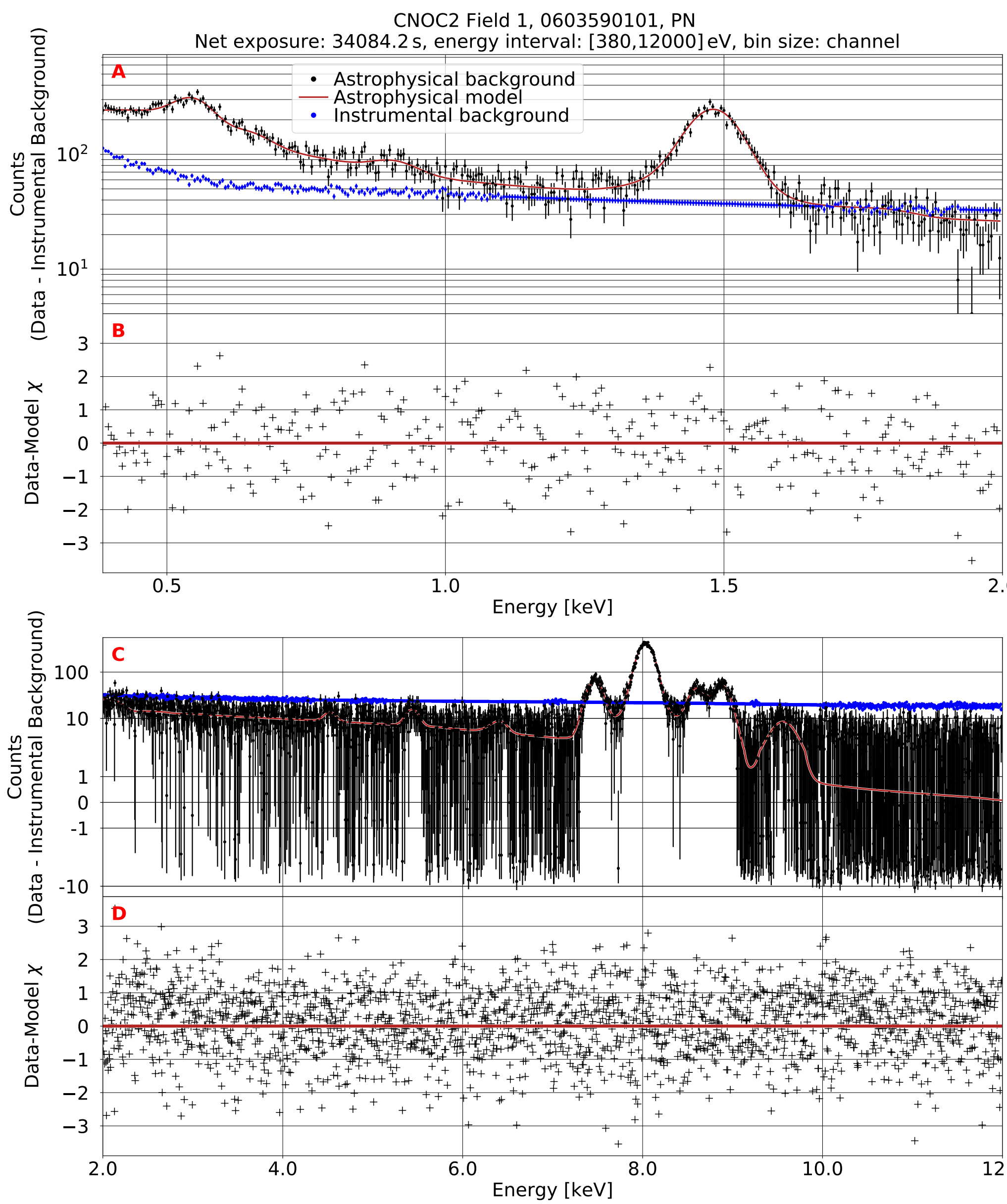

Figure F.46: The panels A and C show the measured spectrum of the data set 0603590101, ($i = 15$, $\mathbf{D_2}$, table 4.2) as black error bars and its fitted null hypothesis model $m_0^{\mathbf{D_2}}$ in an energy range from 0.38 keV to 2 keV (panels A and B) and from 2 keV to 12 keV (panels C and D) as red lines, respectively, while the blue error bars show the instrumental background model. The best-fit values are specified in tables 5.3 and 5.4. The panels B and D show the residuals per energy bin in values of $\chi = \mathrm{sgn}(\mathrm{Data} - \mathrm{Model})\,\sqrt{(\mathrm{Data} - \mathrm{Model})^2}$.

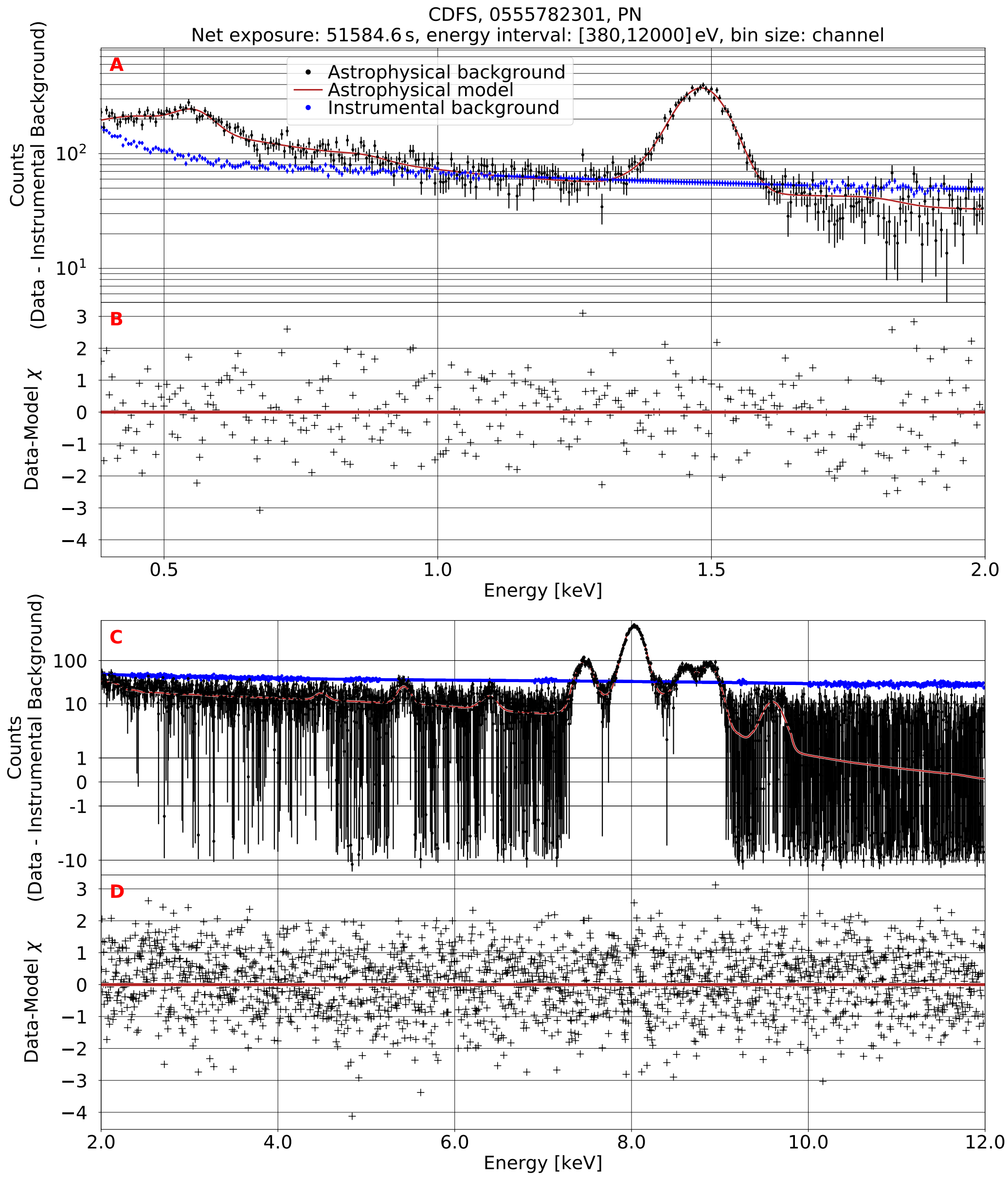

Figure F.47: The panels A and C show the measured spectrum of the data set 0555782301, (i = 16, $\mathbf{D_2}$, table 4.2) as black error bars and its fitted null hypothesis model $m_0^{\mathbf{D_2}}$ in an energy range from 0.38 keV to 2 keV (panels A and B) and from 2 keV to 12 keV (panels C and D) as red lines, respectively, while the blue error bars show the instrumental background model. The best-fit values are specified in tables 5.3 and 5.4. The panels B and D show the residuals per energy bin in values of $\chi = \mathrm{sgn}(\mathrm{Data} - \mathrm{Model})\sqrt{(\mathrm{Data} - \mathrm{Model})^2}$.

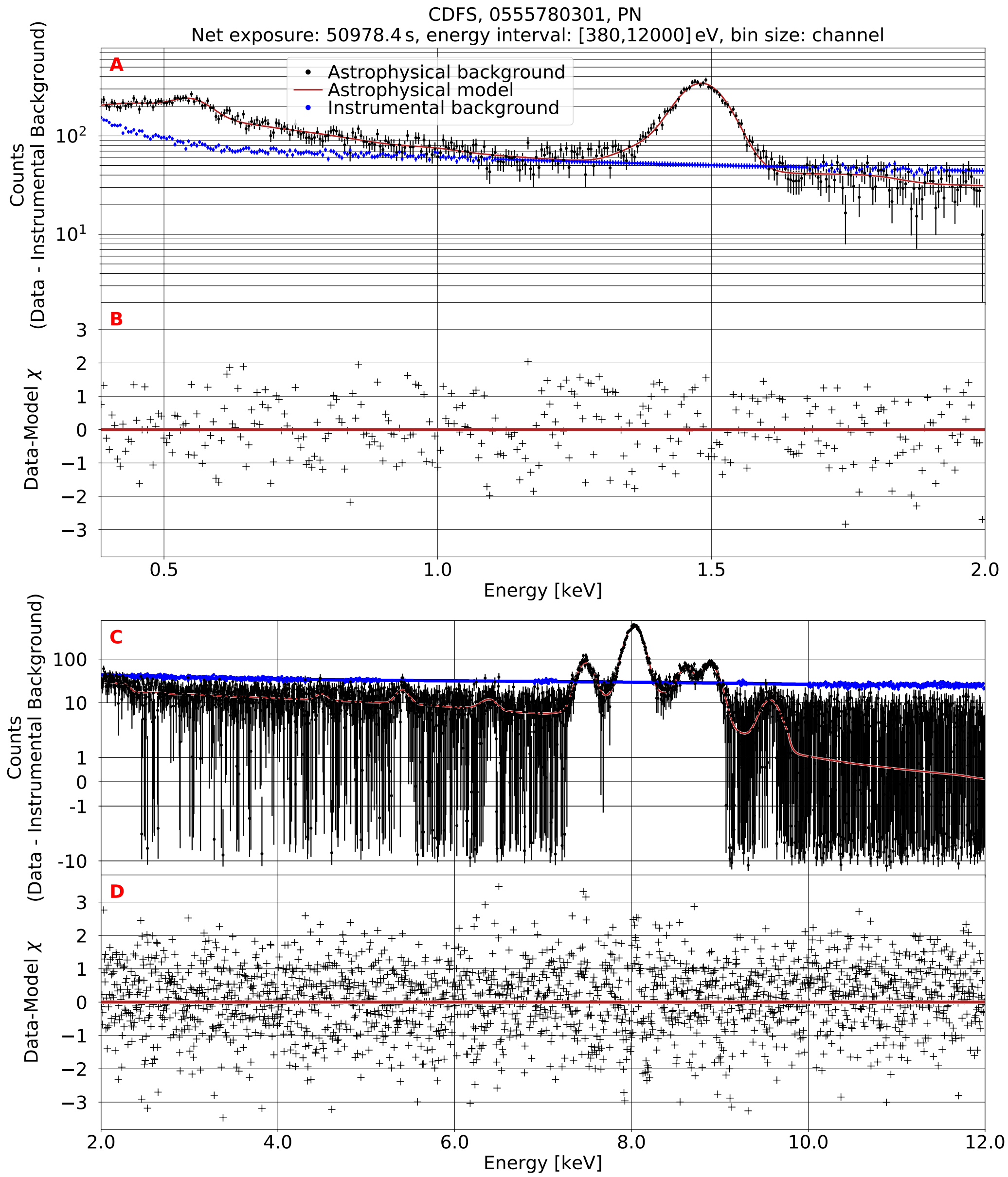

Figure F.48: The panels A and C show the measured spectrum of the data set 0555780301, (i = 17, $\mathbf{D_2}$, table 4.2) as black error bars and its fitted null hypothesis model $m_0^{\mathbf{D_2}}$ in an energy range from $0.38\,\mathrm{keV}$ to $2\,\mathrm{keV}$ (panels A and B) and from $2\,\mathrm{keV}$ to $12\,\mathrm{keV}$ (panels C and D) as red lines, respectively, while the blue error bars show the instrumental background model. The best-fit values are specified in tables 5.3 and 5.4. The panels B and D show the residuals per energy bin in values of $\chi = \mathrm{sgn}(\mathrm{Data} - \mathrm{Model})\sqrt{(\mathrm{Data} - \mathrm{Model})^2}$.

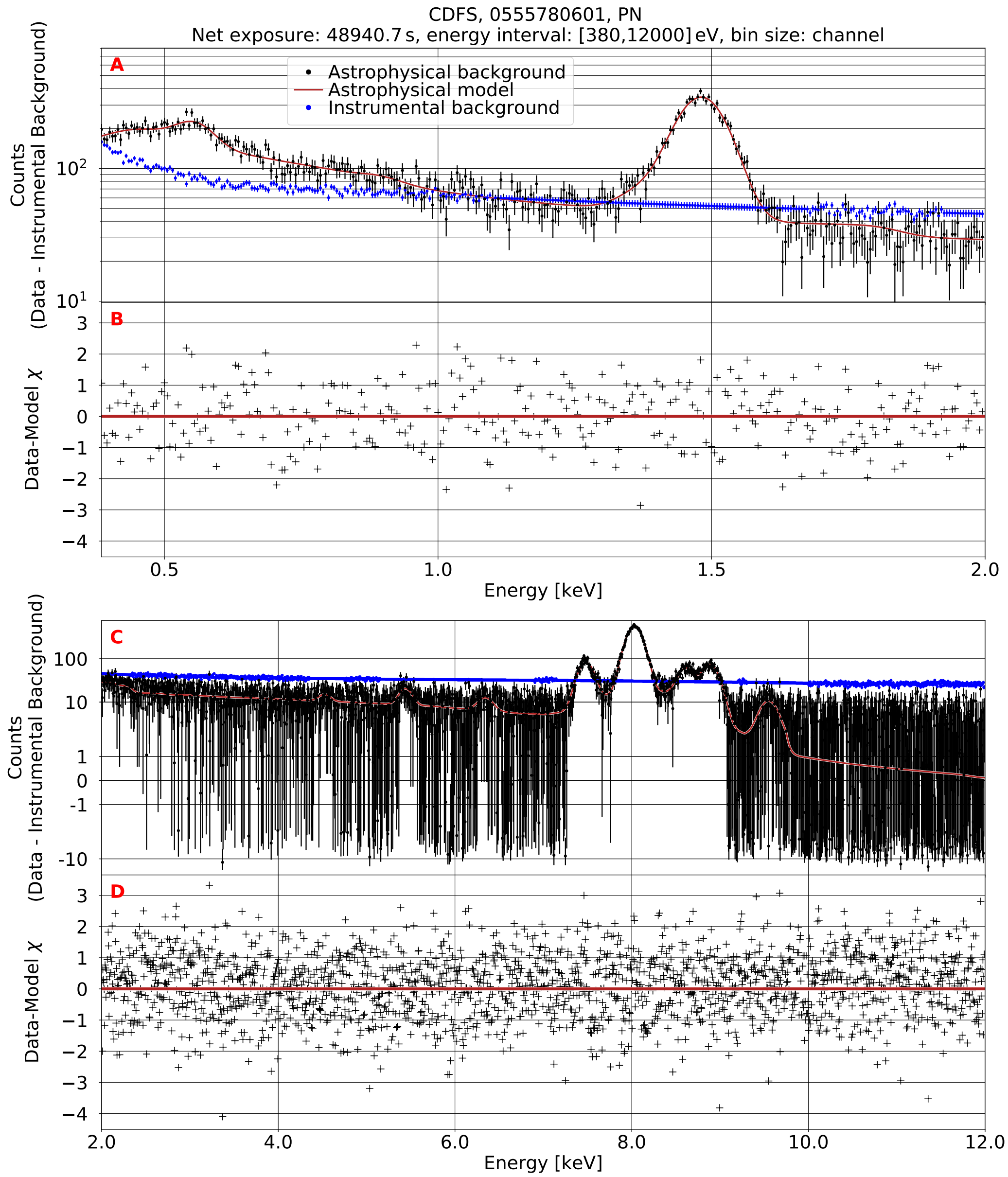

Figure F.49: The panels A and C show the measured spectrum of the data set 0555780601, ($i = 18$, $\mathbf{D_2}$, table 4.2) as black error bars and its fitted null hypothesis model $m_0^{\mathbf{D_2}}$ in an energy range from 0.38 keV to 2 keV (panels A and B) and from 2 keV to 12 keV (panels C and D) as red lines, respectively, while the blue error bars show the instrumental background model. The best-fit values are specified in tables 5.3 and 5.4. The panels B and D show the residuals per energy bin in values of $\chi = \mathrm{sgn}(\mathrm{Data} - \mathrm{Model})\sqrt{(\mathrm{Data} - \mathrm{Model})^2}$.

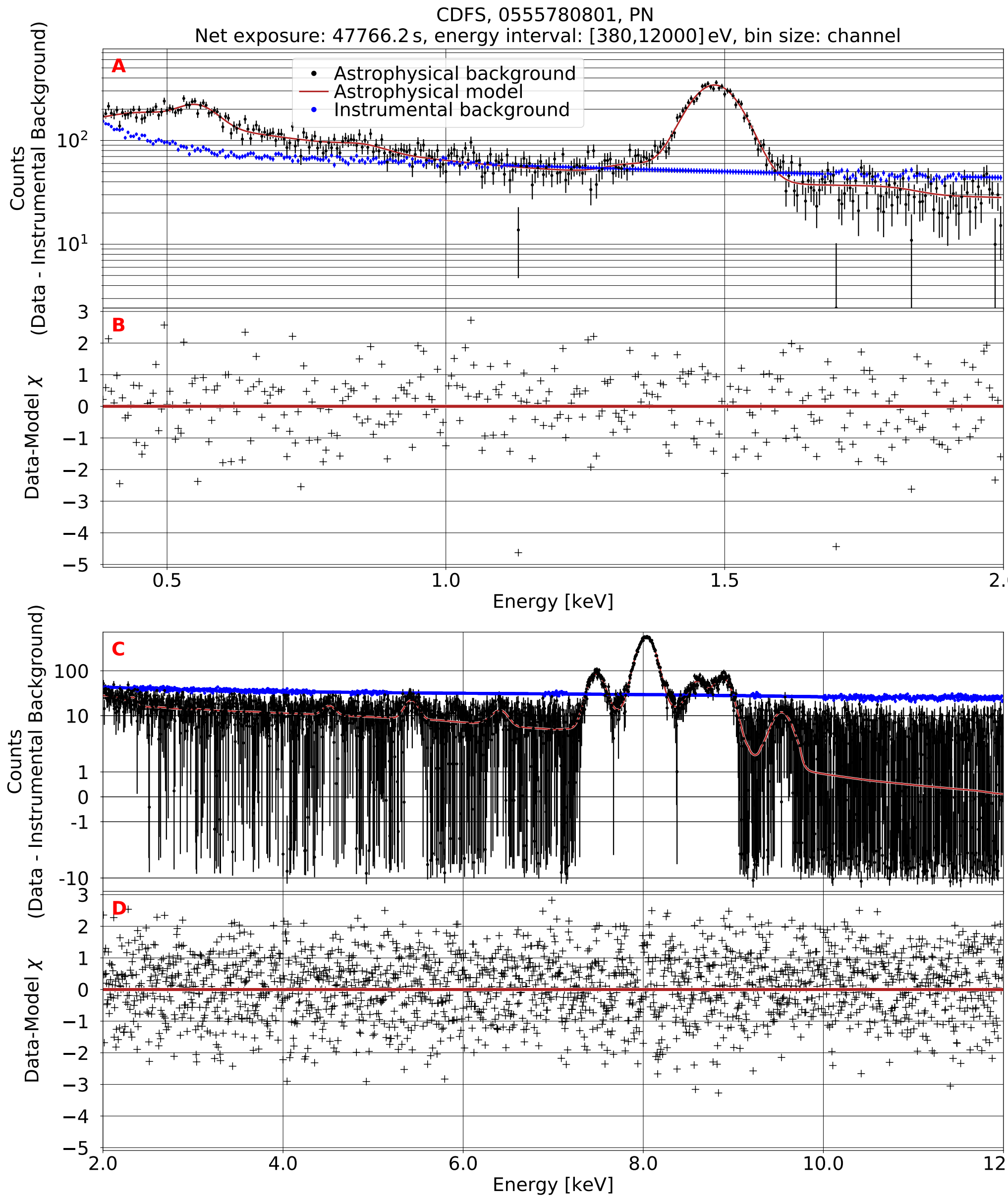

Figure F.50: The panels A and C show the measured spectrum of the data set 0555780801, ($i = 19$, $\mathbf{D_2}$, table 4.2) as black error bars and its fitted null hypothesis model $m_0^{\mathbf{D_2}}$ in an energy range from 0.38 keV to 2 keV (panels A and B) and from 2 keV to 12 keV (panels C and D) as red lines, respectively, while the blue error bars show the instrumental background model. The best-fit values are specified in tables 5.3 and 5.4. The panels B and D show the residuals per energy bin in values of $\chi = \mathrm{sgn}(\mathrm{Data} - \mathrm{Model})\sqrt{(\mathrm{Data} - \mathrm{Model})^2}$.

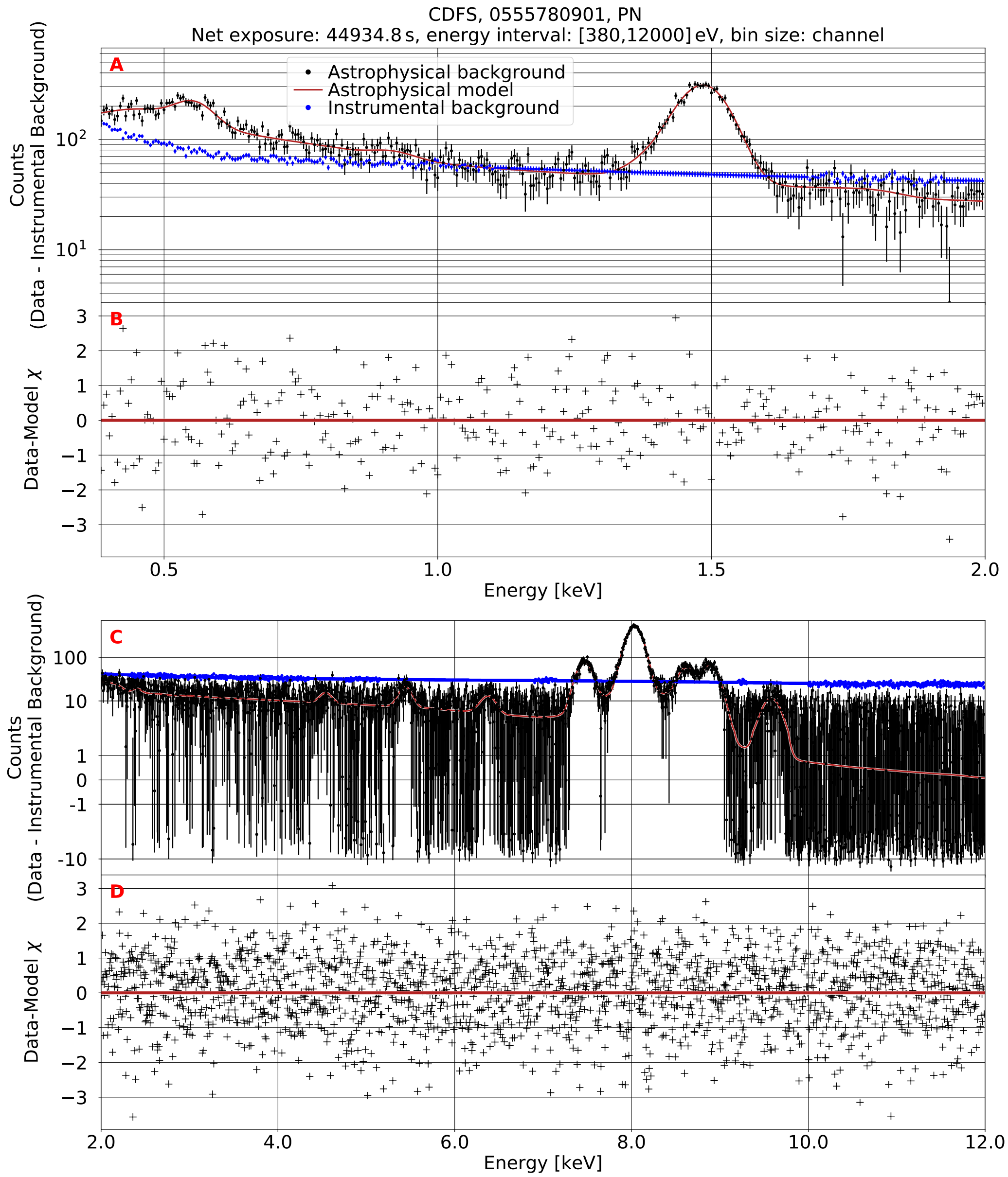

Figure F.51: The panels A and C show the measured spectrum of the data set 0555780901, ($i = 20$, $\mathbf{D_2}$, table 4.2) as black error bars and its fitted null hypothesis model $m_0^{\mathbf{D_2}}$ in an energy range from $0.38\,\mathrm{keV}$ to $2\,\mathrm{keV}$ (panels A and B) and from $2\,\mathrm{keV}$ to $12\,\mathrm{keV}$ (panels C and D) as red lines, respectively, while the blue error bars show the instrumental background model. The best-fit values are specified in tables 5.3 and 5.4. The panels B and D show the residuals per energy bin in values of $\chi = \mathrm{sgn}(\mathrm{Data} - \mathrm{Model})\sqrt{(\mathrm{Data} - \mathrm{Model})^2}$.

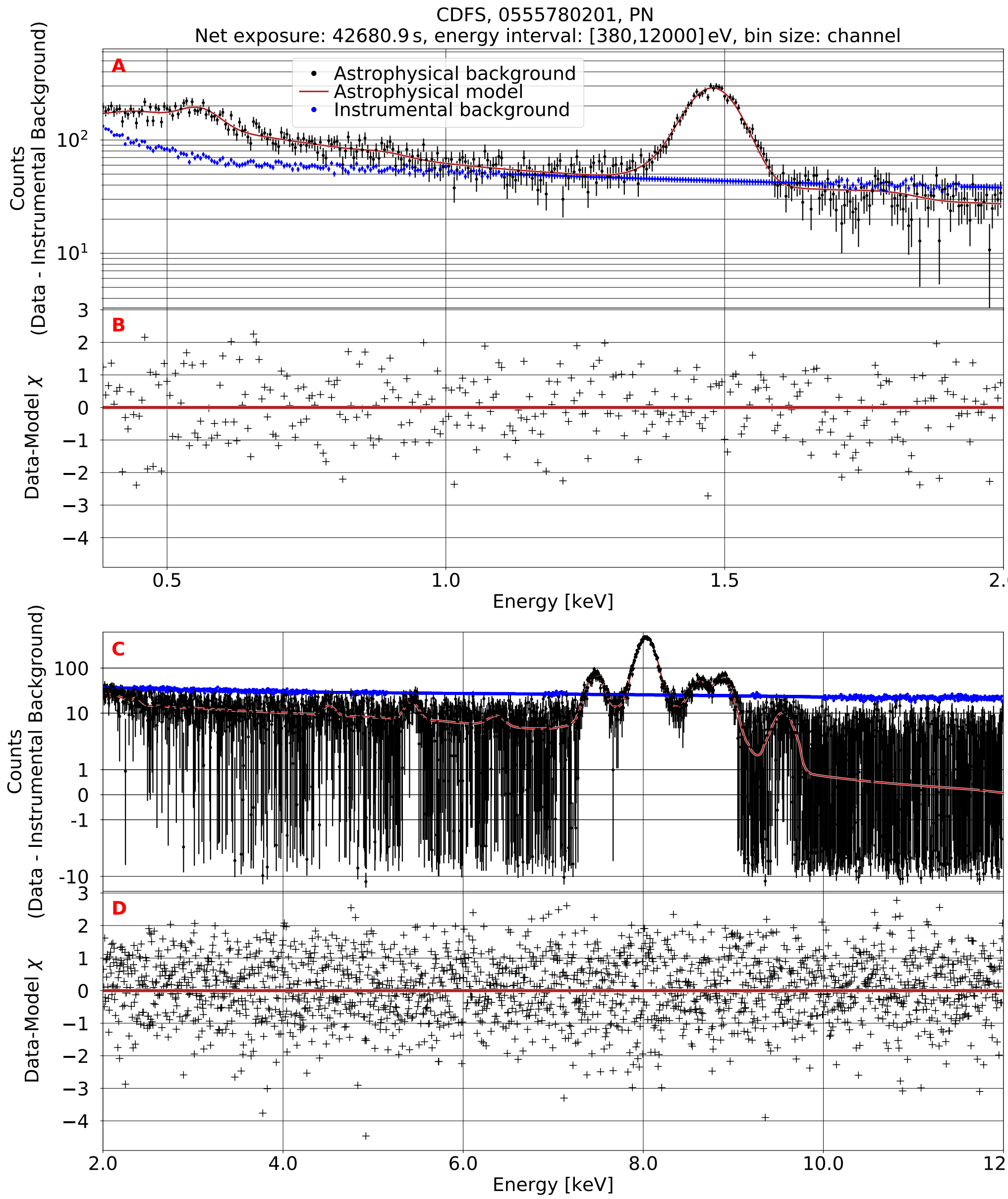

Figure F.52: The panels A and C show the measured spectrum of the data set 0555780201, (i = 21, $\mathbf{D_2}$, table 4.2) as black error bars and its fitted null hypothesis model $m_0^{\mathbf{D_2}}$ in an energy range from 0.38 keV to 2 keV (panels A and B) and from 2 keV to 12 keV (panels C and D) as red lines, respectively, while the blue error bars show the instrumental background model. The best-fit values are specified in tables 5.3 and 5.4. The panels B and D show the residuals per energy bin in values of $\chi = \mathrm{sgn}(\mathrm{Data} - \mathrm{Model})\sqrt{(\mathrm{Data} - \mathrm{Model})^2}$.

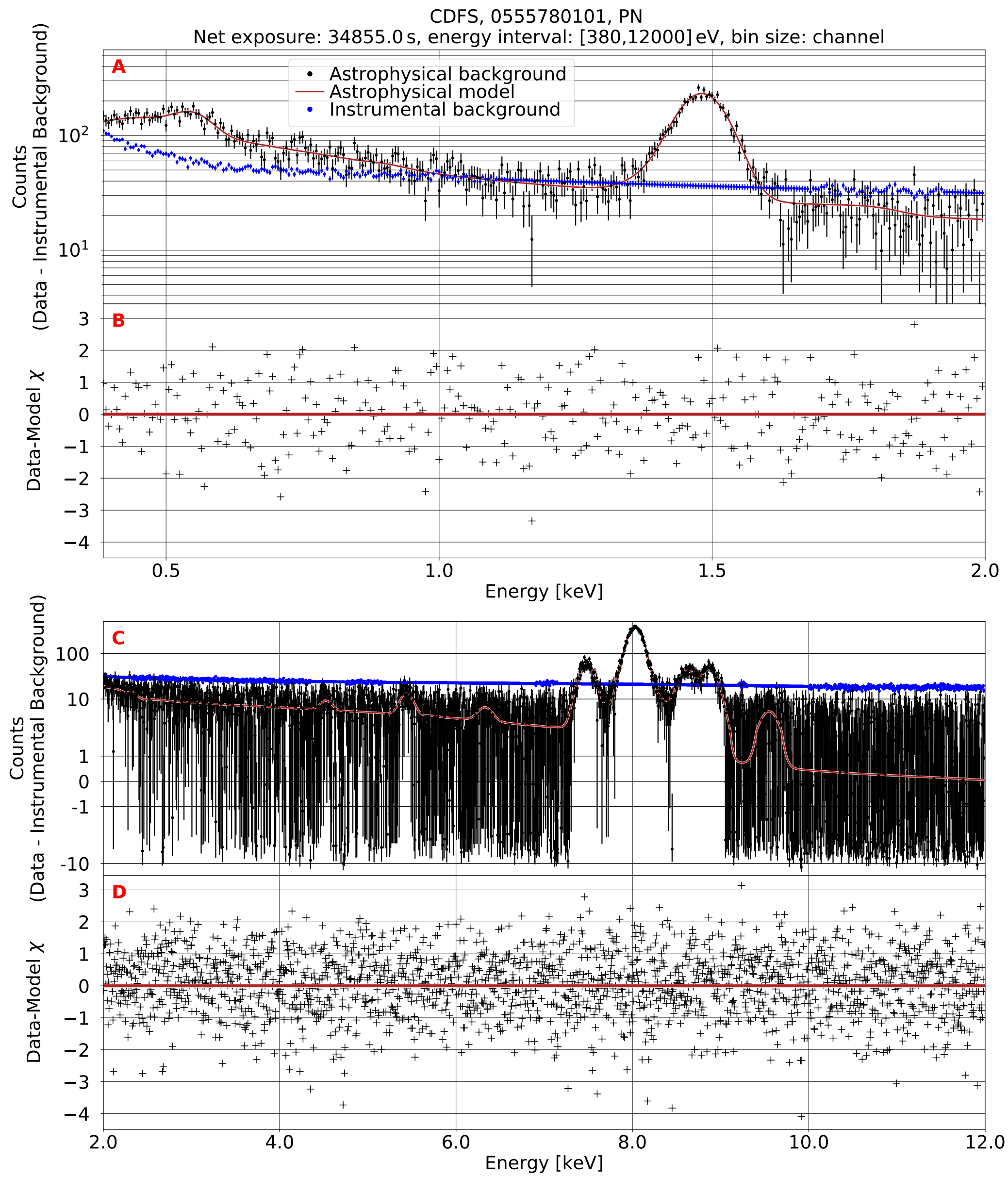

Figure F.53: The panels A and C show the measured spectrum of the data set 0555780101, (i = 22, $\mathbf{D_2}$, table 4.2) as black error bars and its fitted null hypothesis model $m_0^{\mathbf{D_2}}$ in an energy range from 0.38 keV to 2 keV (panels A and B) and from 2 keV to 12 keV (panels C and D) as red lines, respectively, while the blue error bars show the instrumental background model. The best-fit values are specified in tables 5.3 and 5.4. The panels B and D show the residuals per energy bin in values of $\chi = \mathrm{sgn}(\mathrm{Data} - \mathrm{Model})\sqrt{(\mathrm{Data} - \mathrm{Model})^2}$.

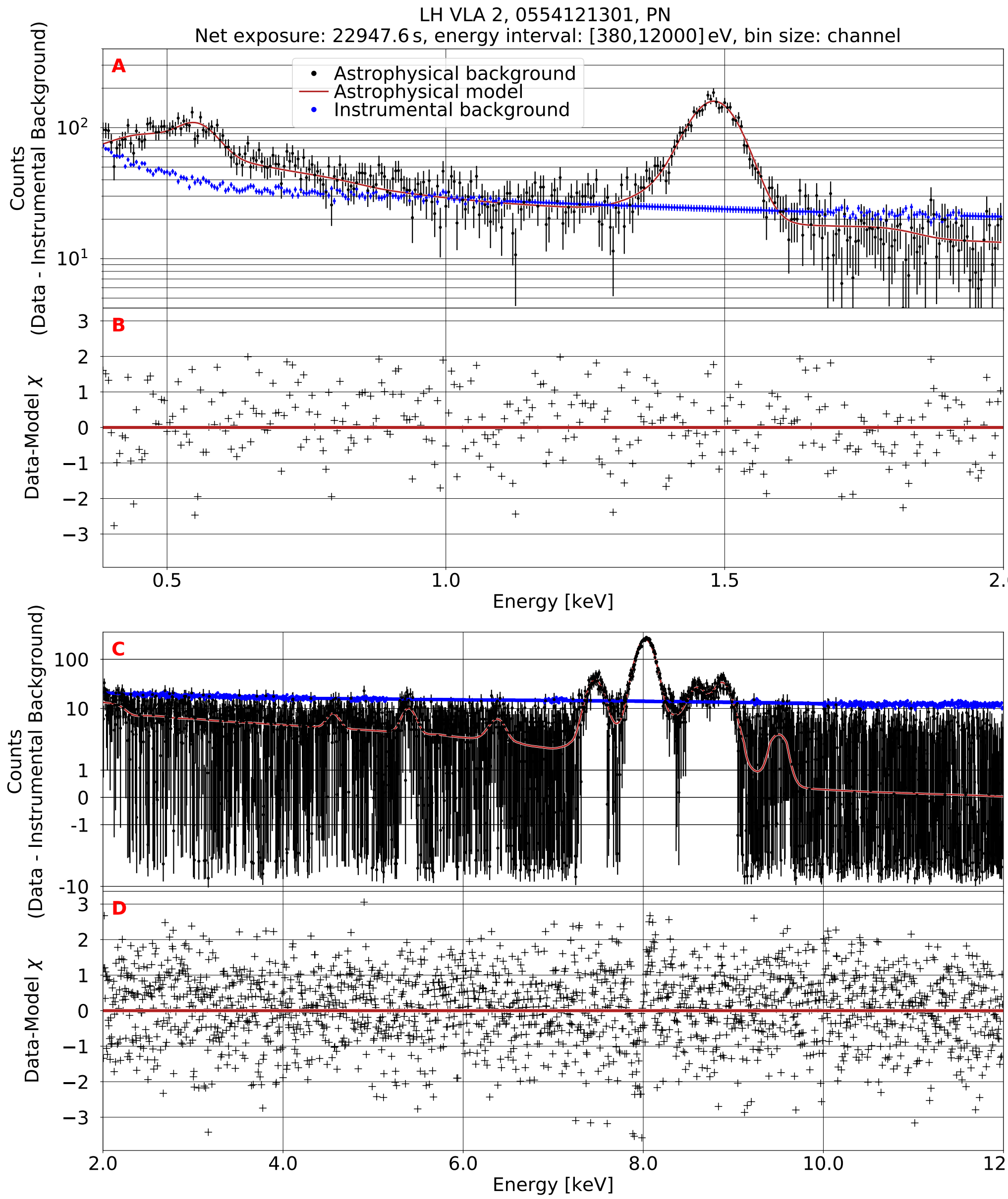

Figure F.54: The panels A and C show the measured spectrum of the data set 0554121301, (i = 23, $\mathbf{D_2}$, table 4.2) as black error bars and its fitted null hypothesis model $m_0^{\mathbf{D_2}}$ in an energy range from 0.38 keV to 2 keV (panels A and B) and from 2 keV to 12 keV (panels C and D) as red lines, respectively, while the blue error bars show the instrumental background model. The best-fit values are specified in tables 5.3 and 5.4. The panels B and D show the residuals per energy bin in values of $\chi = \mathrm{sgn}(\mathrm{Data} - \mathrm{Model})\,\sqrt{(\mathrm{Data} - \mathrm{Model})^2}$.

Chapter Appendices

Bibliography

[1] Röntgen, W. C. 1898, Annalen der Physik, 300, 1

[2] Wood, R. W. 1904, **nat**, 70, 530

[3] Giacconi, R., Gursky, H., Paolini, F. R., & Rossi, B. B. 1962, Physical Review Letters, 9, 439

[4] Giacconi, R., Kellogg, E., Gorenstein, P., Gursky, H., & Tananbaum, H. 1971, **apjl**, 165, L27

[5] Weinberg, S. 2005, The Quantum Theory of Fields, by Steven Weinberg, pp. 512. ISBN 0521670543. Cambridge, UK: Cambridge University Press, May 2005., 512

[6] M. E. Peskin and D. V. Schroeder,

[7] Schmüser, P. 1988, Feynman-Graphen und Eichtheorien für Experimentalphysiker, 295,

[8] K. Zuber, Phys. Rept. **305** (1998) 295 doi:10.1016/S0370-1573(98)00033-7 [hep-ph/9811267].

[9] R. Morrison and D. McCammon, Astrophys. J. **270** (1983) 119.

[10] Rybicki, G. B., & Lightman, A. P. 1986, Radiative Processes in Astrophysics, by George B. Rybicki, Alan P. Lightman, pp. 400. ISBN 0-471-82759-2. Wiley-VCH , June 1986.,

[11] Chandrasekhar, S. 1960, New York: Dover, 1960,

[12] Erickson G. W., 1977, JPCRD, 6, 831

[13] Krause, M. O., & Oliver, J. H. 1979, Journal of Physical and Chemical Reference Data, 8, 329

[14] Johnson W. R., Soff G., 1985, ADNDT, 33, 405

[15] Drake G. W., 1988, CaJPh, 66, 586

[16] Ghez, A. M., Salim, S., Weinberg, N. N., et al. 2008, **apj**, 689, 1044-1062

[17] Gillessen, S., Eisenhauer, F., Trippe, S., et al. 2009, **apj**, 692, 1075

[18] J. F. Navarro, C. S. Frenk and S. D. M. White, Astrophys. J. **462** (1996) 563 [astro-ph/9508025].

[19] A. Klypin, H. Zhao and R. S. Somerville, Astrophys. J. **573** (2002) 597 [astro-ph/0110390].

[20] J. J. Geehan, M. A. Fardal, A. Babul and P. Guhathakurta, Mon. Not. Roy. Astron. Soc. **366** (2006) 996 [astro-ph/0501240].

[21] E. Kerins *et al.* [(POINT-AGAPE) ((1)Theoretical Physics Collaboration], Mon. Not. Roy. Astron. Soc. **323** (2001) 13 [astro-ph/0002256].

[22] I. King, Astron. J. **67** (1962) 471.

[23] Einasto, J., Jaaniste, J., Jôeveer, M., et al. 1974, Tartu Astrofuusika Observatoorium Teated, 48, 3

[24] B. Moore, T. R. Quinn, F. Governato, J. Stadel and G. Lake, Mon. Not. Roy. Astron. Soc. **310** (1999) 1147 [astro-ph/9903164].

[25] J. F. Navarro, E. Hayashi, C. Power, A. Jenkins, C. S. Frenk, S. D. M. White, V. Springel and J. Stadel *et al.*, Mon. Not. Roy. Astron. Soc. **349** (2004) 1039 [astro-ph/0311231].

[26] A. Burkert, IAU Symp. **171** (1996) 175 [Astrophys. J. **447** (1995) L25] [astro-ph/9504041].

[27] K. G. Begeman, A. H. Broeils and R. H. Sanders, Mon. Not. Roy. Astron. Soc. **249** (1991) 523.

[28] Bertone, G., Buchmüller, W., Covi, L., & Ibarra, A. 2007, **jcap**, 11, 003

[29] Boyarsky, A., Neronov, A., Ruchayskiy, O., & Tkachev, I. 2010, Physical Review Letters, 104, 191301

[30] Zwicky, F. 1933, Helvetica Physica Acta, 6, 110

[31] Zwicky, F. 1937, **apj**, 86, 217

[32] Milgrom, M. 1983, **apj**, 270, 365

[33] Bekenstein, J. D. 2004, **prd**, 70, 083509

[34] Jungman, G., Kamionkowski, M., & Griest, K. 1996, **physrep**, 267, 195

[35] P. A. R. Ade *et al.* [Planck Collaboration], arXiv:1502.01589 [astro-ph.CO].

[36] F. Iocco, M. Pato and G. Bertone, Nature Phys. **11** (2015) 245âĂŞ248 doi:10.1038/nphys3237 [arXiv:1502.03821 [astro-ph.GA]].

[37] Y. Sofue and V. Rubin, Ann. Rev. Astron. Astrophys. **39** (2001) 137 doi:10.1146/annurev.astro.39.1.137 [astro-ph/0010594].

[38] Peter, A. H. G. 2012, arXiv:1201.3942

[39] Lumb, D. H, Schartel, N., & Jansen, F. A 2012, arXiv:1202.1651

[40] Jansen, F., Lumb, D., Altieri, B., et al. 2001, aap, 365, L1

[41] L. Struder, U. Briel, K. Dennerl, R. Hartmann, E. Kendziorra, N. Meidinger, E. Pfeffermann and C. Reppin *et al.*, Astron. Astrophys. **365** (2001) L18.

[42] Strüder, L., Bräuninger, H., Meier, M., et al. 1990, Nuclear Instruments and Methods in Physics Research A, 288, 227

[43] Gatti, E., & Rehak, P. 1984, Nuclear Instruments and Methods in Physics Research, 225, 608

[44] Strüder, L., Bräuninger, H., Briel, U., et al. 1997, Review of Scientific Instruments, 68, 4271

[45] Soltau, H., Kemmer, J., Meidinger, N., et al. 2000, Nuclear Instruments and Methods in Physics Research A, 439, 547

[46] Aschenbach, B. 1987, **procspie**, 733, 186

[47] Kendziorra, E., Colli, M., Kuster, M., et al. 1999, **procspie**, 3765, 204

[48] Turner, M. J. L., Abbey, A., Arnaud, M., et al. 2001, **aap**, 365, L27

[49] den Herder, J. W., Brinkman, A. C., Kahn, S. M., et al. 2001, **aap**, 365, L7

[50] Mason, K. O., Breeveld, A., Much, R., et al. 2001, **aap**, 365, L36

[51] Arnaud, K. A. 1996, Astronomical Data Analysis Software and Systems V, 101, 17

[52] Avni, Y. 1976, **apj**, 210, 642

[53] Anders, E., & Ebihara, M. 1982, **gca**, 46, 2363

[54] Kellogg, E., Baldwin, J. R., & Koch, D. 1975, **apj**, 199, 299

[55] Karzas, W. J., & Latter, R. 1961, **apjs**, 6, 167

[56] S. L. Snowden, M. R. Collier and K. D. Kuntz, Astrophys. J. **610** (2004) 1182 [astro-ph/0404354].

[57] H. Ebeling and G. Wiedenmann, Phys. Rev. E **47** (1993) 704. doi:10.1103/PhysRevE.47.704

[58] Weisskopf, M. C., Brinkman, B., Canizares, C., et al. 2002, **pasp**, 114, 1

[59] Schwartz, D. A. 2004, International Journal of Modern Physics D, 13, 1239

[60] Fruscione, A., McDowell, J. C., Allen, G. E., et al. 2006, Proc. SPIE, 6270, 62701V

[61] Bradt H. V. D., Ohashi T., Pounds K. A., 1992, ARA&A, 30, 391

[62] H. Katayama, I. Takahashi, Y. Ikebe, K. Matsushita and M. J. Freyberg, Astron. Astrophys. **414** (2004) 767 doi:10.1051/0004-6361:20031687 [astro-ph/0210135].

[63] F. Haberl, G. Hartner, E. Pfeffermann, E. Kendiziorra, M. Kirsch, D. Lumb, M.J. Freyberg, K. Demerl. The EPIC pn-CCD detector aboard XMM-Newton: Status of the background calibration. *Proc. Symposium 'New Visions of the X-ray Universe in the XMM-Newton and Chandra Era.'*, ESA SP-488, 2001.

[64] K. Dennerl, F. Haberl, G. Hartner, E. Kendziorna, M. Kirsch, M.J. Freyberg, U.G. Briel. The XMM-Newton EPIC PN-camera: Spatial and Temporal Properties of the Internal Background. *Proc. Symposium 'New Visions of the X-ray Universe in the XMM-Newton and Chandra Era.'*, ESA SP-488, 2001.

[65] M.J. Freyberg, U.G. Briel, E. Pfeffermann. The XMM-Newton EPIC PN camera: Spatial distribution of the internal background fluorescence lines. *Proc. Symposium 'New Visions of the X-ray Universe in the XMM-Newton and Chandra Era.'*, ESA SP-488, 2002.

[66] F. Zandanel, C. Weniger and S. Ando, JCAP **1509** (2015) no.09, 060 doi:10.1088/1475-7516/2015/09/060 [arXiv:1505.07829 [astro-ph.CO]].

[67] A. Neronov and D. Malyshev, Phys. Rev. D **93** (2016) no.6, 063518 doi:10.1103/PhysRevD.93.063518 [arXiv:1509.02758 [astro-ph.HE]].

[68] Garmire, G. P., Bautz, M. W., Ford, P. G., Nousek, J. A., & Ricker, G. R., Jr. 2003, **procspie**, 4851, 28

[69] Mitsuda, K., Bautz, M., Inoue, H., et al. 2007, **pasj**, 59, S1

[70] Koyama, K., Tsunemi, H., Dotani, T., et al. 2007, **pasj**, 59, 23

[71] De Luca, A., & Molendi, S. 2004, arXiv:astro-ph/0402233

[72] Kuntz, K. D., & Snowden, S. L. 2008, **aap**, 478, 575

[73] Pugh, E. M., Winslow, G. H., 1966, The Analysis of Physical Measurements, by E. M.Pugh and G. H. Winslow, ASIN: B0006BOAL8. Addison-Wesley , June 1966.,

[74] Bevington, P. R. 1969, New York: McGraw-Hill, 1969.

[75] R. Protassov, D. A. van Dyk, A. Connors, V. L. Kashyap and A. Siemiginowska, astro-ph/0201547.

[76] Mattox, J. R., Bertsch, D. L., Chiang, J., et al. 1996, apj, 461, 396

[77] Denison, D. G. T., & Walden, A. T. 1999, apj, 514, 972

[78] Freeman, P. E., Graziani, C., Lamb, D. Q., et al. 1999, apj, 524, 753

[79] Sofue, Y., Tutui, Y., Honma, M., et al. 1999, **apj**, 523, 136

[80] Betancourt-Martinez, G. L., Beiersdorfer, P., Brown, G. V., et al. 2014, **pra**, 90, 052723

[81] Gu, L., Kaastra, J., Raassen, A. J. J., et al. 2015, **aap**, 584, L11

[82] Shah, C., Dobrodey, S., Bernitt, S., et al. 2016, **apj**, 833, 52

[83] Dolgov, A. D., Hansen, S. H., Raffelt, G., & Semikoz, D. V. 2000, Nuclear Physics B, 580, 331

[84] Dolgov, A. D., Hansen, S. H., Raffelt, G., & Semikoz, D. V. 2000, Nuclear Physics B, 590, 562

[85] Tremaine, S., & Gunn, J. E. 1979, Physical Review Letters, 42, 407

[86] T. Bringmann, F. Calore, G. Vertongen and C. Weniger, Phys. Rev. D **84** (2011) 103525 doi:10.1103/PhysRevD.84.103525 [arXiv:1106.1874 [hep-ph]].

[87] Barbieri, R., & Dolgov, A. 1991, Nuclear Physics B, 349, 743

[88] S. Dodelson and L. M. Widrow, Phys. Rev. Lett. **72** (1994) 17 [hep-ph/9303287].

[89] P. B. Pal and L. Wolfenstein, Phys. Rev. D **25** (1982) 766.

[90] V. D. Barger, R. J. N. Phillips and S. Sarkar, Phys. Lett. B **352** (1995) 365 [Phys. Lett. B **356** (1995) 617] [hep-ph/9503295].

[91] Abazajian, K. N., Acero, M. A., Agarwalla, S. K., et al. 2012, arXiv:1204.5379

[92] Adhikari, R., Agostini, M., Ky, N. A., et al. 2017, **jcap**, 1, 025

[93] Boyarsky, A., Drewes, M., Lasserre, T., Mertens, S., & Ruchayskiy, O. 2018, arXiv:1807.07938

[94] Boyarsky, A., Ruchayskiy, O., Iakubovskyi, D., et al. 2010, **mnras**, 407, 1188

[95] den Herder, J. W., Boyarsky, A., Ruchayskiy, O., et al. 2009, arXiv:0906.1788

[96] Adhikari, R., Agostini, M., Ky, N. A., et al. 2017, **jcap**, 1, 025

[97] P. Arias, D. Cadamuro, M. Goodsell, J. Jaeckel, J. Redondo and A. Ringwald, JCAP **1206** (2012) 013 [arXiv:1201.5902 [hep-ph]].

[98] Lovell, M. R., Frenk, C. S., Eke, V. R., et al. 2014, **mnras**, 439, 300

[99] H. Ishida, K. S. Jeong and F. Takahashi, Phys. Lett. B **732** (2014) 196 [arXiv:1402.5837 [hep-ph]].

[100] K. N. Abazajian, Phys. Rev. Lett. **112** (2014) 161303 [arXiv:1403.0954 [astro-ph.CO]].

[101] S. Baek and H. Okada, arXiv:1403.1710 [hep-ph].

[102] T. Tsuyuki, Phys. Rev. D **90** (2014) 013007 [arXiv:1403.5053 [hep-ph]].

[103] R. Allahverdi, B. Dutta and Y. Gao, Phys. Rev. D **89** (2014) 127305 [arXiv:1403.5717 [hep-ph]].

[104] K. P. Modak, arXiv:1404.3676 [hep-ph].

[105] J. M. Cline, Y. Farzan, Z. Liu, G. D. Moore and W. Xue, Phys. Rev. D **89** (2014) 121302 [arXiv:1404.3729 [hep-ph]].

[106] D. J. Robinson and Y. Tsai, Phys. Rev. D **90** (2014) 045030 [arXiv:1404.7118 [hep-ph]].

[107] A. Abada, G. Arcadi and M. Lucente, arXiv:1406.6556 [hep-ph].

[108] H. Okada and Y. Orikasa, arXiv:1407.2543 [hep-ph].

[109] N. Haba, H. Ishida and R. Takahashi, arXiv:1407.6827 [hep-ph].

[110] D. P. Finkbeiner and N. Weiner, arXiv:1402.6671 [hep-ph].

[111] H. Okada and T. Toma, Phys. Lett. B **737** (2014) 162 [arXiv:1404.4795 [hep-ph]].

[112] T. Higaki, K. S. Jeong and F. Takahashi, Phys. Lett. B **733** (2014) 25 [arXiv:1402.6965 [hep-ph]].

[113] J. Jaeckel, J. Redondo and A. Ringwald, Phys. Rev. D **89** (2014) 103511 [arXiv:1402.7335 [hep-ph]].

[114] H. M. Lee, S. C. Park and W. I. Park, arXiv:1403.0865 [astro-ph.CO].

[115] M. Cicoli, J. P. Conlon, M. C. D. Marsh and M. Rummel, Phys. Rev. D **90** (2014) 023540 [arXiv:1403.2370 [hep-ph]].

[116] J. C. Park, S. C. Park and K. Kong, Phys. Lett. B **733** (2014) 217 [arXiv:1403.1536 [hep-ph]].

[117] K. Y. Choi and O. Seto, Phys. Lett. B **735** (2014) 92 [arXiv:1403.1782 [hep-ph]].

[118] A. G. Dias, A. C. B. Machado, C. C. Nishi, A. Ringwald and P. Vaudrevange, JHEP **1406** (2014) 037 [arXiv:1403.5760 [hep-ph]].

[119] S. P. Liew, JCAP **1405** (2014) 044 [arXiv:1403.6621 [hep-ph], arXiv:1403.6621].

[120] J. P. Conlon and F. V. Day, arXiv:1404.7741 [hep-ph].

[121] N.-E. Bomark and L. Roszkowski, Phys. Rev. D **90** (2014) 011701 [arXiv:1403.6503 [hep-ph]].

[122] S. V. Demidov and D. S. Gorbunov, arXiv:1404.1339 [hep-ph].

[123] K. Nakayama, F. Takahashi and T. T. Yanagida, Phys. Lett. B **735** (2014) 338 [arXiv:1403.1733 [hep-ph]].

[124] C. W. Chiang and T. Yamada, JHEP **1409** (2014) 006 [arXiv:1407.0460 [hep-ph]].

[125] C. Kolda and J. Unwin, Phys. Rev. D **90** (2014) 023535 [arXiv:1403.5580 [hep-ph]].

[126] B. Dutta, I. Gogoladze, R. Khalid and Q. Shafi, arXiv:1407.0863 [hep-ph].

[127] F. S. Queiroz and K. Sinha, Phys. Lett. B **735** (2014) 69 [arXiv:1404.1400 [hep-ph]].

[128] H. M. Lee, arXiv:1404.5446 [hep-ph].

[129] C. Q. Geng, D. Huang and L. H. Tsai, JHEP **1408** (2014) 086 [arXiv:1406.6481 [hep-ph]].

[130] J. M. Cline and A. R. Frey, arXiv:1408.0233 [hep-ph].

[131] R. Krall, M. Reece and T. Roxlo, arXiv:1403.1240 [hep-ph].

[132] M. T. Frandsen, F. Sannino, I. M. Shoemaker and O. Svendsen, JCAP **1405** (2014) 033 [arXiv:1403.1570 [hep-ph]].

[133] E. Dudas, L. Heurtier and Y. Mambrini, Phys. Rev. D **90** (2014) 035002 [arXiv:1404.1927 [hep-ph]].

[134] S. Baek, P. Ko and W. I. Park, arXiv:1405.3730 [hep-ph].

[135] J. Franse *et al.*, arXiv:1604.01759 [astro-ph.CO].

[136] Peccei, R. D., & Quinn, H. R. 1977, Physical Review Letters, 38, 1440

[137] Peccei, R. D., & Quinn, H. R. 1977, **prd**, 16, 1791

[138] S. Weinberg, Phys. Rev. Lett. **40** (1978) 223. doi:10.1103/PhysRevLett.40.223

[139] F. Wilczek, Phys. Rev. Lett. **40** (1978) 279. doi:10.1103/PhysRevLett.40.279

[140] H. Georgi, D. B. Kaplan and L. Randall, Phys. Lett. **169B** (1986) 73. doi:10.1016/0370-2693(86)90688-X

[141] Ringwald, A. 2012, Physics of the Dark Universe, 1, 116

[142] Koyama, K., Hyodo, Y., Inui, T., et al. 2007, **pasj**, 59, 245

[143] Prokhorov, D., & Silk, J. 2010, **apjl**, 725, L131

[144] Koyama, K., Kataoka, J., Nobukawa, M., et al. 2014, arXiv:1412.1170

[145] Boyarsky, A., Franse, J., Iakubovskyi, D., & Ruchayskiy, O. 2015, Physical Review Letters, 115, 161301

[146] O. Ruchayskiy, A. Boyarsky, D. Iakubovskyi, E. Bulbul, D. Eckert, J. Franse, D. Malyshev, M. Markevitch, A. Neronov, Monthly Notices of the Royal Astronomical Society **460** (2) (2016): 1390-1398.

[147] A. Boyarsky, J. Franse, D. Iakubovskyi and O. Ruchayskiy, arXiv:1408.4388 [astro-ph.CO].

[148] T. E. Jeltema and S. Profumo, arXiv:1408.1699 [astro-ph.HE].

[149] D. Malyshev, A. Neronov and D. Eckert, arXiv:1408.3531 [astro-ph.HE].

[150] M. E. Anderson, E. Churazov and J. N. Bregman, arXiv:1408.4115 [astro-ph.HE].

[151] A. Boyarsky, J. Franse, D. Iakubovskyi and O. Ruchayskiy, arXiv:1408.2503 [astro-ph.CO].

[152] S. Riemer-Sorensen, arXiv:1405.7943 [astro-ph.CO].

[153] A. Boyarsky, O. Ruchayskiy, D. Iakubovskyi and J. Franse, Phys. Rev. Lett. **113** (2014) 251301 doi:10.1103/PhysRevLett.113.251301 [arXiv:1402.4119 [astro-ph.CO]].

[154] E. Bulbul, M. Markevitch, A. Foster, R. K. Smith, M. Loewenstein and S. W. Randall, Astrophys. J. **789** (2014) 13 [arXiv:1402.2301 [astro-ph.CO]].

[155] Cappelluti, N., Bulbul, E., Foster, A., et al. 2018, **apj**, 854, 179

[156] Riemer-Sørensen, S., Wik, D., Madejski, G., et al. 2015, **apj**, 810, 48

[157] Figueroa-Feliciano, E., Anderson, A. J., Castro, D., et al. 2015, **apj**, 814, 82

[158] Sekiya, N., Yamasaki, N. Y., & Mitsuda, K. 2016, **pasj**, 68, S31

[159] Tamura, T., Iizuka, R., Maeda, Y., Mitsuda, K., & Yamasaki, N. Y. 2015, **pasj**, 67, 23

[160] Perez, K., Ng, K. C. Y., Beacom, J. F., et al. 2017, **prd**, 95, 123002

[161] Neronov, A., Malyshev, D., & Eckert, D. 2016, **prd**, 94, 123504

[162] Ruchayskiy, O., Boyarsky, A., Iakubovskyi, D., et al. 2016, **mnras**, 460, 1390

[163] Iakubovskyi, D., Bulbul, E., Foster, A. R., Savchenko, D., & Sadova, V. 2015, arXiv:1508.05186

[164] Urban, O., Werner, N., Allen, S. W., et al. 2015, **mnras**, 451, 2447

[165] S. Horiuchi, P. J. Humphrey, J. Onorbe, K. N. Abazajian, M. Kaplinghat and S. Garrison-Kimmel, Phys. Rev. D **89** (2014) 025017 [arXiv:1311.0282 [astro-ph.CO]].

[166] R. Essig, E. Kuflik, S. D. McDermott, T. Volansky and K. M. Zurek, JHEP **1311** (2013) 193 [arXiv:1309.4091 [hep-ph]].

[167] E. Borriello, M. Paolillo, G. Miele, G. Longo and R. Owen, Mon. Not. Roy. Astron. Soc. **425** (2012) 1628 [arXiv:1109.5943 [astro-ph.GA]].

[168] C. R. Watson, Z. Y. Li and N. K. Polley, JCAP **1203** (2012) 018 [arXiv:1111.4217 [astro-ph.CO]].

[169] A. Boyarsky, D. Iakubovskyi, O. Ruchayskiy and V. Savchenko, Mon. Not. Roy. Astron. Soc. **387** (2008) 1361 [arXiv:0709.2301 [astro-ph]].

[170] A. Boyarsky, O. Ruchayskiy and M. Markevitch, Astrophys. J. **673** (2008) 752 [astro-ph/0611168].

[171] A. Boyarsky, J. Nevalainen and O. Ruchayskiy, Astron. Astrophys. **471** (2007) 51 [astro-ph/0610961].

[172] C. R. Watson, J. F. Beacom, H. Yuksel and T. P. Walker, Phys. Rev. D **74** (2006) 033009 [astro-ph/0605424].

[173] A. Boyarsky, A. Neronov, O. Ruchayskiy and M. Shaposhnikov, Mon. Not. Roy. Astron. Soc. **370** (2006) 213 [astro-ph/0512509].

[174] F. A. Aharonian *et al.* [Hitomi Collaboration], arXiv:1607.07420 [astro-ph.HE].

[175] C. Shah, S. Dobrodey, S. Bernitt, R. SteinbrÃijgge, J. R. C. LÃşpez-Urrutia, L. Gu and J. Kaastra, arXiv:1608.04751 [astro-ph.HE].

[176] A. Boyarsky, A. Neronov, O. Ruchayskiy, M. Shaposhnikov and I. Tkachev, Phys. Rev. Lett. **97** (2006) 261302 doi:10.1103/PhysRevLett.97.261302 [astro-ph/0603660].

[177] K. Abazajian, G. M. Fuller and W. H. Tucker, Astrophys. J. **562** (2001) 593 doi:10.1086/323867 [astro-ph/0106002].

[178] A. D. Dolgov and S. H. Hansen, Astropart. Phys. **16** (2002) 339 doi:10.1016/S0927-6505(01)00115-3 [hep-ph/0009083].

[179] K. Abazajian and S. M. Koushiappas, Phys. Rev. D **74** (2006) 023527 doi:10.1103/PhysRevD.74.023527 [astro-ph/0605271].

[180] K. N. Abazajian, M. Markevitch, S. M. Koushiappas and R. C. Hickox, Phys. Rev. D **75** (2007) 063511 doi:10.1103/PhysRevD.75.063511 [astro-ph/0611144].

[181] S. Riemer-Sorensen, S. H. Hansen and K. Pedersen, Astrophys. J. **644** (2006) L33 doi:10.1086/505330 [astro-ph/0603661].

[182] A. Boyarsky, D. Malyshev, A. Neronov and O. Ruchayskiy, Mon. Not. Roy. Astron. Soc. **387** (2008) 1345 doi:10.1111/j.1365-2966.2008.13003.x [arXiv:0710.4922 [astro-ph]].

[183] M. Loewenstein, A. Kusenko and P. L. Biermann, Astrophys. J. **700** (2009) 426 doi:10.1088/0004-637X/700/1/426 [arXiv:0812.2710 [astro-ph]].

[184] M. Loewenstein and A. Kusenko, Astrophys. J. **714** (2010) 652 doi:10.1088/0004-637X/714/1/652 [arXiv:0912.0552 [astro-ph.HE]].

[185] A. Boyarsky, A. Neronov, O. Ruchayskiy and M. Shaposhnikov, JETP Lett. **83** (2006) 133 doi:10.1134/S0021364006040011 [hep-ph/0601098].

[186] A. Boyarsky, A. Neronov, O. Ruchayskiy and M. Shaposhnikov, Phys. Rev. D **74** (2006) 103506 doi:10.1103/PhysRevD.74.103506 [astro-ph/0603368].

[187] S. Riemer-Sorensen, S. H. Hansen, 2009, [arXiv:0901.2569]

[188] N. Mirabal and D. Nieto, arXiv:1003.3745 [astro-ph.CO].

[189] N. Mirabal, Mon. Not. Roy. Astron. Soc. **409** (2010) 128 doi:10.1111/j.1745-3933.2010.00963.x [arXiv:1010.4706 [astro-ph.HE]].

[190] M. Loewenstein and A. Kusenko, Astrophys. J. **751** (2012) 82 doi:10.1088/0004-637X/751/2/82 [arXiv:1203.5229 [astro-ph.CO]].

[191] S. Riemer-Sorensen, K. Pedersen, S. H. Hansen and H. Dahle, Phys. Rev. D **76** (2007) 043524 doi:10.1103/PhysRevD.76.043524 [astro-ph/0610034].

[192] H. Yuksel, J. F. Beacom and C. R. Watson, Phys. Rev. Lett. **101** (2008) 121301 doi:10.1103/PhysRevLett.101.121301 [arXiv:0706.4084 [astro-ph]].

[193] A. Boyarsky, J. W. den Herder, A. Neronov and O. Ruchayskiy, Astropart. Phys. **28** (2007) 303 doi:10.1016/j.astropartphys.2007.06.003 [astro-ph/0612219].

[194] E. Borriello, M. Paolillo, G. Miele, G. Longo, R. Owen, Monthly Notices of the Royal Astronomical Society **425** (2012): 1628.

[195] D. Iakubovskyi, "Constraining properties of dark matter particles using astrophysical data, PhD thesis, Leiden University, 2013."

[196] K. C. Y. Ng, S. Horiuchi, J. M. Gaskins, M. Smith and R. Preece, Phys. Rev. D **92** (2015) no.4, 043503 doi:10.1103/PhysRevD.92.043503 [arXiv:1504.04027 [astro-ph.CO]].

[197] Conlon, J. P., Day, F., Jennings, N., Krippendorf, S., & Rummel, M. 2017, **prd**, 96, 123009

[198] Berg, M., Conlon, J. P., Day, F., et al. 2017, **apj**, 847, 101

[199] Gewering-Peine, A., Horns, D., & Schmitt, J. H. M. M. 2017, **jcap**, 6, 036

Acknowledgements/Danksagung

Ich möchte mich bei Prof. Dr. Dieter Horns und Prof. Dr. Jürgen H. M. M. Schmitt für die Ermöglichung und die Betreuung der vorliegenden Arbeit bedanken, insbesondere auch in Hinblick auf die Herausforderungen, welche in den letzten Jahren durch die räumliche Distanz zwischen uns entstanden sind.
Insbesondere habe ich Dr. Michael Freyberg dafür zu danken, dass er sich nicht nur bereit erklärte, als Gutachter meiner Disputation zu fungieren, sondern diesbezüglich auch die beschwerliche Reise in den hohen Norden absolvierte.
Weiter gilt mein ganz besonderer Dank Prof. Dr. Peter E. Toschek, welcher mir in zahlreichen Gesprächen nicht nur sein eigenes Forschungsfeld sondern auch das Wesen der Wissenschaft an sich näher brachte und mich diesbezüglich an seinem unermesslichen Erfahrungsschatz teilhaben ließ.
Großer Dank gilt meinen ehemaligen und noch bestehenden Mitstreitern, Kollegen und/oder Freunden der Arbeitsgruppe von Prof. Dr. Dieter Horns für die spannenden und tiefgehenden Diskussionen, welche jedoch auch hin und wieder von rein fachlichen Themen abwichen. Insbesondere bedanke ich mich hier bei Dr. Max Kastendieck, Dr. Milton Virgílio Fernandes, Dr. Franziska Spies (geb. Laatz) und Dr. Andreas Spies, Dr. Eike von Seggern, Dr. Hannes-Sebastian Zechlin, Dr. Tanja Kneiske, Dr. Björn Opitz, Attila Abramowski, Alicia Hirt, Moritz Habermehl, Dr. Noëmie Bastidon, Dr. Manuel Meyer, Dr. Sergey Epimakhov, Dr. Ngoc-Lan Nelly Nguyen, Marco Prüser, Dr. Jan Dreyling-Eschweiler, Dr. Andrei Lobanov, Dr. Daniel Hampf, Dr. Martin Tlucykont und Dr. Martin Raue.
Ganz besonders habe ich Dr. Michael Cursio zu danken, welcher mir als Philosoph nicht nur erkenntnistheoretische Fragestellungen nahelegte und diese erörterte.
Auch habe ich Rainer-Peter Feller und Ronald Mohrmann für Ihre Unterstützung und vor allem Geduld in allen Fragen zur IT und darüber hinaus zu danken.
Ohne die Unterstützung und die Ermunterungen von Seiten meiner Familie, insbesondere meiner Mutter und meinem Vater sowie meinen Brüdern Johannes und Thomas, hätte diese Arbeit wohl nicht entstehen können. Ich danke Maria Alessandra Kenner zutiefst für Ihre Unterstützung und ihren Beistand. Weiter

danke ich meinen Freunden für die Zuversicht und die positiven Perspektiven, welche sie mir in Hinblick auf die vorliegende Arbeit mit unendlicher Geduld immer wieder nahegelegten, insbesondere Dr. Matthias Scholz, Maria Müller, Sophia Zeeden, Dr. Franziska Schubert, Maren Bergmann, Liene Rieksta, Julia Ladu, Dr. Klaus Geyer, Anne C. Spies, Dr. Oliver Welzel, Dr. Karina Rojas und Stevan Veljovic.

I am thankful that this work was supported by the Deutsche Forschungsgemeinschaft (DFG) through the Sonderforschungsbereich SFB 676 TP C2 "Particles, Strings, and the Early Universe" over the first four years. Moreover, I have to thank Mr. Jürgen Raeke and Mr. Norbert Zinsinger as my respective former and current employers for their understanding of my wish to finish the present work.

I thank Keith Arnaud and Craig Gordon and the SAS-team, especially Ignacio de la Calle, for many fruitful discussions related to XSPEC and the SAS software, respectively.

Declaration/Erklärung

Hiermit erkläre ich, Alexander Gewering-Peine, an Eides statt, dass ich die vorliegende Dissertationsschrift selbst verfasst habe und keine anderen als die angegebenen Quellen und Hilfsmittel benutzt habe.

Alexander Gewering-Peine